



ORNL/TM-10308

**OAK RIDGE  
NATIONAL  
LABORATORY**

**MARTIN MARIETTA**

**Ceramic Technology for  
Advanced Heat Engines Project  
Semiannual Progress Report for  
April Through September 1986**

Prepared for  
U.S. Department of Energy  
Assistant Secretary for Conservation and Renewable Energy  
Office of Transportation Systems  
Advanced Materials Development Program

**DISTRIBUTION STATEMENT A**  
Approved for Public Release  
Distribution Unlimited

**20070828059**

OPERATED BY  
MARTIN MARIETTA ENERGY SYSTEMS, INC.  
FOR THE UNITED STATES  
DEPARTMENT OF ENERGY



SEP 10 1990

505760

CLAS

Printed in the United States of America. Available from  
National Technical Information Service  
U.S. Department of Commerce  
5285 Port Royal Road, Springfield, Virginia 22161  
NTIS price codes—Printed Copy: A16 Microfiche A01

This report was prepared as an account of work sponsored by an agency of the United States Government. Neither the United States Government nor any agency thereof, nor any of their employees, makes any warranty, express or implied, or assumes any legal liability or responsibility for the accuracy, completeness, or usefulness of any information, apparatus, product, or process disclosed, or represents that its use would not infringe privately owned rights. Reference herein to any specific commercial product, process, or service by trade name, trademark, manufacturer, or otherwise, does not necessarily constitute or imply its endorsement, recommendation, or favoring by the United States Government or any agency thereof. The views and opinions of authors expressed herein do not necessarily state or reflect those of the United States Government or any agency thereof.



METALS AND CERAMICS DIVISION

CERAMIC TECHNOLOGY FOR ADVANCED HEAT ENGINES PROJECT  
SEMIANNUAL PROGRESS REPORT FOR  
APRIL THROUGH SEPTEMBER 1986

D. R. Johnson  
Project Manager

Date Published: March 1987

NOTICE: This document contains information of a preliminary nature. It is subject to revision or correction and therefore does not represent a final report.

Prepared for  
U.S. Department of Energy  
Assistant Secretary for Conservation and Renewable Energy  
Office of Transportation Systems  
Advanced Materials Development Program

Prepared by the  
OAK RIDGE NATIONAL LABORATORY  
Oak Ridge, Tennessee 37831  
operated by  
MARTIN MARIETTA ENERGY SYSTEMS, INC.  
for the  
U.S. DEPARTMENT OF ENERGY  
under Contract DE-AC05-84OR21400

## REPORTS PREVIOUSLY ISSUED

ORNL/TM-9325	Period March 1983-September 1983
ORNL/TM-9466	Period October 1983-March 1984
ORNL/TM-9497	Period April 1984-September 1984
ORNL/TM-9673	Period October 1984-March 1985
ORNL/TM-9947	Period April 1985-September 1985
ORNL/TM-10079	Period October 1985-March 1986

## CONTENTS

SUMMARY . . . . .	1
0.0 PROJECT MANAGEMENT AND COORDINATION . . . . .	3
1.0 MATERIALS AND PROCESSING . . . . .	5
INTRODUCTION . . . . .	5
1.1 MONOLITHICS . . . . .	7
1.1.1 Silicon Carbide . . . . .	7
<i>Synthesis of High-Purity Sinterable Silicon Carbide Powders (SOHIO)</i> . . . . .	7
1.1.2 Silicon Nitride . . . . .	20
<i>Sintering of Silicon Nitride (AMTL)</i> . . . . .	20
<i>Synthesis of High Purity Sinterable <math>Si_3N_4</math> Powders (Ford)</i> . . . . .	26
1.2 CERAMIC COMPOSITES . . . . .	35
1.2.2 Silicon Nitride Matrix . . . . .	35
<i>Transformation-Toughened Silicon Nitride (Rocketdyne)</i> . . . . .	35
<i>Silicon-Nitride-Metal Carbide Composites (GTE)</i> . . . . .	44
<i>SiC-Whisker-Toughened Silicon Nitride (AiResearch)</i> . . . . .	54
1.2.3 Oxide Matrix . . . . .	74
<i>Dispersion-Toughened Oxide Composites (ORNL)</i> . . . . .	74
<i>Sol-Gel Oxide Powder (ORNL)</i> . . . . .	77
<i>Processing of Improved Transformation-Toughened Ceramics (Norton)</i> . . . . .	80
<i>Advanced Transformation-Toughened Oxides (University of Michigan)</i> . . . . .	105
<i>Processing and Characterization of Transformation-Toughened Ceramics With Strength Retention to Elevated Temperatures (Ceramatec)</i> . . . . .	107
<i>Injection Molded Composites (ORNL)</i> . . . . .	122
1.2.4 Silicate Matrix . . . . .	127
<i>Mullite-SiC Whisker Composites (GE)</i> . . . . .	127
<i>Low Expansion Ceramics for Diesel Engine Applications (VPI&amp;SU)</i> . . . . .	138
1.4 JOINING . . . . .	171
1.4.1 Ceramic-Metal Joints . . . . .	171
<i>Joining Ceramics for Heat Engine Applications (ORNL)</i> . . . . .	171



2.0 MATERIALS DESIGN METHODOLOGY . . . . .	177
INTRODUCTION . . . . .	177
2.2 CONTACT INTERFACES . . . . .	179
2.2.2 Dynamic Interfaces . . . . .	179
<i>Studies of Dynamic Contact of Ceramics and     Alloys for Advanced Heat Engines (Battelle)</i> . . . .	179
2.3 NEW CONCEPTS . . . . .	189
<i>Advanced Statistics (ORNL)</i> . . . . .	189
<i>Advanced Statistical Concepts of Fracture in     Brittle Materials (GE)</i> . . . . .	190
3.0 DATA BASE AND LIFE PREDICTION . . . . .	199
INTRODUCTION . . . . .	199
3.1 STRUCTURAL QUALIFICATION . . . . .	200
<i>Microstructural Analysis of Corrosive Reactions     in Structural Ceramics (NBS)</i> . . . . .	200
<i>Physical Properties of Structural Ceramics (ORNL)</i> .	201
<i>Effect of Translucence of Engineering Ceramics on     Heat Transfer in Diesel Engines (ITI)</i> . . . . .	205
3.2 TIME-DEPENDENT BEHAVIOR . . . . .	216
<i>Characterization of Transformation-Toughened     Ceramics (AMTL)</i> . . . . .	216
<i>Fracture Behavior of Toughened Ceramics (ORNL)</i> . .	222
<i>Cyclic Fatigue of Toughened Ceramics (ORNL)</i> . . . .	226
3.3 ENVIRONMENTAL EFFECTS . . . . .	229
<i>Static Behavior of Toughened Ceramics     (U. of Illinois)</i> . . . . .	229
<i>Environmental Effects in Toughened Ceramics     (U. of Dayton)</i> . . . . .	251
3.4 FRACTURE MECHANICS . . . . .	290
<i>Improved Methods for Measuring the Fracture     Resistance of Structural Ceramics     (U. of Washington)</i> . . . . .	290
<i>Testing and Evaluation of Advanced Ceramics at High     Temperature in Uniaxial Tension (North Carolina A&amp;T     University)</i> . . . . .	296
<i>Standard Tensile Test Development (NBS)</i> . . . . .	301

3.5	NONDESTRUCTIVE EVALUATION DEVELOPMENT . . . . .	309
	<i>Nondestructive Characterization</i> (ORNL) . . . . .	309
	<i>Computed Tomography</i> (ANL) . . . . .	316
	<i>Methodology for Intelligent Processing of</i> <i>Reliable Engineering Ceramics</i> (AMTL) . . . . .	324
4.0	TECHNOLOGY TRANSFER (ORNL) . . . . .	331
	<i>Technology Transfer</i> (ORNL) . . . . .	331
	<i>IEA Annex II specimens and Support</i> (ORNL) . . . . .	332
	<i>Standard Reference Materials</i> (NBS) . . . . .	334

CERAMIC TECHNOLOGY FOR ADVANCED HEAT ENGINES PROJECT SEMIANNUAL  
PROGRESS REPORT FOR APRIL THROUGH SEPTEMBER 1986

SUMMARY

The Ceramic Technology For Advanced Heat Engines Project was developed by the Department of Energy's Office of Transportation Systems (OTS) in Conservation and Renewable Energy. This project, part of the OTS's Advanced Materials Development Program, was developed to meet the ceramic technology requirements of the OTS's automotive technology programs.

Significant accomplishments in fabricating ceramic components for the Department of Energy (DOE), National Aeronautics and Space Administration (NASA), and Department of Defense (DOD) advanced heat engine programs have provided evidence that the operation of ceramic parts in high-temperature engine environments is feasible. However, these programs have also demonstrated that additional research is needed in materials and processing development, design methodology, and data base and life prediction before industry will have a sufficient technology base from which to produce reliable cost-effective ceramic engine components commercially.

An assessment of needs was completed, and a five-year project plan was developed with extensive input from private industry. The objective of the project is to develop the industrial technology base required for reliable ceramics for application in advanced automotive heat engines. The project approach includes determining the mechanisms controlling reliability, improving processes for fabricating existing ceramics, developing new materials with increased reliability, and testing these materials in simulated engine environments to confirm reliability. Although this is a generic materials project, the focus is on structural ceramics for advanced gas turbine and diesel engines, ceramic bearings and attachments, and ceramic coatings for thermal barrier and wear applications in these engines. This advanced materials technology is being developed in parallel and close coordination with the ongoing DOE and industry proof-of-concept engine development programs. To facilitate the rapid transfer of this technology to U.S. industry, the major portion of the work is being done in the ceramic industry, with technological support from government laboratories, other industrial laboratories, and universities.

This project is managed by ORNL for the Office of Transportation Systems, Heat Engine Propulsion Division, and is closely coordinated with complementary ceramics tasks funded by other DOE offices, NASA, DOD, and industry. A joint DOE and NASA technical plan has been established, with DOE focus on automotive applications and NASA focus on aerospace applications. A common work breakdown structure (WBS) was developed to facilitate coordination. The work described in this report is organized according to the following WBS project elements:



## 0.0 Management and Coordination

## 1.0 Materials and Processing

- 1.1 Monolithics
- 1.2 Ceramic Composites
- 1.3 Thermal and Wear Coatings
- 1.4 Joining

## 2.0 Materials Design Methodology

- 2.1 Modeling
- 2.2 Contact Interfaces
- 2.3 New Concepts

## 3.0 Data Base and Life Prediction

- 3.1 Structural Qualification
- 3.2 Time-Dependent Behavior
- 3.3 Environmental Effects
- 3.4 Fracture Mechanics
- 3.5 NDE Development

## 4.0 Technology Transfer

This report includes contributions from all currently active project participants. The contributions are arranged according to the work breakdown structure outline.

## 0.0 PROJECT MANAGEMENT AND COORDINATION

D. R. Johnson  
Oak Ridge National Laboratory

This task includes the technical management of the project in accordance with the project plans and management plan approved by the Department of Energy (DOE) Oak Ridge Operations Office (ORO) and the Office of Transportation Systems. This task includes preparation of annual field task proposals, initiation and management of subcontracts and interagency agreements, and management of ORNL technical tasks. Monthly management reports and bimonthly reports are provided to DOE; highlights and semi-annual technical reports are provided to DOE and program participants. In addition, the program is coordinated with interfacing programs sponsored by other DOE offices and federal agencies, including the National Aeronautics and Space Administration (NASA) and the Department of Defense (DOD). This coordination is accomplished by participation in bimonthly DOE and NASA joint management meetings, annual interagency heat engine ceramics coordination meetings, DOE contractor coordination meetings, and DOE Energy Materials Coordinating Committee (EMaCC) meetings, as well as special coordination meetings.

## 1.0 MATERIALS AND PROCESSING

### INTRODUCTION

This portion of the project is identified as project element 1.0 within the work breakdown structure (WBS). It contains four subelements: (1) Monolithics, (2) Ceramic Composites, (3) Thermal and Wear Coatings, and (4) Joining. Ceramic research conducted within the Monolithics subelement currently includes work activities on green state ceramic fabrication, characterization, and densification and on structural, mechanical, and physical properties of these ceramics. Research conducted within the Ceramic Composites subelement currently includes silicon carbide and oxide-based composites, which, in addition to the work activities cited for Monolithics, include fiber synthesis and characterization. Research conducted in the Thermal and Wear Coatings subelement is currently limited to oxide-base coatings and involves coating synthesis, characterization, and determination of the mechanical and physical properties of the coatings. Research conducted in the Joining subelement currently includes studies of processes to produce strong stable joints between zirconia ceramics and iron-base alloys.

A major objective of the research in the Materials and Processing project element is to systematically advance the understanding of the relationships between ceramic raw materials such as powders and reactant gases, the processing variables involved in producing the ceramic materials, and the resultant microstructures and physical and mechanical properties of the ceramic materials. Success in meeting this objective will provide U.S. companies with new or improved ways for producing economical highly reliable ceramic components for advanced heat engines.



## 1.1 MONOLITHICS

### 1.1.1 Silicon Carbide

#### Synthesis of High-Purity Sinterable Silicon Carbide Powders

J. M. Halstead, V. Venkateswaran [SOHIO Engineered Materials Company (Carborundum)] and B. L. Mehosky (SOHIO Research and Development)

#### Objective/Scope

The objective of this program is to develop a volume scaleable process to produce high purity, high surface area sinterable silicon carbide powder.

The program is organized in two phases. Phase I includes the following elements:

- . Verify the technical feasibility of the gas phase synthesis route.
- . Identify the best silicon feedstock on the basis of performance and cost.
- . Optimize the production process at the bench scale.
- . Fully characterize the powders produced and compare with commercially available alternatives.
- . Develop a theoretical model to assist in understanding the synthesis process, optimization of operating conditions and scale-up.

Phase II, which was authorized during the period, will scale the process to 5 - 10 times the bench scale quantities in order to perform confirmatory experiments, produce process flowsheets and to perform economic analysis.

#### Technical Highlights

##### Background - The Gas Phase Synthesis Route

Given the objective of producing a submicron silicon carbide powder purer and with more controllable properties than could be produced via the Acheson process, Standard Oil-Carborundum evaluated three candidate process routes:

- 1) Sol-Gel
- 2) Polymer Pyrolysis
- 3) Gas Phase Reactions

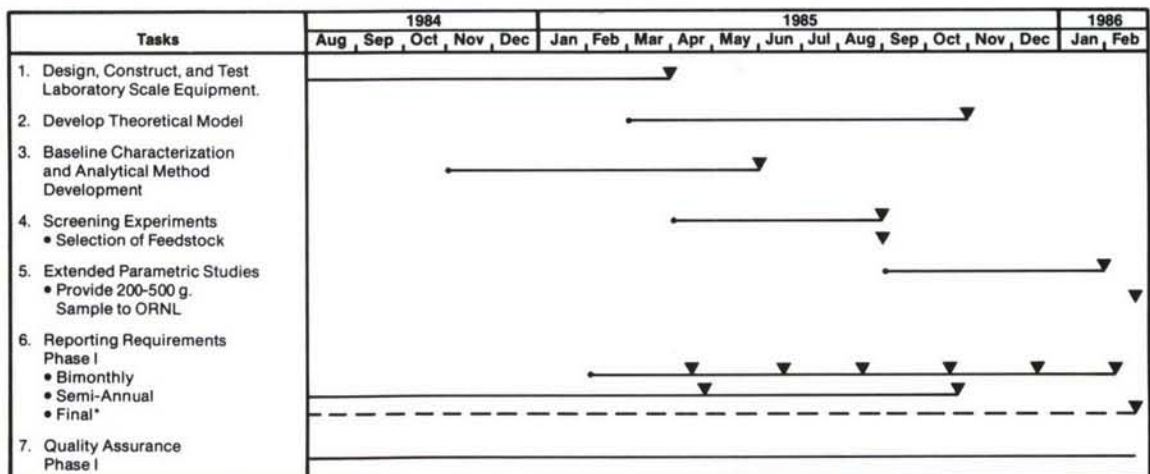
A gas phase route utilizing plasma heating was chosen as having the most proven technology, the highest product yield and good scaleability potential.

Further, Carborundum had previously sponsored proprietary research in gas phase synthesis and had demonstrated the feasibility of the approach.

<sup>1</sup> Research sponsored by the Advanced Materials Development Program, Office of Transportation Systems, U.S. Department of Energy under Contract DE-AC05-84OR21400 with Martin Marietta Energy Systems, Inc.

## Workplan

A breakdown of major tasks and milestones is shown in Figure 1. Subtasks have been developed for Task 4 - Screening Experiments and will be developed for Task 5 - Extended Parametric Studies.



\*Only required if decision is made not to go on to Phase II.

Figure 1. Milestone Chart

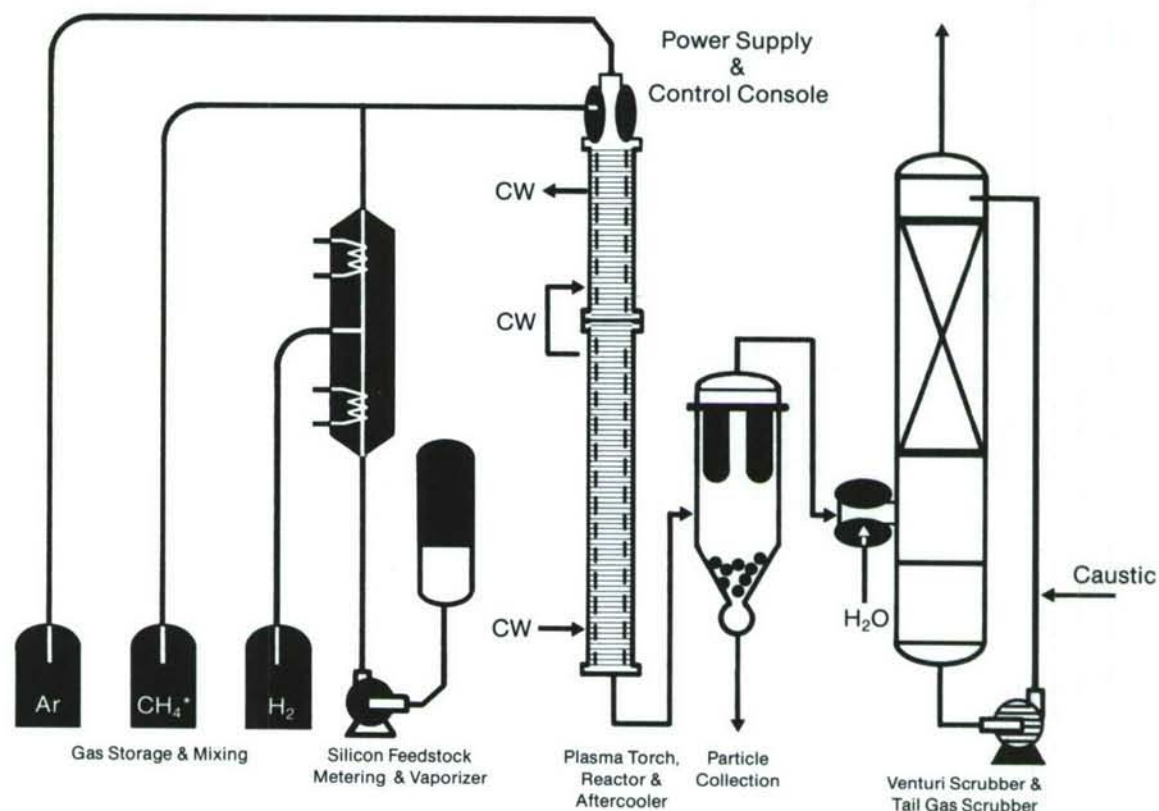
ORNL granted a no-cost extension of Phase I thru June 30, 1986.

### Task 1. Design, Construct and Test Laboratory Scale Equipment

The Standard Oil Research and Development Center at Warrensville, Ohio was chosen as the site for the laboratory scale gas phase synthesis system due to the ready availability of applicable engineering and technical resources. The proximity to other related research which is being performed by Standard Oil on behalf of Standard Oil-Carborundum's structural ceramics effort was also a factor.

The design phase involved a complete review of the preliminary conceptual design and specifying appropriate subsystems in order to evaluate and control critical process parameters.

The conceptual design is shown in figure 1, a photographic overview is shown in figure 2.



\*Optional depending  
on Silicon Feedstock

Figure 2. Conceptual Design and Simplified Process Flow Chart

### Plasma Torch Subsystem

The heart of the system is the plasma torch. This was obtained from Plasma Materials, Inc. with whom Standard Oil-Carborundum has previously worked. The torch system is rated at 50KW. This is significantly higher than required for this application, but the unit has excellent turn-down capability and will be sufficient for future scale-up. It is installed atop the reactor vessel which is constructed of copper and wrapped with copper tubing through which the cooling water flows. Thermocouples are installed along the entire length of the reactor.

The DC power supply has a 75KW effective rating. A simple thimble type collector with an isolation valve is affixed to the lower end of the reactor. Alternative powder collection techniques will be evaluated in preparation for Phase II scale-up.



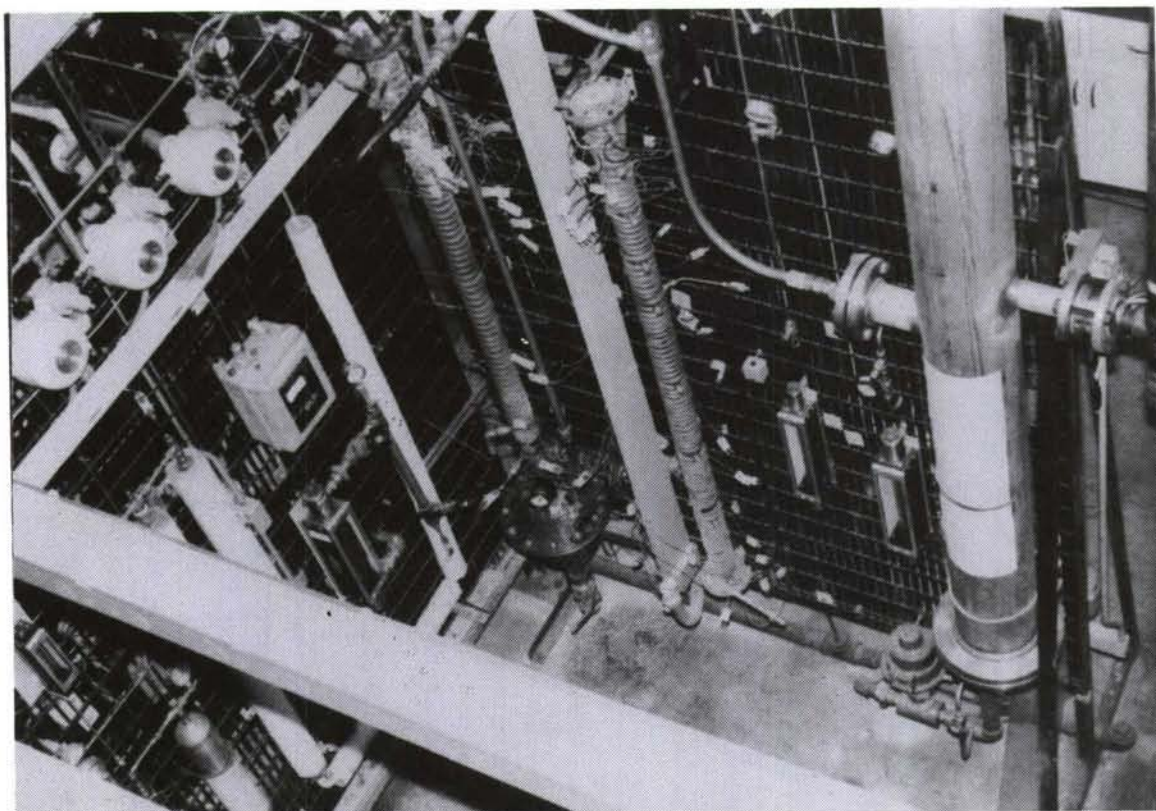


Figure 3. Photographic Overview of Laboratory Scale System

### **Task 2. Development of a Theoretical Model**

The development of a theoretical model was intended to correlate particle surface area with major operational parameters. An expansion of previous Carborundum sponsored work, the goal was to develop a fundamental standing of process reactions.

After consultation with the ORNL Technical Monitor, the modeling work was subcontracted to International Thermal Plasma Engineering, Inc. (Professor Boulous - University of Sherbrooke, Quebec, Canada, et al).

The model was developed in stages:

- 1) Development of a model to describe the flow and temperature field in the reactor.
- 2) The calculation of thermodynamic equilibrium for the  $H_2$ -Ar- $CH_4$ - $SiCl_4$  system and the study of the chemical kinetics of possible homogenous reactions occurring in the plasma process.
- 3) A literature review of nucleation and growth in an aerosol system which could be of relevance to this work.

Although a turbulent model was initially developed to describe the flow in the reactor, the actual flow experienced at the present operating conditions was found to be laminar. This necessitated the development of a laminar flow based model. The turbulent model is used to describe the

flow and temperature fields in the entrance region of the reactor (first 150mm) and thereafter the laminar code is used. Since a mixture of hydrogen and argon is used in the present reactor, the transport properties have been calculated using the rule of mixtures. The model was calibrated using measured temperatures and then used in a predictive mode to describe temperature and flow fields obtained under a wide range of operating conditions.

This model will be used to assist with scale-up of the process during Phase II.

### **Task 3. Baseline Characterization and Analytical Method Development**

The objectives for this task included:

- .. Firmly establish the methodologies to be used for powder characterization.
- .. Define basic powder characteristics which may be utilized to assess property control and improvements as the program progresses.

Initially, two commercially produced SiC powders were to be characterized: H.C. Starck, Inc. (West Germany), A10 Grade; and Standard Oil-Carborundum submicron alpha SiC.

As both of the above powders were alpha phase, it was decided to characterize one beta phase powder in addition, Starck B-10 Grade.

The parameters characterized and the methodologies used include the following:

<u>Characteristic</u>	<u>Methodology</u>
..Pressureless sinterability	--Percentage of theoretical density achieved with and without sintering aids.
..Surface area	--B.E.T. surface analysis.
..Degree of agglomeration	--Tap density.
..Particle size distribution	--Horiba particle size analyzer.
..Bulk composition	--Wet chemistry
..Phase distribution	--X-ray diffraction.

The results of characterization of powders produced under this sub-contract with the three baseline powders is shown at the conclusion of this report.

### **Task 4. Screening Experiments**

Task 4 was divided into subtasks for management and reporting purposes.

The first subtask was to characterize the operation of the plasma torch using a hydrogen/argon blend. It should be noted that the original workscope included a short series of experiments to investigate the feasibility of using a hydrogen plasma in lieu of argon. This could be advantageous as hydrogen is a reactant (to scavenge chlorine from the silicon source) and the argon (necessary only as a carrier of energy) could potentially be reduced or eliminated.



As both Standard Oil and the torch vendor, Plasma Materials, Inc. were confident that the torch would operate with a very rich hydrogen to argon blend, it was decided to accomplish this subtask first.

Concurrent with that subtask, careful consideration was given to the choice of the individual variables for the screening experiments. The candidate feedstocks were described in the statement of work, but the values (or range of values) for temperature, carbon/silicon ratio and reactant concentration had to be established.

A matrix of screening experiments was developed to incorporate two levels of each of the variables for each feedstock. The candidate feedstocks are as follows:

- Reactant 1: silicon tetrachloride ( $\text{SiCl}_4$ )
- Reactant 2: dimethyl dichlorosilane  $[(\text{CH}_3)_2\text{SiCl}_2]$
- Reactant 3: methyl trichlorosilane ( $\text{CH}_3\text{SiCl}_3$ )

### Proposed Test Matrix: Screening Experiments

Reactant	Temperature	Carbon/Silicon Ratio	Reactant Concentration
Reactant 1	Hi	Hi	Hi
			Lo
		Lo	Hi
			Lo
	Lo	Hi	Hi
			Lo
		Lo	Hi
			Lo
Reactant 2	Hi	Hi	Hi
			Lo
		Lo	Hi
			Lo
	Lo	Hi	Hi
			Lo
		Lo	Hi
			Lo
Reactant 3	Hi	Hi	Hi
			Lo
		Lo	Hi
			Lo
	Lo	Hi	Hi
			Lo
		Lo	Hi
			Lo

Figure 4. Screening Experiment Test Matrix



Once the plasma torch had been stabilized on a very rich  $H_2/Ar$  blend, silicon feedstock ( $SiCl_4$ ) and methane were added to the system. Several short runs were made and powder was produced. Analysis later proved the powder to be beta silicon carbide.

Several debugging problems occurred which aborted many of the initial runs. Some of these problems included the silicon feed pump, the tail gas scrubber level transducer and a cooling water leak into the plasma torch. All items were satisfactorily resolved.

The torch and reactor system also experienced plugging problems which limited run times; some as short as 5 minutes. Minor anode configuration changes were made which has since allowed runs up to 3 hours in duration. Although this problem has not been completely solved, the present configuration is capable of running long enough to accomplish the tasks planned for Phase I. Runs of approximately one hour duration have generated representative material in sufficient quantities for analysis.

At this point, the workplan called for the initiation of screening experiments; a matrix of 24 variations of temperature, carbon to silicon ratio and reactant concentration (defined as hydrogen to chlorine ratio). However, a priority was placed upon establishing the consistency and reproducibility of the process. The workplan was modified to first run four pre-screening experiments to establish a consistent baseline; then to prioritize the screening experiments (focusing primarily on feedstock one). Eight experiments (six of Feedstock 1 and two of Feedstock 2) were initially run and the results analyzed. Upon completion of the analytical results of those powders, the remainder of the matrix was completed.

Table 1 summarizes the results of the screening experiments. The prime determinants of the quality of the powders produced were: Percent SiC, Percent Free Carbon, and Percent Free Silicon.

TABLE 1  
RESULTS OF SCREENING EXPERIMENTS

	<u>No. of Conditions</u>	<u>% SiC</u>	<u>% Free Carbon</u>	<u>% Free Silicon</u>
Silicon Tetrachloride	8	43.9 - 81.4	2.89 - 9.32	1.04 - 3.63
Dimethyl Dichlorosilane	7	46.8 - 91.2	0.60 - 4.46	0.16 - 8.38
Methyl Trichlorosilane	8	76.1 - 97.9	1.09 - 3.23	0.03 - 1.04
Goal		>95.0	<2.0	Minimum

### Conclusions - Screening Experiments

Based on the results of the screening experiments, methyl trichlorosilane was chosen as the best feedstock to be carried forward to the parametric studies.

Though the other feedstocks may also be suitable, methyl trichlorosilane provided the widest operating window.

### Task 5. Extended Parametric Studies

This task was intended to further evaluate the process parameters of the feedstock selected at the conclusion of the screening experiments: Methyl trichlorosilane. The parameters to be evaluated included temperature, silicon feedstock flow rate, and hydrogen/chlorine ratio.

One of the first activities for this task was to produce a substantial amount of powder by running methyl trichlorosilane at the best known conditions in order to perform some initial sinterability studies.

Approximately 80 grams of powder were produced, analyzed, and sintering trials were performed.

Analysis of the powder revealed very good chemistry:

Percent SiC	98.5
Percent Free Carbon	0.15
Percent Free Silicon	0.13

Sintering to 89% and 92% of theoretical density was achieved with normal sintering additives. Though sintering conditions for beta SiC powders have not been optimized; these initial results are considered to have established the ability to sinter the powder produced by this process. Photomicrographs of powder and one of the sintered specimens are shown in Figure 5.

**TABLE 2**  
**PARAMETRIC STUDIES**

		<u>High</u>	<u>Medium</u>	<u>Low</u>
Temperature $\Rightarrow$	Net Input Energy (KW)	6.5 - 8.2	5.5 - 6.4	4 - 5.4
	Hydrogen/Chlorine Ratio	33.9	25.4	16.9
Feedstock Feed $\Rightarrow$	Theoretical SiC	450	350	250
Rate	Production Rate (g/hr)			

The H/Cl ratio could be specifically controlled but temperature could not, nor could it be precisely measured. Therefore, net input power (kw) was varied instead, to provide the desired variation in temperature. Also, the flow of feedstock through the system is described by the theoretical rate of SiC production in grams per hour.

A total of 14 sets of unique conditions were run as shown in Table 3.

These were selected based upon being the most promising areas of the matrix and being within the operating range of the reactor.

**TABLE 3**  
**SUMMARY OF PARAMETRIC STUDIES**

<b>Total SiC %</b>	<b>Theoretical SiC Production Rate</b>	<b>H/Cl Ratio</b>	<b>Net Input Energy</b>
97.5	High	Medium	High
97.5	Medium	Medium	Low
96.1	Medium	Low	Medium
95.8	Low	High	Low
95.7	High	Medium	Medium
95.3	High	Low	Low
95.2	Medium	High	Low
94.9	Medium	High	High
93.6	Low	Medium	Medium
92.8	High	Low	Low
92.6	Medium	High	High
92.4	Low	High	Low
91.9	Medium	Medium	High
84.8	Medium	High	Low



Powders were produced with a very wide range of operating conditions during the parametric studies. All except one experiment yielded greater than 90% SiC purity. The analytical results for the low 84.8% SiC content had a very poor material balance closure, so that particular number is suspect.

There appears to be little correlation of the three chosen parameters with the analytical results obtained. However, half of the conditions run gave powders with 95% purity or higher indicating a wide range of acceptable conditions.

At the completion of the parametric studies, a small sample was prepared for submission to the ORNL Technical Monitor to complete Phase I.

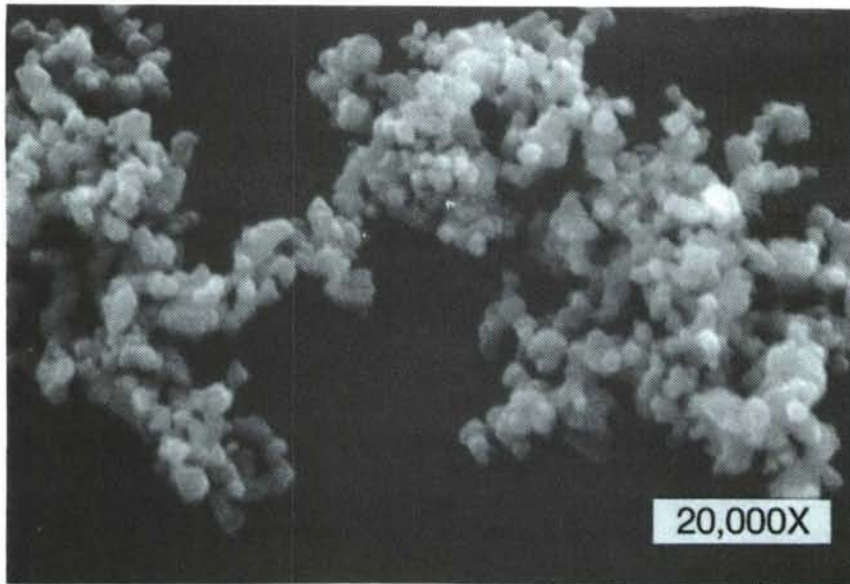
A sinterability trial of this sample of powder achieved 86% of theoretical density. A summary of the characteristics of this powder compared to the baseline powders is shown in Table 4. A photograph of a similar sample of powder with a sintered specimen is shown in Figure 6.

**TABLE 4**  
**SUMMARY OF THE CHARACTERISTICS OF THE POWDER PRODUCED UNDER**  
**THIS SUBCONTRACT COMPARED TO THE BASELINE POWDERS**

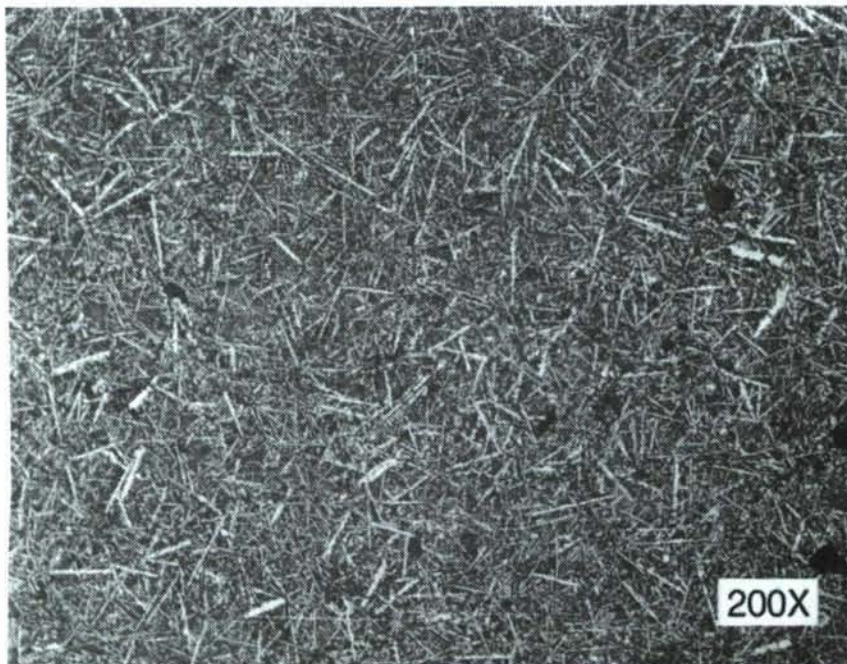
	<b><u>Phase I</u></b> <b><u>Gas Phase</u></b>	<b><u>Starck</u></b> <b><u>B-10</u></b>	<b><u>Starck</u></b> <b><u>A-10</u></b>	<b><u>Standard</u></b> <b><u>Oil</u></b>
<b>Chemistry (wt. %)</b>				
Total Carbon	29.55	30.49	30.30	29.95
Free Carbon	0.35	1.83	1.54	0.36
Free Silicon	0.09	0.40	0.29	0.09
Oxygen	0.58	0.90	0.76	0.27
Iron	< 0.01	0.04	0.03	< 0.01
Silicon Carbide <sup>1</sup>	97.33	95.50	96.60	98.80
<b>Physical Properties</b>				
Major Phase	Beta	Beta	Alpha	Alpha
Median Particle Size ( $\mu\text{m}$ )	0.75	1.0	1.4	1.2
Surface Area ( $\text{m}^2/\text{g}$ )	10.0	15.3	14.3	9.4
<b>Sinterability<sup>2</sup></b>				
Green Density ( $\text{g}/\text{cm}^3$ )	1.89	2.01	2.09	1.67
Fired Density ( $\text{g}/\text{cm}^3$ )	2.76	3.03	3.09	3.20

<sup>1</sup>Obtained from Carbon Balance

<sup>2</sup>With Typical Sintering Aids



Powder (20,000X)



Sintered Specimen:  
92% Theoretical  
Density (200X)

Figure 5. Photomicrographs of powder and sintered specimen



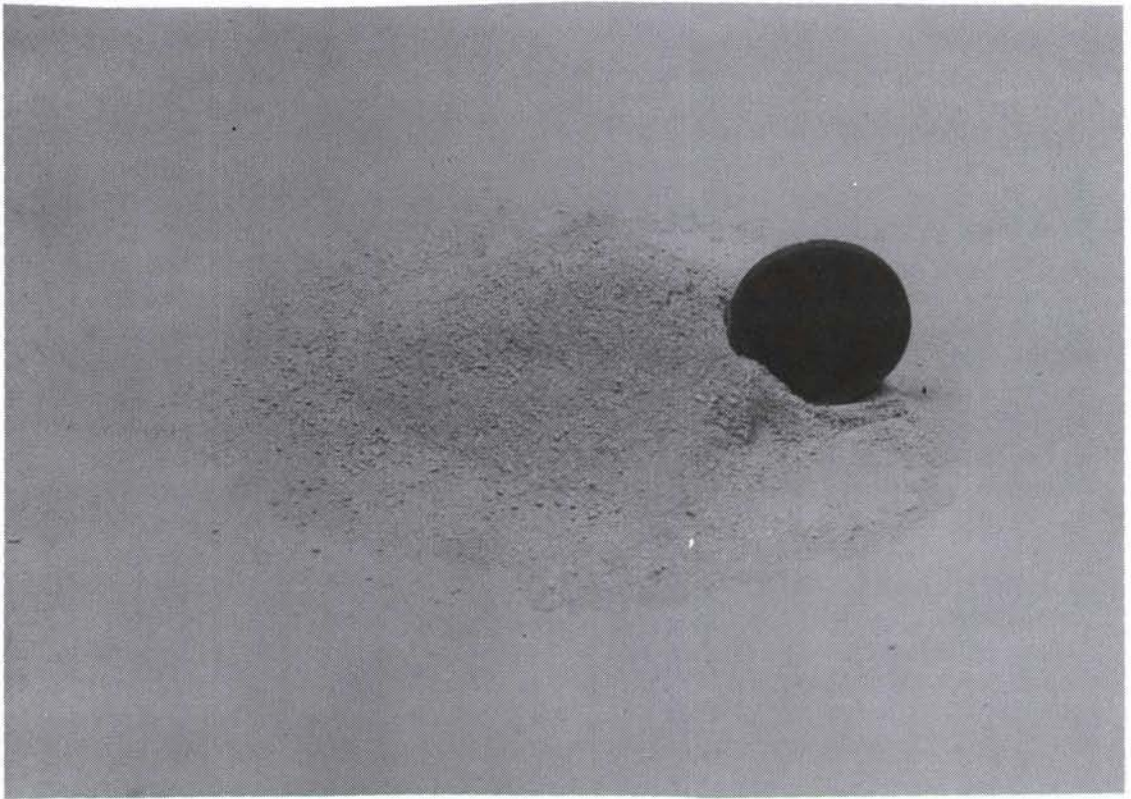


Figure 6. A sample of powder and sintered specimen similar to that which was provided to ORNL to complete Phase II.



**Status of Milestones**

Task 1.	Design, Construct and Test Laboratory Scale Equipment	- Complete
Task 2.	Develop Theoretical Model	- Complete
Task 3.	Baseline Characterization and Analytical Model Development	- Complete
Task 4.	Screening Experiments	- Complete
	.. Selection of Feedstock	- Complete
Task 5.	Extended Parametric Studies	- Complete
	.. Delivery of Powder Sample to ORNL	- Complete
Task 6.	Reporting Requirements	- Complete
Task 7.	Quality Assurance	- Complete

**Publications**

None during the period.

### 1.1.2 Silicon Nitride

#### Sintering of Silicon Nitride

G. E. Gazza (Army Materials Technology Laboratory)

#### Objective/Scope

The program is concentrating on sintering compositions in the  $\text{Si}_3\text{N}_4\text{-Y}_2\text{O}_3\text{-SiO}_2$  system using a two-step sintering method where the nitrogen gas pressure is raised to 7-8 MPa during the second step of the process. During the sintering, dissociation reactions are suppressed by the use of high nitrogen pressure and cover powder of suitable composition over the specimen. Resultant properties determined are room temperature modulus of rupture, high temperature stress-rupture, oxidation resistance, and fracture toughness. Successful densification of selected compositions with suitable properties will lead to densification of injected molded or slip cast components for engine testing.

#### Technical Progress

Compositions of interest in this program lie generally in the  $\text{Si}_3\text{N}_4\text{-Y}_2\text{SiO}_5\text{-Si}_2\text{N}_2\text{O}$  triangle (subsequently referred to as triangle 1) and the  $\text{Si}_3\text{N}_4\text{-Y}_2\text{SiO}_7\text{-Y}_5(\text{SiO}_4)_3\text{N}$  triangle (subsequently referred to as triangle 2) as previously reported (1). Total volume percent of  $\text{Y}_2\text{O}_3$  and  $\text{SiO}_2$  additives used in specimen compositions range from 8 to 14 v/o and  $\text{Y}_2\text{O}_3/\text{SiO}_2$  ratios range from 0.28 to 1.11. It has been previously shown in hot pressing (2,3) and sintering studies (4) that compositions located in triangle 1 possess excellent oxidation resistance and are not susceptible to thermal instability at intermediate temperatures, i.e., 700-1000C. However, little information is available on the creep resistance or static fatigue properties of these compositions which is of concern due to the high silica content in the compositions and the potential for producing low viscosity or low melting phases. Processing problems can also be encountered working in this compositional range due to dissociation reactions involving  $\text{Si}_3\text{N}_4$  and  $\text{SiO}_2$  producing  $\text{SiO}$  and  $\text{N}_2$ . The evolution of these gas species drives the composition toward the  $\text{Y}_2\text{O}_3$ -rich end of the phase diagram and may cross into a different phase field, particularly if weight losses are high during sintering. Compositional gradients (particularly with respect to oxygen) may occur in specimens causing different phases to develop near the specimen surface than in the interior. Therefore, control of such reactions is a prerequisite for successful densification of silicon nitride where strict compositional and phase control are required. Although a broad range of compositions may be evaluated in the overall program, this paper will focus on a series of compositions located in triangle 1 where the total volume percent of combined additive, i.e.,  $\text{Y}_2\text{O}_3 + \text{SiO}_2$ , for each composition is essentially constant at 10.2% but the  $\text{Y}_2\text{O}_3/\text{SiO}_2$  ratio varies from 0.28 to 0.50.

Publications

"Effect of Oxidation on the Densification of Sinterable RBSN", MTL Technical Report TR86-1.

TABLE 1

SINTERING RESULTS OBTAINED FOR SAMPLES
CONTAINING WC ADDITIONS  
 (COMP. # 39)

<u>SAMPLE</u>	<u>% WC</u>	<u>SINTERED</u> <u>DENSITY (g/cc)</u>	<u>% THEORETICAL</u> <u>DENSITY</u>	<u>% WT.</u> <u>CHANGE</u>
T12-A	.48	3.27	99.1	-.37
T24-A	.98	3.27	98.5	-.68
T48-A	.90	3.26	98.2	-.51
T96-A	1.17	3.27	98.2	-.68
S7-A	.55	3.29	99.8	+.02
S12-A	1.43	3.31	98.9	-.91
S24-A	2.90	3.34	97.9	-1.77
S96-A	3.46	3.34	97.4	-2.57

(T = TS-7 S = Silicon)



TABLE 2

## OXIDATION OF SINTERED SILICON NITRIDE COMPOSITIONS

SPEC. I.D.	OXID. TEMP. (C)	TIME (hrs.)	OXID. RATE CONST. ( $k_p$ ) ( $\text{kg}^2\text{m}^{-4}\text{sec}^{-1}$ )
17	1000	155	$2.66 \times 10^{-13}$
17	1200	144	$2.32 \times 10^{-12}$
37	1000	297	$4.88 \times 10^{-12}$
37	1200	297	$3.47 \times 10^{-12}$
39	1200	152	$2.48 \times 10^{-12}$
25	1000	155	$7.47 \times 10^{-11}$
25	1200	144	$1.80 \times 10^{-11}$

(17) 84.7m/oSi<sub>3</sub>N<sub>4</sub>-3.4m/oY<sub>2</sub>O<sub>3</sub>-11.9m/oSiO<sub>2</sub>(37) 85.4m/oSi<sub>3</sub>N<sub>4</sub>-4.3m/oY<sub>2</sub>O<sub>3</sub>-10.3m/oSiO<sub>2</sub>(39) 85.8m/oSi<sub>3</sub>N<sub>4</sub>-4.73m/oY<sub>2</sub>O<sub>3</sub>-9.47m/oSiO<sub>2</sub>(25) 82.0m/oSi<sub>3</sub>N<sub>4</sub>-8.0m/oY<sub>2</sub>O<sub>3</sub>-10.0m/oSiO<sub>2</sub>

TABLE 3

EFFECT OF COMPOSITION AND CRYSTALLIZATION ON STRESS-RUPTURE PROPERTIES  
OF TWO SINTERED SILICON NITRIDE MATERIALS  
(stress=300MPa)

SPEC ID	Y2O3/SiO2	SR TEMP	SR TIME(hrs)	CRYST.(Y/N)
17	0.28	1000	240+	N
17	0.28	1100	150+	N
17	0.28	1200	0.01	N
17	0.28	1200	0.5	Y
17	0.28	1200	1.1	Y
37	0.42	1200	3	N
37	0.42	1200	170+ ( $\epsilon < 0.1\%$ )	Y

## Experimental Procedure

### Preparation of Starting Composition

In formulating the compositions to be studied and evaluated, the source of the starting powders and their characteristics are known to influence the process parameters required for sintering and the resultant microstructure and properties. Sources of silicon nitride powder being studied include Toyo-Soda TS-7 powder, UBE SN-E-10 powder, and KemaNord Siconide 1152 grade powder. The Toyo-Soda and UBE powders are from Japan while the KemaNord powder is from Sweden. The powders are 90-95% alpha phase and contain 1.0-1.5% oxygen. The KemaNord contained less than 1200 ppm of Fe, Al, and Ca while the Japanese powders contained less than 200 ppm of these impurities. The surface areas of the Toyo-Soda and UBE powders are 12-13 m<sup>2</sup>/g while the 1152 powder is approximately 8.5 m<sup>2</sup>/g. Both Japanese powders contain Cl with UBE reporting less than 100 ppm and Toyo-Soda 1000 ppm max. The various compositions selected for sintering were prepared by mixing one of the Si<sub>3</sub>N<sub>4</sub> starting powders with Y<sub>2</sub>O<sub>3</sub> and SiO<sub>2</sub> powders also including the amount of surface silica on the Si<sub>3</sub>N<sub>4</sub> particles. The powder mixtures were milled in plastic jars using either WC or Si<sub>3</sub>N<sub>4</sub> milling balls and ethanol. Milling times were usually 18-24 hours but were varied in some experiments using WC media in order to control WC contamination into the powder mixture. The 18-24 hour milling times were selected as sufficient to produce adequate mixing of components while attempting to minimize the amount of plastic container material incorporated into the powder. Longer milling times were found to produce only modest increases in surface area (reductions in particle size). Significant increases in surface area can be achieved by using both Si<sub>3</sub>N<sub>4</sub> milling jars and balls. After milling, the powders were dried and sieved through a -325 mesh screen to remove agglomerates. The powder was uniaxially die pressed to a disc shape, then cold isostatically pressed at 150 MPa to increase the "green" density. Compositions focused upon in this paper are compositions 17: 84.7m/oSi<sub>3</sub>N<sub>4</sub>-3.4m/oY<sub>2</sub>O<sub>3</sub>-11.9m/oSiO<sub>2</sub>; composition 37: 85.4m/oSi<sub>3</sub>N<sub>4</sub>-4.3m/oY<sub>2</sub>O<sub>3</sub>-10.3m/oSiO<sub>2</sub>; and composition 39: 85.8m/oSi<sub>3</sub>N<sub>4</sub>-4.73m/oY<sub>2</sub>O<sub>3</sub>-9.47m/oSiO<sub>2</sub>.

### Sintering

All sintering runs were made in a high temperature-high gas pressure furnace with graphite heating elements. Specimens were enclosed in a RBSN crucible with a loose fitting lid and embedded in a cover powder of appropriate composition to control specimen composition (weight changes) during sintering. A two-step sintering method was used where the gas pressure in the first step, 1.5-2.0 MPa, was held for 45-90 minutes, then raised in the second step to 7.0-8.0 MPa and held for 15-30 minutes. The sintering temperature used for the first step was 1950-1960C. For the second step (higher pressure), the temperature was either held at 1950-1960C or raised to 2000C for some sintering runs. After high temperature densification, some specimens were held at 1200°C for 60-120 minutes to partially crystallize the specimen for XRD



measurements to determine whether compositional control during the sintering was sufficient to produce the desired phase development. The use of first step temperatures of 1950-1960°C were based on sintering data (Figure 1) showing that these temperatures produced higher, more uniform densities for compositions ranging from 0.28 to 0.42  $\text{Y}_2\text{O}_3/\text{SiO}_2$  additive ratios (at 10.2v/o additive level). At additive ratios above 0.28, it does not appear that the closed pore stage was attained after a 1940°C initial temperature hold as raising the temperature to 2000°C in the second step resulted in a lower density. Since the use of WC milling media (as well as  $\text{Si}_3\text{N}_4$  media) is being studied for powder processing, the influence of milling media impurity pickup on sintering the compositions of interest was also examined. Using two different starting powders, Toyo-Soda TS-7 and KemaNord 1152, several batches of composition 39 were prepared and milled with WC balls for different milling times to produce various amounts of WC impurity in the samples, as shown in Table 1. Milling times ranged from 7 to 96 hours. The KemaNord 1152 powder appeared to pickup the milling media impurity at a faster rate than the TS-7 powder. This may be related to its lower surface area and broader particle size distribution. Sintering of the samples was accomplished at 1960°C, 60 min., 2 MPa, then 1960°C, 30 min., 8 MPa  $\text{N}_2$  gas pressure. The four samples for each different starting powder were sintered in two separate runs but using the same sintering parameters. The best densities were obtained when the WC content was approximately 0.5%. Weight losses increased with increasing WC impurity content.

### Properties

Specimens were machined from dense, sintered discs approximately 1.5 in. diameter x 0.375 in. thick for determination of room temperature modulus of rupture (RT MOR), fracture toughness, oxidation resistance, and stress-rupture properties. RT MOR tests were conducted using four point bending with specimens 0.080 in. wide x 0.105 in. thick. MOR values ranged from 580 to 675 MPa for the three compositions of interest. Fracture toughness values generated by the indentation method were calculated to be 5.0-5.4  $\text{MPa}\cdot\text{m}^{-1/2}$ .

Oxidation resistance of compositions 17, 37 and 39 were determined, in air, at temperatures of 1000°C and 1200°C. The compositions, in the triangle 1 phase compatibility range, all demonstrated good oxidation resistance as shown in Table 2. Oxidation times ranged from 144 to 297 hours. The rate constants were calculated for each composition and fell in the range of  $10^{-12}$  to  $10^{-13}$ . The oxidation resistance of composition 25 (composition in triangle 2 and shown in Table 2) contained 14v/o additives content was also determined for similar temperatures and times. The rate constant increased into the  $10^{-11}$  range.



Since ceramic materials intended for use as heat engine components must endure prolonged periods at high temperature and stress, their time dependent properties are particularly important because performance limiting defects usually manifest themselves in a time dependent manner related to the high temperature properties of the grain boundary phase. Preliminary stress-rupture studies were carried out with compositions 17 and 37 at temperatures of 1000°C and 1200°C under 300 MPa stress in four point bending. Data was obtained from specimens in the as-sintered condition and after crystallization heat treatments, in air, for 125-150 hours. Table 3 shows the results of this study. Composition 17 was stress-rupture tested at temperatures of 1000°C and 1200°C. In the as-sintered condition, specimens at 1000°C lasted 240 hours without failure. At 1100°C they lasted 150 hours without failing. But at 1200°C specimens failed in approximately 0.01 hours (30-40 seconds) after application of load. The large reduction in static fatigue resistance at 1200°C suggests that composition 17 may be located near a low melting compound or eutectic. Some specimens were given crystallization treatments for 125-150 hours in air at temperatures of 1000°C to 1200°C prior to stress-rupture testing. The average time to failure of these specimens was 0.5 hour, still relatively short but more than an order of magnitude increase over as-sintered specimens. If the crystallization temperature was raised to 1200°C, the stress-rupture life increased to 1.1 hours. A specimen that was stress-rupture tested at 1100°C for 150 hours without failure was retested at 1200°C. It failed in 1.4 hours. If the composition was shifted toward the  $\text{Si}_3\text{N}_4\text{-Y}_2\text{Si}_2\text{O}_7$  join, composition 37, stress-rupture properties improve. Specimens of composition 37 tested at 1200°C in the as-sintered condition lasted 3 hours before failure. If a 1200°C crystallization treatment was given before stress-rupture testing, specimens lasted 170 hours without failure. Permanent strain in the specimens was estimated to be less than 0.1%.

#### Status of Milestones

(a) Process and composition -- sintering parameters have been established as 1950-1960°C initial process temperature with second step between 1950°C and 2000°C. Pressure in first step 1-2 MPa increasing to 6-8 MPa for second step. Compositions focused upon are near the  $\text{Si}_3\text{N}_4\text{-Y}_2\text{Si}_2\text{O}_7$  join. Total volume percent of  $\text{Y}_2\text{O}_3\text{-SiO}_2$  additive is approximately 10%. Lower amounts are desirable. Process parameters and use of cover powder should result in a small weight loss (<1%) for high density and compositional and phase stability.

(b) Scale up of compacts -- compacts 1.5-2.0 in. diameter x 3/8 in. thick are being produced in order that specimens may be machined from them for property measurements. Properties being determined are RT modulus of rupture, fracture toughness, oxidation resistance, and stress-rupture at 1000°C and 1200°C.



Synthesis of High Purity Sinterable  $\text{Si}_3\text{N}_4$  Powders -- G. M. Crosbie  
(Research Staff, Ford Motor Company, Dearborn, Michigan)

Objective/scope

The goal of this task is to achieve major improvements in the quantitative understanding of how to produce sinterable  $\text{Si}_3\text{N}_4$  powders having highly controlled particle size, shape, surface area, impurity content and phase content. Through the availability of improved powders, new ceramic materials are expected to be developed to provide reliable and cost-effective structural ceramics for application in advanced heat engines.

Of interest to the present powder needs is a silicon nitride powder of high cation and anion purity without carbon residue.

The process study is directed towards a modification of the low temperature reaction of  $\text{SiCl}_4$  with liquid  $\text{NH}_3$  which is characterized 1) by absence of organics (a source of carbon contamination), 2) by pressurization (for improved by-product extraction efficiency), and 3) by use of a non-reactive gas diluent for  $\text{SiCl}_4$  (for reaction exotherm control).

Technical progress

In this paper, we present key experimental results, describe the process flowsheet, discuss the current status of powder qualities, and outline future plans.

To obtain a silicon nitride powder of high cation and anion purity without carbon residue, we are working on a modification of the preparation of  $\text{Si}_3\text{N}_4$  from low temperature reaction of  $\text{SiCl}_4$  with ammonia. The specific objective of the current work is to design and operate a laboratory version of a chemical process for synthesis of nitride powder to meet the special needs of vehicular applications.

The central concept of this process study is the rate control of the  $\text{SiCl}_4$ - $\text{NH}_3$  reaction by use of a carrier gas to bring  $\text{SiCl}_4$  vapor into contact with liquid ammonia. A second feature is the use of pressure in the process apparatus to reduce processing cost, in part by increased solubility of the chloride by-product in liquid ammonia (above its normal boiling point) and in part by reduced refrigeration cost (by operation near room temperature).

This chloride vapor - liquid ammonia approach is intended to combine the attractive properties of imide-derived silicon nitride powders (e.g., high chlorine purity) with the exclusion of carbon contamination due to process organics. Additionally, process features have been demonstrated which are desired for scale-up: a nearly heat neutral reaction zone and self-clearing lines.

Key results

Key results have been achieved in the areas of phase and microstructure, carbon purity, heat balance, and materials handling:

*Phase and microstructure* --  $\text{Si}_3\text{N}_4$  powder was produced with phase content, particle size and shape which are close to those characteristics considered desirable for pressureless sinterability. Specifically, the powder derived by thermal decomposition of an intermediate imide product



Figure 1. Scanning electron micrograph of powder produced by decomposition of imide synthesized under pressure reaction of  $\text{SiCl}_4(\text{g})$  with  $\text{NH}_3(\text{l})$ .

(from reaction of  $\text{SiCl}_4$  with liquid  $\text{NH}_3$  at  $0^\circ\text{C}$  and 75 psig) was principally alpha silicon nitride with crystallite size of 0.2 to 0.3  $\mu\text{m}$  and primarily equi-axed particle shape shown in Fig. 1. Other key results have been achieved:

*Carbon purity* -- Purity with respect to carbon is important for consistent grain boundary phase development, elevated temperature corrosion and strength of sintered silicon nitrides, and room temperature mechanical properties. In one case for sinterable reaction bonded silicon nitride, a maximum of 0.05 wt.% C has been stated.<sup>1</sup> Organic diluents have been used previously to control the  $\text{SiCl}_4\text{-NH}_3$  reaction rate.<sup>2</sup> Initially present in hydrocarbon molecules adsorbed on the high surface area imide intermediate, carbon remains with the  $\text{Si}_3\text{N}_4$  product powder.

In our work, we have produced submicron, alpha-silicon nitride with 0.02 to 0.08 wt.% C, which is less than half that of organic diluent nitride powders (typical value of 0.17 wt.% C). (For discussion of other powder purities, see "Resulting powder characteristics" section below).

*Heat balance* -- A nearly heat neutral reaction zone is closely related to carrier gas reaction control. The balance is between the heating from the reaction exotherm and the cooling by the latent heat of vaporization of ammonia into the residual carrier gas.

As expected from a model calculation,<sup>3</sup> an overall endotherm has been observed at  $0^\circ\text{C}$  as the reaction proceeds. The near neutrality of heat balance (of the model calculation near room temperature) is important for uniformity of reaction zone temperature and for low cost scale-up of the



solids forming process.

*Materials handling* -- In our experience, the carrier gas approach has a benefit in the imide-forming process by direct reaction, where inlet clogging is a concern. Potentially solid by-product chloride is kept in solution in liquid ammonia.

In combination with the nature of the imide produced, the liquid ammonia has had a clearing action which leaves lines for the inlet, transfer lines, and the reactor itself clear at the end of a run. This absence of solids accumulation is of practical importance for extended semi-continuous operation.

## Process flowsheet development

The primary emphasis in this work has been placed on process flowsheet development. Highlights are as follows:

1) We have synthesized powder with desirable characteristics, as described above.

2) We have prepared a process flowsheet diagram and a mathematical model of mass and heat balances. Estimates were reported (in the 1985 ATD-CCM paper<sup>3</sup>) for endothermic values of the (extensive) net reactor heat and (S.T.P.) volume of carrier gas. We have observed that this cooling more than offsets the heat of reaction at 0°C and 75 psig, as predicted.

3) In addition to the heat balance offset, other important scalability considerations have been demonstrated. The apparatus has no moving parts except valves. The reactants and products are moved cleanly as fluid streams, with no exposure to air.

*Flowsheet description* -- In the overall process flowsheet (Fig. 2), the intermediate product vessel separates the apparatus into two halves which correspond to the two reactions for the preparation of alpha-silicon nitride: 1) synthesis of the silicon diimide and 2) decomposition of the imide. Representative chemical reactions are given at the top of the diagram.

The nitrogen source for the imide synthesis is liquid ammonia. The silicon source is silicon tetrachloride. A nitrogen stream is saturated with  $\text{SiCl}_4$  (at room temperature) and this stream is diluted with a bypass stream to form a slightly undersaturated stream at the reactor temperature.

The reactor is kept below r.t. by the latent heat of vaporization of  $\text{NH}_3$  into the carrier gas. We have observed that this cooling more than offsets the heat of reaction at 0°C. Estimates have been previously reported<sup>3</sup> for flowsheet values of the (extensive) net reactor heat and (S.T.P.) volume of carrier gas. The carrier gas flow is also the means for control of the system pressure as it exits through the system back-pressure valve.

In testing for scalability of the process through longer runs, new solutions are being found for extended operation without clogging. In the present case, the improvement was to keep to the design conditions. It was previously suggested that heat might be needed.<sup>3</sup>

Earlier, runs had been made over 1 hour in length, but those runs ended with a partially or fully clogged inlet path. Improvement to that point was based on revised geometries of the inlet arrangement and

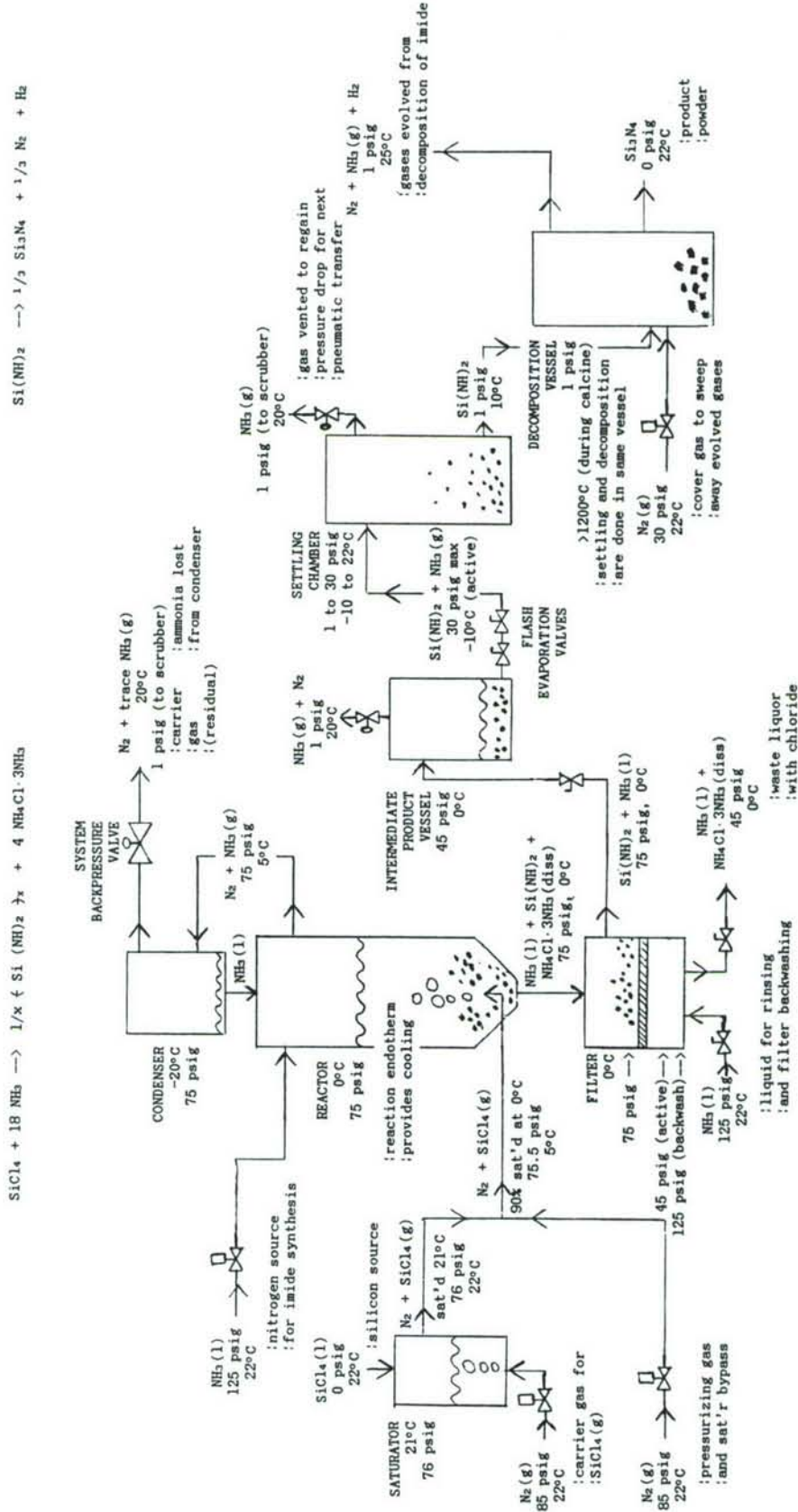


Figure 2. Process flow diagram for pressurized synthesis of  $\alpha\text{-Si}_3\text{N}_4$  from silicon tetrachloride in a carrier gas and liquid ammonia.



revisions of start-up procedures. In those previous runs, ice had built up around the inlet assembly. Although this icing demonstrated the net reaction endotherm at 0°C (and the prospect for a heat neutral reaction at a higher temperature), the thick icing also meant that the interior temperature was well below the design temperature of 0°C. Consequently,  $\text{SiCl}_4$  vapor probably condensed as liquid after the ice reached some critical thickness. From prior experience, reaction of liquid ammonia with liquid  $\text{SiCl}_4$  is a likely source of inlet occlusion. The inlet heater is apparently effective through prevention of  $\text{SiCl}_4$  condensation.

The intermediate imide product is pressure filtered and backwashed to remove chlorine. For the filtering conditions shown, only a moderate excess of  $\text{NH}_3$  is needed to keep all of the  $\text{NH}_4\text{Cl} \cdot 3\text{NH}_3$  in solution. However, we have determined (in this reporting period) that in the absence of rinsing there is sufficient Cl (dissolved in the ammonia held within an imide slurry sediment) to cause 800 ppm Cl to be retained in the silicon nitride which is subsequently formed by decomposition. (For comparison, a value of 180 ppmw Cl is contained in organic-diluent  $\text{Si}_3\text{N}_4$ .) Because the Cl is in solution, the rinsing can be rapid and efficient. Thus, by-product extraction efficiency (which is expected from pressurized operation) can be realized with high solids retention.

The backwashed imide- $\text{NH}_3$  slurry is transferred to the intermediate product vessel and the next reaction can be started.

We have upgraded the process apparatus to have larger volumes for the saturator, reactor, and intermediate product vessel. Various other apparatus design modifications have been carried out. Operating sequence checklists were prepared and computer programs were implemented for multiple-access logging of temperatures, flows, and operator actions.

As part of the process flowsheet task requirements, a flow diagram was prepared. The diagram has also been adapted for an operator's console display with an overlay of continually updated readouts of temperatures and flows at various locations.

Independently, the intermediate product vessel is emptied as aliquots of slurry are flash-dried and pneumatically transported to a settling chamber. The  $\text{NH}_3$  gas is released from the chamber after the particles have settled from each expansion.

The settling chamber doubles as a decomposition vessel, which is heated to  $>1200^\circ\text{C}$  with a flowing cover gas to produce the  $\text{Si}_3\text{N}_4$  product powder.

A design shown in Fig. 2 was implemented for transfer of the air-sensitive imide solids. The imide-containing slurry was produced by the reaction of  $\text{SiCl}_4$  with liquid ammonia. In the present equipment, the slurry is stored in a pressure vessel after low-temperature synthesis. The imide-ammonia slurry is transferred to a controlled atmosphere furnace. The anaerobic transfer is accomplished with a pressure differential and a volume expansion on boiling of  $\text{NH}_3$ . A workable degree of pressure control has been achieved by valving to limit the maximum  $\text{NH}_3$  volume on each unit transferred.

An automated control loop was built-up and used for the flash evaporation segment, which had become tedious to operate by hand. The cycle involves releasing of liquid ammonia-imide slurry with expansion of the ammonia to gas, waiting for particles to settle, and then bleeding down the gaseous pressure slowly. When pressure is down, another cycle begins.

This automation involved sensors, actuators, and software. By use of relay outputs and digital inputs on the existing data acquisition and



control system, the loop was completed with the addition of a sensor for decomposition vessel pressure and electrically-driven valves. These now automatically cycle through repetitive expansion of aliquots of liquid ammonia-imide slurries to transport pneumatically the imide to the settling and decomposition vessel.

The program incorporates a rule-driven approval system, which is designed to prevent the inadvertent release of liquid ammonia under pressure in large volumes to the near-ambient pressure decomposition reactor. This software design covers errors in automatic operation whether from failure of a valve to operate or a program bug in a driving routine or from an error in keyboard commands. The reading back of current valve states is a critical element which is incorporated into the design. In this approval system, the adjacent valves must be indicated as closed, before the next valve can be opened. Manual operation for start-up and shutdown are provided by physical overrides (manually turning valve with deactivated actuator) and a computer terminal valve-command-prompting routine.

Progress has been made in this period with respect to decreasing the oxygen contamination and the amorphous content of the powder under development. Oxygen reduction is a key intermediate variable in preparation for sintering improvements.

Calculations based on input impurities suggest that oxygen contamination can be kept low in cases where the volume of carrier gas is reasonable. In turn, these cases are the more practical cases where the reaction is run under pressure above  $-20^{\circ}\text{C}$ . In practice, there are many places where oxygen can be picked up. In one case, a BET surface area of  $23 \text{ m}^2/\text{g}$  was measured. This level of specific surface area is considered too high and alone would contribute substantial surface oxygen.

To address the oxygen contamination issue, the imide preparation system was reworked to enlarge vacuum lines to make start-up evacuate/purge routines more effective. Also, changes were made in the decomposition system, which will be described now in more detail.

The decomposition furnace was reprofiled (for temperature distribution) and an improved degree of nitride crystallization was obtained. This crystallization is reflected in narrower alpha-silicon nitride peaks in x-ray diffraction patterns and a flat backgrounds of those patterns. The leak rates for the decomposition system were reduced (although still higher than the imide preparation section) and the small exit bubbler pressure was raised. Also, a small amount of  $\text{NH}_3$  gas was added to the decomposition carrier gas flow to lead to positively non-oxidizing conditions.

Process refinements are continuing and more analyses are pending. Results from solid state (magic angle spinning) nmr are being used to follow crystallization extent and to distinguish among amorphous species. These results are provided courtesy of K. R. Carduner of Ford Research Staff. It is from these m.a.s.-n.m.r. results that we know that improvements have been made in the reduction of particular amorphous species and oxygen content.

### Resulting powder characteristics

Powder characterizations have been carried out with impacts on process choices. Some consequences follow from the flowsheet described above: requisite purity of precursors, system tightness, backfill and



purge procedures, residence times, decomposition gas, decomposition environment. Because of these continuing changes, no single set of characteristics is yet appropriate to list as definitive values for the chloride vapor - liquid ammonia process. Continuing emphasis in this work is in refining the process development to approach more closely the goals.

The primary characterizations on each lot made have been x-ray diffraction (XRD) and scanning electron microscopy (SEM). These have shown (in every lot made) that the major crystalline phase is 85 to 95% alpha-silicon nitride. With process refinements, the secondary phase has become beta silicon nitride rather than oxynitride. SEM images, such as Fig. 1, show that the dimensions of predominantly equi-axed particles are 0.2 to 0.3  $\mu\text{m}$ . These phase and morphology features are expected from an imide intermediate process and meet goals for phase, particle size, and shape. Although the surface area goal is  $>10\text{m}^2/\text{g}$ , the achieved level of  $23\text{m}^2/\text{g}$  is considered excessive.

A second category of characterizations is for cation impurities. The target value is  $<0.1\text{ wt.}\%$  total cation impurities. Given a high purity silicon source and minimal corrosion of the apparatus, the cation impurities are primarily a reflection of environment during decomposition. With an  $\text{Al}_2\text{O}_3$  refractory, Al is the principal cation impurity at 0.6%Al with next highest for Fe at 0.16%, Ca 0.06%, and Ti at 0.03%. Except for these three cations, we meet target values.

In one trial without additional  $\text{Al}_2\text{O}_3$ , a sintered density of 83% theoretical density was obtained with 8 wt.%  $\text{Y}_2\text{O}_3$  sintering aid. Therefore, a substantial degree of sinterability was shown for the powder.

In a third group, anions other than nitrogen are detected in products. Sulfur is 60 ppmw, which is below the program target of 100 ppmw. This sulfur is traceable to impurity in the  $\text{SiCl}_4$ . We had 800 ppmw Cl without  $\text{NH}_3$  rinsing. Non-chloride halides are at a desirably low level, except for 200 ppmw F. Oxygen has been discussed in the "Thermal decomposition" section above and is estimated at 5 to 11 wt.%. Crystalline oxynitride has been eliminated, but amorphous and surface oxide content are still undergoing refinement.

## Conclusions

The "chloride vapor - liquid ammonia" route to silicon nitride powders:

- . is a modification of imide route which works;
- . leads to many desired powder and process characteristics now demonstrated:
  - . equi-axed, submicron morphology
  - . low carbon (0.08 wt.%)
  - . nearly heat neutral reaction (scalable)
  - . semi-continuous (liquid-like) transfers;

and

- . is responding to process modification.

## Future plans

By the end of the two-year contract initiated in February 1985, we want to gain more experience with extended manual operation, to carry out sintering retrials with reduced oxygen content powders, and to refine cost estimates with inclusion of refrigeration costs as a function of tempera-

ture.

Beyond the two-year period, we plan to carry out sensor and automation development, to design a pilot plant, to develop flowsheets for the transients in the semi-continuous operation, and to increase the effort for sintering and characterization of the sintered materials.

### Summary

We have prepared a novel process flowsheet for preparation of  $\text{Si}_3\text{N}_4$  with a block flow diagram and a mathematical model of mass and heat balances. We have observed that the cooling from latent heat of vaporization of  $\text{NH}_3$  more than offsets the heat of reaction at  $0^\circ\text{C}$  and 75 psig.

The central concept of this process study is the rate control of the  $\text{SiCl}_4\text{-NH}_3$  reaction by use of a carrier gas to bring  $\text{SiCl}_4$  vapor into contact with liquid ammonia. A second concept is the use of pressure in the process apparatus to reduce processing cost, in part by increased solubility of the chloride by-product in liquid ammonia above its normal boiling point and in part by reduced refrigeration cost.

Powder characteristics meet or are approaching target values. Key results have been achieved in the areas of phase and microstructure, and carbon purity.  $\text{Si}_3\text{N}_4$  powder was produced with phase content, particle size and shape which are close to those characteristics considered desirable for pressureless sinterability. Specifically, the powder derived by thermal decomposition of an intermediate imide product (from reaction of  $\text{SiCl}_4$  with liquid  $\text{NH}_3$  at  $0^\circ\text{C}$  and 75 psig) was principally alpha silicon nitride with crystallite size of 0.2 to 0.3  $\mu\text{m}$  and primarily equi-axed particle shape.

The process has features which are important for scale-up. Key features of near-neutral heat balance and liquid-like materials handling have been demonstrated.

### Acknowledgement

The author thanks R. L. Predmesky and W. B. Copple for construction and operation of the apparatus and is grateful to R. L. Gealer, A. F. McLean, M. E. Milberg, and E. L. Long, Jr. (ORNL) for helpful discussions.

### Status of milestones

The milestones "complete process flow sheet analysis" and "demonstration of sinterability of synthesized  $\text{Si}_3\text{N}_4$  powder" have been met on time in this semi-annual report period. The following milestones are on schedule for this program:

Demonstration of proof of scalability	November 1986
Complete draft technical report describing the process	March 1987

### Publications

G. M. Crosbie, "Preparation of Silicon Nitride Powders," *Ceram. Eng. Sci. Proc.*, 7 [9-10] 1144-49 (1986).



G. M. Crosbie, *Method of Making a Special Purity Silicon Nitride Powder*, U.S. Patent No. 4,582,696 (April 15, 1986).

G. M. Crosbie and R. L. Predmesky, *Method of Making a High Purity Silicon Nitride Precursor*, U.S. Patent Appl. No. 853,539 filed April 18, 1986.

G. M. Crosbie, "Silicon Nitride Synthesis -- A Progress Report," Paper 1-JIII-86 presented at the American Ceramic Society Annual Meeting, Chicago, Illinois, April 29, 1986.

G. M. Crosbie, "Synthesis of High Purity Sinterable Powder  $\text{Si}_3\text{N}_4$ ," pp.191-94 in *Proc. of the 23rd Automotive Technology Development Contractors' Coordination Meeting*, Soc. of Automotive Engineers, Warrendale, Pa., 1986. (P-165)

"Purer  $\text{Si}_3\text{N}_4$  Powders," High-Tech Materials Alert, Technical Insights, Inc., Englewood, New Jersey, July 1986, p.7.

G. M. Crosbie, "Synthesis of High Purity, Sinterable Silicon Nitride Powders," pp. 25-8 in *Ceramic Technology for Advanced Heat Engines Project Semiannual Progress Report for Period October 1985 Through March 1986*, ORNL/TM-10079, Oak Ridge National Laboratory, Oak Ridge, Tenn., August 1986.

G. M. Crosbie, " $\text{Si}_3\text{N}_4$  Powder Synthesis," presented at the 24th Automotive Technology Development Contractors' Coordination Meeting, Dearborn, Michigan, October 27-30, 1986. Manuscript submitted for publication by the Society of Automotive Engineers, Warrendale, Pa. in 1987.

#### References

1. A. Ezis, *Method of Making a Silicon Nitride Body from the  $\text{Y}_2\text{O}_3/\text{SiO}_2/-\text{Si}_3\text{N}_4/\text{Al}_2\text{O}_3$* , U.S. Patent No. 4,443,394 (Apr. 17, 1984).

2. T. Iwai, T. Kawahito, T. Yamada, *Process for Producing Metallic Nitride Powder*, U.S. Patent No. 4,196,178 (Apr. 1, 1980).

3. G. M. Crosbie, "Synthesis of High-Purity Sinterable Powder  $\text{Si}_3\text{N}_4$ ," pp. 191-94 in *Proceedings of the Twenty-Third Automotive Technology Development Contractors' Coordination Meeting*, Dearborn, Michigan, October 21-24, 1985. Society of Automotive Engineers, Warrendale, Pa., No. P-165.

## 1.2 CERAMIC COMPOSITES

### 1.2.2 Silicon Nitride Matrix

#### Transformation-Toughened Silicon Nitride

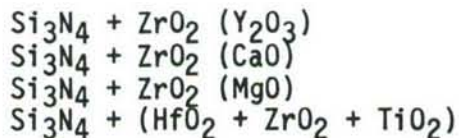
H. W. Carpenter (Rocketdyne Division, Rockwell International) and  
F. F. Lange (Rockwell Science Center)

#### Objective/scope

The objective of this program is to develop high toughness, high strength refractory ceramic matrix composites that can be made at low cost and to near net shape for heat engine applications. The composite system selected for development is based on a silicon nitride matrix toughened by dispersions of  $ZrO_2$ ,  $HfO_2$ , or  $(Hf,Zr)O_2$  modified with suitable additions of other refractory ceramics to control the physical behavior. The desired microstructure and optimum mechanical properties will be developed by expeditious laboratory methods including colloidal suspension, press forming, sintering, and hot pressing. Once the best composition and microstructure have been demonstrated, parameters will be optimized for producing samples by the injection molding process.

#### Technical progress

Four  $Si_3N_4/ZrO_2$  composite systems were evaluated this period and each system was distinguished by the alloying content in the  $ZrO_2$  particulate. The four systems were:



A small amount of sintering aid was also added to each system.

Initial results for the  $Y_2O_3$ - and  $CaO$ -modified composites were highly encouraging. The first exhibited strength to 1200 MPa while the second exhibited high strength plus toughness values to 13.8 MPa  $m^{1/2}$ . The  $MgO$ -modified composite exhibited high toughness but erratic strength, and the  $HfO_2$ - $TiO_2$ -modified composite disintegrated at intermediate temperatures. Thus, only the first two composites are being pursued. These systems are discussed below.

$Si_3N_4 + ZrO_2 (Y_2O_3) + Al_2O_3$  Composite - The problem experienced in the past is that  $Si_3N_4$  and  $ZrO_2$  react to form Zr-oxynitride, an undesirable compound because it depletes the  $ZrO_2$  content without increasing toughness and oxidizes at intermediate temperatures to monoclinic  $ZrO_2$ . The monoclinic  $ZrO_2$ , in turn, results in serious surface cracking. F.F. Lange (Ref. 1) has shown evidence that the formation of Zr-oxynitride can be prevented or retarded and that a transformable tetragonal  $ZrO_2$  phase can be obtained by using  $ZrO_2$  alloyed with  $Y_2O_3$ . It has been shown in this study that at least 8 w/o  $Y_2O_3$  alloy content in the  $ZrO_2$  is



necessary to prevent the formation of Zr-oxynitride. Two or 4 w/o  $\text{Al}_2\text{O}_3$  was added as a sintering aid.

Submicron powders free of agglomerates were obtained by multiple sedimentation processes and the selected components were intimately mixed in an ultrasonic mixing chamber. Discs, 5 cm in diameter, were filter pressed, dried (green density was 40% of theoretical), and hot pressed or sintered to near full density. Compositions of  $\text{Si}_3\text{N}_4$  + 20 v/o or 30 v/o  $\text{ZrO}_2$  + 2 or 4 w/o  $\text{Al}_2\text{O}_3$  sintered easily (Table 1), whereas a composition of  $\text{Si}_3\text{N}_4$  + 10 v/o  $\text{ZrO}_2$  + 4 w/o  $\text{Al}_2\text{O}_3$  did not sinter to a high density and samples cracked into several pieces.

Table 1. Density (g/cc) of Sintered and Hot Pressed Materials Composed of  $\text{Si}_3\text{N}_4$  +  $\text{ZrO}_2$  (9 w/o  $\text{Y}_2\text{O}_3$ ) + 4 w/o  $\text{Al}_2\text{O}_3$

Densification Process	Vol % $\text{ZrO}_2$	
	20	30
Hot Pressed, 1700°C, 1 h	3.65	3.88
Sintered, 1750°C, 1 h	3.63	3.91

Soft agglomerates that formed during the colloidal processing route resulted in large inclusions in the densified material (Fig. 1). Causes of these soft agglomerates were (1) dried slurry on the side of the storage vessel that fell back into the wet slurry, (2) polymers incorporated to improve green strength that changed the electronic nature of the suspended particles, (3) inadequate sonication, and possibly (4) chemical reaction between  $\text{Si}_3\text{N}_4$  and water. However, modification of slurry handling practices eliminated all inclusions and resulted in an excellent dispersion of  $\text{ZrO}_2$  in  $\text{Si}_3\text{N}_4$  (Fig. 2).

Results obtained during this period showed that the strength of both hot pressed and sintered material was very high, and that strength can be further increased by heat treatment. Data from a set of samples cut from the same hot pressed billet are shown in Table 2. Strength increased from 827 MPa (4 pt MOR) in the as-hot-pressed condition to 1164 MPa after heating at 1350°C, 2 h. The strength of sintered material was 10 to 20% lower.



Table 2. Heat Treatment Improves Strength of Hot Pressed  $\text{Si}_3\text{N}_4$  +  $\text{ZrO}_2$  (9 w/o  $\text{Y}_2\text{O}_3$ ) + 4 w/o  $\text{Al}_2\text{O}_3$  Composite

Condition	30 Vol % $\text{ZrO}_2$		20 Vol % $\text{ZrO}_2$	
	4-Point MOR (MPa)	3-Point MOR (MPa)	4-Point MOR (MPa)	3-Point MOR (MPa)
As Hot Pressed	827	951	861	1096
700°C, 250 h	806	806	1096	1075
1200°C, 2 h*	841	896	806	779
1200°C, 2 h* + 700°C, 250 h	930	1006	799	830
1350°C, 2 h** + 700°C, 250 h	1164	1213	1102	1199

\* No Cleanup After Heat Treat

\*\* Surface Polished After Heat Treat

A few samples of both sintered and hot pressed exhibited degradation by oxidation at 700C. The phenomenon was related to an excessively high oxidation rate, especially at such a low temperature, of anion-deficient  $\text{ZrO}_2$  (the result of sintering or hot pressing in a  $\text{N}_2$  atmosphere) back to stoichiometric  $\text{ZrO}_2$ . Analyses of samples indicates that this phenomenon is caused by an inadequate  $\text{Y}_2\text{O}_3$  alloying content and improper processing temperature. Chemical analysis showed that the  $\text{Y}_2\text{O}_3$  content in the  $\text{ZrO}_2$  was 9 w/o rather than the specified 12 w/o, and all samples sintered at 1750C exhibited this problem whereas all samples sintered at 1800C were immune to the problem. SEM and TEM studies will be preformed to elucidate the mechanism but the higher sintering temperature apparently eliminates the oxidation problem.

This material does not exhibit transformation toughening. Nevertheless, this composition would be a promising candidate for an adiabatic diesel engine due to its low thermal conductivity and high strength, and it could be toughened by adding SiC whiskers or by admixing an appropriate amount of  $\text{ZrO}_2$  alloyed with CaO or MgO, which does result in increased toughness. During the next reporting period the high temperature strength will be measured and it will be improved by using a sintering aid, such as  $\text{Y}_2\text{O}_3$ , that produces in a more refractory grain boundary phase than does  $\text{Al}_2\text{O}_3$ .



Figure 1. Dense  $\text{Si}_3\text{N}_4$  + 30 v/o  $\text{ZrO}_2$  + 4 w/o  $\text{Al}_2\text{O}_3$  with large  $\text{Si}_3\text{N}_4$  and  $\text{ZrO}_2$  inclusions.

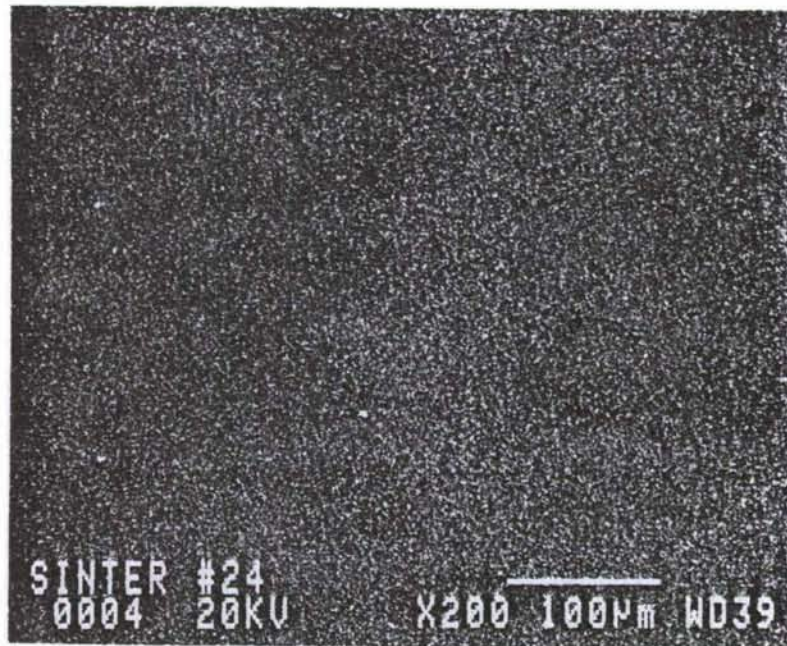


Figure 2. Dense  $\text{Si}_3\text{N}_4$  + 30 v/o  $\text{ZrO}_2$  + 4 w/o  $\text{Al}_2\text{O}_3$  with good dispersion and no inclusions.



Si<sub>3</sub>N<sub>4</sub> + ZrO<sub>2</sub>(CaO) + 2 1/2 MgO Composite - Initial samples were prepared by hot pressing at 1700°C for 1 h. Compositions included Si<sub>3</sub>N<sub>4</sub> + 10, 20, and 30 v/o ZrO<sub>2</sub> alloyed with 5 w/o CaO. Two and one-half percent by weight MgO was added as a densification aid and to retard removal of the CaO from the ZrO<sub>2</sub> during densification. Initial results show significant increases in both fracture toughness and strength.

The fracture toughness of all samples was substantially higher than that of the Si<sub>3</sub>N<sub>4</sub> matrix. The baseline matrix toughness is 4.1 MPa m<sup>1/2</sup> which was measured and calculated by the same diamond indentation technique (Ref. 2) on NC132 samples. Toughness values measured on as hot-pressed samples and samples subjected to selected heat treat conditions are listed below. All of these samples were composed of Si<sub>3</sub>N<sub>4</sub> + 30 v/o ZrO<sub>2</sub> (5 w/o CaO) + 2 1/2 w/o MgO.

<u>CONDITION</u>	<u>K<sub>IC</sub> (MPa m<sup>1/2</sup>)</u>
1. As Hot Pressed	6.8 - 7.6
2. Oxidized at 700C, 64 h	9.1 - 9.9
3. Aged at 1350C, 2 h	9.9 - 12.5
4. Aged at 1350C, 8 h	10.7 - 13.8
5. Aged at 1350C, 2 h + 700C, 120 h	12.8

A large portion of the high measured toughness in the aged samples is due to surface compression stresses that develop as Zr-oxynitride oxides to form monoclinic ZrO<sub>2</sub> on the surface, but annealing at 700C for 120 h after aging at 1380C for 2 h did not decrease toughness.

The 4-point modulus of rupture was measured as a function of (1) volume loading of ZrO<sub>2</sub> and (2) exposure to oxidation at 700C for durations to 250 h. The strength of these compositions is degraded by microcracking at moderate temperatures, and a temperature of 700C was selected to study this microcracking phenomenon. The degree of strength degradation for volume loadings of 10, 20, and 30% ZrO<sub>2</sub> is shown in Fig. 3. Reduction in MOR at a volume loading of 30% ZrO<sub>2</sub> is substantial, but the degradation can be reduced by pre-aging at an elevated temperature. A temperature of 1350C was selected for evaluation but a complete parametric study will be required to find the optimum aging temperature. The strength of samples aged at 1350C for 2 h and then exposed at 700C for selected periods is given in Fig. 4. There is no apparent reduction in strength at volume loadings of 10% and 20% ZrO<sub>2</sub> composites. The strength of the 30% ZrO<sub>2</sub> composite, on the other hand, decreased about 33% as a result of heating at 700C in air.

Two-inch diameter samples of the composition Si<sub>3</sub>N<sub>4</sub> + 30 v/o ZrO<sub>2</sub> + 2 1/2 w/o MgO were press formed and sintered at 1700C to 1800C. Even at 1800C, sintered density was slightly lower than that of hot-pressed samples (Fig. 5). Samples containing 10, 20, and 30



v/o  $ZrO_2$  were sintered at 1800C and MOR bars are being prepared for evaluation. The final densities of hot-pressed and sintered samples are shown in Fig. 6.

The  $ZrO_2$  + 5 w/o CaO powder used to make the above samples had a coarse particle size and, consequently, it was not ideal for the colloidal processing route used. Powders with a submicron particle size, which is much more suitable for colloidal processing, were procured. Three different alloy compositions (3, 5, and 10 w/o CaO) were obtained for characterization of the toughening mechanism.

$Si_3N_4$  +  $ZrO_2$  (MgO) + MgO Composite - A water slurry of 70 v/o  $Si_3N_4$  + 30 v/o  $ZrO_2$  (5 w/o MgO) + 2 1/2 w/o MgO was prepared by milling for 16 h with  $ZrO_2$  grinding medium. Discs, 3.8 cm in diameter, were prepared by filter pressing, dried, and hot pressed at 1700C, 1 h, 1600C, 1 h, and 1550C, 1/4 h. Results (Table 3) show that this composite has merit. The toughness of samples hot pressed at 1700C, and 1600C was almost double that of the  $Si_3N_4$  matrix and it was triple that of the  $Si_3N_4$  baseline after heat treatment at 1350C, 2 h. However, the strength was low and erratic. The low strength was believed to be due to microcracking that occurred during hot pressing. The sample that was hot pressed at 1600C cracked into two pieces at temperature which was evidenced by a loud sound. Although this composite system showed promise based on high toughness, it was not pursued at this time because of the cracking problem.

Table 3. Results of hot Pressed  $Si_3N_4$  +  $ZrO_2$  (5 w/o MgO) + 2 1/2 w/o MgO Composite

Properties	Hot Pressed Temperature (°C)		
	1700	1600	1550
Density (g/cm <sup>3</sup> )	3.87	3.91	4.08
K <sub>IC</sub> (MPa m <sup>1/2</sup> )			
As HP	7.4, 7.8	6.4	3.9
1350°C, 2 h	10.1	13.4	9.2
MOR (MPa)			
As HP	138-696	599	324
700°C, 64 h	103-620	186	69
1350°C, 2 h	-	-	413
1350°C, 3 h + 700°C, 64 h	-	41-241	41

$Si_3N_4$  + ( $HfO_2$ - $ZrO_2$ - $TiO_2$ ) Composite - Submicron powder of the desired alloy (60 m/o  $HfO_2$  + 20 m/o  $ZrO_2$  + 20 m/o  $TiO_2$ ) was obtained from a vendor and a composition of 70 v/o  $Si_3N_4$  + 30 v/o (60  $HfO_2$ -20  $ZrO_2$ -20  $TiO_2$ ) was prepared by a colloidal processing route. A 3.8 cm diameter disc was filter pressed, dried, and hot

pressed to near full density. The fracture toughness was only 2.7 MPa m<sup>1/2</sup> and samples disintegrated when oxidized at 700C. Investigation of this alloy as a dispersoid was not pursued due to the poor initial results.

#### Status of Milestones

All past milestones have been completed on time and the milestones for the next report period are on schedule.

#### Publications

H. W. Carpenter, G. D. Schnittgrund, and F. F. Lange, "Transformation Toughened Silicon Nitride", presented at 24th Automotive Technology Development Contractor's Coordination Meeting, Dearborn, MI, 29 October 1986.

#### References

1. F.F.Lange, L. K. L. Falk, and B.I. Davis, "Structural Ceramics Composites Based on Si<sub>3</sub>N<sub>4</sub>-ZrO<sub>2</sub>(+Y<sub>2</sub>O<sub>3</sub>) Compositions", unpublished, October 1985.
2. Anstis, G.R., et al., "A critical Evaluation of Indentation Techniques for Measuring Fracture Toughness; I Direct Crack Measurements Strength Method," Jour. Amer. Ceram. Soc., 64 (9), 533-538, 1981.



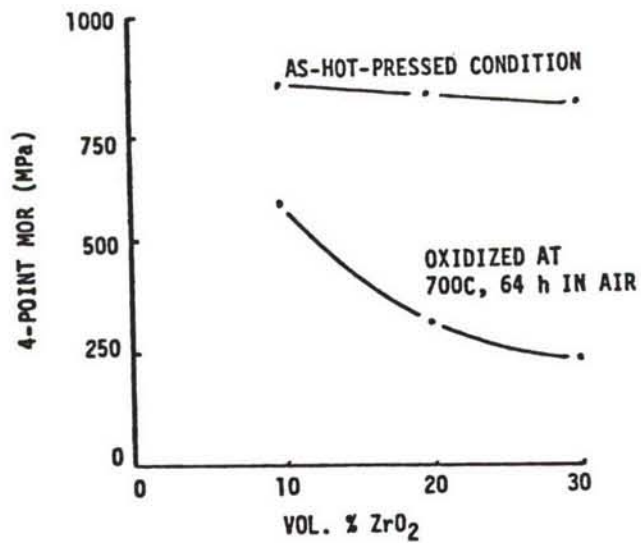


Figure 3. Room Temperature Strength vs Volume Content of  $ZrO_2$  (5 w/o CaO) Particulates

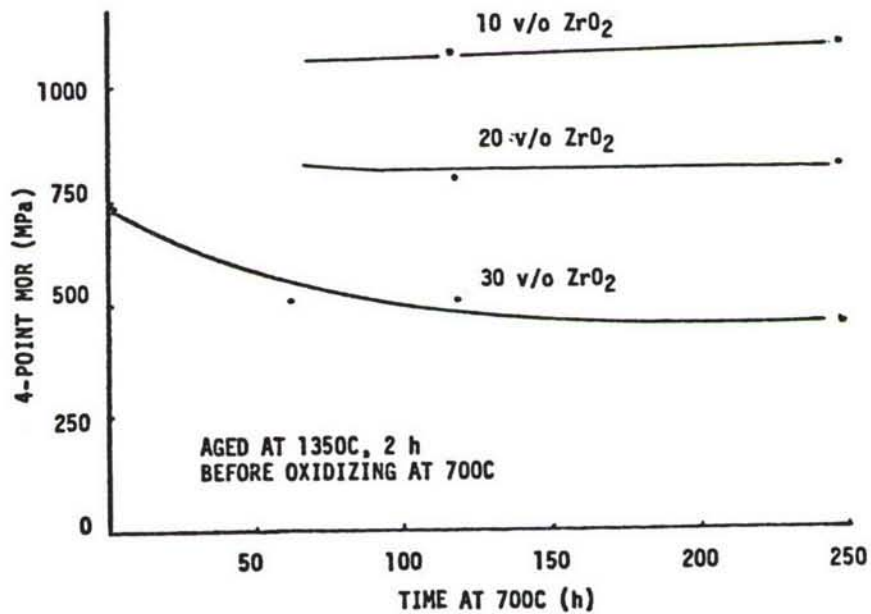


Figure 4. Room Temperature Strength of  $Si_3N_4/ZrO_2$  (5 w/o CaO) Composites vs Duration at 700C in Air After Aging at 1350C, 2 h.

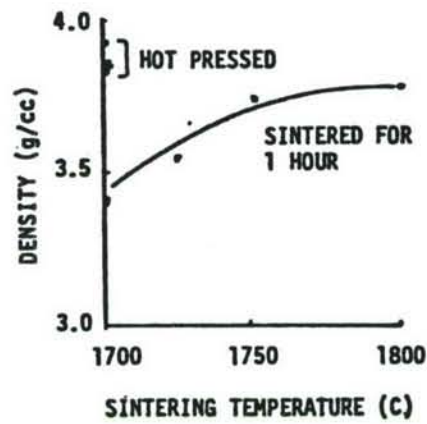


Figure 5. Sintered Density of  $\text{Si}_3\text{N}_4$   $\text{ZrO}_2$  (5 w/o  $\text{CaO}$ ) + 2 1/2  $\text{MgO}$ . (Hot-Pressed Densities are Presented for Reference)

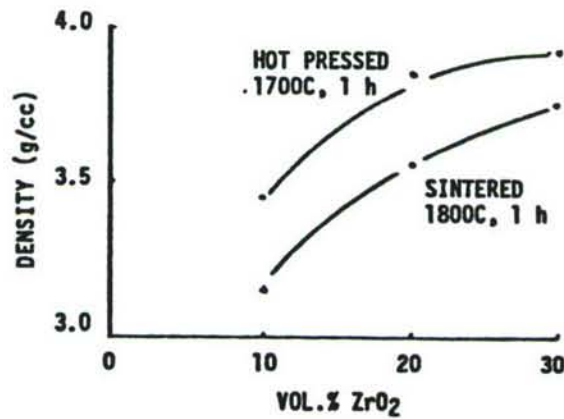


Figure 6. Sintered and Hot-Pressed Densities of  $\text{Si}_3\text{N}_4$  +  $\text{ZrO}_2$  (5 w/o  $\text{CaO}$ ) + 2 1/2 w/o  $\text{MgO}$  Compositions.



Silicon-Nitride-Metal Carbide Composites  
S. T. Buljan (GTE Laboratories, Inc.)

Objective/Scope

The objective of this program is to develop silicon nitride-based composites of improved toughness, utilizing SiC and TiC as particulate or whisker dispersoids, and to develop and demonstrate a process for near net shape part fabrication. Near net shape process development will explore forming by injection molding and consolidation by hot isostatic pressing or conventional sintering.

Technical Progress

Summary

Based on the data generated, it was decided that the  $\text{Si}_3\text{N}_4$ -SiC (whisker) system has the highest potential to meet the program goals on schedule. Further efforts were concentrated on the study of composite microstructure/property relations and characterization.

Work directed towards development of a low cost process for near net shape part fabrication has been initiated. Composites containing 30 v/o of whisker dispersoid have been successfully injection molded. Program execution is on schedule.

Material Studies

Based on the data generated to date, it was decided that the  $\text{Si}_3\text{N}_4$ -SiC (whisker) system has, at this stage of development, the highest potential to meet the program goals on schedule. The reactivity of TiC in the composite requires strict control of sintering parameters in order to obtain a composite of the required properties. In view of the program requirements, which are directed toward the development of a low cost process for near net shape part fabrication, this reduced flexibility further favors the  $\text{Si}_3\text{N}_4$ -SiC system.

Fracture toughness improvements, with dispersoid additions, deviate from predictions based on models which assume "continuum" matrices. The toughness of a single or polyphase polycrystalline ceramic matrix which exhibits to a large extent intergranular fracture is a function of the morphology and the size of grains. It follows then that dispersoids have to meet certain minimum size requirements (with respect to matrix) in order to effect toughening. In the process of densification, added dispersoids may also chemically or physically modify the development of the matrix microstructure, further contributing to deviations from toughening/strengthening predictions.

In order to evaluate the influence of matrix grain size on properties,  $\text{Si}_3\text{N}_4$ -SiC (whisker) composites have been hot pressed for extended time (400 min.) at sintering temperature to enhance  $\text{Si}_3\text{N}_4$  grain growth. As can be seen in Figure 1, extended sintering time results in a coarser  $\text{Si}_3\text{N}_4$ -base material grain structure, which in turn produces an increase in fracture toughness of the monolithic base material.

As with the monolithic  $\text{Si}_3\text{N}_4$ , variation in densification parameters of the composite is anticipated to result in differences in matrix microstructures and hence mechanical properties. It follows that the resultant matrix microstructures of the densified composites may not be identical in grain size distribution. Hence, the toughening behavior observed through whisker additions would not be expected to be a singular function such as that based on models which assume a homogeneous continuum matrix. The observed functional dependence consists of individual points on a family of toughening curves, each point depending on the microstructure of the individual composite matrix, since the degree of toughening achieved with a whisker dispersoid is dependent upon its size relative to the polycrystalline matrix grain size. Composites of finer matrix microstructure (shorter sintering time: solid line, Fig. 2) exhibit a high degree of toughening with an increased amount of dispersoid additions. The fracture toughness of composites held at sintering temperature for an extended time (400 min., dashed line, Fig. 2) shows higher toughness mainly due to coarsening of the matrix. The diminished contribution of dispersoid to fracture toughness improvement results from the decreased matrix-dispersoid size ratio.

In a material with typical intergranular fracture, the energy expended to propagate a crack is directly proportional to the amplitude and frequency of crack deflection by the grains. Based on geometrical considerations, the expected change in fracture toughness due to grain size can be approximated by the expression below:

$$\Delta K_{IC} = CK_{IC}^0 (D/D^0 - 1) \quad (1)$$

where  $C$  is a geometrical factor which, for an assumed close-packed arrangement of hexagonal, equisized particles (Figure 3), can be set at  $C = 0.25$ . The  $K_{IC}^0$  term represents the measured fracture toughness of the material with  $D^0$  average grain size. In the absence of other toughening effects and changes of fracture mode, the change of grain size from  $D^0$  to  $D$  would produce an increase/decrease of fracture toughness directly proportional to  $D/D^0$ . Based on the same assumptions, the fracture toughness of the composite can be estimated using appropriate fractional contributions of the matrix and dispersoid grain size.

In this study,  $\beta\text{-Si}_3\text{N}_4$  grain size (equivalent diameter) of the monolith and composite matrix was determined from transmission electron photomicrographs (25,000X magnification), with total counts ranging from 1500 - 2000 grains. The equivalent diameter of the dispersoid was  $1.95 \mu\text{m}$  corresponding to a whisker of an average length of  $6 \mu\text{m}$  and 12:1 aspect ratio (see Table 1). Measured values for grain size and fracture toughness are in fair agreement, suggesting that the increase in composite fracture toughness as well as that of the monolith is most likely derived from increased crack deflection due to enlarged grain size (effected by the addition of large whiskers in the case of composites).



Table 1: Characterization of SiC Whiskers  
(Average Diameter =  $0.5 \pm 0.2$ )

Processing Step	Average Length ( $\mu\text{m}$ )/Counts	Aspect Ratio
As-Received	$18 \pm 12/1574$	33
After Sedimentation	$18 \pm 9/1430$	33
After Homogenization	$5 \pm 3/1439$	10
Hot Pressed Composite	$6 \pm 3/1780$	12

Table 2: Comparison of Measured and Calculated  $K_{IC}$ -Based  
on Changes in Matrix Grain Size

Material	Average Grain Size <sup>+</sup>		$K_{IC}$ ( $\text{MPa}\cdot\text{m}^{1/2}$ )	
	$\text{Si}_3\text{N}_4$	Composite	Measured	Calculated*
AY6 <sup>1</sup>	$0.37 \pm 0.27$	0.37	$4.7 \pm 0.3$	4.7
AY6 <sup>2</sup>	$0.59 \pm 0.41$	0.59	$5.4 \pm 0.5$	5.4
AY6 + 10 v/o SiC	$0.36 \pm 0.24$	0.51	$4.4 \pm 0.1$	5.1
AY6 + 20 v/o SiC	$0.24 \pm 0.14$	0.58	$4.8 \pm 0.3$	5.4
AY6 + 30 v/o SiC	$0.36 \pm 0.24$	0.84	$6.4 \pm 0.5$	6.2
<sup>+</sup> Equivalent diameter				
*Calculated from Equation 1, the grain size of whisker used is				
$1.95 \mu\text{m } K_{IC}^0 = 4.7 \text{ MPa}\cdot\text{m}^{1/2}$				
<sup>1</sup> Hot pressed for 90 minutes				
<sup>2</sup> Hot pressed for 400 minutes				

Elevated temperature (1200°C) mechanical property characterization of  $\text{Si}_3\text{N}_4$  matrix composites containing SiC whiskers has shown that the whisker additions increase both fracture toughness and strength (Figure 4). Examination of the controlled surface flaw specimens used for fracture toughness determinations shows that the enhanced mechanical properties at 1200°C are reflected in a reduced susceptibility to subcritical crack growth for the composites, compared to the monolithic base materials (Table 3). In all cases examined to date the whisker-containing composites experience substantially less slow crack growth prior to fast fracture at 1200°C. This phenomenon is attributed to enhanced whisker pullout mechanism at high temperature.

Table 3: Evaluation of Subcritical Crack Growth of AY6 and AY6-Based Composites at 1200°C

	Increase in Surface Flaw Crack Dimensions(%)	
	<u>a</u>	<u>c</u>
AY6	82	229
AY6 + 10 v/o SiC whiskers	49	100
AY6 + 20 v/o SiC whiskers	33	94
AY6 + 30 v/o SiC whiskers	63	139

a = minor elliptic axis of precrack

c = 1/2 major elliptic axis of precrack

Testing to evaluate the effects of oxidation on the strength of these materials has been completed. Test bars of AY6 and AY6-containing 30 v/o SiC whiskers (Arco SC-9) were oxidized at 1200°C for 100 hours and, subsequently, broken at room temperature in standard four-point loading. The results (Table 4) show that the MOR of the composite was reduced slightly (12%) by the oxidation, while that of the monolithic AY6 was unaffected. However, even after oxidation, the strength of the composite is higher (10%) than that of the monolith. Further extended time oxidation studies are in progress.

Table 4: Room Temperature MOR of Standard and Oxidized Silicon Nitride-Based Materials

<u>Material</u>	<u>Standard</u>	<u>Oxidized</u>	<u>Change</u>
AY6	773 ± 67	791 ± 66	+2%
AY6 + 30 v/o SiC whiskers (SC-9)	975 ± 39	859 ± 117	-12%

#### Process Development

Work on the injection molding process development was initiated. The approach is given in Figure 5.

Batches of AY6-SiC (30 v/o Tateho) have been compounded at four loading levels of solids for trial injection molding. The loading levels are 54, 56, 58, and 60 v/o solids.



Table 5 describes the results of the compounding, injection molding and binder burnout trials to date. In the initial runs, injection molding of the 58 v/o material did not fill the bar cavity uniformly. The 54 v/o material showed complete uniform filling of the cavities in the 4-bar die (Figure 6).

Table 5: Compounding and Molding Behavior of AY6 Silicon Nitride + 30 v/o Tateho SiC Whisker Composite

Solids Loading (volume %)	Compounding Behavior	Molding Behavior	Burnout Behavior
60	Difficult	N/D	N/D
58	Acceptable	Difficult	Good
54	Good	Good	Good

N/D = Not Determined

The bars from these runs were successfully put through the binder burnout cycle and will be encapsulated for HIPing and sintering studies. SEM examination of fracture surfaces of the burned out materials showed the presence of intact whiskers protruding from the matrix material (Figure 7).

#### Status of Milestones

Milestone 122302 and 122303 have been completed. Overall program execution is on schedule.

#### Publications

None.

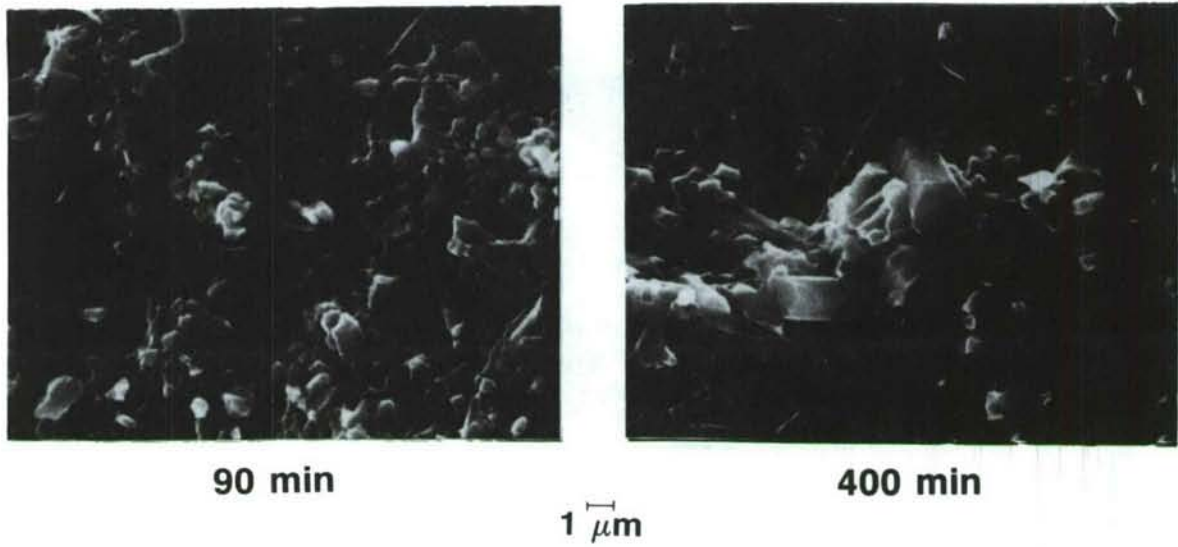


Figure 1: Fracture surface of Silicon Nitride Base Material Held at at Sintering Temperature 90 min. and 400 min.



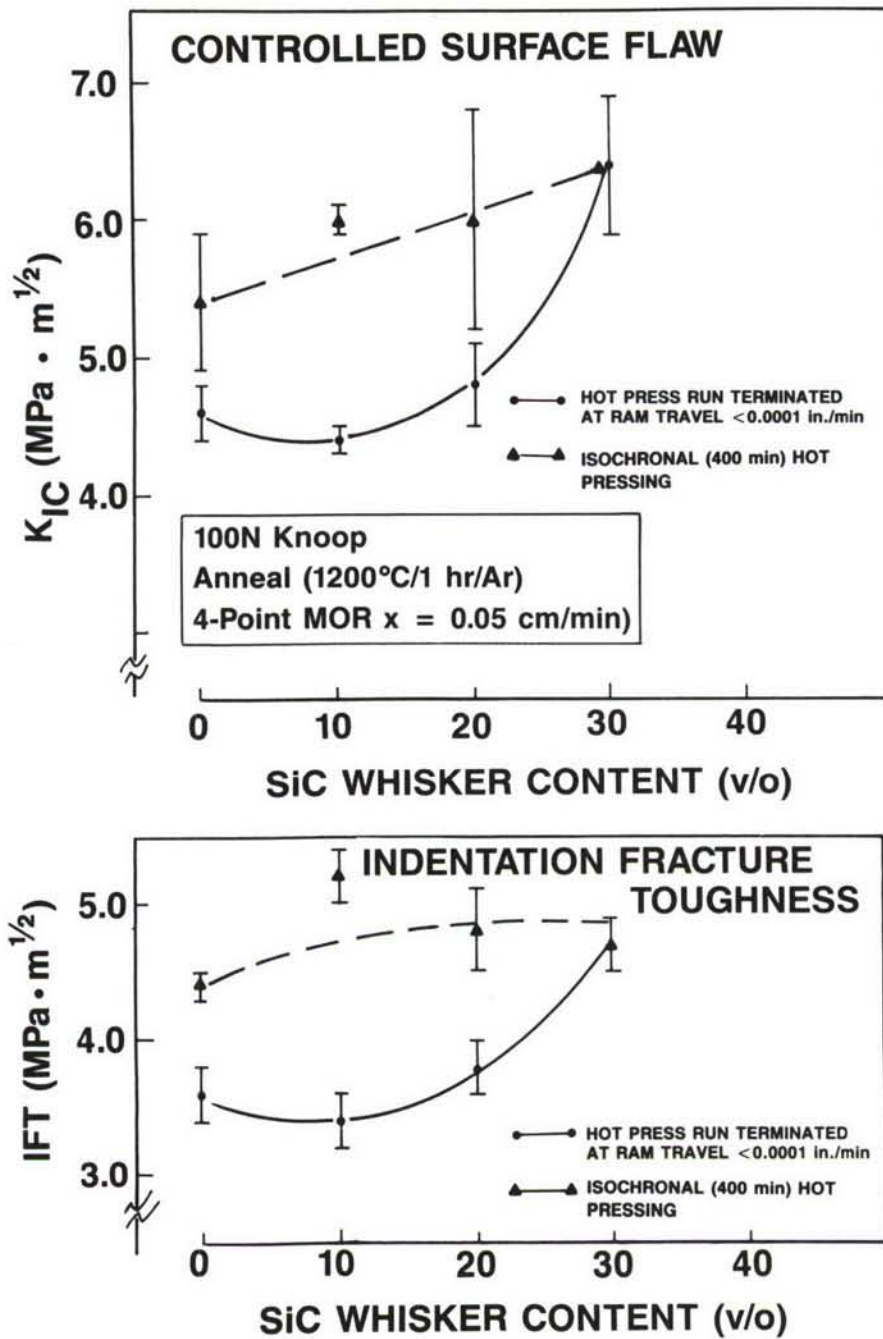


Figure 2: Fracture Toughness of  $\text{Si}_3\text{N}_3$ -SiC (Whisker) Composites

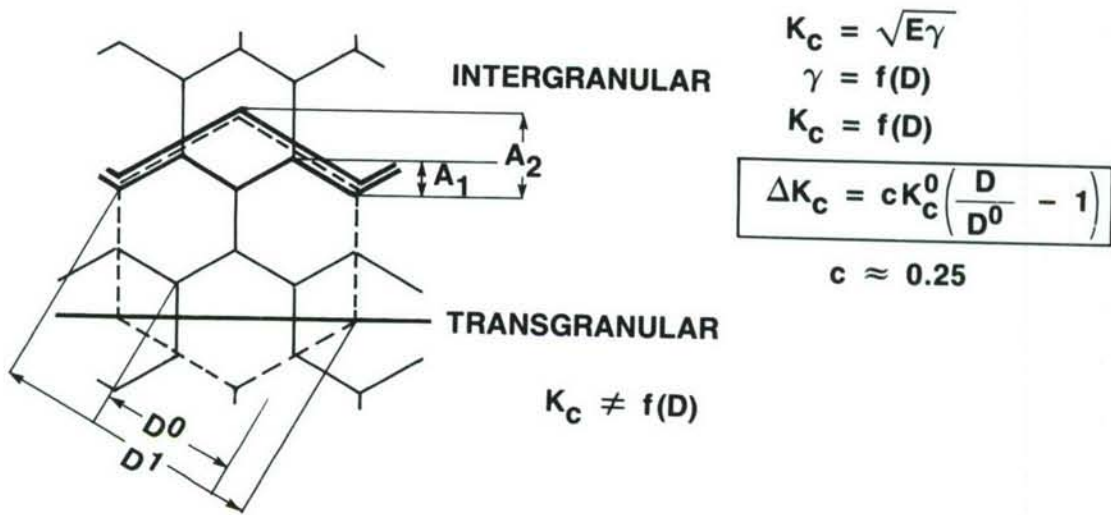


Figure 3: Model of Grain Size Effect on Crack Deflection Amplitude and Frequency

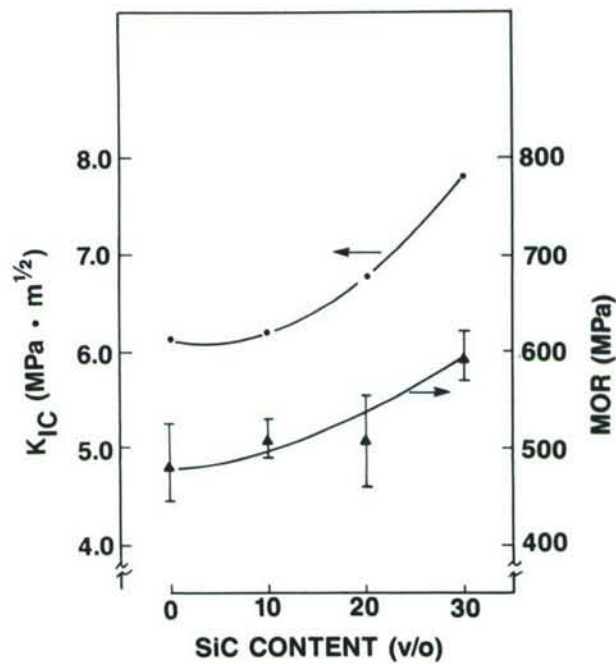


Figure 4: Modulus of Rupture (MOR) and Fracture Toughness ( $K_{IC}$ ) of  $Si_3N_4$ -Based Ceramics at 1200°C



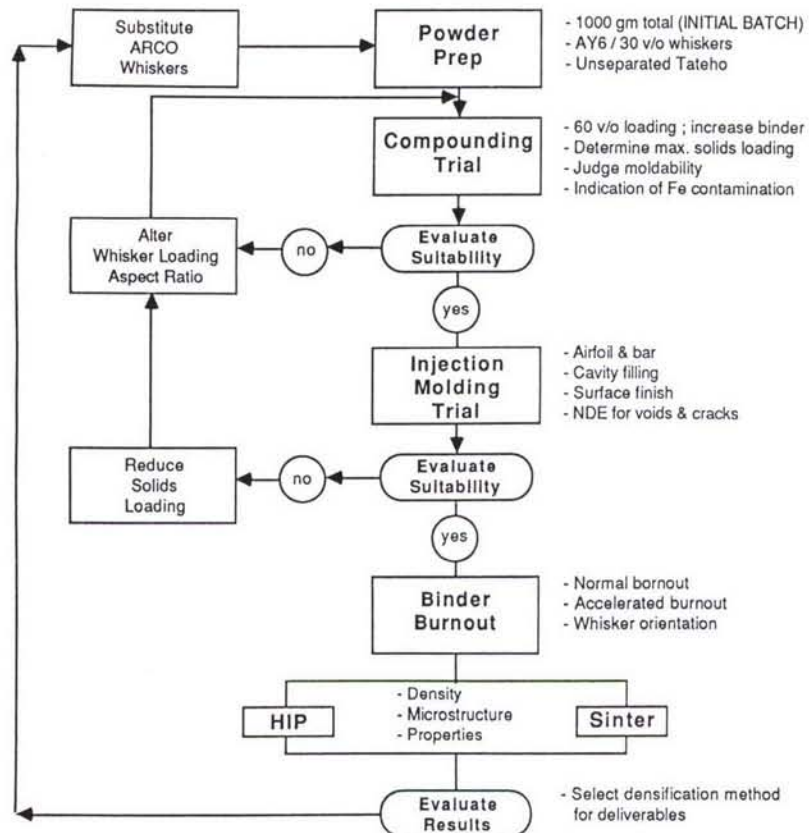


Figure 5: Process Development Approach for Injection Molding  $\text{Si}_3\text{N}_4$ -SiC (Whisker) Composites

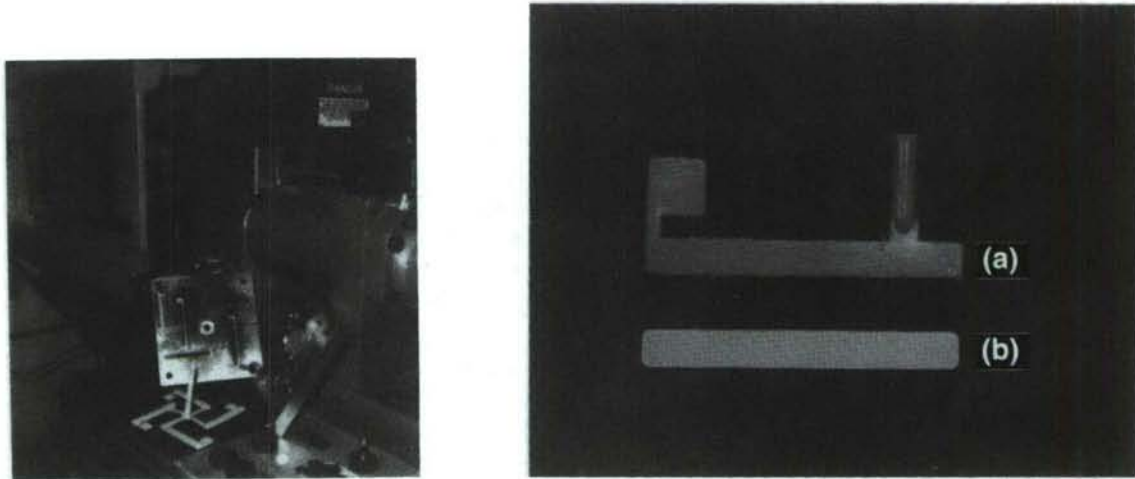


Figure 6: A. Four Bar Injection Molding Die and B.  $\text{Si}_3\text{N}_4$ -30 v/o SiC (Whisker) Composite Test Bars a) as Molded and b) Burned Out

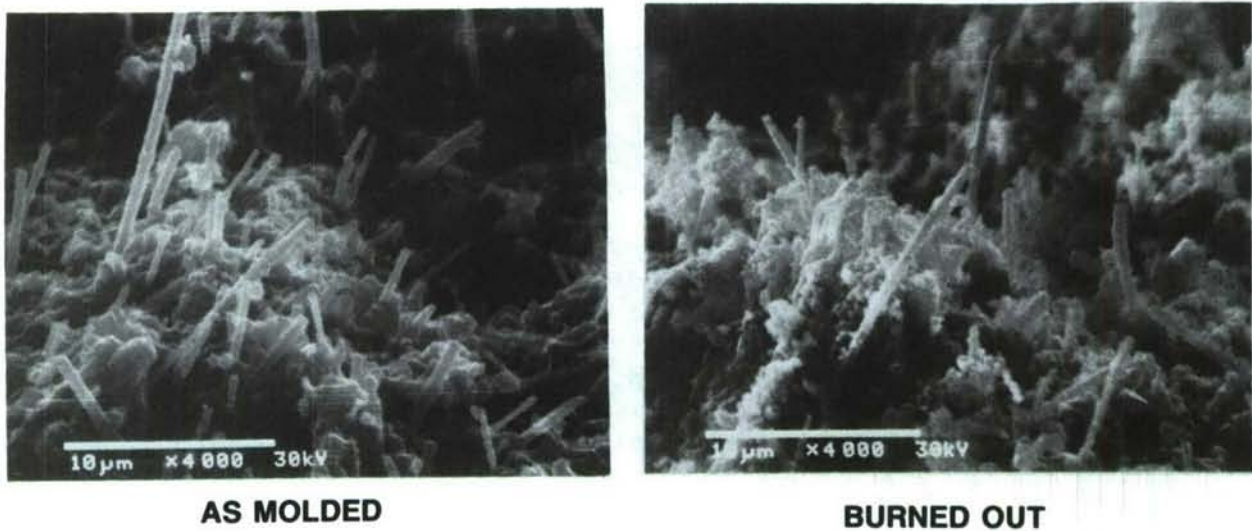


Figure 7: Fracture Surfaces of Injection Molded  $\text{Si}_3\text{N}_4$ -30 v/o SiC (Whisker) Composites a) as Molded and b) After Binder Burnout

SiC-Whisker-Toughened Silicon Nitride

K. Haynes, M. Martin, and H. Yeh (AiResearch Casting Company)

Objective/scope

The objective of this twenty-four month program is to develop the technology base for fabricating a ceramic composite consisting of silicon carbide whiskers dispersed in a dense silicon nitride matrix. This is to be accomplished by slip casting as the green shape forming method, and HIP'ing or sinter/HIP as the densification method. An iterative experimental approach is used throughout the entire program.

The original goal of the program is a two-fold increase in fracture toughness over the unreinforced silicon nitride matrix (92% GTE Sylvania (GTE) SN-502  $\text{Si}_3\text{N}_4$  + 6%  $\text{Y}_2\text{O}_3$  + 2%  $\text{Al}_2\text{O}_3$ , designated as Code 2) without a degradation of other properties. AiResearch Casting Company (ACC) is responsible for developing the fabrication techniques and providing specimens to Garrett Turbine Engine Company (GTEC). GTEC is responsible for determining the physical and mechanical properties, including fracture toughness, and for evaluating the microstructure. Allied-Signal Engineered Materials Research Center (EMRC) provides analytical assistance to ACC.<sup>1</sup>

Technical/progressMaterials and Procedures

Test cylinders containing 20% ARCO SC-9, 30% Tateho SCW #1, and 20% Tateho SCW #1-S silicon carbide whiskers in the silicon nitride matrix (two cylinders of each) were fabricated via slip casting along with baseline monolithic silicon nitride cylinders. All cylinders have been processed through presintering and niobium encapsulation. Half of the  $\text{Si}_3\text{N}_4/\text{SiC}$  composite cylinders have been HIP'ped and sent to GTEC for machining and testing. The remaining  $\text{Si}_3\text{N}_4/\text{SiC}$  composite samples and the baseline  $\text{Si}_3\text{N}_4$  samples await HIP.

The niobium encapsulated samples (baseline Code 2  $\text{Si}_3\text{N}_4$ ,  $\text{Si}_3\text{N}_4/20\%$  Tateho SCW #1-S,  $\text{Si}_3\text{N}_4/30\%$  Tateho-SCW #1, and  $\text{Si}_3\text{N}_4/20\%$  ARCO SC-9) sent to GTEC from ACC were HIP'ped at 1750°C for 4 hours. The baseline billet had a density of only 2.75 g/cc, while the composite billets were HIP'ped to between 3.23 and 3.24 g/cc. The composite billets were to be machined into test bars for strength and fracture toughness measurements. The baseline monolithic  $\text{Si}_3\text{N}_4$  billet was not to be machined at this time due to its low density. Additional baseline billets will be processed to optimize the density of the baseline  $\text{Si}_3\text{N}_4$ .

<sup>1</sup> Drs. K. Karasek and S. Bradley, Engineered Materials Research Center, Allied-Signal Corporation.



Two samples previously sent to GTEC (#11074 containing 20% ARCO SC-9 SiC whiskers and #0125603 containing 30% Tateho SCW #1 SiC whiskers) were machined for room temperature flexural strength and fracture toughness evaluation. These two billets were HIP'ed at 1800°C and 28 ksi for 2 hours. Flexural strength testing was conducted at GTEC using 2" X 0.250" X 0.125" test bars. Fracture toughness testing was conducted at the University of Washington, using 2" X 0.250" X 0.250" chevron notch bend bars. The results are summarized in Table 1. The flexure strength results correlated well with the microstructures observed in metallographic analysis. ARCO strength values may be due partially to the possible preferred orientation of the whiskers along the length of the test bar. Fractography was conducted on all specimens (up to 40X) using an optical binocular microscope. Both tensile face and internal fracture origins were observed from the ARCO composite. The Tateho composite showed failure at inclusions similar to those identified using metallography. SEM analysis conducted at GTEC will be summarized later in this report.

TABLE 1  
FLEXURAL STRENGTH/FRACTURE TOUGHNESS

Material	Density, g/cm <sup>3</sup>	Strength, ksi	Fracture Toughness (Chevron Notch), ksi·in. <sup>1/2</sup>
Sintered Code 2	3.25	100	5.37
HIP'ed Code 2/20 w/o ARCO	3.24	131.5	6.45
HIP'ed Code 2/30 w/o Tateho	3.23	63.1	5.08

Based on suggestions from Dr. R. Bradt and his staff at the University of Washington, GTEC has fabricated a new fracture toughness test flexure fixture and has developed new procedures for machining the notch, both aimed at increasing the reproducibility and reliability of chevron notch fracture toughness tests.

A 1 kg sample of Tokai Carbon silicon carbide whiskers (brand name "Tokawhisker") was received by ACC. In addition, ACC received from GTEC a quantity of ARCO SC-9 silicon carbide whiskers. Composite formulations containing GTE Si<sub>3</sub>N<sub>4</sub> with 20% Tokai Carbon "Tokawhisker" silicon carbide whiskers and GTE Si<sub>3</sub>N<sub>4</sub> with 20% ARCO SC-9 silicon carbide whiskers were produced. Milling times used to incorporate the silicon carbide whiskers to the Si<sub>3</sub>N<sub>4</sub> were reduced from 2 hours to 15 minutes.

Slips have been prepared from the composite powder. Billets have been cast from both the ARCO and the Tokai silicon carbide whiskers.

Information from ORNL has indicated that J. M. Huber has produced a silicon carbide whisker with good potential. Inquiries were made by ACC to acquire a sample of Huber's silicon carbide whiskers for evaluation. ACC will receive an initial sample of silicon carbide whiskers by the second or third week of November.

## ANALYSIS

Extensive analysis of composite materials in various stages of processing has been performed by GTEC and EMRC. The majority of the following analysis presented will focus on presintered and HIP composite microstructures. Additional morphology work done on silicon carbide whiskers will also be presented.

### Presintered Microstructure

EMRC analyzed the microstructure of both ARCO SC-9/Si<sub>3</sub>N<sub>4</sub> and Tateho SCW #1/Si<sub>3</sub>N<sub>4</sub> composites in a presintered state.

The ARCO presintered sample contained much porosity and a very fine structure. The microstructure exhibits a grain size of 0.05-0.2 micron. Grain boundary pockets tended to be higher in Y/Si ratio than the sintered sample. However, the sintering aids tended to be present in a variety of Y-Al-Si combinations; this reflects the distribution of the additives prior to full sintering, but during liquid phase sintering a more homogeneous composition results. As with the sintered sample some degraded regions were present; these were non-crystalline and rarely were associated with the sintering aids. There was some bonding between the SiC whiskers and the Si<sub>3</sub>N<sub>4</sub>.

The Tateho presintered composite had a much different microstructure. There were very few regions exhibiting the initial stages of a fine microstructure. Instead, the silicon nitride was irregularly shaped and joined to other particles at a neck. There were 1-10 micron size dense Si-rich and sintering aid particles. Outside of these dense particles the sintering aids were not observed. In addition, the SiC whiskers seemed to be degrading as some have through holes and others appeared to be reacting with the Si<sub>3</sub>N<sub>4</sub>.

Since the presintered specimen containing Tateho whiskers showed extensive whisker degradation, EMRC, to simulate the presintering environment, conducted an experiment to see if the whiskers were susceptible to nitridation at the temperature and atmosphere involved. Tateho SCW #1 whiskers were heated in one atmosphere of flowing nitrogen at 1550°C ±25°C for 2 hours. Ramp times up and down were 8 hours each (with flowing nitrogen atmosphere maintained). The whiskers were then submitted for X-ray diffraction. The X-ray results indicated a sizable amount of Si<sub>3</sub>N<sub>4</sub> formation. A similar experiment performed with ARCO SC-9 whiskers showed no detectable Si<sub>3</sub>N<sub>4</sub>.



## HIP Microstructure

At GTEC, metallographic analysis on polished sections was conducted on billets #11074 (20% ARCO/Si<sub>3</sub>N<sub>4</sub>) and #0125603 (30% Tateho/Si<sub>3</sub>N<sub>4</sub>). Microstructures taken were representative of the 2" test bars cut lengthwise from cylindrical billets. Both ARCO (Figure 1) and Tateho (Figure 2) samples show good SiC whisker distribution in the Si<sub>3</sub>N<sub>4</sub> matrix. (Some SiC whisker agglomeration was noted in the Tateho sample). The ARCO sample showed slight preferred orientation in the lengthwise direction of the test bar, while the Tateho sample retained little or no whisker aspect ratio characteristics, suggesting severe whisker degradation/breakage. In addition, the Tateho sample contained inclusions not shown in the ARCO sample.

SEM analysis was also conducted at GTEC on composite specimens from billets #11074 (20% ARCO SC-9/Si<sub>3</sub>N<sub>4</sub>) and #0125603 (30% Tateho SCW #1/Si<sub>3</sub>N<sub>4</sub>). The analysis was conducted on the fracture surfaces of flexure strength and fracture toughness specimens. The composite microstructures showed the SiC whiskers in the ARCO composite to be intact, having some degree of preferred orientation. The whiskers in the Tateho composite degraded to the point of having a significant reduction in the whisker aspect ratio characteristics or the elimination of whisker aspect ratio during processing. The microstructure of both composites contained regions of unreinforced matrix which appeared to be large Si<sub>3</sub>N<sub>4</sub> grains 20 to 50 microns in diameter.

The fracture surfaces of the flexure strength specimens did not indicate any evidence of whisker pullout on the fracture surface. SiC whiskers were not observed on the fracture surfaces of either composite. The failure origins were primarily surface flaws in the case of the ARCO composite which exhibited 131.5 ksi strength (Figure 3). The Tateho composite exhibited much lower strength (65 ksi) which was associated with the gross flaws such as internal porosity (Figure 4) and large Si<sub>3</sub>N<sub>4</sub> grains (Figure 5).

The fracture surfaces of the ARCO fracture toughness specimens did indicate some evidence of whisker pullout/crack deflection (Figure 6). These fracture characteristics explain the 20% improvement in toughness ( $K_{I0} = 6.45 \pm 0.53 \text{ ksi}\cdot\text{in.}^{1/2}$  by chevron notch) compared to the toughness of monolithic Code 2 Si<sub>3</sub>N<sub>4</sub> ( $5.39 \pm 0.52 \text{ ksi}\cdot\text{in.}^{1/2}$  by chevron notch). All whiskers observed on this particular fracture surface were perpendicular to the fracture plane. No whiskers were found lying in the fracture plane. This suggests the possibility of preferred orientation in the ARCO composite.



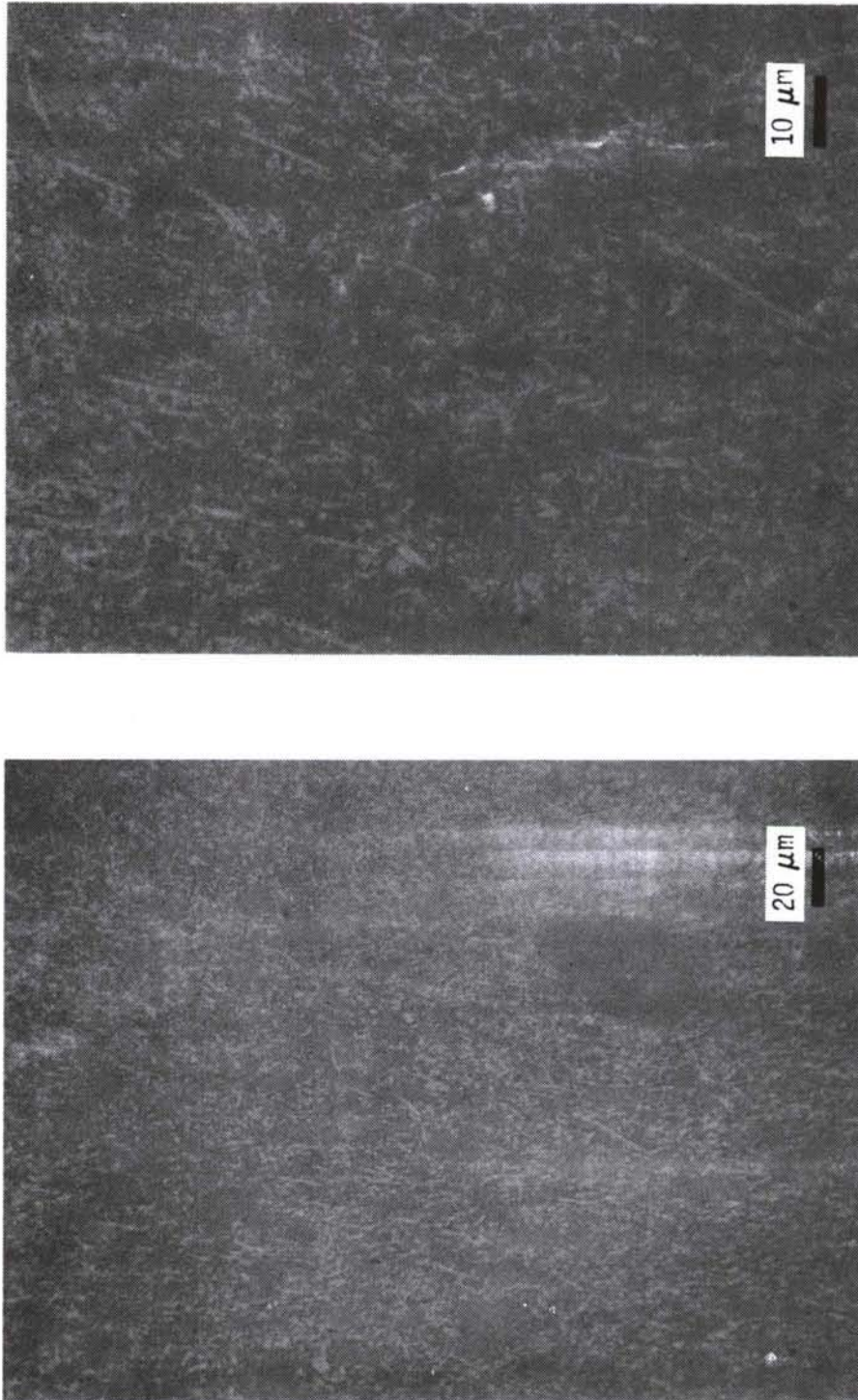


Figure 1. 20% ARCO SC-9/Si<sub>3</sub>N<sub>4</sub> (Billet #11074)

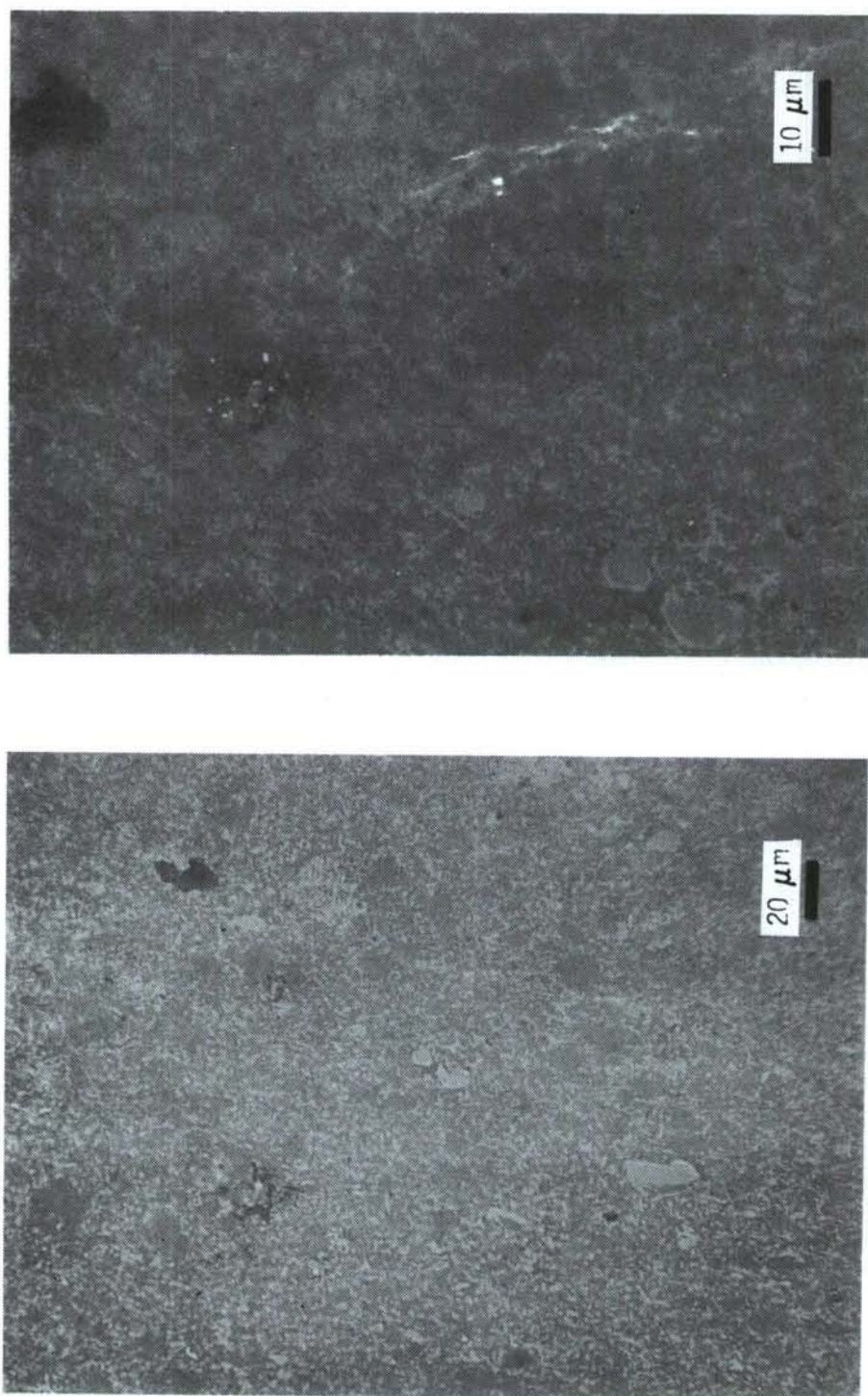


Figure 2. 30% Tatanite SCW #1/Si<sub>3</sub>N<sub>4</sub> (Billet #0125603)



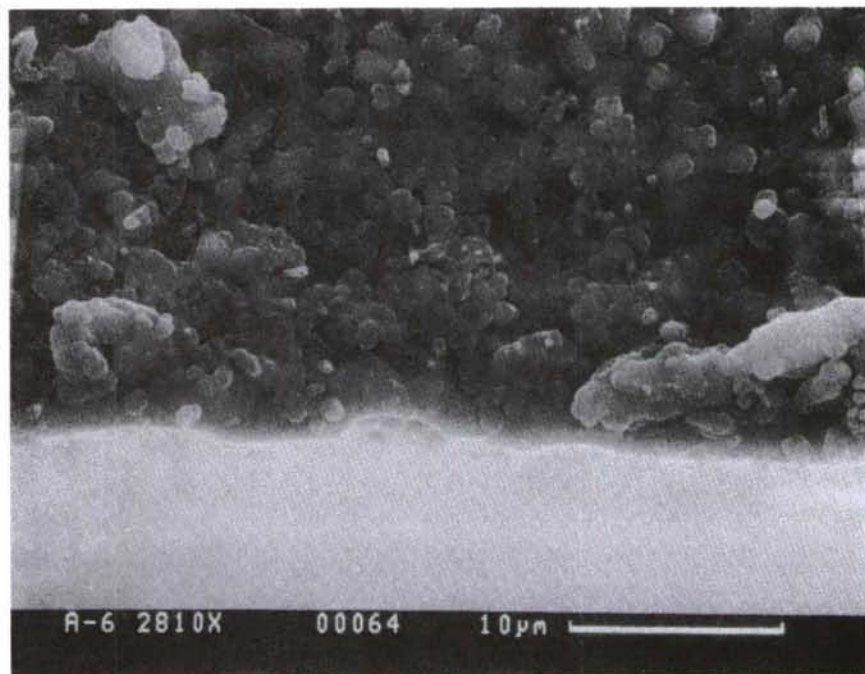
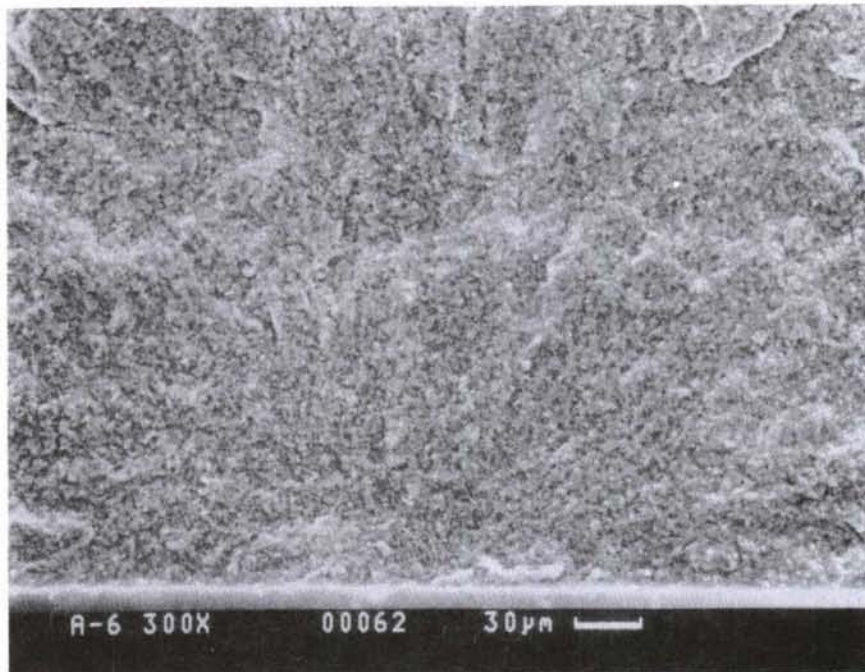


Figure 3. ARCO SC-9 Flexural Strength Samples Showing Failure at the Tensile Surface



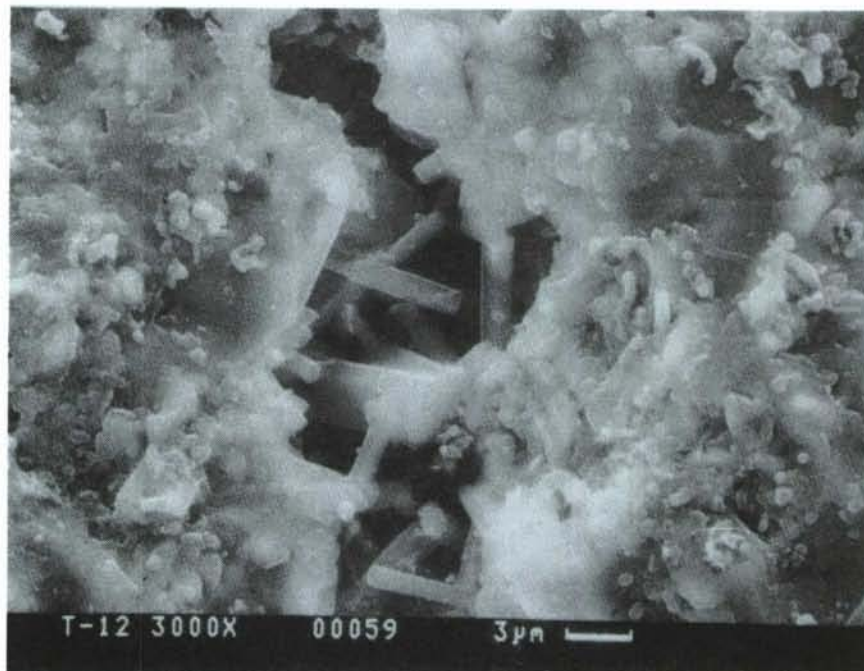
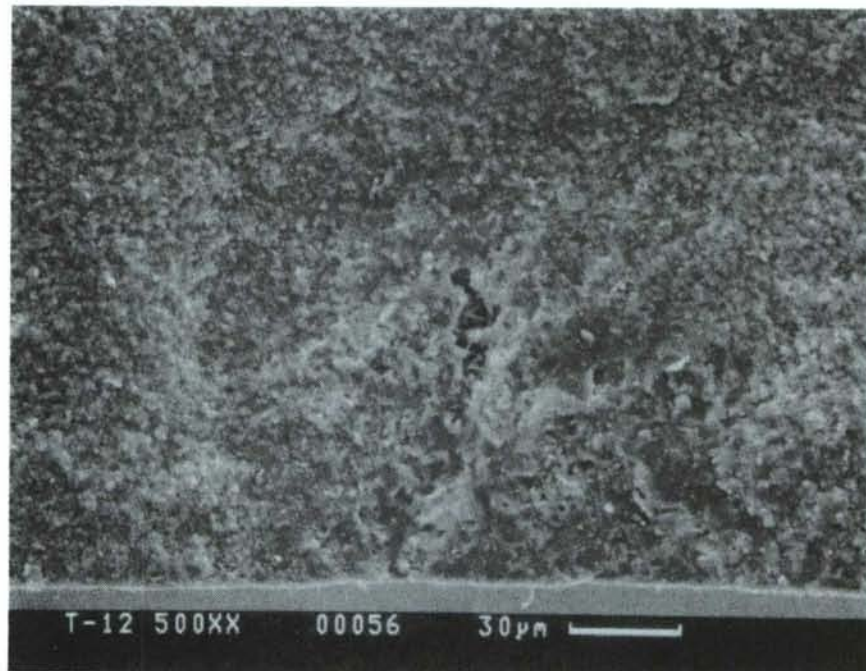


Figure 4. Tateho SCW #1 Flexural Strength Samples Showing Internal Porosity on the Fracture Surface

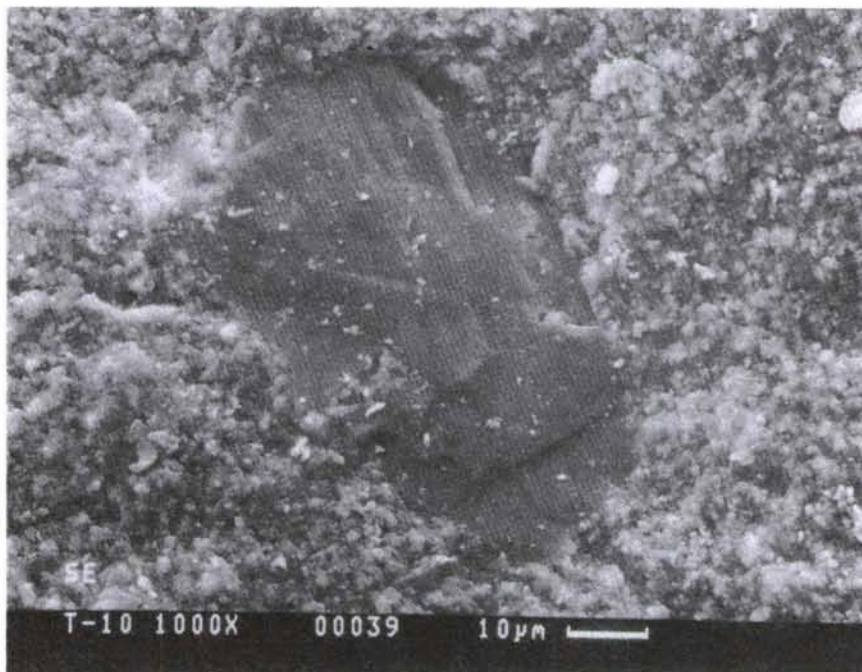
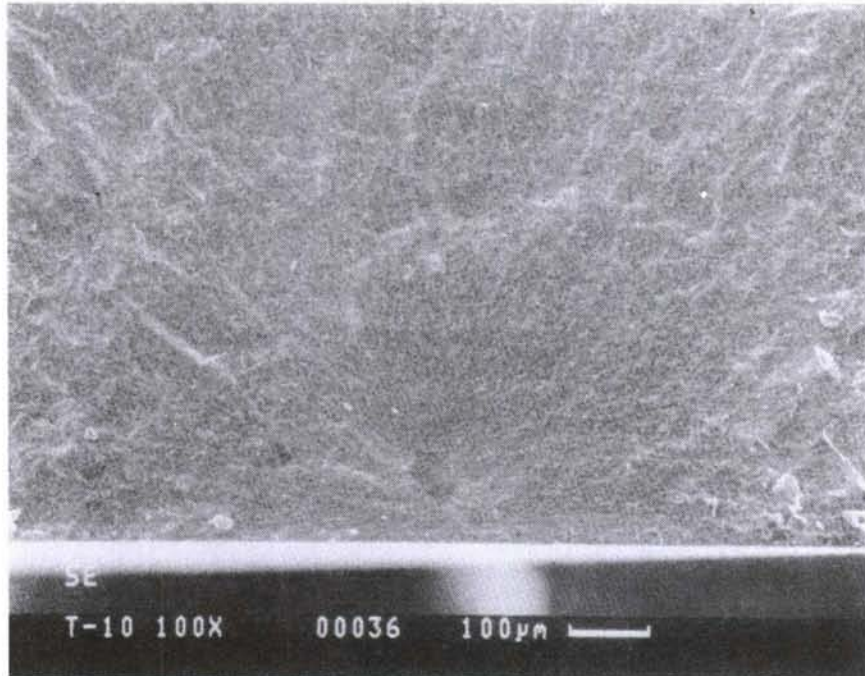


Figure 5. Tateho SCW #1 Flexural Strength Samples Showing Large  $\text{Si}_3\text{N}_4$  Grains on the Fracture Surface

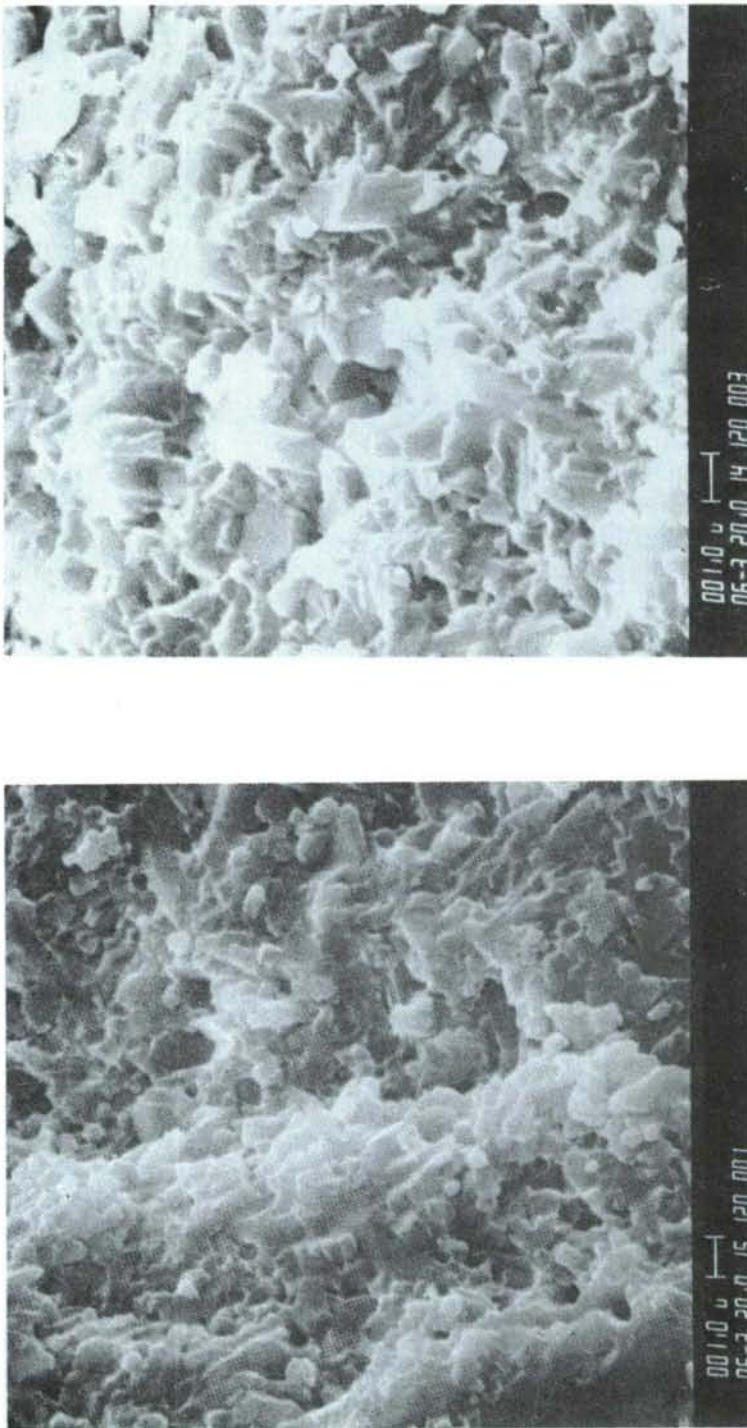


Figure 6. ARCO SC-9 Flexural Strength Samples Showing Crack Deflection/Whisker Pullout



The results from the Tateho composite were not as encouraging. Whiskers were not observed on the fracture surfaces (Figure 7). The speculation is that these whiskers were significantly degraded (which agrees with the metallography results) and cannot be distinguished from among the surrounding grain boundary phases.

EMRC performed Scanning Transmission Electron Microscopy (STEM) analysis on the fully processed 20% ARCO composite sample (Figures 8 through 13). The grain size was about  $0.5\ \mu\text{m}$ . The grain boundary pocket size was less than  $0.2\ \mu\text{m}$ . Compositional analysis of the pocket indicated  $13.7 \pm 2.4$  at. % (Atomic %) Al,  $67.8 \pm 2.8$  at. % Si and  $18.5 \pm 1.1$  at. % Y. The longest SiC whisker observed was  $5\ \mu\text{m}$ . Most whiskers observed were much shorter, possibly due to sample preparation/orientation.

Non-crystalline regions were found throughout, appearing to be associated with degradation of SiC whiskers and  $\text{Si}_3\text{N}_4$ . EMRC's hypothesis is based upon the presence of some very fine whiskers; the micro-crystalline areas could not be unambiguously identified as either  $\text{Si}_3\text{N}_4$  or  $\text{SiO}_2$ . Non-crystalline films were found surrounding all whiskers. The Al content in the  $\text{Si}_3\text{N}_4$  grains was quite varied ( $1.4 \pm 1.1$  at. %); about 25% of the grains contained no Al. Approximately 25% of the SiC whiskers had detectable Al.

#### Whisker Morphology

EMRC has done additional work on SiC whisker morphology using STEM. (A summary comparing whisker morphology is given in Table 2.) The ARCO SC-9 SiC whiskers exhibited a variety of morphologies, consisting of stacking faults lying normal to the whisker axis. The spacings between faults ranged from 2-200 nm. The diameters of the whiskers also varied from 50 nm to 0.5 micron. Many whiskers had surfaces that undulated coincident with the stacking faults. Other ARCO whiskers had smooth surfaces, while some had very irregular stackings. On occasion a branched whisker was noted. There also was a considerable amount of amorphous material; some contained low levels of Ca. Overall, the ARCO whisker morphology was more consistent than those from Tateho and Tokai.



Figure 7. Tateho SCW #1 Flexural Strength Sample Showing No Observed Whisker Pullout or Crack Deflection

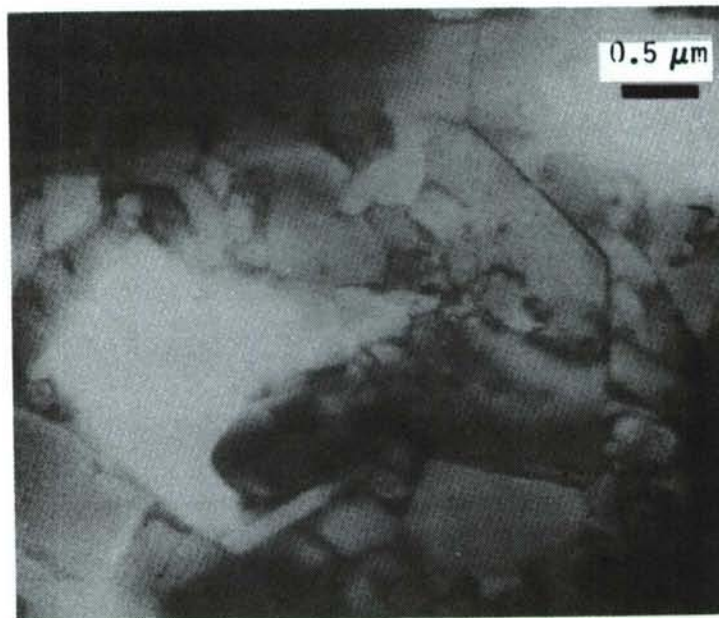


Figure 8. General View of SiC Whisker Reinforced  $\text{Si}_3\text{N}_4$

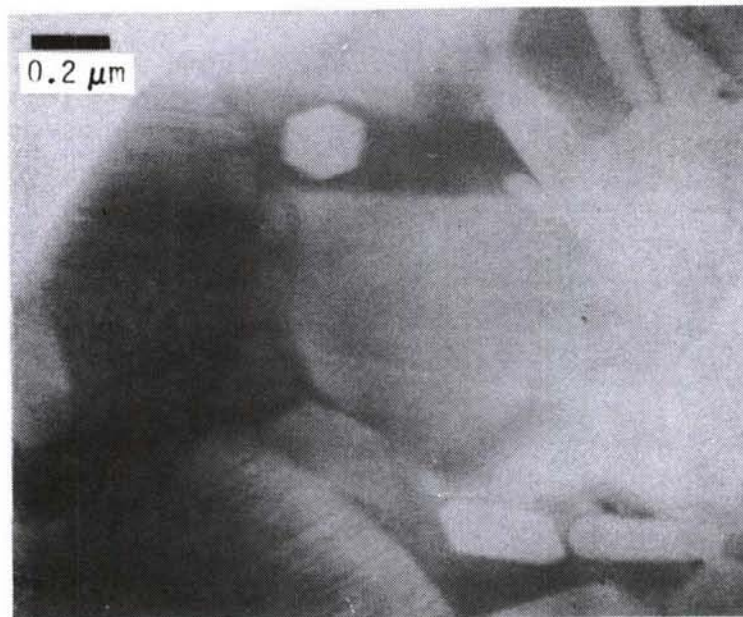
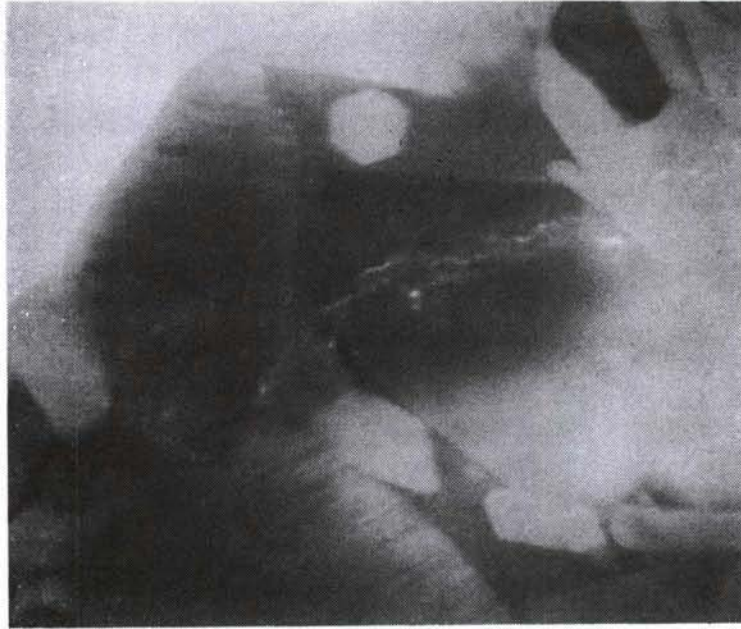


Figure 9. Non-Crystalline Grain Boundary Pockets as Demonstrated by Tilting the Sample



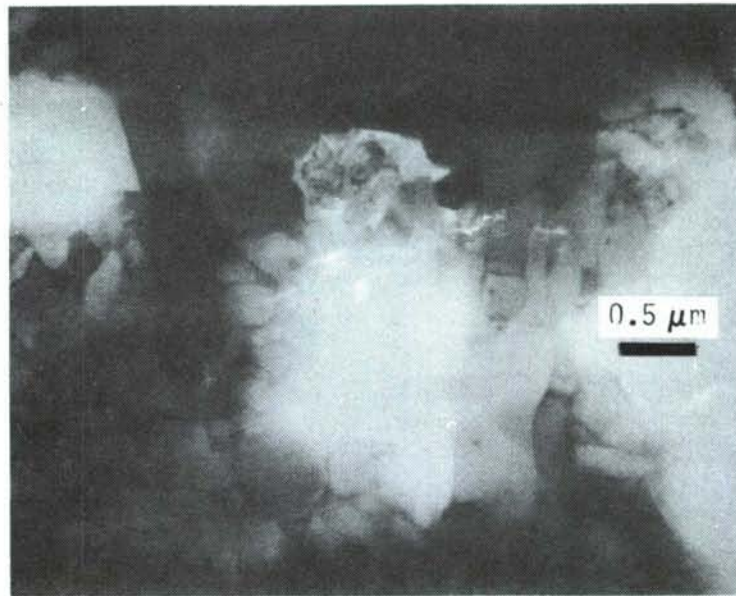


Figure 10. Degraded Area in SiC Whisker Reinforced  $\text{Si}_3\text{N}_4$

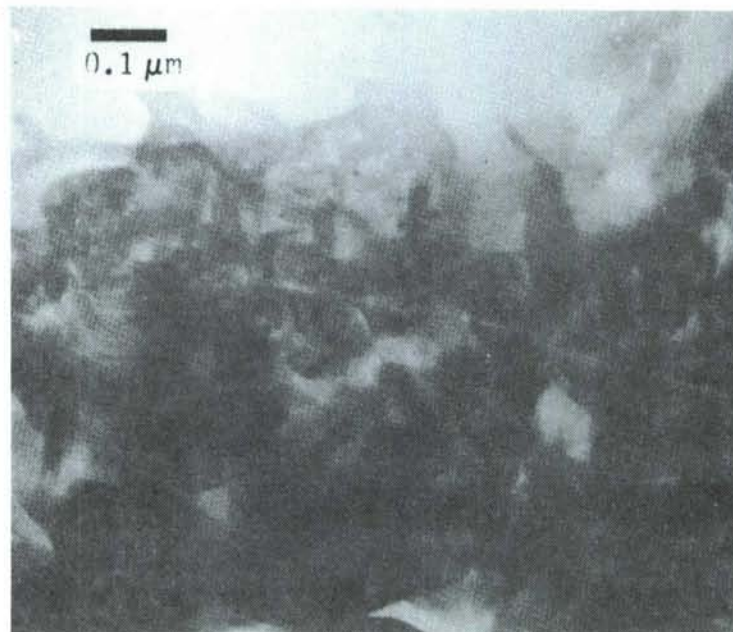


Figure 11. Fine SiC Whiskers in Degraded Area

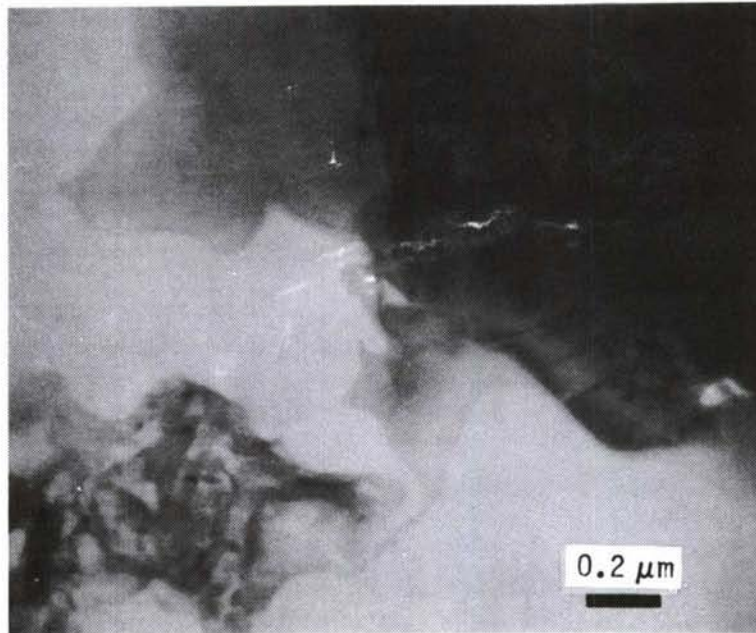


Figure 12. Start of Degradation of SiC Whisker and Si<sub>3</sub>N<sub>4</sub> Grain

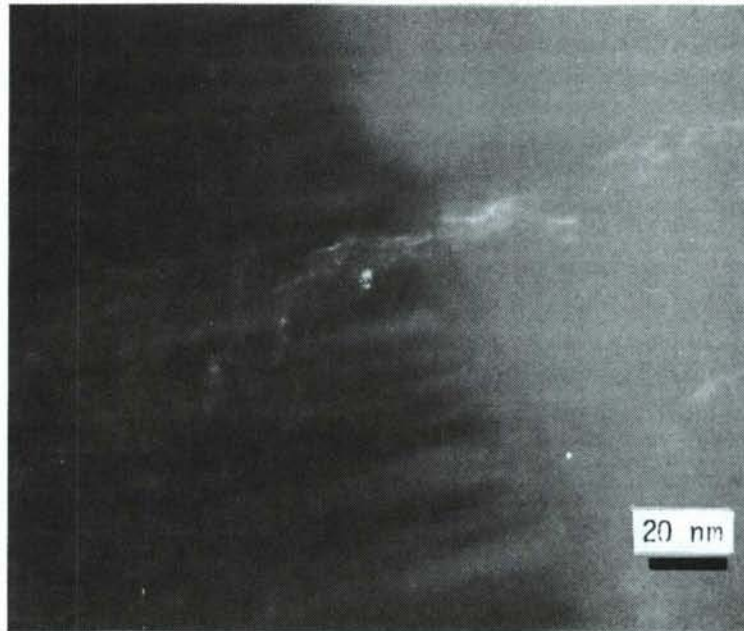


Figure 13. Y-Rich Layer between SiC Whisker and Si<sub>3</sub>N<sub>4</sub> Grain

The Tateho #1 and #1-S SiC whiskers tended to have smooth surfaces; stacking faults were still commonly observed (Figure 14). However, many whiskers had a highly irregular structure and appeared quite contorted (Figure 15). The diameter of the whiskers ranged from 50 nm to 1 micron. A few branched structures were also found. The debris was both micro-crystalline and non-crystalline. Some whiskers appeared hollow or had axial defects (Figures 14 and 15). The Tateho #1 whiskers seemed to have substantially fewer defects and debris than the Tateho #1-S sample.

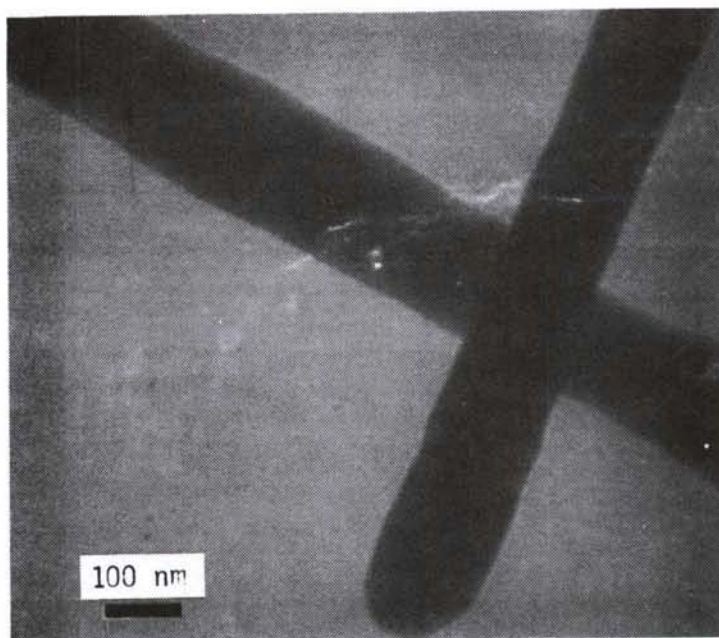
The Tokai SiC whiskers consisted of both smooth and irregularly shaped whiskers. The smoothly shaped whiskers often varied in diameter. The irregularly shaped whiskers were often extensively contorted. The diameter of the whiskers varied from 50 nm to 0.5 micron. Stacking faults lying normal to the whisker axis were common but some areas exhibited no stacking faults. Some branching was present as well; non-crystalline debris was found also. Small crystallites (10 nm) rich in Co were noted; these most likely were the catalyst.

#### PROBLEMS ENCOUNTERED

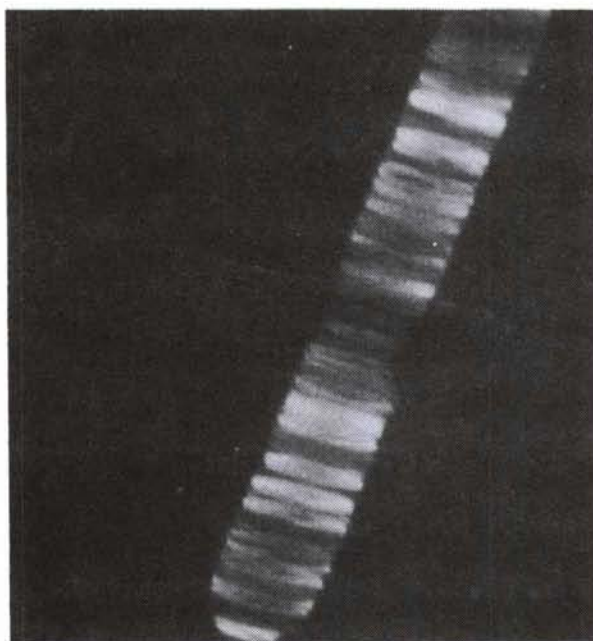
##### Supply of ARCO SC-9 SiC Whiskers

In the original scope of the program, the primary source of SiC whiskers was to be ARCO Metals, utilizing the ARCO Silar SC-9 SiC whisker. Alternate sources of SiC whiskers could be incorporated into the program parallel with the ARCO SC-9. ARCO's decision to initially





Bright Field



Dark Field

Figure 14. STEM of Tateho SCW #1 SiC Whiskers Showing Stacking Faults Lying Normal to (111) Whisker Axis

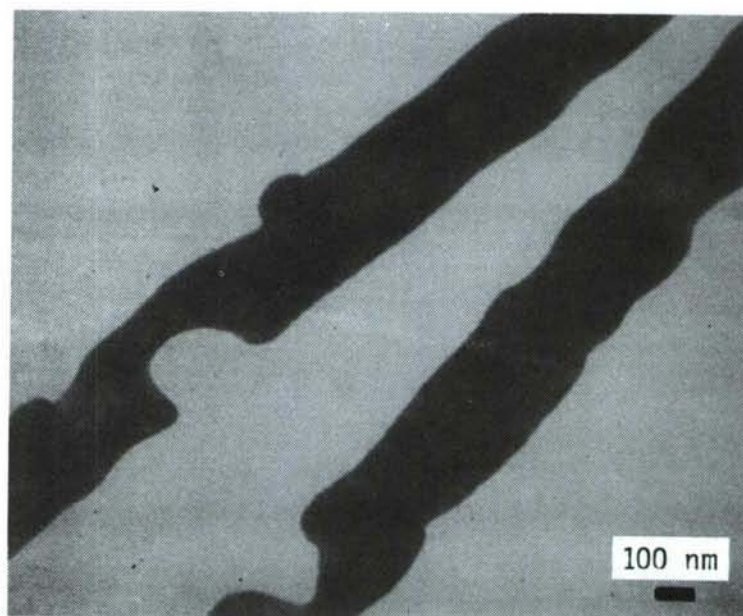
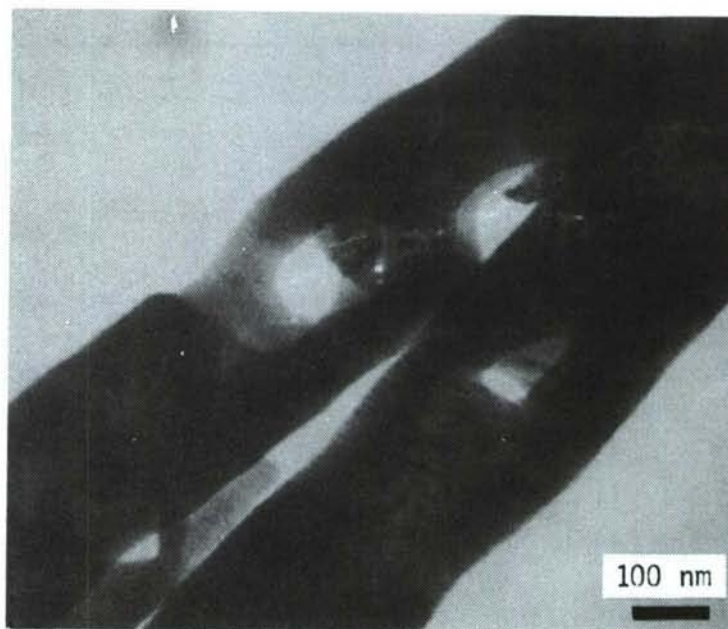


Figure 15. STEM of Tateho SCW #1 Whiskers  
Showing Irregular, Contorted Structure

TABLE 2  
STEM COMPARISON OF SiC WHISKERS

	ARCO SC-9	Tateho SCW #1 and SCW #1-S1	Tokai
Morphology consistency	High	Low	Moderate
Whisker diameter, $\mu\text{m}$	0.05 - 0.5	0.05 - 1.0	0.05 - 0.5
Stacking faults	5	5	4
Smooth surface	4	5	4
Undulation	4	3	2
Irregularities/contortions	2	4	4
Branching	1	2	2
Debris	B2	A/B2	A/B2
Axial holes	NA3	2	NA3

Scale based on 1  $\rightarrow$  least, 5  $\rightarrow$  most.

NOTES: 1 SCW #1 has fewer defects and debris than SCW #1-S  
 2 A - Crystalline debris; B - Non-crystalline debris  
 3 NA - Not available



restrict SiC whisker availability and eventually to discontinue supplying SC-9 SiC whiskers, experimental iterations involving ARCO SC-9 had to be restricted. Tateho SCW #1 and SCW #1-S SiC whiskers were the only commercially available SiC whiskers.

#### HIP Processing Problems

The more recent property results seen with the processed samples have been encouraging. However, the malfunctioning of the in-house 30 ksi HIP unit has resulted in loss of samples and delay in progress. In addition, as indicated in Table 3, glass and tantalum encapsulation has shown poor reliability. Niobium can fabrication has shown better reliability, but delivery has taken up to 10 weeks. Thus, the processing of samples through HIP has been slow.

TABLE 3

SUMMARY OF HIP EFFORTS (FEBRUARY 1985 - AUGUST 1986)

No. of HIP Runs	No. of Capsules HIP ped	No. of Capsules Successfully Collapsed
20*	Quartz 21	1
	Tantalum 7	2
	Niobium 7	6

\*Including five runs aborted due to equipment failure.

#### Status of milestones

The milestones are in the process of being revised.

### 1.2.3 Oxide Matrix

#### Dispersion-Toughened Oxide Composites

T. N. Tiegs, P. F. Becher, L. A. Harris, J. W. Geer, and W. H. Warwick (Oak Ridge National Laboratory)

#### Objective/scope

This work involves development and characterization of SiC-whisker-reinforced oxide composites for improved mechanical performance. To date, most of the work has dealt with alumina as the matrix because it was deemed a promising material for initial study. However, optimization of matrix materials is also explored. The approach to fabrication is to first use hot pressing to identify compositions for toughening and then to explore pressureless sintering for fabrication to near net shape.

#### Technical progress

SiC whiskers X-ray photoelectron spectroscopy (XPS) scans made on the surfaces of ARCO and Tateho SiC whiskers showed that the Tateho whiskers were much richer in oxygen than the ARCO whiskers and appeared to have some surface silica. Alumina-20 vol % SiC whisker composites made from these two whisker batches had significantly different fracture toughness values. The fracture toughnesses were  $K_{IC} = 4.2 \text{ MPa}\cdot\text{m}^{1/2}$  and  $8.3 \text{ MPa}\cdot\text{m}^{1/2}$  for the composites made with Tateho and ARCO whiskers, respectively. In addition, SEM examination showed a very smooth fracture surface for the composite made with Tateho whiskers indicating little crack deflection by the whiskers. Evidently the surface characteristics of the whiskers influence the bonding between the matrix and the whiskers, and this affects the fracture toughness.

Further testing of the role of the whisker-matrix interface bond indicated that by controlling the surface chemistry of the whiskers the fracture toughness can be altered. The whiskers with the high surface silica, used in the composite with a toughness of  $K_{IC} = 4.2 \text{ MPa}\cdot\text{m}^{1/2}$ , were subjected to acid leaching with HCl and HF. XPS showed a significant reduction in the surface oxygen content. An alumina-20 vol % SiC composite made with these whiskers had a fracture toughness of  $K_{IC} = 6.0 \text{ MPa}\cdot\text{m}^{1/2}$ . Conversely, the whiskers with the low surface silica, used in the composite with a toughness of  $K_{IC} = 8.3 \text{ MPa}\cdot\text{m}^{1/2}$ , were oxidized at  $1000^\circ\text{C}$  for 60 minutes. XPS revealed a high surface silica content, and consequently the fracture toughness of a similar composite was  $K_{IC} = 7.0 \text{ MPa}\cdot\text{m}^{1/2}$ . Evidently, the crack propagation behavior, which determines the fracture toughness, can be modified by changing the surface chemistry of the whiskers. Further testing is under way to improve the fracture toughness by surface treatments.

Samples of alumina-20 vol % SiC whisker composite material fabricated with the ARCO and Tateho whiskers were examined by transmission electron microscopy (TEM). A comparison of TEM micrographs for the two samples revealed no marked differences in the general appearance of the microstructures. The matrices consisted of relatively large well-defined alumina grains. Boundaries between alumina-alumina and alumina-SiC whisker were sharp and did not indicate material transfer between these phases. However, examination of micrographs from the composite made with



Tateho whiskers at high magnification showed a possible glassy phase surrounding some of the SiC whiskers. Because the microstructures between the two composites were generally similar, the properties of the alumina-SiC whisker interface are again believed to be the major factor affecting the mechanical properties of the whisker-reinforced composites.

#### Long-term oxidation tests

The long-term oxidation resistance of alumina-SiC whisker composites was examined to determine if any degradation of the mechanical properties occurs. The oxidation weight gains for two different composites of alumina-20 vol % SiC whiskers show that oxidation of the composites at elevated temperatures does occur (Fig. 1).

ORNL-DWG 86-1988

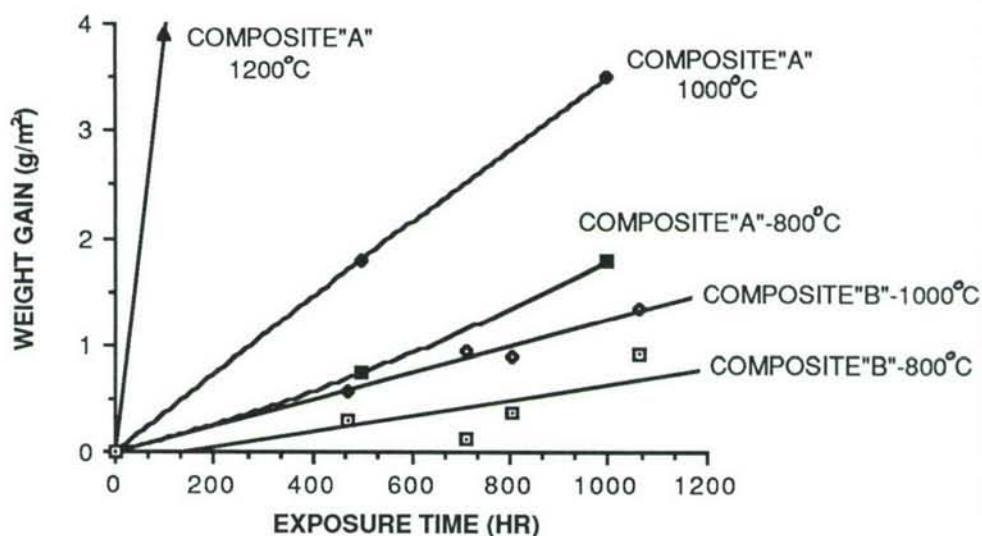


Fig. 1. Summary of results of isothermal oxidation of alumina-20 vol % SiC whisker composites.

The initial work<sup>1</sup> performed with composite "A" showed that the oxidation rates up to 1000 h at 800 and 1000°C are relatively linear, indicating oxygen transport through the alumina matrix with no formation of a protective layer at the surface as is common with SiC and Si<sub>3</sub>N<sub>4</sub> materials. Apparently oxygen transports along grain boundaries, and the rate is accelerated by the presence of monovalent and divalent atoms such as Na, Mg, and Ca. The alumina powder used for composite "A" was 99.5% pure with the balance mostly Na<sub>2</sub>O and MgO. In this matrix, oxygen is apparently transported readily.

Composite "B" is compositionally identical to composite "A" except that the alumina used was 99.99% pure with the Na, Mg, and Ca content <50 ppm, and the SiC whiskers were "cleaned" by sedimentation. Oxidation weight gain is reduced, apparently because of reduced oxygen transport.



The effect of oxidation on the composite flexural strength is illustrated in Fig. 2. As shown, composite "A," which showed higher oxidative weight gain, also exhibits significant degradation of the flexural strength. Composite "B," on the other hand, shows little strength degradation with exposure time. These results indicate that oxidation-produced property degradation is a potential long-term problem for the application of alumina-SiC whisker composites in heat engines. The problem could be even more severe in matrices such as zirconia, where oxygen transport occurs rapidly as compared with the rate in alumina.

ORNL-DWG 86-1989

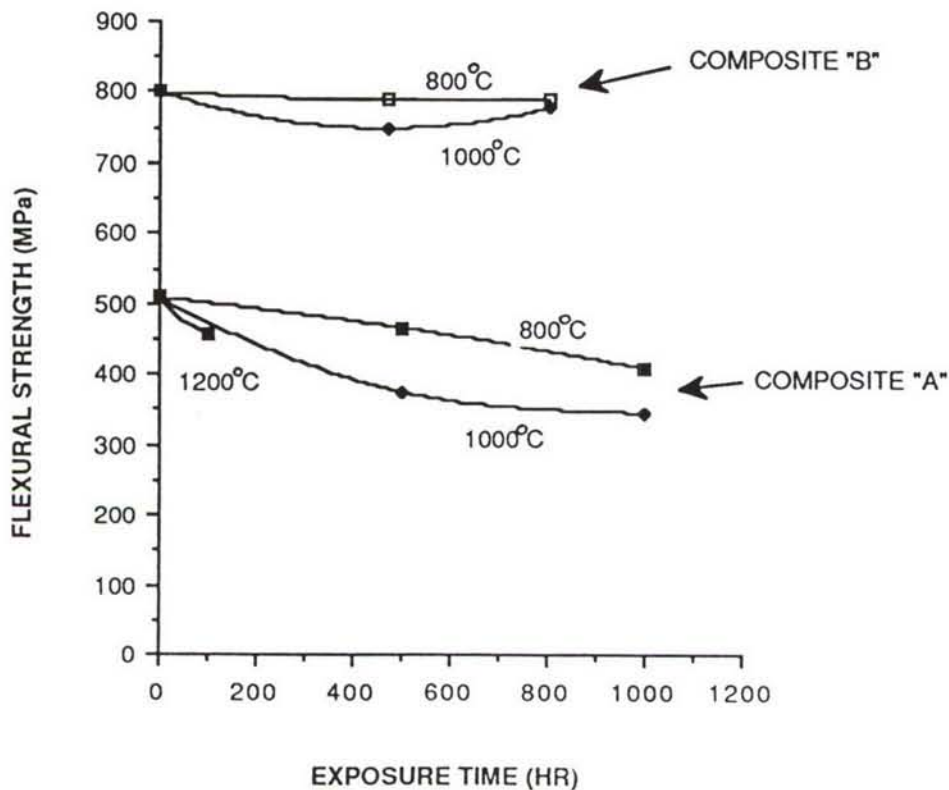


Fig. 2. Flexural strength at room temperature following isothermal oxidation for alumina-20 vol % SiC whisker composites.

#### Pressureless sintering

Alumina-10 vol % SiC whisker composites were fabricated from various alumina powders. All compositions contained ARCO whiskers, contained 2 wt %  $Y_2O_3$  as a sintering aid, and were fabricated under the same conditions. A summary of the results is presented in Table 1. As shown, high densities were achieved with all the powders, with the best densities obtained using Reynolds RC-HP DBM and Baikowski CR-10. Further improvements are being made by using combinations of these powders to maximize reactivity and particle packing.

Sol-Gel Oxide Powder

W. D. Bond, P. F. Becher, and T. N. Tiegs (Oak Ridge National Laboratory)

Objective/scope

Sol-gel processes have the potential for the synthesis of materials that can be processed at modest temperatures while obtaining highly uniform composition in dense, fine-grain ceramics that incorporate dispersed second phases to increase fracture toughness. This research emphasizes the determination of the feasibility of sol-gel processes for (1) synthesizing powders of phase stabilized zirconia and alumina and (2) coating whiskers to control their interface properties to matrix phases.

Sol-gel processes take advantage of the high degree of homogeneity that can be achieved by mixing on the colloidal scale and the surface properties of the colloidal particles. The excellent bonding and sintering properties of colloids are a result of their very high specific surface energy.

The work reported here is performed in a collaborative effort in the Material Sciences Program tasks of the Structural Ceramics Group in the Metals and Ceramics Division. The synthesis of sol-gel materials is carried out in the Ceramics for Advanced Heat Engines Project. The densification, characterization, and mechanical properties studies on compacts of the sol-gel powders are performed in the Materials Sciences Program.

Technical progress

Studies were continued on the preparation of colloidal zirconia and hafnia by thermal hydrolysis reactions in an autoclave and the characterization of the product colloidal oxides. Studies were also initiated on the preparation of fibrous, colloidal alumina (boehmite) by hydrothermal reaction methods similar to those reported by Bugosh.<sup>1,2</sup>

Electron microscopy studies show that zirconia and hafnia particles prepared by hydrolyzing 1 M salt solution at 175 to 200°C for 4 h are roughly spherical (75- to 100-nm diam) and consist of agglomerated 7-nm-diam crystallites. Surface area measurements (BET method) indicate that the crystallites are not tightly packed into the agglomerate (Table 1). The surface of the crystallites is available for nitrogen absorption as indicated by the calculated equivalent particle size. The amount of nitric required for dispersing the  $ZrO_2$  or  $HfO_2$  colloids to the stable sol state was 0.1 mol  $HNO_3$  per mol of the metal oxide and a pH value of ~4. At lower reaction temperatures, the crystallites grow at a much slower rate, and at 125°C the oxides are essentially amorphous (<2-nm diam) for our nominal 4-h reaction time.

Acid-stabilized sols (pH ~4) of 1 M  $ZrO_2$  or  $HfO_2$  of low electrolyte content are readily prepared from the colloidal oxides formed by thermal hydrolysis. Zirconia sols with nitrate-to- $ZrO_2$  mole ratios of 0.05 to 0.1 and hafnia sols with chloride-to- $HfO_2$  mole ratios of 0.05 have been found to be highly stable. The yields of colloidal oxides from the thermal hydrolysis reactions of zirconyl and hafnynl salts are essentially quantitative at 200°C after a 4-h reaction time.

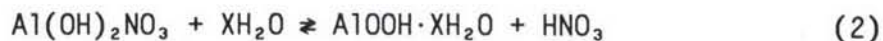
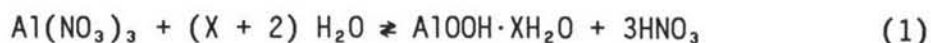


Table 1. Surface area of gels synthesized from  $\text{ZrO}_2$  and  $\text{HfO}_2$  particles prepared by thermal hydrolysis

Oxide	Hydrolysis temperature (°C)	Surface area ( $\text{m}^2/\text{g}$ )	Calculated equivalent particle diameter (nm)
$\text{ZrO}_2$	175	149	7.2
$\text{HfO}_2$	175	91.0	6.8
$\text{HfO}_2$	200	85.9	7.2

In some initial studies we have obtained evidence that additional aging of the colloidal oxides produces more uniform particles. In studies with  $\text{HfO}_2$ , the colloidal particles were more uniform in size and spherical when aged in the mother liquor from the hydrothermal reaction for an additional 3 h at 175°C. Electron microscopy indicated that restructuring of the agglomerates of crystallites may have occurred. It appeared that uniformly sized (500-nm-diam) spherical agglomerates were formed from the more irregularly shaped and smaller agglomerates of 7-nm crystallites that were initially present in the sample. However, a complete restructuring did not occur. Additional studies on the effects of aging time and of the pH and electrolyte concentration of the aging liquor are in progress.

To obtain good yields of hydrous, colloidal boehmite ( $\text{Al}(\text{OH})_3 \cdot \text{XH}_2\text{O}$ ) by hydrothermal reaction, it is necessary to employ partially hydrolyzed aluminum nitrate (e.g.,  $[\text{Al}(\text{OH})_2\text{NO}_3]$ ) rather than the stoichiometric salt  $[\text{Al}(\text{NO}_3)_3]$ . The position of equilibrium with the stoichiometric salt [Eq. (1)] is too far to the left to give good yields; whereas the thermal hydrolysis of  $\text{Al}(\text{OH})_2\text{NO}_3$  proceeds to near completion according to Eq. (2).



Colloidal alumina produced by the thermal hydrolysis of 0.25 M  $\text{Al}(\text{OH})_2\text{NO}_3$  at 175 to 200°C after a 4-h reaction time was composed of irregular-shaped agglomerates (average diameter  $\sim 1 \mu\text{m}$ ) of fibrous alumina monohydrate (boehmite) crystallites (1-nm diam and 50 nm long). The minimum amount of nitric acid for dispersion to the stable sol state was 0.07 mol  $\text{HNO}_3$  per mol of oxide and a pH value of  $\sim 4$ . The hydrothermally synthesized alumina, zirconia, and hafnia are compatible when codispersed to mixed hydrosols.



Status of milestones

Progress on gel powder synthesis variables (Milestone 12 33 03) is on schedule.

Publications

None.

References

1. J. Bugosh, "Fibrous Alumina Monohydrate and Its Production," U.S. Patent 2,915,475 (Dec. 1, 1959).
2. J. Bugosh et al., "A Novel Fine Alumina Powder, Fibrillar Boehmite," *I&EC Prod. Res. Dev.* 1, 1962.

Processing of Improved Transformation-Toughened Ceramics  
J. B. Blum, C. E. Knapp, and G. A. Rossi (Norton Company)

Objective/scope

The objective of this program is the production of zirconia toughened ceramics (ZTC) which exhibit mechanical properties (strength and toughness) superior to those of the "state of the art" toughened ceramics, particularly at high temperature and after prolonged aging at high temperature. In addition, such ceramics should possess low thermal conductivity to minimize energy losses in heat engine applications.

The scope includes the powder synthesis and characterization, shape forming, pressureless sintering, characterization of the sintered ceramics, and reporting of results.

In order to meet the program objectives, research will be focussed on comparing the performance of two types of powders, i.e. rapidly solidified and chemically derived, one of which will be chosen for the final part of the program. The most promising compositions will be studied, which will produce three classes of zirconia toughened ceramics, i.e. Mg-PSZ, (MgO-partially stabilized zirconia), Y-TZP ( $Y_2O_3$ -Tetragonal Zirconia Polycrystals) and ZTA (Zirconia Toughened Alumina), with the intention of identifying the best one, which will be eventually used for final property optimization. Several shape forming methods will also be investigated, with particular emphasis on those which are based on colloidal suspensions, and the best method will be selected, based on the properties of the green and sintered ceramics. Hot isostatic pressing will be used in the exploratory phase of the program, to try to separate the influence of composition and microstructure from that of flaws on the mechanical properties. Microstructural and fractographic analysis will be used for a better understanding of strength and fracture toughness.

Technical progress

1. Experimental Procedure

1.1 Powder preparation

The rapidly solidified (R/S) powders were prepared by melting a charge of the desired composition and rapidly quenching with a blast of compressed air.

Hollow bubbles were obtained, which were crushed and wet milled to get a powder with mostly sub-micron particles. Such powder was classified in some instances to obtain the desired particle size distribution.

The chemically derived (C/D) powders were made by coprecipitation from ethanolic solutions of precursors. The slurry was filtered and the cake dried to remove the alcohol, then washed to eliminate the salt by-product. The amorphous powder so obtained was then crystallized, either by air calcination or by hydrothermal treatment. The ethanolic solutions were used to avoid the formation of a gel, which produces a coarse unsinterable powder.

## 1.2 Powder characterization

The powders were characterized for physical and chemical properties. Properties measured included BET surface area, particle size distribution, phase composition by X ray diffraction, morphology and state of agglomeration by SEM, purity by spectrographic analysis, weight loss vs. temperature by TGA and crystallization by DTA.

## 1.3 Shape forming methods

The shape forming methods used were: dry pressing (die pressing followed by cold isostatic pressing or direct isostatic pressing), slip-casting and pressure assisted casting using air at about 700 KPa. The suspensions were prepared using water and selected dispersing agents and their rheological properties were measured with a viscometer. The objective was the preparation of a stable suspension with the highest solid loading. Deairing was done before casting.

## 1.4 Sintering and HIPing

Pressureless sintering was done in electric muffle furnaces with a temperature controller/programmer. Dilatometry was frequently performed for exploratory study and to identify the best sintering conditions. HIPing was done on presintered billets in Ar pressure of 207 MPa.



### 1.5 Measurement of physical and mechanical properties

The density of the ceramic was measured with the Archimedes method in water. Strength was measured in 4 Pt bending on MOR bars of 3x3x30 mm, with spans of 25.4 mm and 12.7 mm, using a crosshead speed of 0.5 mm/min. MOR values were obtained at room temperature and at 1000°C. For the hot MOR test, the bars were introduced in the furnace at about 300°C and the temperature was raised to 1000°C in about 15 min. A fixture of hot pressed SiC (NC-203) was used. The fracture toughness at room temperature was measured with the microindentation (MI)<sup>(1)</sup> and with the multiple controlled flaw (MCF)<sup>(2)</sup> methods. The latter method was used for measuring  $K_{IC}$  at 1000°C and the bars were heated at the same rate used for the MOR test.

### 1.6 Microstructure and fractographic analysis

The microstructures of the densified ceramics were obtained by SEM on polished and thermally etched samples. The fracture surface was obtained also by SEM and the analysis of the impurities was performed by SEM/EDS.

## 2. Results

### 2.1 Powder characterization and shape forming methods

The rapidly solidified (R/S) and chemically derived (C/D) powders were characterized for physical and chemical properties. Table 1 shows the results of the spectrographic analysis for some of these powders. The first generation of lower purity R/S powders produces yellow sintered ceramics, whereas the second generation of purer powders produces ivory materials. The chemically derived powders, as previously mentioned, can be crystallized either by air calcination or hydrothermally. The chemical analysis of this powder is shown also in Table 1. The impurity levels are lower than in the case of the R/S powders, except for sodium, which cannot be completely washed out.

Table 2 shows some typical properties of the various powders. Table 3 summarizes their advantages and drawbacks.

## 2.2 Shape forming methods

### A) Dry pressing

Most of the work has concentrated on two compositions: 4 w/o  $Y_2O_3$ - $ZrO_2$  (abbreviated as Z4Y) and 80 w/o (4 w/o  $Y_2O_3$ - $ZrO_2$ )-20 w/o  $Al_2O_3$  (abbreviated as Z4Y20A). Both R/S and C/D powders were used. The R/S powder gives a higher green density after cold isostatic pressing, typically 50-55% of TD at 200 MPa, compared to about 40% of TD for the C/D powder, either calcined at 700°C or autoclaved at 250°C. However, the C/D powder densifies at a lower temperature (about 1450-1500°C vs. 1600°C for the milled R/S powder).

### B) Slip casting

In order to systematically compare different forming techniques it was decided to focus on the Z4Y20A composition and use the R/S, C/D and Toyo-Soda Super Z powders. Previous experience has indicated that wet forming methods offer a higher probability of yielding the requisite green body characteristics.

In the case of the R/S powder, 75 w/o (36 v/o) solid loadings were obtained. The green densities of the pressure cast billets were 58-61% of TD. After cold isostatic pressing at 210 MPa, the density increased to 61-65% of TD. All green billets were fired at 1600°C to >99% of TD.

No difference was observed in the green densities of slip cast and gas pressure cast pieces. Mercury porosimetry revealed little differences in porosity and pore size distribution. An average pore size of 0.09 - 0.1  $\mu m$  was obtained. The major difference between the two techniques is the time required for casting, i.e. about 20 min. for pressure casting vs. 4-6 hrs. for slip casting.



### 2.3 Mg-PSZ ceramics (3 w/o MgO)

During this period rapidly solidified batches of higher purity were made. The chemical analysis of one of these materials, with a 2.95 w/o MgO, is shown in Table 1. After sintering and aging, these Mg-PSZ ceramics have shown the typical microstructure already found for the ceramics of lower purity, illustrated in Fig. 1. Efforts to produce billets to be used for the standard MOR bars have failed; difficulties were encountered in sintering these materials, i.e. formation of  $m\text{-ZrO}_2$  and concurrent cracking. Work will be continued with the purpose of evaluating these fine grained Mg-PSZ vis a vis the NILCRA Mg-PSZ ceramics.

Efforts to produce Mg-PSZ and Mg-TZP ceramics by using the chemically derived powders have failed. Extensive cracking occurred when the MgO content was reduced to 1 m/o (0.33 w/o) in order to obtain the Mg-TZP ceramics. Even with 1.3 w/o MgO cracking occurred. This composition was obtained from a nominal 3 w/o MgO-ZrO<sub>2</sub> after MgO was lost during the washing of the powder. The microstructure of a billet sintered at 1500°C, containing composite grains, is shown in Fig. 2. When a 3 w/o MgO-ZrO<sub>2</sub> powder was prepared by adding a solution of magnesium nitrate to a pure ZrO<sub>2</sub> powder made with the alcohol method, densification was not complete at 1500°C and a heterogeneous microstructure (Fig. 3) containing pores and large grains was obtained, probably reflecting a poor MgO distribution in the powder. Because of these disappointing results, the use of chemical powders for the production of Mg-PSZ ceramics has been discontinued.

### 2.4 Y-TZP Ceramics ( 4 w/o Y<sub>2</sub>O<sub>3</sub>-ZrO<sub>2</sub>)

#### A) Ceramics made with the rapidly solidified (R/S) powders

Recently a 4 w/o Y<sub>2</sub>O<sub>3</sub>-ZrO<sub>2</sub> powder of higher purity was made by using purer graphite electrodes in the arc melting process and improved collection equipment for the rapidly solidified bubbles. Ceramics made with this powder are ivory, instead of yellow, which is the color of the lower purity materials. A



typical microstructure for a higher purity Y-TZP ceramic pressureless sintered is shown in Fig. 4. Most of the grains are tetragonal and submicron in size. This sample was sintered at  $1600^{\circ}\text{C}$ , 1 hr., and made with a mill grade (unclassified) powder. Fig. 5 shows for comparison, the microstructure of a ceramic produced using the lower purity R/S powder of the same composition.

The strength values at room temperature and at  $1000^{\circ}\text{C}$  for Y-TZP ceramics made with the R/S (low purity) and C/D powders are shown in Table 4. Recent results, not shown in this table, indicate that the Y-TZP ceramics fabricated with the high purity powder possess a higher strength at  $1000^{\circ}\text{C}$ , but a firm conclusion cannot be drawn due to insufficient data.

Figs. 6 and 7 show the fracture surface of two Y-TZP ceramics, made with low purity and high purity R/S powders, respectively. The MOR bars were fractured at room temperature and the strength values are reported in the captions.

Table 5 reports the fracture toughness values for these materials, both at room temperature and at  $1000^{\circ}\text{C}$ . A large drop in toughness occurs at  $1000^{\circ}\text{C}$ , which is expected, since the t- $\text{ZrO}_2$  polymorph is thermodynamically stable at this temperature and, therefore, no stress induced toughening should occur.

#### B) Ceramics made with the chemically derived (C/D) powders

Fig. 8 shows the typical microstructure of a 4 w/o  $\text{Y}_2\text{O}_3$ - $\text{ZrO}_2$  TZP ceramic made with a chemically derived powder (ethanol method). By comparison with Fig. 4, it appears that the microstructure is more uniform. This material was made by pressing a powder calcined at  $700^{\circ}\text{C}$  and milled in water to achieve deagglomeration. The typical strengths at room temperature and at  $1000^{\circ}\text{C}$  are reported in Table 4, whereas the fracture toughness values are shown in Table 5. These Y-TZP materials, when compared with those made with the rapidly solidified powders, exhibit a similar strength at room temperature but are slightly less strong at  $1000^{\circ}\text{C}$ .

Since the powder calcined at  $700^{\circ}\text{C}$  must be deagglomerated by milling, which may introduce impurities, in some experiments the amorphous, as prepared 4 w/o  $\text{Y}_2\text{O}_3$ - $\text{ZrO}_2$  powder was crystallized in an autoclave with water at  $250^{\circ}\text{C}$  and 4 MPa steam pressure. After the hydrothermal treatment the powder contained about 5% water and consisted of a mixture of t- $\text{ZrO}_2$  and m- $\text{ZrO}_2$ . In comparison with the powder calcined at  $700^{\circ}\text{C}$ ,<sup>(2)</sup> this powder contains softer agglomerates, as shown by the smaller average agglomerate size obtained from the particle size distribution curve. Pressed green billets contain pores around 10 nm in diameter, with a narrow size distribution. A dilatometer samples was densified to >98% of TD at  $1300^{\circ}\text{C}$ , instead of  $1450$ - $1500^{\circ}\text{C}$  required for similar samples made with the calcined powder. Unfortunately, larger billets (50x50x6mm) cracked during firing and mechanical properties could not be obtained. This problem is now under study. The results of this work were recently presented at the Zirconia III Conference in Tokyo<sup>(3)</sup>.

## 2.5 Y-TZP ceramics containing alumina as dispersed phase

It has been recently reported<sup>(4)</sup> that the presence of alpha alumina in a HIPed Y-TZP ceramic strongly enhances the room temperature strength and toughness. During the past six months, two compositions were studied, i.e. 4 w/o  $\text{Y}_2\text{O}_3$  TZP with 10 w/o and 20 w/o  $\text{Al}_2\text{O}_3$ . The first composition was made with the chemical method, i.e. by mixing two ethanolic solutions, one containing  $\text{ZrCl}_4$ ,  $\text{AlCl}_3$  and  $\text{YCl}_3 \cdot 6\text{H}_2\text{O}$  and the other containing  $\text{NaOH}$ .<sup>3</sup> The second composition was made by using both C/D and R/S powders.

Fig. 9 shows the microstructure of the Y-TZP with 10 w/o  $\text{Al}_2\text{O}_3$ . The distribution of the alpha alumina grains throughout the zirconia matrix is fairly uniform. The density is about 98.5% of TD and the strength of 1x1x10mm bars (3 pt.) was 1316 MPa, which is higher than that measured on bars of the same size for the Y-TZP ceramics without alumina, (about 1100 MPa).



The Y-TZP ceramics containing 20 w/o  $\text{Al}_2\text{O}_3$  were more thoroughly investigated. They were prepared with both C/D and high purity R/S powders. For the sake of comparison, ceramics were also made using the Super-Z powder of similar composition sold by the Toyo Soda Mfg Co. (Japan). The microstructures of these ceramics are shown in Figs. 10, 11 and 12. All materials show a good distribution of alumina grains. The mechanical properties are reported in Tables 4 and 5. It can be observed that the addition of alumina lowers the room temperature toughness but raises the strength. At  $1000^\circ\text{C}$  the  $\text{Al}_2\text{O}_3$  containing Y-TZP ceramics retain a higher strength, in comparison with the Y-TZP materials, and also a higher fraction of the toughness. However, the toughness values at  $1000^\circ\text{C}$  are not reliable, since difficulties were encountered in measuring the length of the cracks perpendicular to the bar length. A surprising result was the relatively low strength of the HIPed materials, much lower than that reported by the Toyo Soda researchers<sup>(4)</sup>,<sup>(5)</sup>. A possible explanation is the use of higher sintering and HIPing temperatures in the present study.

## 2.6 ZTA ceramics

It was previously reported that rapidly solidified batches of three compositions had been prepared and preliminary strength data at room temperature and at  $1000^\circ\text{C}$  were obtained for the composition  $\text{Al}_2\text{O}_3$ -38 w/o  $\text{ZrO}_2$ -1.4 w/o  $\text{Y}_2\text{O}_3$ . RT MOR (3 pt) measured on  $1\times 1\times 10\text{mm}$  bars was 1378 MPa and  $1000^\circ\text{C}$  MOR (3 pt) on  $3\times 3\times 30\text{mm}$  bars was 378 MPa.

Recently, four more batches with higher purity were made and billets were sintered at  $1600^\circ\text{C}$ . Table 6 shows compositions and MOR (3 pt) values obtained using  $1\times 1\times 10\text{mm}$  bars. Material #4 has shown t- $\text{ZrO}_2$  and alpha-alumina by XRD, whereas material #1 contained substantial amounts of m- $\text{ZrO}_2$  on the surface, which could explain the much lower strength. Of these four materials, the one with highest RT strength and, hopefully, the lowest  $\text{Y}_2\text{O}_3$  level, will be tested for MOR and  $K_{\text{IC}}$  at  $1000^\circ\text{C}$ . The microstructure of materials #4 is shown in Figs. 13 and 14.



### 3. Discussion

Considerable efforts in the past period have been devoted to the powder preparation and characterization, in order to understand the relationship between powder properties and those of the green parts, which in turn affect microstructure and properties of the ceramics.

The R/S powders have shown in general better performance than the C/D ones, in terms of green density, good dispersibility (low agglomeration) in aqueous media, and better sinterability in the case of the Z4Y20A composition. Another interesting feature of these powders is the presence of metastable phases produced by the rapid solidification, i.e. delta alumina in the  $\text{ZrO}_2\text{-Y}_2\text{O}_3\text{-Al}_2\text{O}_3$  powders.

The C/D powders, on the other hand, possess some desirable features, such as purity and small crystallite size and can be sintered at a lower temperature, but a serious drawback is the agglomeration, which results in low green density, non-uniform pore size distribution in the pressed parts and difficulty in preparing good dispersions in aqueous media. Their higher purity could be a potential advantage for high temperature properties and for the problem of degradation of the Y-TZP materials around 200-300°C in a humid environment.

The Y-TZP (4 w/o  $\text{Y}_2\text{O}_3$ ) ceramics made with the high purity R/S powder have shown a better strength retention at 1000°C, in comparison with the low purity materials of the same composition. The reason for this is not understood at present and more work is needed. The loss in strength at 1000°C is probably caused not only by the drop in toughness, but also by the elimination of the compressive surface layer generated by the  $t\text{-ZrO}_2 \rightarrow m\text{-ZrO}_2$  transformation. From the data already obtained, it appears that the purity difference does not play an important role since MOR bars made with the purer C/D powder have shown a similar percent drop in strength at 1000°C.

The ceramics with the Z4Y20A composition have shown higher room temperature strength when compared to the Y-TZP materials. These results agree with those reported in a recent Toyo-Soda patent<sup>(5)</sup>, but the strengths after HIPing are much lower than those shown in the same patent (2400 MPa in 3 pt). The room temperature toughness is increased by the addition of alumina, but only a small fraction is retained at 1000°C<sup>(6)</sup>. This is contrast with the results of C. Tsukuma et al<sup>(6)</sup>, who reported a value of about 6 MPa.m<sup>1/2</sup> for  $K_{IC}$  at 1000°C, measured with the SENB technique.

Obviously, more work is needed to find a reliable technique for measuring high temperature toughness and considerable effort will be devoted to this problem in the next months.

Future efforts will be focused in finding other compositions in which more toughness is retained at high temperature. Good candidates, are, for example,  $\text{CeO}_2\text{-ZrO}_2$  toughened alumina and  $\text{CeO}_2\text{-ZrO}_2\text{-HfO}_2$  toughened alumina, since the  $\text{CeO}_2\text{-TZP}$  ceramics appear to exhibit a new type of toughening mechanism<sup>(7)</sup> which makes these materials good candidates for high temperature applications.



## Status of the Milestones

### Milestone #1 (properties of Mg-PSZ ceramics)

A preliminary evaluation of the potential of these materials has been done. Further work will be limited to compare their properties with those of the NILCRA ceramics.

### Milestone #2 (Equipment for high purity R/S powders)

This milestone has been met, the equipment was built and evaluation of several powders has been done or is in progress.

### Milestone #3 (Initial evaluation of R/S and C/D powders)

The evaluation has been done and the R/S powders have shown better performance.

### Milestone #4 (Evaluation and optimization of Y-TZP ceramics)

The evaluation has been done for these materials with and without alumina as dispersed phase. They have shown a potential for meeting the program objectives.

### Milestone #5 (Paper for the Proceedings of the 24th CCM meeting)

The paper is being written and will be submitted before the deadline of Nov. 28, 1986.

### Milestone #6 (Choice of the two best forming methods)

It was agreed with the program manager of ORNL that it is premature to exclude now potentially promising methods, therefore the deadline has been extended.

### Milestone #7 (First results for the ZTA ceramics)

The milestone has been met.

### Publications

1. KNSiebein, RRBiederman and GARossi, "Microchemical analysis of  $Y_2O_3$ -doped  $ZrO_2$  powders" presented at the 1986 Conference on Ceramic Powder Science and Technology, Boston, MA, Aug.3-6, 1986.
2. GARossi and PJPelletier, " $Y_2O_3$ -doped  $ZrO_2$  Powder Prepared in a Non Aqueous Medium. Influence of the Crystallization Method on Powder Sinterability and Properties of the Y-TZP Ceramics". Presented at the Third International Conference on the Science and Technology of Zirconia, Tokyo, Japan, Sept. 9-11, 1986.
3. CEKnapp, KEManwiller and DBArvidson, "Microstructures of Zirconia Toughened Ceramics Produced Using Prealloyed Rapidly Solidified Powders". Presented at the Third International Conference on the Science and Technology of Zirconia, Tokyo, Japan, Sept. 9-11, 1986.

### References

1. GRANstis, PChantikul, BRLawn and BBMarshall, "A Critical Evaluation of Indentation Techniques for Measuring Fracture Toughness: I, Direct Crack Measurements" J. Am. Ceram. Soc. Vol 64, p. 533-543, 1981.
2. RFCook and BRLawn, "A Modified Indentation Toughness Technique" Comm. Am. Ceram. Soc. C 200-C 201, Nov. 1983.
3. GARossi and PJPelletier, " $Y_2O_3$ -doped  $ZrO_2$  Powder Prepared in a Non Aqueous Medium. Influence of the Crystallization Method on Powder Sinterability and Properties of the Y-TZP Ceramics". Presented at the Third International Conference on the Science and Technology of Zirconia, Tokyo, Japan, Sept. 9-11, 1986.
4. KTsukuma, KUeda and MShimada, "Strength and Fracture Toughness of Isostatically Hot Pressed Composites of  $Al_2O_3$  and  $Y_2O_3$ -Partially Stabilized Zirconia" Comm. Am. Ceram. Soc., C4-C5, Jan. 1985.
5. KTsukuma, KUeda, TTsukidate, "High-Strength Zirconia Type Sintered Body", U. S. Pat. 4,587,225, May 6, 1986.
6. KTsukuma, KUeda, KMatsushita and MShimada, "High Temperature Strength and Fracture Toughness of  $Y_2O_3$ -Partially Stabilized  $ZrO_2$ - $Al_2O_3$  Composites" Comm. Am. Ceram. Soc., C56-C58, Feb. 1985.
7. AVVirkar and RLKMatsumoto, "Ferroelastic Domain Switching as a Toughening Mechanism in Tetragonal Zirconia". Comm. Am. Ceram. Soc., C224-C226, Oct. 1986.



TABLE 1

## CHEMICAL ANALYSIS OF R/S AND C/D POWDERS

(concentrations in w/o)

POWDER	Na	Ca	Mg	Fe	Ti	Si	Al	Y
$4w/oY_2O_3-ZrO_2$ (R/S) HIGH PURITY	ND	0.03	0.05	0.03	0.04	0.03	0.04	3.25
$4w/oY_2O_3-ZrO_2$ (R/S) LOW PURITY	ND	0.03	0.05	0.07	0.15	0.03	0.45	3.10
$4w/oY_2O_3-ZrO_2$ (C/D) CALCINED $700^\circ C$	<0.1	0.01	0.005	0.001	ND	0.001	0.005	3.15
$3w/oMgO-ZrO_2$ (R/S) HIGH PURITY	ND	0.02	1.78	0.03	0.04	0.01	0.04	ND

NOTE: All elements analyzed by Spectrographic Analysis, except Mg and Y, analyzed by Atomic Absorption

ND = Not Detected; R/S = Rapidly Solidified; C/D = Chemically Derived

TABLE 2

## PHYSICAL PROPERTIES OF R/S AND C/D POWDERS

POWDER	BET Surface Area (m <sup>2</sup> /g)	XRD PHASES	L O I (w/o) (1000°C)	APS (nm)
4w/oY <sub>2</sub> O <sub>3</sub> -ZrO <sub>2</sub> (R/S/ HIGH PURITY	6-8	tet. (major) mono. (mod.)	<0.5	0.7
4w/oY <sub>2</sub> O <sub>3</sub> -ZrO <sub>2</sub> (R/S/ LOW PURITY	6-8	tet. (major) mono. (mod.)	<0.5	0.8
4w/oY <sub>2</sub> O <sub>3</sub> -ZrO <sub>2</sub> (C/D) CALCINED 700°C	25-30	100% tet.	<1.0	0.4-0.8*
3 w/oMgO-ZrO <sub>2</sub> (R/S) HIGH PURITY	6-8	100% tet.	<0.5	0.7

NOTE: L O I = Loss on Ignition; APS = average particle size

\* agglomerate size



TABLE 3  
ADVANTAGES AND DRAWBACKS OF R/S AND C/D POWDERS

<u>POWDER</u>	<u>ADVANTAGES</u>	<u>DRAWBACKS</u>
R/S	<ul style="list-style-type: none"> <li>○ HIGH GREEN DENSITIES</li> <li>○ METASTABLE PHASES</li> <li>○ LOW AGGLOMERATION</li> <li>○ RELATIVELY LOW COST</li> </ul>	<ul style="list-style-type: none"> <li>○ IMPURITIES</li> <li>○ POSSIBLE PHASE SEGREGATION AFTER MILLING</li> </ul>
C/D	<ul style="list-style-type: none"> <li>○ HIGH PURITY</li> <li>○ SMALL CRYSTALLITE SIZE</li> <li>○ LOWER SINTERING TEMPERATURE</li> <li>○ FINER MICROSTRUCTURE</li> <li>○ POTENTIALLY BETTER HIGH TEMPERATURE PROPERTIES</li> </ul>	<ul style="list-style-type: none"> <li>○ AGGLOMERATION</li> <li>○ LOW GREEN DENSITIES</li> <li>○ PRESENCE OF VOLATILE SPECIES</li> <li>○ GEL FORMATION FOR HIGH <math>Al_2O_3/ZrO_2</math> RATIOS</li> <li>○ RELATIVELY HIGH COST</li> </ul>

TABLE 4

MOR (4 PT) OF 3x3x30mm BARS (MPa)

COMPOSITION	R/S	25°C	C/D	R/S	1000°C	C/D
2.7w/oMqO-ZrO <sub>2</sub> (Mq-PSZ)	690*	SINT.	--	--	SINT.	--
	--	SINT. + HIP	--	--	SINT. + HIP	--
4w/oY <sub>2</sub> O <sub>3</sub> -ZrO <sub>2</sub> (Y-TZP)	970	SINT.	950	311 <sup>Δ</sup>	SINT	276 <sup>Δ</sup>
	1520	SINT. + HIP	1580	539 <sup>Δ</sup>	SINT. + HIP	--
						--
80w/o(4w/oY <sub>2</sub> O <sub>3</sub> -ZrO <sub>2</sub> ) 20w/oAl <sub>2</sub> O <sub>3</sub>	1096	SINT.	--	425	SINT.	--
	--	SINT. + HIP	1647	--	SINT. + HIP	276

\* 1x1x10mm bars, 3pt. bending

Δ 3 pt. bending

TABLE 5

COMPOSITION	POWDER	$\frac{K_{IC}}{1000} \text{ (MPa} \cdot \text{m}^{\frac{1}{2}} \text{)}$		1000°	MI
		25°C			
4w/oY <sub>2</sub> O <sub>3</sub> -ZrO <sub>2</sub>	R/S	MCF	MI	MCF	MI
	C/D	12.6	9.6	1.6	--
80w/o(4w/oY <sub>2</sub> O <sub>3</sub> -ZrO <sub>2</sub> ) 20w/oAl <sub>2</sub> O <sub>3</sub>		11.2	9.2	0.4	--
	R/S	11.0	6.7	1.7	--
	C/D	8.0	4.8	2.5	--
	SUPER Z*	6.3	4.0	1.8	--

NOTE: R/S = RAPIDLY SOLIDIFIED

C/D = CHEMICALLY DERIVED

MCF = MULTIPLE CONTROLLED FLAW METHOD

MI = MICROINDENTATION METHOD

\* = TOYO SODA MFG. CO. (JAPAN)



TABLE 6  
CHEMICAL COMPOSITION OF SOME HIGH ALUMINA R/S  
POWDERS AND RT MOR (3 PT) OF 1x1x10mm BARS

POWDER #	w/o $\text{Al}_2\text{O}_3$	w/o $\text{ZrO}_2$	w/o $\text{Y}_2\text{O}_3$	w/o $\text{Y}_2\text{O}_3$ in $\text{ZrO}_2$	MOR (MPa)
1	78.6	21.4	0	0	214
2	76.5	23.2	0.33	1.4	N/A
3	76.4	23.0	0.60	2.6	N/A
4	76.1	22.9	1.02	4.4	1061

NOTE: N/A = Not Available; mill grade (unclassified) powder billets sintered at 1600°C, 1 hr.

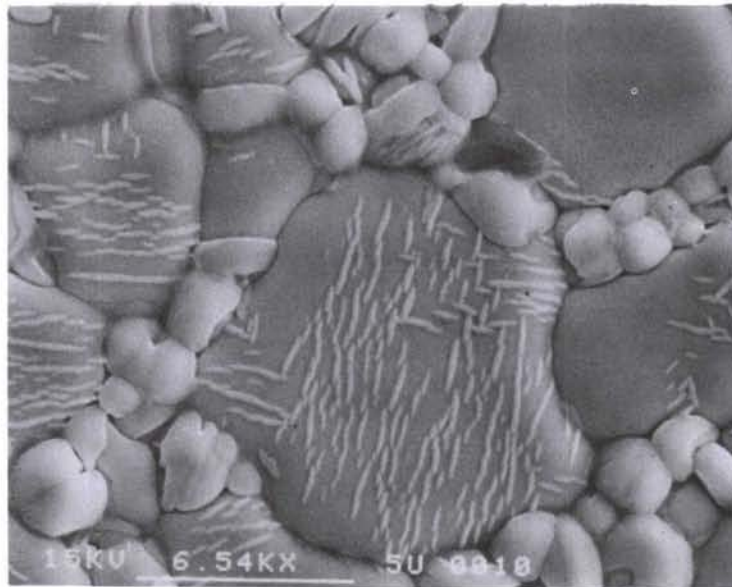


Fig. 1 SEM micrographs (polished and thermally etched surface) of a 2.95w/oMgO-ZrO<sub>2</sub> ceramic sintered at 1500°C and aged at 1400°C. High purity, mill grade powder prepared by rapid solidification.



Fig. 2 SEM micrograph (polished and thermally etched surface) of a 1.31 w/o MgO-ZrO<sub>2</sub> ceramic sintered at 1500°C. Powder prepared by ethanol method.



Fig. 3 SEM micrograph (polished and thermally etched surface) of a 3.0w/oMgO-ZrO<sub>2</sub> ceramic sintered at 1500°C. Pure ZrO<sub>2</sub> powder prepared with the ethanol method and doped with magnesium nitrate.

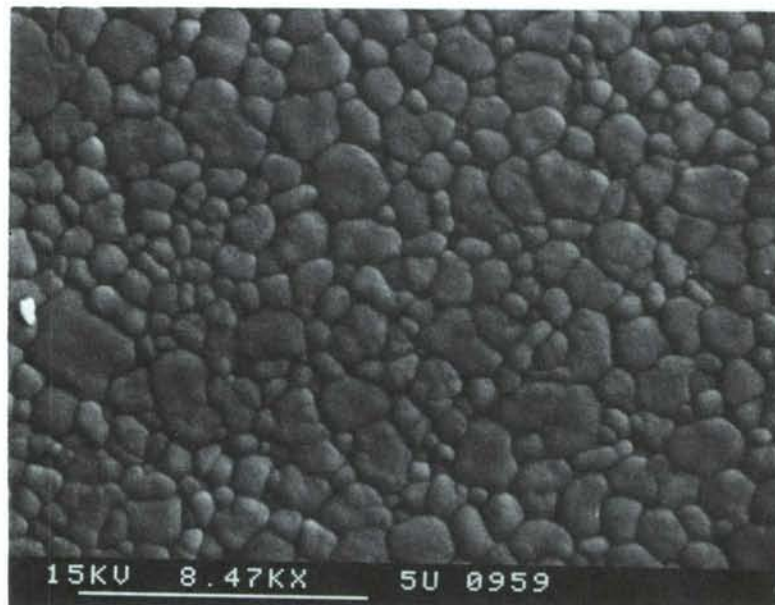


Fig. 4 SEM micrograph (polished and thermally etched surface) of a 4w/oY<sub>2</sub>O<sub>3</sub>-ZrO<sub>2</sub> ceramic sintered at 1600°C. High purity, mill grade powder prepared by rapid solidification.



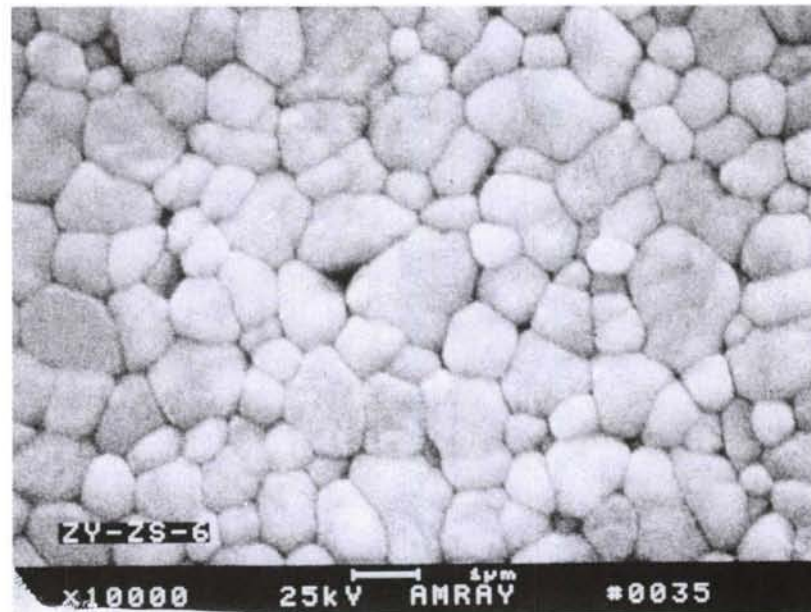


Fig. 5 SEM micrograph (polished and thermally etched surface) of a 4w/o  $Y_2O_3$ - $ZrO_2$  ceramic sintered at  $1600^\circ C$ . Low purity, mill grade powder prepared by rapid solidification.

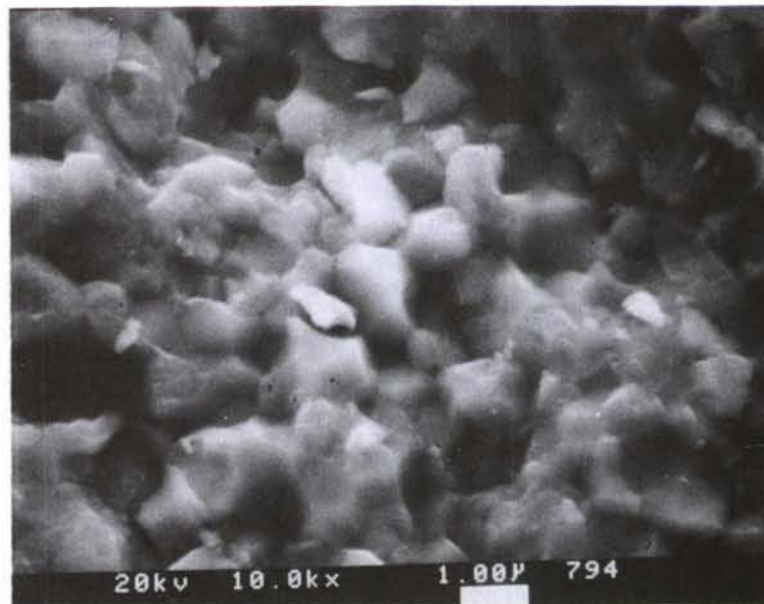


Fig. 6 Fracture surface (SEM) of sample shown in Fig. 5. (MOR = 890 MPa)

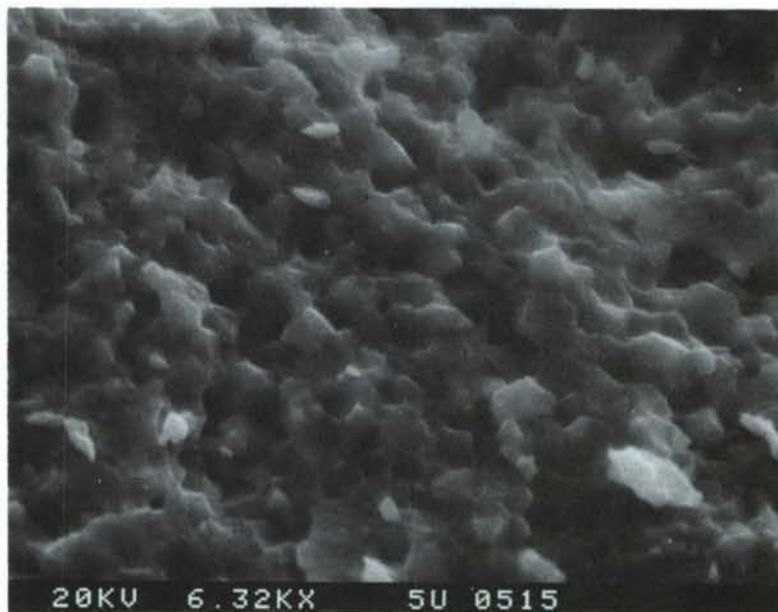


Fig. 7 Fracture surface (SEM) of sample shown in Fig. 4.  
(MOR = 935 MPa)



Fig. 8 SEM micrograph (polished and thermally etched surface) of a  $4w/oY_2O_3-ZrO_2$  ceramic sintered at  $1500^\circ C$ . Powder prepared with the ethanol method, calcined at  $700^\circ C$  and deagglomerated by milling.

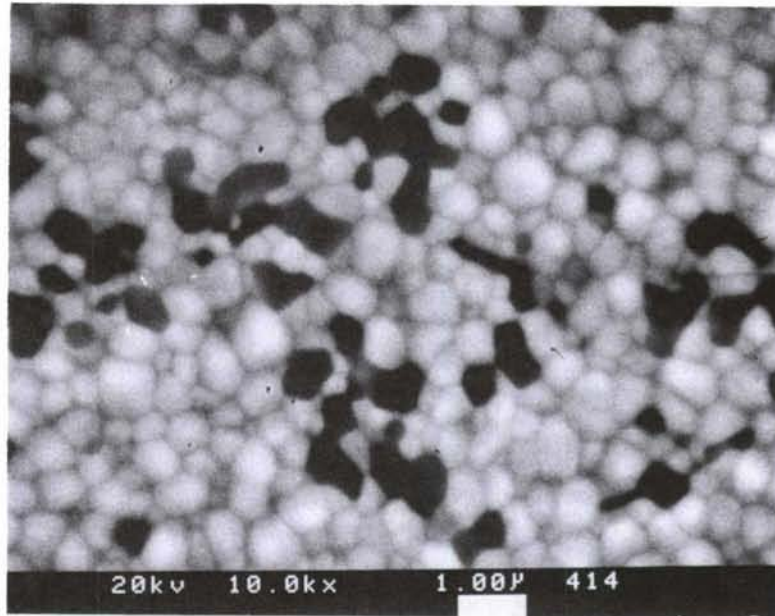


Fig. 9 SEM micrograph (polished and thermally etched surface) of a 90w/o (4w/o  $\text{Y}_2\text{O}_3$ - $\text{ZrO}_2$ )-10w/o  $\text{Al}_2\text{O}_3$  ceramic sintered at  $1500^\circ\text{C}$ . Powder prepared with the ethanol method, calcined at  $700^\circ\text{C}$  and deagglomerated by milling.

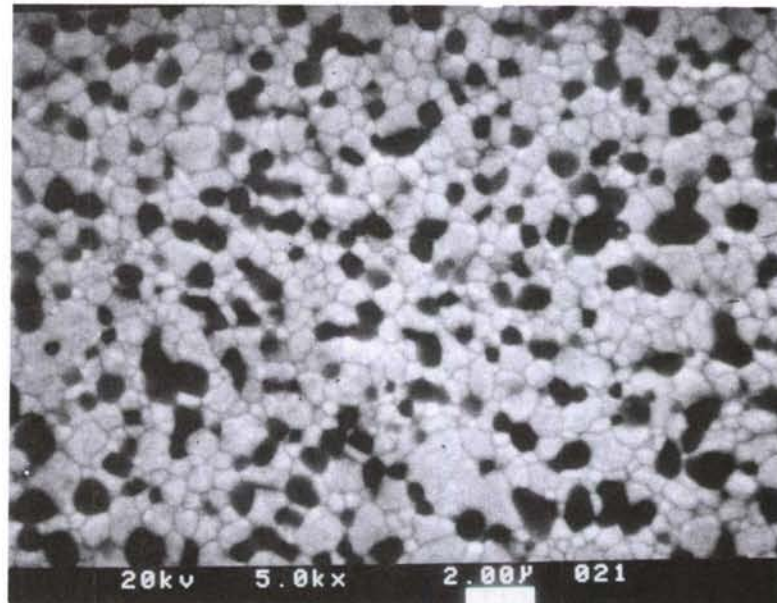


Fig. 10 SEM micrograph (polished and thermally etched surface) of a ceramic of composition 80w/o (4w/o  $\text{Y}_2\text{O}_3$ - $\text{ZrO}_2$ )-20 w/o  $\text{Al}_2\text{O}_3$  sintered at  $1600^\circ\text{C}$ . High purity, mill grade powder made by rapid solidification.



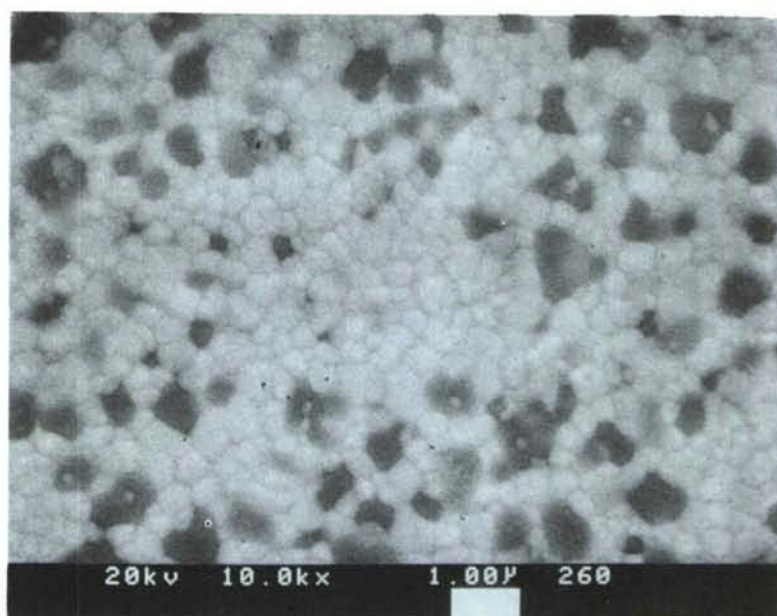


Fig. 11 SEM micrograph (polished and thermally etched surface) of a ceramic of composition 80w/o (4w/o  $\text{Y}_2\text{O}_3$ - $\text{ZrO}_2$ ) -20w/o  $\text{Al}_2\text{O}_3$  sintered at  $1500^\circ\text{C}$  and HIPed at  $1550^\circ\text{C}$ . Powder made with the ethanol method, calcined at  $700^\circ\text{C}$  and deagglomerated by milling.

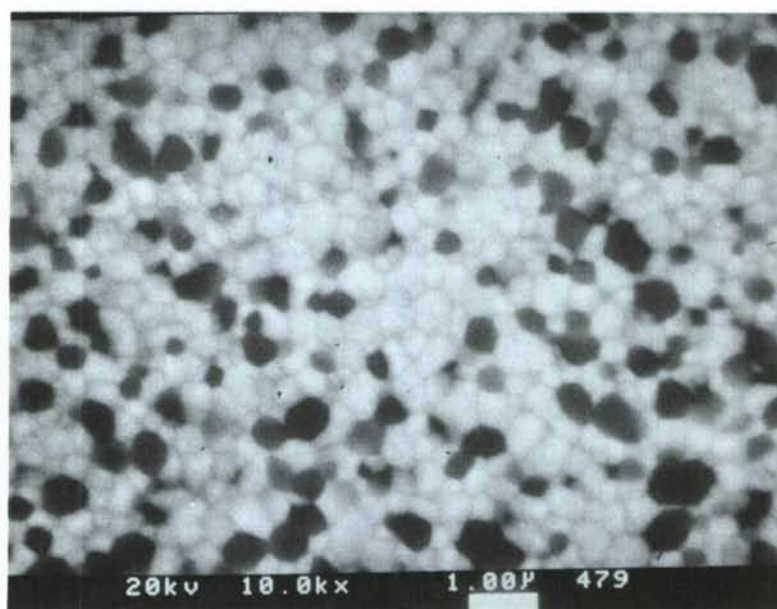


Fig. 12 SEM micrograph (polished and thermally etched surface) of a ceramic of composition 80w/o (5.3w/o  $\text{Y}_2\text{O}_3$ - $\text{ZrO}_3$ ) -20w/o  $\text{Al}_2\text{O}_3$  sintered at  $1500^\circ\text{C}$  and HIPed at  $1550^\circ\text{C}$ . Powder supplied by Toyo Soda Mfg. Co. (Japan).

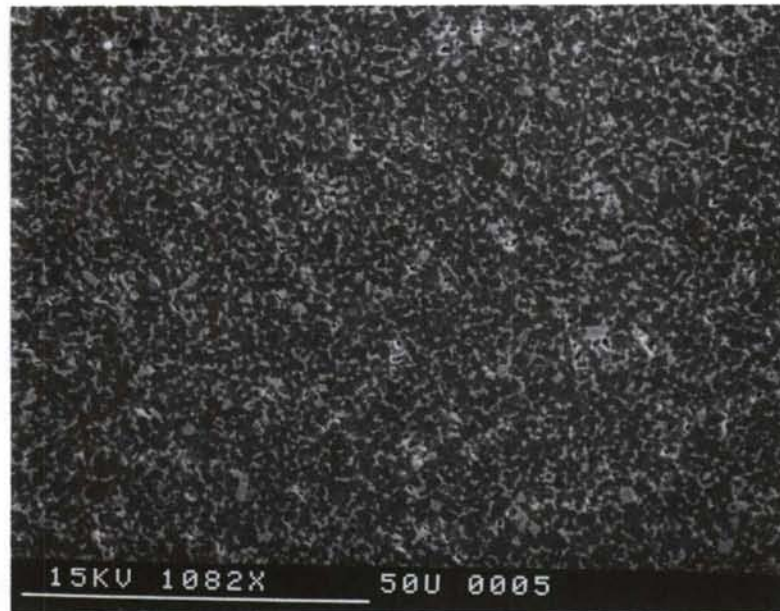


Fig. 13 SEM micrograph (polished and thermally etched surface) of a ZTA ceramic with composition 76.1 w/o  $\text{Al}_2\text{O}_3$ -22.9w/o  $\text{ZrO}_2$ -1.02w/o  $\text{Y}_2\text{O}_3$ , sintered at 1600°C. High purity, mill<sup>2</sup> grade powder made by rapid solidification.

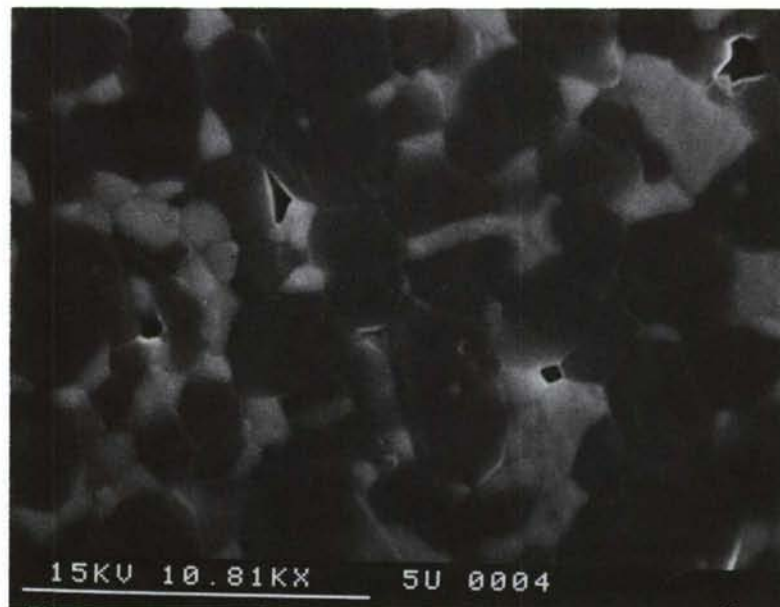


Fig. 14 SEM micrograph (polished and thermally etched surface) of a ZTA ceramic with composition 76.1w/o  $\text{Al}_2\text{O}_3$ -22.9w/o  $\text{ZrO}_2$ -1.02w/o  $\text{Y}_2\text{O}_3$ , sintered at 1600°C. High purity, mill<sup>2</sup> grade powder made by rapid solidification.

Advanced Transformation-Toughened Oxides

T. Y. Tien (University of Michigan)

Objective/Scope

The objective of this project is to develop a thermal insulating material has sufficient strength and toughness for heat engine applications. The approach is to explore the composite materials in the system  $\text{Al}_2\text{O}_3\text{:Cr}_2\text{O}_3\text{/ZrO}_2\text{:HfO}_2$ .

Technical Highlight

The goal of the present work is to optimize the strength and toughness of compositions in the system  $\text{Al}_2\text{O}_3\text{:Cr}_2\text{O}_3\text{/ZrO}_2\text{:HfO}_2$  by optimizing the processing and the microstructures of the composites. Previous results indicated that the toughness could be increased by the controlling the tetragonal to monoclinic ratio of the dispersed zirconia particles ( $\text{ZrO}_2\text{:HfO}_2$ ). It has also been demonstrated that the high strength and high toughness can be only obtained when the dispersed particles remain small and agglomeration is avoided.

Technical Progress

The current research will emphasize development of procedures to produce material with single dispersed zirconia particles by the use of organic surfactant.

Specimens of different matrix and dispersed phase compositions with 15 vol % of  $\text{ZrO}_2\text{:HfO}_2$  particles were produced. Starting powders were produced by co-precipitation from ethanol solution of aluminum and chromium nitrate and zirconium and hafnium oxychloride. Precipitated powders were dried, calcined and dispersed in aqueous solutions of polyelectrolytes. Polyelectrolyte molecules will absorb on the oxide surfaces and will cause repulsion between particles. Slurries containing co-precipitated oxide powders with different amount of polyelectrolyte molecules were prepared. Green compacts were made by forced filtration. The results (Table I) showed that a better distribution of zirconia were obtained with slurries containing higher amount of polyelectrolyte. Toughness of these specimens were measured by micro-indentation method and the values were confirmed by four point bend. The results are given in Figure 1. It should be noted that a peak value toughness of  $>10 \text{ MN/m}^{3/2}$  was obtained for specimens with a 40% tetragonal content.



Table 1, Co-precipitated powder mixtures (ZrO<sub>2</sub> from oxy-cl), different levels of polyelectrolyte addition.

	% of polyelectrolyte saturation adsorption			
	0	25	50	100
green density (%)	45	45	45	50
sintered density (%) (1½ hr., 1500°C)	97	97	99	>99
%tet (1½ hr, 1500°C)	48	44	47	45
%tet (1 hr., 1500°C)	30	25	35	42

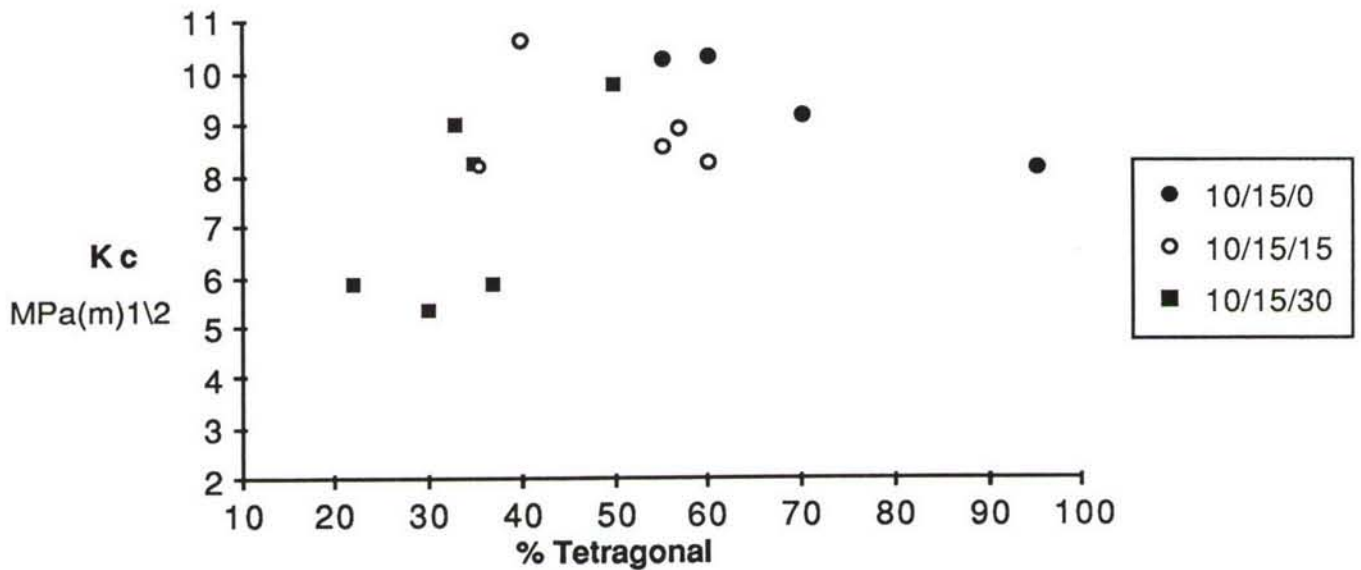


Fig. 1, Toughness vs. %tetragonal for colloidal filtration samples. Composition is indicated in key as,  $\text{m}\text{Cr}_2\text{O}_3/\text{m}\text{ZrO}_2/\text{m}\text{HfO}_2$ .

Processing and Characterization of Transformation-Toughened Ceramics with Strength Retention to Elevated Temperatures

R. A. Cutler, J. D. Bright, J. J. Hansen, D. W. Prouse (Ceramtec, Inc.) A. V. Virkar and D. K. Shetty (University of Utah)

Objective/Scope

Previous work[1] has shown that it is possible to increase the strength of  $\text{Al}_2\text{O}_3\text{-ZrO}_2$  ceramics by incorporating transformation-induced residual stresses in sintered specimens consisting of three layers. The outer layers contained  $\text{Al}_2\text{O}_3$  and unstabilized  $\text{ZrO}_2$ , while the central layer contained  $\text{Al}_2\text{O}_3$  and partially stabilized  $\text{ZrO}_2$ . When cooled from the sintering temperature, some of the zirconia in the outer layers transformed to the monoclinic form while zirconia in the central layer was retained in the tetragonal polymorph. The transformation of zirconia in the outer layers led to the establishment of surface compressive stresses and balancing tensile stresses in the bulk. In theory, the residual stresses will not decrease with temperature until the monoclinic to tetragonal transformation temperature is reached since monoclinic and tetragonal  $\text{ZrO}_2$  polymorphs have nearly the same coefficients of thermal expansion. The demonstration of the retention of residual stresses with temperature is a primary purpose of this project.

Previous work was accomplished using dry pressing techniques. The development of slip casting technology for layered composites will allow for better dispersion of zirconia in alumina and thereby facilitate higher volume monoclinic  $\text{ZrO}_2$  in outer layers without strength degrading microcracking. A comparison between slip casting and dry pressing techniques will be made to identify higher strength materials for more detailed characterization during the second year of the project.

Technical Highlights

Experimental Procedures

Monolithic and three layered  $\text{Al}_2\text{O}_3\text{-10 vol. \% ZrO}_2$  bars used for room temperature testing[2] required too high of loads for testing at elevated temperatures due to their large cross-section (6 mm x 12 mm). Consequently, bars of smaller cross-section (nominally 4.5 mm x 5 mm) were made. It was also determined, due to the relatively low monoclinic content (36-38%)[2] in the unstabilized zirconia, to increase the residual compressive stresses by increasing the zirconia content from 10 volume percent to 15 volume percent. Unstabilized ( $\text{Al}_2\text{O}_3\text{-15ZrO}_2$ ) and partially stabilized ( $\text{Al}_2\text{O}_3\text{-15ZrO}_2(2 \text{ mole \% Y}_2\text{O}_3)$ ) powders



were dispersed and spray dried as reported previously[2], to make powders for the outer and inner layers, respectively. The powders were uniaxially pressed at 35 MPa, followed by isostatic pressing at 207 MPa. Monolithic bars were made of the inner and outer layer powders, as well as three sets of composite bars in which the outer layer thickness,  $d_1$ , was 1/3, 1/6, and 1/12 the total thickness,  $d$ , of the bar. Specimens were chamfered in the green state, unless otherwise stated, to avoid stress-induced transformations which occur upon grinding. Bar shaped specimens were sintered at 1585°C for 60 minutes and hot isostatically pressed (HIP) at 1500°C for 30 minutes in 175 MPa Ar overpressure.

X-ray diffraction (XRD) was used to determine the  $ZrO_2$  polymorph type[3] and calculate the theoretical density. Density was determined by water displacement. Strength bars were broken in four-point bending (20 mm inner span and 40 mm outer span) at a crosshead speed of 0.5 mm/min. Fractography using a stereo microscope was coupled with electron microscopy to determine fracture origins. Hardness and indentation fracture toughness[4] were determined on one fractured specimen (picked at random) after polishing to a one micron finish.

## Results and Discussion

XRD showed that the monoclinic content ranged between 60 and 70 percent, depending on the  $ZrO_2$  particle size used (i.e., Daiichi DK1 or DK2) and sintering conditions. Room temperature characterization data are given in Table 1. Although surface grinding increases the strength by roughly 25% for the bars in question, it was determined to test the bars in the unground condition because it was then certain that the increase in strength was due to the residual compressive transformation-induced stresses[1] and not to compressive stresses created within the near surface region due to grinding.

The strength data (see Table 1) indicated that compressive stresses in the three layer composites having layers of equal thickness are on the order of 130 MPa. Assuming a modulus of 355 GPa and  $\Delta\epsilon_o$  [1] to be  $1.7 \times 10^{-3}$  (taking the percent monoclinic in the 15 vol. %  $ZrO_2$  to be 70% and the volume change of tetragonal to monoclinic to be 4.9%), the calculated residual compressive stress should be 270 MPa. All of the bars failed from the tensile surface or chamfer region suggesting that thinner outer layers (i.e., increased residual compressive stresses) will result in improved strength. Based on these tests, it was also determined to use the powder with coarser  $ZrO_2$  particles (DK2) for further testing.

Density, strength, hardness, and fracture toughness[4] data for monolithic, as well as three-layered bars (all



Table 1  
Characterization of  $\text{Al}_2\text{O}_3\text{-15ZrO}_2$

Code	Shrinkage (%)	Density(g/cc)		Monoclinic (%) <sup>b</sup>	Strength (MPa) <sup>a</sup>	
		Sintered	HIP		"as-sintered"	"as-HIPped"
A <sup>c</sup>	16.5	4.18	4.29	2.3	418±68	494±55
B <sup>d</sup>	16.8	4.23	4.27	68.9	318±64	439±37
C <sup>e</sup>	16.8	4.23	4.27	71.6	363±20	453±21
D <sup>f</sup>	16.4	4.21	4.28	---g	490±99	571±83
E <sup>h</sup>	16.2	4.20	4.29	---i	527±40	588±49

- a. Strength data for 5 bars broken in four point bending.  
b. Percent monoclinic  $\text{ZrO}_2$  [3] (balance is tetragonal).  
c. Monolithic inner material ( $\text{ZrO}_2$  partially stabilized (Zircar)).  
d. Monolithic outer material (unstabilized DK-1 Zirconia (Daichi)).  
e. Monolithic outer material (unstabilized DK-2 Zirconia (Daichi)).  
f. Three layer composite using Code A for inner material and Code B for outer layers. All layers of equal thickness.  
g. Not measured (similar to B).  
h. Three layer composite using Code A for inner layer and Code C for outer layers. All layers of equal thickness.  
i. Not measured (similar to C).

bars having a total thickness of 4.5 mm) with outer layer thicknesses of 375, 750, and 1500 microns, are given in Table 2. The strength data are depicted graphically in Figures 1 and 2. The higher strengths observed, as compared

Table 2  
Mechanical Property Data for  $\text{Al}_2\text{O}_3\text{-15ZrO}_2$

Code	$d_1$ ( $\mu\text{m}$ )	Strength Data(MPa) <sup>a</sup>				H(GPa) <sup>b</sup>		$K_{IC}$ (MPa-m <sup>1/2</sup> ) <sup>g</sup>	
		# <sup>c</sup>	$\bar{x}$ <sup>d</sup>	se <sup>e</sup>	m <sup>f</sup>	x	s	x	s
40A	---h	18	451.4	47.7	9.9	17.1	0.53	3.79	0.24
40B	---i	18	545.1	50.1	11.4	16.7	0.31	3.80	0.39
40C	1500	10	570.4	62.0	8.8	17.4	0.58	3.20	0.27
40D	750	20	696.1	87.7	8.3	17.0	0.71	4.84	0.34
40E	375	18	825.0	53.7	16.1	17.4	0.27	4.70	0.21

- a. Four point bend strength on 4.5 mm x 5 mm x 50 mm bars.  
b. Vicker's hardness determined at loads between 75 and 225N.  
c. Number of bars broken.  
d. Mean value.  
e. Standard deviation.  
f. Weibull modulus.  
g. Indentation toughness[4].  
h. Monolithic "outer layer"  $\text{Al}_2\text{O}_3\text{-15ZrO}_2$ .  
i. Monolithic "inner layer"  $\text{Al}_2\text{O}_3\text{-15ZrO}_2$ (2.0 mole %  $\text{Y}_2\text{O}_3$ ).

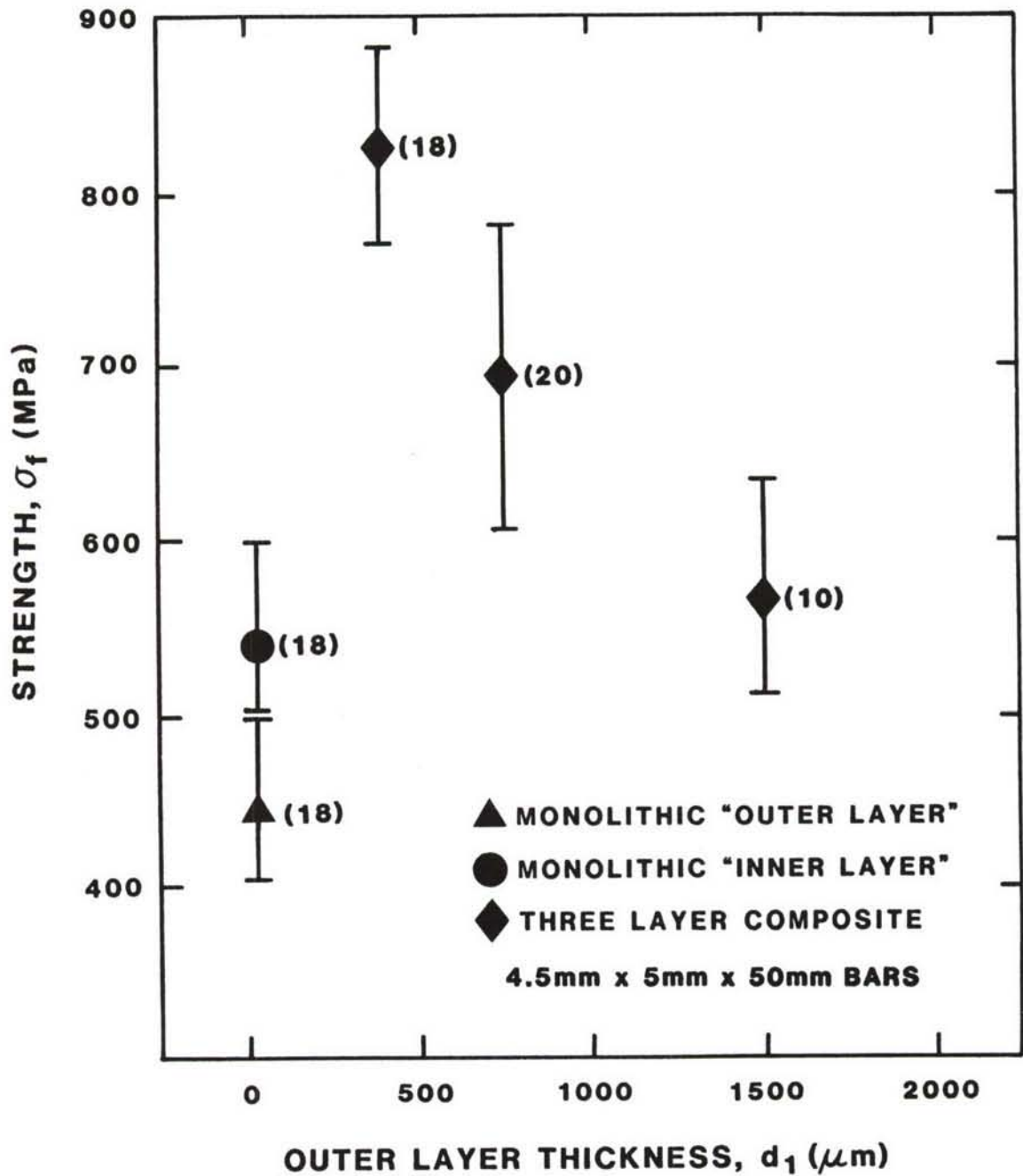


Figure 1. Room temperature strength comparison between monolithic and three layer  $\text{Al}_2\text{O}_3$ -15 vol. %  $\text{ZrO}_2$  composites.

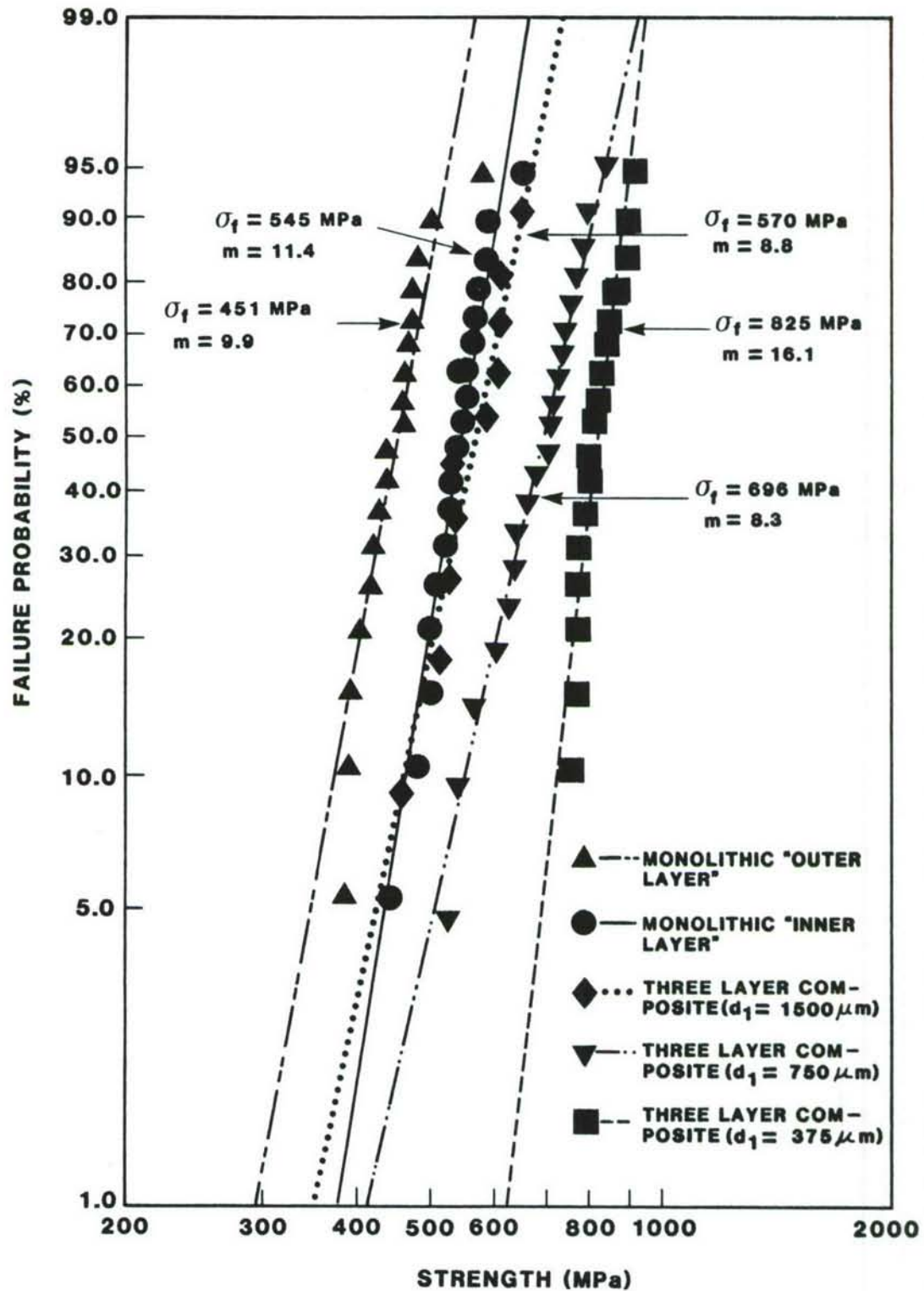


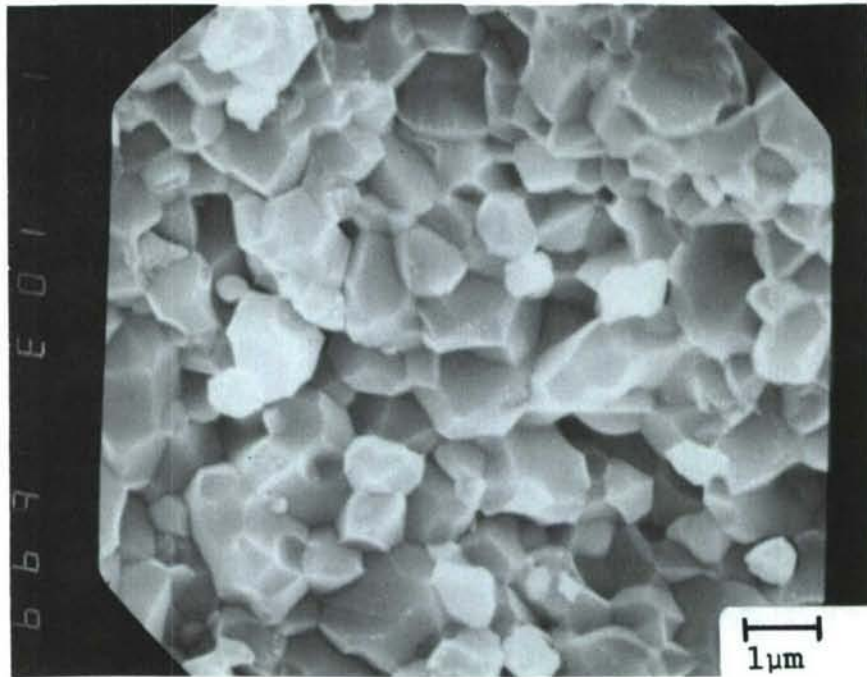
Figure 2. Failure probabilities of monolithic and three layered  $\text{Al}_2\text{O}_3$ -15 $\text{ZrO}_2$  composites.



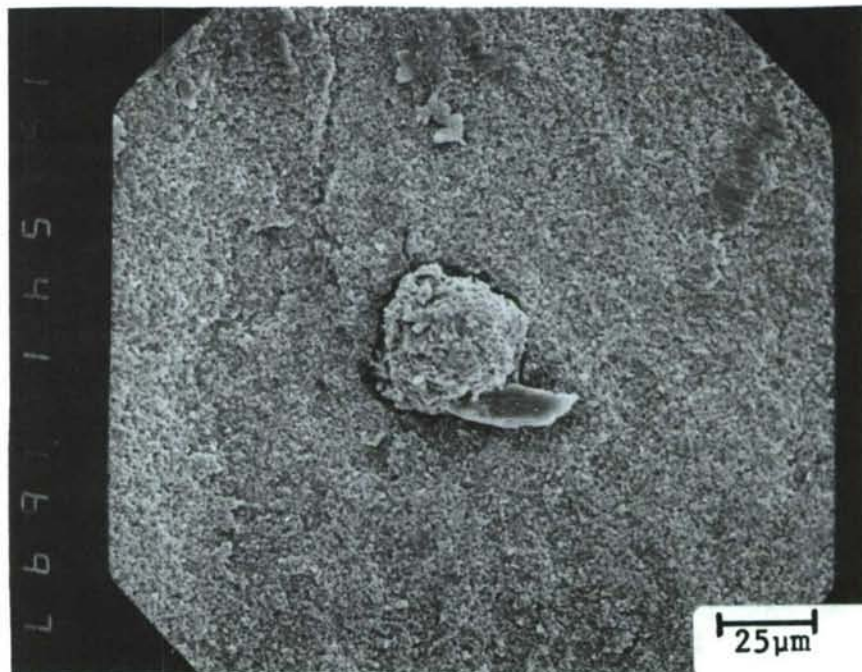
to data for  $\text{Al}_2\text{O}_3$ -10ZrO<sub>2</sub> reported previously[2], are the result of higher monoclinic zirconia content in the outer layers leading to higher compressive stresses in the outer layers and improved processing (elimination of CeO<sub>2</sub> inclusions and uniformity of outer constraining layers). The strength increases with decreasing outer layer thickness, as predicted[2], indicative of failure from near surface defects in the outer layers. Fractography showed that surface flaws controlled failure in most cases. Although the microstructure was fine grained (see Figure 3a), internal failures occurred due to agglomerates (Figure 3b), voids, or regions containing exaggerated grain growth (Figure 3c). Further optimization of processing conditions and zirconia particle size should improve strength.

Failures originated in the outer layer of three-layer composites, suggesting that residual stresses are on the order of 375 MPa, 245 MPa, and 120 MPa for 375, 750, and 1500 microns outer layer thicknesses, respectively (total bar thickness in all cases was approximately 4.5 mm). If the monoclinic content in the bulk of the outer layer is 70%, the value measured by XRD, the stresses introduced are only one half of those predicted[5]. It is possible, however, that the monoclinic content is higher in the near surface region which is penetrated by x-rays than in the bulk of the outer layers. It is noteworthy that the strength of the monolithic composite was doubled by incorporating stresses, without a post-sintering surface treatment. This was verified by heating the samples to 1500°C for one hour and again measuring room temperature strength, with no observed strength change.

The usefulness of this technique is seen when one compares Weibull plots of monolithic versus three layer specimens. The lowest strength specimen of the 375 micron outer layer bars had strength greater than the highest strengths of the monolithic bars (see Figure 2). The increase in Weibull modulus (16.1 for three layer specimens with  $d_1 = 375$  micrometers as compared to 9.9 for monolithic "outer layer" specimens) can be explained by superposition of stresses. If 374 MPa (the difference in strength between the three layer composite with the highest strength ( $d_1=375$  micrometers) and the monolithic "outer layer" material) is added to the failure stress of each monolithic outer layer specimen, the mean strengths are identical (825 MPa) and the Weibull modulus of the monolithic material increases from 9.9 to 17.6. This is in excellent agreement with the experimentally determined Weibull modulus of 16.1 (see Figure 2). Using the same logic, the Weibull modulus of the intermediate thickness three layer composite ( $d_1 = 750$  microns) would increase to 13.0, contrary to observation ( $m = 8.3$  as shown in Figure 2). Further characterization of stresses are underway for the  $\text{Al}_2\text{O}_3$ -15 ZrO<sub>2</sub> composites.



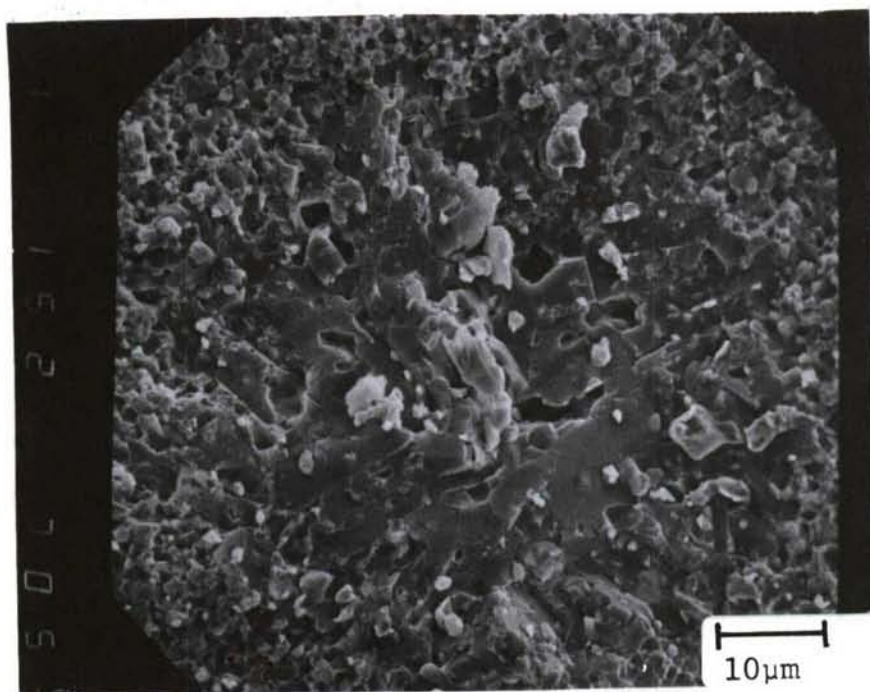
(a)



(b)

Figure 3. Fracture surfaces of  $\text{Al}_2\text{O}_3\text{-15ZrO}_2$ . (a) Typical microstructure, and (b) agglomerate remnant from spray drying.





(c)

Figure 3 (continued). (c) Exaggerated grain growth.

While this technique is valuable for components failing due to contact stresses or thermal stresses, as is the case for most ceramics, it will lead to degraded strength for materials failing in uniform tension, due to the balancing internal residual tensile stresses.

Data from elevated temperature bend tests are shown in Figure 4. The residual stresses decrease as the monoclinic  $\text{ZrO}_2$  converts to tetragonal zirconia with increasing temperature. The decrease in strength is initially similar to transformation toughened  $\text{Al}_2\text{O}_3$ -15 $\text{ZrO}_2$  (see Figure 4) and zirconia ceramics reported previously[6.7], but falls precipitously at temperatures above 750°C. Strength data in Figure 4 suggest that the residual stresses are non-existent by 1000°C. Substantial stresses, however, still exist at 750°C, as evidenced by the layered composite being 200 MPa stronger than the monolithic "outer layer" composite. The decrease in strength is expected to be a function of particle size among other parameters, and a narrow  $\text{ZrO}_2$  size distribution in the outer layer would result in transformation from tetragonal to monoclinic over a smaller temperature range. One must use larger  $\text{ZrO}_2$  particle size to avoid the m  $\rightarrow$  t transformation at temperatures below



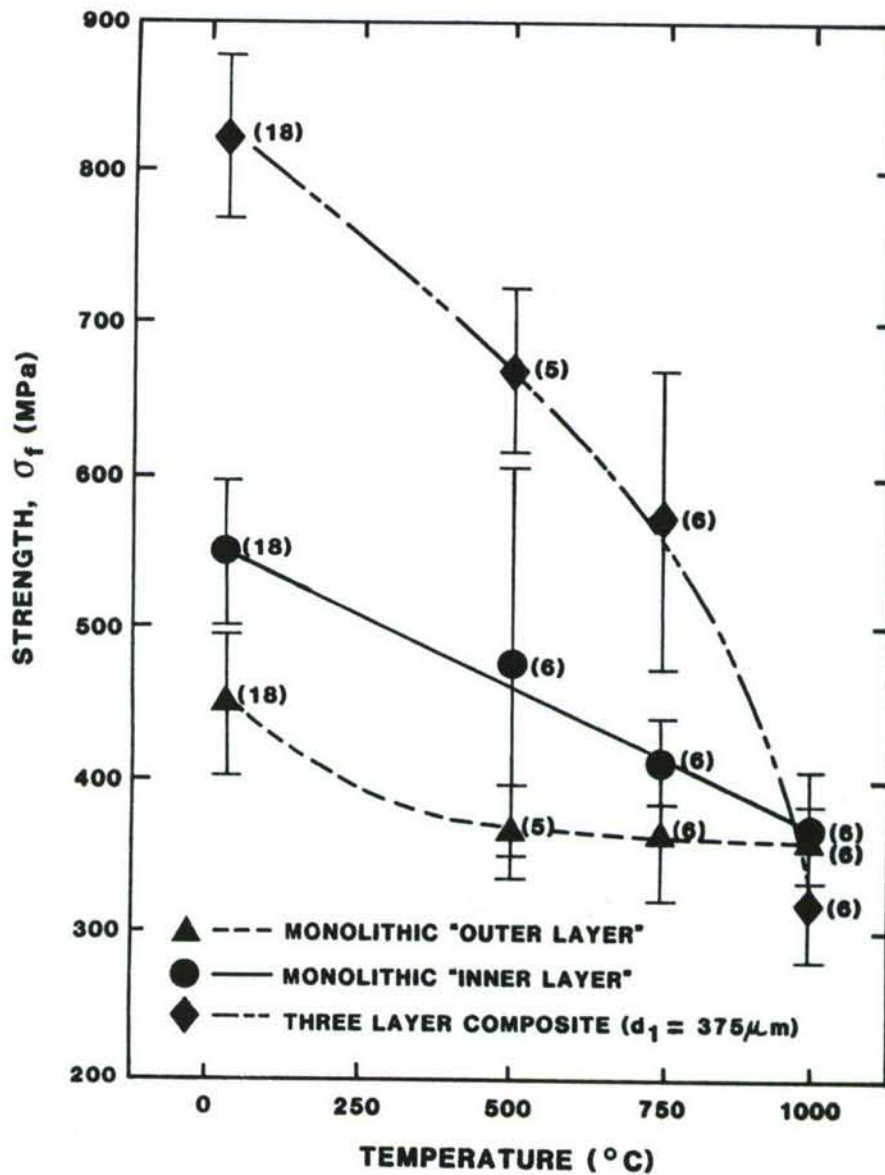


Figure 4. Strength of  $\text{Al}_2\text{O}_3\text{-15ZrO}_2$  as a function of temperature. Note that substantial residual stresses are retained to  $750^\circ\text{C}$ .

$1000^\circ\text{C}$ , and yet ensure that microcracking which can lower the strength, does not occur. The retention of over half of the room temperature residual stresses to  $750^\circ\text{C}$  suggests that further optimization of  $\text{ZrO}_2$  particle size will increase the temperature at which stresses can be retained. The substitution of  $\text{HfO}_2$ , or  $\text{ZrO}_2\text{-HfO}_2$  solid solutions, for  $\text{ZrO}_2$  will substantially increase the temperature at which stresses are retained.

The change in strength between the three layer composite and the monolithic outer layer ceramic is compared in Figure 5. The residual stresses decrease slightly between room temperature and 500°C, more significantly between 500 and 750°C, and rapidly between 750 and 1000°C (Figure 5).

In order to understand the strength decrease, the coefficients of thermal expansion were measured for the monolithic "inner" and "outer" materials. The "outer layer" material ( $\text{Al}_2\text{O}_3\text{-15ZrO}_2$ ) had a thermal expansion coefficient of  $6.5 \times 10^{-6}/^\circ\text{C}$  between 25 and 1000°C while the "inner layer" material ( $\text{Al}_2\text{O}_3\text{-15ZrO}_2(\text{Y}_2\text{O}_3)$ ) had a thermal expansion coefficient of  $8.0 \times 10^{-6}/^\circ\text{C}$  over the same temperature range. These values, as measured by an outside laboratory, would suggest that large temperature stresses (on the order of 593 MPa (assuming a stress free body above 1000°C)) are superimposed on the transformation stresses. As can be seen in Figure 6, significant hysteresis exists for the "outer layer material" suggesting that the transformation to tetragonal  $\text{ZrO}_2$  occurs between 920 and 980°C on heating, and the  $t \rightarrow m$  transformation upon cooling occurs between 540 and 180°C. Additionally, the absolute magnitude of the thermal expansion coefficients is low, relative to published data for  $\text{Al}_2\text{O}_3$  and  $\text{ZrO}_2$  and places some doubt on the measurements. The laboratory was able to duplicate their thermal expansion data. If significant temperature stresses are present, one would predict a linear strength decrease, contrary to observation. Thermal expansion data will be measured in-house within the next two months, as a dilatometer system is currently being installed.

In order to find an alternative explanation for the decrease in strength with increasing temperature, Dr. R. Winterton of Dow Chemical Company performed x-ray diffraction on the monolithic outer layer material (sample thickness constraints (250 micrometers) did not allow three layer composites to be tested in this apparatus) as a function of temperature. The percent monoclinic was initially 66.5%, and decreased slightly at temperatures up to 700°C, with rapid conversion to tetragonal  $\text{ZrO}_2$  above 700°C (see Figure 7). The x-ray diffraction data are in excellent agreement with the strength change measured experimentally (compare Figures 5 and 7). It should be noted that one would expect monoclinic zirconia in the outside layers of a three layer composite to convert to tetragonal  $\text{ZrO}_2$  at lower temperatures than the monolithic specimen due to constraint imposed on the particles by the residual compressive stress. The observed decrease in strength of the three layer composite between room temperature and 500°C could alternatively be due to moisture sensitivity of the  $\text{Al}_2\text{O}_3\text{-ZrO}_2$  composite. The important conclusion from the data in Figures 5 and 7 is the verification that significant transformation-induced stresses were introduced in  $\text{Al}_2\text{O}_3\text{-ZrO}_2$  composites by the technique described previously[1.5].



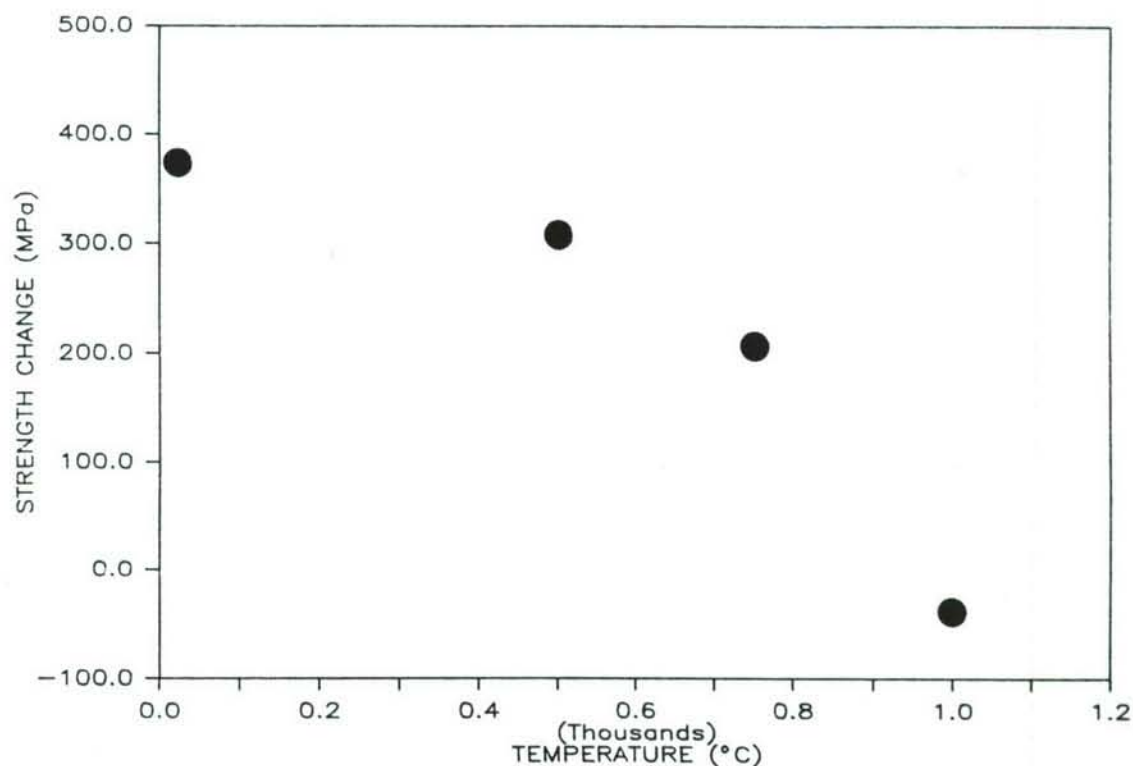
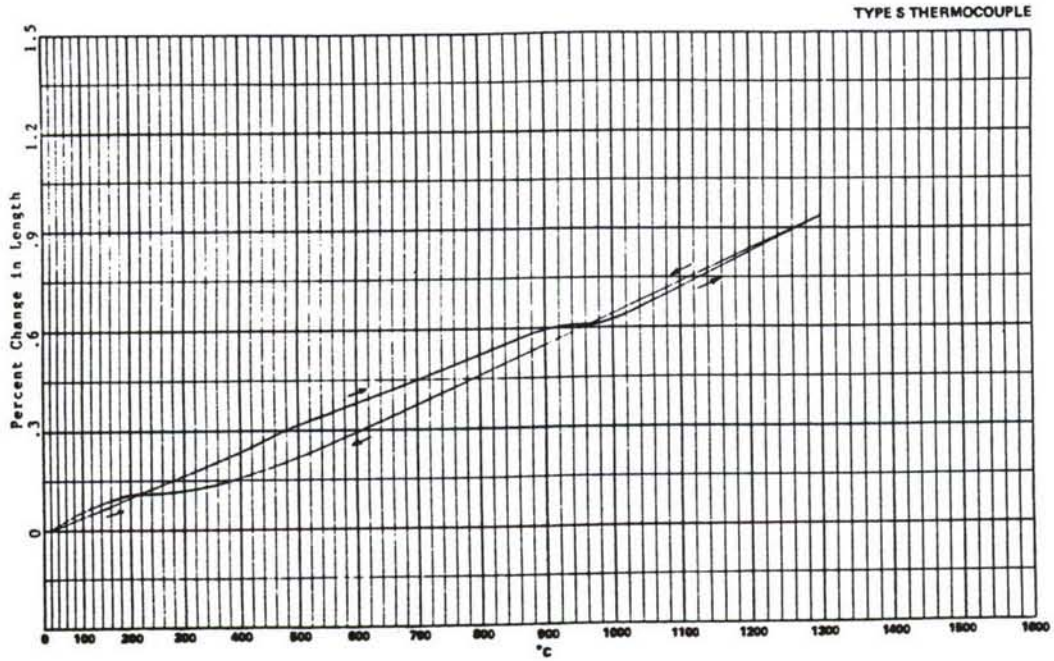


Figure 5. Strength change (in four point bending) between three layer composites with residual stresses and monolithic "outer layer" specimens as a function of temperature.

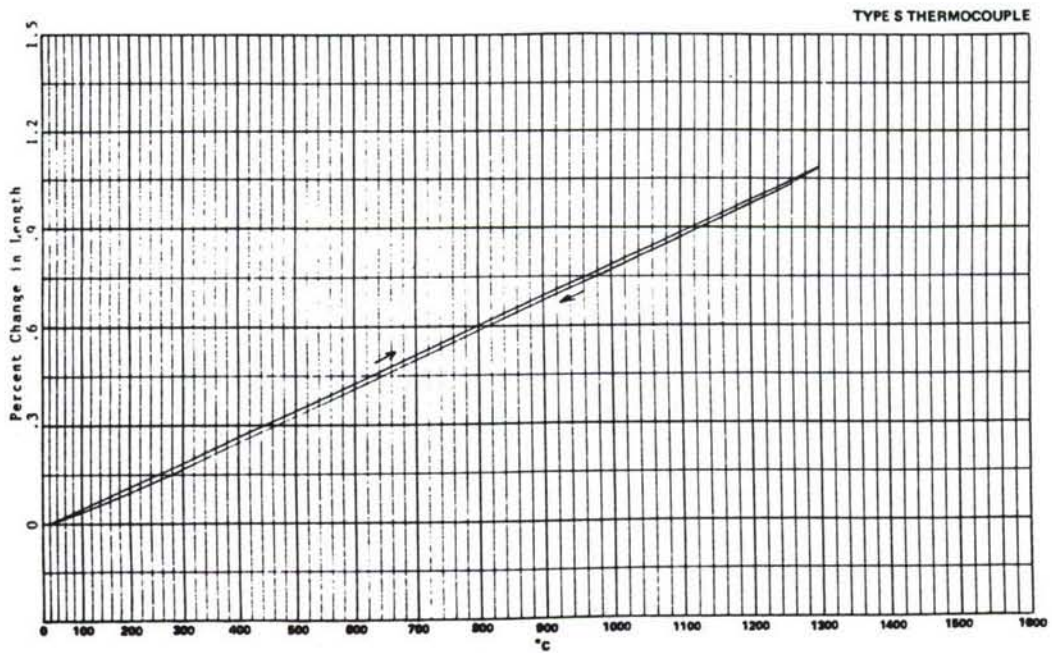
In order to improve the retention of residual stresses above 750°C, high temperature annealing was performed to change the  $ZrO_2$  grain size distribution (i.e., grow small grains without inducing microcracking). Annealing at 1300°C for 16 hours did not significantly affect the amount of monoclinic in the material. Annealing at 1400°C for 16 hours, or 1500°C for 4 hours increased the monoclinic content from 59% to 67%. although room temperature strengths were unchanged. Cursory electron microscopy showed no evidence of grain growth or microcracking.

Changing the size distribution of the starting  $ZrO_2$  powder was also investigated. A zirconia powder (K906) with a median particle size of 1.35 microns (all particles less than 3.7 microns, 90% less than 2.2 microns, and 90% greater than 0.65 microns) was obtained from J. Peterson of Teledyne Wah Chang Albany. The powder was processed in an identical manner to previous work[2]. This "narrow"  $ZrO_2$  size distribution  $Al_2O_3$ -15 $ZrO_2$  powder was compared to  $ZrO_2$  powder currently used [5] which has 100% of the powder less than 1.8 microns and an average particle size





(a)



(b)

Figure 6. Thermal expansion data obtained on monolithic bar specimens. (a) Outer layer ( $\text{Al}_2\text{O}_3\text{-15ZrO}_2$ ), (b) inner layer material ( $\text{Al}_2\text{O}_3\text{-15ZrO}_2(\text{Y}_2\text{O}_3)$ ).

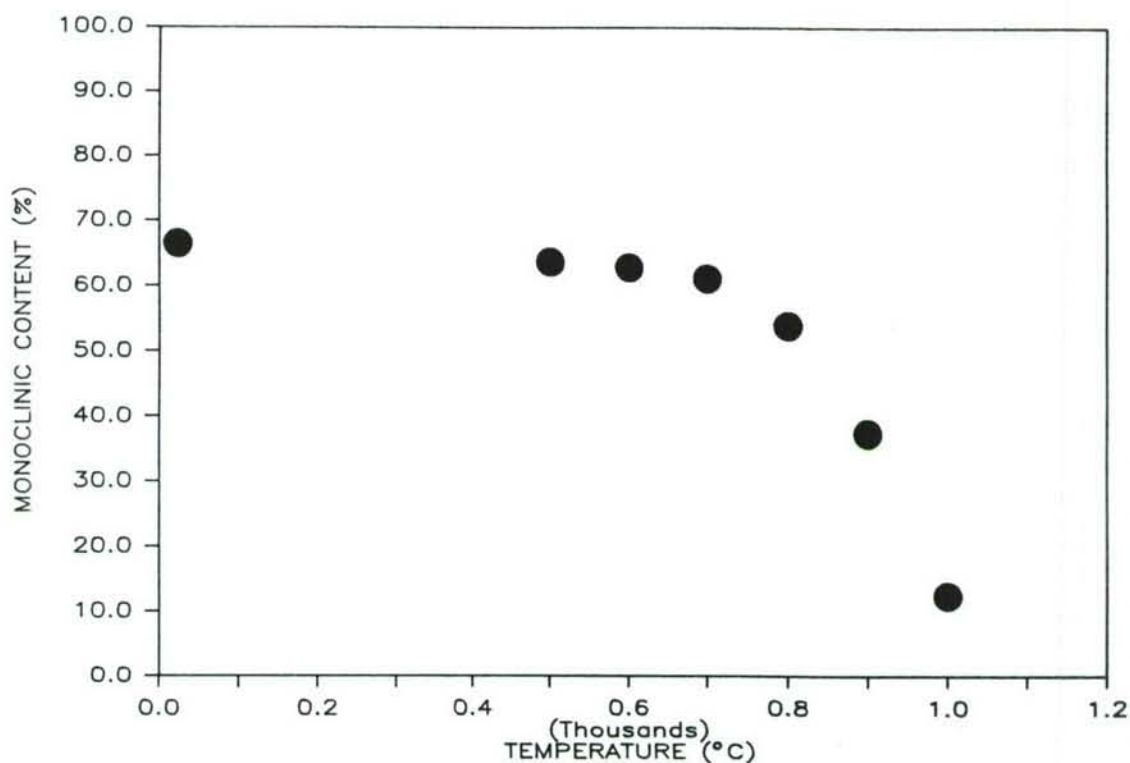


Figure 7. X-ray diffraction data showing the percent monoclinic  $ZrO_2$  in a monolithic  $Al_2O_3-15ZrO_2$  (outer layer material) specimen as a function of temperature.

of 0.4 microns (90% less than 1.2 microns and 70% greater than 0.2 microns). Three layer composites made with the Teledyne material had room temperature strengths of 795 MPa ( $s=72$  MPa) as compared to 752 MPa ( $s=86$  MPa) for the "current" three layer material when 8-10 bars of each material were tested. The percent monoclinic  $ZrO_2$  was also very comparable, with values of 59.7 and 63.4 measured for the "narrow" and "current" monolithic outer layer specimens, respectively. Percent monoclinic values of 54.3 and 52.1 were determined for the three layer composites using "narrow" and "current"  $ZrO_2$  powders, respectively. The decrease in percent monoclinic of the three layered composites, as compared to the monolithic materials, is believed to be due to the constraint factor discussed above. High temperature x-ray diffraction will be performed on a "narrow" (Teledyne  $ZrO_2$ ) monolithic specimen to see if improved high temperature strength is to be expected.

The largest improvement in strength occurred by surface treatments to the "as-sintered" bars. Using the "current"  $Al_2O_3-15 ZrO_2$  bars discussed above, the strength improved from 752 MPa for "as-sintered" bars, to 877 MPa ( $s=57$  MPa)



for bars tumbled in a deburring machine, to 934 MPa ( $\sigma = 116$  MPa) for bars which had approximately 75 microns removed from both sides using a 320 grit wheel. This strength increase is to be expected since fractography had shown that failure initiated from the tensile surface in "as-sintered" bars. X-ray diffraction is needed to determine if the light tumbling increased the monoclinic content. Weibull plots of the strength of monolithic and three layer composites which have been sintered and tumbled will be compared.

Dispersion of  $\text{Al}_2\text{O}_3$ - $\text{ZrO}_2$  powders was investigated with both pH control and surface active agents used in spray drying[2]. Based on room temperature strength testing it was determined to use the same dispersion system in slip casting as previously used in spray drying. Slip cast billets (100 mm by 100 mm) were prepared using vacuum degassed slips of  $\text{Al}_2\text{O}_3$ -15 $\text{ZrO}_2$  powder. These billets demonstrated that it was possible to control the outer layer thickness and make uniform layers via this process. Sintering and strength testing of bars cut from these billets, in comparison to specimens made from spray dried powder, is in progress.

Tape casting was evaluated as an alternative method of fabrication, as compared to powder pressing, due to the ability to control the layers to precise thicknesses. Individual layers of  $\text{Al}_2\text{O}_3$ -15 $\text{ZrO}_2$  were laminated together using conventional ceramic packaging techniques and equipment. The resulting composite (5 mm thick) was sintered to make a three layer composite. Although the above results demonstrate that tape casting can be used to make layered composites of considerable thickness, slip casting is preferable due to problems associated with binder removal from tape cast composites.

#### Status of Milestones

Both "elevated temperature toughness testing (part of milestone 123702)" and "slip casting/spray drying comparison (milestone 123703)" tasks are in progress and will be completed by the next reporting period.

#### Publications

A paper entitled "Transformation-Toughened Alumina with Improved Strength at Elevated Temperatures" by R.A. Cutler, J.D. Bright, A.V. Virkar, and D.K. Shetty was submitted to the Am. Ceram. Soc. The paper includes results of the first eight months of the ORNL funded program.



### References

1. A. V. Virkar, J. L. Huang, and R. A. Cutler, "Strengthening of Oxide Ceramics by Transformation Induced Stresses," to appear in J. Am. Ceram. Soc.
2. R. A. Cutler and J. D. Bright, "Processing and Characterization of Transformation Toughened Ceramics with Strength Retention to 1000°C," pp. 122-133 in Ceramic Technology for Advanced Heat Engines Project Semi-Annual Technical Progress Report for period Oct. 1985-April 1986, ORNL TM-10079, Oak Ridge National Laboratory. Oak Ridge, Tenn., August 1986.
3. H. Toraya, M. Yoshimura, and S. Somiya, "Calibration Curve for Quantitative Analysis of the Monoclinic-Tetragonal  $ZrO_2$  System by X-Ray Diffraction," J. Am. Ceram. Soc., 68 C-119-C-121 (1984).
4. G.R. Anstis, P. Chantikul, B.R. Lawn, and D.B. Marshall, "A Critical Evaluation of Indentation Techniques for Measuring Fracture Toughness: I, Direct Crack Measurements," J. Am. Ceram. Soc., 64[9] 533-38 (1981).
5. R. A. Cutler, J. D. Bright, A. V. Virkar and D. K. Shetty, "Transformation Toughened Alumina With Improved Strength at Elevated Temperatures," submitted to Am. Ceram. Soc. for publication.
6. F. F. Lange, "Transformation Toughening," J. Mater. Sci., 17 225-263 (1982).
7. D. C. Larsen and J. W. Adams, "Long-Term Stability and Properties of Zirconia Ceramics for Heavy Duty Diesel Engine Components," NASA report CR-174943, 40-46 (Sept. 1985).

Injection Molded Composites

M. A. Janney (Oak Ridge National Laboratory)

Objective/scope

The goals of this activity are twofold: (1) to evaluate the ability of advanced ceramic-ceramic composites to be injection molded and processed using standard wax- and/or polymer-based binder systems; and (2) to develop advanced complex-shape forming technologies that will eliminate some of the problems associated with wax- and polymer-based binder systems such as long binder removal times, cracking, and low green strength.

Technical progress

Work this period has focused on defining the effects of whisker content and solids loading on the flow properties of  $\text{Al}_2\text{O}_3$ -SiC whisker slurries. Total solids contents from 25 to 55 vol % and whisker contents up to 60% were investigated. Rheological measurements have demonstrated that both the total solids loading and the whisker content of the solid affect the processability of the slurries.

Aqueous slurries were prepared from A16SG alumina,\* SCW1S SiC whiskers,† and Darvan 7‡ and citric acid\*\* as dispersants. Dispersant levels were held constant at 0.25 wt % Darvan 7 and 0.07 wt % citric acid based on the weight of solid in the slurry. The pH was adjusted to  $9.2 \pm 0.1$  for all slurries. The dry  $\text{Al}_2\text{O}_3$  and SiC were added to an aqueous solution of the dispersants mixed by hand to incorporate the powders in the liquid, then sonicated using a 300-W ultrasonic probe.†† Some difficulty was encountered in preparing the high-solids and high-whisker-content slurries; they tended to be dilatant in the hand-mixed condition and became fluid only after intensive ultrasonic mixing. After mixing, the slurries were aged, with continuous agitation, for 4 days prior to testing. Flow behavior was determined with a Model RFS-8400 fluids spectrometer\*\*\* using a parallel plate geometry.

Flow curves for slurries with 25, 40, and 55 vol % solids are shown in Figs. 1-4. For each solids loading there was a distinctive change in flow behavior from Newtonian or shear rate thinning (pseudoplastic) flow to dilatant flow at a characteristic whisker content. For the slurries studied here, the changes to dilatant flow occurred as follows: (1) at 25 vol % solids, between 40 and 60% whiskers; (2) at 40 % solids, between 30 and 40% whiskers; and (3) at 55 vol % solids, between 15 and 20%

---

\*Alcoa, Pittsburgh, Pa.

†Tateho Chemical Co., Japan.

‡R. T. Vanderbilt Co, Norwalk, Conn.

\*\*Fisher Scientific Co, Pittsburgh, Pa.

††Model 300, Fisher Scientific Co, Pittsburgh, Pa.

\*\*\*Rheometrics, Inc., Piscataway, N. J.

ORNL-DWG-86-18264

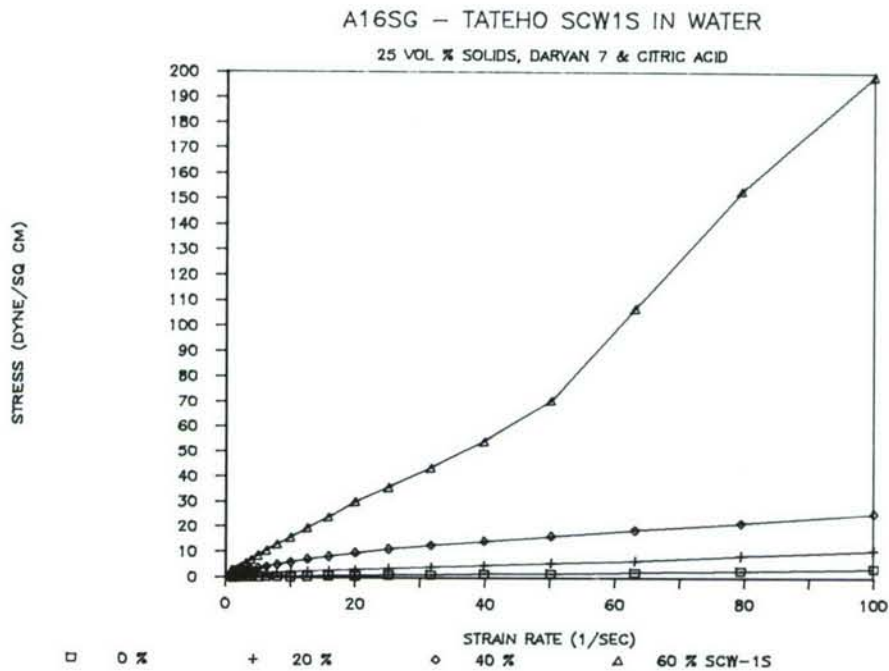


Fig. 1. Flow curves for 25 vol % A16SG-SCW1S slurries with 0, 20, 40, and 60% SCW1S whiskers.

ORNL-DWG-86-18265

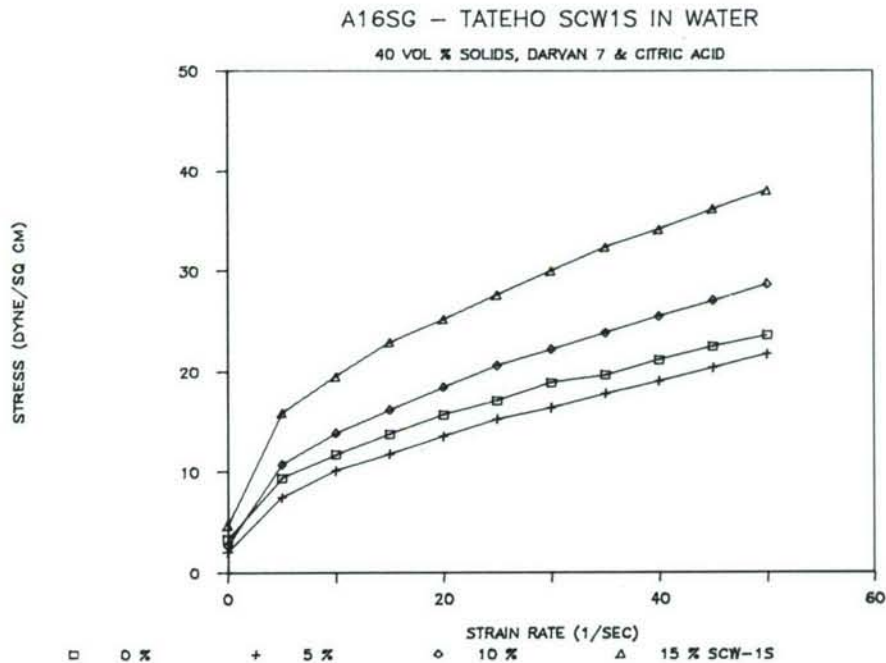


Fig. 2. Flow curves for 40 vol % A16SG-SCW1S slurries containing 0, 5, 10, and 15% SCW1S whiskers.



ORNL-DWG-86-18266

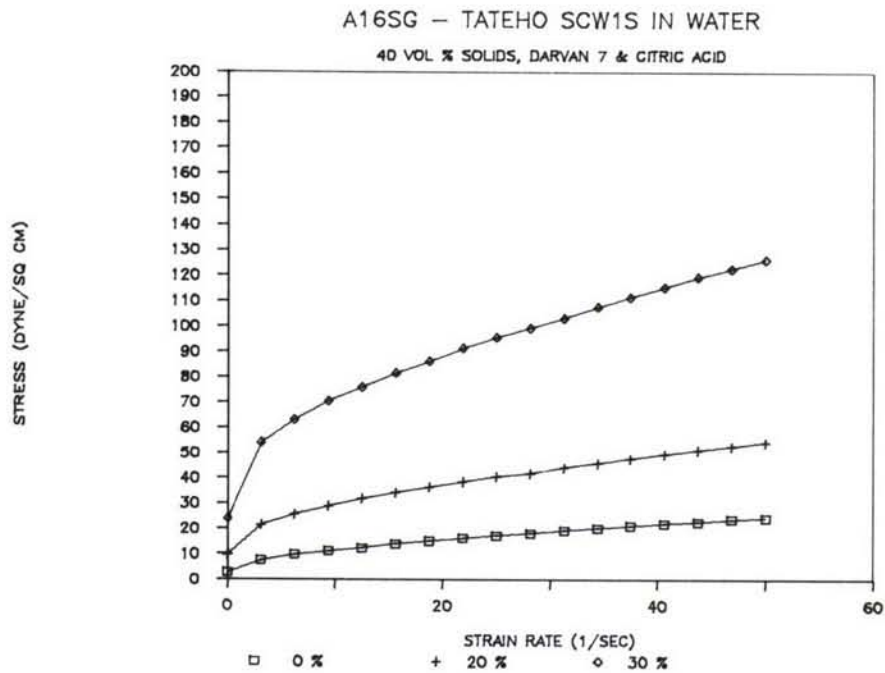


Fig. 3. Flow curves for 40 vol % A16SG-SCW1S slurries containing 0, 20, and 30% SCW1S whiskers.

ORNL-DWG-86-18267

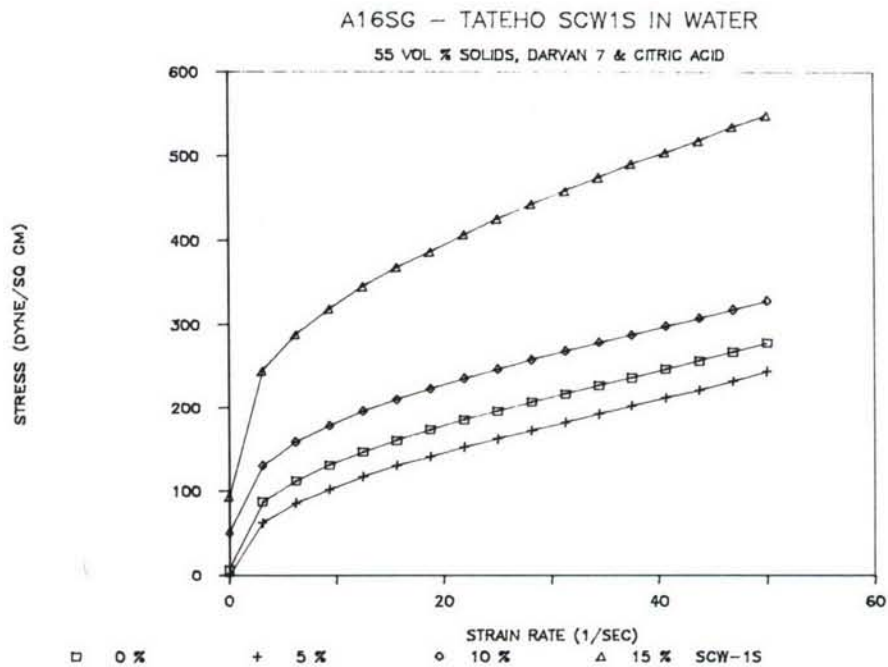


Fig. 4. Flow curves for 55 vol % A16SG-SCW1S slurries containing 0, 5, 10, and 15% SCW1S whiskers.

arise at high solids loading. The occurrence of dilatancy at relatively low loadings such as at 25 vol % solids (60% whiskers) and 40 vol % solids (40% whiskers) indicates that the "effective" solids loading is higher than the actual solids loading. For whisker-containing slurries, such an effect is not surprising; the "volume of influence" of a whisker is greater than its actual volume because of its large aspect ratio.

Figures 2 and 4 show the presence of a small, yet real, anomaly in the flow of the slurries with 40 vol % and 55 vol % solids. In both cases, the flow curves for the slurries containing 5% whiskers fall *below* the flow curves for the slurries containing no whiskers. We believe that the packing of particles in the slurries containing 5% whiskers is somewhat more efficient than in the straight alumina slurries.

Summaries of the viscosity behavior for these  $\text{Al}_2\text{O}_3$ -SiC Whisker slurries are shown in Figs. 5 and 6. Figure 5 shows the viscosity at  $50 \text{ s}^{-1}$  plotted against the whisker content in the solid phase at 25, 40, and 55 vol % total solids. As the total solids loading increases, the viscosity of the slurries also increases, and the amount of whiskers that can be incorporated into a flowable composition decreases. Figure 6 shows the same data as Fig. 5, replotted as viscosity at  $50 \text{ s}^{-1}$  versus volume fraction total solids, at various whisker loadings. We observe that the slopes of the curves for viscosity vs. volume fraction solids are relatively insensitive to the presence or absence of whiskers, at least up to 15% whiskers.

Flowable slurries containing a maximum of (1) 60% whiskers at 25 vol % solids, (2) 30% whiskers at 40 vol % solids, and (3) 15% whiskers at 55 vol % solids were produced in the Al6SG-SCW1S-Darvan 7-citric acid-water system. Rheological characterization was used to define limits of processability for the slurries based on a transition from Newtonian or pseudoplastic flow to dilatant flow.

#### Status of milestone

No activity.

#### Publications

None.

ORNL-DWG-86-18268

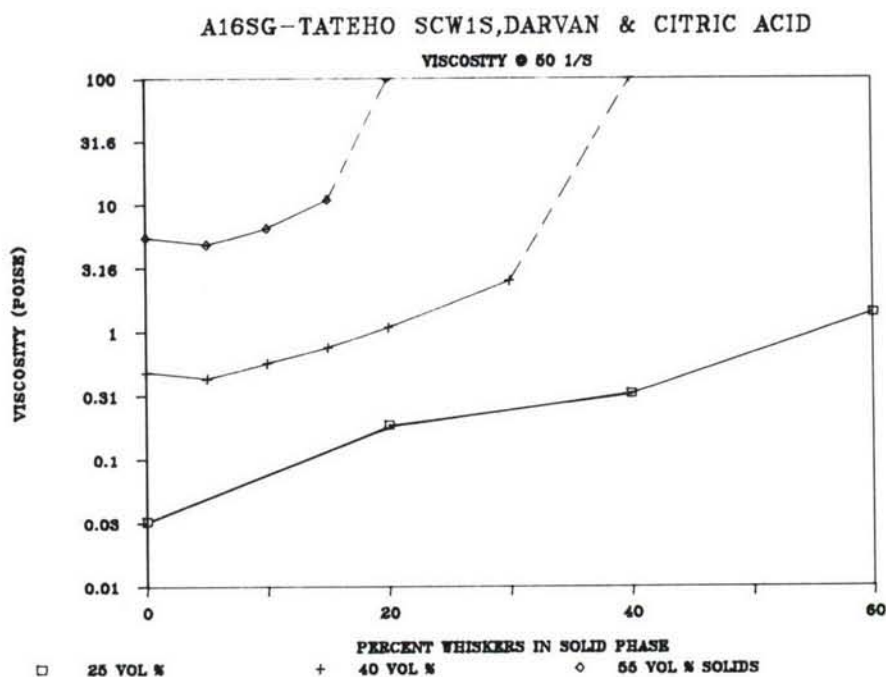


Fig. 5. Summary plot for A16SG-SCW1S slurries showing variation of viscosity (at  $50 \text{ s}^{-1}$ ) with whisker content.

ORNL-DWG-86-18269

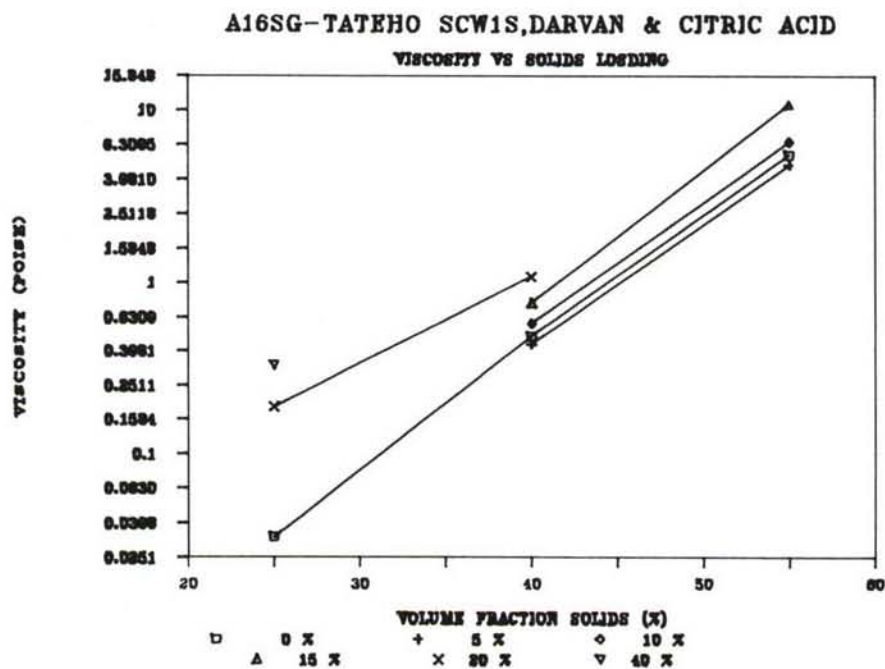


Fig. 6. Summary graph for A16SG-SCW1S slurries showing variation of viscosity (at  $50 \text{ s}^{-1}$ ) with volume fraction solids.



#### 1.2.4 Silicate Matrix

##### Mullite-SiC Whisker Composites

Solomon Musikant and S. Samanta (General Electric Co., Space Systems Division)

##### Objective/Scope

The objective of this program is to develop high toughness, high strength, refractory ceramic matrix composites which are amenable to low cost, near net shape forming for application to automotive engines.

In this program, the General Electric Company, Space Systems Division, is pursuing the development of SiC whisker reinforced mullite ( $3\text{Al}_2\text{O}_3 \cdot 2\text{SiO}_2$ ) matrix ceramic composite. In addition, the enhancement of the mullite matrix fracture toughness by the incorporation of transformation toughening by additions of  $\text{Zr}_{0.5}\text{Hf}_{0.5}\text{O}_2$  is proposed. This mullite matrix composite can meet a very significant need in the ceramic heat engine technology. That specific need is for a low thermal conductivity, high strength, tough, hard and wear resistant ceramic with intrinsically good thermal shock resistance. The intrinsically good thermal shock resistance is due to mullite's moderately low modulus of elasticity,  $30 \times 10^6$  psi (207 GPa), and relatively low coefficient of thermal expansion (CTE),  $5 \times 10^{-6}/^\circ\text{C}$ , as well as good levels of strength. The thermal conductivity is low, being approximately equal to that of  $\text{ZrO}_2$ . Since the coefficient of thermal expansion (CTE) is about half that of  $\text{ZrO}_2$ , mullite experiences for lower thermal stresses than  $\text{ZrO}_2$  when exposed to the same thermal gradient.

Similarly, in comparison to alumina, mullite is intrinsically superior with respect to thermal shock because of mullite's lower CTE and lower modulus of elasticity. Any matrix with a high CTE tends to have lower resistance to thermal shock.

The initial aim of the investigation is to prepare a composite with fracture toughness of  $> 4.0 \text{ MPa}\sqrt{\text{m}}$ .

In order to achieve this goal, we have initiated investigation of the mullite-SiC whiskers compositions with varying parameters.

The major steps in this investigation are as follows:

1. Prepare mullite/SiC whisker compositions using fine particle size mullite powder. Whisker compositions may range between 15 and 30 wt %. Whiskers may be milled for size reduction before incorporating into a batch composition.
2. Investigate sintering aids which will assist in composite consolidation.
3. Investigate the addition of a transformation toughening agent,  $\text{Zr}_{0.5}\text{Hf}_{0.5}\text{O}_2$ , to mullite SiC compositions to enhance the fracture toughness of the matrix material.
4. Consolidation methods include:
  - (a) Cold isostatic pressing and sintering.
  - (b) Hot isostatic pressing (HIP).
  - (c) Cold isostatic pressing (CIP), sintering, and hot isostatic pressing (HIP).

5. Explore the application of coating materials to whiskers to control the bonding strength of whisker to matrix; incorporating diffusion barriers at the whisker/matrix interface to minimize chemical reactions between the matrix and whisker.
6. Characterize the composites for mechanical, physical, chemical and thermal properties at room temperature and at elevated temperatures.



Technical/progressBillet Preparation and Processing

During this reporting period, preparation of finer particle size raw materials, namely, Baikowski mullite, Norton alumina,  $Nb_2O_5$ , glass I and  $ZrO_2-HfO_2$  (1:1 molar) solid solution was completed. Each of the above raw materials was first attrition milled in 2-propanol for six hours and the finer fraction of each was separated by repeated gravity sedimentation of coarse particles from an aqueous slurry of each attrition milled material. Top aqueous layers containing finer fractions of each material were siphoned off, dried and used for composite batch preparation.

As mentioned in the previous Technical Progress Report No. 8, a series of composite batch compositions have been planned to be fabricated from the above fine particle size raw material powders and clean milled Arco SC9 SiC whiskers. The procedures for fabrication of these composite billets is to include sintering of CIP'ed (cold isostatically pressed) billets in argon or nitrogen in order to minimize oxidation of SiC whiskers and then HIP'ing in Nb-1Zr metal cans using SiC powders/whiskers as a load transfer and separation medium in-between the billet and the Nb-1Zr can. The planned compositions are shown in Table I. So far, the first four composite batches (Nos. 1-4, Table I) have been prepared and are ready to be fabricated into billets.

Two preliminary billets were densified with compositions similar to 1 and 2 of Table I except that non attrition milled powders were used to conserve the limited supply of attrition milled powders. Clean, milled Arco SiC whiskers were used. The objective of these two billets was to check out the processing steps before committing the attrition milled powder prepared composites. The billets were CIP'ed at 50-55 Ksi and then sintered. Billet No. Y1 (mullite A/SiC whiskers, 70/30, wt %) was sintered in flowing argon at 1700°C for 2 hours and billet No. Y2 (mullite A/ $Nb_2O_5$ /SiC whiskers, 65.3/4.7/30.0, wt %) was sintered in flowing nitrogen at 1750°C for 2 hours. The billets were buried inside a layer of mullite-SiC whisker mixture (50:50, by weight) during sintering. Sintered billets' densities were relatively low, approximately 58% theoretical. Sintered billets were then encapsulated in Nb-1Zr cans by helium-arc welding (work performed by Mr. E. Gorsky, University of Maryland) and HIP'ed at 1600°C, 25 Ksi for 30 minutes. After HIP'ing, the Nb-1Zr cans were cut and billets surrounded by a layer of SiC powder/SiC whiskers, 70/30 wt %, used as the separation medium between the billet and Nb-1Zr can, were taken out rather easily.

However, the final densities of billets Nos. Y1 and Y2 were 93% and 57% of theoretical. It is deduced that the HIP'ing can failed in the case of billet Y2.

However, in the case of Y1, there are two changes from prior practice which may be operating to produce a billet of <95% theoretical density:

- (a) Argon sintering in lieu of air sintering.



- (b) The addition of  $\text{Al}_2\text{O}_3$  to the batch in an attempt to reduce the glassy grain boundary created by the slight excess of  $\text{SiO}_2$  in the Baikowski 193CR mullite.

To check out these effects, two more billets (Y3 and Y4) will be prepared similar to Y1 except that we will reduce the added  $\text{Al}_2\text{O}_3$  content as indicated in Table II. In order to improve sinterability, composition No. Y3 uses Mullite A2 which has a lower alumina addition than Mullite A, while composition Y4 uses as received Baikowski mullite 193CR.

The alumina/silica contents of these three mullites are as follows:

	WT %	
	$\text{Al}_2\text{O}_3$	$\text{SiO}_2$
Mullite A**	74.0	26.0
Mullite A2**	70.2	29.8
Mullite (193CR)*	68.2	31.8

\*Composition determined by EDX analysis

\*\*Composition by calculation

Composition No.Y3 contains mullite A2/SiC whiskers, 70/30, wt %, where mullite A2 is 95/5 V% Baikowski mullite/Norton alumina, instead of 85/15 V%. Composition No.Y4 contains no extra alumina added to Baikowski mullite, 193CR. No. Y4 may be considered as a baseline composition. Thus, the results should show the effect of alumina addition to the original mullite in the range of 0-15 V% on the properties of final mullite-SiC whisker composites.

#### Whisker Coating

Preliminary investigation of coating of SiC whiskers with carbon was performed during this reporting period. Such a coating on the whiskers may be beneficial in controlling matrix/whisker interface bonding. Thus, such a coating could promote more whisker pull-outs and hence increase the fracture toughness of composites. In this preliminary investigation, dilute solutions (2-10 V%) of an organic (furfuryl alcohol based) resin in iso-propyl alcohol were prepared. SiC whiskers were then impregnated with these solutions, cured, dried, and carbonized followed by hand milling. SEM examination of such treated SiC whiskers indicated the formation of a coating on the whiskers' surfaces (Figures 1, 2, and 3). It is planned to prepare an additional composite billet (Y5) using SiC whiskers, which have been coated with the 5 V% organic resin solution, in order to investigate possible  $K_{IC}$  enhancement of such ceramic composites.

We plan to prepare billets Y3, Y4 and Y5 (Table II) in the next period.

Publications

Table III lists the Milestone schedule for this study. All scheduled milestones are on target except 3.3.2 and 3.3.3. Work on these has been delayed due to funding restrictions.

None

TABLE I

MULLITE-SiC WHISKER COMPOSITES  
COMPOSITION, PERCENT BY WEIGHT

No.	Mullite A	Nb <sub>2</sub> O <sub>5</sub>	ZrO <sub>2</sub> -HfO <sub>2</sub> (1:1 molar)	Glass I	Al <sub>2</sub> O <sub>3</sub>	SiC Whisker
1	70.0	--	--	--	--	30.0
2	65.3	4.7	--	--	--	30.0
3	56.0	--	14.0	--	--	30.0
4	35.5	--	--	10.2	24.3	30.0
5	67.6	2.4	--	--	--	30.0
6	85.3	4.7	--	--	--	10.0
7	52.2	4.7	13.1	--	--	30.0

NOTE: Mullite A - Baikowski mullite, 193CR/Norton Alumina, 38-900  
85/15 V% (81.8/18.2 W%); calculated Al<sub>2</sub>O<sub>3</sub>/SiO<sub>2</sub> = 74.0/26.0 W%

Glass I - SiO<sub>2</sub>/Al<sub>2</sub>O<sub>3</sub>, 95/5 mole % (91.8/8.2 W%)



TABLE II

## MULLITE-SiC WHISKER COMPOSITES

## COMPOSITION, PERCENT BY WEIGHT

No.	Mullite	Nb <sub>2</sub> O <sub>5</sub>	ZrO <sub>2</sub> -HfO <sub>2</sub>	Glass I	Al <sub>2</sub> O <sub>3</sub>	SiC Whisker	Notes
Y1	70 (A)					30 (U)	Sinter in Ar 1700°C, 2 Hr HIP 1600°C/ 25 Ksi/30 Min
Y2	65.3 (A)	4.7				30 (U)	Sinter in N <sub>2</sub> ; 1750°C, 2 Hr HIP 1600°C/ 25 Ksi/30 Min
Y3	70 (A2)					30 (U)	
Y4	70 (M)					30 (U)	
Y5	70 (A2)					30 (F)	

**NOTE:**

Mullite (A) - Baikowski mullite, 193CR/Norton alumina, 38-900, 95/15 V%

Mullite (A2) - Baikowski mullite, 193CR/Norton alumina, 38-900, 95/5 V%

Mullite (M) - Baikowski mullite, 193CR

SiC Whiskers (U) - Sedimentation cleaned, dried, milled 1/2 hr

SiC Whiskers (F) - Same as (U) except coated with furfuryl alcohol based resin\*  
from a 5 V% solution in iso-propyl alcohol

\*Furcarb LP-340, Chem., Div., Quaker Oats, Co., Chicago, IL 60654

TABLE III

Development of Ceramic Matrix Composites for Application in the Ceramic Technology for Advanced Heat Engine Program - Mullite Si C Whisker Composites  
Subcontract 86X-00218C

Milestone Schedule

<u>Task</u>	<u>Date</u>
1. Feasibility demonstration	
1.1 Establish performance goals	12/14/84
1.2 Fabricate initial specimens	1/7/85
1.3 Characterize initial specimens	2/1/85
2. Develop process flow sheets	
2.1 Develop low cost near net shape process	
Fabricate initial liquid phase sintered specimens	4/1/85
Fabricate initial HIP specimens	4/5/85
Fabricate improved liquid phase sintered specimens	8/2/85
Fabricate improved HIP specimens	8/2/85
Select best process for optimization	1/3/86
2.2 Develop optimized process	
Document optimized process flow sheet for intermediate level of optimization	5/2/86
Document process flow sheet for final level of optimization	8/1/86
3.0 Property measurements	
3.1 Characterize microstructure of each stage of process development	
initial	5/3/85
improved	9/6/85

December 1, 1984

Task

Page 2 of 2

Date

3.1	intermediate optimization	5/2/86
	final optimization	8/1/86
3.2	Submit detailed test plan to ORNL	2/1/85
3.3	Property measurements	
3.3.1	(a) Measure MOR, $K_{IC}$ at RT and 1200C	5/3/85
	(b) Measure MOR, E, $K_{IC}$ CTE, k at RT and 1200C.	9/6/85
	Thermal soak at 1000C/500 hrs. and repeat tests.	
	(c) Repeat (b)	7/4/86
3.3.2	Perform cyclic fatigue test and fatigue crack propagation test	5/16/86
3.3.3	Model MOR of composite	8/16/85
3.3.4	Perform thermal shock analysis	8/15/86
4.0	Reports	
	Milestone schedule	12/1/84
	Bimonthly reports	1/15/85
		3/15/85
		5/15/85
		7/15/85
		9/15/85
		11/15/85
		1/15/86
		3/15/86
		5/15/86
		7/15/86
	Semi annual reports	6/15/85
		12/15/85
		6/15/86
	Final report	10/31/86



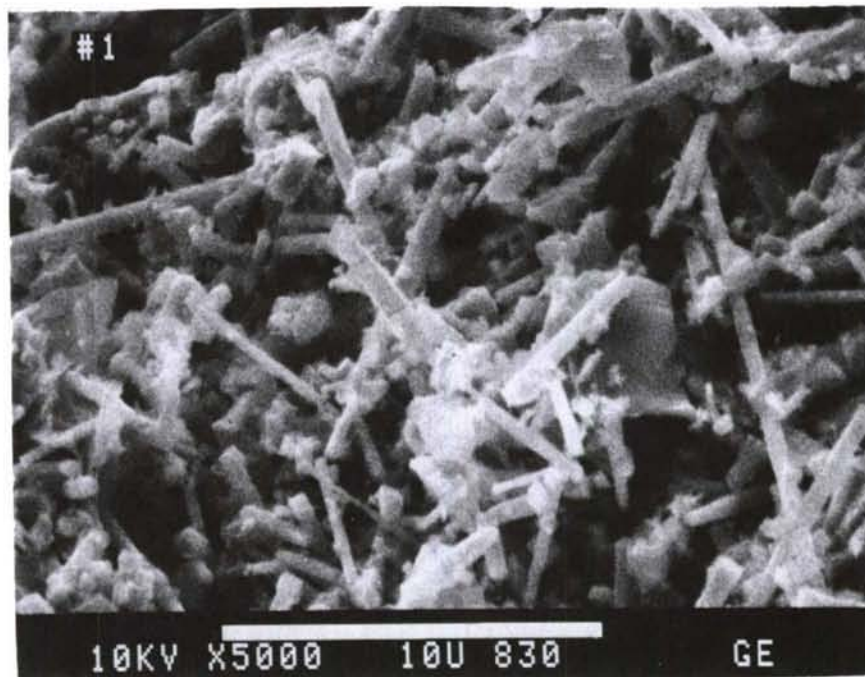


Figure 1 SiC whiskers coated with 10% resin solution, carbonized in N<sub>2</sub> at 980°C 1 hr, then separated by manual milling.

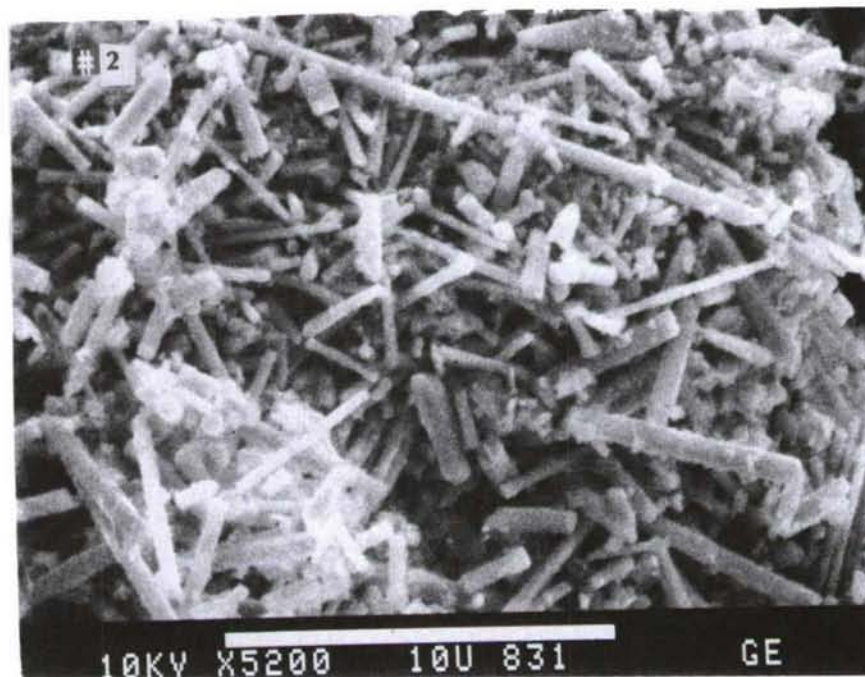


Figure 2 SiC whiskers coated with 5% resin solution, carbonized in N<sub>2</sub> at 980°C 1 hr, then separated by manual milling.

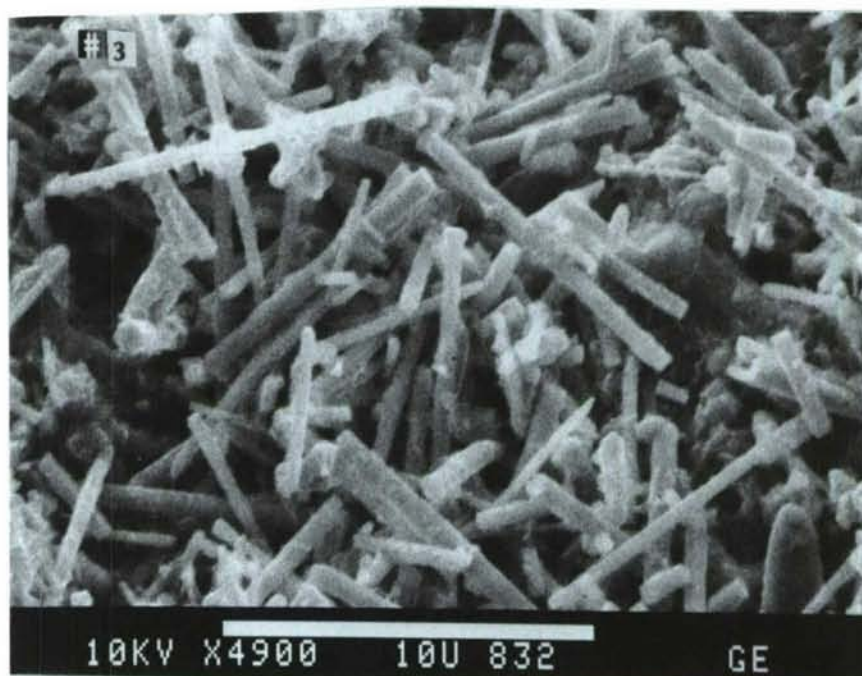


Figure 3 SiC whiskers coated with 2% resin solution, carbonized in N<sub>2</sub> at 980°C 1 hr, then separated by manual milling.

Low Expansion Ceramics for Diesel Engine Applications

J. J. Brown, Jr., R. E. Swanson (Virginia Polytechnic Institute and State University) and F. A. Hummel (Consultant)

### I. Objectives and Scope of Work

The major objective of this research is to investigate selected oxide systems for the development of a low expansion, high thermal shock resistant ceramic. Specifically, it is the goal of this study to develop an isotropic, ultra-low expansion ceramic which can be used above 1200°C and which is relatively inexpensive.

### II. Introduction

The need for stable fabricable low thermal expansion ceramics for use in advanced heat engines was first recognized in the Department of Energy Advanced Gas Turbine (AGT) technology programs. More recently, the need for ceramic materials having low thermal expansion for use in components of advanced low heat rejection diesel engines has also been recognized. Components for the AGT, including the regenerator and other parts in the hot flow path, operate under thermal cyclic or other conditions which require low thermal expansion in order for the components to have satisfactory life. Only two major ceramic systems --magnesia-alumina-silica and the lithia-alumina-silica -- have been evaluated extensively for use in fabricating these low expansion ceramic components. Compositions evaluated extensively in the magnesia-alumina-silica system are near the composition of the compound cordierite, whereas compositions evaluated in the lithia-alumina-silica system are near that of the compound spodumene. Advanced low heat rejection diesel



engine designs also have demonstrated the need for low thermal expansion ceramics which also have relatively high mechanical strength. Ceramic materials based upon either spodumene or cordierite have relatively low strength and high thermal expansion compared to fused silica, for example. It is of considerable importance to determine whether other ceramic systems exist in which the thermal expansion can be tailored so as to be very near zero over a relatively wide temperature range, extending to at least 1200°C.

The research program includes the following tasks: synthesis, property characterization, and fabrication of candidate low thermal expansion ceramics from four systems based upon aluminum phosphate, silica, mullite, and zircon. In the first two systems, the goal is to stabilize low thermal expansion, high temperature, high crystal symmetry phases via solid solution formation. In mullite, deviation from stoichiometry and solid solution formation is utilized to reduce the thermal expansion. In zircon, the crystal anisotropy and thermal expansion are reduced via solid solution formation. Based upon earlier data of the investigators, compositional ranges are evaluated by fabricating experimental specimens and determining phase content plus microstructure, thermal expansion, solidus temperature, and density. Those compositions which exhibit acceptable sintering, phase composition, and expansion characteristics are studied in more detail, including flexure strength, creep, thermal conductivity, and crystal structure. Finally, those ceramic compositions exhibiting the best

combination of properties are evaluated as to their fabrication behavior in the form of specimens having masses up to about 0.5 kg.

### III. Technical Progress for Aluminum Phosphate

#### A. Background

The value of an ultra-low coefficient of thermal expansion corresponds to the desire to find a ceramic material with high thermal shock resistance. Most of the analytical equations for thermal shock resistance are based on the following equation:

$$R = \frac{\sigma_f (1-\mu)}{E\alpha}$$

where  $\sigma_f$  is the stress required to fracture,  $\mu$  is Poisson's ratio,  $E$  is the modulus of elasticity, and  $\alpha$  is the linear expansion coefficient (1). Since  $\alpha$  is in the denominator, as its value approaches zero, the resistance to thermal shock will theoretically approach infinity. According to Hummel (2), it has been shown experimentally that dense, low porosity materials with this ultra-low coefficient of expansion do indeed have the best resistance to thermal shock.

Three materials,  $\text{AlPO}_4$ ,  $\text{BPO}_4$ , and  $\text{Li}_2\text{O} \cdot \text{Al}_2\text{O}_3 \cdot 2\text{SiO}_2$  ( $\beta$ -eucryptite) have been targeted as comprising a system that has potential for ultra-low expansion.  $\beta$ -eucryptite is of interest in that it has an overall negative coefficient of thermal expansion up to  $1000^\circ\text{C}$  (3). Work has previously been conducted with  $\beta$ -eucryptite to bring its coefficient nearer to zero. Increasing the  $\text{SiO}_2$  content as a solid solution in

$\beta$ -eucryptite was successful in bringing the coefficient closer to zero (4). However, substituting  $\text{Ge}^{4+}$  for  $\text{Si}^{4+}$  produced no significant difference in the thermal expansion coefficient (5). Another study investigated the substitution of  $\text{N}^{3-}$  for  $\text{O}^{2-}$  in  $\beta$ -eucryptite. This substitution raised the overall expansion to a positive value, but reduced the expansion anisotropy (6). Hummel and Langensiepen have found that a solid solution of 50%  $\text{AlPO}_4$  and 50%  $\beta$ -eucryptite will produce a thermal expansion as low as that of fused silica (7).

The crystal structures of  $\text{AlPO}_4$ ,  $\text{BPO}_4$ , and  $\beta$ -eucryptite are known. Eucryptite,  $\text{Li}_2\text{O} \cdot \text{Al}_2\text{O}_3 \cdot 2\text{SiO}_2$ , exists in two forms:  $\alpha$  and  $\beta$ . The  $\alpha$ -eucryptite form is the low temperature form which occurs in nature. At  $970^\circ\text{C} \pm 10^\circ\text{C}$ , this form converts to  $\beta$ -eucryptite, the form obtained when starting materials are fired in air (8).  $\beta$ -eucryptite has a structure similar to high-quartz (space group  $\text{P6}_222$ ) with half the  $\text{Si}^{4+}$  ions replaced by  $\text{Al}^{3+}$  ions (6). The charge balance is maintained by  $\text{Li}^+$  ions which locate themselves in channels running parallel to the c-axis. At  $460^\circ\text{C}$ , an order/disorder transition occurs in which the  $\text{Li}^+$  atoms begin to occupy 6-fold coordination sites as well as the 4-fold coordination sites they occupied below  $460^\circ\text{C}$  (9,10). This reaction is reversible and shows no discontinuities.

$\text{AlPO}_4$  is a half-breed derivative of silica, with  $\text{Al}^{3+}$  and  $\text{P}^{5+}$  ions occupying the sites occupied by  $\text{Si}^{4+}$  in silica. The transformations in  $\text{AlPO}_4$  are given in Figure 1.



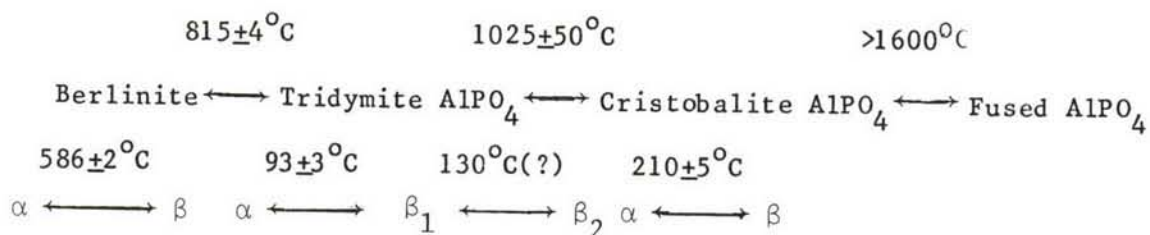


Figure 1. Transformations in  $\text{AlPO}_4$  (11).

These conversions are more rapid and occur at a lower temperature than those corresponding to silica (11).

$\text{BPO}_4$  is also a half-breed derivative of silica, with  $\text{B}^{3+}$  and  $\text{P}^{5+}$  ions occupying the sites occupied by  $\text{Si}^{4+}$  in silica. The structures of  $\text{AlPO}_4$  and  $\text{BPO}_4$  are more closely related to each other than to that of silica (12).

Even though a significant difference exists in the ionic radii of  $\text{Al}^{3+}$  and  $\text{B}^{3+}$ , the compounds  $\text{AlPO}_4$  and  $\text{BPO}_4$  form a continuous solid solution above  $1200^{\circ}\text{C}$  (13). This is possible since both compounds exhibit an ordered, tetragonal, high cristobalite structure at this temperature (12). This solid solution can be quenched in a metastable form to room temperature. The stabilization of this  $\beta$ -cristobalite solid solution is chemical, not mechanical. Long-term heat treatments will cause exsolution and the appearance of  $\text{Al}(\text{PO}_3)_3$ . Non-equilibrium conditions will arise during heat treatments due to the volatility of  $\text{B}_2\text{O}_3$  and  $\text{P}_2\text{O}_5$  and their subsequent loss from the composition (14). Horn and Hummel have developed tentative equilibrium and non-equilibrium phase diagrams for the system  $\text{BPO}_4$ - $\text{AlPO}_4$ . These are reproduced in

Figures 2 and 3.  $\beta$ -eucryptite has also been shown to form solid solutions with  $\text{AlPO}_4$  (7).

Some of the physical properties of  $\beta$ -eucryptite,  $\text{AlPO}_4$ , and  $\text{BPO}_4$  have been documented.  $\beta$ -eucryptite melts incongruently at about  $1400^\circ\text{C}$  (8). When it is heated,  $\beta$ -eucryptite undergoes a net reduction in volume, but it behaves with high anisotropy with its a-unit cell axis expanding and its c-unit cell axis contracting (6). The melting point of  $\text{AlPO}_4$  is between  $1850$  and  $2000^\circ\text{C}$ . It tends to decompose in air before melting by losing  $\text{P}_2\text{O}_5$  (15). The thermal expansion of  $\text{AlPO}_4$  is similar to that of the analogous silica structures (16).  $\text{BPO}_4$  has a melting point in the vicinity of  $1300^\circ\text{C}$  (13).

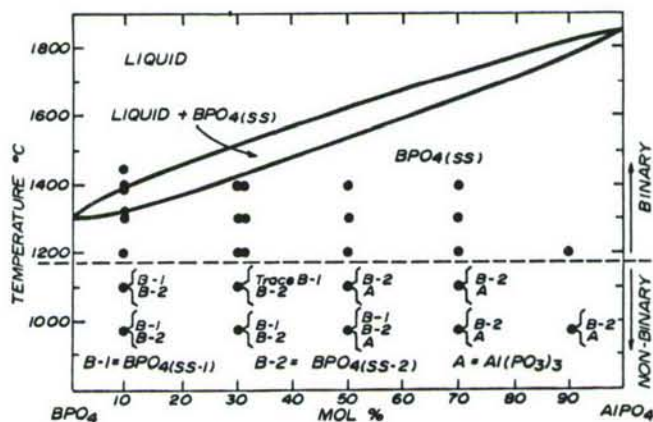


Figure 2. The binary system  $\text{BPO}_4$  -  $\text{AlPO}_4$ .

Many of the compositions studied previously were prepared by first melting the raw materials to form a glass, then by recrystallizing the glass. Horn and Hummel reported that in the system  $\text{BPO}_4$ - $\text{AlPO}_4$ , glasses

could only be obtained from compositions containing 10 to 70 mole percent  $\text{AlPO}_4$  (13).

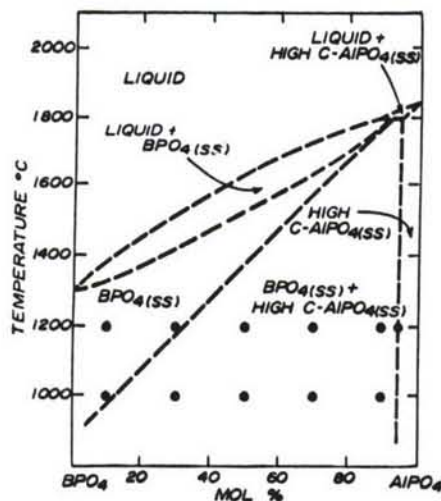


Figure 3. Tentative non-equilibrium diagram of the system  $\text{BPO}_4$  -  $\text{AlPO}_4$ .

Solid-state reactions have been used to obtain the compounds as well. Hummel used  $\text{Li}_2\text{CO}_3$ ,  $\text{Al}_2\text{O}_3$ , and Potter's flint to form  $\beta$ -eucryptite (3).

Some difficulties have been encountered in evaluating systems containing  $\text{AlPO}_4$  and  $\text{BPO}_4$ . The volatility of  $\text{B}_2\text{O}_3$  and  $\text{P}_2\text{O}_5$  requires that compositions containing these compounds be sealed in platinum. The seals sometimes fail due to either the internal pressure from  $\text{B}_2\text{O}_3$  or  $\text{P}_2\text{O}_5$  or from the deleterious reaction of  $\text{P}_2\text{O}_5$  with the platinum (17).

The ternary phase equilibria between  $\text{AlPO}_4$ ,  $\text{BPO}_4$ , and  $\beta$ -eucryptite are being studied. Initial work will concentrate on mapping the binary phase diagrams of the system primarily using differential thermal



analysis (DTA). X-ray diffraction and optical and electron microscopy will be used to supplement the DTA. Eventually ternary compositions will be studied.

Concurrent with the phase diagram work, thermal expansion data will be collected with a dilatometer.  $\text{AlPO}_4$ ,  $\text{BPO}_4$ , and  $\beta$ -eucryptite are to be tested alone, in binary compositions, and in ternary compositions. After initial screening work is completed, regions with the most promising results will be studied in greater detail.

Initial work includes determining a consistent method for preparation of  $\text{AlPO}_4$ ,  $\text{BPO}_4$  and  $\beta$ -eucryptite.

#### B. Procedure

Processes have been developed for the consistent formation of  $\text{AlPO}_4$ ,  $\text{BPO}_4$ , and  $\beta$ -eucryptite in the laboratory. The starting materials for the  $\text{AlPO}_4$  are aluminum hydroxide,  $\text{Al}(\text{OH})_3 \cdot n\text{H}_2\text{O}$ , and dibasic ammonium phosphate  $(\text{NH}_4)_2\text{HPO}_4$ , weighed to give a 1:1  $\text{Al}_2\text{O}_3$  to  $\text{P}_2\text{O}_5$  ratio after accounting for weight loss. The starting materials for  $\text{BPO}_4$  are boric acid,  $\text{H}_3\text{BO}_3$ , and dibasic ammonium phosphate, weighed to give a 1:1  $\text{B}_2\text{O}_3$  to  $\text{P}_2\text{O}_5$  ratio after weight loss. The starting materials for the  $\beta$ -eucryptite are lithium carbonate,  $\text{Li}_2\text{CO}_3$ ; alumina,  $\text{Al}_2\text{O}_3$ ; and silica gel,  $\text{SiO}_2$ . These are weighed to give a ratio of 1:1:2  $\text{Li}_2\text{O}/\text{Al}_2\text{O}_3/\text{SiO}_2$  after weight loss. In the case of the  $\beta$ -eucryptite, the raw materials were calcined at  $200^\circ\text{C}$  for 24 hours before weighing, and in the case of the  $\text{AlPO}_4$ , a weight factor for the  $\text{Al}(\text{OH})_3 \cdot n\text{H}_2\text{O}$  was determined.

The heat treatments and containers used for all samples are shown in Table 1. The raw materials for each batch are mixed under acetone using a mortar and pestle. The process is repeated between each firing.

After the final firing, samples are removed and reground dry with a mortar and pestle. The samples are then analyzed by X-ray diffraction to determine whether the reaction is complete. Finally, samples are stored in a desiccator.

Samples have been prepared for DTA and have been run. All samples were weighed on a mole percent basis then sealed in a platinum tube.  $\text{AlPO}_4$  and  $\text{BPO}_4$  were purchased from Aldrich Chemical Company and have been used for these experiments. The 100%  $\text{AlPO}_4$  and  $\text{BPO}_4$  samples received no heat treatment prior to analysis. The 90 mole percent  $\text{AlPO}_4$ -10 mole percent  $\text{BPO}_4$  sample was prefired at  $1300^\circ\text{C}$  for 48 hours, then furnace cooled before analysis. The rest of the  $\text{AlPO}_4$ - $\text{BPO}_4$  samples, 70-30, 50-50, 30-70, and 10-90, were heated to  $1650^\circ\text{C}$  as determined by optical pyrometer in a strip furnace, then quenched in water to retain a glassy phase. Laboratory synthesized  $\beta$ -eucryptite was used for analysis. The pure sample had no heat treatment prior to DTA other than that involved in forming it.

X-ray diffraction patterns were run on a few of the samples to ensure that a glassy phase had formed. In the future, optical microscopy will be used to determine the index of refraction to aid in assuring that a glassy phase has been obtained.

Table 1. Sample compositions and processing.

Sample	Compound	First Firing Temp. °C/Time h/ Container	Second Firing Temp. °C/Time h/Container	Third Firing Temp. °C/Time h/Container
KE-A1	AlPO <sub>4</sub>	1200/8/ alumina	1300/4/ alumina	1300/34.5/platinum
KE-A2	AlPO <sub>4</sub>	1200/8/ alumina	1300/4/ alumina	
KE-A3	AlPO <sub>4</sub>	1200/8/ alumina	1300/4/ alumina	
KE-A4	AlPO <sub>4</sub>	1200/8/ alumina	1300/4/ alumina	
KE-A5	AlPO <sub>4</sub>	825/6/ alumina	1100/54/platinum tube	1300/36/platinum
KE-A6	AlPO <sub>4</sub>	825/6/ alumina		
KE-B1	BPO <sub>4</sub>	800/5/ alumina	1150/7.5/ alumina	
KE-B2	BPO <sub>4</sub>	800/5/ alumina	1150/7.5/ alumina	
KE-B3	BPO <sub>4</sub>	825/6/ alumina	1100/54/platinum tube	
KE-B4	BPO <sub>4</sub>	825/6/ alumina		
KE-A7	AlPO <sub>4</sub>	400/12/platinum	1300/72/platinum	
KE-A7	AlPO <sub>4</sub>	400/12/platinum	1300/72/platinum tube	
KE-A7	AlPO <sub>4</sub>	400/12/ alumina	1090/72/ alumina	
KE-B5	BPO <sub>4</sub>	400/12/platinum	1090/72/platinum	
KE-B5	BPO <sub>4</sub>	400/12/platinum	1090/72/platinum tube	
KE-B5	BPO <sub>4</sub>	400/12/ alumina		
KE-A8	AlPO <sub>4</sub>	400/18/platinum	1090/72/ alumina	
KE-A9	AlPO <sub>4</sub>	400/12.5/platinum	1080/70/platinum	
KE-B6	BPO <sub>4</sub>	400/12.5/ alumina	1090/73/platinum	
KE-A10	AlPO <sub>4</sub>	400/15/platinum	1090/73/ alumina	
KE-B7	BPO <sub>4</sub>	400/15/ alumina	1080/72/platinum	
KE-E1	β-eucryptite	120/24/ alumina	1080/72/ alumina	
			1300/48/platinum	



### C. Results and Discussion

Pure  $\text{AlPO}_4$  and  $\text{BPO}_4$  were not formed using the compositions KE-Al-6 and KE-B1-4 listed in Table 1. Varying amounts of constituent oxides were identified using X-ray diffraction. The successful heat treatments for both the  $\text{AlPO}_4$  and the  $\text{BPO}_4$  (KE-A8-10 and KE-B5-6) were identical.  $\text{BPO}_4$  can be synthesized equally well in an alumina crucible, a platinum crucible, or a sealed platinum tube; however,  $\text{AlPO}_4$  can be best synthesized in a platinum tube or in a platinum crucible at a lower temperature than the  $1300^\circ\text{C}$  previously used. Both compositions are fired at  $175^\circ\text{C}$  for one hour,  $400^\circ\text{C}$  for about 12 hours, and  $1080\text{--}1090^\circ\text{C}$  for 72 hours. This heat treatment gives  $\text{AlPO}_4$  and  $\text{BPO}_4$  according to X-ray diffraction analysis.

The procedure listed in Table 1 for forming  $\beta$ -eucryptite gives a material which contains small amounts of impurities.

$\text{AlPO}_4$  and  $\text{BPO}_4$  do not sinter hard when heated. Both are white powders that remain easy to grind.  $\beta$ -eucryptite sinters to a very hard mass.

The heat treatments used for forming  $\text{AlPO}_4$  and  $\text{BPO}_4$  are successful for a couple of reasons. The low temperature first firing holds the temperature at  $175^\circ\text{C}$  for an hour to allow the  $155^\circ\text{C}$  decomposition of  $(\text{NH}_4)_2\cdot\text{HPO}_4$  to begin. The temperature is then raised to  $400^\circ\text{C}$  to allow the evolution of water from  $\text{H}_3\text{BO}_3$  and  $\text{Al}(\text{OH})_3\cdot\text{H}_2\text{O}$ . This allows for a slow initiation of the reactions and helps to tie up  $\text{B}_2\text{O}_3$  and  $\text{P}_2\text{O}_5$  in the compounds and prevents their volatilization during the second

firing. The second firing at nearly  $1100^{\circ}\text{C}$  is high enough to allow the reactions to go to completion, yet low enough to minimize volatilization of  $\text{B}_2\text{O}_3$  and  $\text{P}_2\text{O}_5$ .

Earlier heat treatments that failed to produce  $\text{AlPO}_4$  and  $\text{BPO}_4$  may be unsuccessful for a number of reasons. The initial firing temperatures are too high. In the case of  $\text{AlPO}_4$ , at  $1200^{\circ}\text{C}$  the volatilization of  $\text{P}_2\text{O}_5$  is appreciable, so the  $1300^{\circ}\text{C}$  second firing is much too high for a system open to air. In the case of  $\text{BPO}_4$ ,  $800^{\circ}\text{C}$  is above the melting points of both  $\text{B}_2\text{O}_3$  ( $T_m = 488-452^{\circ}\text{C}$ ) and  $\text{P}_2\text{O}_5$  ( $T_m = 580-585^{\circ}\text{C}$ ).

#### IV. Technical Progress for Silica

##### A. Background

An ideal material for thermal shock resistance will possess very low thermal expansion as well as thermal expansion anisotropy, giving virtually no dimensional change. The isotropic property is important in that localized stresses at the grain boundaries and within the crystals usually result from the anisotropic thermal behaviors along different crystallographic directions during thermal cycling. Therefore, a negligible volume change from the thermal expansion measurement does not necessarily indicate dimensional stability since this can be accomplished by large expansion in one crystallographic direction and large contraction in another. In general, phases with low symmetry, open structure, and high elastic constants tend to have low expansion

coefficients. Other factors, such as heat capacity, heat of formation, and melting point also seem to control or have a relationship with thermal expansion (18). However, the actual mechanism is still not clear, and the simple anharmonic thermal vibration model appears to be of little use in complex crystal structures.

The crystal lattice thermal expansion is usually very sensitive to minute chemical changes. It can be expected that the thermal expansion of a pure compound can be modified by introducing foreign atoms. The work of Kirchner (19) and Kirchner, et al. (20) showed that the thermal expansion and the expansion anisotropy can be reduced by changing the lattice constants or defect structure when solute atoms are added. In addition, anion substitution seems to have the same effect as cation substitution. Geiger, et al. (21) found that by partially substituting nitrogen for oxygen in  $\beta$ -eucryptite, the anisotropic expansion was greatly reduced. An interesting phenomenon of  $\beta$ -eucryptite is that it undergoes negative volume change upon heating (22). It is also interesting that crystals with thermal contraction in one crystallographic direction usually have a screw axis of symmetry along the c direction (23). The spiral of the tetrahedra can extend or contract depending on the torsional stress as pointed out by Gillery and Bush (24).

Knowing that thermal expansion can be modified by forming a solid solution, and knowing that the high temperature form of cristobalite ( $\text{SiO}_2$ ) is most structurally and thermodynamically similar to fused



silica (14), it is reasonable to choose silica as a matrix for developing new low thermal expansion ceramics. To do so, it is necessary to find the compounds that are isostructural with silica. These compounds can be of either half-breed or stuffed derivative structure of silica.  $\text{AlPO}_4$  and  $\text{BPO}_4$  are examples of the former, and lithium aluminum silicates are examples of the latter. Also, the symmetry is always lower for derivative structures. Therefore, the phase relations as well as thermal expansion behaviors will be studied by adding  $\text{AlPO}_4$ ,  $\text{BPO}_4$ ,  $\text{TiO}_2$ , and possibly  $\text{P}_2\text{O}_5$  to  $\text{SiO}_2$ . It is anticipated that the high cristobalite phase can be stabilized by the solution method.

According to Tien and Hummel (25), the  $\text{SiO}_2$ - $\text{TiO}_2$  system consists of a maximum solubility of approximately 10 wt% of  $\text{TiO}_2$  in  $\text{SiO}_2$  at  $1540^\circ\text{C}$  and a solubility limit of approximately 20% of  $\text{SiO}_2$  in  $\text{TiO}_2$ , the eutectic point being at 20%  $\text{TiO}_2$  and  $1540^\circ\text{C}$ . It was also pointed out that the thermal expansion of both  $\text{SiO}_2$  and  $\text{TiO}_2$  was changed by forming a solution.

#### B. Procedure

The compositions prepared for studying the phase relationships between  $\text{SiO}_2$ - $\text{TiO}_2$  are listed in Table 2. Batches of 20 g each were prepared by mixing silicic acid and titanic oxide in acetone, and then were calcined at  $1000^\circ\text{C}$  for 2 hours.

After calcining, samples were fired in platinum crucibles at  $1630^\circ\text{C}$  for 40 hours. After the heat-treatments the furnace cooled to below

1000°C in approximately twelve minutes. Samples were then analyzed by standard X-ray diffraction methods.

### C. Results and Discussion

The crystalline phase formed for each composition is listed in Table 2. The solid solution of  $\text{TiO}_2$  in  $\text{SiO}_2$  was evident since the X-ray

Table 2. Phase analyses of  $\text{SiO}_2$  -  $\text{TiO}_2$  compositions at 1630°C.

Sample No.	Composition, wt %		Phases
	$\text{SiO}_2$	$\text{TiO}_2$	
TS-1	95	5	$\alpha$ -cristobalite
TS-2	90	10	Glass
TS-3	85	15	Rutile (SS)*+Glass
TS-4	80	20	Rutile (SS)+Glass
TS-5	75	25	Rutile (SS)+Glass
TS-6	65	35	Rutile (SS)+Glass
TS-7	55	45	Rutile (SS)+Glass
TS-8	45	55	Rutile (SS)+Glass
TS-9	35	65	Rutile (SS)+Glass
TS-10	25	75	Rutile (SS)+Glass
TS-11	20	80	Rutile (SS)
TS-12	15	85	Rutile (SS)
TS-13	10	90	Rutile (SS)
TS-14	5	95	Rutile (SS)

---

\*\* SS indicates solid solution.

diffraction pattern of composition TS-1 before firing showed the peaks of anatase, and only  $\alpha$ -cristobalite was detected after firing. It was found the d-spacing change of cristobalite (at this low angle) was too small to be distinguished (26).

## V. Technical Progress for Mullite

### A. Background

Mullite-base ceramics have potential for use in advanced heat engines because of their low expansion, high strength, high stability, and relatively low expense compared to carbide and nitride ceramics which have been investigated extensively.

The ideal mullite should have three characteristics:

- (i) Very low coefficient of thermal expansion over a large temperature interval (up to at least 1200°C);
- (ii) High mechanical strength;
- (iii) High thermal shock resistance.

### 1. Phase Equilibria

It is well known that mullite is the only stable compound under normal atmospheric pressure in the alumina-silica binary system. It has been used extensively in refractories because of its high melting temperature. Klug (27) showed that mullite melts incongruently at 1790  $\pm$  10°C, and its solid solution limits were defined as a function of temperature. The phase diagrams are shown in Figure 4 (28) and Figure 5 (27).



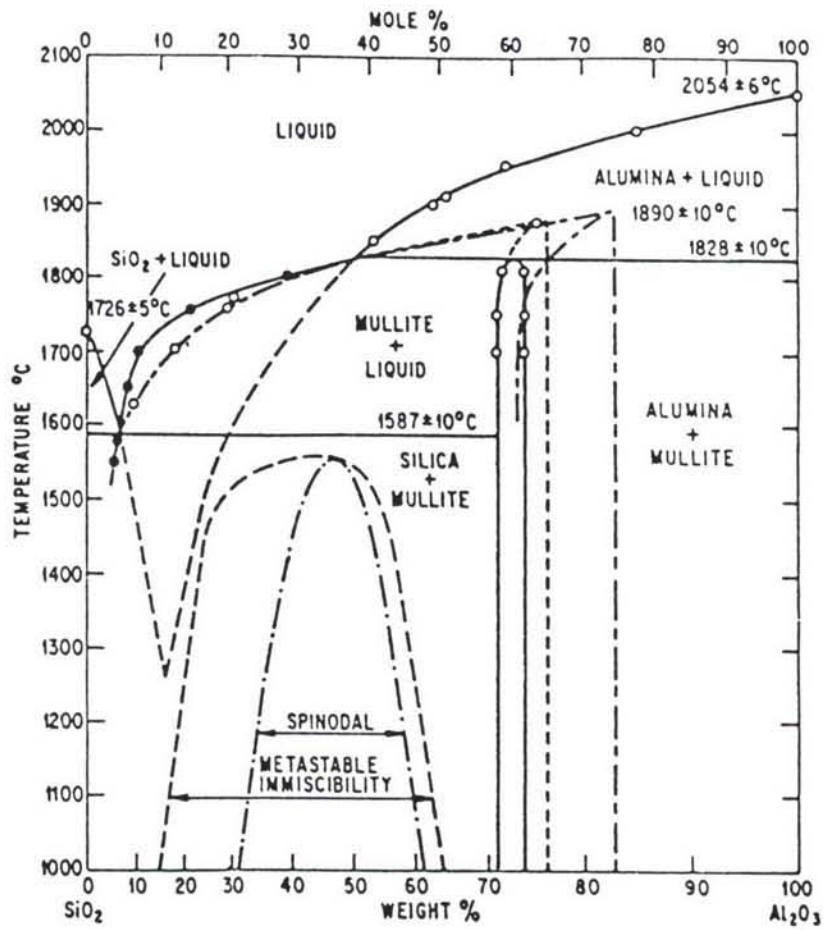


Figure 4. Alumina-silica equilibrium phase diagram.

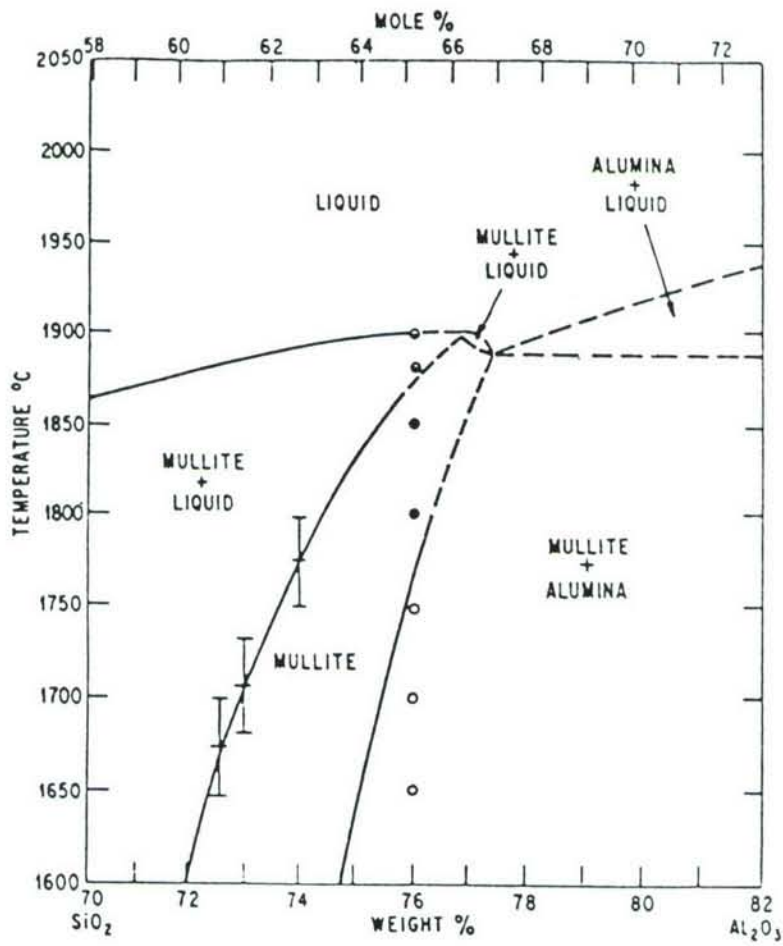


Figure 5. Alumina-rich side of phase diagram.

Mullite composition varies in a narrow region from 71.8 wt% (3:2 mullite) to 77.3 wt % (2:1 mullite)  $\text{Al}_2\text{O}_3$ . However, there is no definitive boundary between 2:1 mullite and the corundum phase region.

## 2. Crystal Structure

Using the Zoltai (29) classification scheme, mullite with its corner-sharing  $[\text{AlO}_4]$  and  $[\text{SiO}_4]$  tetrahedra is considered to be a double chain aluminosilicate with sharing coefficient 1.75. The structure formula of mullite is expressed as  $\text{Al}^{\text{VI}} [\text{Al}_{1+2X} \text{Si}_{1-2X}]^{\text{IV}} \text{O}_{5-X}$  with X ranging from 0.125 to 0.2 (3:2 - 2:1 mullite) (30). X is number of oxygen vacancies per formula unit. Sadanaga, et al. (31) and Burnham (32) found the average structure of mullite to be very similar to that of sillimanite with straight chains of edge-sharing  $[\text{AlO}_6]$  octahedra, but with oxygen vacancies appearing when excessing  $\text{Al}^{3+}$  in the tetrahedral sites. The charge - balancing substitution is  $2\text{Al}^{3+} + \square = 2\text{Si}^{4+} + \text{O}^{2-}$ . From 3:2 to 2:1 mullite, the number of oxygen vacancies increases. The unit cell dimensions and densities change non-linearly (33) upon varying the composition. When the  $\text{Al}_2\text{O}_3$  content increases, a and c increase, b decreases, and density decreases.

Burnham (34) considered mullite to have a disordered Al, Si distribution, but this is true for the average unit cell. Nakajima and Ribbe (35) interpreted the complex diffraction patterns of Al-rich mullites as indicating that mullite has an incommensurate antiphase domain structure with a nonintegral periodicity ranging from 9 to  $15\frac{1}{2}$  Å. McConnell and Heine (36) were first to demonstrate a new scheme of



symmetry analysis for incommensurate modulated structure to determine the ordering patterns both of the Al-Si atoms and of the oxygen vacancies. Mullite has to lower its free energy by ordering oxygen. This thereby establishes the Al-Si ordering: two Al atoms move apart in the ab plane when a vacancy occurs between them. By introducing parameter  $C_1$  (ordering in  $\text{Al}_2\text{O}_3 \cdot \text{SiO}_2$ ) and  $C_2$  (ordering in  $\text{Al}_2\text{O}_3$ ), overlapping occurs to modulate  $3\text{Al}_2\text{O}_3 \cdot 2\text{SiO}_2$  and  $2\text{Al}_2\text{O}_3 \cdot \text{SiO}_2$ . They were able to demonstrate that maximum overlapping of  $C_1$  and  $C_2$  boundary results in very stable mullite with the number of oxygen vacancies ranging from  $x = 0.25$  to  $x = 0.4$  in this given expression  $\text{Al}_2(\text{Al}_{2+2X} \text{Si}_{2-2X}) \text{O}_{10-X} \square_X$ .

### 3. Thermal Expansion

The goal of this study is to develop an ultra-low expansion mullite. Hummel (37) classified mullite within the intermediate expansion group which has the region of the coefficients of expansion from  $20 \times 10^{-7} \text{ K}^{-1}$  to  $80 \times 10^{-7} \text{ K}^{-1}$ . The expansion data given by Shaffer (28) are shown in Table 3.

Although little work has been done on the axial thermal expansion measurement because of the lack of high temperature X-ray diffractometry, Fenstermacher and Hummel (39) point out that mullite crystals do not have an exceptionally high degree of thermal expansion anisotropy.

Leopold and Sibold (40) investigated potential methods for varying the thermal expansion and other properties of mullite bodies at

Table 3. Thermal expansion of  $3\text{Al}_2\text{O}_3 \cdot 2\text{SiO}_2$ .

Temperature Interval	Coefficient of Thermal Expansion $10^{-7} \text{ K}^{-1}$
20 - 1325°C	45.0
20 - 500°C	46.3
20 - 1000°C	51.3
20 - 1500°C	56.2

temperatures to 800°C. They observed that the ratio of  $\text{Al}_2\text{O}_3/\text{SiO}_2$  in the starting materials slightly affected thermal expansion of the mullite composites, and that a composition of 63.6% mullite plus 36.4%  $\text{SiO}_2$  showed the lowest thermal expansion coefficient.

Again, the goal of this research is to obtain mullite which is as pure as possible and has a coefficient of expansion below  $20 \times 10^{-7} \text{ K}^{-1}$  in a much larger temperature interval (up to at least 1200°C). So, attention is paid to the mullite rather than mullite composites in the initial stages.

#### The Relationship between Crystal Structure and Thermal Expansion of Mullite

Grimvall (41) stated that an insulator with harmonic lattice vibration has no thermal expansion. The reason is that the restoring forces perpendicular to the direction of an atomic displacement depend on the strain state. The microscopic model for mullite is not simple.

For its complicated structure, mullite research can benefit by comparison with cordierite which has a very low thermal expansion and has been studied extensively. Hochella, Ross, and Gibbs (42) studied tetrahedral and octahedral bond length variations in cordierite upon heating and the effect on its channel constituents. They gave the structural interpretation of the axial expansion of cordierite. The case in mullite is remarkably similar. In mullite, the volumes of  $[\text{AlO}_4]$  and  $[\text{SiO}_4]$  tetrahedra sites are expected to show little or no change upon heating because of their high bonding strength. With increased  $\text{Al}_2\text{O}_3/\text{SiO}_2$  ratio, more  $\text{Al}^{3+}$  ions will enter tetrahedral sites. The stability of  $[\text{AlO}_4]$  is less than that of  $[\text{AlO}_6]$  by using Pauling's electrostatic theory. Smaller sized and higher charged  $\text{Si}^{4+}$  ions play an important role here. This will result in a slightly weaker bonding in a tetrahedral site. However, the overall effect on thermal expansion depends on the bonding strength of  $[\text{AlO}_6]$  octahedral site. It has the weakest bond strength ( $S = 1/2$ ) in the structure of mullite and is the least stable due to the edge-sharing.

## 5. Approach

Synthetic mullite is developed mainly by solid-state reaction, but, if necessary, another method such as sol-gel decomposition will be employed to achieve the minimum expansion.

When using other oxides to substitute for  $\text{Si}^{4+}$  or  $\text{Al}^{3+}$  in mullite, the sizes and charges of the substitutes should be compatible or at least close to  $\text{Si}^{4+}$  and  $\text{Al}^{3+}$ . The charge causes the number of oxygen



vacancies to vary and the size determines which site between tetrahedra and octahedra the cation occupies. The latter, in fact, determines the coordination number of substituting cations. For the above reason,  $\text{TiO}_2$ ,  $\text{BPO}_4$ ,  $\text{P}_2\text{O}_4$ , and  $\text{AlPO}_4$  are selected as substitutes in mullite.

If the solubility of the solute oxides, such as  $\text{TiO}_2$ , in mullite is exceeded, a second phase will be present. At this stage, increasing its solubility limit by rapid cooling or increasing the temperature should be tried. The amount of other phases present should be minimized.

By using other cations to substitute for  $\text{Si}^{4+}$  or  $\text{Al}^{3+}$  to increase the bond strength in the tetrahedral or octahedral sites in mullite, the thermal expansion data with varying amount of substitutes will be obtained from dilatometry and high temperature X-ray diffractometry for the axial expansion. The results will be compared to pure mullite made under the same conditions.

#### B. Procedure and Initial Results

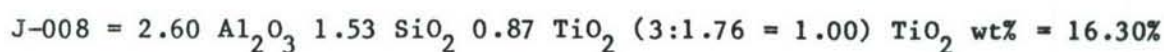
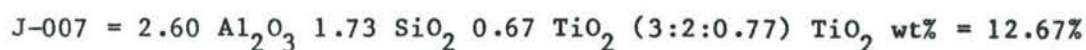
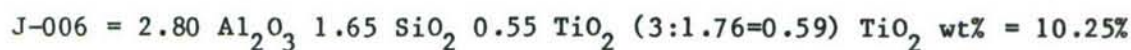
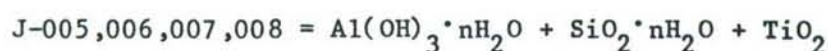
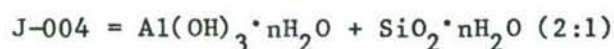
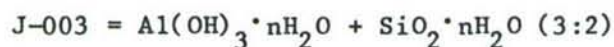
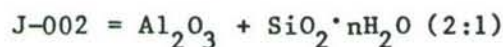
Four oxides are being used for substitution effects on the thermal expansion of mullite, with  $\text{TiO}_2$  being the first tested in initial solid-state reactions. The solubility limit of  $\text{TiO}_2$  in mullite is low (43) and efforts are being made to exceed the limit.

Table 4 shows the compositions and processing conditions. Samples J-001 to J-004 were fired to make pure mullite. Samples J-005 to J-008 were fired with different molar amounts of  $\text{Al}_2\text{O}_3$  and  $\text{SiO}_2$  and different additions of  $\text{TiO}_2$  for evaluation of the solubility and the effect on thermal expansion.

Table 4. Mullite compositions and processing.

Sample No.	Desired Compound	First Firing Temp. <sup>°</sup> C/Time h/Container	Second Firing Temp. <sup>°</sup> C/Time h/Container
J-001	3Al <sub>2</sub> O <sub>3</sub> ·2SiO <sub>2</sub>	1200/6/alumina	
J-002	2Al <sub>2</sub> O <sub>3</sub> ·SiO <sub>2</sub>	1200/6/alumina	
J-003	3Al <sub>2</sub> O <sub>3</sub> ·2SiO <sub>2</sub>	1300/6/alumina	1390/24/alumina
J-004	2Al <sub>2</sub> O <sub>3</sub> ·SiO <sub>2</sub>	1300/6/alumina	1390/24/alumina
J-005	mullite	1500/24/alumina	
J-006	mullite	1500/24/alumina	
J-007	mullite	1500/6*/alumina	1500/18**/alumina
J-008	mullite	1500/6*/alumina	1500/18**/alumina

## Remarks:




---

\*fired in the old furnace

\*\*fired in the new furnace

Samples J-009 to J-012 will be fired with the same ratio of  $\text{Al}_2\text{O}_3/\text{SiO}_2$  (3:2) but with 1 to 4 weight percent of  $\text{TiO}_2$ . The thermal expansion data will be collected.

All fired samples are analyzed by X-ray diffraction to identify the phases presented in order to decide whether the further firing is needed.

The unit cell parameters of mullite from samples J-005 to J-008 were determined by the multiple regression method. The refraction planes used are (110), (120), (210), (001), (220), (111), (130), (401), (141), (230), (320), (041), (331), and (002). The results could only be compared relative to each other but could not be used as the precise cell parameters since the  $2\theta$  errors were corrected, but not based on internal standards. The results showed no significant changes in cell parameters and volume upon varying the compositions. Note that the purpose of determining cell parameters of mullite is to try to determine whether one particular composition will have cell edges a and b closest, since it is desired to have close cell edges in order to gain the low axial expansion.

Samples were prepared as follows:

(i) The weight factors of pure  $\text{SiO}_2 \cdot n\text{H}_2\text{O}$  and  $\text{Al}(\text{OH})_3 \cdot n\text{H}_2\text{O}$  were determined.

(ii) Samples of 10-g batches were prepared by mixing the powders in acetone, and carefully grinding for about one-half hour.

(iii) Samples then were prefired at  $100^\circ\text{C}$  -  $200^\circ\text{C}$  overnight.



(iv) Samples then were fired in covered alumina crucibles.

(v) The furnace was turned off and allowed to cool to room temperature.

The pure  $\text{SiO}_2 \cdot n\text{H}_2\text{O}$  powder was fired at  $1500^\circ\text{C}$  for 8 hours in an alumina crucible. X-ray powder diffractometry was used to determine that no mullite could be formed. Thus, it is appropriate to use alumina crucibles to make mullite below that temperature.

The  $\text{TiO}_2$  phase was found in samples J-006 to J-008, which means that the solubility of  $\text{TiO}_2$  in mullite is exceeded when the weight percent of  $\text{TiO}_2$  is greater than 6.22%, based on this series of experiment.

#### VI. Zircon

No progress to report.

#### VII. Status of Milestones

Status of milestones is presented in Table 5 and Figure 6.

One of the principal investigators participated in the Annual Contractor's Meeting in Dearborn and the Conference for Processing for Reliability of Advanced Ceramics in Corning.

Two new high-temperature furnaces as well as an analytical balance have been received and are in use. The hot press and X-ray diffractometer have been serviced and calibrated.

A surface area and pure volume analyzer has also been received and is being set up.

Table 5. Key to major milestones.

VPI 1.1	Process selection for phosphate- and silicate-based systems (Oct. 31, 1986)
VPI 1.2	Process selection for mullite- and zircon-based systems (Oct. 31, 1986)
VPI 2.1	Complete literature review (Oct. 31, 1986)
VPI 3.1	Complete upgrade of characterization facility (Dec. 31, 1986)
VPI 3.2	Complete upgrade of specimen fabrication, processing facilities (June 30, 1987)
VPI 4.1	Complete initial screening of phosphate-based systems (Dec. 31, 1987)
VPI 4.2	Complete initial screening of silicate-based systems (Dec. 31, 1987)
VPI 4.3	Complete initial screening of zircon-based systems (Dec. 31, 1987)
VPI 4.4	Complete initial screening of mullite-based systems (Dec. 31, 1987)
VPI 5.1	Complete second-stage property and characterization evaluation of phosphate-based systems (Sept. 30, 1988)
VPI 5.2	Complete second-stage property and characterization evaluation of silicate-based systems (Oct. 31, 1988)
VPI 5.3	Complete second-stage property and characterization evaluation of mullite-based systems (Nov. 30, 1988)
VPI 5.4	Complete second-stage property and characterization evaluation of zircon-based systems (Dec. 31, 1988)
VPI 6.0	Complete scale-up specimen fabrication of most promising low-expansion ceramics (Feb. 28, 1989)

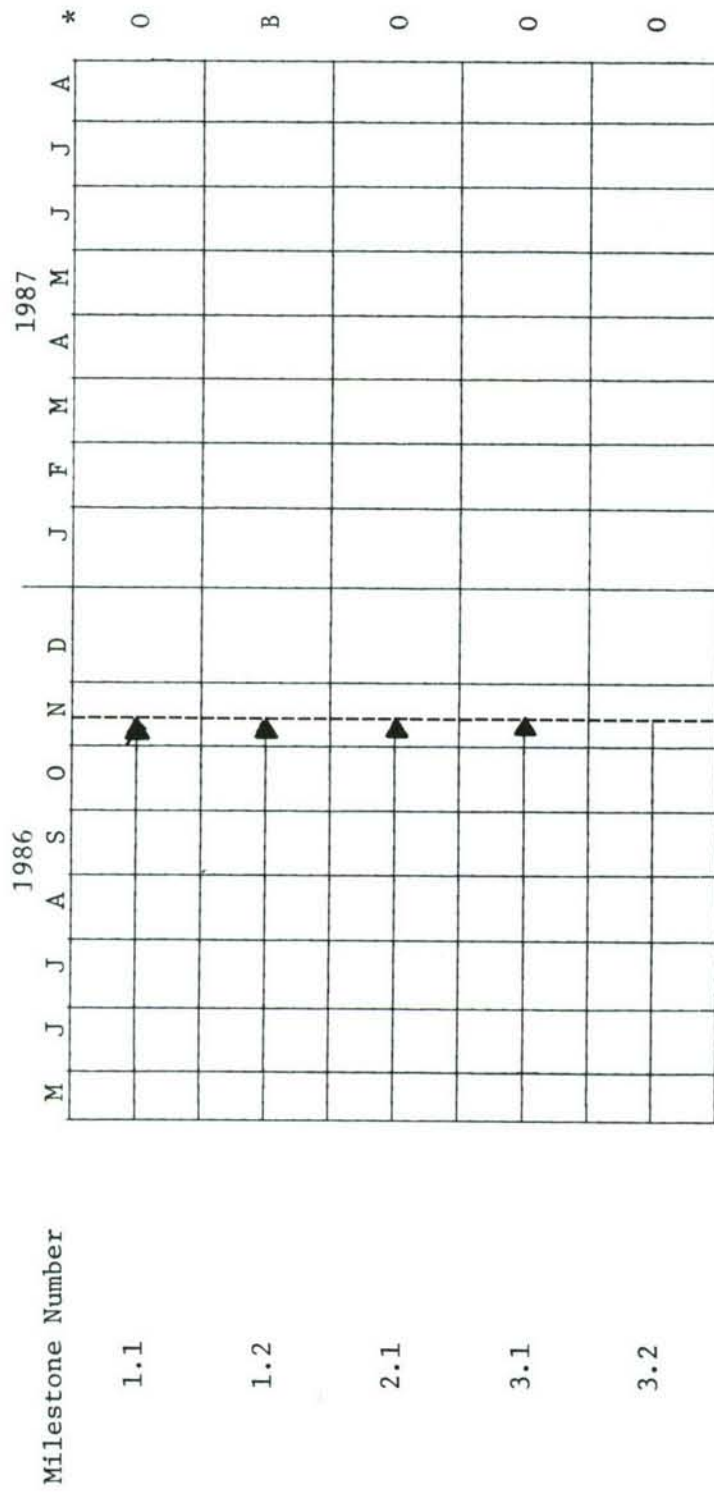


Figure 6. Milestone status.



Bids have been received and are being evaluated for a thermal expansion measuring system.

#### VIII. Publications

None this period.

## IX. References

1. W. D. Kingery, H. K. Bowen, D. R. Uhlmann, Introduction to Ceramics, 2nd Ed., John Wiley & Sons, New York, 1976.
2. F. A. Hummel, "A Review of Thermal Expansion Data of Ceramic Materials, Especially Ultra-Low Expansion Compositions," *Interceram*, 27-30 (Dec. 1984).
3. F. A. Hummel, "Thermal Expansion Properties of Some Synthetic Lithia Minerals," *J. Am. Ceram. Soc.*, 34 (8) 235-239 (1951).
4. J. S. Moya, A. G. Verduch, and M. Hortal, "Thermal Expansion of Beta-Eucryptite Solid Solutions," *Trans. J. Brit. Ceram. Soc.*, 73 (6) 177-78 (1974).
5. T. Y. Tien and F. A. Hummel, "Studies in Lithium Oxide Systems: XIII,  $\text{Li}_2\text{O}:\text{Al}_2\text{O}_3:2\text{SiO}_2$ - $\text{Li}_2\text{O}:\text{Al}_2\text{O}_3:2\text{GeO}_2$ ," *J. Am. Ceram. Soc.*, 47 (11) 582-584 (1964).
6. G. R. Fischer, R. R. Wusirika, and J. E. Geiger, "The Crystal Lattice Thermal Expansion of an Oxynitride Glass-Ceramic Material of High-Quartz Structure," *J. Mat. Sci.*, 20, 4117-4122 (1985).
7. F. A. Hummel and Jelena Brun Langensiepen, "Elimination of Alpha-Beta Cristobalite Inversion of  $\text{AlPO}_4$ ," unpublished research.
8. F. A. Hummel, "Significant Aspects of Certain Ternary Compounds and Solid Solutions," *J. Am. Ceram. Soc.*, 35 (3) 64-66 (1952).
9. W. W. Pillars and D. R. Peacor, "The Crystal Structure of Beta Eucryptite as a Function of Temperature," *Am. Mineralogist*, 58, 681-690 (1973).
10. H. Schulz, "Thermal Expansion of Beta Eucryptite," *J. Am. Cer. Soc.*, 57 (7) 313-318 (1974).
11. W. R. Beck, "Crystallographic Inversions of the Aluminum Orthophosphate Polymorphs and Their Relation to Those of Silica," *J. Am. Cer. Soc.*, 32 (4) 147-151 (1949).
12. W. F. Horn and F. A. Hummel, "The System  $\text{BPO}_4$ - $\text{AlPO}_4$ - $\text{SiO}_2$  at 1200C," *Trans. J. Brit. Ceram. Soc.*, 79, 109-111 (1980).
13. W. F. Horn and F. A. Hummel, "The System  $\text{BPO}_4$ - $\text{AlPO}_4$ ," *Trans. J. Brit. Ceram. Soc.*, 77 (5) 158-162 (1978).

14. W. F. Horn and F. A. Hummel, "Progress Report on the System  $\text{BPO}_4\text{-SiO}_2$ ," Trans. J. Brit. Ceram. Soc., 78 (4) 77-80 (1979).
15. W. F. Horn and F. A. Hummel, "The System  $\text{AlPO}_4\text{-SiO}_2$ ," Glass and Ceramic Research Bulletin, 26 (1-4) 47-59 (1979).
16. F. A. Hummel, "Properties of Some Substances Isostructural with Silica," J. Am. Ceram. Soc., 32 (10) 320-326 (1949).
17. W. F. Horn and F. A. Hummel, "The Quaternary System  $\text{B}_2\text{O}_3\text{-Al}_2\text{O}_3\text{-SiO}_2\text{-P}_2\text{O}_5$ : II. Exploratory Data," J. Austral. Ceram. Soc., 17 (2) 33-36 (1981).
18. J. B. Austin, "Thermal Expansion of Nonmetallic Crystals," J. Am. Ceram. Soc., 35 (10) 243-53 (1952).
19. H. P. Kirchner, "Thermal Expansion Anisotropy of Oxides and Oxide Solid Solutions," J. Am. Ceram. Soc., 52 (7) 379-86 (1969).
20. K. M. Merz, W. R. Brown, and H. P. Kirchner, "Thermal Expansion Anisotropy of Oxide Solid Solutions," J. Am. Ceram. Soc., 45 [11] 531-36 (1962).
21. G. R. Fischer, R. R. Wusirika, and J. E. Geiger, "The Crystal Lattice Thermal Expansion of an Oxynitride Glass-Ceramic Material of High-Quartz Structure," J. Materials Science, 20, 27-102 (1985).
22. F. A. Hummel, "Thermal Expansion Properties of Some Synthetic Lithia Minerals," J. Am. Ceram. Soc., 34 (8) 235-9 (1951).
23. W. Ostertag, G. R. Fischer, and J. P. Williams, "Thermal Expansion of Synthetic  $\beta$ -Spodumene and  $\beta$ -Spodumene-Silica Solid Solutions," J. Am. Ceram. Soc., 51 (11) 651-4 (1968).
24. F. H. Gillery and E. A. Bush, "Thermal Contraction of  $\beta$ -Eucryptite ( $\text{LiO Al}_2\text{O}_3 \cdot 2\text{SiO}_2$ ) by X-Ray and Dilatometer Methods," J. Am. Ceram. Soc., 42 (4) 175-7 (1959).
25. R. W. Ricker and F. A. Hummel, "Reactions in the System  $\text{TiO}_2\text{-SiO}_2$ , Revision of the Phase Diagram," J. Am. Ceram. Soc., 34 (9) 271-9 (1951).
26. D. L. Evans, "Solid Solution of  $\text{TiO}_2$  in  $\text{SiO}_2$ ," J. Am. Ceram. Soc., 53 (7) 418-9 (1970).
27. F. J. Klug, "Alumina-Silica Phase Equilibria in the Mullite System," University Microfilm International, Ann Arbor, MI, 1984.



28. I. A. Aksay and J. A. Pask, "Stable and Metastable Phase Equilibria in the System  $\text{Al}_2\text{O}_3\text{-SiO}_2$ ," J. Am. Ceram. Soc., 58 (11-12) 507-12 (1975).
29. T. Zoltai, "Classification of Silicates and Other Minerals with Tetrahedral Structure," Am. Mineral, 45, 960-73 (1960).
30. P. H. Ribbe, Orthosilicates, Reviews in Mineralogy, Vol. 5, 2nd Edition, Mineralogical Society of America, 1982.
31. R. Sadanaga, M. Tokonami, and Y. Takeuchi, "Structure of Mullite  $2\text{Al}_2\text{O}_3\text{SiO}_2$ , and Relationship with the Structures of Sillimanite and Andalusite," Acta. Crystallogr., 15, 65-8 (1962).
32. C. M. Burnham, "Crystal Structure of Mullite," Carnegie Inst. Wash. Year Book, 62, 223-7 (1963).
33. W. E. Cameron, "Exsolution in Stoichiometric Mullite," Nature, 264, 736-8 (1976).
34. C. W. Burnham, "Composition Limits of Mullite and the Sillimanite-Mullite Solid Solution Problem," Carnegie Inst. Wash. Year Book, 62, 227-8 (1963).
35. Y. Nakajima and P. H. Ribbe, "Twinning and Superstructure of Al-Rich Mullite," Am. Mineral., 66, 142-7 (1980).
36. J. D. C. McConnell and V. Heine, "Incommensurate Structure and Stability of Mullite," Phys. Rev. B: Condens. Matter, 31 (9) 6140-2 (1985).
37. F. A. Hummel, "A Review of Thermal Expansion Data of Ceramic Materials, Especially Ultra-Low Expansion Compositions," INTERCERAM, 27-30, 1984.
38. T. B. Shaffer, "Materials Index 1," 407-8 (1964).
39. J. E. Fenstermacher and F. A. Hummel, "High-Temperature Mechanical Properties of Ceramic Materials: IV, Sintered Mullite Bodies," J. Am. Ceram. Soc., 44 (6) 185-7 (1961).
40. M. H. Lepold and J. D. Sibold, "Development of Low-Thermal Expansion Mullite Bodies," J. Am. Ceram. Soc., 65 (9) C-147-C-149 (1982).
41. G. Grimvall, Thermophysical Properties of Materials, Amsterdam New York, 1986.

42. M. F. Hochella, Jr., G. E. Brown, Jr., F. K. Ross and G. V. Gibbs, "High Temperature Crystal Chemistry of Hydrous Mg- and Fe-Cordierite," *Am. Mineral*, 64, 337-51 (1979).
43. C. Bandin, M. I. Osendi, and J. S. Moya, "Solid Solution of  $\text{TiO}_2$  in Mullite," *J. Mater. Sci. Lett.*, 2 (5) 185-7 (1983).

## 1.4 JOINING

### 1.4.1 Ceramic-Metal Joints

#### Joining of Ceramics for Heat Engine Applications

M. L. Santella (Oak Ridge National Laboratory)

#### Objective/scope

The objective of this task is to develop strong reliable joints containing ceramic components for application in advanced heat engines. Presently, this work is focused on the joining of partially stabilized zirconia to nodular cast iron by brazing. Joints of this arrangement will be required for attaching monolithic pieces of partially stabilized zirconia to cast iron piston caps in order for the ceramic to provide the insulation necessary for use in uncooled diesel engines. A novel method for brazing zirconia to cast iron has already been established. The emphasis of this activity for FY 1986 will be to improve the integrity of joints between zirconia and cast iron, to assess their mechanical properties at room temperature and elevated temperature (primarily by shear testing), and to investigate their thermal aging behavior.

#### Technical progress

There was activity in three areas during this reporting period:

1. assessing the strength of joints between zirconia and cast iron and between zirconia and titanium by shear testing,
2. the use of alternate alloys for joining to zirconia, and
3. a method of estimating residual stress in braze joints between ceramics and metals.

The work done in these areas is outlined in the following paragraphs.

#### Joint strength

Joints between zirconia and cast iron, and between zirconia and titanium, were subjected to shear testing at temperatures of 25 and 400°C. The specimens were tested in the unaged condition or after aging at 400°C for 100 h. Both the aging and the testing of specimens at 400°C were done in air. The temperature of 400°C was selected because it is in the range where the brazed interface between zirconia and cast iron is expected to be under steady-state operating conditions for an insulated piston cap in an uncooled diesel engine.

The joints were made by two different brazing processes:

1. The active substrate process, in which the zirconia is vapor coated with titanium prior to brazing. This technique uses a so-called non-reactive filler metal, AWS BVAg-18 (Ag-30Cu-10Sn). The brazing was done in vacuum at 735°C.



2. The active filler metal process, in which no coating of the zirconia is required. The filler metal used for these joints was Incusil 15ABA, which is produced by GTE Wesgo and has the composition of AG-23.5Cu-14.5In-1.25Ti. In this case the brazing was done in vacuum at 775°C.

The materials used for both processes were Nilcra grade MS partially stabilized zirconia, grade 8003 nodular cast iron electroplated with copper, and commercially pure titanium.

The results of the shear tests are given in Table 1 for the active-substrate joints and in Table 2 for the active-filler-metal joints. For the joints of zirconia to cast iron, both sets of data show that aging or testing at 400°C significantly reduces joint strength. The joints that were aged and tested at 400°C had strength far below the target minimum of 100 MPa, suggesting that obtaining high-strength joints by brazing zirconia directly to cast iron may not be possible with the techniques presently being studied.

The data for joints of zirconia to titanium also show that aging or testing at 400°C reduces joint strength. In this case, however, the joints were generally much stronger than the joints of zirconia to cast iron joints for the same set of test conditions. Table 1 shows that even after aging the joints made between zirconia and titanium by the active-substrate process still had high strength at 25 and 400°C. The closeness of the strength of the aged specimens suggests that these joints are relatively resistant to strength degradation due to thermal aging. Table 2 shows that the zirconia-to-titanium joints brazed by the active-filler-metal technique also had very good strength, but in this case the trend of the data suggests that these joints may not be as thermally stable as the active-substrate joints.

Titanium was selected as an alternate to cast iron for these experiments because its thermal expansion coefficient is very close to that of zirconia ( $9.5$  to  $10.0 \times 10^{-6}/^{\circ}\text{C}$ ), and it has relatively high ductility up to the brazing temperatures used to form the joints with zirconia. It was anticipated, therefore, that residual stresses would be minimized in the joints made with titanium as compared to those made with cast iron. The better strength of the joints between zirconia and titanium indicates that residual stress may be important in determining mechanical behavior, and this aspect of ceramic-to-metal joints is being studied in more detail.

#### Alternate alloys

In an effort to examine the substitution of alternate alloys for nodular cast iron, active-substrate braze joints were made between zirconia and two iron-based heat-resistant alloys: alloy 800H, a solid solution alloy, and A286, a precipitation hardened alloy. The zirconia used for these joints was a tetragonal type obtained from NGK, and it was vapor coated with  $0.6 \mu\text{m}$  of titanium prior to brazing. Handy and Harmon Lithobraz 720 was the filler metal selected because of its relatively low brazing temperature and compatibility with heat-resistant alloys. The nominal composition of Lithobraz 720 is 71.7Ag-28Cu-0.3Li wt %. Vacuum brazing at 790°C was used to form the joints between zirconia and the alloys. The joints were cross sectioned and examined metallographically. The

Table 1. Shear test results for active-substrate braze joints

Specimen	Interface	Aging	Test temperature (°C)	Shear strength (MPa)
MCB-64	ZrO <sub>2</sub> Fe	None	25	188
MCB-71	ZrO <sub>2</sub> Fe	None	400	91
MCB-72	ZrO <sub>2</sub> Fe	400°C/100 h	25	114
MCB-73	ZrO <sub>2</sub> Fe	400°C/100 h	400	30
MCB-97	ZrO <sub>2</sub> Ti	None	25	262
MCB-98	ZrO <sub>2</sub> Ti	None	400	133
MCB-99	ZrO <sub>2</sub> Ti	400°C/100 h	25	123
MCB-100	ZrO <sub>2</sub> Ti	400°C/100 h	400	123

Table 2. Shear test results for active-filler-metal braze joints

Specimen	Interface	Aging	Test temperature (°C)	Shear strength (MPa)
MCB-61	ZrO <sub>2</sub> Fe	None	25	165
MCB-79	ZrO <sub>2</sub> Fe	None	400	140
MCB-95	ZrO <sub>2</sub> Fe	400°C/100 h	25	61
MCB-96	ZrO <sub>2</sub> Fe	400°C/100 h	400	28
MCB-108	ZrO <sub>2</sub> Ti	None	25	289
MCB-109	ZrO <sub>2</sub> Ti	None	400	123
MCB-110	ZrO <sub>2</sub> Ti	400°C/100 h	25	103
MCB-111	ZrO <sub>2</sub> Ti	400°C/100 h	400	67



microstructure of the joint between zirconia and alloy 800H is shown in Fig. 1. Sound joints with similar microstructures were formed in both cases. This experiment shows that substitution of iron-based heat-resistant alloys for nodular cast iron appears feasible from a brazing standpoint, and additional evaluation of this approach is proceeding.

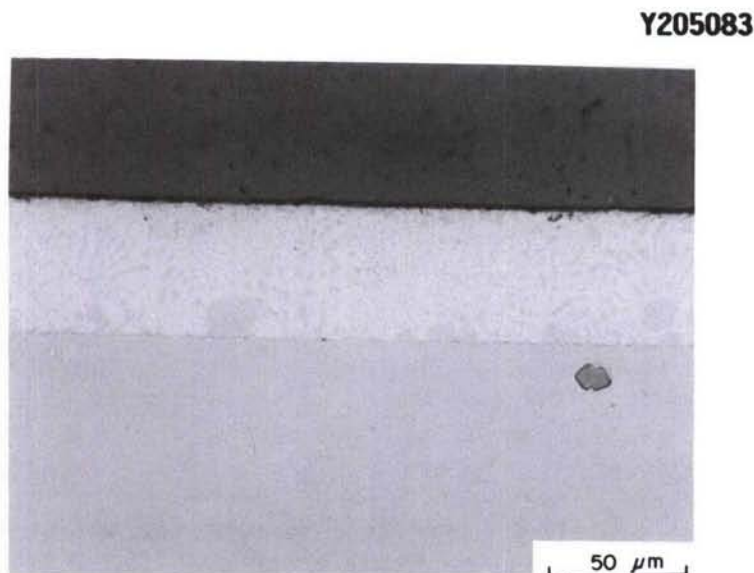


Fig. 1. Optical micrograph of braze joint between zirconia (top) and alloy 800H. Braze filler metal is Lithobraz 720.

### Residual stress

An indentation technique using a Vickers indenter on a standard hardness tester has been adapted for estimating residual stress patterns in ceramic braze joints. The result of using this approach on a zirconia-to-A286 joint is illustrated in Fig. 2. The indentation at position A in Fig. 2 clearly shows greater extension of cracks parallel to the joint than indentations farther away, e.g., at position B. This cracking pattern indicates that there is a sizable residual tensile stress in the zirconia acting normal to the brazed surface. Comparing the crack lengths in stressed and unstressed regions allows estimation of the magnitude of residual stress at any point. The residual stress acting normal to the brazed surface at position A in Fig. 2 was estimated to be about 200 MPa. The development of this technique as a means of identifying residual stress patterns in ceramic-to-metal braze joints is continuing.



YP2782

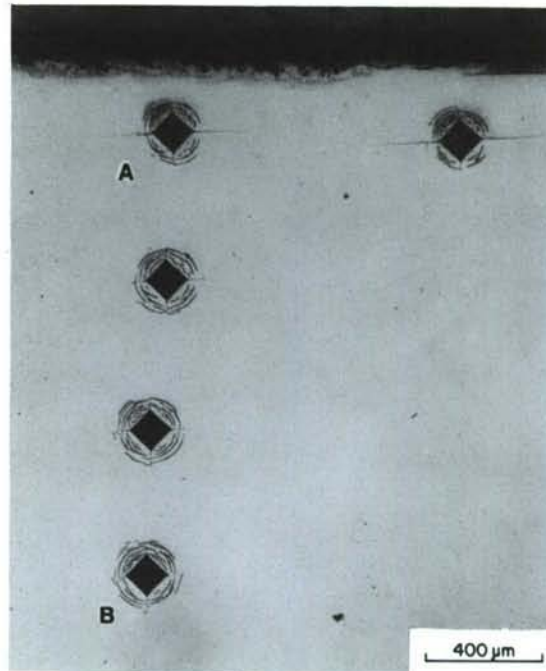


Fig. 2. Optical micrograph of braze joint between zirconia and A286 showing indentations made in zirconia to determine sense and magnitude of residual stress produced by brazing. The braze joint is parallel to the top of the micrograph.

#### Status of milestones

None.

#### Publications

1. M. L. Santella, "Joining Ceramics to Metals by Active Substrate Brazing," presented at the 17th International AWS Brazing Conference, April 15, 1986, Atlanta, Georgia.
2. A. J. Moorhead and M. L. Santella, "Development and Characterization of Brazed Joints in Ceramic Materials," presented at the Materials Science and Engineering Symposium, Oak Ridge National Laboratory, May 16, 1986.

## 2.0 MATERIALS DESIGN METHODOLOGY

### INTRODUCTION

This portion of the project is identified as project element 2 within the work breakdown structure (WBS). It contains three subelements: (1) Three-Dimensional Modeling, (2) Contact Interfaces, and (3) New Concepts. The subelements include macromodeling and micromodeling of ceramic microstructures, properties of static and dynamic interfaces between ceramics and between ceramics and alloys, and advanced statistical and design approaches for describing mechanical behavior and for employing ceramics in structural design.

The major objectives of research in Materials Design Methodology elements include determining analytical techniques for predicting structural ceramic mechanical behavior from mechanical properties and microstructure, tribological behavior at high temperatures, and improved methods for describing the fracture statistics of structural ceramics. Success in meeting these objectives will provide U.S. companies with methods for optimizing mechanical properties through microstructural control, for predicting and controlling interfacial bonding and minimizing interfacial friction, and for developing a properly descriptive statistical data base for their structural ceramics.

## 2.2 CONTACT INTERFACES

### 2.2.2 Dynamic Interfaces

*Studies of Dynamic Contact of Ceramics and Alloys for Advanced Heat Engines*  
K. F. Dufrane and W. A. Glaeser (Battelle Columbus Division)

#### Objective/scope

The objective of the study is to develop mathematical models of the friction and wear processes of ceramic interfaces based on experimental data. The supporting experiments are to be conducted at temperatures to 650 C under reciprocating sliding conditions reproducing the loads, speeds, and environment of the ring/cylinder interface of advanced engines. The test specimens are to be carefully characterized before and after testing to provide detailed input to the model. The results are intended to provide the basis for identifying solutions to the tribology problems limiting the development of these engines.

#### Technical progress

##### Apparatus

The apparatus developed for this program uses specimens of a simple flat-on-flat geometry, which facilitates procurement, finishing, and testing. The apparatus reproduces the important operating conditions of the piston/ring interface of advanced engines. The specimen configuration and loading is shown in Figure 1. The contact surface of the ring specimen is 3.2 x 19 mm. A crown with a 32 mm radius is ground on the ring specimen to insure uniform contact. The ring specimen holders are pivoted at their centers to provide self-alignment. A chamber surrounding the specimens is used to control the atmosphere and contains heating elements to control the temperature. The exhaust from a 4500 watt diesel engine is heated to the specimen temperature and passed through the chamber to provide an atmosphere similar to that of actual diesel engine service. A summary of the testing conditions is presented in Table 1.

##### Materials

Monolithic alpha silicon carbide, silicon nitride, and three zirconia compounds were selected for the cylinder specimens. The compositions of the materials are presented in Table 2.

Plasma-sprayed coatings of chromium carbide and chromium oxide were applied on mild steel base metal for both ring and cylinder specimens. Chromium plated ring specimens and gray cast iron cylinder specimens were used for baseline data. Monolithic ring specimens were cut from the sides of the cylinder specimens.

##### Silicon nitride without lubrication

Earlier non-lubricated experiments with silicon carbide, all three zirconias, and various plasma-sprayed metallic and ceramic coatings resulted in high wear rates, high friction coefficients, and extensive surface damage.



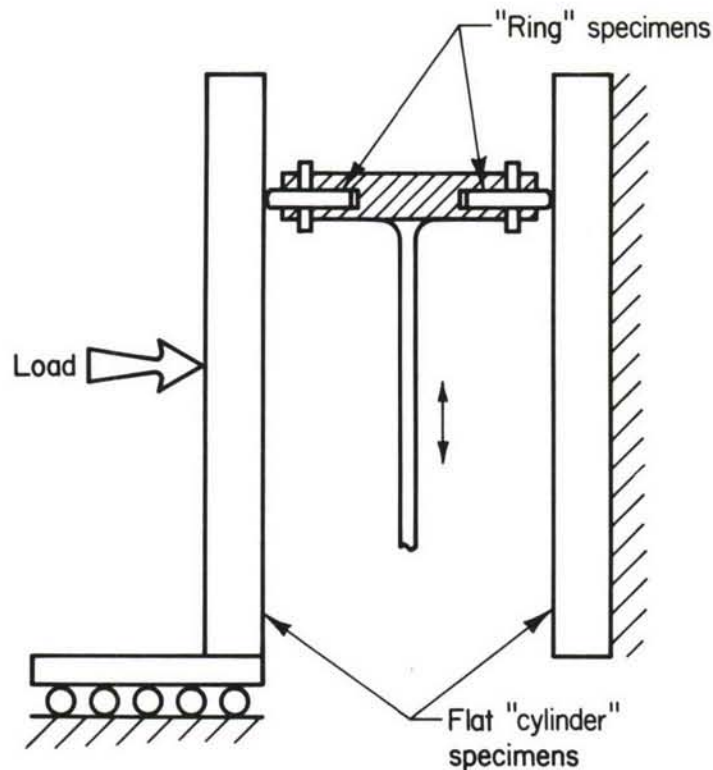


Figure 1. Test specimen configuration and loading

An experiment using self-mated silicon nitride without lubrication produced similar results. As shown in Figure 2, the ring specimen was worn across its entire width in 8 minutes of sliding at a light load of 12 N/mm. The measured friction coefficient was 0.23 for most of the experiment. The edges of the specimen were chipped, but there were no overall fractures. The wear surfaces were generally smooth overall with local bands of heavier wear. At higher magnification, Figure 3a, the wear bands consisted of extensive smearing and apparent transfer between the two sliding surfaces, similar to that experienced with metals. The remaining overall surfaces, which appeared smooth at low magnifications, consisted of local pitting, as in Figure 3b. The pits appeared to be formed by the brittle removal of individual grains from the microstructure. In spite of the severe sliding conditions experienced without lubrication, there was no evidence of thermal shock cracking on the worn surfaces.

#### Experiments with lubrication

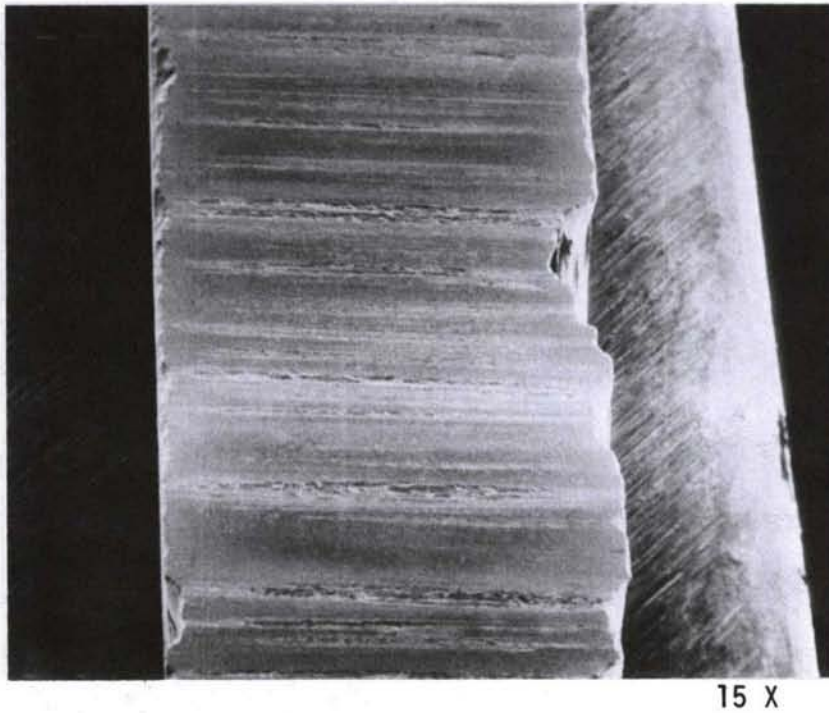
An experiment with self-mated silicon nitride and SAE 10 mineral oil lubrication produced excellent results in that the wear was limited to a polishing mechanism. As shown in Figure 4a, the overall wear surface of the ring specimen was smooth with only the pits remaining from the original grinding visible. At higher magnification, Figure 4b, the contacting wear surface was polished and without features. A few local areas experienced

Table 1. Summary of testing conditions

Sliding Contact:	Dual flat-on-flat
"Cylinder" Specimens:	12.7 x 32 x 127 mm
"Ring" Specimens:	3.2 x 19 x 19 mm
"Ring" crown radius:	32 mm
Motion:	Reciprocating, 108 mm stroke
Speed:	500 to 1500 rpm
Load:	to 950 N
Ring Loading:	to 50 N/mm
Atmosphere:	Diesel exhaust or other gases
Measurements:	Friction and wear (after test)

Table 2. Current cylinder and ring specimens

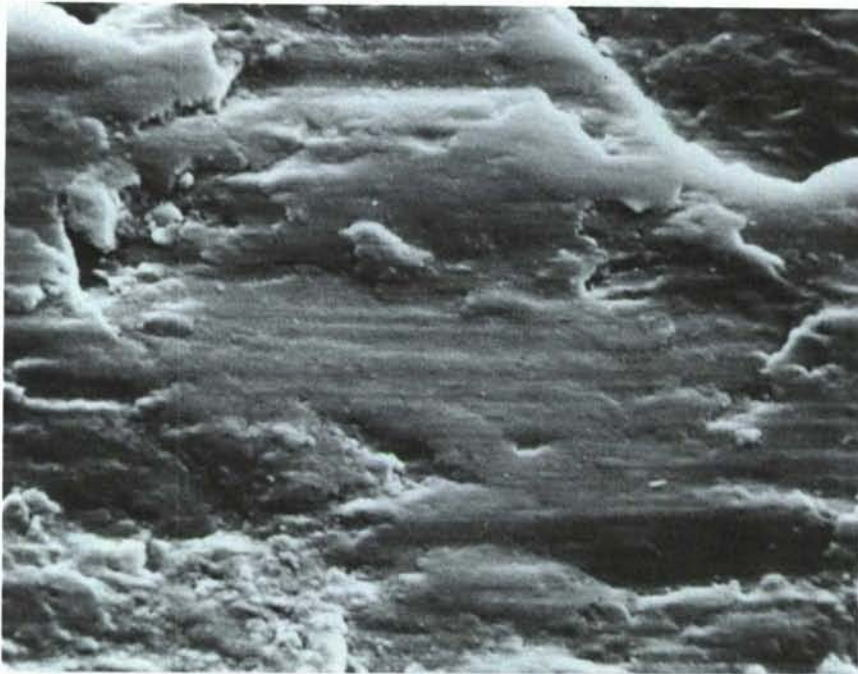
Material	Abbreviation	Nominal Composition, Weight Percent
Magnesia Partially Stabilized Zirconia	MPSZ	3.3 % MgO 3 % HfO <sub>2</sub> , bal ZrO <sub>2</sub>
Yttria Partially Stabilized Zirconia (Z-191)	YPSZ	5.4 % Y <sub>2</sub> O <sub>3</sub> , bal ZrO <sub>2</sub>
Alumina Transformation Toughened Zirconia	ATTZ	3.6 % Y <sub>2</sub> O <sub>3</sub> , 20 % Al <sub>2</sub> O <sub>3</sub> , bal ZrO <sub>2</sub>
Sintered Alpha Silicon Carbide	SiC	SiC
Silicon Nitride	Si <sub>3</sub> N <sub>4</sub>	2 % W, 0.5 % Mg, 0.25 % Al, bal Si <sub>3</sub> N <sub>4</sub>
Chromium Carbide	Cr <sub>3</sub> C <sub>2</sub>	20 % Cr <sub>3</sub> C <sub>2</sub> , 12 % Ni, 9 % W, bal Cr
Chromium Oxide	Cr <sub>2</sub> O <sub>3</sub>	5 % Cr, bal Cr <sub>2</sub> O <sub>3</sub>
Chromium Plate	Cr	Cr
Gray Cast Iron	--	3.3 % C, 2.3 % Si, 0.7 % Mn, bal Fe



15 X

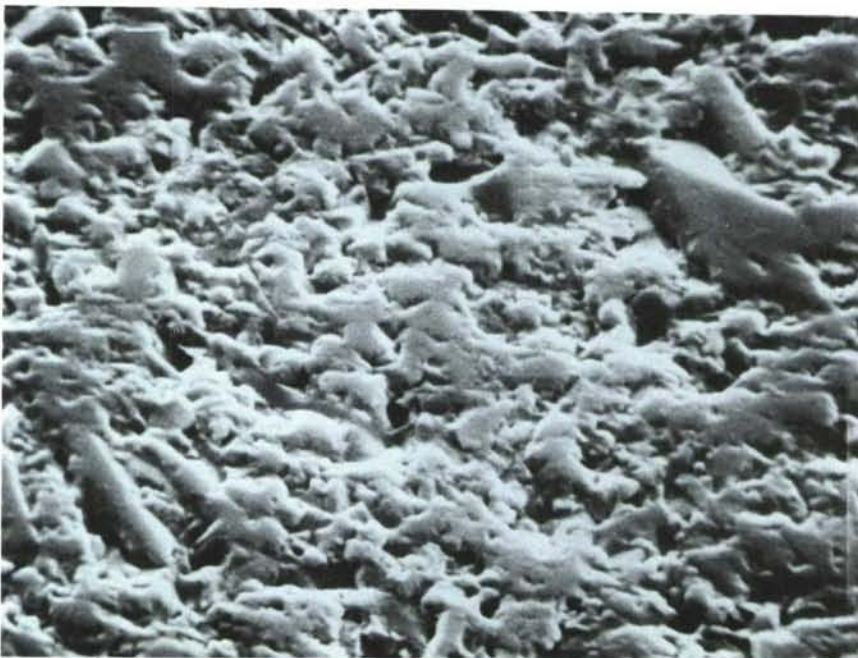
Figure 2. Wear bands and edge chipping on ring specimen of silicon nitride run without lubrication





5000 X

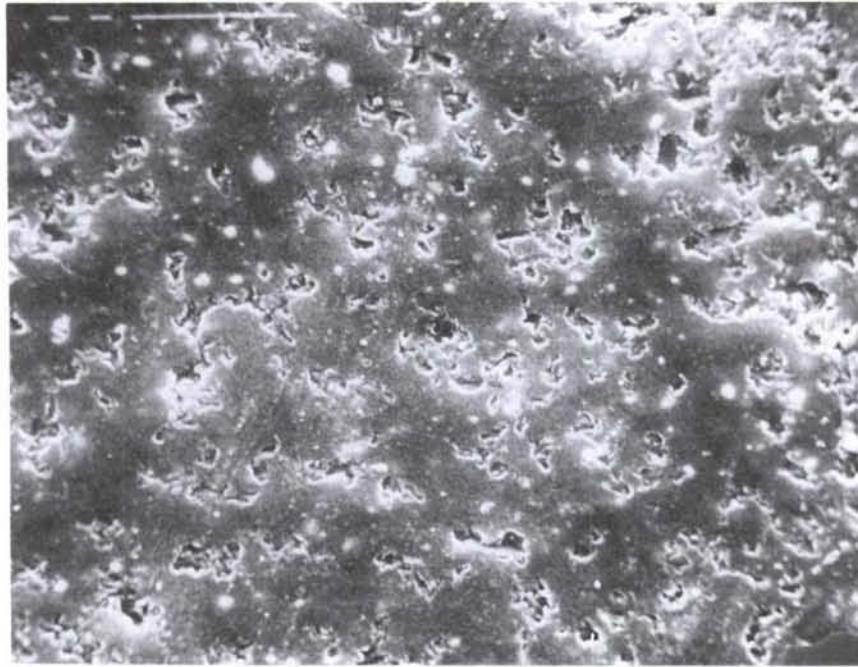
a. smearing and transfer in heavy wear band



5000 X

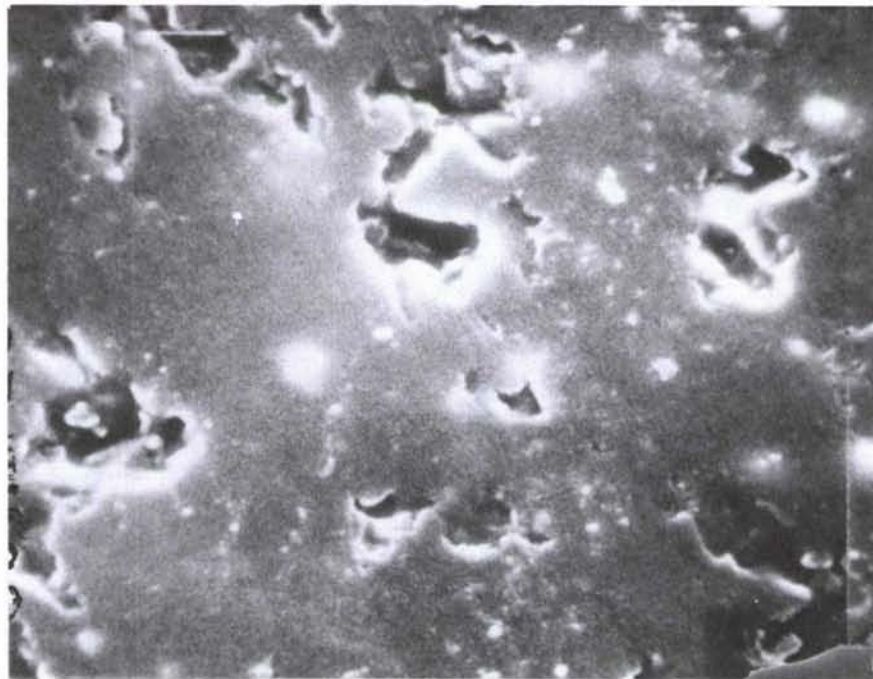
b. local spalling in smooth areas between heavy wear bands

Figure 3. Surface damage on silicon nitride run without lubrication



2000X

a. smooth surface with pits remaining from original grinding



10,000X

b. polished contacting wear surface

Figure 4. Smooth wear surfaces on silicon nitride run with SAE mineral oil lubrication



more extensive pitting and removal of surface grains. However, since the total depth of wear was very limited and had not removed the pitting associated with the original grinding, these areas may have been the result of remaining damage from the original surface preparation. As with the specimens from the unlubricated tests, there was no evidence of thermal shock cracking on the silicon nitride wear surfaces.

With the completion of the room-temperature baseline experiments using SAE 10 mineral oil lubrication, experiments were conducted using SDL-1 diesel engine oil, a polyalphaolefin, as the lubricant. The initial experiments used chromium-plated rings against cast iron, YPSZ, and silicon nitride. The results are summarized in Table 3. The baseline experiment at room temperature with cast iron cylinder specimens resulted in low ring wear and friction coefficients in the hydrodynamic range. With ring loadings to 16 N/mm and running for over 2 hours, the wear was confined to less than 0.013 mm. The ring surfaces were highly polished, and most of the measured wear probably occurred in the early break-in portion of the run.

Table 3. Results of elevated temperatures experiments with SDL-1 lubricant and chromium-plated rings

Cylinder Material	Temperature C	Friction Coefficient	Ring Wear
Cast iron	20	0.06-0.07	less than 0.013 mm
Cast iron	310	0.13	through Cr
Cast iron	260	0.07-0.01	No. 1-0.051 mm No. 2- through Cr
YPSZ (Z191)	260	0.2-0.3	through Cr
Si <sub>3</sub> N <sub>4</sub> (NC132)	260	0.14	through Cr

The experiment with cast iron at 310 C, the temperature SDL-1 was reportedly capable of withstanding, resulted in a high friction coefficient and high ring wear. After only 1 hour of running at a ring loading of 10 N/mm, the 0.10 mm of chromium plate was worn through to the base metal. Also, the entire test chamber was coated with a tenacious black layer of lubricant decomposition products. The cast iron cylinder specimens were grooved from the sliding contact and heavily coated with a tenacious layer of wear debris and lubricant decomposition products.

With the inability of SDL-1 to operate at 310 C in the apparatus, a heating experiment was conducted to observe its behavior at elevated temperatures. Drops of the lubricant were placed on a steel plate heated to increasing temperatures. At temperatures above 260 C, the SDL-1 left a



dark residue after evaporating. The residue became darker and more tenacious as the temperature was increased. On this basis, 260 C was determined to be the maximum allowable operating temperature for the SDL-1 and was used in the subsequent tests.

As shown in Table 3, the results of the cast iron baseline experiment at 260 C were much better than obtained at 310 C. However, the ring wear was substantial after 4 hours of running at a ring loading of 10 N/mm. One specimen was worn through the 0.10 mm of chromium plating, while the other had worn approximately 0.051 inch.

The yttria partially stabilized zirconia experienced high friction coefficients and the chromium plating was rapidly worn away with a ring loading of 10 N/mm. Visible hot spots associated with thermoelastic instability (TEI) were very pronounced throughout the test. The surfaces of the zirconia cylinder specimens were badly cracked from the thermal shock associated with the TEI.

The friction coefficient measured with the silicon nitride cylinder specimens at 260 C was also relatively high (0.14), but better than that measured with the zirconia cylinder specimens. The wear on the ring specimens was also rapid in that the chromium plating was worn through in 1 hour of running at a ring loading of 10 N/mm.

The poor results with the cast iron and silicon nitride at 260 C compared with those at room temperature suggest that the SDL-1 is not providing adequate lubrication at this temperature. Piston rings depend upon hydrodynamic lubricant films to minimize wear. The primary problem is probably the greatly reduced viscosity at the high temperature. The inherent wear resistance of the chromium plating is apparently inadequate to survive with the marginal lubricant films provided by the SDL-1 at 260 C. Experiments are being conducted using  $\text{Cr}_3\text{C}_2$  and  $\text{Cr}_2\text{O}_3$  rings and cylinder specimens with SDL-1 at 260 C to determine the extent of improved performance over the chromium plating.

Calculations were made of the approximate wear coefficients obtained with the various experiments for a direct comparison. The wear coefficients were calculated using the relationship<sup>1</sup>:

$$k = \frac{3pV}{Lx},$$

where:  $k$  = wear coefficient  
 $p$  = hardness of wearing member  
 $V$  = wear volume  
 $L$  = applied load  
 $x$  = sliding distance.

The results are presented in Table 4.

For a basis of comparison, the wear coefficient of a conventional diesel truck engine was calculated. A wear depth of 0.25 mm was assumed for 6000 hrs of service at an average ring loading of 18 N/mm. The resulting wear coefficient of  $5 \times 10^{-9}$  is indicative of the very low wear rates associated with hydrodynamic lubrication. The wear coefficients of  $10^{-6}$  obtained with the chromium plate and  $\text{Si}_3\text{N}_4$  at room temperature are indicative of excellent lubrication, but are significantly higher than the field service

Table 4. Comparison of approximate ring wear coefficients

Ring Material	Cylinder Material	Lubricant	Temperature, C	Ring Wear Coefficient, k
Cr	cast iron	SDL-1	~100	$5 \times 10^{-9*}$
YPSZ	YPSZ	none	540	$8 \times 10^{-4}$
YPSZ	YPSZ	SAE 10	20	$2 \times 10^{-4}$
Si <sub>3</sub> N <sub>4</sub>	Si <sub>3</sub> N <sub>4</sub>	SAE 10	20	$1 \times 10^{-6}$
Cr	cast iron	SAE 10	20	$2 \times 10^{-6}$
Cr	cast iron	SDL-1	310	$1 \times 10^{-4}$
Cr	cast iron	SDL-1	260	$1 \times 10^{-5}$
Cr	YPSZ	SDL-1	260	$1 \times 10^{-5}$
Cr	Si <sub>3</sub> N <sub>4</sub>	SDL-1	260	$1 \times 10^{-4}$

\* Typical actual diesel truck engine experience

example. This is probably due to the influence of the high wear rates experienced during the break-in portion of the short laboratory experiments. Wear coefficients of  $10^{-4}$  indicate poor lubrication and aggressive wear mechanisms. The  $10^{-4}$  values obtained with the SDL-1 lubricant at 260 C suggest that the viscosity is too low at this temperature to produce hydrodynamic oil films. Future experiments with Cr<sub>3</sub>C<sub>2</sub> and C<sub>2</sub>O<sub>3</sub> ring specimen coatings will help to determine the improvement that can be expected using SDL-1 with materials having higher wear resistance than chromium plate.

#### Status of milestones

The milestones of constructing the friction and wear apparatus, obtaining specimens, performing initial wear experiments, and initiating modeling of the wear processes have been met and are progressing in general accordance with the milestone schedule.

#### Publications

1. K. F. Dufrane, "Sliding Performance of Ceramics for Advanced Heat Engines", v. 7, n. 7-8, *Ceramic Engineering and Science Proceedings*, July-August 1986.

2. K. F. Dufrane and W. A. Glaeser, "Wear of Ceramics in Advanced Heat Engine Applications", submitted for the *1987 Wear of Materials Conference*.

3. K. F. Dufrane and W. A. Glaeser, "Performance of Ceramics in Ring/Cylinder Applications", submitted for the *1987 SAE International Congress and Exposition*.

#### References

1. E. Rabinowicz, *Friction and Wear of Materials*, p. 138, John Wiley and Sons, Inc., New York, 1966.



2.3 NEW CONCEPTS

Advanced Statistics  
W. P. Eatherly (ORNL)

No Report Received

Advanced Statistical Concepts of Fracture in Brittle Materials

C. A. Johnson and W. T. Tucker (General Electric Corporate R&D)

Objective/scope

The design and application of reliable load-bearing structural components from ceramic materials requires a detailed understanding of the statistical nature of fracture in brittle materials. The overall objective of this program is to advance the current understanding of fracture statistics, especially in the following three areas:

- Optimum testing plans and data analysis techniques.
- Consequences of time-dependent crack growth on the evolution of initial strength distributions.
- Confidence and tolerance bounds on predictions that use the Weibull distribution function.

The studies are being carried out largely by analytical and computer simulation techniques. Actual fracture data are then used as appropriate to confirm and demonstrate the resulting data analysis techniques.

Technical/progress

During the previous reporting period, work was carried out on all three of the primary objectives listed above. The work described herein concentrates on progress toward the second objective: Prediction of the evolution of initial strength and flaw size distributions during slow crack growth. As will be demonstrated below, strength degradation due to subcritical crack growth (SCG) modifies the distribution of initial strengths. The distribution obviously shifts downward in strength as SCG proceeds, but less obvious is a change in the form of the distribution function such that there is less scatter in strengths (lower coefficient of variation) after SCG than before.

Figure 1 illustrates the interrelationship of three important complicating factors in the analysis of structural reliability. Models of behavior and methods of analysis are available for each factor when present individually. For instance, in the case of non-uniform flaw sizes, the Weibull distribution is a model that is often found to be reasonable in describing the strength variability and size effects that result from non-uniform flaw sizes. For the case of uniform, uniaxial stressed bodies, the Weibull distribution is of the form:

## COMPLEXITIES IN THE ANALYSIS OF STRUCTURAL RELIABILITY

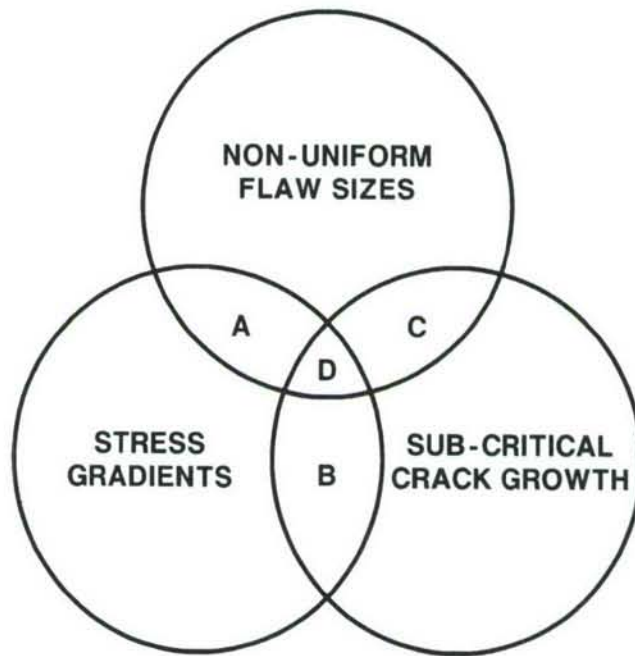


Fig. 1 Interrelationship of three important factors in the analysis of structural reliability.

$$P = 1 - e^{-V(\sigma/\sigma_0)^m} \quad (1)$$

where  $P$  is the cumulative probability of failure,  $V$  is the volume under uniform stress,  $\sigma$  is the magnitude of that stress,  $m$  is the Weibull modulus, and  $\sigma_0$  is a normalizing parameter. The empirically derived parameters,  $m$  and  $\sigma_0$ , can be thought of as material properties for materials that are properly described by the Weibull distribution.

Referring to Figure 1 again, if SCG is the only complicating factor, then models of crack growth rates are available that allow the strength degradation of a material to be predicted. One crack velocity relationship that is often found to be reasonable in describing ceramic materials is:

$$v = A K^n \quad (2)$$

where  $v$  is the velocity of crack growth,  $K$  is the applied stress intensity factor for the defect of interest, and  $A$  and  $n$  are empirically derived parameters.

In the case shown on Figure 1 where stress gradients are the only complicating factor, either analytical or numerical methods of analysis are available to determine the complete stress state for virtually any geometry and loading configuration.



In the above three cases where only one of the three complicating factors are present, the methodologies used for design and/or prediction of reliability are straightforward. When two of the three complicating factors are present simultaneously (corresponding to regions A, B, and C of Figure 1), the analysis is more involved. For instance, when both non-uniform flaw sizes and stress gradients are present (region A), the more general form of the Weibull distribution involving area or volume integrals is necessary:

$$P = 1 - e^{-\int (\sigma/\sigma_0)^m dV} \quad (3)$$

where the integration of the stress term is carried out over all volume elements,  $dV$ , that are under tensile stress. When both stress gradients and SCG are present at the same time (region B), very little added complexity arises since the flaw at the highest stressed point will always control failure. The structure will behave similar to a uniformly stressed body loaded to the same stress. The situation is more complex, however, when both non-uniform flaw sizes and SCG are present simultaneously (region C). In this region, the initial strength and flaw size distributions evolve in a way that is not normally expected. When all three complicating factors of Figure 1 are present simultaneously (region D), the analysis is even more complex because unlike the previous cases, the flaw that would cause failure in the absence of SCG may or may not be the flaw that causes failure after SCG. The following two sections describe characteristics of materials tested in regions C and D respectively.

#### I. Non-Uniform Flaw Sizes and Sub-Critical Crack Growth

Dynamic fatigue testing is a popular method to characterize SCG that involves loading the specimen to progressively higher loads on a linear loading schedule (stress is proportional to time) until failure occurs. When several uniform, uniaxial-stress specimens are tested at each of a number of loading rates, the results can be plotted as shown schematically on Figure 2. Each data point corresponds to the average strength of specimens tested at a particular loading rate. The error bars indicate the standard deviation or some other measure of variability of strengths within each group. The error bars are drawn with a slope of unity on the log-log scale (higher strength specimens fail at longer times to failure in dynamic fatigue, therefore the error bars are not vertical). Different loading rates result in different average times to failure. The measured average strengths as shown by the data points reflect the true behavior of the average strength which is represented here as the solid line. At very short times to failure (very fast loading rates), the strength is independent of time and is often described as the "inert strength" of the material. As the loading rate is progressively decreased there is more time for SCG and the strengths also decrease. For the case of SCG according to Equation 2, the solid line asymptotically approaches a straight line at very long times to failure where the slope of the straight line is  $-1/n$ .

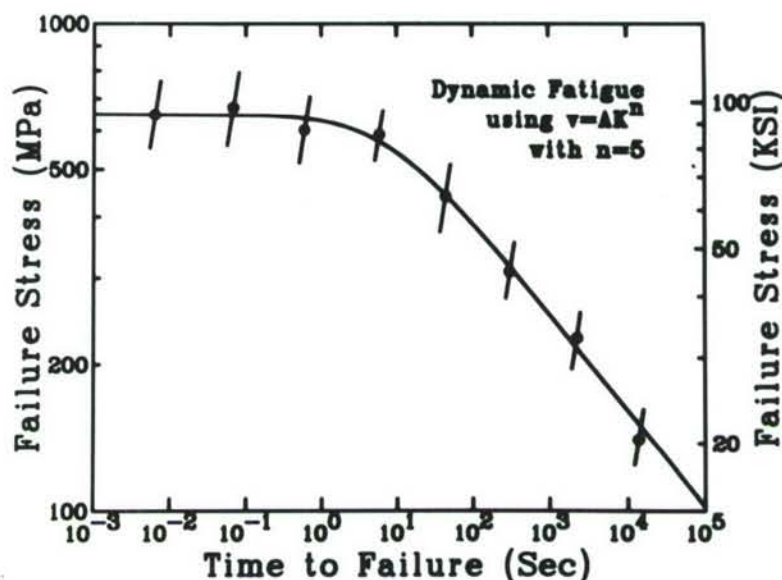


Fig. 2 Log stress vs. log time to failure showing typical dynamic fatigue behavior.

Figure 3 is similar to Figure 2 except that a family of nine curves are shown representing the 10, 20,...90 percentile behaviors of a Weibull distribution (where the initial strengths have a Weibull modulus of 5). The lowest curve, for instance, represents the behavior of specimens with an initial strength equal to the 10 percentile behavior of the distribution (approximately 450 MPa for this choice of parameters). At any given loading rate, the strength distribution that would be observed can be predicted by the intersections of the family of dynamic fatigue curves with the straight line of unity slope representing the loading curves of interest. Two such loading rates are shown on Figure 3 and are labelled as "fast loading" and "slow loading".

The important point to be illustrated on Figure 3 is that the distribution of initial strengths or inert strengths is different than the distribution of strengths in the asymptotic region of the dynamic fatigue curves. Not only have the strengths decreased, but the variability in strengths has also decreased. It has been shown by derivation that if the inert strengths have a Weibull distribution with modulus  $m_{\text{inert}}$ , and if SCG is properly described by Equation 2, then the strengths at very slow loading rates (in the asymptotic region of Figure 3) also have a Weibull distribution, but with a higher modulus,  $m_{\text{slow}}$ . The  $m$  at slow loading rates is a function of the inert  $m$  and the slow crack growth exponent,  $n$ , as follows:

$$m_{\text{slow}} = m_{\text{inert}} \frac{(n+1)}{(n-2)} \quad (4)$$

It is interesting to note that at intermediate loading rates on Figure 3 (neither on the plateau nor the asymptote), the distribution is no longer a simple Weibull distribution.



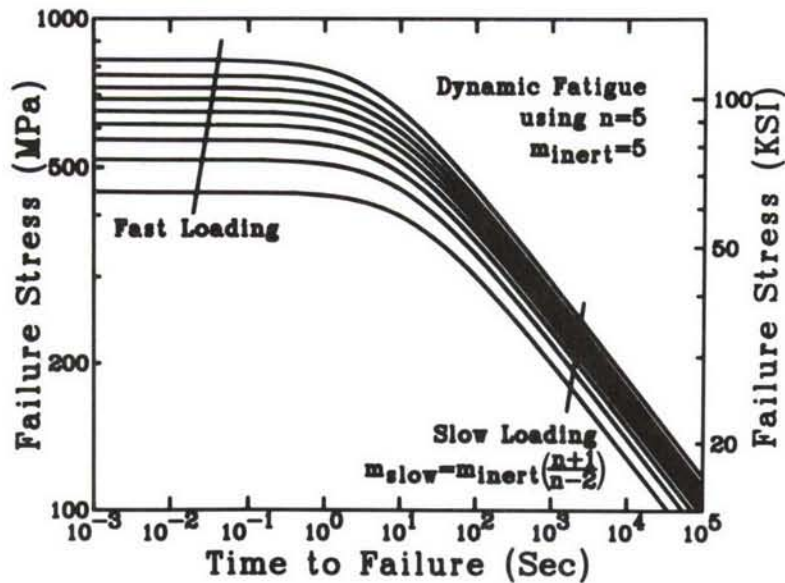


Fig. 3 Dynamic fatigue behavior for a family of initially Weibull strengths.

The relationship between  $m$ 's and  $n$  is shown on Figure 4 where the ratio of  $m_{\text{slow}}$  to  $m_{\text{inert}}$  is plotted versus  $n$ . As  $n$  approaches infinity, the two  $m$  values approach each other. As  $n$  approaches 2, the ratio of  $m$ 's approaches infinity (i.e., a material with an  $n$  incrementally greater than 2 tested at very slow loading rates has virtually no scatter in strength).

Some of the more significant conclusions from this part of the study include:

- Sub-critical crack growth reduces the scatter in strengths regardless of the form of the initial strength distribution.
- If the initial strength distribution is Weibull, the distribution at slow loading rates is also Weibull but with a higher  $m$  value as described by Equation 4.
- The  $m$  value at slow loading rates can be used for size-scaling calculations if the predicted strengths are also in the "asymptotic" region.
- Instead of the previous method, however, it is recommended that size scaling be done by deducing the initial strength distribution, scaling the inert strength to the new specimens size, and calculating the degradation of the scaled specimen using the loading schedule of interest.



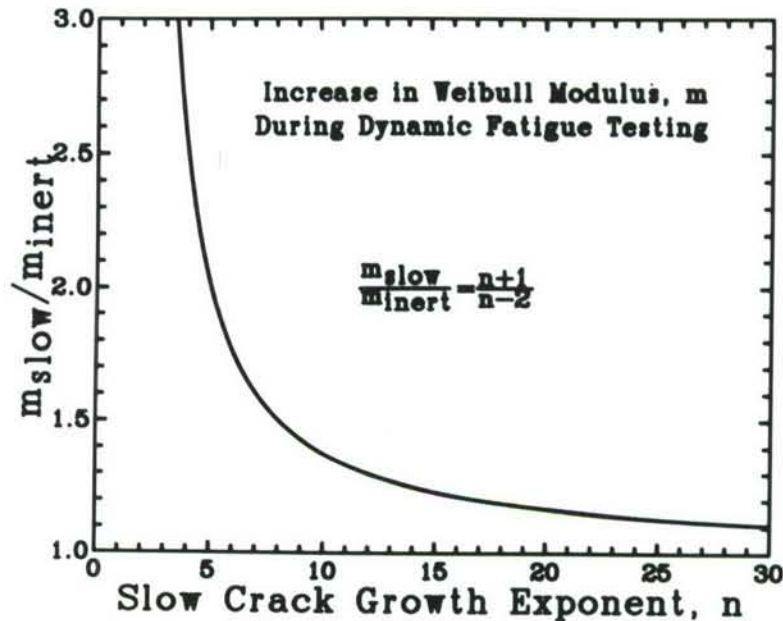


Fig. 4 Dependence of the asymptotic Weibull modulus on the slow crack growth exponent.

## II. Non-Uniform Flaw Sizes, Sub-Critical Crack Growth, and Stress Gradients

In the previous section, the problem was simplified somewhat because the action of SCG was only important for one defect in each specimen. Of course SCG acted on all stressed defects, but for a particular specimen, the defect that would be strength controlling under inert conditions would be the same defect that would be strength controlling in that specimen regardless of the stress-time schedule. Unfortunately, this simplification is not justified in region D of Figure 1 where all three complexities are present simultaneously. In this case, a particular specimen may fail from one defect if tested at a fast loading rate, but would fail from a different defect in a different location if that same specimen had been tested at a slow loading rate. The consequences of this situation are difficult to predict, but one could imagine that an initially Weibull strength distribution might be modified during SCG because different flaws would become strength controlling.

Figure 5 is a schematic of a three-point bend specimen with two defects that can illustrate the problem. One defect is of size "a" and is located at the point of maximum stress. The other defect is of size "4a" and is located halfway between the center and the right-hand load point. Because of this special situation, the stress intensity factors for the two defects are identical, therefore failure is equally likely to occur from either flaw. If SCG acts on the flaws during loading, the defects will grow at the same absolute rate

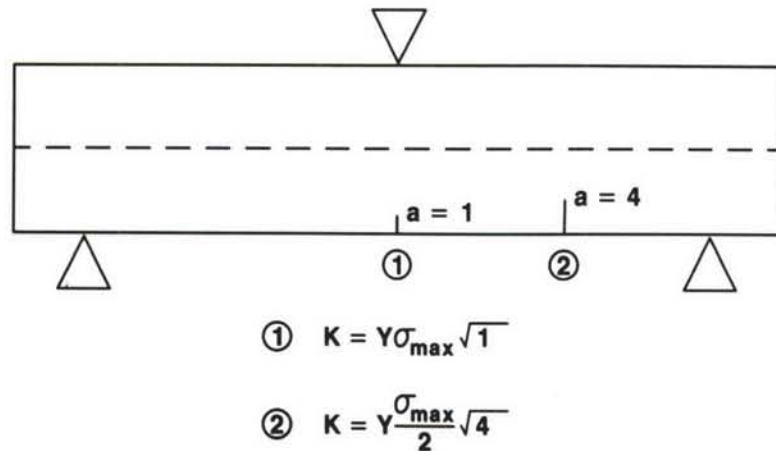


Fig. 5 Schematic of a bend specimen with two competing flaws.

(assuming a relationship such as Equation 2). However, in order to maintain equal stress intensity factors for the two, the second flaw would have to grow at four times the rate of the first. This does not happen, therefore, after the first increment of SCG, the center defect will become the strength limiting defect. Similar effects of competing defects are expected in any structure with stress gradients during SCG. At long times to failure there is a greater likelihood of fracture initiating from a defect near the point of maximum stress than at short times to failure.

Figure 6 illustrates the "clouds" of fracture origin positions that are expected for materials with two different Weibull moduli when tested in three-point bending with no SCG (2). In each of the two side views, the data points record the positions of the strength initiating defect in each of 50 specimens chosen randomly from a population of Weibull strengths. From the earlier discussion of Figure 5, one could predict that after SCG, the cloud of origins in each case of Figure 6 would be more densely packed around the point of maximum stress than that shown for the inert strengths. Not obvious, however, is whether extremely long times to failure will result in all origins occurring at the point of maximum stress, or whether the cloud reaches a limiting density that does not change with longer testing times.

The "two-body" model of Figure 7 is a very simple structure that was used to better understand the consequences of SCG in bodies with stress gradients. The model is composed of two uniformly stressed sub-volumes that are loaded in series. When loaded to failure, the fracture origin will be located in either region A or region B. Computer simulation of data and analytical derivations were both utilized to gain insight into the behavior of two-body specimens when tested under conditions that promote SCG. The most important conclusions of the two-body studies include:

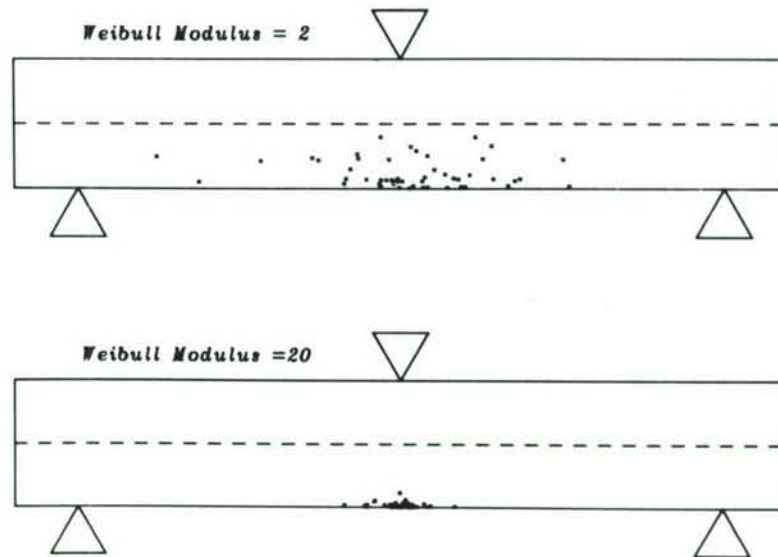


Fig. 6 Results of fracture origin position study showing that positions of fracture origins are dependent on Weibull modulus.

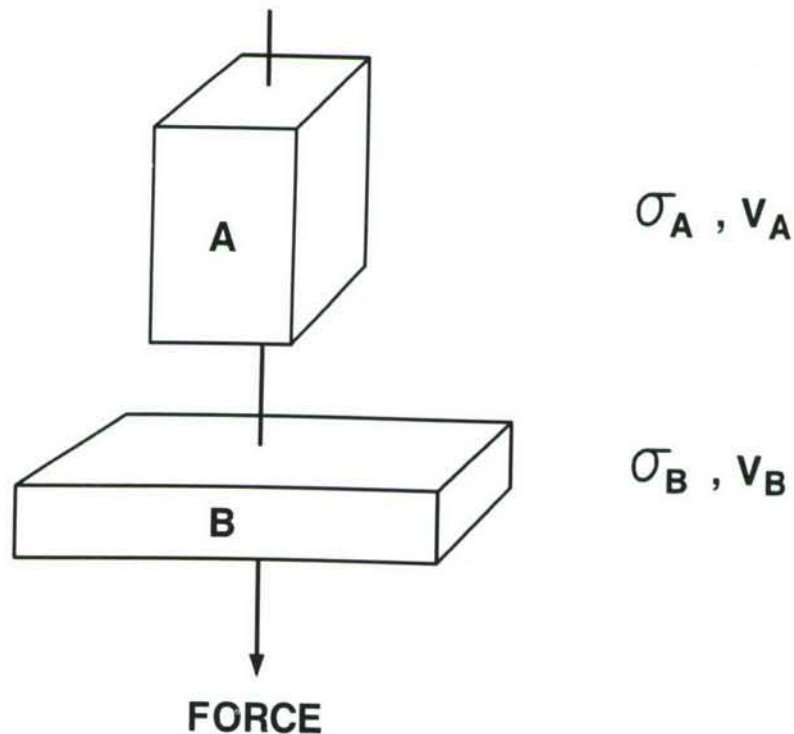


Fig. 7 Schematic of the "two-body" model which is useful as a simple structure with a stress gradient.



- For all continuous strength distribution<sup>5</sup>, as sub-critical crack growth proceeds, the proportion of failures in the higher stressed sub-volume increases.
- The proportion of failures in the higher stressed sub-volume asymptotically approaches a fixed value at very slow loading rates.
- For Weibull materials tested at slow loading rates,  $m$  estimated from strengths follows the same relationship as that for uniformly stressed bodies (Equation 4).
- For Weibull materials tested at slow loading rates,  $m$  estimated from origin positions follows a different relationship:

$$m_{\text{slow}} = m_{\text{inert}} \frac{n}{(n-2)} \quad (5)$$

It is expected (but not yet demonstrated or proven) that similar conclusions are valid for bodies with arbitrary stress gradients.

#### Status of milestones

On schedule.

#### Publications

None.

#### References

1. W. Weibull, "A Statistical Distribution Function of Wide Applicability", J. Appl. Mech., 18, 293, 1951.
2. C. A. Johnson and W. T. Tucker, "Advanced Statistical Concepts of Fracture in Brittle Materials", Proceedings of the Twenty-third Automotive Technology Development Contractors' Coordination Meeting, Dearborn, MI, Published by SAE, p. 265, 1986.

### 3.0 DATA BASE AND LIFE PREDICTION

#### INTRODUCTION

This portion of the project is identified as project element 3 within the work breakdown structure (WBS). It contains five subelements, including (1) Structural Qualification, (2) Time-Dependent Behavior, (3) Environmental Effects, (4) Fracture Mechanics, and (5) Nondestructive Evaluation (NDE) Development. Research conducted during this period includes activities in subelements (1), (2), and (3). Work in the Structural Qualification subelement includes proof testing, correlations with NDE results and microstructure, and application to components. Work in the Time-Dependent Behavior subelement includes studies of fatigue and creep in structural ceramics at high temperatures. Research in the Environmental Effects subelement includes study of the long-term effects of oxidation, corrosion, and erosion on the mechanical properties and microstructures of structural ceramics.

The research content of the Data Base and Life Prediction project element includes (1) experimental life testing and microstructural analysis of  $\text{Si}_3\text{N}_4$  and  $\text{SiC}$  ceramics, (2) time-temperature strength dependence of  $\text{Si}_3\text{N}_4$  ceramics, and (3) static fatigue behavior of PSZ ceramics.

Major objectives of research in the Data Base and Life Prediction project element are understanding and application of predictive models for structural ceramic mechanical reliability, measurement techniques for long-term mechanical property behavior in structural ceramics, and physical understanding of time-dependent mechanical failure. Success in meeting these objectives will provide U.S. companies with the tools needed for accurately predicting the mechanical reliability of ceramic heat engine components, including the effects of applied stress, time, temperature, and atmosphere on the critical ceramic properties.

### 3.1 STRUCTURAL QUALIFICATION

*Microstructural Analysis of Corrosive Reactions in Structural Ceramics*  
N. J. Tighe (National Bureau of Standards, Gaithersburg, Md.)

No Report Received



Physical Properties of Structural Ceramics

R. K. Williams, R. S. Graves, and M. A. Janney (Oak Ridge National Laboratory)

Objective/scope

The structural ceramics presently considered for use in advanced heat engine applications usually contain more than one phase and several components. The thermal conductivities of these materials are low relative to metals, and this characteristic, along with thermal expansion plus fracture strength and toughness, is a prime factor in determining suitability of a given ceramic for a particular advanced engine component. The purpose of this research is to develop an improved understanding of the factors that determine the thermal conductivities of these complex structural materials at high temperatures.

Technical progress

A study of the effects of  $\text{Cr}_2\text{O}_3$  and  $\text{Fe}_2\text{O}_3$  additions on the thermal conductivity,  $\lambda$ , of  $\text{Al}_2\text{O}_3$  has been completed. The purpose of this investigation was to determine whether the effect of point defect scattering on the thermal conductivity,  $\lambda$ , of alumina-based ceramics could be explained by available theories. Interest in the problem arose because alumina is an excellent high-temperature structural material, but for some applications its thermal conductivity is too high, and dissolving other  $\text{M}_2\text{O}_3$  oxides shows promise as a method of controlling thermal conductivity. Consequently, there is general interest in developing a reliable method for predicting this effect.

All of the data were obtained in a comparative longitudinal heat flow apparatus that has been in service for many years.<sup>2,3</sup> In this apparatus an uninstrumented sample is compressed between two gold-plated Armco Iron heat meter bars, and the sample temperature drop and heat flux are inferred from temperature-distance data obtained on the two heat meters. Indium foils, under a compressive load of 34 MPa, are used to minimize resistance to heat flow at the two sample-meter bar interfaces, and the interfacial resistance is determined by making measurements on standard samples. Nonlinear flow of heat is minimized by the gold plating and by operating in a vacuum. The method used in calculating  $\lambda$  allows for heat losses, which are typically 1 to 2%. The experimental uncertainty has been assessed by making measurements on samples of known thermal conductivity; it is less than  $\pm 3\%$  (ref. 2).

Two groups of hot-pressed compacts were prepared for this study, a pure  $\text{Al}_2\text{O}_3$  series and seven  $\text{Al}_2\text{O}_3$ -base compositions containing  $\text{Cr}_2\text{O}_3$ ,  $\text{Fe}_2\text{O}_3$ , or both  $\text{Cr}_2\text{O}_3$  and  $\text{Fe}_2\text{O}_3$ . The data for the pure  $\text{Al}_2\text{O}_3$  samples have been presented previously.<sup>3</sup> Sintering aids were not used for any of the samples, and all of the pellets were hot pressed for 1 h.

The solid solution compacts were formed by adding an alcohol solution of the appropriate nitrate salt to  $\text{Al}_2\text{O}_3$  powder, drying, calcining at  $1150^\circ\text{C}$  in air, and hot pressing in a graphite die. Grain size measurements were obtained from photomicrographs, and checks of longitudinal and transverse sections showed no obvious anisotropy. Scanning electron micrographs were required for some of the fine-grained material, and the

grain sizes ranged from 2 to 71  $\mu\text{m}$ . Adding 2 mol %  $\text{Fe}_2\text{O}_3$  greatly enhanced grain growth, yielding the 71- $\mu\text{m}$  grain size. Presumably the presence of a small amount of a second phase inhibited grain growth in the 4 mol %  $\text{Fe}_2\text{O}_3$  compact. Elemental analyses were obtained with a quantitative microprobe apparatus. Checks by wet chemistry on three different compacts showed maximum differences of about 0.4 mol %  $\text{Cr}_2\text{O}_3$ .

Thermal conductivity samples, 6.35 mm in diameter and 5.1 mm tall, were machined from the compacts, and the surface carbide reaction layer was avoided. Geometrical density measurements were made on all of these carefully machined samples, and these values were compared with the X-ray values. The least dense samples contained about 3% porosity, and the porosity,  $P$ , values obtained in this manner were used to correct the measured thermal conductivity,  $\lambda$ , values using Maxwell's equation<sup>4</sup>:

$$\lambda_{T.D.} = \lambda \frac{1 + 0.5P}{1 - P} .$$

The experimental data are shown in Fig. 1.

The thermal conductivity of unalloyed  $\text{Al}_2\text{O}_3$  is limited by 3-phonon Umklapp processes and by phonon-grain boundary scattering. These two scattering processes also occur in alloyed ceramics, and they must be accounted for in order to identify the strength of the phonon-point defect scattering introduced by alloying. Data for unalloyed  $\text{Al}_2\text{O}_3$  were used to determine the strength of the Umklapp process and boundary scattering, and a Callaway<sup>5</sup> model was adopted for the analysis. The highest temperature data, at 360 K, were used in the analysis because the formula for Umklapp scattering is valid at high temperatures.

After identifying the point defect contribution to the total phonon scattering rate, the results were compared with several theories.<sup>6-9</sup> These theories indicate that the scattering is determined by the mass difference, elastic strain, and local force constant changes associated with the foreign atoms. The results of this study indicate that the strain and force constant changes are negligible and that the scattering is entirely due to the difference in atomic mass. This is shown in Fig. 2. The results also are consistent with the suggestion that a light atom in a heavy matrix produces more scattering than a heavy atom in a light matrix.<sup>10</sup> The results of this study therefore provide a good basis for predicting the effects of point defect scattering of phonons in other ceramics.



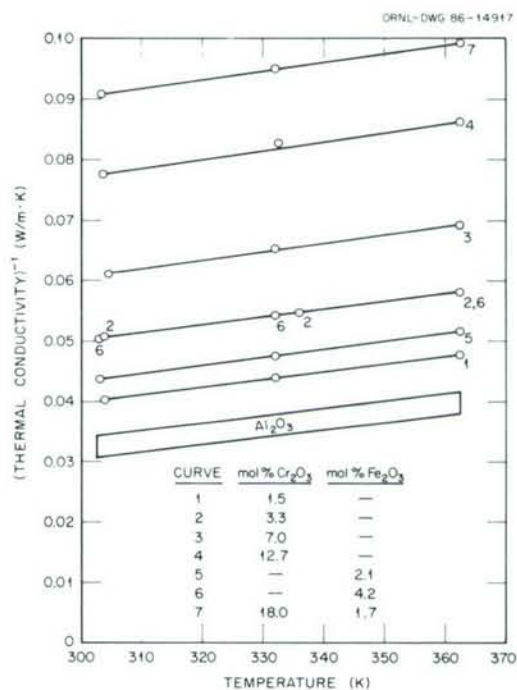


Fig. 1. Experimental thermal conductivity data for  $\text{Al}_2\text{O}_3$ -based solid solutions.

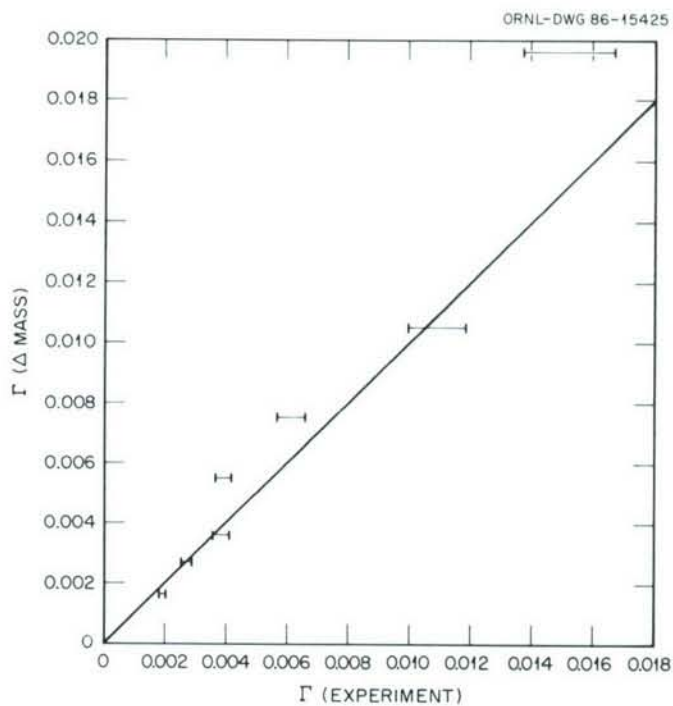


Fig. 2. The phonon-point defect scattering strength,  $\Gamma$ , can be calculated from the mass difference between  $\text{Al}_2\text{O}_3$  and the solutes  $\text{Cr}_2\text{O}_3$  and  $\text{Fe}_2\text{O}_3$ .



Status of milestones

311201 Complete study of  $\text{Cr}_2\text{O}_3$  and  $\text{Fe}_2\text{O}_3$  effects on thermal conductivity, was completed.

September 30, 1986

Publications

R. K. Williams, R. S. Graves, M. A. Janey, T. N. Tiegs, and D. W. Yarbrough, "The Effects of  $\text{Cr}_2\text{O}_3$  and  $\text{Fe}_2\text{O}_3$  Additions on the Thermal Conductivity of  $\text{Al}_2\text{O}_3$ ," paper submitted to *Journal of Applied Physics* on September 30, 1986.

References

1. T. Y. Tien, T. K. Brog, and A. K. Li, p. 215 in *Proceedings of the 23rd Automotive Technology Development Contractors Coordination Meeting*, P.165, of Automotive Engineers, Inc., Warrendale, Pa, 1985.
2. R. K. Williams, R. K. Nanstad, R. S. Graves, and R. G. Berggren, *J. Nucl. Mater.*, **115**, 115 (1983).
3. R. K. Williams, R. S. Graves, and M. A. Janney, "Physical Properties of Structural Ceramics," pp. 232-34 in *Ceramic Technology for Advanced Heat Engines Project Semiannual Progress Report for Period October 1985 through March 1986*, ORNL/TM-10079, August 1986.
4. J. M. Wimmer, H. C. Graham, and N. M. Tallan, p. 619 in *Electrical Conductivity in Ceramics and Glass, Part B*, ed. N. M. Tallan, Marcel Dekker, Inc., New York, 1974.
5. J. Callaway, *Phys. Rev.* **113**, 1046 (1959).
6. P. G. Klemens, *Proc. Phys. Soc. (London)* **A68**, 1113 (1955).
7. J. A. Krumhansl and J. A. D. Matthew, *Phys. Rev.* **140**, A1812 (1965).
8. C. Y. Ho, M. W. Ackerman, K. Y. Wu, S. G. Oh, and T. N. Havill, *J. Phy. Chem. Ref. Data* **7**, 959 (1978).
9. N. Morton, *Cryogenics* **17**, 225 (1977).
10. J. Tavernier, *Compt. Rend.* **245**, 1705 (1957).

*Effect of Translucence of Engineering Ceramics on Heat Transfer in Diesel Engines* - Thomas Morel and Syed Wahiduzzaman (Integral Technologies Incorporated)

Objective/scope

Ceramic materials are being used as thermal barrier materials, separating the engine metal substructure from the convective and radiative heat fluxes originating in the combustion gases. The heat transfer through the ceramic layer to the substructure will be increased by any translucence, which would allow a part of the radiation heat flux to pass through the barrier material. To quantify the effect of translucence of engineering ceramics on the heat transfer in diesel engines, Integral Technologies is conducting analytical studies using detailed computer codes which describe a realistic engine thermal environment including gas-to-wall heat fluxes, as well as the combined radiation/conduction heat transfer through a thermal barrier layer. A detailed parametric study will be carried out in which the following parameters will be varied, and their effect on heat barrier effectiveness will be studied: 1) material absorption coefficient, 2) material conductivity, 3) material thickness and 4) engine operating conditions (speed, fuel/air ratio, boost). An analysis of the results will yield bounds on critical properties, beyond which there is a reason for concern about this effect. Also, suggestions will be made for methods to control any adverse effects.

Technical progress

In order to study the effects of translucence in ceramic layers, one needs to describe the main heat transfer processes within such layers, which are conduction and radiation. An extensive literature review was performed in order to select a radiation model accurate enough to describe the effect of pertinent parameters on total heat transfer, and yet tractable enough to be practical.

Once such a model is constructed, its success in answering the posed questions will be largely dependent on the proper choice of physical parameters, which in this case includes the complex refractive index, single scattering albedo, thermal conductivity and the specific heat of the medium. Unfortunately, information on properties for ceramic materials is sparse, especially for radiative properties. In the absence of reliable property data, the only feasible approach is to perform a parametric analysis over a broad range of possible values of the properties in order to account for the uncertainty of the chosen property values and to determine the sensitivity of the calculated results to the selected property values. Thus, an important part of the work is to determine the lower and upper bounds on these parameters, which should be comprehensive, yet not overly broad, to allow meaningful conclusions to be drawn.



## Combined Radiation/Conduction Model

The general scheme of evaluating the gas-to-wall heat transfer in diesel engines will involve the solution of a one-dimensional energy (heat transfer) equation within the wall, coupled with the appropriate boundary conditions. The wall is assumed to be composed of two layers: an insulating coating material facing the combustion gas and a metallic substrate (Figure 1). The gas side boundary condition (gas-to-wall convection and radiation) will be provided by an engine simulation code IRIS, described in Morel et al.<sup>1</sup> The energy equation will be solved for two distinct regions: a semitransparent region within the ceramic, and a fully opaque region within the substrate. The energy equation for both of these regions is given by

$$\rho c \frac{\partial T}{\partial t} = -\nabla \cdot q \quad (1a)$$

where  $\rho$  is density,  $c$  is specific heat,  $T$  is temperature,  $q$  is heat flux vector  $= -k\nabla T + F$  (combined conduction and radiation),  $k$  is thermal conductivity, and  $F$  is radiative component of the heat flux vector.

The gas side boundary condition (see Figure 1) is given by

$$-k \frac{\partial T}{\partial x} = h(T_{\infty} - T) + \int_{\lambda_c}^{\infty} (\alpha_{\lambda} G_{\lambda} - \epsilon_{\lambda} E_{b\lambda}) \quad (1b)$$

$\alpha_{\lambda}$  is absorptivity of the surface,  $G_{\lambda}$  is incident radiant heat flux,  $\epsilon_{\lambda}$  emissivity of the surface,  $E_{b\lambda}$  blackbody emissive power at temperature  $T$ ,  $h$  is the convective heat transfer coefficient at the gas-wall interface, and  $k_1$  is the conductivity of the ceramic layer. It should be noted here that the above temperature boundary condition involves only the portion of the radiant energy spectrum which is beyond  $\lambda_c$ , since only this portion of the energy interacts at the surface and must therefore be conducted directly from the surface. This is because the ceramic layer is assumed to be opaque to radiation at wavelengths beyond  $\lambda_c$  (the substrate is opaque at all wavelengths). The rest of the energy penetrates inside and interacts volumetrically with the ceramic, and will be taken into account by the radiative heat flux vector  $F$ , as will be discussed in detail subsequently. The other boundary condition is

$$T_L^c = T_L^s \quad (1c)$$

where superscripts  $c$  and  $s$  denote ceramic layers and substrate respectively.

The radiative heat flux vector, which is an integral over the whole spectrum, is computed separately by solving the equation of transfer describing the radiative intensity distribution in the medium. In the opaque region of the medium (substrate),  $F$  is identically zero and the energy equation becomes the familiar unsteady conduction equation.



## Radiation Heat Flux in Ceramics

The governing equation for radiation transfer can be treated very accurately as quasi-stationary for most engineering applications (Viskanta<sup>2</sup>), because the time-scales of radiation are an order of magnitude below the scales typically encountered, and this holds also here. It should be pointed out that the time dependence of the radiative flux is, however, still included, as it is coupled through the transient temperature distribution of the medium and through the time dependence of the gas-radiation process. Even though the term involving the time derivative in the equation of transfer can be neglected, the solution of the very complex integro-differential radiative transfer equation is still a formidable task. The exact solution of this equation exists for very few simple geometrical situations and almost exclusively for non-scattering medium (Viskanta and Anderson,<sup>3</sup> Love,<sup>4</sup> and Viskanta and Song<sup>5</sup>).

Because of the intractability of the exact equation, many approximate schemes of solution of radiative transfer equation have been developed. Among them, several applicable to the problem at hand are available, requiring different degrees of computational efforts. Two commonly used approaches are the discrete ordinate method (Houf and Incropera<sup>6</sup>), and the spherical harmonics method (Menguc and Viskanta<sup>7</sup>). In the former method, radiant energy is divided into discrete streams and the phase function is expanded into a series of Legendre polynomials about the scattering angle, and in addition the integral is replaced by a suitable quadrature. The six flux, three flux and two flux methods are, essentially, subsets of this method. In the spherical harmonics method, on the other hand, the radiation field is expanded in terms of Legendre polynomial. In both methods the resulting system of non-homogeneous equations has to be solved to obtain the radiation field. In the simplest spherical harmonics method where only two terms of the expansion are retained ( $P_1$  method), this becomes identical to Milne-Eddington's approximation which is applicable only in the optically thick limit (Ozisik<sup>8</sup>). The accuracy of the spherical harmonics method improves as more terms are retained, but that comes at the cost of increased computational effort. In a comparison of radiative transfer approximations for a highly forward scattering planar medium (Menguc and Viskanta<sup>7</sup>), it was observed that the two-flux method compares favorably with the discrete ordinates method and higher order spherical harmonics methods, but it requires a considerably smaller computational effort.

In view of the above, the two-flux method was chosen for the present study. The general expression of the two-flux model is of the form

$$\frac{dF_{\lambda}^{\pm}(\tau)}{d\tau} = -AF_{\lambda}^{+}(\tau) + BF_{\lambda}^{-}(\tau) + C\lambda(\tau) \quad (2a)$$

$$-\frac{dF_{\lambda}^{-}(\tau)}{d\tau} = -AF_{\lambda}^{-}(\tau) + BF_{\lambda}^{+}(\tau) + C_{\lambda}(\tau) \quad (2b)$$

$$F(\tau) = \int_0^{\lambda} (F_{\lambda}^{+}(\tau) - F_{\lambda}^{-}(\tau)) d\lambda \quad (2c)$$

where

$F_{\lambda}^{+}$  is the forward radiative flux,  $F_{\lambda}^{-}$  is the backward radiative flux and  $\tau$  is the optical depth defined as

$$\tau = \int_0^x (k_{\lambda} + \alpha_{\lambda}) d\xi \quad (2d)$$

where  $x$  is the normal distance from the surface into the interior of the ceramic. It may be noted that the integration limits in eq (2c) extend only over the wavelengths over which the material is translucent and for which the radiant energy penetrates into the interior of the ceramic.

#### Method of Solution

The energy equation has to be solved simultaneously for the semi-transparent ceramic layer and the opaque substrate. An additional boundary condition will be required to completely specify the system of equations. This may be a convective boundary condition for the coolant side of the engine, or a fixed prescribed temperature on that interface.

The governing equation (2) has to be solved for each  $\lambda$  and then integrated over the semitransparent region of the coating. This is accomplished by discretizing the semitransparent wavelength region into a number of bands over which radiative properties are assumed constant. Each of these equations is integrated over the wavelength band, over which the radiative properties and boundary conditions are assumed to be uniform. This operation leaves the form of the flux equations unaltered, except for the emission term which is replaced by an a quantity integrated over the band of wavelengths. Then a solution of a pair of differential equations is obtained for each band. The solution of these equations provides the radiative flux integrated over the bandwidth. The sum of the heat fluxes over all bands then gives the total radiative flux. These equations are solved with the temperature distribution of the previous time step. As already discussed, this is an acceptable scheme since the changes in the temperature field will be very small from one time step to the next.



The chromatically integrated forward and backward flux equations are further spatially discretized so that they can be solved numerically. The spatial grid points are generated by a grid generator, which provides compact grid spacings at both interfaces, where higher resolution is required for accuracy. The resulting two sets of linear equations are interlaced to avoid iterative solution.

### Model Validation

To validate the implementation of the model, its results were compared to a highly accurate and involved numerical solution of Menguc and Viskanta.<sup>7</sup> The specific test case for comparison was chosen to be one in which scattering plays a significant role, because this is expected to be an important factor in the ceramics application. Menguc and Viskanta compared performances of various radiation models in a geometrically simple situation, where the scattering medium is a plane parallel slab of unity refractive index. Since the expressed purpose of their exercise was to compare models under different scattering properties, the medium was assumed to be cold so that the emission term could be neglected. In the present computation, this term was retained, but the medium was set at 500K so that its contribution was negligible. The boundaries were nonreflecting and nonemitting. The scattering particles were assumed to be suspended in air, and diffuse heat flux incident on one of the boundaries was assumed. In Figure 2 is shown a comparison of present calculations (modified two-flux) with the benchmark calculations of Menguc and Viskanta employing the  $F_0$  method of the transmittance through the medium for a highly forward scattering medium. The comparisons are also shown in Table I. It is seen that the agreement in transmittance is excellent, but that predictions of reflectance tend to be lower than the benchmark calculations (Table I). The predictions, however, get better as medium becomes less forward scattering (see  $b = 0.345$ , Table I). It should be noted, that in terms of the total energy transmitted, the discrepancy in reflectance is small and is not considered to be serious. In summary, it is found that the model was implemented correctly and reproduces well the results obtained for a relevant test case by a much more involved method.

### Parametric Study

A study has been undertaken to assess the sensitivity of different parameters contributing to the radiative heat transfer process. This was done using the radiation flux model in a stand-alone mode prior to coupling it to the heat conduction calculations. The base-line conditions chosen as follows:

Uniform medium temperature = 1000K  
 Back scattering fraction,  $b = 0.5$   
 Sample thickness,  $L = 10\text{mm}$   
 Scattering albedo,  $\omega = 0.8$   
 Incident heat flux = 1MW  
 Refractive index,  $n = 1.6$   
 Outside reflectance of first surface,  $r_0 = 0.2$



Second surface reflectance = 0.7  
 Second surface emittance = 0.3

and the inside reflectance of the first surface was calculated using the following equation, which takes into account the total internal reflection:

$$r_i = (n^2 - 1 + r_o) / n^2$$

Figures 3 to 6 show several samples from parametric study. Figure 3 pertains to the effects of scattering albedo. It is plotted (as are all remaining figures) with respect to the optical thickness  $\tau = kL/(1-\omega)$ . It appears to indicate that increasing the scattering albedo increases the transmittance. In fact, when the effect of  $\omega$  on  $\tau$  is taken into consideration, one finds that increasing the albedo decreases the transmittance. Figure 4 shows that the effect of the back scattering fraction is small, especially as the phase function becomes less anisotropic (approaching 0.5). The effect of increasing refractive index is to increase the transmittance moderately (Figure 5). It should be noted that the refractive index of ceramic material is expected to be quite close to 1.5, and the present results indicate that the uncertainty in its value is not expected to lead to significant errors. By contrast, as would be expected, the influence of the front surface reflectivity is rather substantial (Figure 6). This implies surface finish and deposition will greatly influence total radiative heat transfer. In all these plots, it can be seen that optical depth is of prime parameter influencing the load of radiation heat transfer.

#### Status of Milestones

Milestone 11a, model formulation was reached in March, 1986.  
 Milestone 11b, model development was completed in August, 1986.

#### Publications

No publications concerning this work were prepared during this period.

#### References

1. Morel, T., Keribar, R., Blumberg, P. N. and Fort, E. F. (1986) "Examination of Key Issues in Low Heat Rejection Engines," SAE Paper 860316.
2. Viskanta, R. (1966), in Irvine, T. F. Jr., Hartnett, J. P. (eds): Advances in Heat Transfer, Vol. 3. New York, London, Academic Press.
3. Viskanta, R., Anderson, E. E. (1975), "Heat Transfer in Semi-transparent Solids." in Irvine, T. F. Jr., Hartnett, S. P. (eds). Advances in Heat Transfer, Vol. 11, New York, London; Academic Press.
4. Love (1968), Radiation Heat Transfer, C. E. Merrill Pub. Co.

5. Viskanta, R. and Song, Tae-Ho (1985), "On the Diffusion Approximation for Radiation Transfer in Glass." *Glastechnische Berichte*, Vol. 58, No. 4, pp. 80-86.
6. Houf, W. G. and Incropera, F. P. (1980), "An Assessment of Techniques for Predicting Radiation Transfer in Aquaeous Media," *Journal of Quantitative Spectroscopy and Radiation Heat Transfer*, Vol. 23, pp. 101-115.
7. Mengüç, M. P. and Viskanta, R. (1983), "Comparison of Radiative Transfer Approximations for a Highly Forward Scattering Planar Medium," *Journal of Quantitative Spectroscopy and Radiation Heat Transfer*, Vol. 29, No. 5, pp. 381-394.
8. Ozisik, M. N. (1985) Radiative Heat Transfer, Werbel and Peck, New York.

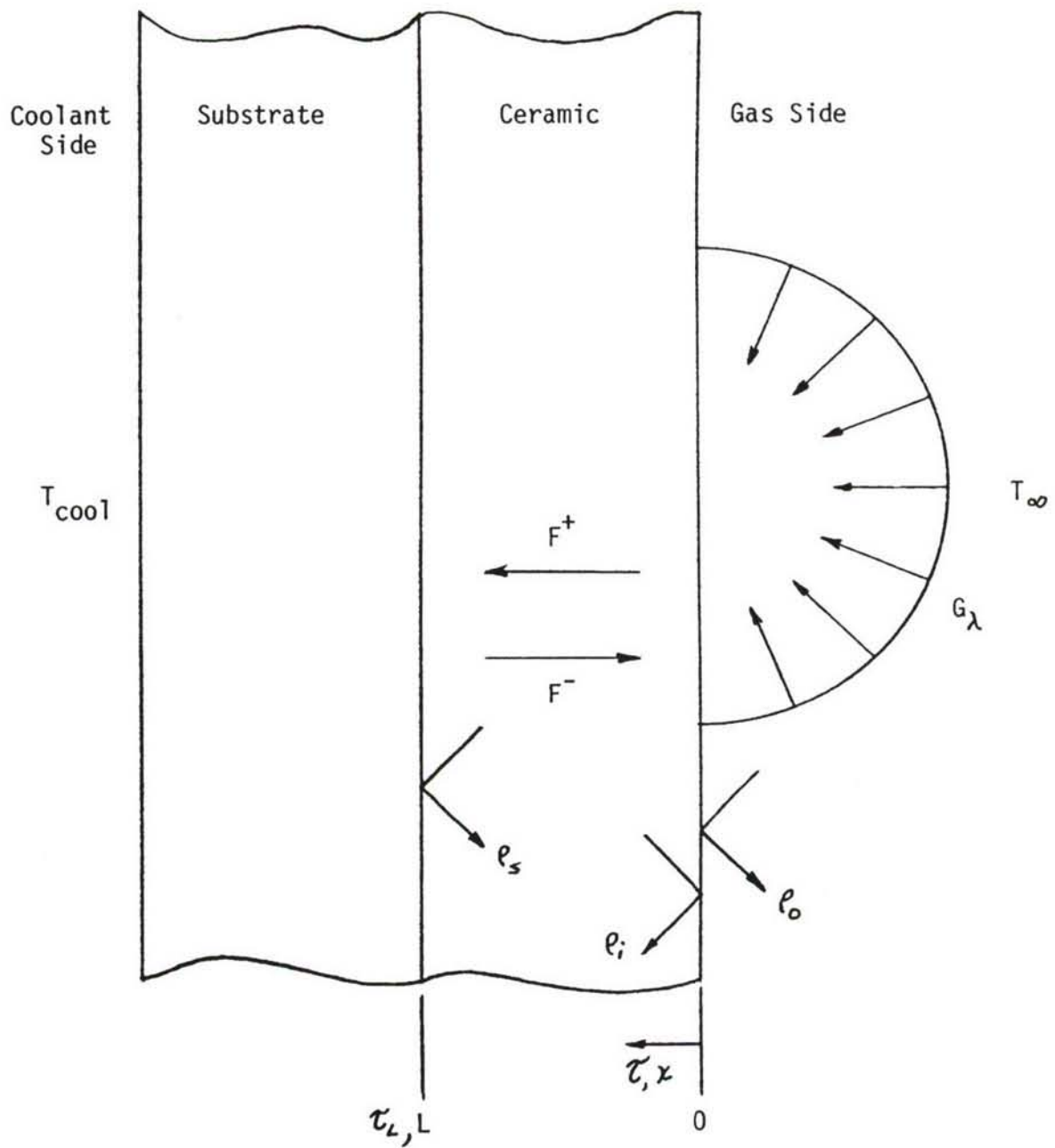


Figure 1: Physical Model of the Insulating Coating



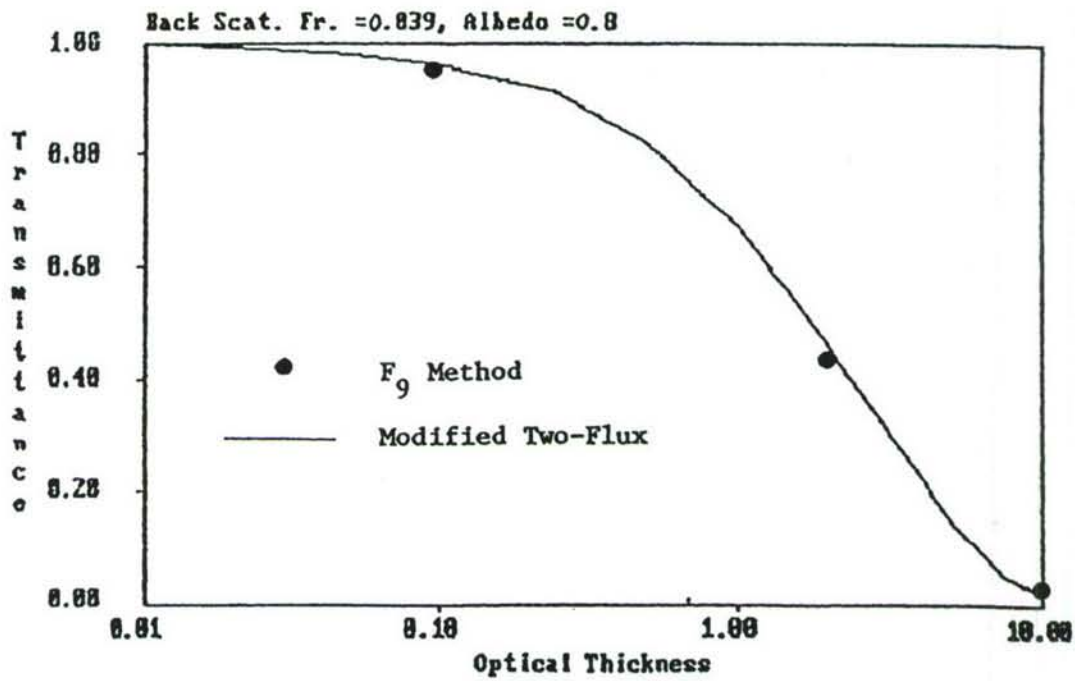


Figure 2: Comparison of model predictions to accurate literature results of Menguc and Viskanta (1982) for a scattering radiation medium.

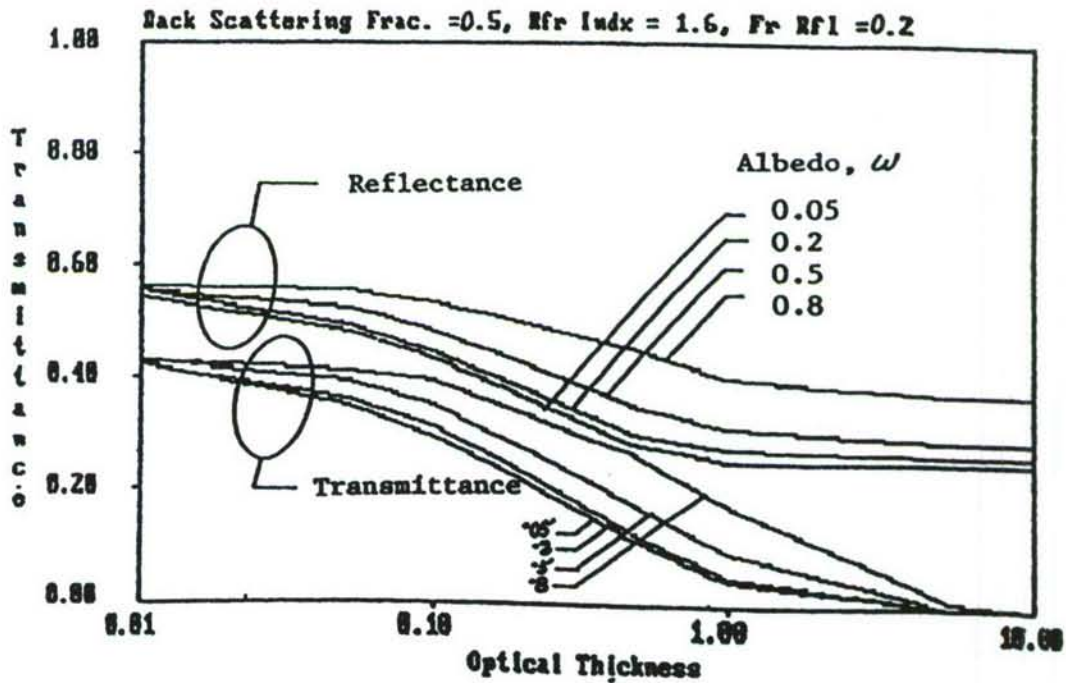


Figure 3: Effect of scattering albedo.

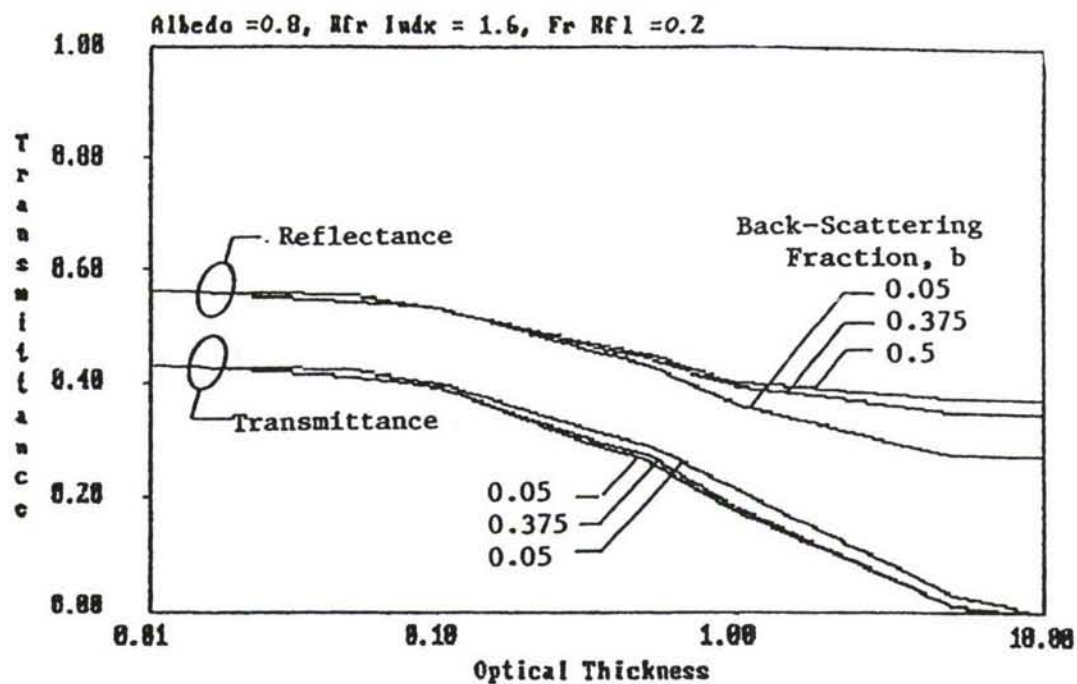


Figure 4: Effect of back-scattering fraction.

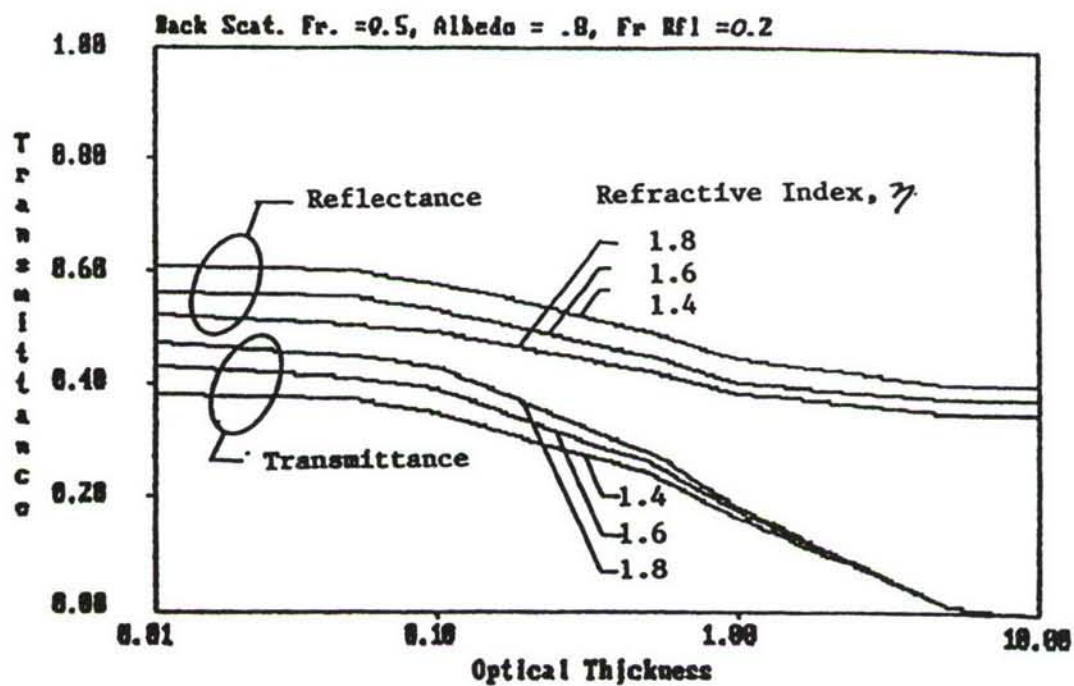


Figure 5: Effect of refractive index.

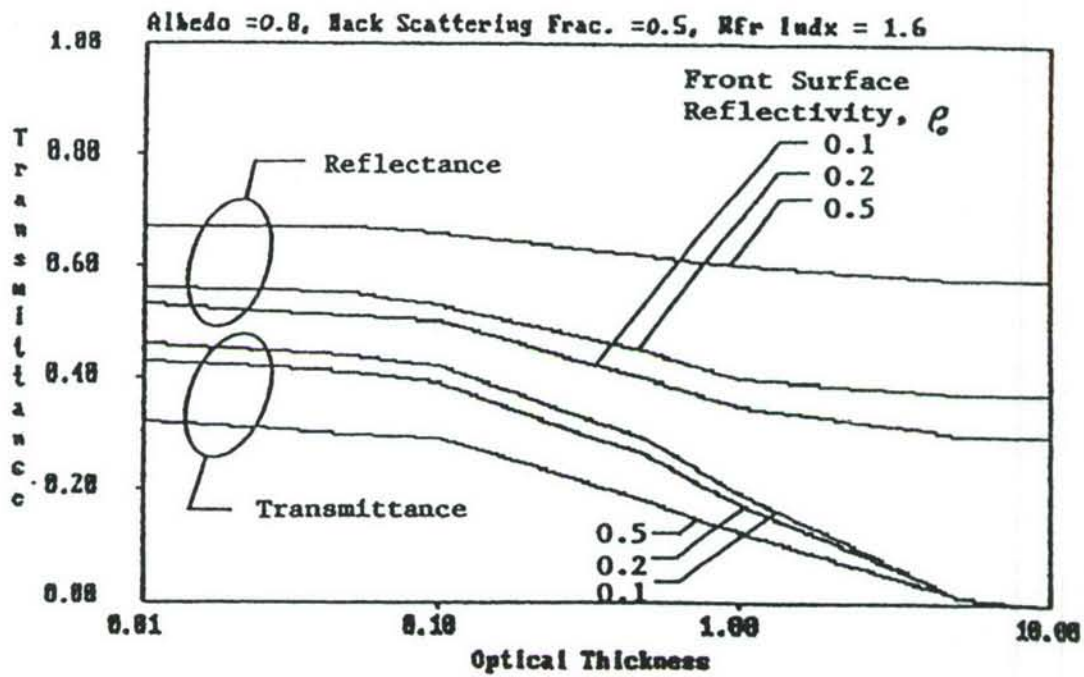


Figure 6: Effect of front surface reflectivity.

Optical Depth $\tau$	Back Scattering Fraction	Single Scattering Albedo $w$	Modified Two Flux of the Present Work		F <sub>9</sub> Method Calculation of Menguc & Viskanta	
			Reflectance	Transmittance	Reflectance	Transmittance
0.1	0.039	0.8	0.005	0.961	0.013	0.948
2	0.039	0.8	0.056	0.452	0.075	0.430
10	0.039	0.8	0.071	0.022	0.087	0.024
1	0.345	0.8	0.244	0.472	0.240	0.456
1	0.075	0.8	0.070	0.641	0.093	0.602
1	0.039	0.8	0.038	0.672	0.058	0.638

Table I. Comparison of model predictions to accurate literature results of Menguc and Viskanta (1982) for a scattering radiation medium



### 3.2 TIME-DEPENDENT BEHAVIOR

#### Characterization of Transformation-Toughened Ceramics

J. J. Swab and R. H. Katz (Army Materials Technology Laboratory)

#### Objective/Scope

Because of their unusual combination of properties, transformation toughened zirconias (TTZ) are leading candidates for cylinder liners, piston caps, head plates, valve seats and other components for the adiabatic diesel engine. These materials are age-hardened ceramic alloy systems and as such, they are likely to be susceptible to overaging and loss of strength after long times at high temperatures (i.e., close to the age-hardening temperatures). The possibility of overaging, with its likely negative impact on materials performance, was identified as a critical area of ignorance in the preliminary technology assessment on ceramics for diesel engines previously prepared by AMMRC. Accordingly, a task was initiated to a) define the extent and magnitude of the overaging (if any) and b) to develop toughened ceramic alloy systems which would not be susceptible to overaging at temperatures which may be encountered in advanced diesel engines (1000C-1200C).

#### Technical Progress

Originally, eight yttria-stabilized transformation toughened zirconias (TTZ) were to be examined by this study. However, one Japanese manufacturer informed me that his company could not supply me with their material.

Of the seven TTZ's examined, the Koransha "Hipped" (KH) has the best as-received room temperature strength, 1261 MPa. After heat treatments of 100 and 500 hours at 1000 °C, it retained over 80% of its strength. However, the Hitachi (HIT) still exhibits the best strength retention after heat treatment, losing only 7% of its as-received strength. Because of their excellent strength properties both of these TTZ's have undergone additional heat treatments at 1100 °C, for 500 hours with strengths of 1170 and 1135 MPa, respectively. Heat treatment at 1200 °C for 500 hours has been completed on HIT and again it shows no further strength loss with a strength of 1098 MPa. The KH is now undergoing the 1200 °C heat treatment.

High temperature testing is proceeding. Stepped-temperature stress rupture has been completed on the following: HIT, AC Sparkplug (AC), NGK-Locke (NGK) and Koransha "sintered" (KS). All but the AC, Fig. 2, show typical time-dependent failure with increasing temperature and applied stress. The AC has a clustering of failures below 900 °C and above 1100 °C. This could be a consequence of the size

Table 1. Summary of Zirconia Data

PROPERTY	MATERIAL	UNITS	KY	AC	TOSH	HIT	KS	KH	NGK
DENSITY:	COMPANY LISTING	g/cc	5.9	NDA	6.05	6.08	6.05	NDA	5.91
	AS-RECEIVED		5.853	5.840	5.880	6.038	5.966	6.045	5.869
	100 HRS @ 1000°C		5.803	5.835	5.884	6.029	5.967	6.056	5.861
	500 HRS @ 1000°C		5.772	5.863	5.877	6.037	5.967	6.064	5.863
SONIC MOE:	COMPANY LISTING	GPa	206	NDA	180	209	NDA	NDA	205
	AS-RECEIVED		201	204	200	213	210	214	208
	100 HRS @ 1000°C		203	206	200	213	211	212	207
	500 HRS @ 1000°C		205	208	200	214	210	213	208
MOR (4-PT):	COMPANY LISTING	MPa	980a	NDA	900a	1000	1100	NDA	1020
(CHAKAC)	AS-RECEIVED		745	753	633	1169	640	1261	873
STRENGTH OF	100 HRS @ 1000°C		470	683	581	1053	600	1070	754
BEND BAR)	500 HRS @ 1000°C		334	671	576	1062	663	1045	754
WEIBULL NO.:	COMPANY LISTING	NONE	NDA	NDA	NDA	NDA	10.2	NDA	NDA
	AS-RECEIVED		8.8	12.2	6.2	3.6	9.5	8.8	15.2
	100 HRS @ 1000°C		2.3	18.7	14.2	5.9	8.9	5.2	10.0
	500 HRS @ 1000°C		3.0	5.2	13.8	5.0	4.0	12.5	10.6
MOR (4-PT):	COMPANY LISTING	MPa	NDA	NDA	NDA	NDA	NDA	NDA	NDA
(MEAN)	AS-RECEIVED		704	722	587	1045	608	1192	884
	100 HRS @ 1000°C		413	664	561	975	567	974	718
	500 HRS @ 1000°C		296	613	555	974	589	1003	719
STANDARD	COMPANY LISTING	MPa	NDA	NDA	NDA	NDA	NDA	NDA	NDA
DEVIATION:	AS-RECEIVED		75	70	96	265	75	140	65
	100 HRS @ 1000°C		183	42	47	181	76	132	83
	500 HRS @ 1000°C		122	101	48	215	98	89	80
HARDNESS:	COMPANY LISTING	GPa	12.3b	NDA	11.8c	13.3b	14.7c	NDA	11.7
(KNOOP)	AS-RECEIVED		10.5	11.1	10.1	12.4	10.8		10.9
(300g LOAD)	100 HRS @ 1000°C		9.4	11.1	10.0	12.2	11.3		11.3
	500 HRS @ 1000°C		9.4	11.0	10.4	12.2	11.0		10.4

KY - KYOCERA Z201  
 AC - AC SPARKPLUG  
 TOSH - TOSHIBA "TAS21C"  
 HIT - HITACHI  
 KS - KORANSHA "SINTERED"  
 KH - KORANSHA "HIPPED"  
 NGK - NGK-LOCKE Z191  
 NDA - NO DATA AVAILABLE  
 a - BELIEVED TO BE 3-PT BEND RESULTS  
 b - VICKERS 500g LOAD  
 c - VICKERS

Figure 1. Room Temperature Strength vs Heat Treatment Time

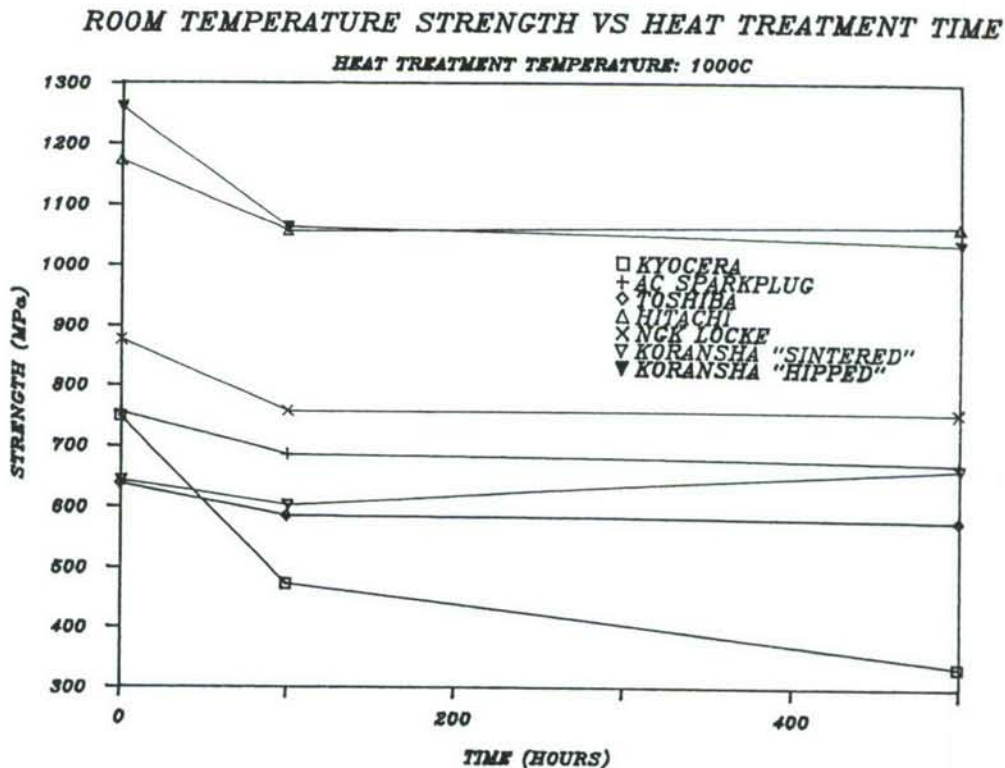


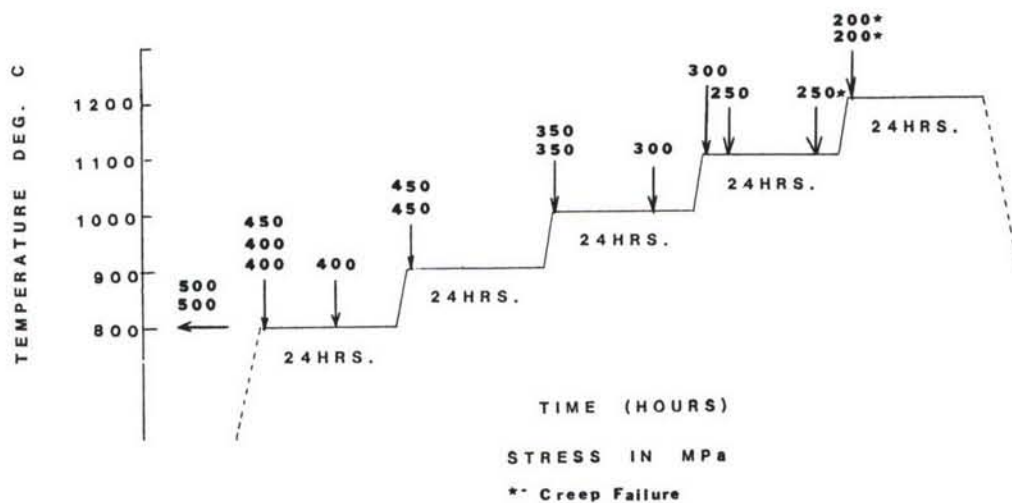
TABLE 2  
STRENGTH DATA FOR HIT AND KH AFTER ADDITIONAL HEAT TREATMENTS

MATERIAL	HITACHI	KORANSHA "HIPED"
CONDITION		
As-Received MOR (MPa)	1169	1261
StD	265	140
500 Hours @ 1000°C MOR (MPa)	1062	1045
StD	215	89
500 Hours @ 1100°C MOR (MPa)*	1170	1135
StD	130	102
500 Hours @ 1200°C MOR (MPa)*	1098	
StD	74	

\* Sample size = 15

Figure 2. Hitachi Stepped-Temperature Stress Rupture

### STSR - HITACHI

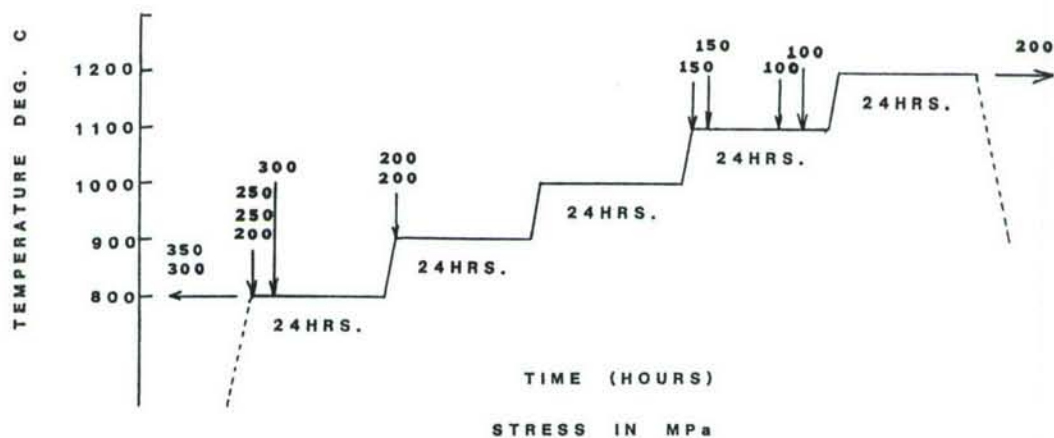


ROOM TEMPERATURE CHARACTERISTIC STRENGTH = 1169 MPa

HEAT-UP RATE 10 MIN. BETWEEN STEPS



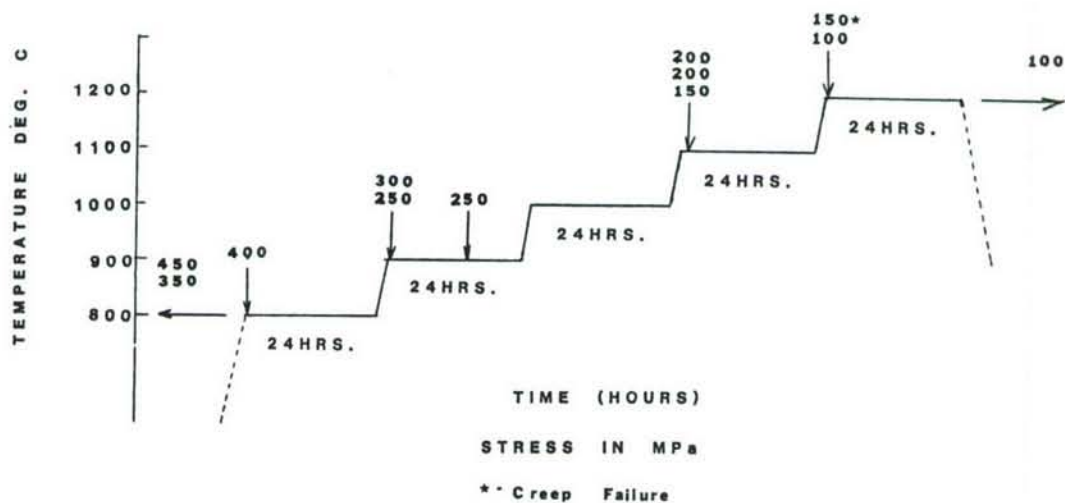
Figure 3. AC Sparkplug Stepped-Temperature Stress Rupture

**STSR-AC SPARKPLUG**

ROOM TEMPERATURE CHARACTERISTIC STRENGTH = 753 MPa

HEAT-UP RATE 10 MIN. BETWEEN STEPS

Figure 4. NGK-Locke Stepped-Temperature Stress Rupture

**STSR-NGK LOCKE**

ROOM TEMPERATURE CHARACTERISTIC STRENGTH = 873 MPa

HEAT-UP RATE 10 MIN. BETWEEN STEPS

of the bars, Army MIL-STD "A". The smaller bars are much harder to align in the furnace and if they are not properly centered it could result in erroneous data. A majority of failures very close to the beginning of the steps are occurring within 30 minutes of reaching the designated temperature. Stress rupture testing is continuing on the HIT and NGK TTZ's.

Fracture toughness evaluation of the TTZ's has started. It has been decided to use the indent and break method. This method was chosen because the technique is relatively easy to do and can be done on the same size bars that are used for flexure testing.

Post heat treatment characterization has revealed that, as expected, the monoclinic phase content (%m) changes with heat treatment time. For the HIT the %m is very low and stays low throughout the tests. The AC and TOSH also had constant %m throughout testing, but the content is about 3 times higher than HIT. The %m for the KY increases with increasing heat treatment time. This increase correlates well with decrease in density and strength with heat treatment time.

Hardness remains essentially constant for all TTZ's except KY which shows a slight decrease after 100 hrs of heat treatment time.

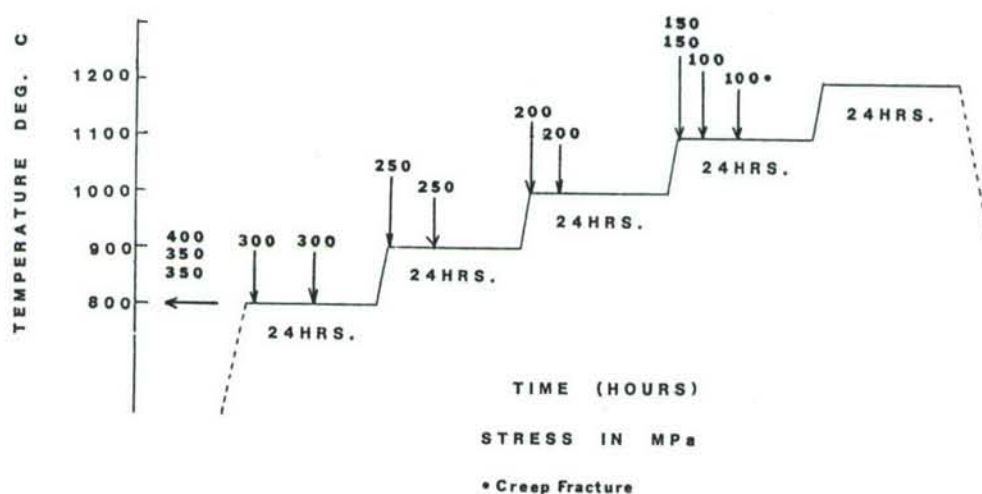
#### Status of Milestones

The final draft of the in-house technical report, authored by Lise Schioler, on the work done for the last three years has been edited and corrections are now being made.

#### Publications

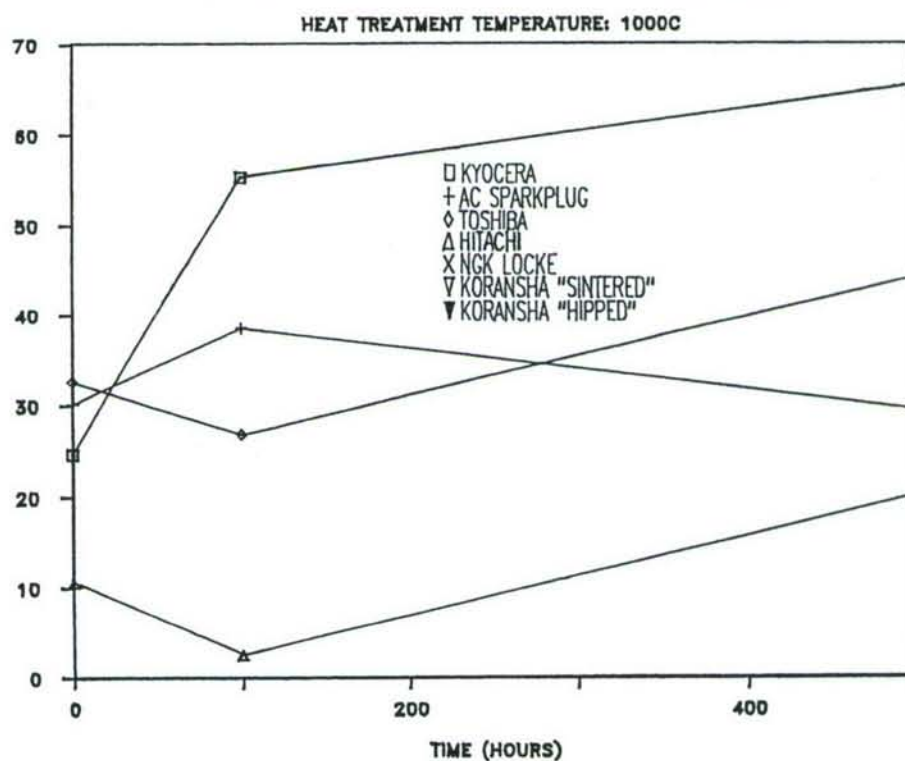
None

Figure 5. Koransha "Sintered" Stepped-Temperature Stress Rupture

**STSR - KORANSHA "sintered"**

ROOM TEMPERATURE CHARACTERISTIC STRENGTH = 640 MPa

HEAT-UP RATE 10 MIN. BETWEEN STEPS

Figure 6. % Monoclinic Content vs Heat Treatment Time  
% MONOCLINIC VS HEAT TREATMENT TIME



### Fracture Behavior of Toughened Ceramics

P. F. Becher and W. H. Warwick (Oak Ridge National Laboratory)

#### Objective/scope

Because of their excellent toughness, oxide ceramics such as partially stabilized zirconia (PSZ), dispersion-toughened alumina (DTA), and whisker-reinforced ceramics are prime candidates for many diesel engine components. The enhanced toughness of the PSZ and DTA materials is thought to be due to a stress-induced transformation (of the dispersed tetragonal  $ZrO_2$  phase) that requires additional energy in order for catastrophic fracture to occur. However, these materials are still susceptible to slow crack growth and thus strength degradation. Also there is limited evidence that at temperatures above 700°C, time-dependent aging effects can reduce the concentration of the phase involved in the transformation process leading to significant losses in toughness and strength. It is essential that mechanisms responsible for both the slow crack growth and aging behavior be well understood. Similarly the toughening behavior in whisker-reinforced ceramics and their high-temperature performance must be evaluated in order to develop materials for particular applications.

In response to these needs, studies have been initiated to examine toughening and fatigue properties of transformation-toughened and whisker-reinforced materials. Particular emphasis has been placed on understanding the effect of microstructure on processes responsible for time-dependent variations in toughness and high-temperature strength. In addition, fundamental insight into the slow crack growth behavior associated with these materials is being obtained.

#### Technical progress

Experimental results were obtained on the high-temperature fracture strength behavior in air of the alumina-20 vol % SiC whisker reinforced composites. Four-point flexure (6.35-mm and 19.05-mm inner and outer spans respectively) strengths are determined for rectangular cross section bars (2.5-mm thick by 2.6-mm wide by >20-mm long) whose surfaces are finished with a 220-grit diamond resinoid-bonded grinding wheel. The bar edges are beveled using a 6- $\mu$ m diamond lap with the direction of polishing parallel to the length of the bar. The flexure tests include (1) fast fracture strengths obtained by equilibrating the sample and fixture for 15 min at the test temperature and then fracturing the samples at a stressing rate of >30 MPa/s, and (2) fracture strengths retained after exposing the sample at a selected temperature to a fixed applied stress (2/3 of the fast fracture strength at that temperature) for a desired time. The latter test [an interrupted static fatigue (ISF) test] provides data on the long-term stability of the mechanical properties at elevated temperatures.

As noted by Becher and Wei,<sup>1</sup> the flexure strengths of such composites are sensitive to the degree of microstructural homogeneity (i.e., the uniformity of dispersion of the whiskers in the dense matrix). This can be seen by the improved strengths, Fig. 1, which are

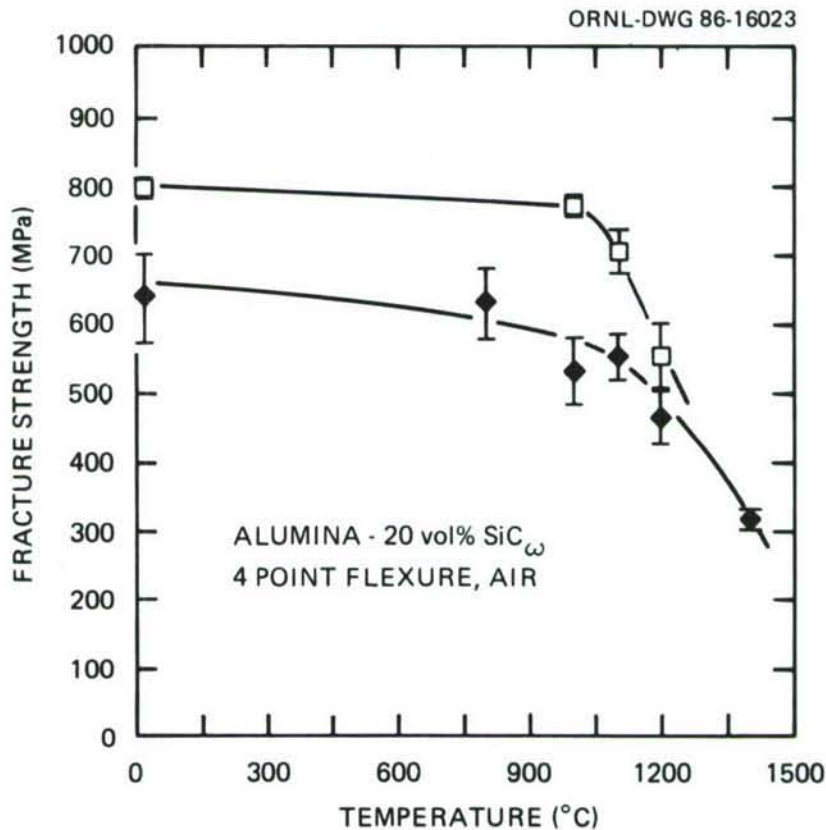


Fig. 1. The high fracture strengths of the alumina-20 vol % SiC whisker composites are maintained to temperatures approaching 1200°C. The two plots are representative of the temperature dependence of the fracture strengths for composites fabricated by different processes. The lower curve is representative of materials fabricated by techniques utilized in the past. The improved strengths illustrated by the upper curve are representative of materials fabricated using improved whisker dispersion techniques.

obtained when further refinements are made in the elimination of whisker and matrix powder agglomerates and in improving the dispersion of the whiskers in the matrix. In the case of pressureless-sintered composites where comparable toughness values are obtained, the fracture strengths are lower as a result of the lower densities currently achieved by this processing route.<sup>2</sup>

The alumina-20 vol % SiC whisker composites retain their high fracture strengths in an oxidizing environment (air) to temperatures in excess of 1000°C as shown in Fig. 1. The two alumina-20 vol % SiC whisker composites exhibit very slight changes in strength between room temperature and 1100°C; however, at 1200°C and above there is a marked loss in strength.



Studies of the rate of oxidation of the alumina-20 vol % SiC whisker reinforced composites, as determined by weight change as a function of time, reveal a substantial increase in oxidation rates with increase in temperature. For example, for exposure times of under 100 h, the oxidation rate at 1200°C is 10- to 15-fold greater than that at 1000°C, which is 2- to 4-fold greater than that at 800°C.<sup>3</sup> The substantial increase in oxidation rates, due to the SiC-oxygen reaction, at 1200°C coincides with the loss in fracture strength in the composites.

A surface layer formed during the exposure of these composites to air at elevated temperatures can penetrate locally into the composite to form larger defects. The loss in strength in air at temperatures above 1100°C is related to this oxidation behavior. The surface layer formation is a result of the oxidation of the SiC whiskers and their chemical interaction with the alumina matrix. With the generation of a surface layer of SiO<sub>2</sub> during oxidation of the SiC whiskers, thermodynamics would predict that mullite should form at the Al<sub>2</sub>O<sub>3</sub>-SiO<sub>2</sub>

interface. Indeed, the formation of fine mullite particles has been observed at the alumina-SiC whisker interface at elevated temperature.<sup>4</sup> The kinetics of mullite formation are enhanced by impurities, and in pure systems the reaction rates are quite slow. If one desires long-term stability of the phases present and thus improved mechanical properties at temperatures  $\geq 1200^\circ\text{C}$ , either impurities must be controlled or matrix materials that result in greater thermodynamic stability must be selected.

The fracture strengths retained after various times of exposure to an applied stress at 800, 1000, and 1100°C are shown in Fig. 2. At 1000°C, the samples were subjected to an applied stress of 355 MPa (2/3 of the fast fracture strength at 1000°C). The retained fracture strengths increase with exposure times of up to 1000 h. Similar behavior is also observed at 800°C with an applied stress of 405 MPa (2/3 of the fast fracture strength at 800°C). At 1100°C with an applied stress of 370 MPa (2/3 of the fast fracture strength at 1100°C), the retained fracture strength initially increases for an exposure time of 100 h. After 100 h, the retained fracture strengths at 1100°C remain constant with continued exposure times of up to 1000 h. Thus the SiC-Whisker-reinforced aluminas exhibit considerable promise for long-term applications in oxidizing environments at temperatures of up to 1100°C with applied stresses of up to 2/3 the fracture strength.

#### Status of milestones

None.

#### Publications

None.

#### References

1. P. F. Becher and G. C. Wei, "Toughening Behavior in SiC-Whisker-Reinforced Alumina," *J. Am. Ceram. Soc.* **67**(12), C-267-C-269 (1984).
2. T. N. Tiegs and P. F. Becher, "Whisker Reinforced Ceramic Composites," in *Tailoring of Multiphase and Composite Ceramics*, ed. R. Tressler and G. Messing, Plenum Press, New York, in press.



3. T. N. Tiegs and P. F. Becher, "Alumina-SiC Whisker Composites," *Proceedings of the 23rd Automotive Technology Development Contractors' Coordination Meeting*, Society of Automotive Engineers, Inc., Warrendale, Pa, in press.

4. A. H. Chokshi and J. R. Porter, "The Creep Behavior of an Alumina Matrix-Silicon Carbide Whisker Composite," *Am. Ceram. Soc. Bull.* **64**(10), 1346 (1985).

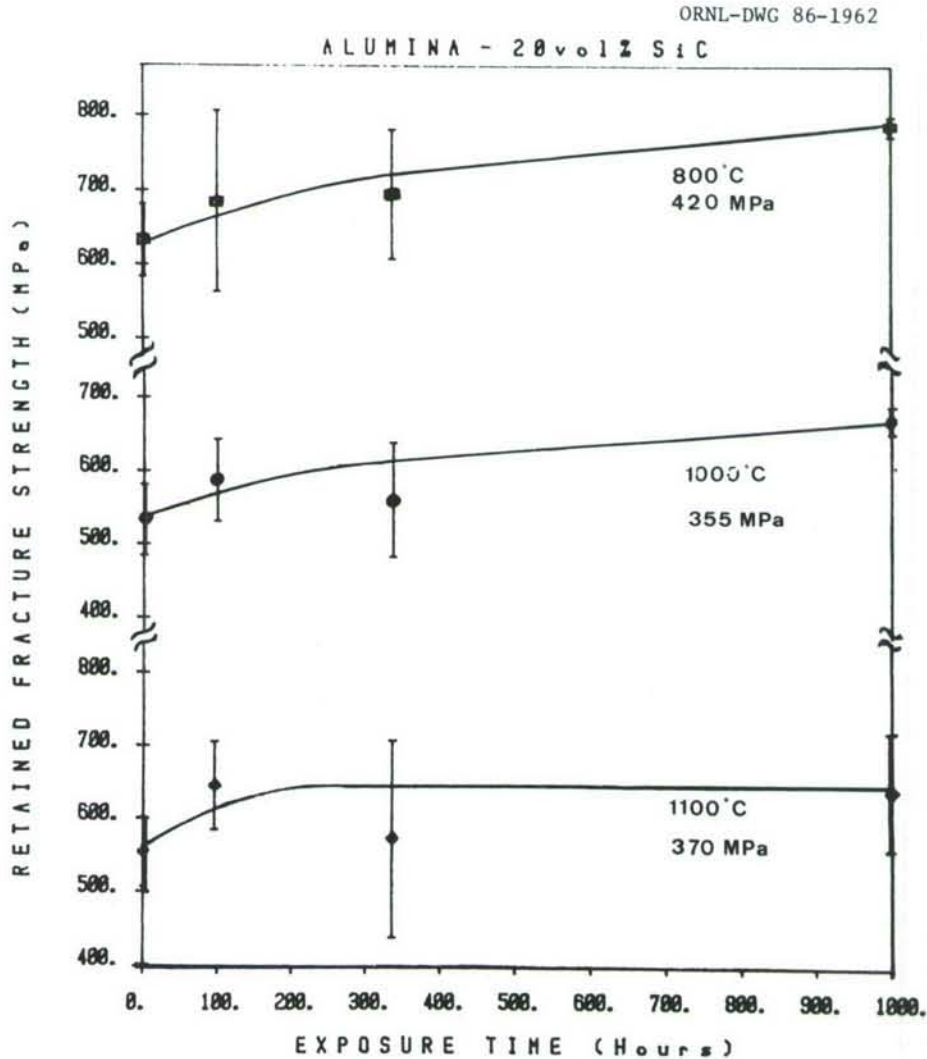


Fig. 2. The retained fracture strengths increase during interrupted static fatigue of alumina reinforced with 20 vol % SiC whiskers at 800, 1000, and 1100°C. The fracture strength retained increase with increasing exposure time for samples subjected to an applied stress equal to 2/3 the fast fracture strength at the desired temperature in an air environment. At 800 and 1000°C, the retained fracture strengths increase with increasing time of exposure. However, at 1100°C, the retained fracture strengths remain constant with increasing exposure time after an initial increase in retained strength after 100 h of exposure.

Cyclic Fatigue Of Toughened Ceramics

K. C. Liu and C. R. Brinkman (Oak Ridge National Laboratory)

Objective/scope

The objective of this task activity is to demonstrate the capability to perform tension-tension dynamic fatigue testing on a uniaxially loaded ceramic specimen at elevated temperatures.

Three areas of research have been identified as the main thrust of this task: (1) design, fabrication, and demonstration of a load train column that truly aligns with the line of specimen loading; (2) development of a simple specimen grip that can effectively link the load train and test specimen without complicating the specimen geometry and, hence, minimize the cost of the test specimen; and (3) design and analysis of a specimen for tensile cyclic fatigue testing.

Technical progress

Two approaches in specimen heating have been pursued, namely resistance and inductance heating methods. The former was discussed in the previous report. Since then the resistance heating furnace was ordered and received. It has six Kanthal Super\* heating elements capable of achieving temperatures as high as 1800°C. The ceramic gripping fixtures associated with the high-temperature test system were received also. Preparations for trial heating are in progress.

The resistance heating method has been used for many years in the testing of ceramics. In contrast, heating by induction power has not been widely used in tensile testing of ceramics. Because of its unique heating characteristic and compactness, we were able to develop a simple and effective method of heating by induction that is especially convenient for high-temperature testing of ceramics. This method permits replacement of the high-cost ceramic gripping fixtures with less expensive pull-rod fixtures made of a nickel-base alloy because the heating power can be focused in the gage section of the specimen. The drawback is that the maximum specimen temperature is limited by the ability of the pull-rod alloy to withstand the stress at temperature (about 1000°C maximum).

An alumina specimen was initially heated for a short time with a 2.5-kW induction generator to 1300°C. The specimen heating was accomplished indirectly via a short tubular susceptor made of silicon carbide as a heating element centered on the specimen and induction load coil. The susceptor is about 50 mm long with an inner diameter of 19 mm and a 6.5-mm wall thickness. To preserve the maximum heating power around the gage section, the susceptor is encapsulated in a cylindrical firebrick shell and capped off at both ends. The heater fits the entire space between the two metal pull-rod fixtures. The specimen temperature was measured to be reasonably uniform within the 25-mm gage length, with a small temperature drop-off of about 25°C at both ends of the gage section. Because the heat source was reasonably well insulated, the heat dissipated from both ends of the specimen to the pull rods did not appear to have overheated the metal fixtures. Overall observations indicate that this heating method is appropriate for applications to fatigue testing of structural ceramics.

---

\*Kanthal Super is the tradename of improved molybdenum disilicide heating elements manufactured by Kanthal Corporation.



Difficulties encountered during initial induction heating experimentation were: (1) the temperature gradient along the gage section could not be measured optically, (2) a mechanical extensometer could not be attached, (3) specimen setup was somewhat cumbersome. To avoid those problems, the heating strategy was modified. First, the tubular susceptor of silicon carbide was cut into two halves along the longitudinal axis. The halves were then assembled back in the firing position after the specimen was loaded in the load train column. The half shells were slightly separated with a gap that provided good visibility of the gage section for the temperature and strain measurements by optical instruments or by a mechanical extensometer. To heat the susceptor efficiently, the load coil was situated horizontally with the windings separated in two sections by about 50 mm and centered on the test specimen, as shown in Fig. 1. The susceptor shell, not visible in Fig. 1, was press fitted in the cavity at the inner ends of the firebricks, which in turn fitted inside the coil opening. The firebricks were held together by glass fiber. No differences were noticed in the heating characteristics of the specimen, except that the latter method required somewhat more power. However, the small power loss was a worthwhile trade-off to get around the difficulties encountered in the previous heating method.

#### Important findings and observations

The induction heating technique, using a 2.5-kW generator, was developed and demonstrated to be a simple and effective method of heating alumina specimens for prolonged periods of time to temperatures of at least 1300°C.

#### Status of milestones

A draft report (Milestone 321403) was completed covering design and initial test results of grips for uniaxial fatigue testing of ceramic materials.

#### Publications

None.



YP2631

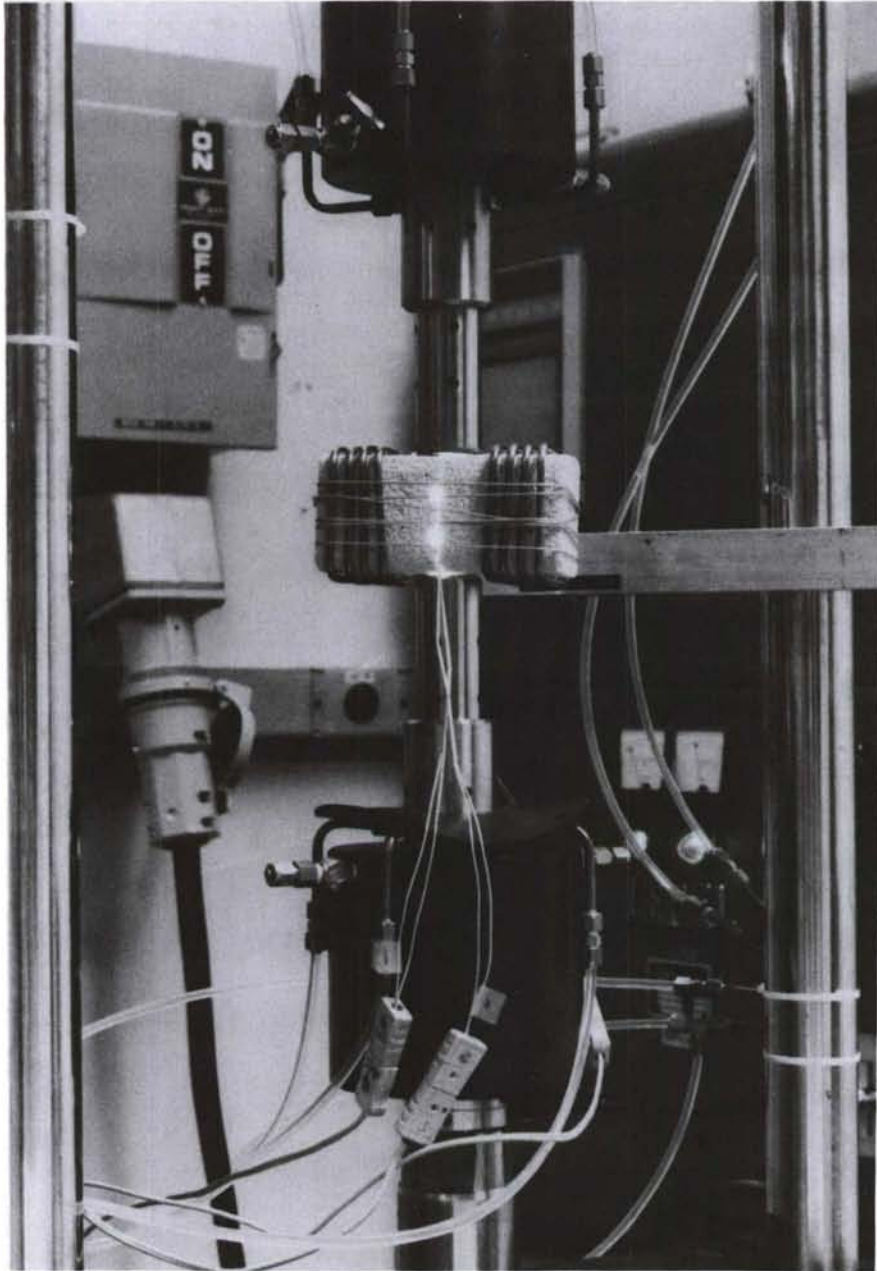


Fig. 1. Load train assembly with ceramic specimen being heated by an induction generator.

### 3.3 ENVIRONMENTAL EFFECTS

#### Static Behavior of Toughened Ceramics

M. K. Ferber, T. Hine, and G. Zeigler (University of Illinois)

#### Objective/scope

The objective of this program is to study the long-term mechanical stability of toughened ceramics for diesel engine applications. The work is divided into the two tasks. The first involves the measurement of the time-dependent strength behavior of ceramic bend-bar samples as a function of temperature and applied stress using the Interrupted Fatigue (I.F.) method. Although a variety of candidate engine materials will be examined, current studies are focusing upon commercially available partially stabilized zirconia (PSZ). In the second task, the microstructures of selected I.F. specimens are characterized using SEM and TEM. In addition, x-ray diffraction and dilatometry studies are used to examine changes in the transformation behavior of the PSZ ceramics resulting from the high-temperature exposure.

#### Technical progress

##### (a) Procedure

Two commercial Mg-PSZ ceramics\* designated TS-PSZ (thermal shock grade) and MS-PSZ (maximum strength grade/1983) were chosen for initial testing since both are prime candidates for use as prototype diesel engine components.<sup>1</sup> Both 1983 and 1984 vintages of the TS PSZ (designated TS (83) and TS (84)) were examined. Starting materials were obtained in the form of either circular discs 100 mm in diameter and 7.6 mm thick or rectangular plates (101.6 x 101.6 x 6.35 mm). Rectangular bend specimens (25.4 X 2.82 X 2.5 mm) were then machined from these shapes for subsequent mechanical property studies. The tensile surface of each sample was polished to a 0.25  $\mu\text{m}$  finish and the edges beveled using a 6  $\mu\text{m}$  diamond wheel.

The fatigue behavior was determined using an interrupted fatigue (I.F.) technique in which the four-point bend strength  $S_f$  was measured as a function of time ( $\tau$ ), temperature ( $T$ ), and applied stress ( $\sigma_a$ ). This method has several advantages over conventional static fatigue<sup>a</sup> testing. First, since time is a controllable quantity, problems associated with an unpredictable fatigue life (as in the case of static fatigue) are avoided. In the present study, this feature allowed for periodic examination of test specimens so that changes in both phase composition and transformation characteristics could be ascertained. A second advantage is that processes responsible for both strength degradation and strength enhancement can be readily distinguished.<sup>2</sup>

\* Manufactured by Nilcra Ceramics, USA Office, Glendale Heights, Illinois.



I.F. studies involving both materials were conducted at temperatures of 500, 800, and 1000°C for exposure times ranging from 1 to 1008 h. The baseline data were established using specimens subjected to a zero stress level. Subsequent tests were then performed with  $\sigma_a$  equal to 60, 70, and 80% of the fast fracture strength (i.e. 60, 70, 80%<sup>a</sup> of  $S_f$  values measured at the same T for  $\tau = 1$  h and  $\sigma_a = 0$ ). Tables 1 and 2 outline specific test conditions considered to date for the MS and TS materials respectively. For each condition,  $S_f$  was determined at temperature by fracturing three or more samples. However, in a few cases specimens were held at temperature but not fractured. As discussed below these samples were used to examine the creep deformation behavior.

All testing was conducted in a specially designed Flexure Test System (F.T.S.)\* capable of holding up to three bend samples.† The general layout of the F.T.S. is shown in Fig. 1. The Test Frame contains the hardware for applying mechanical forces to each of three samples which are supported by aluminum oxide ( $Al_2O_3$ ) four-point bend fixtures. The loads are generated by pneumatically driven air cylinders located at the top of the support frame. These loads are transmitted into the hot zone of the furnace through  $Al_2O_3$  rods. Each of the bottom three  $Al_2O_3$  rods are also attached to a load cell which monitors the applied force as a function of time. Water-cooled adapters connect the aluminum oxide rams to both the load cells and the air cylinders. The computer monitors the load on each specimen and provides necessary adjustments in the air pressure (via the electro-pneumatic transducer) such that the desired stress level is maintained. Following the designated exposure time, the samples are fractured using a prescribed loading rate (345 KPa/s in the present study).

Table 1: I.F. exposure conditions examined for MS PSZ (83 vintage)

T(°C)/ Stress Level (%)/ $\sigma_a$ (MPa)	0.5	24	Exposure Time (h)		1008
			168	336	
800/0/0	X	X	X	X	X
800/60/207	0	X	X	X	X
1000/0/0	X	X	X	X	X
1000/60/172	0	X	X	X	X

Note: X-I.F. test condition; 0-condition not examined.

\* The F.T.S. design is based on a similar system originally developed by S. M. Wiederhorn and N. J. Tighe of the National Bureau of Standards.

† Two manually controlled F.T.S. units were used to supplement the data collection.



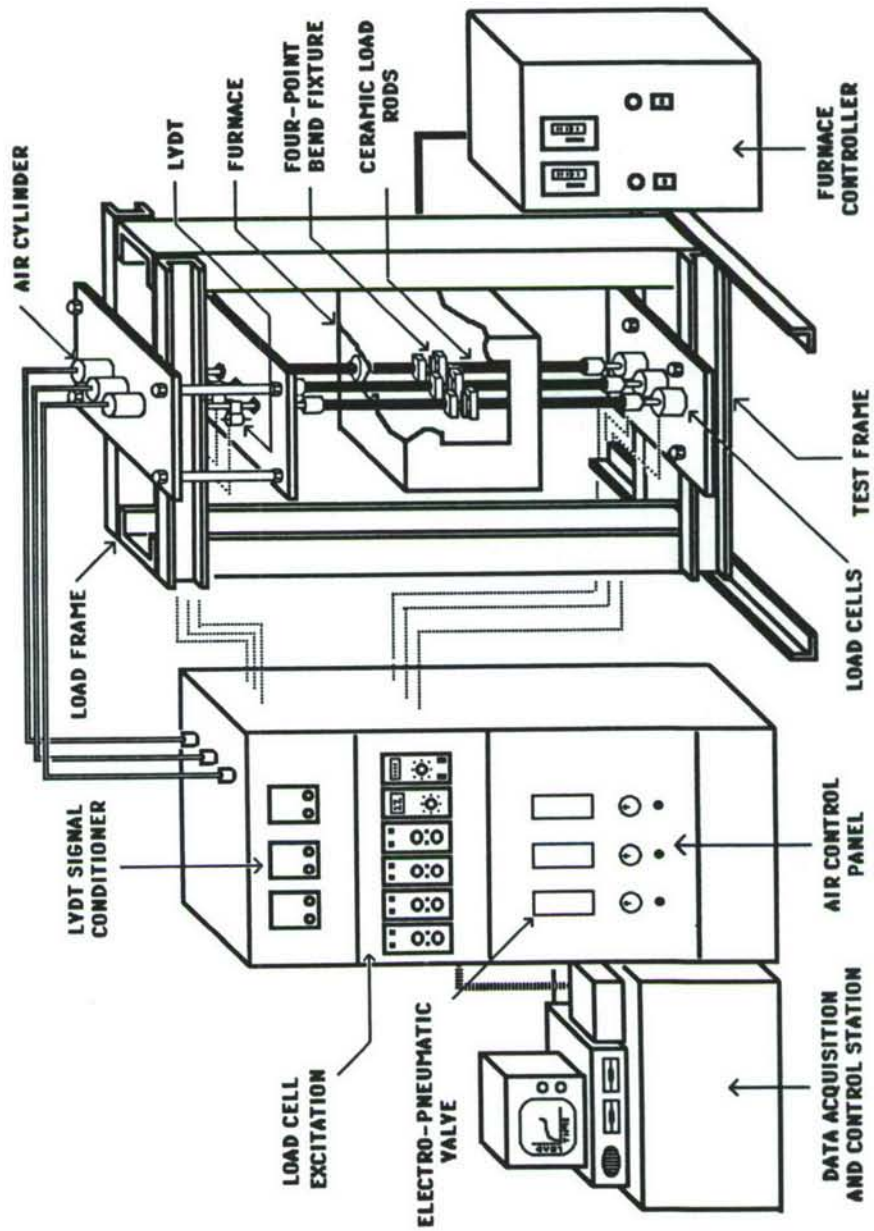


Figure1. I.F. testing was conducted in specially designed Flexure Test System in which applied loads were generated pneumatically.

Table 2: I.F. exposure conditions examined for TS PSZ

Vintage/T(°C)/ Stress Level (%)/ $\sigma_a$ (MPa)	0.5	24	Exposure Time (h)		1008
			168	336	
83/500/0/0	X	0	0	0	0
83/500/60/248	0	X	X	X	X
83/800/0/0	X	0	0	0	0
83/800/60/207	0	X	X	X	X
83/1000/0/0	X	X	X	X	X
83/1000/60/172	0	X	X	X	X
84/800/0/0	X	X	X	X	X
84/800/60/207	0	X	X	X	X
84/800/70/242	0	X	X	X	X
84/800/80/276	0	X	X	X	X
84/1000/0/0	X	0	X	0	X
84/1000/60/172	0	X	X	X	X

Note: X-I.F. test condition; 0-condition not examined.

Several techniques were used to characterize both the as-received and tested I.F. samples. For example, the microstructures were examined using both standard ceramographic methods and SEM. The latter technique also allowed for characterization of fracture surfaces. TEM studies provided additional information concerning microstructural and phase changes occurring in both the tensile and compressive regions of the fractured I.F. specimens. Finally, the volume fractions of the cubic (c), tetragonal (t), and monoclinic (m) phases were determined from x-ray diffraction and Raman spectroscopy studies.\*

The thermal expansion behavior of the MS and TS ceramics was measured using a dual pushrod dilatometer.\*\* The reference standard consisted of an NBS single crystal  $Al_2O_3$ . In order to establish the  $M_s$  temperature or the as-received materials, the dilatometer was modified so that temperatures as low as  $-190^\circ C$  could be achieved. The expansion-contraction characteristics were also measured for selected I.F. samples. The resulting data (percent elongation versus temperature) were used to examine changes in the (t)-(m) transformation characteristics arising from the high-temperature exposure.

The extent of creep deformation resulting from the high-temperature exposure was determined for several of the I.F. samples using two methods. First, the permanent deflection was measured at various positions along the flexure specimens which were exposed but not

\* Measurements provided by P. F. Becher and G. Begun, Oak Ridge National Laboratory, Oak Ridge, TN.

\*\* Dilatronic II, Theta Industries, INC., Port Washington, New York. Low temperature measurements provided by P. F. Becher, Oak Ridge National Laboratory, Oak Ridge, TN.

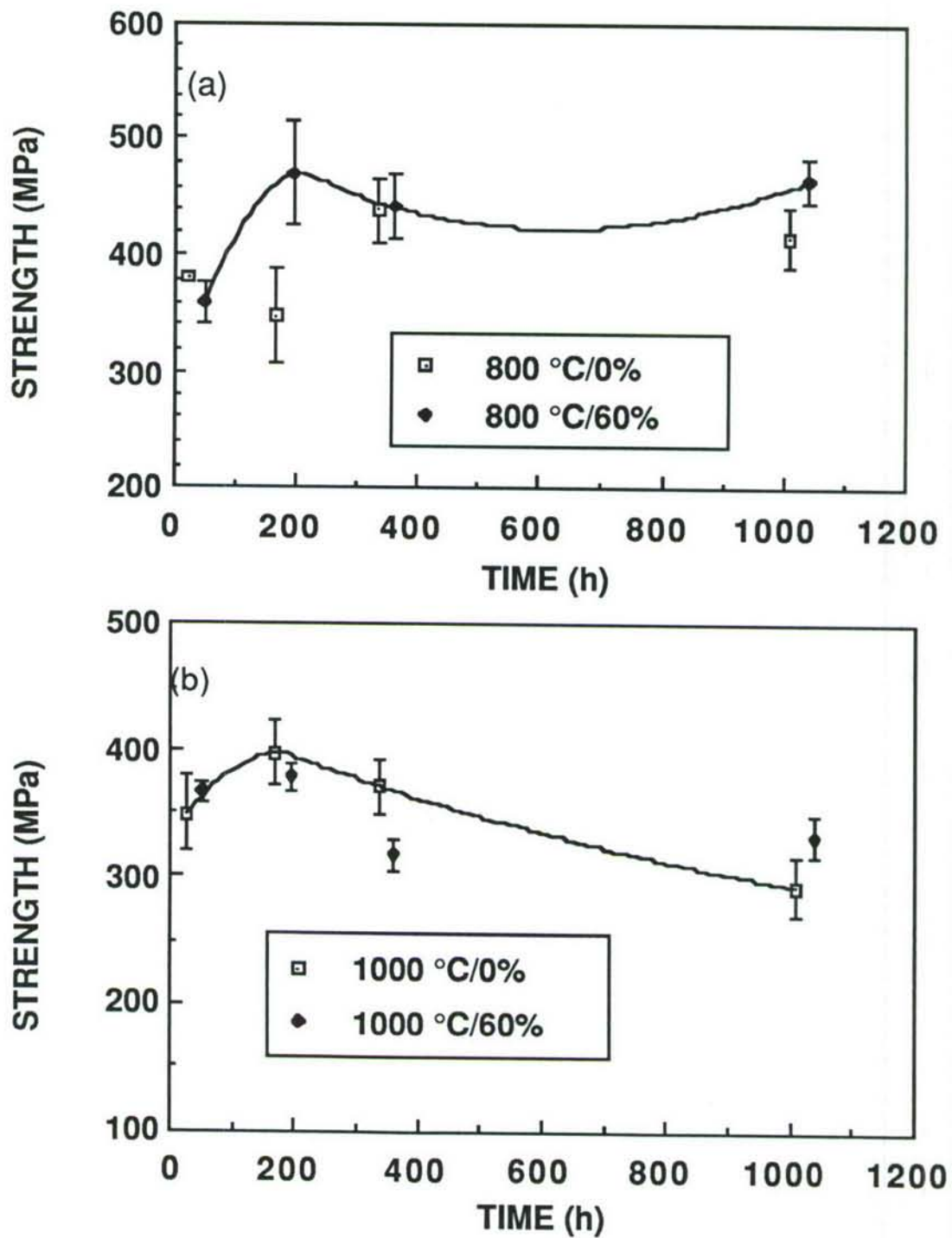


Figure 2. Interrupted fatigue data for MS PSZ tested at (a) 800°C and (b) 1000°C revealed no clear dependency upon applied stress or exposure time.



fractured. Actual measurements were determined with an optical microscope equipped with a filar eyepiece. In the second method, an L.V.D.T. was attached to the F.T.S. so that real time deflection measurements could be made.

## (2) I.F. and Deformation Behavior

The I.F. data for the MS PSZ samples tested at 800° and 1000°C are illustrated in Figs. 2(a) and (b), respectively. At 800°C, the strength at both the 0% and 60% stress levels exhibited a substantial short-term increase and then was relatively independent of time. The extent of this increase in  $S_f$  was only marginally dependent upon the stress level; the strength being slightly greater for the stressed samples ( $\sigma_a = 207$  MPa) at all values of  $\tau$ . The I.F. data at 1000°C (Fig. 2(b)) revealed a modest strength maximum at  $\tau \sim 200$  h for both the stressed and unstressed samples. At longer exposure times,  $S_f$  for the 0% stress level dropped well below the starting strength.

Results from the I.F. measurements for the TS(83) PSZ tested at 500° and 800°C are shown in Fig. 3. At 500°C the strength of the stressed samples (60%) did not change appreciably for exposure times up to 1008 h. However, when the T was raised to 800°C,  $S_f$  initially increased for  $\tau < 200$  h and then decreased after 1008 h to  $373 \pm 56$  MPa, which is comparable to the value obtained after 24 h. Therefore, under application of applied stress,  $S_f$  exhibited a definite definite maximum with increasing exposure time.

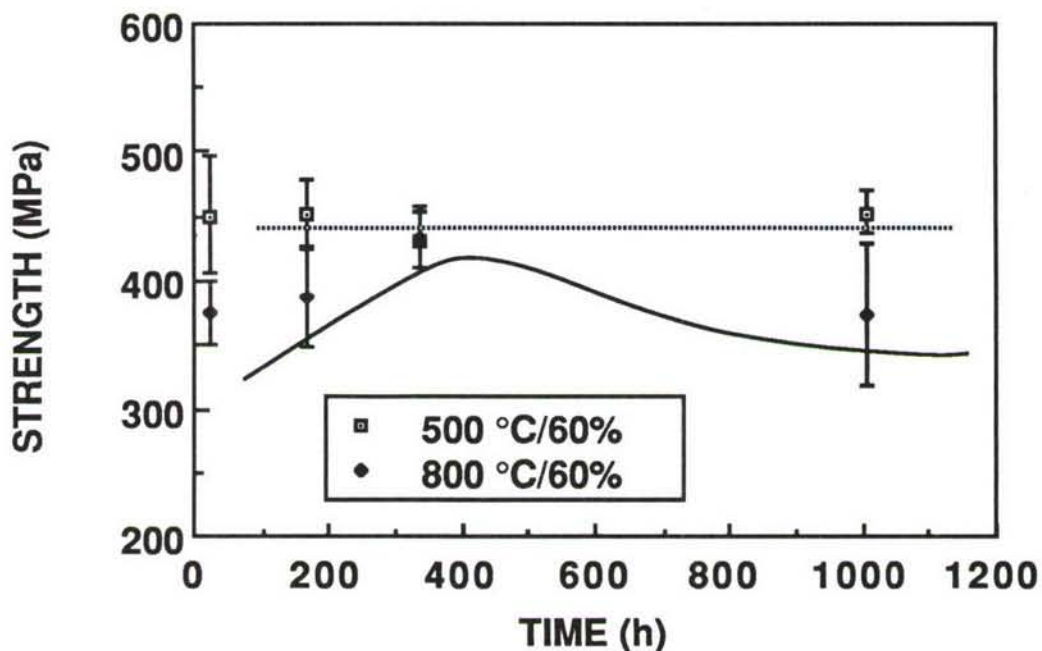


Figure 3. Strength of TS(83) samples stressed at 500°C (a) was independent of time. For tests conducted at 800°C the application of the 60% stress resulted in a strength maximum.

Similar behavior was observed when the TS samples were stressed ( $\sigma = 172$  MPa) at  $1000^\circ\text{C}$  (Fig. 4). However, the average strength after 1008 h was only 85% of its initial short-term value ( $\tau = 24$  h). When no stress was applied, the strength did not change significantly, at least to 360 h, the extent of (83) data. These results suggest that for  $T \geq 800^\circ\text{C}$ , the applied stress level can have a dramatic affect upon the long-term mechanical behavior.

The reproducibility of the I.F. data was examined by testing a second group of TS(84) samples at both  $800^\circ$  and  $1000^\circ\text{C}$ . The general trends obtained at  $1000^\circ\text{C}$  (Fig. 5) were very similar to those for the 1983 vintage specimens. The only apparent difference was that the maximum in the TS(84) curve for the stressed samples occurred at a slightly longer exposure time. This discrepancy may have been due to differences in the short-term ( $\tau = 0.5$  h) strengths:  $304 \pm 26$  MPa for TS(83) and  $375 \pm 20$  MPa for TS(84).

In order to better elucidate the role of  $\sigma$  upon fracture strength, tests involving the TS(84) PSZ exposed at  $800^\circ\text{C}$  were conducted utilizing 60, 70 and 80% applied stress levels. Results for these I.F. tests are shown in Figs. 6(a)-(c). Actual values of  $\sigma_a$  were 207 MPa (60%), 241 MPa (70%) and 276 MPa (80%). At the 60% level (Fig. 6(a)),  $S_f$  exhibited a short-term increase for  $\tau < 336$  h, while no strengthening was observed for the unstressed samples. These results are in agreement with those observed for the 83 material. Data for the 70% stress gave evidence of a small drop in  $S_f$  during the first 168 h of testing (Fig. 6(b)). At longer exposure times, the strength increased in fashion similar to that at the 60% level. Finally, as shown in Fig. 6(c) the short-term decrease in  $S_f$  became even more extensive at the 80% stress level. Therefore, the I.F. behavior of the TS PSZ (84) was characterized by strengthening and weakening processes both of which were strongly dependent upon the applied stress. Possible mechanisms are discussed below.

Both the TS and MS samples tested at  $1000^\circ\text{C}$  under stress experienced significant creep deformation. Preliminary results obtained from post-exposure optical measurements are shown in Fig. 7(a) for the MS PSZ and Fig. 7(b) for the TS (84) PSZ. MS flexure samples tested for 1008 h exhibited a maximum permanent deformation at sample midspan of  $\sim 320$   $\mu\text{m}$  while maximum deflection in TS samples exposed for 336 h was  $\sim 140$   $\mu\text{m}$ . The implications of this behavior concerning strength variations are discussed below.

### (3) X-Ray and Dilatometry Results

X-ray analyses of the polished surfaces of fractured MS and TS specimens were used to determine the volume fraction of (m),  $V_f^m$ . Results for the TS(83) and MS materials are summarized in Fig. 8(a) and (b), respectively. In general,  $V_f^m$  for the  $1000^\circ\text{C}$  test increased significantly with increasing exposure time. More importantly, data for the TS(83) material exposed at  $1000^\circ\text{C}$  indicated that the magnitude of  $V_f^m$  for a given  $\tau$  was significantly greater when a stress was applied. However, the stress dependency for (m) formation in the MS PSZ ceramics tested at  $1000^\circ\text{C}$  was minimal. At  $800^\circ\text{C}$ ,  $V_f^m$  was relatively independent of  $\tau$  and stress for both materials.



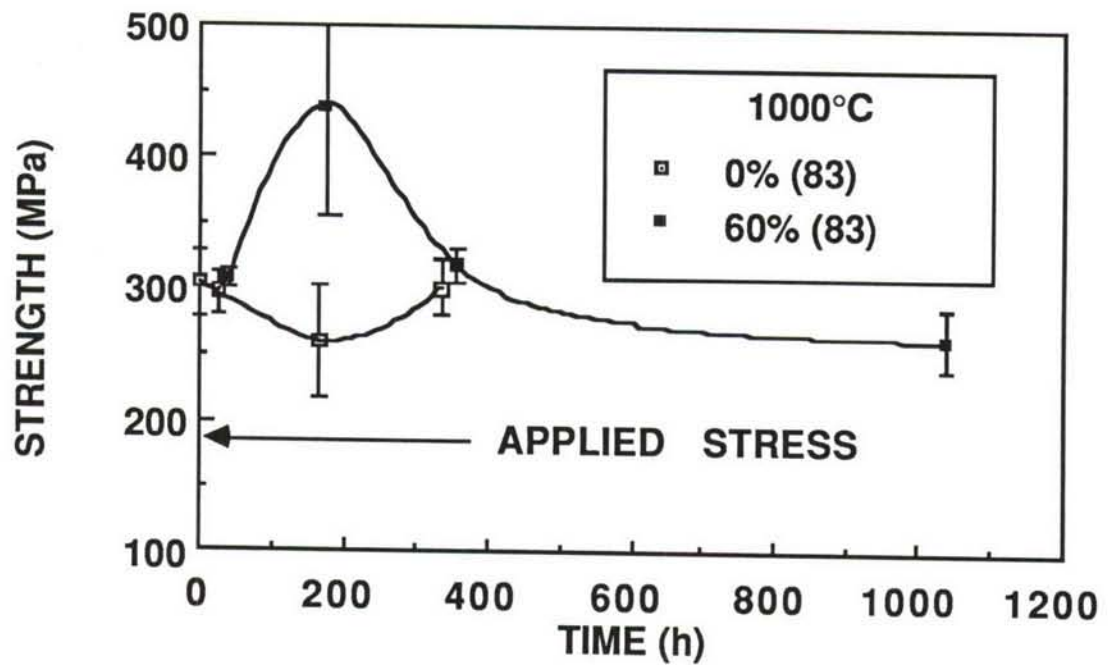


Figure 4. A strength maximum was also observed for TS(83) PSZ tested under stress (60%) at 1000°C. The strength of the unstressed samples remained unchanged with time.

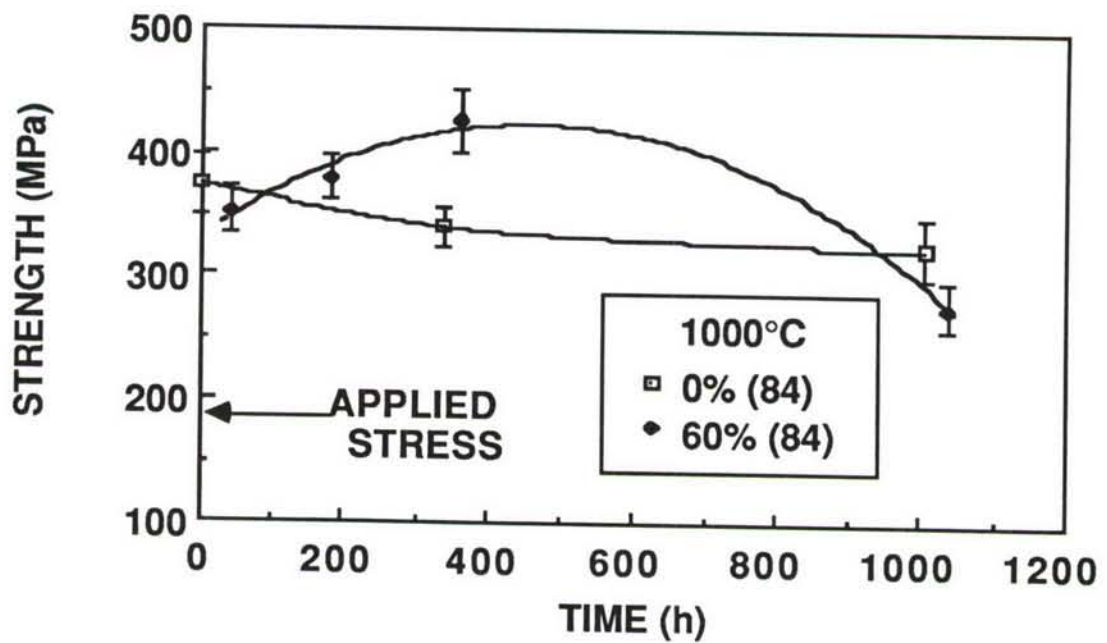


Figure 5. I.F. behavior for the TS (84) samples exposed at 1000°C was similar to that for the TS (83) material.



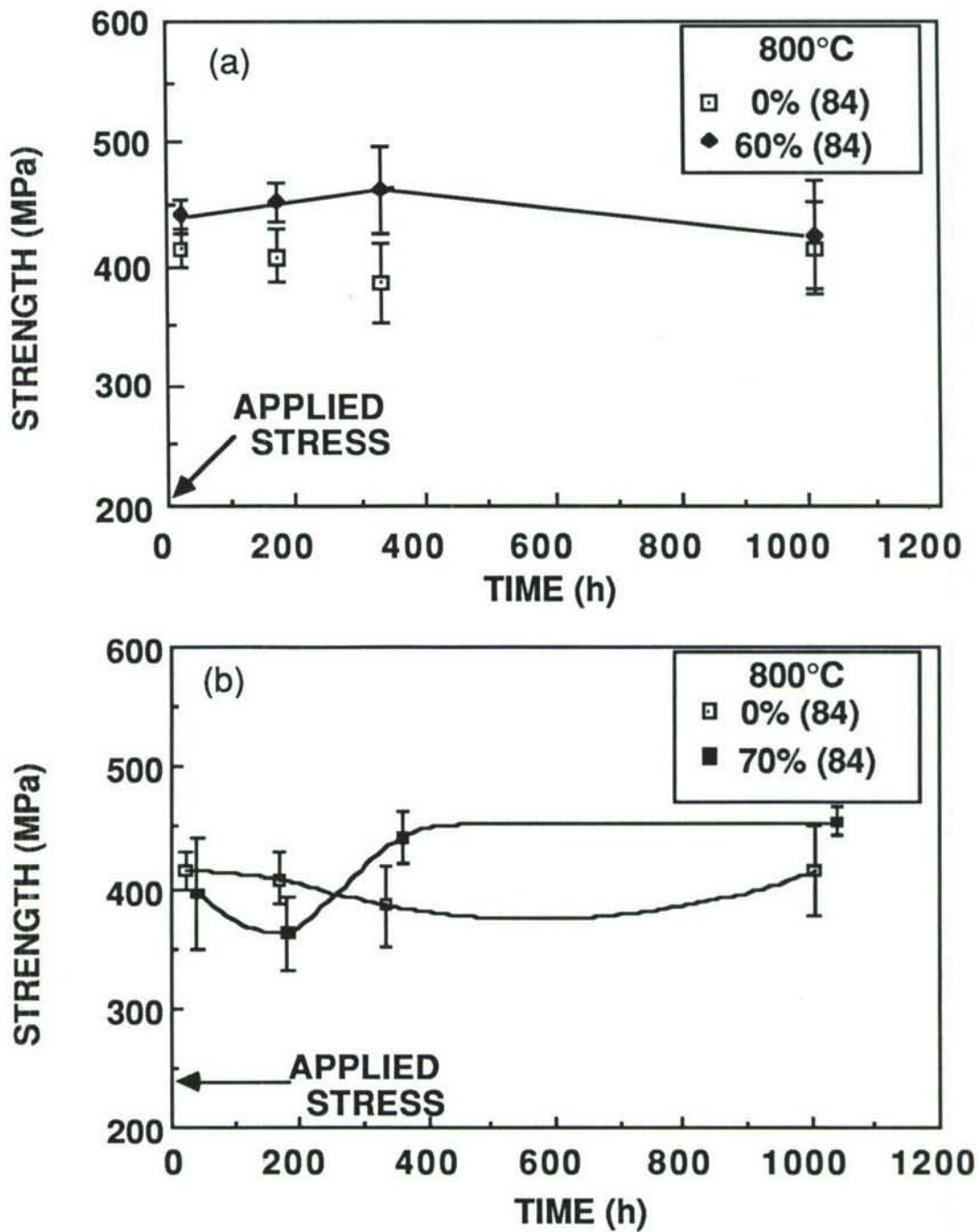
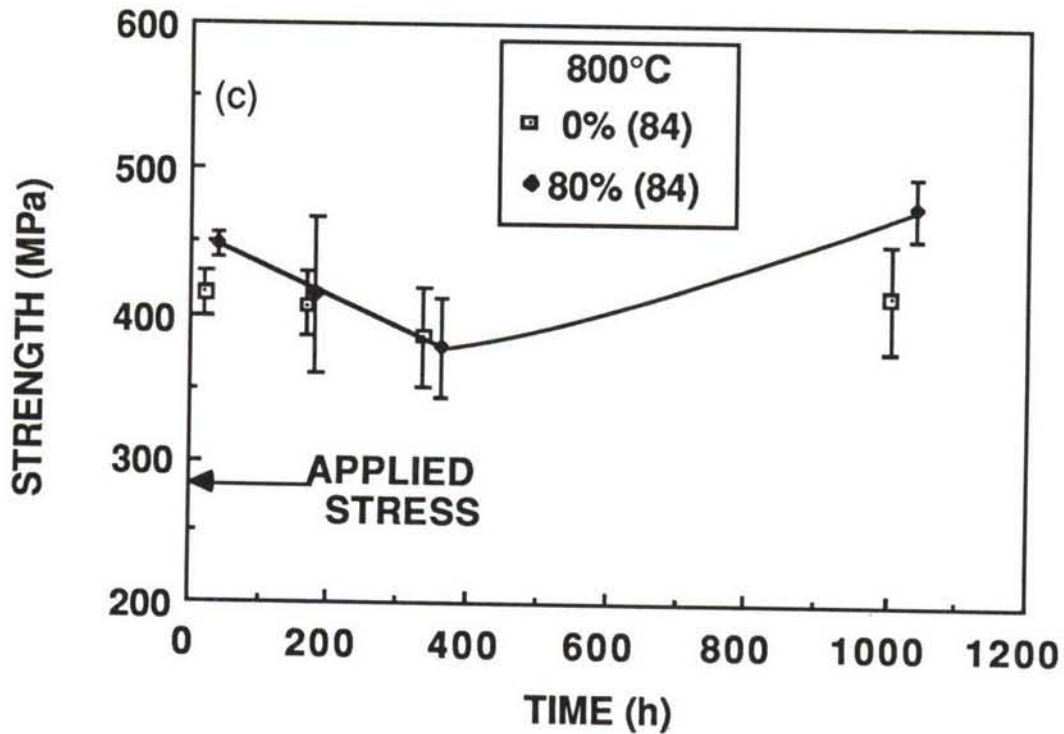


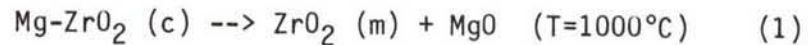
Figure 6. A short-term strength degradation process was observed in the TS (84) material tested at 800°C. The extent of this degradation became more pronounced as the stress level increased: (a) 60%, (b) 70%, and (c) 80%. Data for 0% stress level are included in each plot for comparison.

Figure 6 continued

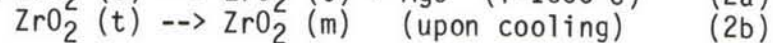
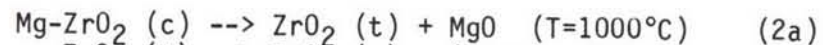


As shown in Fig. 9(a),  $V_f^m$  was again relatively independent of  $\tau$  and applied stress for the TS(84) PSZ exposed at 800°C. The only exception occurred for the samples stressed at the 80% level. The time-dependence of  $V_f^m$  for the TS(84) exposed at 1000°C (Fig. 9 (b)) did not show the same strong stress dependence as the 83 material. As discussed below, subsequent ceramographic studies were used to provide additional insights into the possible stress dependence of the rate of (m) formation.

The fact that  $V_f^m$  values often exceeded the  $V_f^t$  (volume fraction of the (t) phase) for the as-received ceramics indicates that both the (c) and (t) phases were involved in the (m) formation. Recent aging studies conducted at 1100°C<sup>3-7</sup> have shown that at least two types of reactions can lead to the generation of the (m) phase. The first is the eutectoid decomposition of the MgO-stabilized (c) matrix which can occur via two reactions:



and



These reactions generally initiate along grain boundaries and then slowly consume the (c) phase within grain interiors. The resulting (m) phase is often in the form of small 1-5  $\mu\text{m}$  grains.<sup>3,6</sup> The thermal expansion anisotropy associated with these (m) grains can promote extensive microcracking upon cooling. This microcracking is also facilitated by

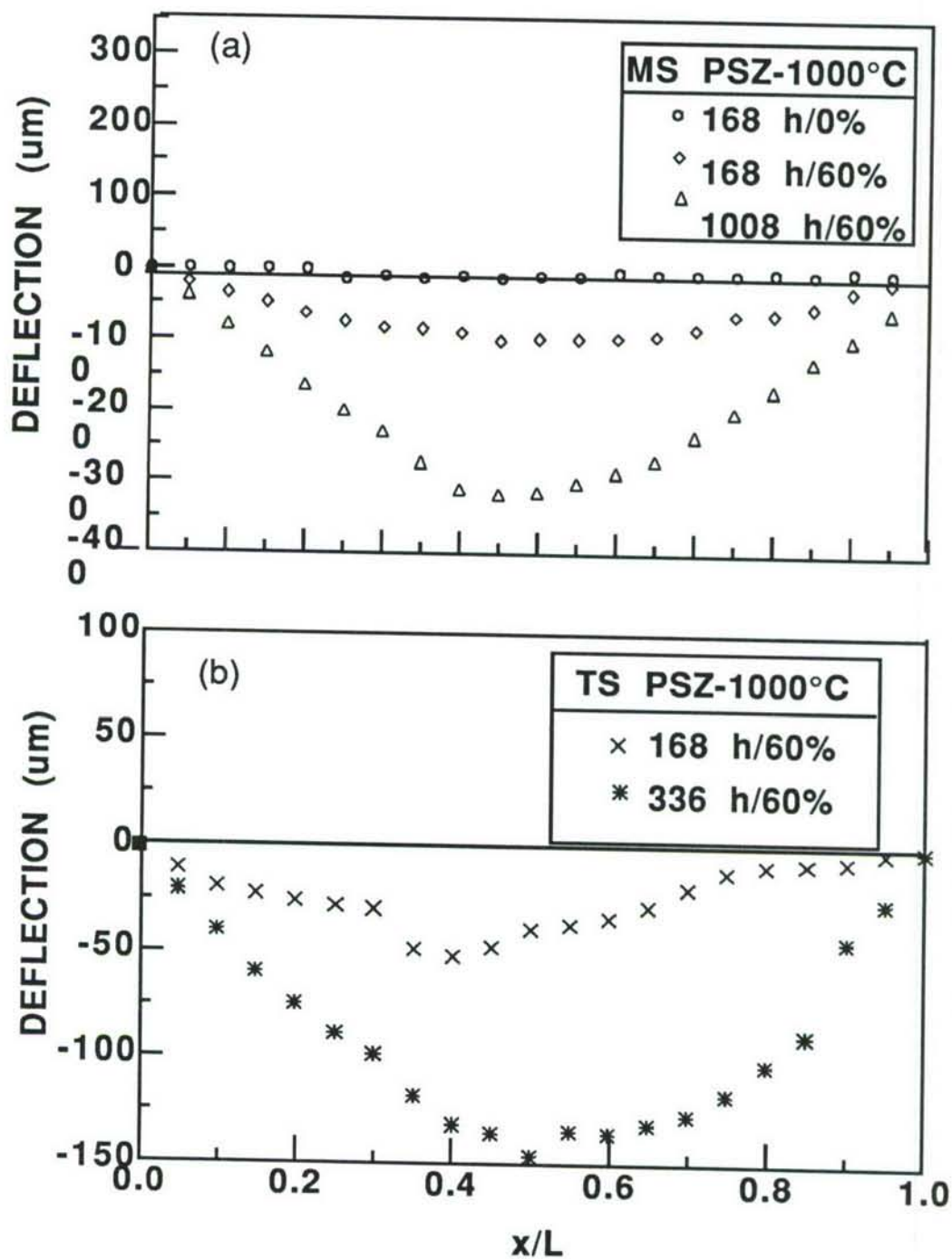


Figure 7. Extensive creep deformation occurred in the stressed (a) MS and (b) TS (84) samples exposed at 1000°C.  $x$  is the distance from the end of the flexure bar of length  $L$ .



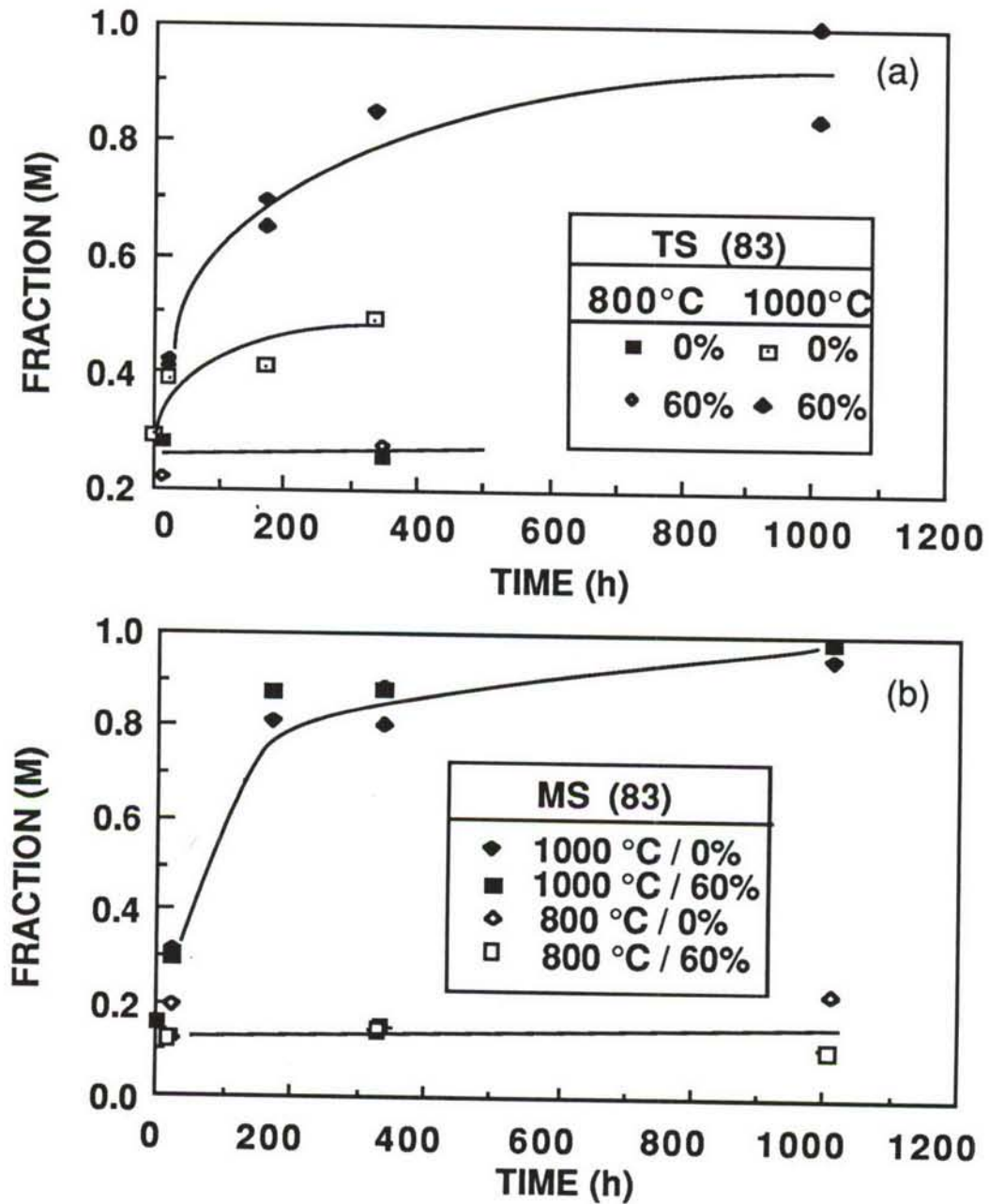


Figure 8. The (m) volume fraction increased significantly with time in the (a) MS and (b) TS (83) samples exposed at 1000°C. Data for the former material gave evidence of a stress dependency associated with the rate of (m) formation. At 800°C, the (m) volume fraction for both materials was insensitive to exposure time and applied stress.

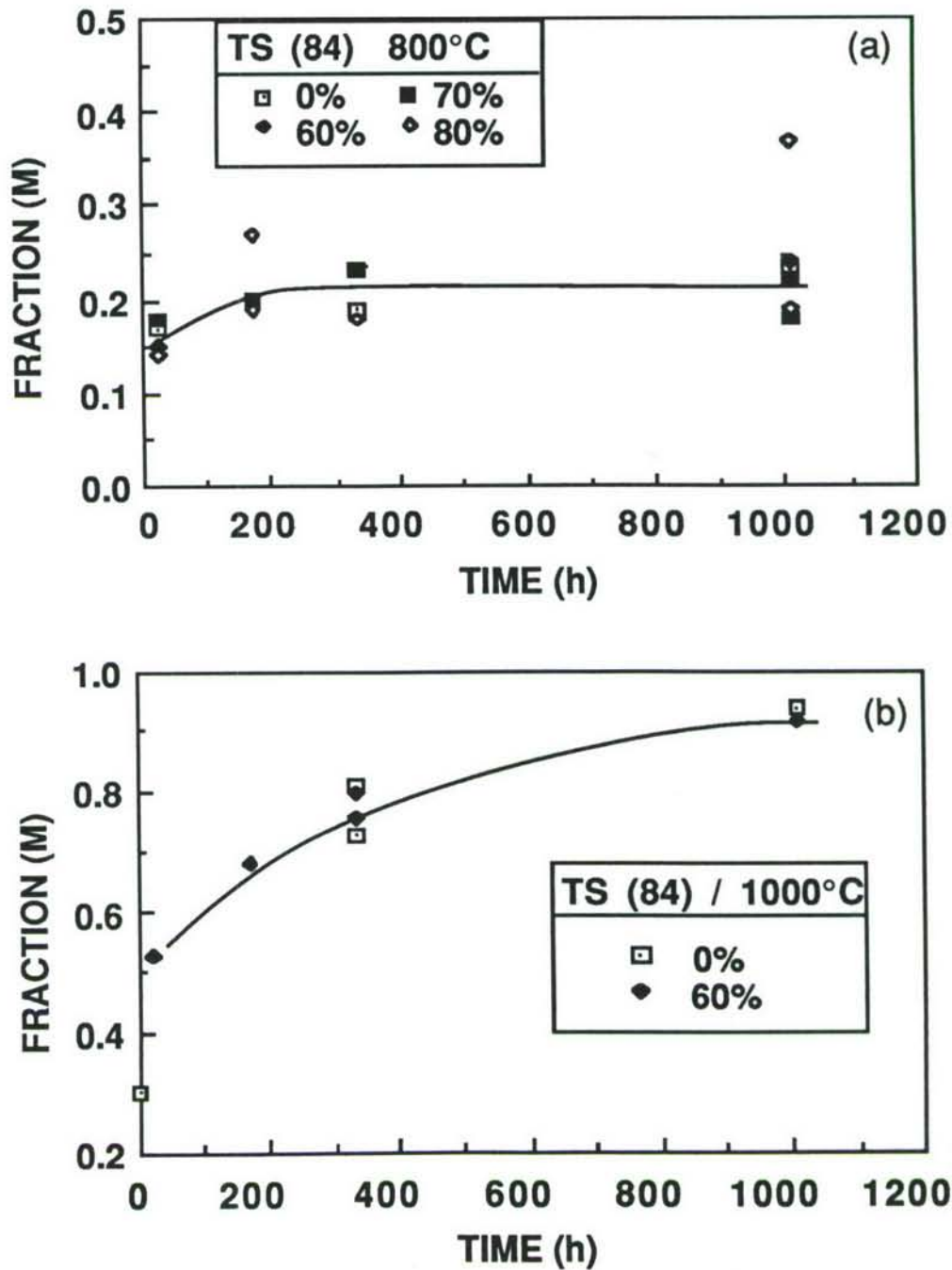


Figure 9. Although extensive quantities of the (m) phase were generated in the TS (84) samples exposed at (a) 1000°C, the rate of (m) formation was independent of applied stress. At 800°C (b), the (m) volume fraction exhibited only a slight dependency upon stress level.

thermal expansion differences between the (m) grains and surrounding matrix.

The second type of reaction involves the formation of an ordered anion vacancy  $\delta$ -phase ( $\text{Mg}_2\text{Zr}_5\text{O}_{12}$ ) within the region between adjacent (t) precipitates.<sup>3-6</sup> The  $\delta$ -phase nucleates at the (t) - (c) interface and then grows into the (c) matrix due to short-range diffusion of Mg. The interfacial strains which accompany this  $\delta$ -phase reaction can destroy the precipitate coherency and thus promote the (t) to (m) transition upon cooling. This results in an increase in the  $M_s$  temperature. The presence of these destabilized precipitates at relatively low concentration levels can lead to improved thermal shock resistance without significantly sacrificing strength and toughness.<sup>3-5</sup>

Dilatometry studies gave direct evidence for both types of (m) generation processes. As discussed previously,<sup>8,9</sup>  $M_s$  for both the TS(83) and MS samples tested at 1000°C increased from the as-received value of -55°C to the ~350°C. The time-dependence associated with this increase, which was due to the precipitate destabilization process ( $\delta$ -phase formation), appeared to be independent of the applied stress. These initial results were obtained from dilatometer measurements conducted in the 25-1000°C temperature range. More recently, data obtained in the 25-1300°C range revealed a second (m)-(t) hysteresis for I.F. samples exposed at 1000°C. As shown in Fig. 10 (Curve B), this hysteresis occurred over a much higher temperature range. Such behavior is consistent with the transformation of the unstabilized  $\text{ZrO}_2$  generated from the eutectoid decomposition.

#### (4) Optical, SEM, and TEM Studies

Standard ceramographic techniques were used to prepare I.F. samples for optical examination. Polished specimens were subsequently etched in boiling phosphoric acid to delineate the grain boundary structure including decomposition phase if present. Initially the etching time was varied between 1 and 10 minutes. Optimum contrast between phases occurred for the 5 minute exposure. Using the linear intercept method<sup>1</sup>, the volume fraction of the eutectoid decomposition phase ( $V_f^d$ ) was then measured from optical micrographs of the tensile region near the fracture surface (Area A in Fig. 11).<sup>\*</sup> In the case of the stressed I.F. samples,  $V_f^d$  was determined at several additional positions on the tested flexure bar (Regions B-D in Fig. 11). This allowed for examination of possible effects of stress upon the extent of the decomposition reaction.

For the samples tested at 1000°C, the grain boundary decomposition phase for both the MS and TS samples increased steadily with increasing exposure time as illustrated in Fig. 12. The y parameter in this figure represents the width of the decomposition zone (calculated using  $V_f^d$  measured from Region A) while G is the average grain diameter. The decomposition rate for the TS material was insensitive to stress level and material vintage. Furthermore for a fixed exposure time,  $V_f^d$  for the stressed samples did not vary significantly with flexure bar position.

<sup>\*</sup> There was no measurable effect of etching time upon  $V_f^d$ .



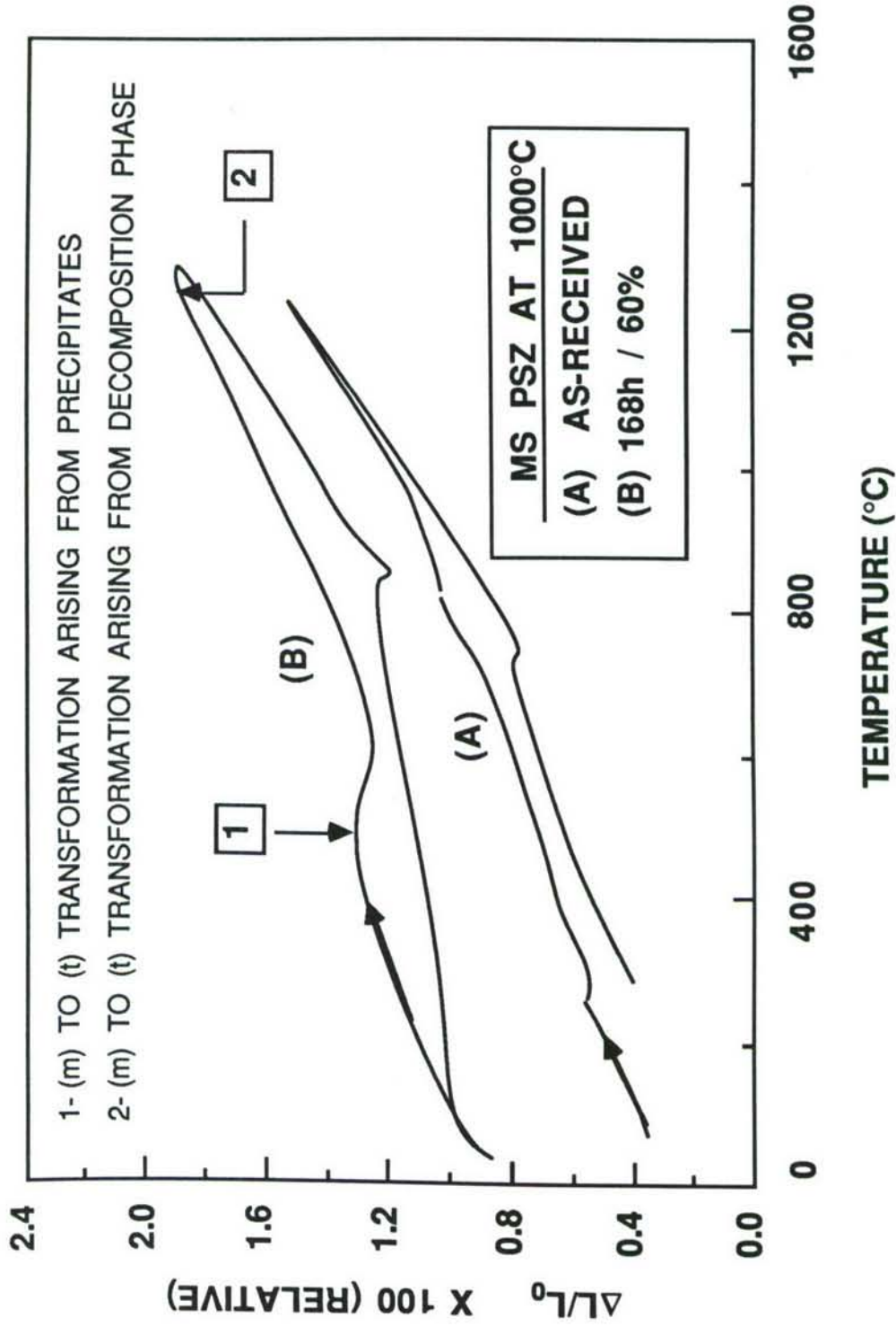


Figure 10. Thermal expansion data for MS PSZ tested for 168 h at 1000°C (B and C) exhibited two distinct (m)-(t) hysteresis curves. Data for the as-received material (A) is included for comparison. Similar behavior was observed for the TS PSZ.

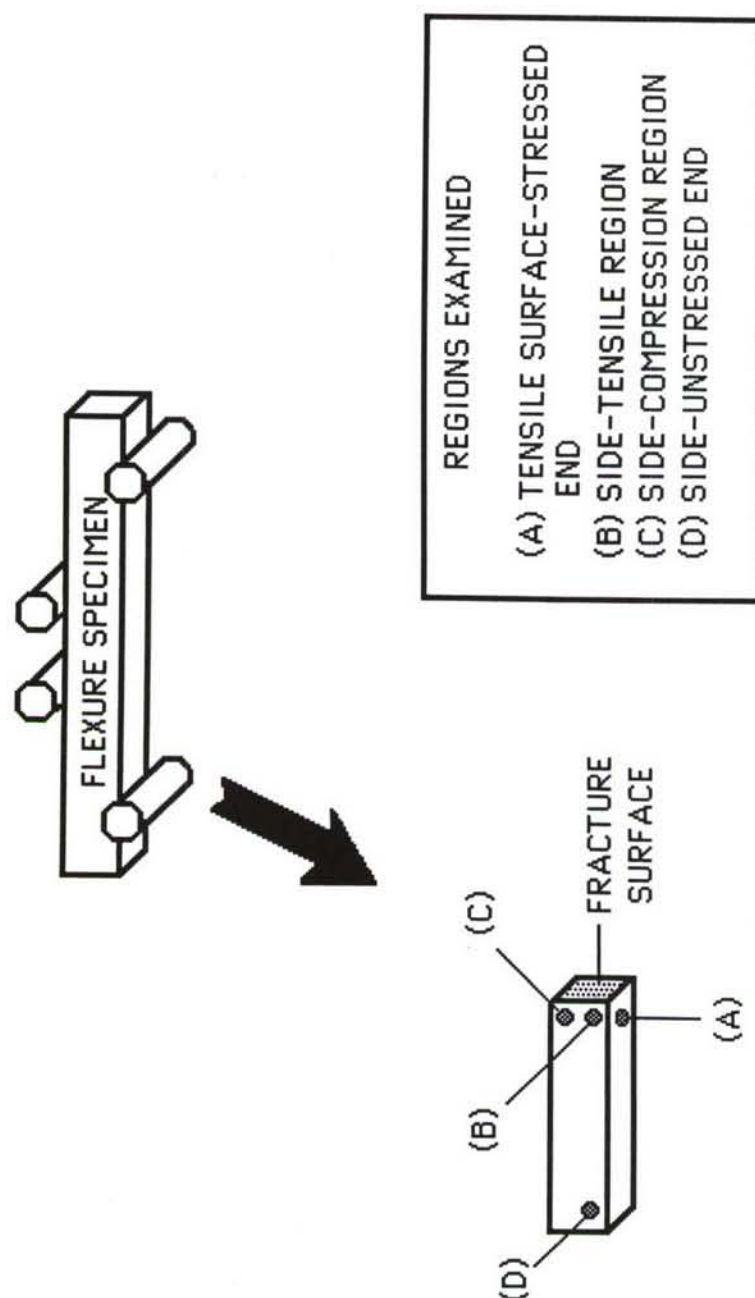


Figure 11. The extent of the eutectoid decomposition was determined at several positions along the polished surface of fractured I.F. flexure samples.

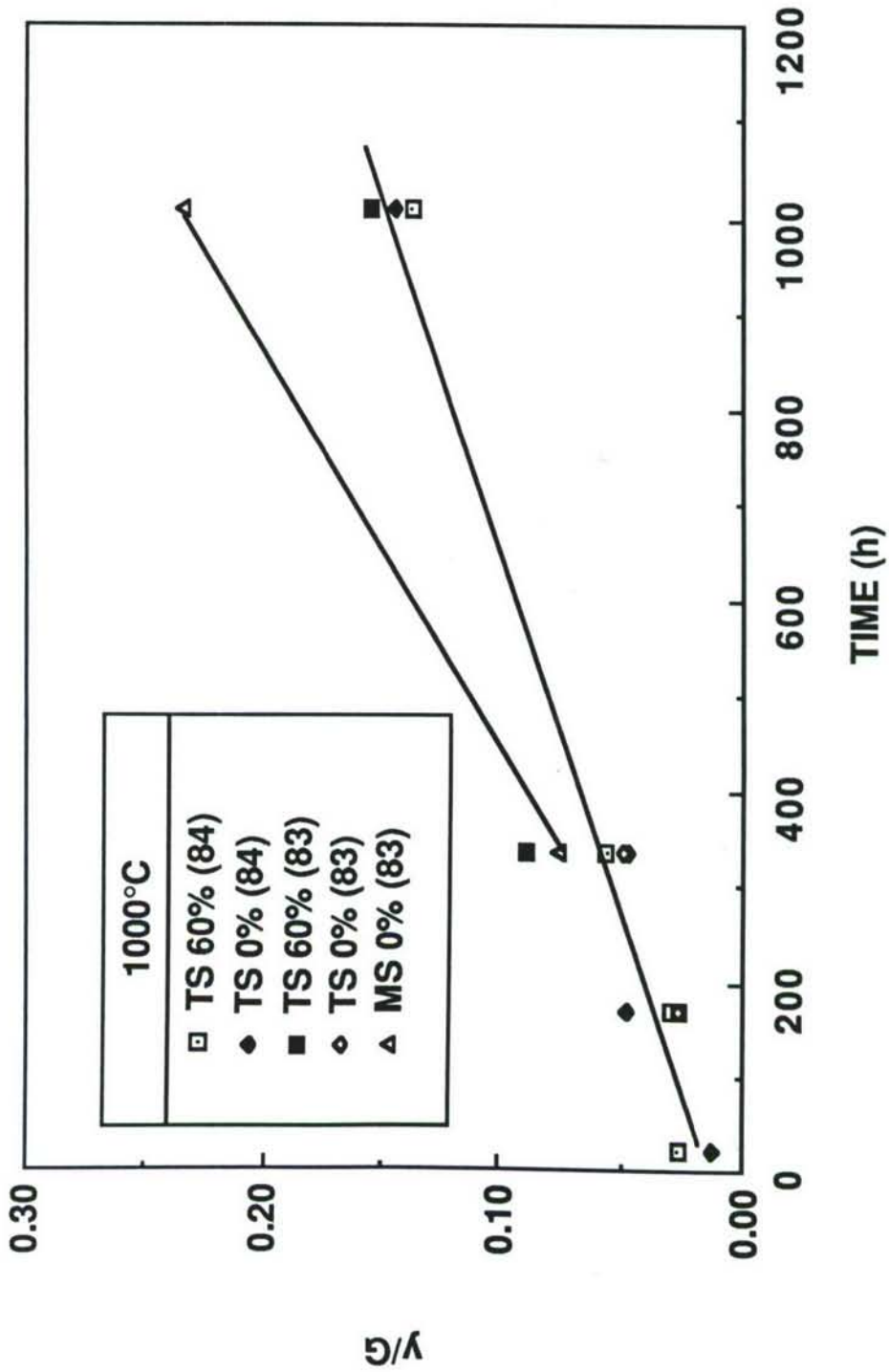


Figure 12. The time dependence of the eutectoid decomposition formation (at 1000°C) was insensitive to stress level.



Similar results were obtained from Raman spectroscopy studies. The lack of a stress dependency for the TS (83) material contradicts the x-ray data shown in Fig. 8(b). This discrepancy is currently under examination. Finally, the decomposition rate for the MS PSZ was significantly larger than that for the TS material. This difference may be attributed to the higher SrO content in the TS PSZ (determined by x-ray fluorescence). SrO has been shown to inhibit the decomposition process.<sup>10</sup>

The SEM examination of the as-exposed (tensile) surfaces of several fractured TS samples (tested at 1000°C) gave additional evidence for the eutectoid decomposition reaction. As discussed previously<sup>11</sup>, extensive formation of the (m) decomposition phase occurred in the TS and MS specimens exposed for 1008 h at the 60% stress level. The surface (m) phase consisted of 1-5  $\mu\text{m}$  diameter grains in agreement with previous studies.<sup>3-5</sup> Numerous microcracks were also observed particularly in regions containing a high density of (m) grains. In general, the concentration of this (m) phase diminished as the exposure time decreased. In addition, no microcracking was observed for  $\tau < 168$  h. Although similar results were obtained for the unstressed samples exposed at 1000°C, the associated microcracking was generally less extensive. At 800°C and below, no microcracking was observed.

The TEM studies of the TS samples exposed at 1000°C provided a number of results. In particular, four distinct areas (designated T1, T2, T2', and T2'') were observed in stressed and unstressed samples fractured after 1008 h. T1 consisted of a precipitate array (characteristic of the as-received material) present within the grain interior. The majority of these precipitates were monoclinic as expected from the dilatometry data. Areas T2, T2', and T2'' were characteristic of the grain boundary decomposition region. In T2, the (m) phase had a regular (undeformed) appearance while the MgO decomposition product was in the form of well-defined pipes. These pipes were often perpendicular to the growth front. Area T2' was similar to T2 except that the (m) phase was highly twinned. This result suggests that T2 and T2' were formed in accordance with Eqs. 1 and 2, respectively. Consequently, the twinning in T2' was associated with (t)-(m) transformation upon cooling. The last area T2'' consisted of small 1-5  $\mu\text{m}$  grains containing an irregular MgO decomposition product.

The above results for the stressed I.F. samples were relatively independent of location within the flexure specimen (tensile versus compressive regions). However, intergranular microcracks were observed in the tensile regions of samples exposed for  $\tau > 336$  h.

#### (5) Possible Mechanisms Affecting Strength

As discussed previously, the time-dependent strength behavior for the TS PSZ tested at 800 and 1000°C exhibited a strong dependence upon the applied stress. In particular, the application of stress promoted both strengthening and weakening processes depending upon time and temperature. Based on results of the microstructural, x-ray, and thermal expansion studies it is clear that several processes could be responsible for such behavior. Table 3 summarizes several of the possible mechanisms. Cases 1-4 are only applicable to the I.F. behavior at 1000°C.



Table 3: A number of potential mechanisms may have been responsible for I.F. behavior at 1000°C

- 
- (1) Enhanced High-Temperature Toughening and Strengthening due to Time-Dependent Shift in  $M_s$  to Higher Temperatures,
  - (2) Preferential Generation of Compressive Stresses Along the Flexure Bar Tensile Surfaces due to Stress Dependency of the Eutectoid Decomposition Reaction (Strengthening Mechanism),
  - (3) Macroscopic Redistribution of Flexure Bar Stresses Arising from Nonlinear Creep (Strengthening Mechanism),
  - (4) Change in Intrinsic Toughness due to Time-Dependent Modifications of the Phase Assemblage (Weakening Mechanism), and
  - (5) Flaw Modification Processes (Strength Loss due to Slow Crack and Microcracking; Strength Enhancement due to Crack Blunting).
- 

Mechanism 1 is based on the observation that the precipitate transformation characteristics changed abruptly with increasing exposure duration. Assuming that transformation toughening dictated the mechanical behavior, then an increase in  $M_s$  (relative to the 800 and 1000°C test temperatures) would raise both the fracture toughness and strength in accordance with a model described previously.<sup>8,9</sup> However, there are two factors which tend to discredit this mechanism. First, calculations based on the transformation toughening model\* predict a maximum strengthening (at  $T = 1000^\circ\text{C}$ ) of only 8% which is substantially less than that observed experimentally (Fig. 5). Secondly, since  $M_s$  also increased for the unstressed samples, one would expect a similar short-term increase in  $S_f$ . This prediction is again inconsistent with the data in Fig. 5.

A second possibility (Mechanism 2), is that the volume increase accompanying the formation of the eutectoid (m) phase led to preferential generation of compressive stresses along the outer tensile surface of the stressed bend bars.\*\* The fact that  $S_f$  only increased when  $\sigma_a$  was nonzero suggests that the rate of (m) formation was proportional to the applied stress level. Initial evidence for this stress dependency was provided by the x-ray data for the TS(83) PSZ exposed at 1000°C. However, in view of the ceramographic studies of the decomposition process (Fig. 11), the existence of this stress dependency is questionable. Therefore, the operation of this mechanism is unlikely.

The apparent flexure strength may have been modified due to a creep-induced redistribution (lowering) of the macroscopic (tensile) flexure stresses. This mechanism, which has been observed in other ceramics,<sup>12</sup> requires that the tensile and compressive creep rates exhibit a nonlinear

---

\* Calculations relied on assumption that  $V_f^t$  at 1000°C was approximately equal to the room-temperature value measured for the as-received material. This assumption is consistent with the thermal expansion data in Fig. 9.

\*\* A similar mechanism is responsible for strengthening effects in samples subjected to surface grinding.<sup>11</sup>

stress exponent. Although the available creep data<sup>13</sup> for the MS material<sup>†</sup> reveal a linear stress dependence, the validity of these results is questionable since the tests were conducted in bending. In particular, recent studies<sup>14</sup> have shown that the stress exponent determined from bend tests is not reliable if the creep rates in tension and compression are different. Therefore, Mechanism 3 may not be ruled out entirely.

The substantial microstructural and phase changes observed at 1000°C could have altered the intrinsic fracture toughness  $K_{IC}$  at that temperature (Mechanism 4). For example, residual stresses generated from the eutectoid decomposition would be expected to lower  $K_{IC}$ . Possible insights into these toughness variations were obtained by measuring the room temperature  $K_{IC}$  for TS(84) samples previously tested at 1000°C. The resulting toughness values were insensitive to both exposure time and stress level suggesting that Mechanism 4 may be inappropriate.

Mechanisms 1-4 are primarily associated with time-dependent variations in the bulk material characteristics. However, one must also consider the possible effects of flaw modification processes (Mechanism 5). For example, the initial drop in strength of the TS(84) samples stressed at 800°C may have resulted from slow crack growth which was activated at stress levels exceeding 60%. As  $\tau$  increased, the strengthening mechanism became the dominant process. The corresponding increase in  $S_f$  may have reflected the influence of crack blunting. A similar transitional behavior has been observed for alumina.<sup>15</sup> In the case of tests at 1000°C, stressed-induced microcracking may have promoted the long-term strength degradation of the stressed TS PSZ (for  $\tau > 200$  h). These potential flaw modification processes will be investigated further by performing additional I.F. tests using indented flexure samples.

#### Status of milestones

The I.F. experimental matrices for the MS and TS PSZ ceramics were completed. A paper entitled, "Time-Dependent Mechanical Behavior of Partially Stabilized Zirconia for Diesel Engine Applications," was also submitted for publication in the Bulletin of the American Ceramic Society. Both tasks were completed by September 30 in accordance with the milestone schedule (331202).

---

<sup>†</sup> Based on results in Ref. 13, the creep behavior for the TS PSZ is expected to be similar to that for the MS PSZ.



## Publications

A paper entitled, "Time-Dependent Mechanical Behavior of Partially Stabilized Zirconia for Diesel Engine Applications," submitted for publication in the Bulletin of the American Ceramic Society.

## References

1. R. Kamo and W. Bryzik, "Cummins/TACOM Advanced Adiabatic Engine," pp. 121-134 in *Proceedings of the Twenty-First Automotive Technology Development Contractors' Coordination Meeting* P-138, Society of Automotive Engineers, Warrendale, PA, March 1984.
2. S. M. Wiederhorn, "A Probabilistic Framework for Structural Ceramics," pp. 197-226 in *Fracture Mechanics of Ceramics*, Vol 5., eds. R. C. Bradt, A. G. Evans, D. P. H. Hasselman, and F. F. Lange. Plenum, New York, 1983.
3. R. Hannink and M. Swain, "Magnesia-Partially Stabilized Zirconia: The Influence of Heat Treatment on Thermomechanical Properties," *J. Aust. Ceram. Soc.* **18** (2), pp. 53-62 (1983).
4. R. Hannink and R. Garvie, "Sub-eutectoid Aged Mg-PSZ Alloy with Enhanced Thermal Upshock Resistance," *J. Mater. Sci.* **17**, pp. 1637-43 (1982).
5. R. Hannink, "Microstructural Development of Sub-eutectoid Aged Mg-ZrO<sub>2</sub> Alloys," *J. Mater. Sci.* **18**, pp. 457-70 (1982).
6. M. V. Swain, R. C. Garvie, R. H. J. Hannink, "Influence of Thermal Decomposition on the Mechanical Properties of Magnesia-Stabilized Cubic Zirconia," *J. Am. Ceram. Soc.* **66** (5), pp. 358-362 (1983).
7. S. C. Farmer, A. H. Heuer, and R. H. J. Hannink, "Eutectoid Decomposition of MgO Partially-Stabilized Zirconia," submitted to the *J. Am. Ceram. Soc.* for publication.
8. V. J. Tennery, M. K. Ferber, P. F. Becher, and S. B. Waters, "Characterization of Fatigue and Slow Crack Growth Behavior of Partially Stabilized Zirconia Ceramics," pp. 409-18 in *Proceedings of the Twenty-Second Automotive Technology Development Contractors' Coordination Meeting*, P-155, Society of Automotive Engineers, Warrendale, PA, March 1985.
9. P. F. Becher and M. K. Ferber, "Mechanical Behavior of MgO-Partially Stabilized ZrO<sub>2</sub> Ceramics at Elevated Temperatures," submitted to the *J. Mater. Sci.* for publication.
10. W. D. Kingery, H. K. Bowen, and D. R. Uhlmann, *Introduction to Ceramics*, pp. 526-32, John Wiley and Sons, New York, 1976.

11. N. Claussen and M. Ruhle, "Design of Transformation-Toughened Ceramics," pp. 137-63, in *Science and Technology of Zirconia, Advances in Ceramics*, Vol. 3, eds. A. H. Heuer and L. W. Gibbs, American Ceramic Society, Ohio, 1981.
12. D. F. Carroll and R. E. Tressler, "Time-Dependent Strength of Siliconized Silicon Carbide Under Stress at 1000°C and 1100°C," *J. Am. Ceram. Soc.* **68** [3] 143-6 (1985).
13. D. C. Larsen and J. W. Adams, "Long-Term Stability and Properties of Partially Stabilized Zirconia," pp. 399-407 in *Proceedings of the Twenty-Second Automotive Technology Development Contractors' Coordination Meeting* P-155, Society of Automotive Engineers, Warrendale, PA, March 1985.
14. T. Chuang, "Estimation of Power-Law Creep Parameters from Bend Test Data," "NBSIR 85-2997 Report, National Bureau of Standards, Feb. 1985.
15. A. G. Evans and B. J. Dalgleish, "Some Aspects of the High Temperature Performance of Ceramics and Ceramic Composites," pp. 1073-95 in *Ceramic Engineering and Science Proceedings*, American Ceramic Society, Sept.-Oct. 1986.



Environmental Effects in Toughened Ceramics

Norman L. Hecht (University of Dayton)

Objective/scope

The University of Dayton Research Institute (UDRI) has continued its study of "The Effect of Environment Upon the Mechanical Behavior of Structural Ceramics for Application in the DOE Ceramic Technology for Advanced Heat Engines Program." This study was initiated in January 1985 through a subcontract with Martin Marietta Energy Systems Inc. The primary goal of this program is to determine the effect of environment upon toughening and strength in commercially available transformation toughened ceramics [partially stabilized  $ZrO_2$  (PSZ) and dispersion toughened  $Al_2O_3$  (DTA)]. Emphasis is focused on understanding the mechanism(s) responsible for environmentally induced strength degradation in the temperature range of 25°C to 1050°C. It is anticipated that the information and insight obtained from this program can be used to determine the long-term applicability of toughened ceramics as diesel engine components.

Dynamic fatigue methods (4 point bend strength measurements as a function of stressing rate) are being used in a three-phase program to investigate strength, slow crack growth, and aging in environments containing controlled amounts of water vapor. Similar tests are also being conducted in inert atmospheres (dry  $N_2$ ) to distinguish intrinsic effects from environmentally induced effects.

In the first phase of the program all commercially available materials were investigated for evaluation. In this phase of the program, manufacturers' data and preliminary characterization studies conducted at the University of Dayton were utilized to screen the candidate PSZ and DTA materials. From the eight candidate materials screened, five were selected for further study in the second phase of the program. A 4 point flexure modulus of rupture (MOR) testing plan (mini-matrix) was developed for the evaluation of the candidate materials. In addition, the effects of aging on the candidate materials and three (UDRI) prepared high purity  $ZrO_2$  powder compacts were also studied. The results of these studies were used to select the two finalist candidate materials which are being more intensively evaluated in the third phase of the program. A description of the activities pursued and the results obtained are presented in this semiannual report.

Work plan

As described in our last semiannual report, the work scope consisted of three major tasks. A description of these tasks is outlined in Table 1. Eight commercial transformation toughened ceramics (Table 2) were identified for screening and initial evaluation as outlined in Task 1. The elements employed in the preliminary screening analysis conducted in Task I are described in Table 3. The mini-matrix test plan developed for evaluating the five candidate materials under Task II is outlined in Table 4. After flexure testing, all fractured samples were examined visually and representative samples were selected for XRD analysis and



Table 1. Work Scope.

TASK I	TASK II	TASK III
Evaluation of Potential Candidate Transformation Toughened Ceramics (TTC) <ul style="list-style-type: none"> <li>● Identification of TTC Suppliers</li> <li>● Screening Evaluation of Potential Candidate TTC Materials</li> <li>● Analysis of TTC Screening Data</li> </ul>	Investigation of five Selected Candidate Materials <ul style="list-style-type: none"> <li>● Finalize Candidate Selection for Matrix Testing Plan (four temperatures, two atmospheres, and two stressing rates)</li> <li>● Conduct Candidate Matrix Test Program</li> <li>● Conduct Aging Studies</li> </ul>	Detailed Investigation of the Two Finalist TTC Materials <ul style="list-style-type: none"> <li>● Selection of the Two Finalist Materials</li> <li>● Finalization of an Expanded Matrix Testing Plan</li> <li>● Implementation of MOR Testing Plan</li> </ul>

Table 2. Transformation Toughened Ceramic Materials Identified for Evaluation.

Material Supplier	Material Designation	Material Description
Ceramatec Inc.	ZTA-XS121	ZrO <sub>2</sub> Dispersion Toughened Al <sub>2</sub> O <sub>3</sub>
Kyocera Int'l.	DTA-AZ301	Dispersion Toughened Al <sub>2</sub> O <sub>3</sub> (19% ZrO <sub>2</sub> )
Nilcra Ceramic (USA) Inc.	MS-PSZ	3 wt. % MgO Stabilized ZrO <sub>2</sub> (heat treated for high strength)
Nilcra Ceramic (USA) Inc.	TS-PSZ	3 wt. % MgO Stabilized ZrO <sub>2</sub> (heat treated for high thermal shock resistance)
Ceramatec Inc.	YTZP-XS241	~5 wt. % Y <sub>2</sub> O <sub>3</sub> Stabilized ZrO <sub>2</sub> (with 10% Al <sub>2</sub> O <sub>3</sub> addition)
NGK Locke Inc.	Z191	5 wt. % Y <sub>2</sub> O <sub>3</sub> Stabilized ZrO <sub>2</sub>
Kyocera Int'l.	PSZ-Z201	5.4 wt. % Y <sub>2</sub> O <sub>3</sub> Stabilized ZrO <sub>2</sub>
Ceramatec Inc.	CTZP	CeO <sub>2</sub> Stabilized ZrO <sub>2</sub> (with 10% Al <sub>2</sub> O <sub>3</sub> addition)

Table 3. Elements of the Preliminary Screening Analysis (Task I).

- 
- Visual Inspection (low power microscope)
  - Surface Finish Measurement
  - SEM/EDAX
  - High Power Optical Microscopy
  - Density
  - Vickers Hardness
  - Coefficient of Thermal Expansion Measurement
  - Modulus of Rupture (MOR) Testing (in dry N<sub>2</sub> at room temperature and at 1050°C)
  - XRD (as-received, after MOR<sub>RT</sub>, and MOR<sub>1050</sub>)
  - Fracture Toughness (controlled surface flaw and micro-indent technique)
- 

Table 4. MOR Matrix Test Plan (Task II).

Temperature (°C)	Atmosphere	MOR Crosshead Speed (cm/s)
25	Dry N <sub>2</sub>	0.0064
25	Dry N <sub>2</sub>	0.00004
25	10% H <sub>2</sub> O	0.0064
25	10% H <sub>2</sub> O	0.00004
250	Dry N <sub>2</sub>	0.0064
250	10% H <sub>2</sub> O	0.0064
250	10% H <sub>2</sub> O	0.00004
800	Dry N <sub>2</sub>	0.0064
800	10% H <sub>2</sub> O	0.0064
800	10% H <sub>2</sub> O	0.00004
1050	Dry N <sub>2</sub>	0.0064
1050	Dry N <sub>2</sub>	0.00004
1050	10% H <sub>2</sub> O	0.0064
1050	10% H <sub>2</sub> O	0.00004

---

fracture analysis by SEM. Aging treatments in 10% water, dry  $N_2$ , and vacuum were employed for additional evaluation of the candidate materials (see Table 5). MOR testing, XRD analysis, Raman spectroscopy, and infrared spectroscopy were used to evaluate the aged samples. In addition to the candidate materials, high purity  $ZrO_2$  powder compacts of 2, 3, and 4 mole percent  $Y_2O_3$  were pressed and sintered for aging studies.

The results of Task II were used for the selection of the two finalist materials to be evaluated more extensively. The detailed matrix test plan used for evaluating the two finalist materials under Task III is presented in Table 6.

### Technical progress

#### Results

Summary of Task I results. The results obtained from the studies conducted under Task I were described in detail in our first semiannual report. The results obtained in Task I are summarized in Table 7 and in Figure 1. Task I was completed with the selection of the five candidate materials to be studied further: NGK Locke Z191, Ceramtec CTZP, Nilcra MS-PSZ, Kyocera AZ301, and Kyocera Z201.

Summary of Task II results. The initial results obtained for the activities under Task II were described in our previous semiannual report. All of the activities listed under Task II have now been completed, and the results obtained are summarized in this section. The flexure testing (MOR) outlined in the mini-matrix test has been completed, and the results obtained are shown graphically in Figures 2 through 6. The linear decrease in strength with increasing temperature was determined by a best fit computer analysis. The MOR results were also statistically analyzed, and the results obtained are summarized in Table 8. As shown in Table 8, the relative precision (the ratio of the half width of the 95% confidence interval to the coverage MOR) is generally less than 25%. These relative precision values calculated reflect both the scatter in the MOR values measured and the size of the sample population used to determine the mean value and the standard deviation.

The effects of subcritical crack growth and the effects of selected environmental conditions were also studied. The procedure used was based on the assumption that if a material is subject to subcritical crack growth, higher strengths will be observed at the higher stressing rate because there is less time for subcritical crack growth. This effect, known as dynamic fatigue can be characterized by a  $\ln\text{-}\ln$  plot of fracture strength versus stressing rate. The relationship between fracture strength and stressing rate is:

$$\sigma_f = A\dot{\sigma}^{\left(\frac{1}{n+1}\right)} \quad (1)$$

which can be expressed by

$$\ln \sigma_f = \ln A + \left(\frac{1}{n+1}\right) \ln \dot{\sigma} \quad (2)$$



Table 5. Aging Investigations.

Material	Aging Treatments in 10% H <sub>2</sub> O, Dry N <sub>2</sub> , and Vacuum
Z191	250°C/120 hrs, 300°C/25 hrs
AZ301	250°C/144 hrs, 300°C/25 hrs, 250°C/120 hrs in dry N <sub>2</sub>
Z201	250°C/120 hrs, 300°C/25 hrs
CTZP	150°C/120 hrs, 250°C/120 hrs, 300°C/25 hrs
XS121	250°C/120 hrs, 300°C/25 hrs, 250°C/120 hrs in dry N <sub>2</sub>
XS241	250°C/120 hrs and 240 hrs, 300°C/25 hrs, 250°C/120 hrs in dry N <sub>2</sub> , 250°C/168 hrs in vacuum
MS-PSZ	250°C/120 hrs and 144 hrs, 800°C/200 hrs, 250°C/120 hrs in dry N <sub>2</sub>
TS-PSZ	250°C/120 hrs, 800°C/200 hrs, 250°C/120 hrs in dry N <sub>2</sub> , 250°C/168 hrs in vacuum
2Y*	250°C/24 hrs, 250°C/24 hrs in dry N <sub>2</sub> , 250°C/168 hrs in vacuum
3Y*	250°C/50 hrs, 250°C/24 hrs in dry N <sub>2</sub> , 250°C/168 hrs in vacuum
4Y*	250°C/24 hrs, 250°C/24 hrs in dry N <sub>2</sub> , 250°C/168 hrs in vacuum

\*Specially prepared fired discs of 2 mole % Y<sub>2</sub>O<sub>3</sub>; 3 mole % Y<sub>2</sub>O<sub>3</sub>, and 4 mole % Y<sub>2</sub>O<sub>3</sub> ZrO<sub>2</sub> for analysis.

Table 6. Finalist MOR Matrix Test Plan.

Temperature	Environment*	MOR Crosshead Speed (cm/sec)		
		0.00004	0.0021	0.0064
25°C	Atm <sub>1</sub>	x	x	x
	Atm <sub>2</sub>	x	x	x
250°C	Atm <sub>1</sub>	x	x	x
	Atm <sub>2</sub>	x	x	x
800°C	Atm <sub>1</sub>	x	x	x
	Atm <sub>2</sub>	x	x	x
1050°C	Atm <sub>1</sub>	x	x	x
	Atm <sub>2</sub>	x	x	x

\*Environmental Conditions: Atm<sub>1</sub> - Dry N<sub>2</sub>; Atm<sub>2</sub> - 90% N<sub>2</sub>/10% H<sub>2</sub>O.

Table 7. Summary of Screening Evaluations for TTC Materials.

Material Designation	Nilcra MS-PSZ	Nilcra TS-PSZ	Kyocera DTA-AZ301	Kyocera PSZ-Z201
Chemistry (Components)	ZrO <sub>2</sub> MgO	ZrO <sub>2</sub> MgO	Al <sub>2</sub> O <sub>3</sub> ZrO <sub>2</sub> SiO <sub>2</sub> - Trace	ZrO <sub>2</sub> Y <sub>2</sub> O <sub>3</sub>
Crystal Structure				
% Monoclinic As-Received	23	33	28	3
% Monoclinic After MOR <sub>1050</sub>	88	69	21	0
Density (g/cc)	5.7	5.7	4.2	5.9
Hardness (kg/mm <sup>2</sup> )	1099	1025	1939	1282
Fracture Toughness (MPa $\sqrt{m}$ )				
By Controlled Flaw	-	-	4.6	5.4
By Micro Indent	7.6	6.0	11.1	8.8
Major Microstructural Features	Porous coarse grained (30-60 $\mu$ ) material.	Porous coarse grained (30-60 $\mu$ ) material.	Dense two phase material with grains $\approx .3 \mu - 2 \mu$ .	Dense fine grained material (0.2-0.5 $\mu$ avg. $\approx .3 \mu$ ).
Average Sample Surface Finish Measurements ( $\mu$ in)	10 (4-15)	9 (4-12)	2.8 (2-4)	6.1 (4-8)
Coefficient of Thermal Expansion ( $\times 10^{-6}/^{\circ}\text{C}$ )	10.3	9.5	8.4	11.0
				(continued)

Table 7. Summary of Screening Evaluations for TTC Materials (concluded).

Material Designation	NGK Z191	Ceramatec ZTA-XS121	Ceramatec YTZP-XS241	Ceramatec CTZP
Chemistry (Components)	ZrO <sub>2</sub> , Y <sub>2</sub> O <sub>3</sub> SiO <sub>2</sub> Al <sub>2</sub> O <sub>3</sub> } Trace	Al <sub>2</sub> O <sub>3</sub> , ZrO <sub>2</sub> SiO <sub>2</sub> K <sub>2</sub> O/CaO-Trace	ZrO <sub>2</sub> Y <sub>2</sub> O <sub>3</sub> Al <sub>2</sub> O <sub>3</sub>	ZrO <sub>2</sub> , SiO <sub>2</sub> Al <sub>2</sub> O <sub>3</sub> , CeO <sub>2</sub> K <sub>2</sub> O/CaO-Trace
Crystal Structure				
% Monoclinic As-Received	7	30	11	1
% Monoclinic After MOR <sub>1050</sub>	0	24	8	0
Density (g/cc)	5.9	4.4	5.4	5.7
Hardness (kg/mm <sup>2</sup> )	1292	1172	1120	864
Fracture Toughness (MPa $\sqrt{m}$ )				
By Controlled Flaw	6.8	2.8	4.8	-
By Micro Indent	7.4	6.9	6.6	7.0
Major Microstructural Features	Dense fine grained material (0.2-0.4 $\mu$ )	Fine grained multi-phase material (0.5-2.5 $\mu$ avg. $\approx$ 1.5 $\mu$ ). Uniform distribution of pores (0.2-2 $\mu$ ).	Fine grained multi-phase material (2-4 $\mu$ ). Uniform distribution of pores (0.5-4 $\mu$ ).	Fine grained two-phase material (1-4 $\mu$ ). Uniform distribution of pores.
Average Sample Surface Finish Measurements ( $\mu$ in)	6.9 (4-16)	3.1 (2-10)	8 (6-10)	3.1 (2-6)
Coefficient of Thermal Expansion ( $\times 10^{-6}/^{\circ}\text{C}$ )	10.1	9.4*	9.9	10.7

\*Slope change @ 625°C.



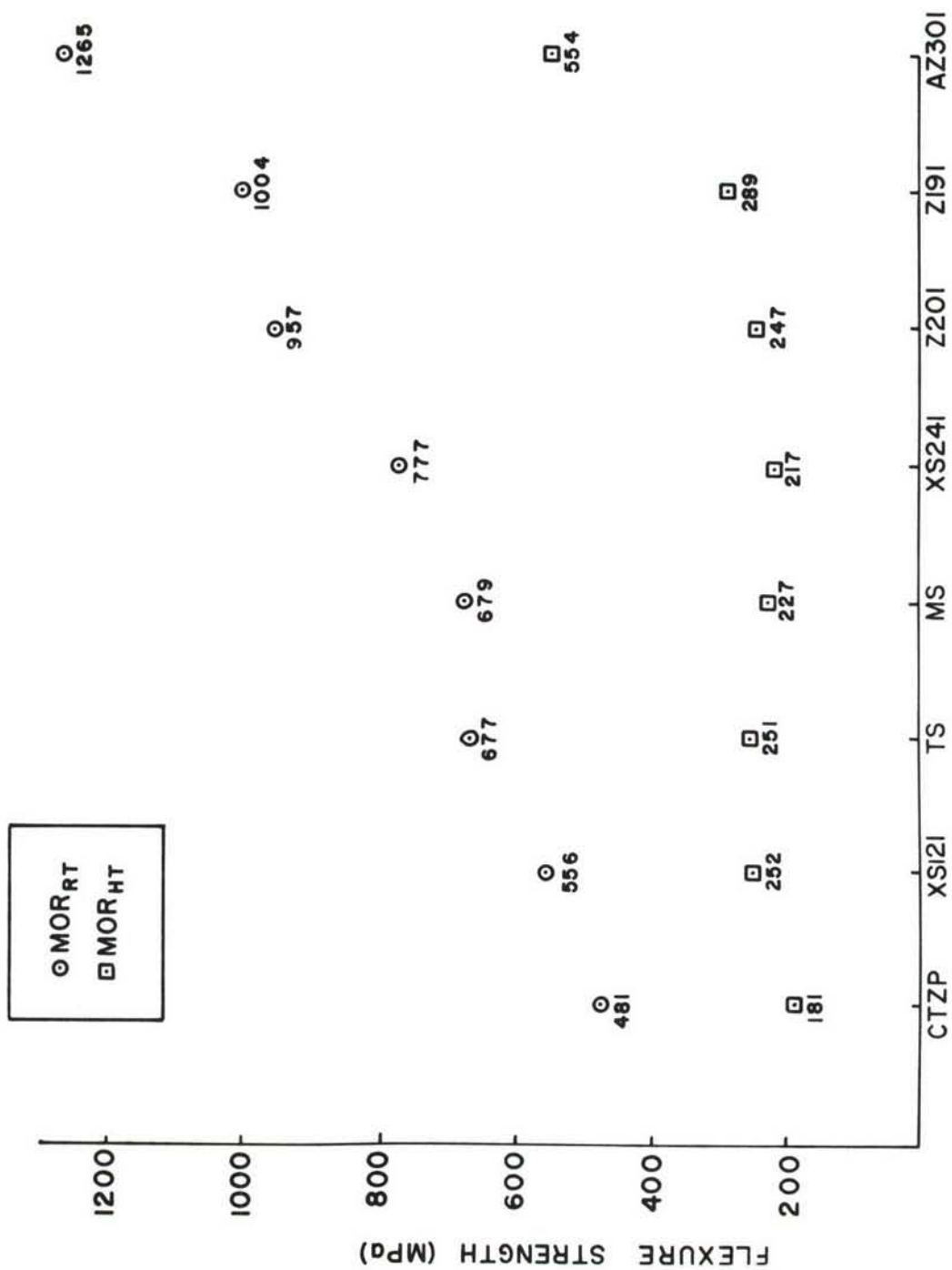


Figure 1. MOR test results from the screening analysis (Task I).

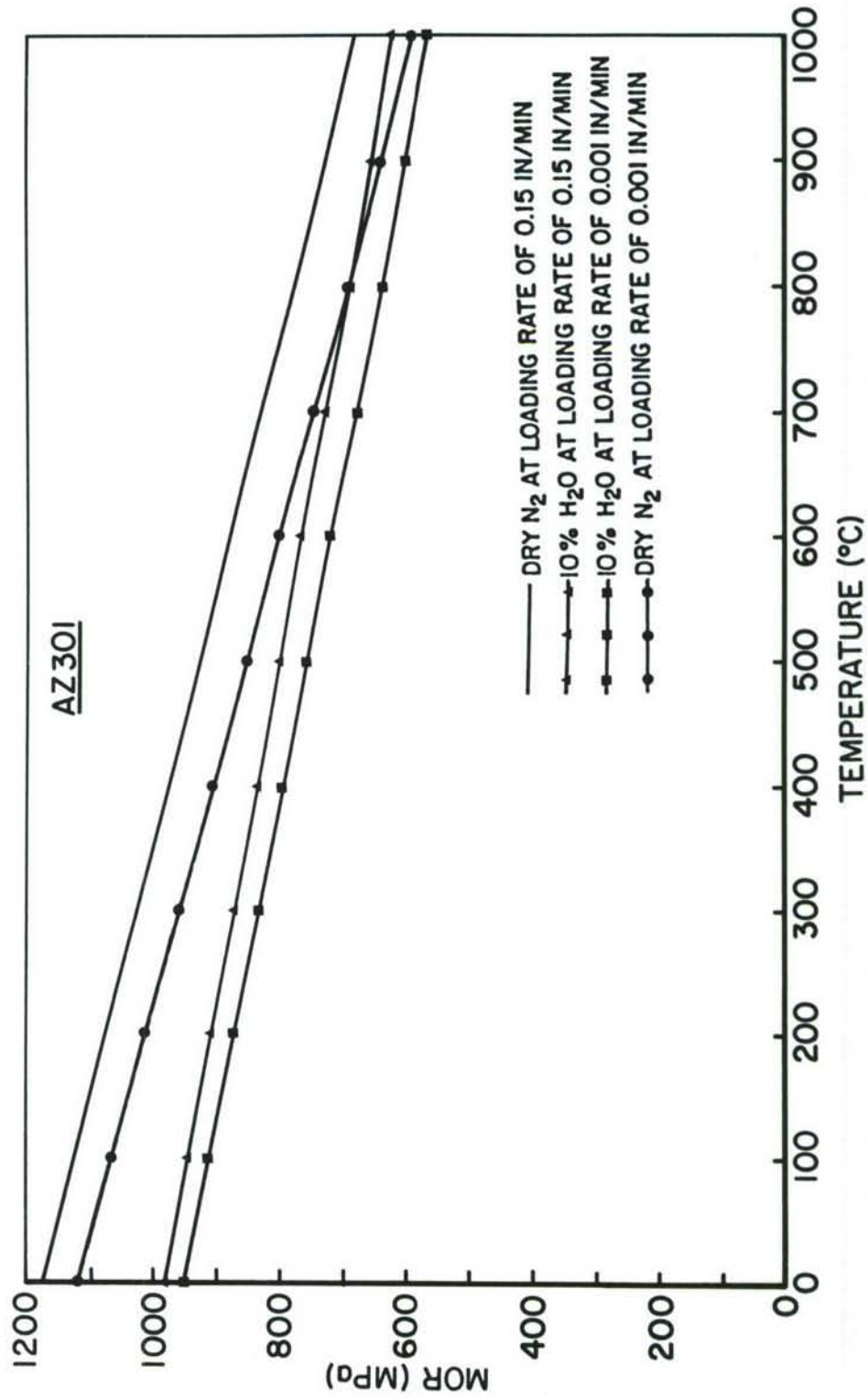


Figure 2. Linear dependency of flexure strength versus temperature for AZ301.

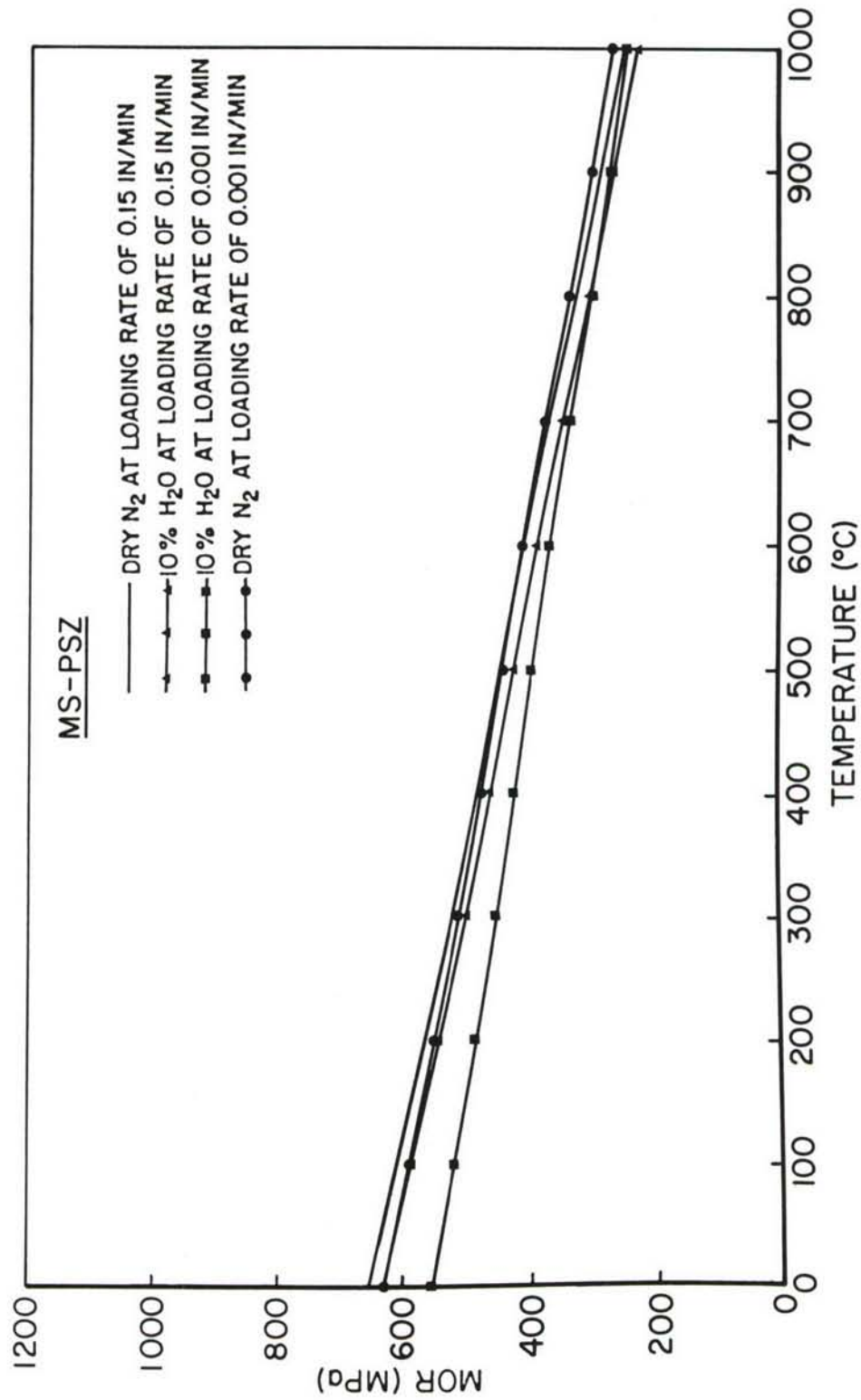


Figure 3. Linear dependency of flexure strength versus temperature for MS-PSZ.



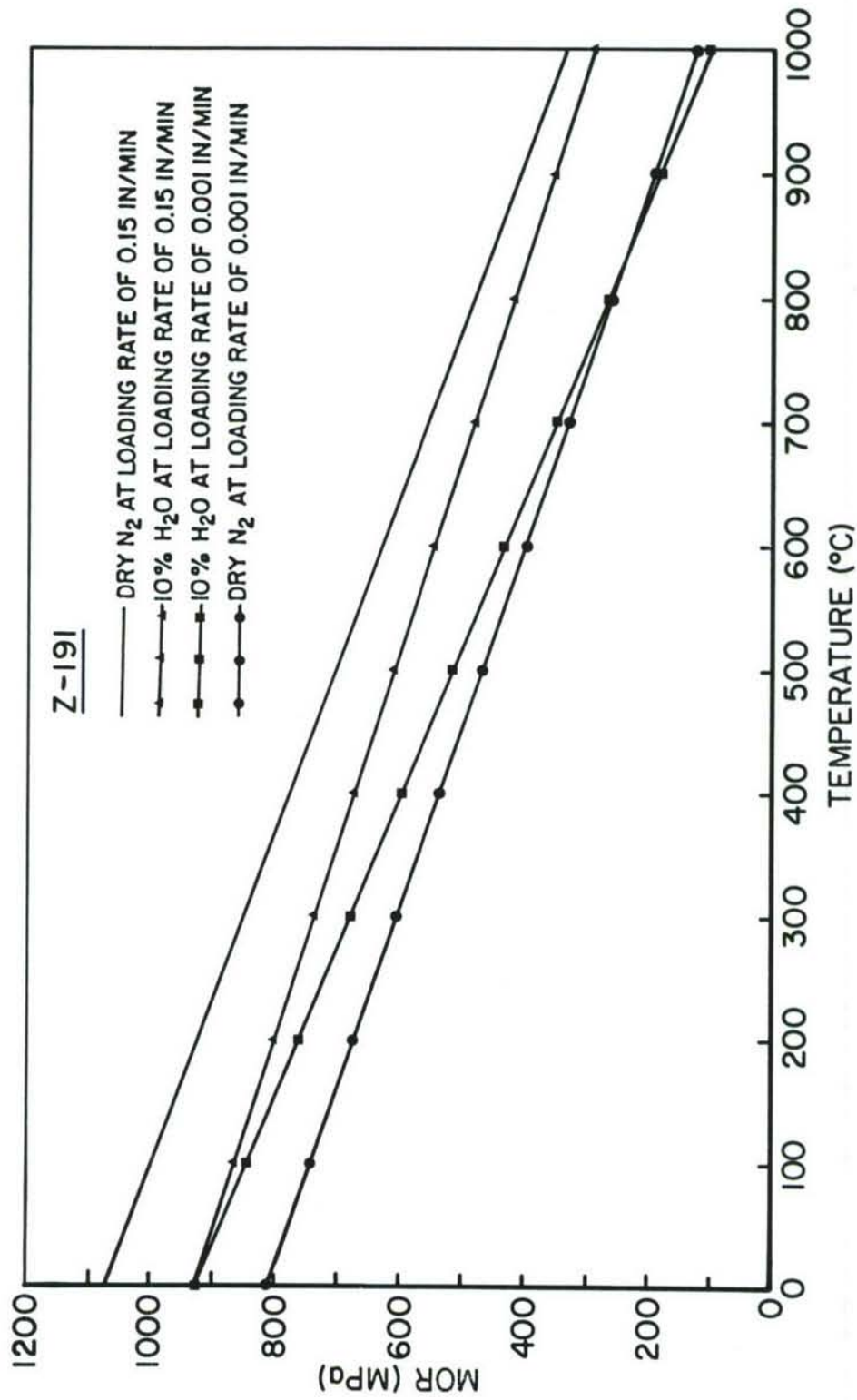


Figure 4. Linear dependency of flexure strength versus temperature for Z191.

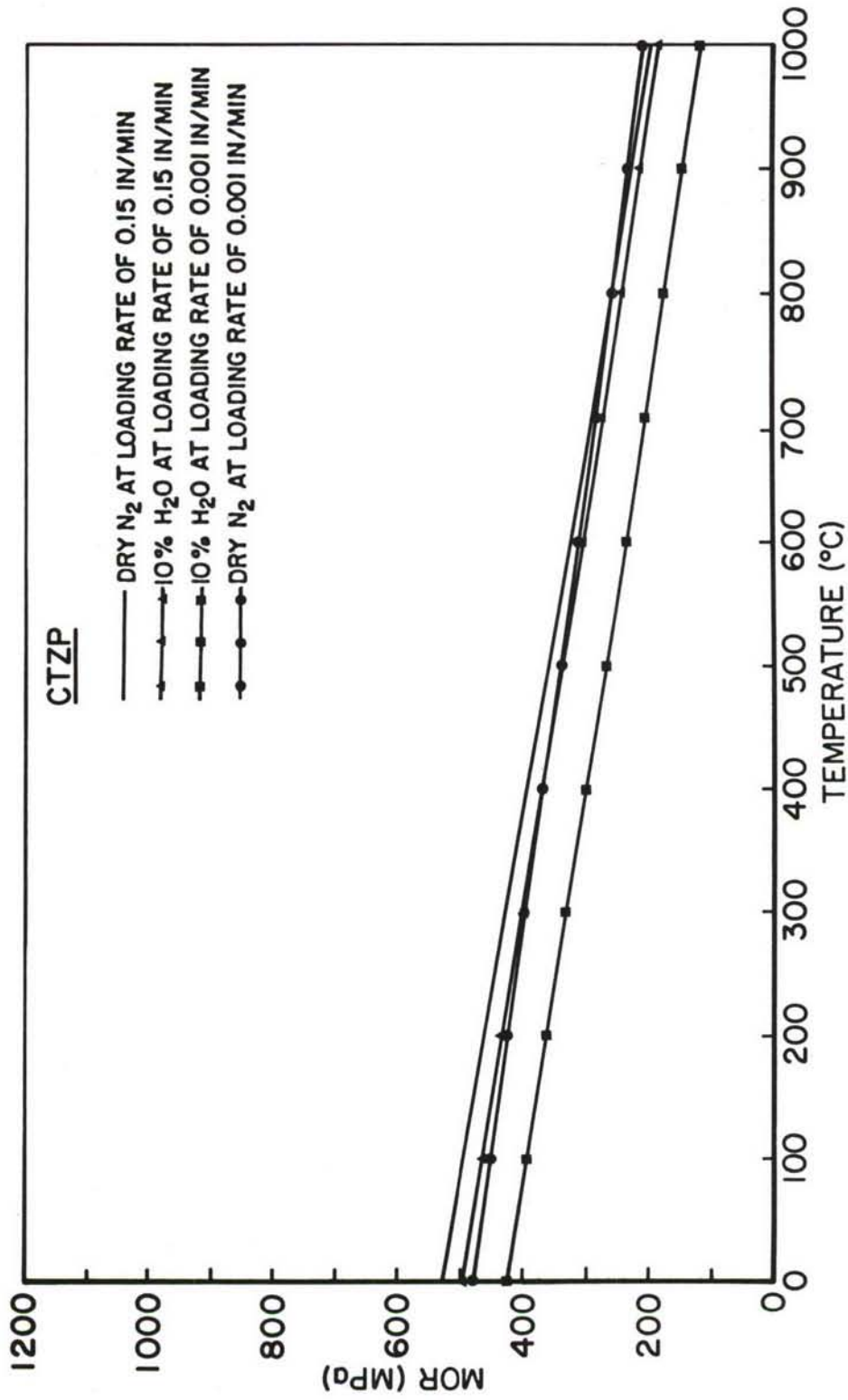


Figure 5. Linear dependency of flexure strength versus temperature for CTZP.

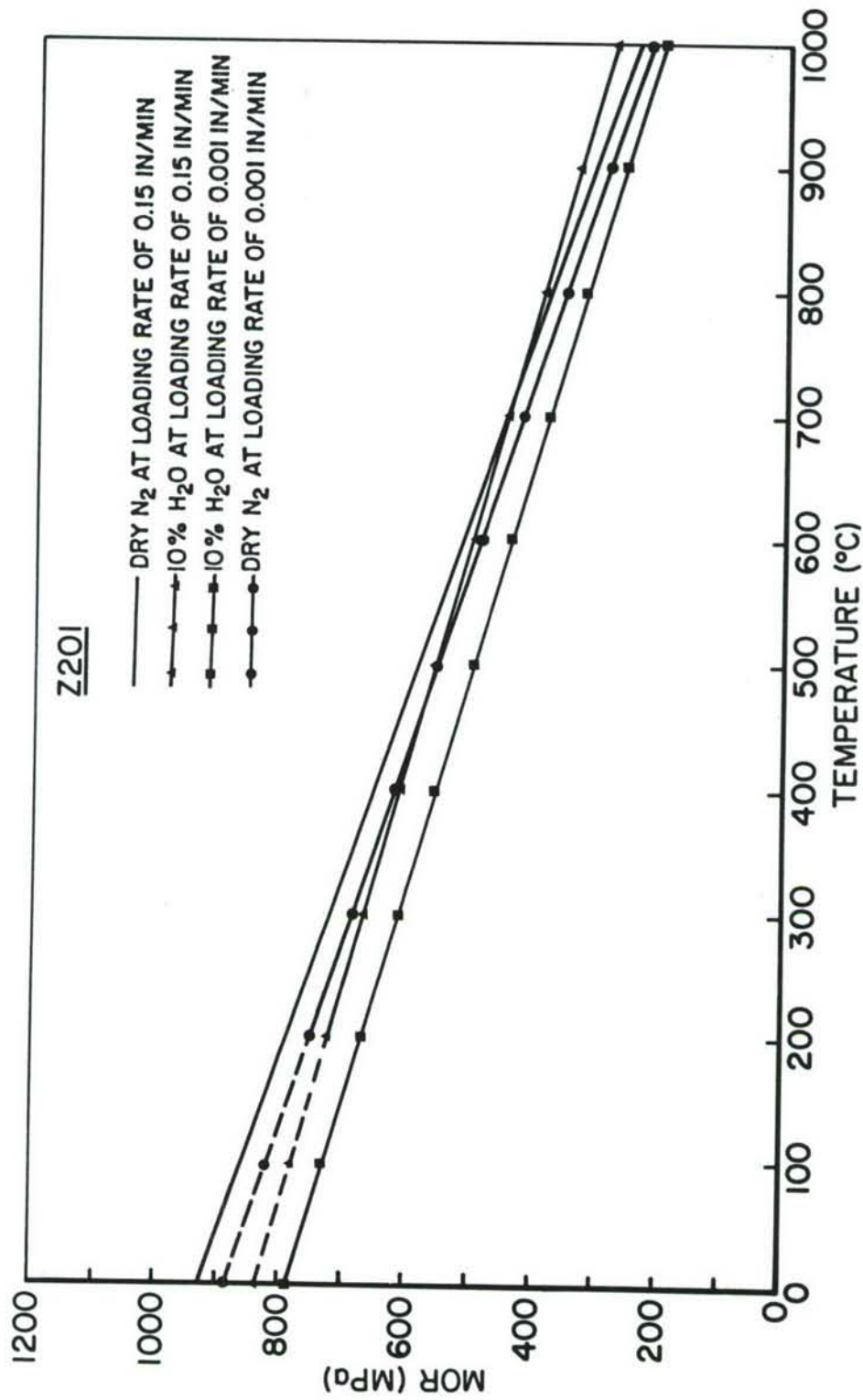


Figure 6. Linear dependency of flexure strength versus temperature for Z201.



Table 8. Analysis of Flexure Test Results (MOR).

Test Conditions			AZ301				MS			
Temp. (°C)	Atm.	Crosshead Speed (cm/s)	Mean MOR (MPa)	Std. Dev.* (MPa)	95% CL* Range (± MPa)	Rel. Prec.* (%)	Mean MOR (MPa)	Std. Dev.* (MPa)	95% CL* Range (± MPa)	Rel. Prec.* (%)
25	Dry N <sub>2</sub>	.0064	1264	137	169.5	13.4	678.6	38.6	48	7.1
25	Dry N <sub>2</sub>	.00004	1107	127	90.5	8.2	620.5	44.0	70.5	11.4
25	10% H <sub>2</sub> O	.0064	849	244	303	35.7	638.2	25.5	31.5	4.9
25	10% H <sub>2</sub> O	.00004	932	109	134	14.4	565.8	20.1	25	4.4
250	Dry N <sub>2</sub>	.0064	897	304	378	42.1	540	66.7	83	15.4
250	10% H <sub>2</sub> O	.0064	1036	192	239	23.1	525.6	28.7	35.5	6.75
250	10% H <sub>2</sub> O	.00004	892.2	61.6	76.5	8.6	448.2	49.6	61.5	13.7
800	Dry N <sub>2</sub>	.0064	832	111	276	33.2	298.7	23.5	58.5	19.6
800	10% H <sub>2</sub> O	.0064	729	221	548.5	75.2	281.3	22.5	56	19.9
800	10% H <sub>2</sub> O	.00004	463	171	424	91.6	270.7	24.4	60.5	22.4
1050	Dry N <sub>2</sub>	.0064	662	236	293.5	44.3	248.4	15.9	19.7	7.9
1050	Dry N <sub>2</sub>	.00004	590	137	169.5	28.7	247.4	13.2	16.4	6.6
1050	10% H <sub>2</sub> O	.0064	554	132	162.5	29.3	224.8	9.07	11.3	5.0
1050	10% H <sub>2</sub> O	.00004	620	149	185	29.8	253.8	13.8	17.1	6.7

(continued)

(continued)

\*CL - Confidence Limit.

\*Rel. Prec. - Relative Precision - the ratio of the 1/2 width.

\*Std. Dev. - Standard Deviation.

Table 8. Analysis of Flexure Test Results (MOR).

(continued)										
Test Conditions			Z191				CTZP			
Temp. (°C)	Atm.	Crosshead Speed (cm/s)	Mean MOR (MPa)	Std. Dev.* (MPa)	95% CL* Range (± MPa)	Rel. Prec.* (%)	Mean MOR (MPa)	Std. Dev.* (MPa)	95% CL* Range (± MPa)	Rel. Prec.* (%)
25	Dry N <sub>2</sub>	.0064	1004	157	194.5	19.4	481.2	16.9	21	4.4
25	Dry N <sub>2</sub>	.00004	1013.8	93.6	149	14.7	472	7.16	11.4	2.4
25	10% H <sub>2</sub> O	.0064	831	111	137.5	16.6	472.8	8.79	10.9	2.3
25	10% H <sub>2</sub> O	.00004	821	67.3	84	10.2	421.8	30.6	38	9.0
250	Dry N <sub>2</sub>	.0064	900.4	71.8	89.5	9.9	523.2	69.0	85.5	16.3
250	10% H <sub>2</sub> O	.0064	826.6	41.2	51.5	6.2	432.8	42.2	52.5	12.1
250	10% H <sub>2</sub> O	.00004	861.8	53.9	67	7.8	340.8	82.3	102	29.9
800	Dry N <sub>2</sub>	.0064	459.7	18.5	46	10.0	215.7	16.3	40.4	18.7
800	10% H <sub>2</sub> O	.0064	324.7	72.6	180.5	55.6	202	25.9	64	31.7
800	10% H <sub>2</sub> O	.00004	261.7	46.4	115.5	44.1	217.7	100	34.9	11.4
1050	Dry N <sub>2</sub>	.0064	319	2	2	0.6	180.7	34.6	86	47.6
1050	Dry N <sub>2</sub>	.00004	119.7	4.51	11.2	9.4	190.6	29	36	18.9
1050	10% H <sub>2</sub> O	.0064	296.4	17.2	21.3	7.2	186	24.4	30	16.1
1050	10% H <sub>2</sub> O	.00004	114.6	13.6	17	14.8	154	36.6	45	29.2
(continued)										

(continued)

\*CL - Confidence Limit.

\* Rel. Prec. - Relative Precision - the ratio of the 1/2 width.

\*Std. Dev. - Standard Deviation.

Table 8. Analysis of Flexure Test Results (MOR).

Test Conditions			Z201			
Temp. (°C)	Atm.	Crosshead Speed (cm/s)	Mean MOR (MPa)	Std. Dev.* (MPa)	95% CL* Range (± MPa)	Rel. Prec.* (%)
25	Dry N <sub>2</sub>	.0064	957.3	52.2	83	8.7
25	Dry N <sub>2</sub>	.00004	775	179	187.5	24.2
25	10% H <sub>2</sub> O	.0064	-	-	-	-
25	10% H <sub>2</sub> O	.00004	-	-	-	-
250	Dry N <sub>2</sub>	.0064	714	121	150	21.0
250	10% H <sub>2</sub> O	.0064	690	128	158.5	23.0
250	10% H <sub>2</sub> O	.00004	708.8	70.8	88	12.4
800	Dry N <sub>2</sub>	.0064	319.7	87	216.5	67.7
800	10% H <sub>2</sub> O	.0064	391	42	104	26.6
800	10% H <sub>2</sub> O	.00004	396	30.6	76	19.2
1050	Dry N <sub>2</sub>	.0064	263.7	58.9	146.5	55.6
1050	Dry N <sub>2</sub>	.00004	174.7	9.71	24.2	13.8
1050	10% H <sub>2</sub> O	.0064	247.2	50.8	63	25.5
1050	10% H <sub>2</sub> O	.00004	173.4	11.2	14	8.1

\*CL - Confidence Limit.

\*Rel. Prec. - Relative Precision - the ratio of the 1/2 width.

\*Std. Dev. - Standard Deviation.



where  $\sigma_f$  = fracture strength  
 $\dot{\sigma}$  = stress rate

A, n = constants

The constant n, the stress intensity factor exponent, gives a measure of the stress corrosion susceptibility of the material. Large n values are synonymous with lower stress corrosion or fatigue susceptibility. A plot of  $\ln \sigma_f$  versus  $\ln \dot{\sigma}$  yields a straight line with a slope of  $\frac{1}{n+1}$ . The stressing rate for crosshead speeds of 0.00004 and 0.0064 cm/s were calculated for the PSZ and DTA materials at 25°C, 250°C, 800°C, and 1050°C using temperature corrected calculated values of elastic modulus. Using the stressing rates established and the MOR values obtained, the values of n and A were determined from equation (1). The results of these calculations for the five materials studied in the mini-matrix test program (Phase II) are presented in Table 9. The statistical validity of the slopes calculated were evaluated at a confidence level of 95%. The validated slopes are also identified in Table 9. Typical computer generated graphs for this dynamic fatigue data are presented in Figures 7 through 13.

Samples from each group of candidate material tested in MOR were evaluated by x-ray diffraction (XRD), scanning electron microscopy (SEM), and Raman spectroscopy. A summary of the XRD data is presented in Table 10.

As reported in previous studies, a shift in the monoclinic fraction present at the stressed and unstressed regions was observed by Raman analysis of the tensile edge of MOR fractured specimens. A Nilcra TS-PSZ fractured sample was used for further investigation of this increase in monoclinic phase. The experimental procedure used was described in our previous semiannual report. The Nilcra sample was found to have a monoclinic fraction of 13% when analyzed on the unstressed end, and analysis on the fractured edge of the sample revealed a monoclinic fraction of 65%, showing the effects of strain on the material. The fracture was 25 mm long with a 5 mm x 2.5 mm cross section. The measurements were taken on the 25 mm side. The purpose of this study was to determine the spatial variation of this stress-induced transition. Figure 14 presents a plot of the monoclinic fraction present along the tensile edge of the fractured specimen.

Aging studies. The extended exposure of the candidate transformation toughened ceramic materials to water vapor, dry  $N_2$ , and vacuum environments at low and moderate temperatures (aging) was also studied. Several different aging treatments were investigated as outlined in Table 5. MOR tests, XRD analysis, infrared spectroscopy, and Raman spectroscopy were used to evaluate the aged samples. The results of the XRD analysis of the aged samples are presented in Table 11, and the MOR results are presented in Table 12. The ATR FTIR spectra obtained for the as-received and the aged samples are presented in Figures 15 through 20.

To better understand some of these aging effects, high purity  $ZrO_2$  powders with 2, 3, and 4 mole percent  $Y_2O_3$  (2Y, 3Y, and 4Y) were obtained

Table 9. Summary of Dynamic Fatigue Test Results.

Test Temp. °C	Conditions Atm.	AZ301 N	A	MS N	A	Z191 N	A	CTZP N	A	Z201 N	A
25	Dry N <sub>2</sub>	+32	1110*	+71	630*	-400	1010	+155	470	+21	795*
25	10% H <sub>2</sub> O	-41	925	+40	575*	+610	821	+42	430*	-	-
250	10% H <sub>2</sub> O	+35	890	+30	460*	+123	850	+18	350*	-140	700
800	10% H <sub>2</sub> O	+10	450	+125	275	+23	270	-64	215	-345	395
1050	Dry N <sub>2</sub>	+34	595	0	250	+4	145*	-66	190	+13	190*
1050	10% H <sub>2</sub> O	-47	600	-45	245	+4.3	140*	+23	160	+14	185*

$$N = \frac{1}{\text{Slope}} - 1.$$

A = Intercept.

\* = Sufficient sample population to determine that the calculated slope value was statistically correct at the 95% confidence limit.

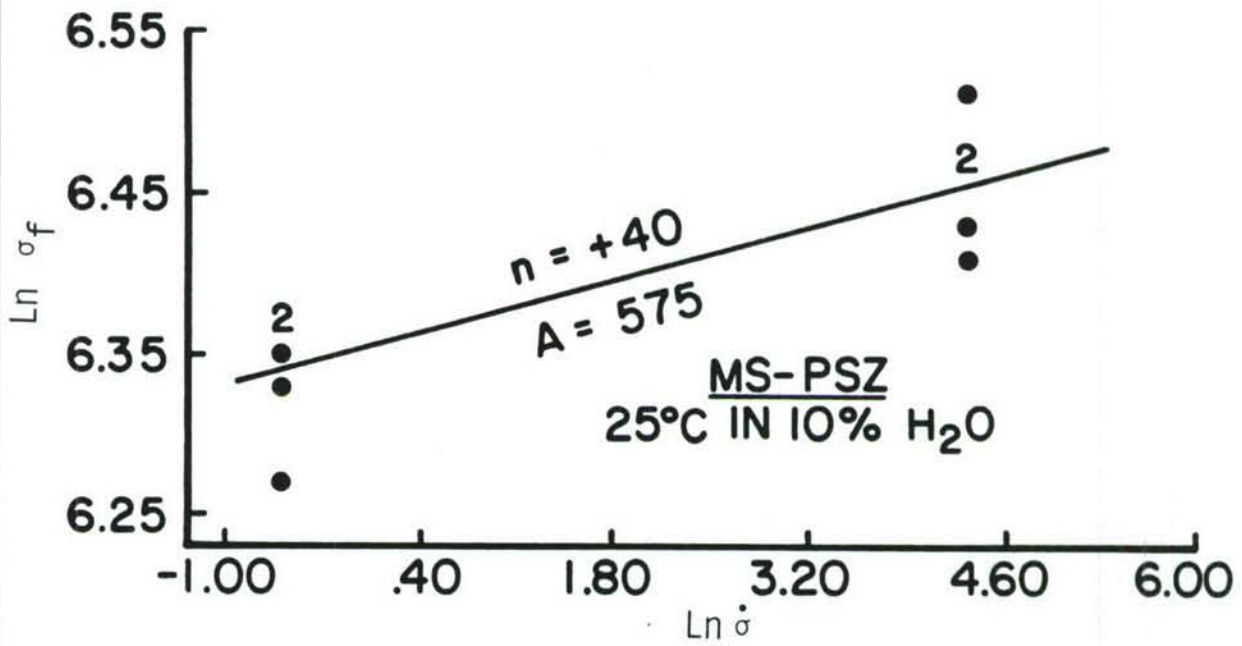


Figure 7. Dynamic fatigue results for MS-PSZ at 25°C in 10% H<sub>2</sub>O.

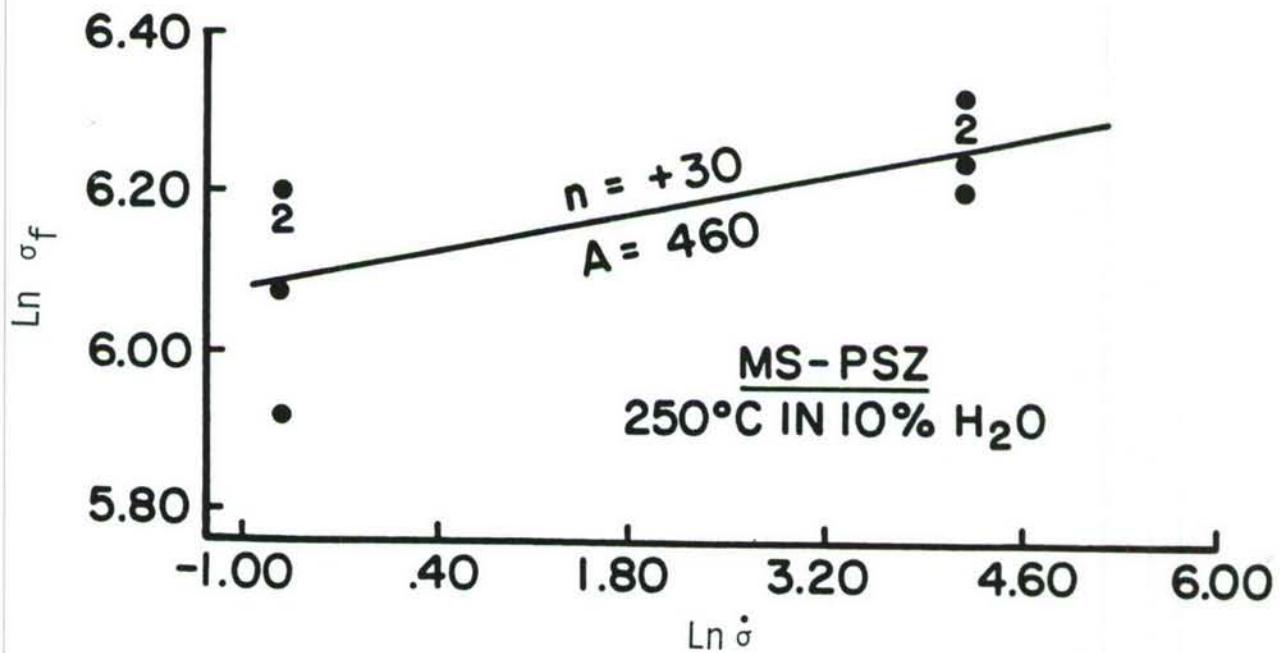


Figure 8. Dynamic fatigue results for MS-PSZ at 250°C in 10% H<sub>2</sub>O.



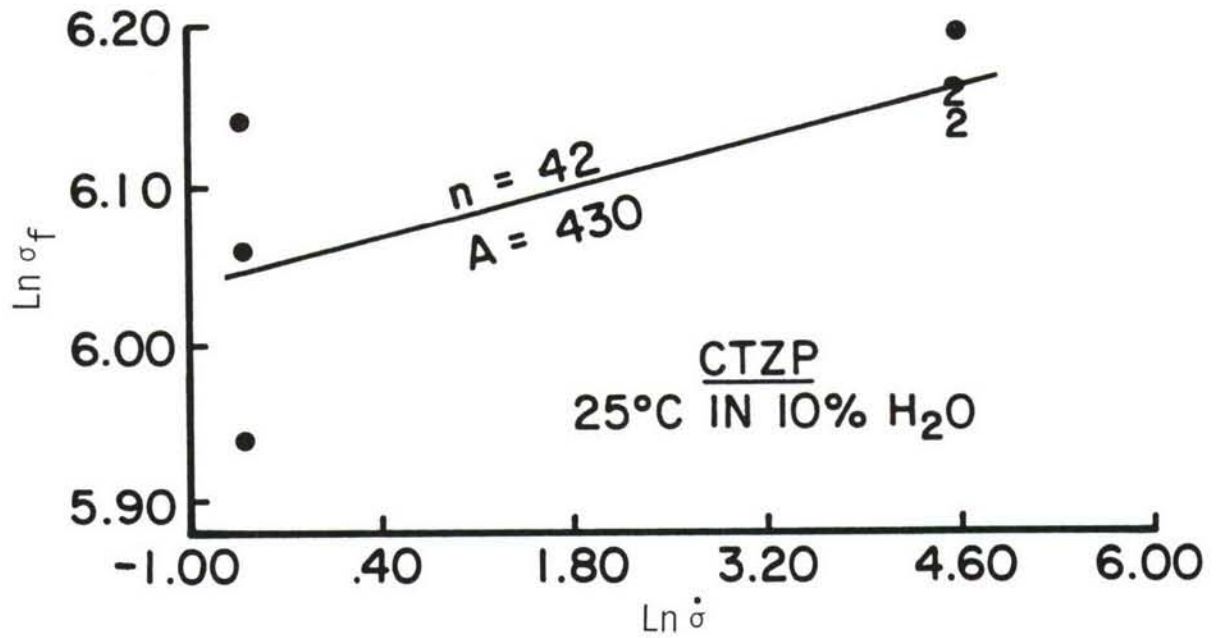


Figure 9. Dynamic fatigue results for CTZP at 25°C in 10%  $\text{H}_2\text{O}$ .

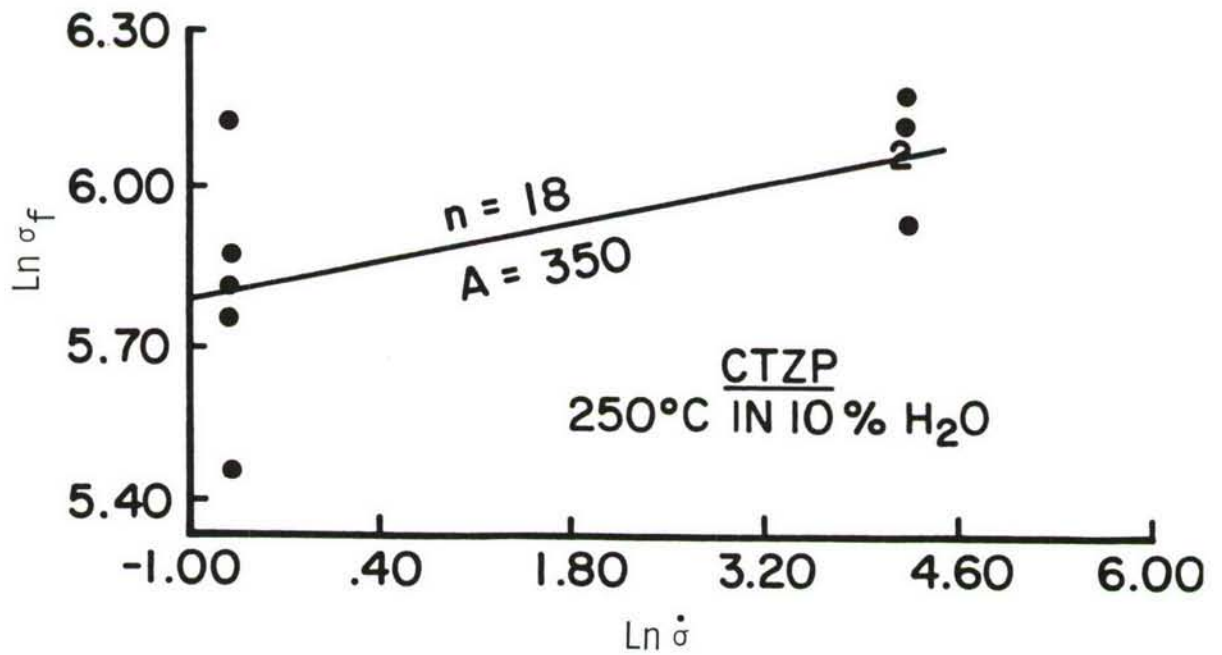


Figure 10. Dynamic fatigue results for CTZP at 250°C in 10%  $\text{H}_2\text{O}$ .

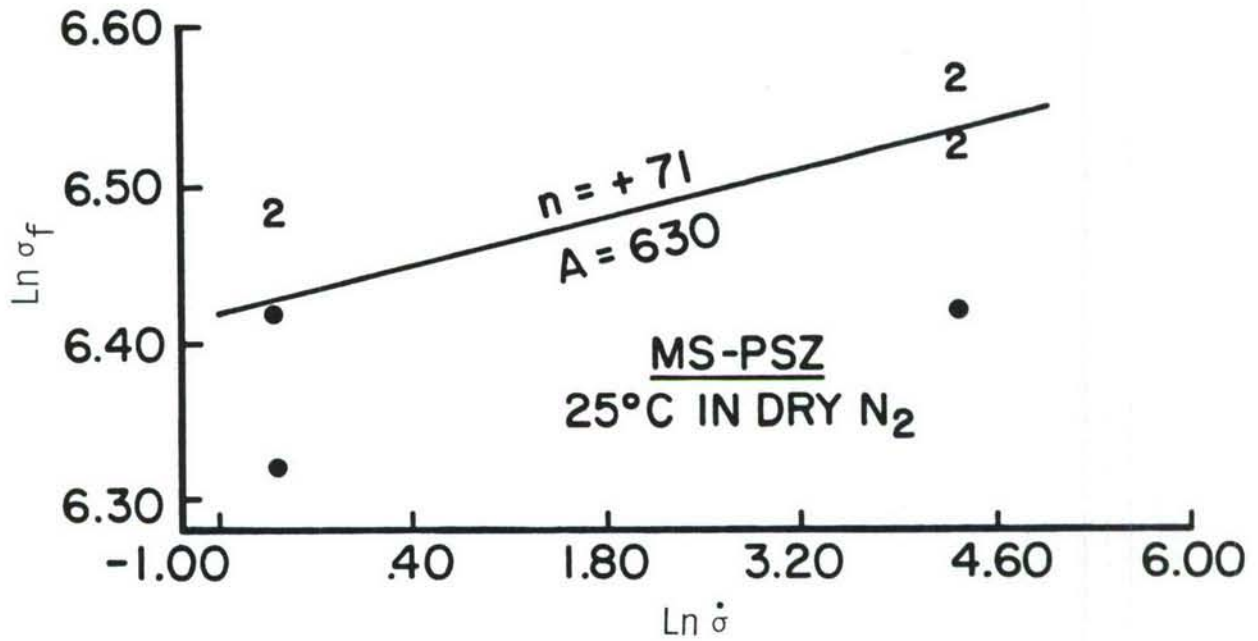


Figure 11. Dynamic fatigue results for MS-PSZ at 25°C in Dry  $\text{N}_2$ .

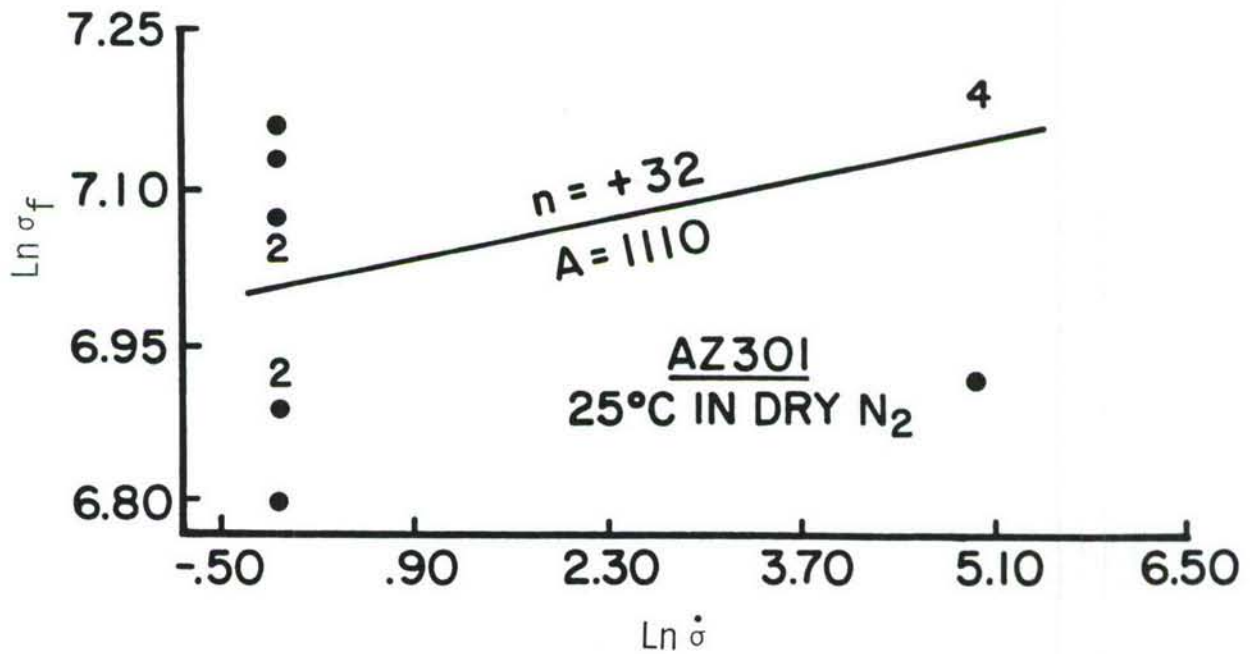


Figure 12. Dynamic fatigue results for AZ301 at 25°C in Dry  $\text{N}_2$ .

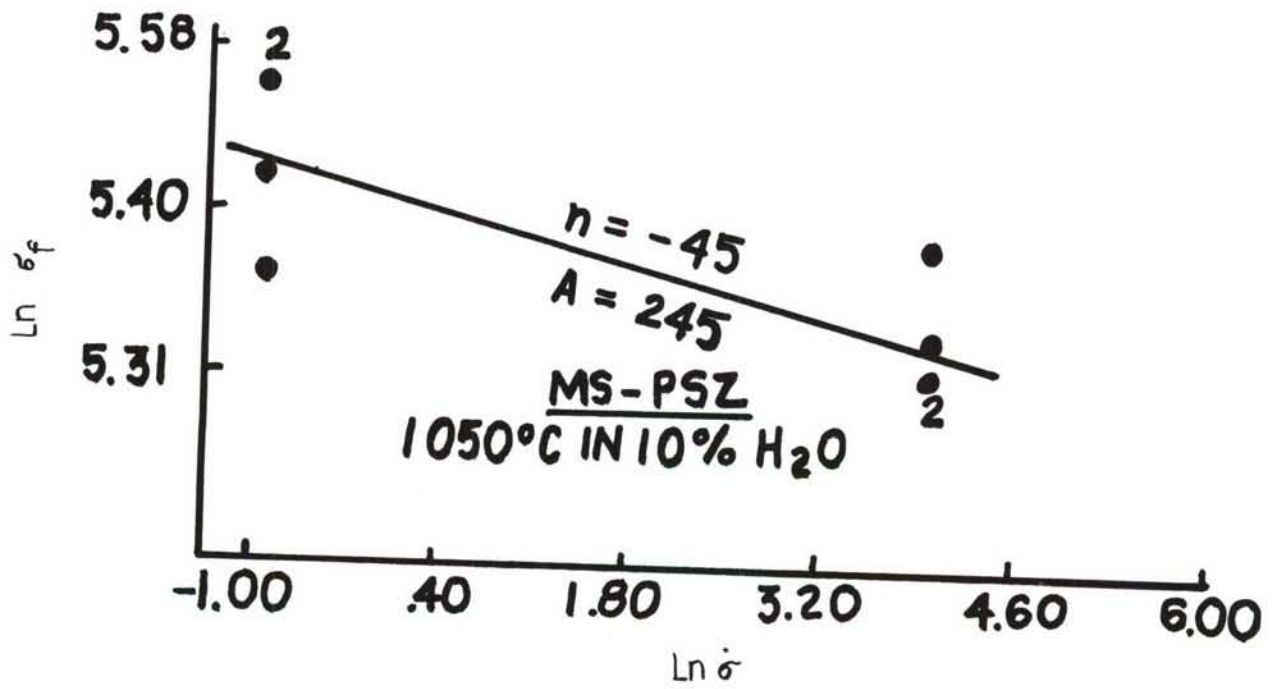


Figure 13. Dynamic fatigue results for MS-PSZ at 1050°C in 10% H<sub>2</sub>O.



Table 10. Summary of XRD Data for Materials Evaluated.

Material/ Condition	Z191		CTZP		MS-PSZ		Z201		AZ301	
	% Mono	Major* Phase	% Mono	Major* Phase	% Mono	Major* Phase	% Mono	Major* Phase	% Mono	Major* Phase
As-Received	7	T	1	T	23	T	3	T	28	T
After MOR <sub>RT</sub>	7	T	0	T	23	T	-	-	36	T
After MOR <sub>250</sub> Dry N <sub>2</sub> (ff)	7	T	0	T	21	T	0	T	33	T
After MOR <sub>250</sub> 10% H <sub>2</sub> O (ff/sf)	7/8	T	0/0	T	24/25	T	3/6	T	42/34	T
After MOR <sub>800</sub> Dry N <sub>2</sub> (ff)	4	T	0	T	17	T	0	T	36	T
After MOR <sub>800</sub> 10% H <sub>2</sub> O (ff/sf)	0/15	T	0/0	T	21/21	T	0/0	T	37/42	T
After MOR <sub>1050</sub> Dry N <sub>2</sub> (ff/sf)	0/0	T	0/0	T	66/77	M	0/0	T	24/25	T
After MOR <sub>1050</sub> 10% H <sub>2</sub> O (ff/sf)	0/0	T	0/0	T	88/50	M	0/0	T	21/17	T

\*Major ZrO<sub>2</sub> phase: T - tetragonal; M - monoclinic (mono).

Table 11. Results of XRD Analysis After Aging.

Material	As-Received	Percent Monoclinic (MP)*			After 250°C Dry N <sub>2</sub>	After Vacuum Treatment
		After 250°C in 10% H <sub>2</sub> O	After 300°C/800°C in 10% H <sub>2</sub> O			
Z191	7(t)	9(t)	10(t)	--	--	--
AZ301	28(t)	33(t)	27(t)	26(t)	--	--
Z201	3(t)	4(t)	4(t)	--	--	--
CTZP	1(t)	0(t)	0(t) <sup>+</sup>	--	--	--
XS121	30(t)	64(m)	60(m)	48(t)	--	--
XS241	11(t)	46(c)	42(c)	31(c)	16(t)	16(t)
MS-PSZ	23(t)	32(t)	33(t) @ 800°C	28(t)	--	--
TS-PSZ	33(t)	43(t)	41(t) @ 800°C	41(t)	37(t)	37(t)

\*MP - Major ZrO<sub>2</sub> crystal phase: m - monoclinic; t = tetragonal; c = cubic.

+CTZP - 0% m @ 300°C and 150°C.

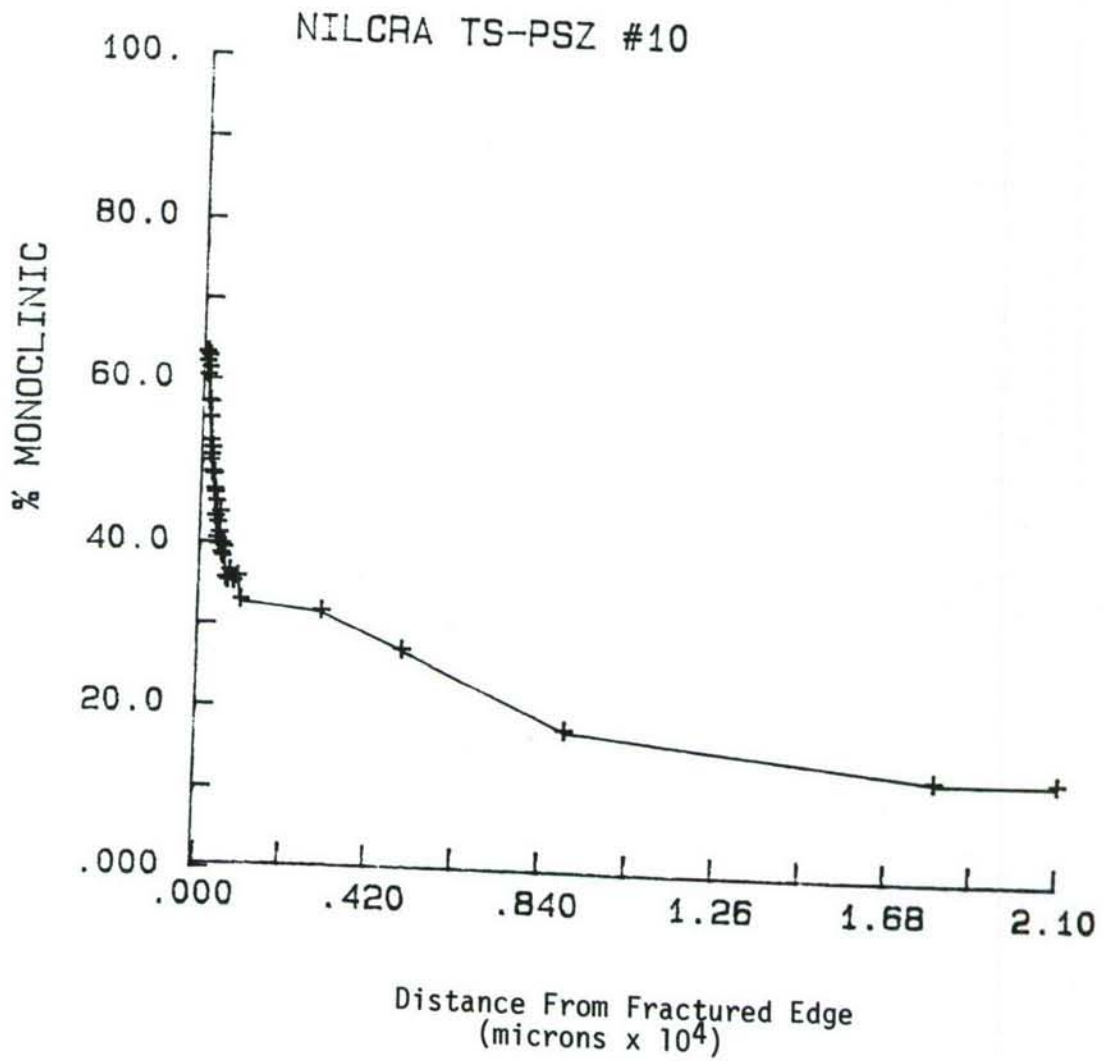


Figure 14. Monoclinic fraction versus distance from fractured edge.



Table 12. MOR Test Results of Aged Samples.

Material	MOR As-Received (MPa)	MOR After Initial Aging (MPa)	MOR After Advanced Aging (MPa)	MOR After Aging in Dry N <sub>2</sub> (MPa)	MOR After Aging in Vacuum (MPa)
Z191	1004	957	-	-	-
AZ301	1265	1206	-	-	-
Z201	957	791	-	-	-
CTZP	481	481	492 (@ 150°C)	-	-
XS121	556	556	645*	607	-
XS241	777	729	519*	475	568**
MS-PSZ	679	674	-	-	-
TS-PSZ	677	608	662*	648	499**

\*120 hrs @ 250°C.

\*\*168 hrs @ 250°C.

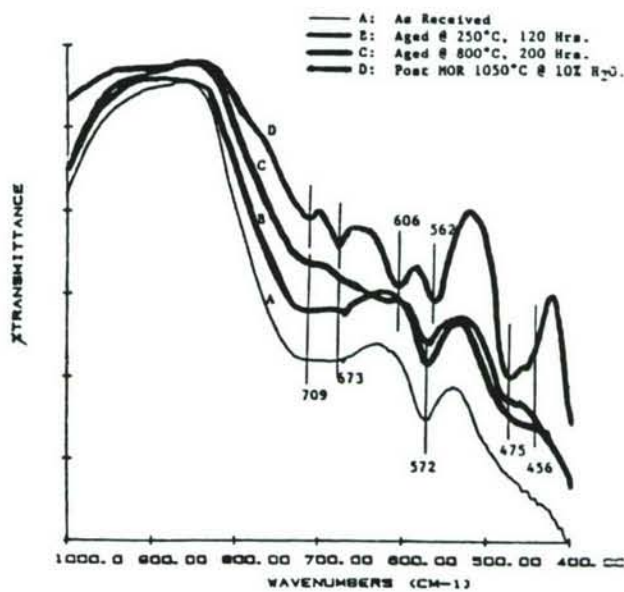


Figure 15. ATR FTIR spectra for MS-PSZ.

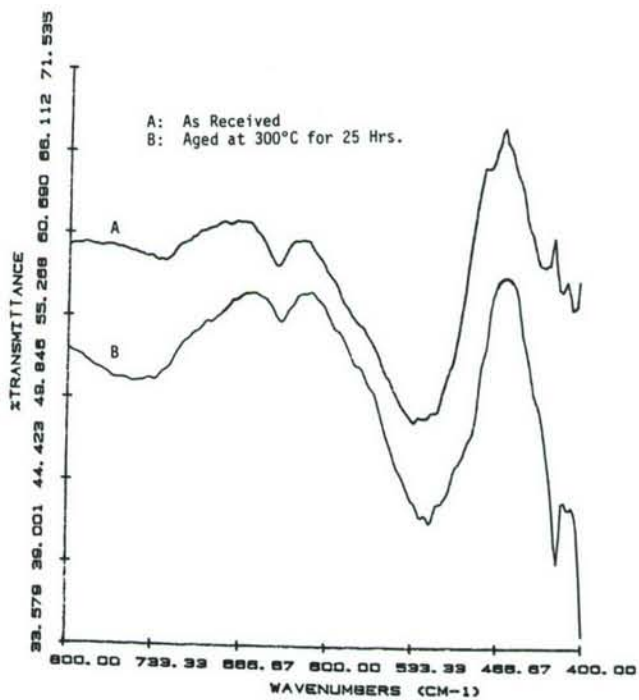


Figure 16. ATR FTIR spectra for AZ301.

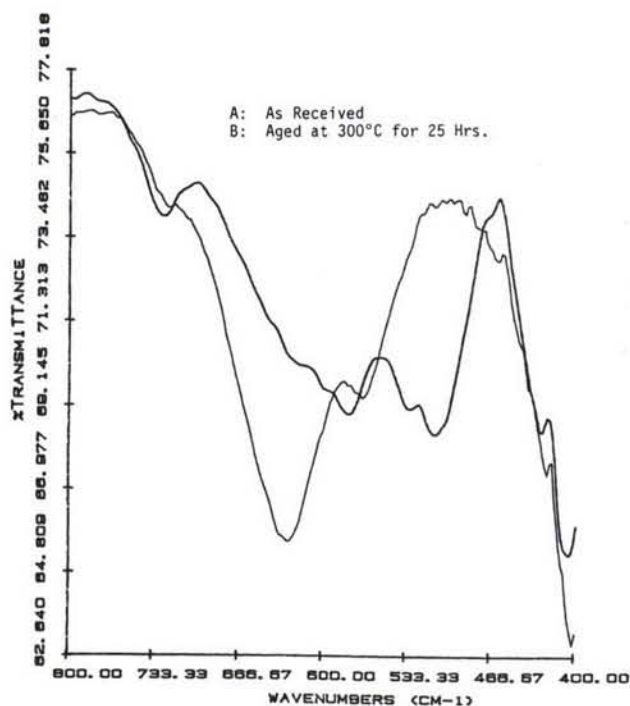


Figure 17. ATR FTIR spectra for Z191.

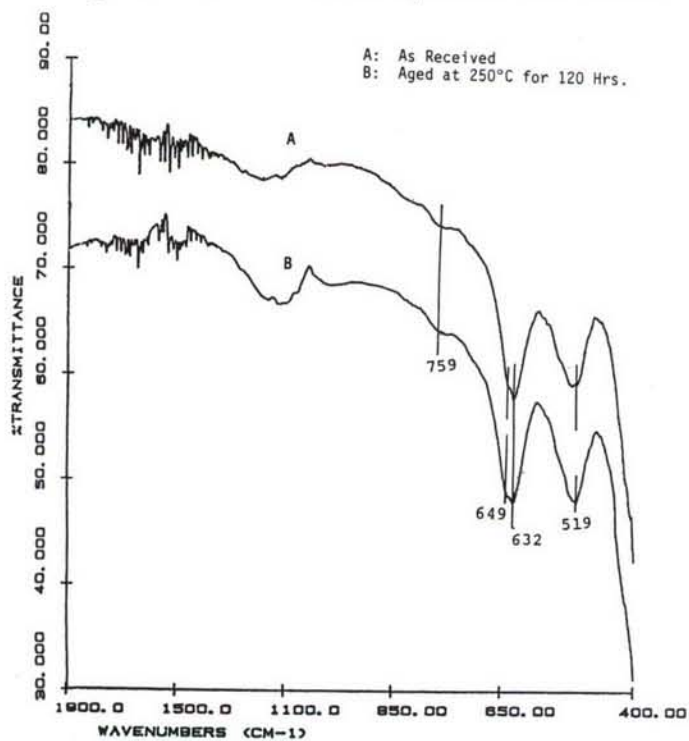


Figure 18. ATR FTIR spectra for CTZP.



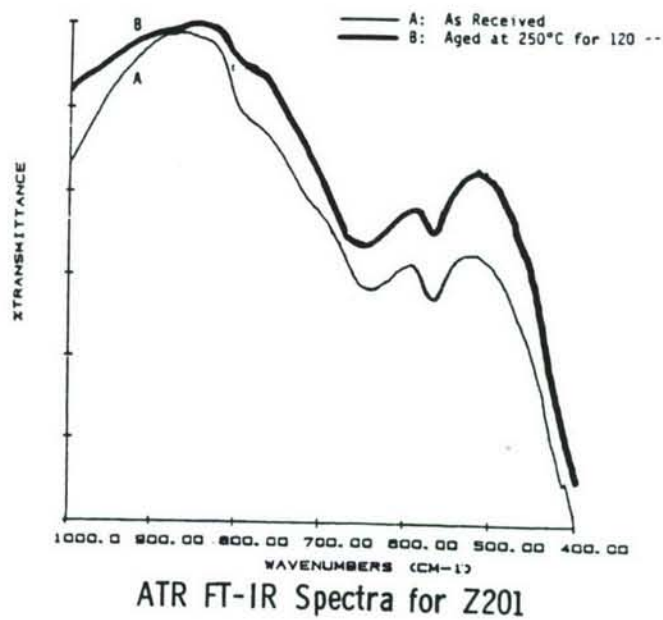


Figure 19. ATR FTIR spectra for Z201.

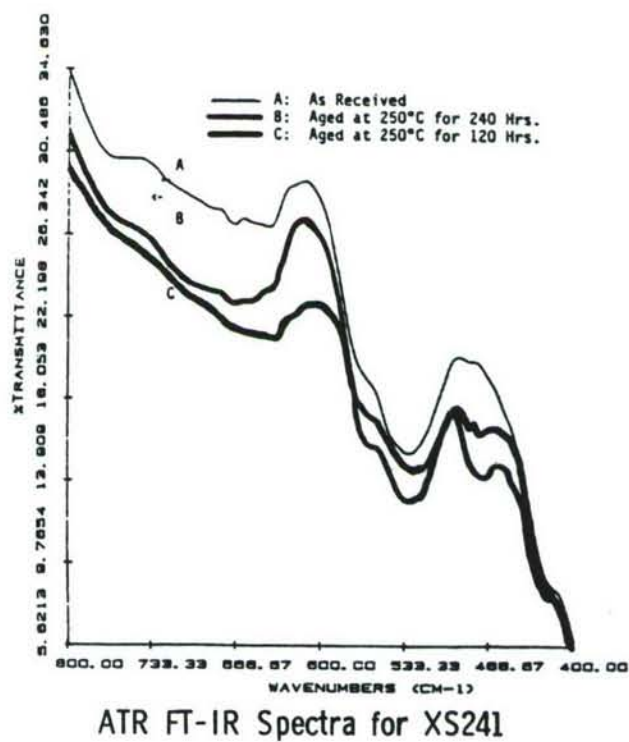


Figure 20. ATR FTIR spectra for XS241.

for study. Discs of each powder were prepared by dry pressing and then sintering at 1400°C for 20 hours. Discs from each group were aged at 250°C in both 10% water vapor, dry N<sub>2</sub>, and vacuum (see Table 5). Discs in the as-prepared state and after aging were analyzed by SEM, XRD, and ATR FTIR. A summary of the XRD data obtained is presented in Table 13, and the IR spectra obtained is presented in Figures 21 through 23. The effects of aging treatments on the 2 and 4 mole percent of the Y<sub>2</sub>O<sub>3</sub> stabilized ZrO<sub>2</sub> was also studied by Raman spectroscopy. The aging of the 2Y and 4Y discs in dry N<sub>2</sub> and 10% H<sub>2</sub>O at 250°C was investigated by the Raman spectroscopy procedures described in our last semiannual report. The tetragonal peak at 146 cm<sup>-1</sup> were selected for computing the monoclinic pair at 178 and 188 cm<sup>-1</sup> were selected for computing the monoclinic fraction present. The spectra obtained for the unaged 2Y material is shown in Figure 24 and the spectra obtained for the 2Y material aged in dry N<sub>2</sub> and 10% H<sub>2</sub>O for 48 hrs at 250°C are presented in Figures 25 and 26. The spectra obtained for the 4Y material in the as-received and after aging at 10% H<sub>2</sub>O for 50 hours at 250°C are presented in Figures 27 and 28. The 2Y and 4Y discs aged in vacuum for 168 hours were also analyzed by Raman. The spectra obtained for the 2Y aged in vacuum is shown in Figure 29, and the spectra for the 4Y aged in vacuum is shown in Figure 30.

Results obtained in Task III. As reported, the Nilcra MS-PSZ and the Kyocera AZ301 material were selected for more detailed investigation. The results of the MOR values obtained for the selected matrix test conditions are presented in Table 14. A statistical analysis of the data obtained and an evaluation of the slow crack growth are under study.

Analysis of Results. The flexure strength of the transformation toughened ceramics decreased linearly with increasing temperature. Except for the AZ301 material, the transformation toughened ceramics have an average flexure strength of about 200 MPa at 1050°C. The AZ301 material has a room temperature flexure strength in excess of 1200 MPa and an average flexure strength of almost 600 MPa at 1050°C. The MOR measurements made in dry N<sub>2</sub> tended to be higher than those made in N<sub>2</sub> with 10% H<sub>2</sub>O. In addition, the MOR measurements made using the rapid loading rate tended to be higher than the measurements made using the slow loading rate. Although the rapid decline in strength with increasing temperature is of concern, it should be recognized that fully stabilized ZrO<sub>2</sub> has an average flexure strength of 245 MPa at room temperature and an average flexure strength of 145 MPa at 1000°C. The transformation toughened ceramics tend to have flexure strength about 40% higher than the values reported for fully stabilized ZrO<sub>2</sub>.

The plastic deformation observed in the Z191 and Z201 when slow loaded at 1050°C is consistent with the creep behavior reported (1). The very fine particle size ~0.3 μ and the presence of SiO<sub>2</sub> is thought to account for the deformation behavior observed. It is believed that this deformation or creep is due to grain boundary sliding and plastic flow.

From the dynamic fatigue data it was found that about 70% of the calculated slopes were positive and the remaining slopes were zero or negative. The significance of the negative values is not completely understood but may be due to the closing of cracks during phase transformation. The

Table 13. Results of XRD Analysis After Aging.

Material	As-Received	Percent Monoclinic (MP)*		
		After 250°C in 10% H <sub>2</sub> O	After 250°C Dry N <sub>2</sub>	After Vacuum Treatment
2Y	11(t)	93(m)	90(m)	74(m)
3Y	0(t)	66(m)	22(t)	0(t)
4Y	0(t)	0(t)	0(t)	0(c)

\*MP - Major ZrO<sub>2</sub> crystal phase: m - monoclinic; t - tetragonal; c - cubic.



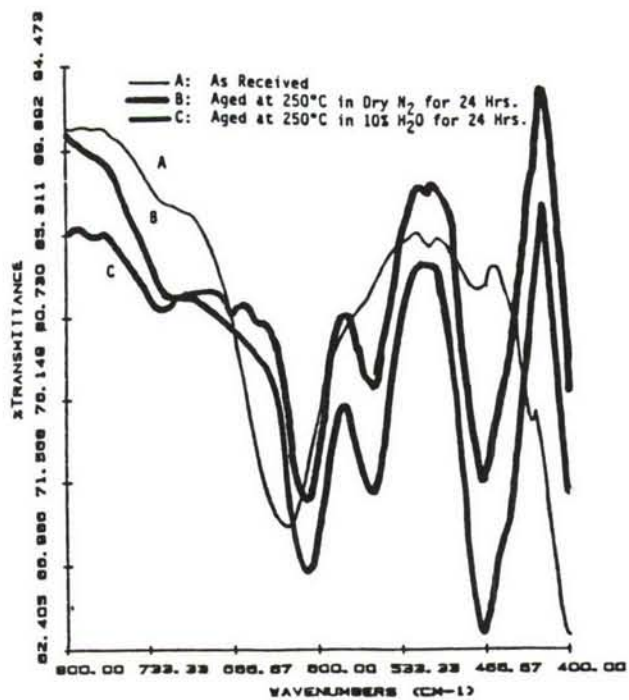


Figure 21. ATR FTIR spectra for Z-2Y.

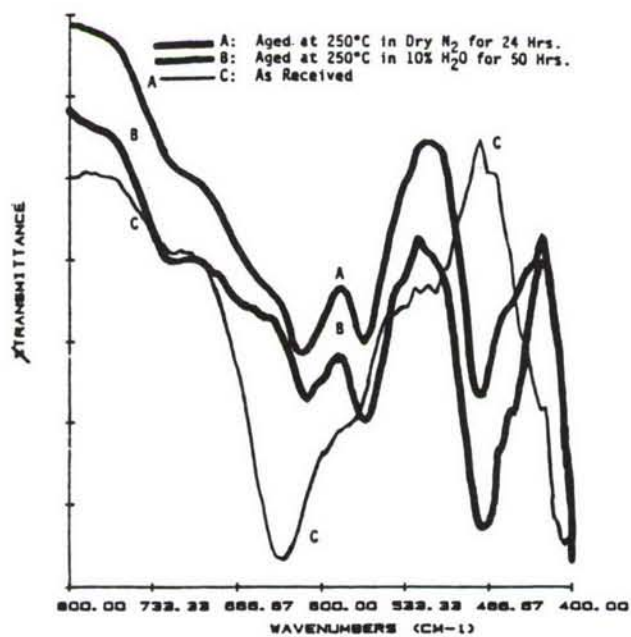


Figure 22. ATR FTIR spectra for Z-3Y.

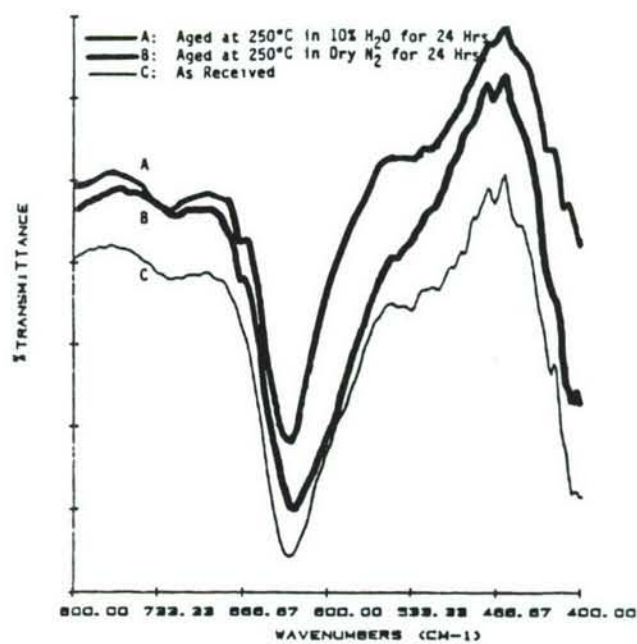


Figure 23. ATR FTIR spectra for Z-4Y.

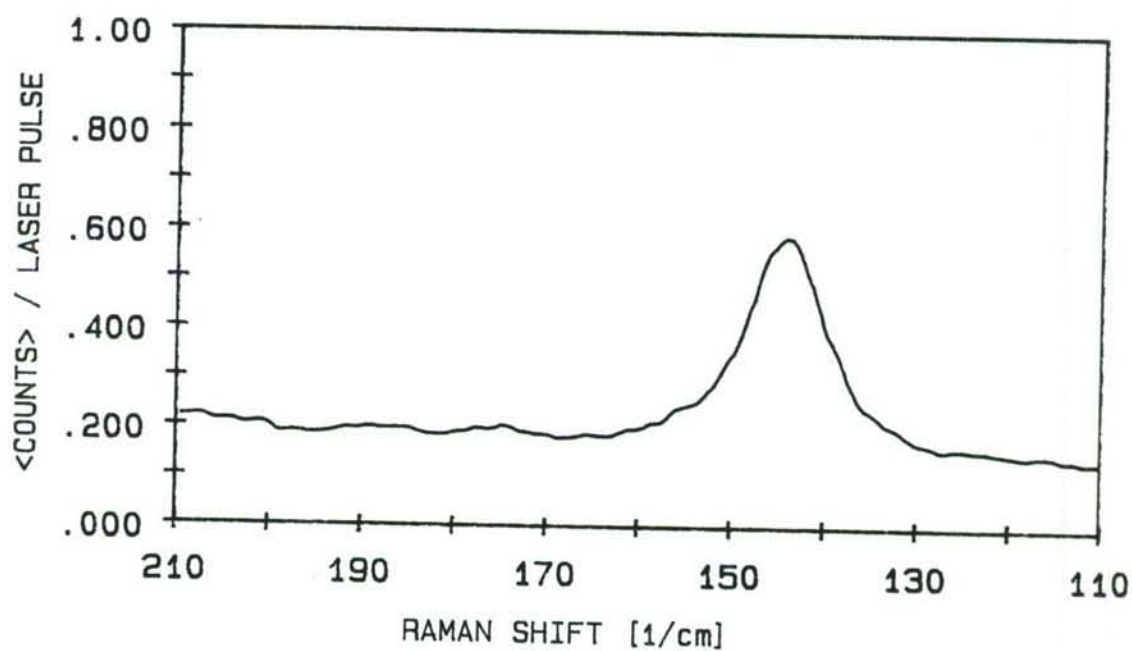


Figure 24. 2% yttria stabilized zirconia, not aged.

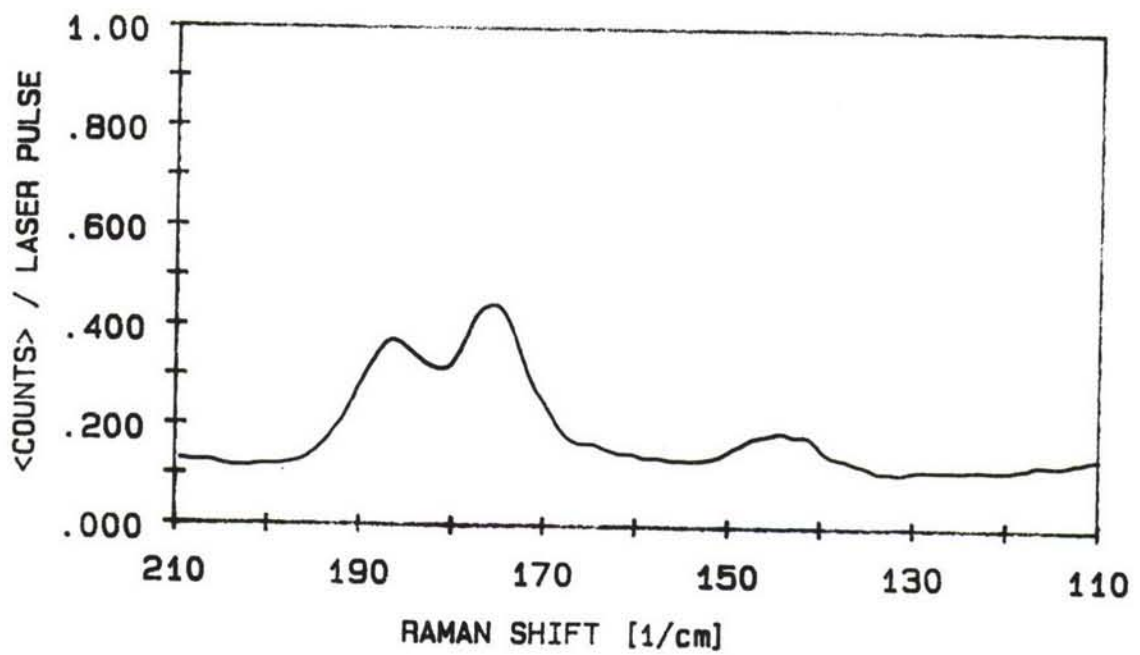


Figure 25. 2% yttria stabilized zirconia, aged 48 hours in dry nitrogen.

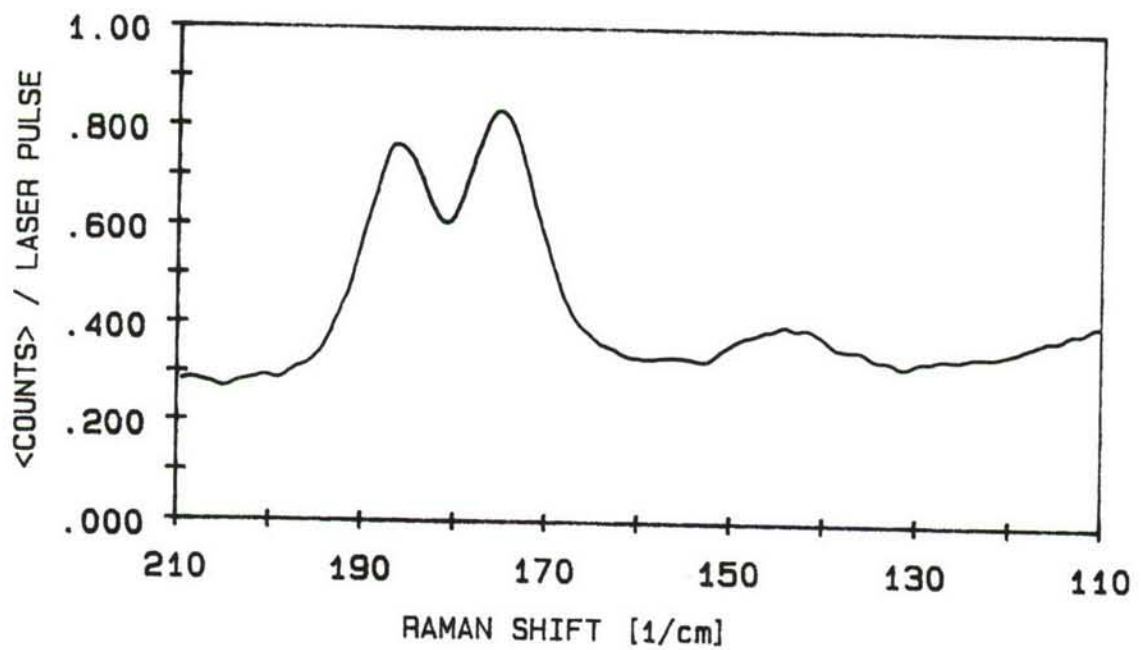


Figure 26. 2% yttria stabilized zirconia, aged 48 hours in 10% water vapor.



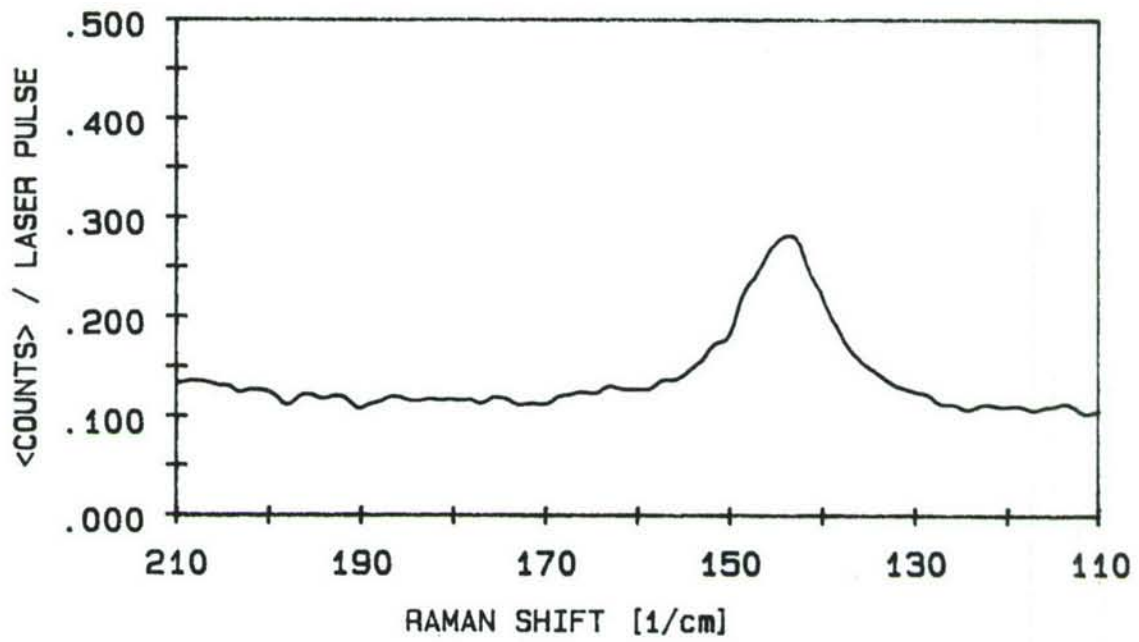


Figure 27. 4% yttria stabilized zirconia, not aged.

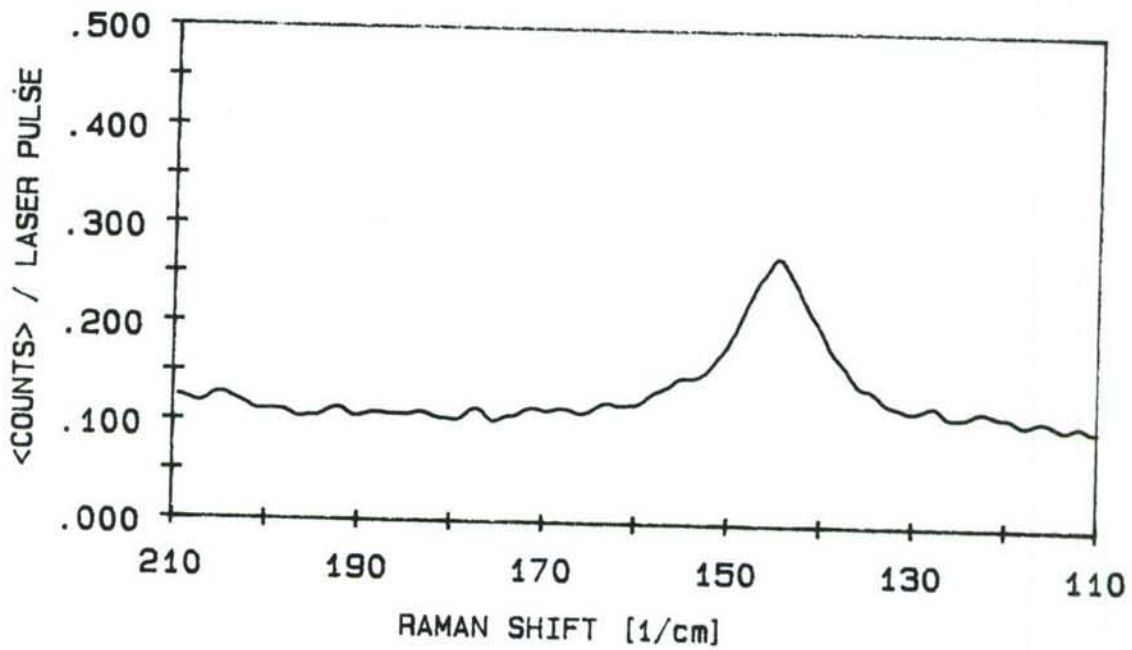


Figure 28. 4% yttria stabilized zirconia, aged 50 hours in 10% water vapor.

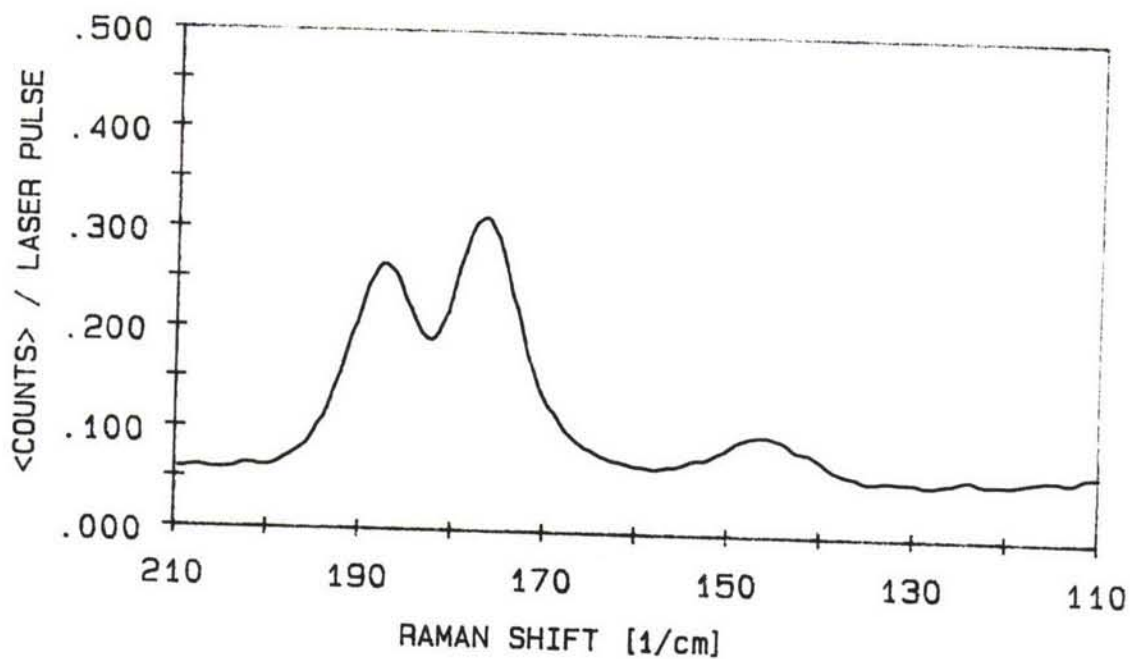


Figure 29. 2% yttria stabilized zirconia, aged 168 hours in vacuum.

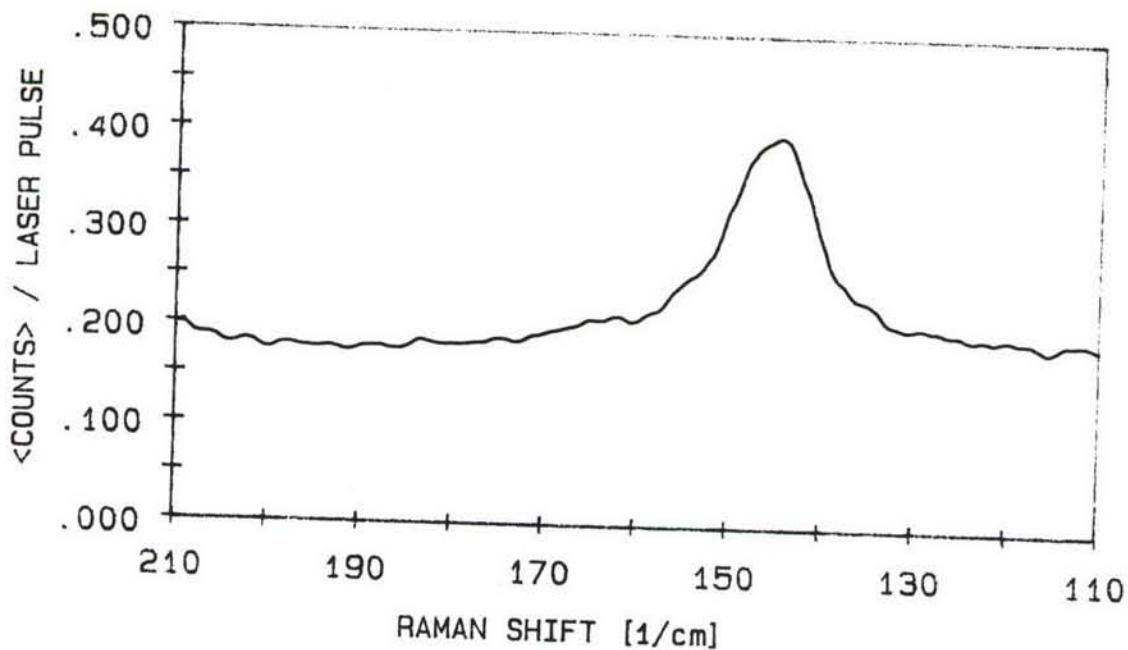


Figure 30. 4% yttria stabilized zirconia, aged 168 hours in vacuum.

Table 14. Flexure Test Results for Task III.

Test Temperature (°C)	Test Atmosphere	<u>Kyocera AZ301</u>		
		Average MOR (MPa)		
		Crosshead Speed (cm/s)		
		0.00004	0.0021	0.0064
25	Dry N <sub>2</sub> 10% H <sub>2</sub> O	1106	1157	1131
		949	920	836
250	Dry N <sub>2</sub> 10% H <sub>2</sub> O	-	-	997
		808	967	938
800	Dry N <sub>2</sub> 10% H <sub>2</sub> O	-	-	813
		655	807	681
		<u>Nilcra MS-PSZ</u>		
25	Dry N <sub>2</sub> 10% H <sub>2</sub> O	615	574	675
		545	557	611
250	Dry N <sub>2</sub> 10% H <sub>2</sub> O	-	-	531
		461	466	523
800	Dry N <sub>2</sub> 10% H <sub>2</sub> O	-	-	250
		249	202	238



positive slopes obtained for the Z191 and Z201 at 1050°C are due to the plastic deformation found to occur at the slow loading rates above 1000°C. About 50% of the calculated  $n$  values were found to be statistically significant. Calculated slope values  $\left(\frac{1}{n+1}\right)$  were designated as statistically valid if the difference between average MOR for the two loading rates was significantly different from zero at 0.05 level of significance (95% level of confidence). It is believed that the poor level of confidence obtained in these calculations is due to the limited number of test samples used for each data point. Ritter et al. (2) have reported that a minimum of 30 test samples and possibly as many as 100 test samples may be required to obtain a statistically reliable evaluation of slow crack growth by dynamic fatigue.

A preliminary analysis of these results indicates subcritical crack growth in the MS and CTZP materials due to water corrosion at 25°C and 250°C. The AZ301, MS, and Z201 materials exhibited subcritical crack growth in dry  $N_2$  at 25°C. This subcrack growth may be due to minute quantities of water trapped at the crack tip or to some other mechanism not associated with water corrosion.

Significant decreases in flexure strength due to aging was only observed in the Z201 and the XS241 materials. Reduction in flexure strength due to aging was the most pronounced in the XS241 material aged for 120 hours at 250°C (~35% reduction). The aging treatment also resulted in an increase in the flexure strength measured for the XS121 material. The TS materials showed a decrease in MOR after aging in vacuum.

The aging studies for the commercial materials provided several unexpected results. The MS and TS materials were found to be susceptible to aging treatments at both 250°C and 800°C. The amount of premature transformation to the monoclinic crystal phase was the same at both aging temperatures. The XS241 material underwent considerable transformation to the monoclinic crystal phase during aging at both 300°C and 250°C. Transformation occurred in both the 10% water vapor and dry  $N_2$  environments. Of particular interest for the XS241 material was the conversion of a majority of the  $ZrO_2$  to the cubic phase. This transformation could not be readily explained, however, it is known that this material contains about 10%  $Al_2O_3$  and this second phase may affect the transformation process. The aging effects observed in the XS241 material under dry  $N_2$  conditions were also observed in the XS121 and TS materials.

For the 2Y, 3Y, and 4Y samples, the XRD data and IR and Raman spectra clearly demonstrated that the 2Y and 3Y materials were susceptible to the effects of aging in the presence of  $H_2O$  vapor and in dry  $N_2$ . The 4Y material was not affected by the different aging treatments and retained the tetragonal crystal structure.

The 2Y, 3Y, and 4Y samples aged in a vacuum underwent some unexpected changes. The 4Y transformed from tetragonal to cubic, the 2Y transformed approximately 70% to monoclinic, and the 3Y remained tetragonal. The transformation of 2Y to monoclinic after vacuum aging has also been reported by Iio, et al. (3). The XS241 and TS materials showed only a small increase in monoclinic phase after vacuum aging, however, they exhibited a significant decrease in MOR. It would appear that thermal

aging without the presence of water can cause degradation of the toughened  $\text{ZrO}_2$  ceramics, under certain conditions of grain size and percent stabilizer.

#### Future plans

The MOR testing matrix plan will be completed for the AZ301 and MS-PSZ materials. The statistical analysis of the test data will be completed, and a research plan for future work will be developed based on the results of the current study program.

#### Status of milestones

Milestone 331402 has been completed and Milestone 331403 has been completed. Milestone 331405 is in progress.

#### References

1. David C. Larsen and Jane W. Adams, Long-Term Stability and Properties of Zirconia Ceramics for Heavy Duty Diesel Engine Components, Final Report, DOE/NASA/0305-1, NASA CR-174943, September 1985.
2. J. E. Ritter, et al., Statistical Reproducibility of the Dynamic and Static Fatigue Experiments, University of Massachusetts, Amherst, MA (U.S. Department of Commerce NTIS), October 1980.
3. S. Iio, M. Watanabe, K. Kuroda, H. Saka, and T. Imura, Tetragonal to Monoclinic Transformation in Y-TZP During Low Temperature Aging, paper presented at The 3rd International Conference on the Science and Technology of Zirconia, Tokyo, Japan, September 9-11, 1986.



### 3.4 FRACTURE MECHANICS

#### Improved Methods for Measuring the Fracture Resistance of Structural Ceramics

R. C. Bradt and A. S. Kobayashi (University of Washington)

##### Objective/Scope

The long-term goals of this study are to develop and demonstrate a technique comprising a single measurement, or a technique comprising a set of correlative measurements for structural ceramics including monolithic and composite materials which will allow for the reliable and accurate determination of their resistance to fracture (crack propagation) over a broad temperature range from 25 C to 1400 C.

##### Technical Progress

The laser interferometric strain gage (LISG) has been successfully used in fracture tests conducted at 1400 C. The tests were performed using monolithic silicon nitride (GTE A2Y6) straight-notched, three-point bend specimens. Successful completion of these tests demonstrates the integrity of the ceramic adhesive bond between the platinum targets and the specimen, and the elevated temperature capability of the LISG. This temperature is the highest temperature application of the LISG reported to date.

The three dimensional finite element analysis of the chevron-notched, three-point bend specimen has been completed. The model consists of eight-noded (3 DOF/node) bricks with approximately 2100 total degrees-of-freedom in the solution. When compared with the Bluhm slice model and the Sakai modified slice model, the 3-D solution has consistently demonstrated a stiffer load point compliance relationship.

The completion of this modeling has produced two important results. The first is the relationship between the crack mouth opening displacement (CMOD) and the load point displacement (LPD). The former is measured by the LISG and the latter is necessary for energy calculations during crack extension. The relationship between the two is a linear elastic one. Since the measurement of the CMOD is completely independent of the machine compliance, the determination of the LPD from the CMOD measurement completely eliminates all of the errors associated with the "test-rig" compliance at elevated temperatures. The second result of the analysis is that modifications have been made to the previously reported solution of Sakai for the dimensionless stress intensity factor of the chevron-notched, three-point bend specimen. An example of the results of these modifications is shown in Figure 1.



The validity of the LPD/CMOD relations and the modification of the stress intensity factor were demonstrated for room temperature tests of the silicon nitride (GTE A2Y6) and the silicon carbide (Hexology). The good agreement between the calculated LPD and the measured LPD is shown in a sample load/displacement plot of Figure 2. Table I contains the comparisons between the three-dimensional finite element results and other methods for the work-of-fracture and fracture toughness.

Crack growth resistance curves (R-curves) were generated for room temperature fracture data for silicon nitride (GTE A2Y6) and silicon carbide (Hexology) chevron-notched, three-point bend specimens. The fracture resistance is determined from the stable crack growth region observed after the maximum test load in the load/displacement plots. The results of the finite element analysis and the revised computer program were used to calculate the R-curves from the digitized load/CMOD data. Figure 3 shows the characteristically flat R-curves generated for both the silicon nitride and the silicon carbide at room temperature.

The arrival of the two types of composite materials has completed the acquisition of all the materials for the test program. The two composites are a 25% SiC whisker/ $\text{Al}_2\text{O}_3$  matrix material from ARCO Metals Co. and a CVD SiC/SiC material from Refractory Composites, Inc.

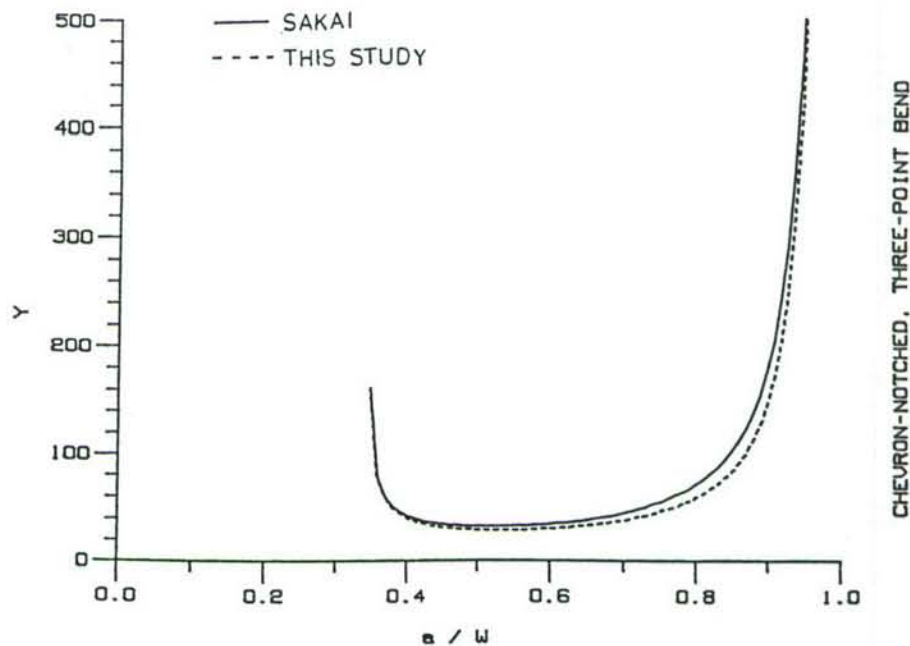
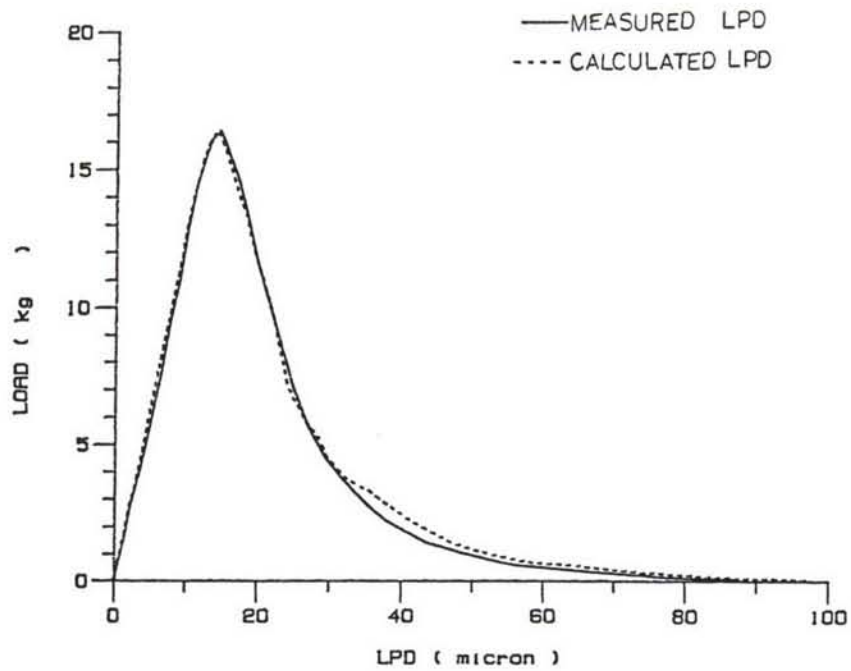
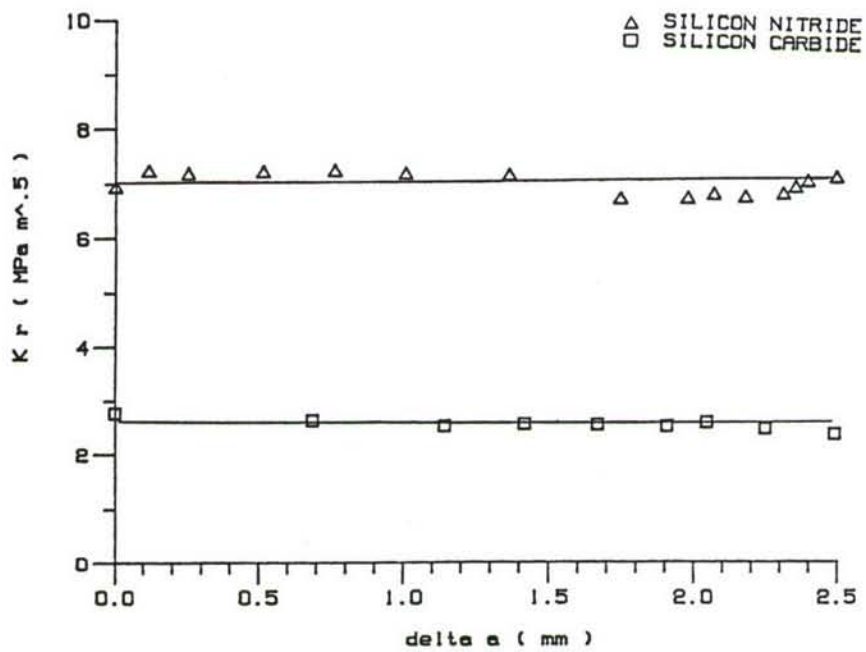


FIGURE 1 COMPARISON OF GEOMETRY CORRECTION FACTOR VERSUS NORMALIZED CRACK LENGTH FOR  $\alpha_0 = 0.35$ .



CHEVRON-NOTCHED, THREE-POINT BEND

FIGURE 2 COMPARISON OF LOAD VERSUS MEASURED AND CALCULATED LPD FOR A SILICON NITRIDE.



CHEVRON-NOTCHED, THREE-POINT BEND

FIGURE 3 R-CURVES FOR A SILICON NITRIDE AND A SILICON CARBIDE AT ROOM TEMPERATURE.

Table I  
Fracture Results for  
Silicon Nitride and Silicon Carbide

Material/ Sample	Work of Fracture ( J / m <sup>2</sup> )		Fracture Toughness ( MPa m <sup>1/2</sup> )	
	LPD measured	LPD from CMOD	From Sakai [8]	From Modified Sakai
Silicon Nitride : GTE A2V6				
1	85.8	89.9	7.71	6.90
2	80.6	91.5	7.61	6.78
3	90.6	103	7.71	6.88
Average s	85.7 5.0	94.8 7.1	7.68 0.06	6.85 0.06
Silicon Carbide : Sohio Hexoloy				
1	9.91	9.35	2.92	2.72
2	8.54	8.11	3.00	2.76
3	9.52	8.98	3.41	3.25
Average s	9.32 0.71	8.81 0.64	3.11 0.27	2.91 0.29

### Status of Milestones

Progress on some of the proposed milestones which involve elevated temperature tests is lagging. However, the progress involving mathematical modeling of fracture behavior is well ahead of schedule.

Specific problems include difficulty in finding readily obtainable supplies of the composite materials. This difficulty has delayed the initial room temperature tests of those materials. However, the composite materials are now in-house and the testing of these materials is underway.

Additional delays have been encountered with the elevated temperature test equipment. Specific problems include delays associated with iterative modifications of the conventional design of the test furnace in order to accommodate the LISG. The conventional design of the elevated temperature test fixture also had to be modified in order to accommodate the LISG and the upper extremes of testing temperatures.

These delays with the macro-flaw tests at elevated temperatures have in turn delayed the micro-flaw and strength tests, since these tests are dependent on the macro-flaw tests. However, with the completion of proof tests of the test machine, LISG and furnace at the temperature extremes, macro-flaw testing of all the materials for the entire temperature range should be completed before the end of this



calendar year, 1986. The completion of the micro-flaw and the strength test for all the materials for the entire temperature range should be completed soon after the completion of the micro-flaw tests.

Although physical testing has been delayed, progress has been substantial in the mathematical modeling of both linear and non-linear behavior during fracture. Completion of room temperature tests of the monolithic and composite materials has allowed the application of this modeling. Analysis of these data has demonstrated consistent, reliable results.

### Publications

The following papers have been submitted for publication:

Fracture Toughness Testing of Ceramics Using a Laser Interferometric Strain Gage, in review by the American Ceramic Society.

Crack Initiation and Arrest in a SiC Whisker/ $\text{Al}_2\text{O}_3$  Ceramic-Ceramic Composite, accepted by the American Ceramic Society.

The following papers are being finalized for submission for publication:

1. Fracture Resistance in a SiC Whisker/ $\text{Al}_2\text{O}_3$  Matrix Composite.
2. A 3-D Finite Element Analysis of the Chevron-Notched, Three-Point Bend Fracture Specimen.
3. Elevated Temperature Fracture Resistance of a Silicon Nitride.

### References

1. Bluhm, J.I., "Slice Synthesis of a Three Dimensional Work of Specimen," *Engineering Fracture Mechanics*, 7, 593-604, (1977).
2. Sakai, M., Yamasaki, K.K., "Numerical Fracture Analysis of Chevron-Notched Specimens: I, Shear Correction Factor, k," *J. Amer. Ceram. Soc.* 66(5) 371-375, (1983).
3. Sakai, M., Yamasaki, K.K., "Numerical Fracture Analysis of Chevron Notched Specimens: II Stability Condition for Crack Growth," *J. Amer. Ceram. Soc.* 66(5), 376-379, (1983).

4. Sakai, M. and Bradt, R.C., "Graphical Methods for Determining the Nonlinear Fracture Parameters of Silica and Graphite Refractory Composites," in: *Proceedings of the Fourth International Symposium on the Fracture Mechanics of Ceramics*, Virginia Polytechnical Institute, (1985).

Testing and Evaluation of Advanced Ceramics at High Temperature in Uniaxial Tension

J. Sankar, V. S. Avva, and R. Vaidyananthan (North Carolina A & T State University)

Objectives/Scope

The purpose of this effort will be to test and evaluate advanced ceramic materials at temperatures up to 1500°C in uniaxial tension. Testing may include fast fracture strength, stepped static fatigue strength, and cyclic fatigue strength, along with analysis of fracture surfaces by scanning electron microscopy. This effort will comprise the following tasks:

- Task 1. Specifications for Testing Machine and Controls + (Procurement)
- Task 2. Identification of Test Material (s) + (Procurement of Specimens)
- Task 3. Identification of Test Specimen Configuration
- Task 4. Specifications for Testing Grips and Extensometer + (Procurement)
- Task 5. Specifications for Testing Furnance and Controls + (Procurement)
- Task 6. Development of Test Plan
- Task 7. High Temperature Tensile Testing
- Task 8. Reporting (Periodic)
- Task 9. Final Report

It is anticipated that this two (2) year program will help in understanding the behavior of ceramic materials at very high temperatures in uniaxial tension.

Technical Progress

During the reporting period calibration and familiarizing of the obtained MTS 880 Automated Materials Testing Machine continued. Further computer programs were developed to conduct both static tension and fatigue tests in this machine. Figure 1 shows the set-up of this machine with computer controls in the background.

Filling up of hydraulic in the hydraulic self-aligning grip system, to be used in the program, consumed part of the reporting period. The hydraulic self-aligning grip system used in this program is similar to the one suggested by K. J. C. Liu of ORNL for his program "Cyclic Fatigue of Toughened Ceramics". Figure 2 shows the close-up view of the hydraulic self-aligning grip system with free floating pistons. The operational principle of the system is that the specimen load which acts through the center of the grip system, will be balanced by the reactive forces generated by the eight pistons in the circular assembly. With



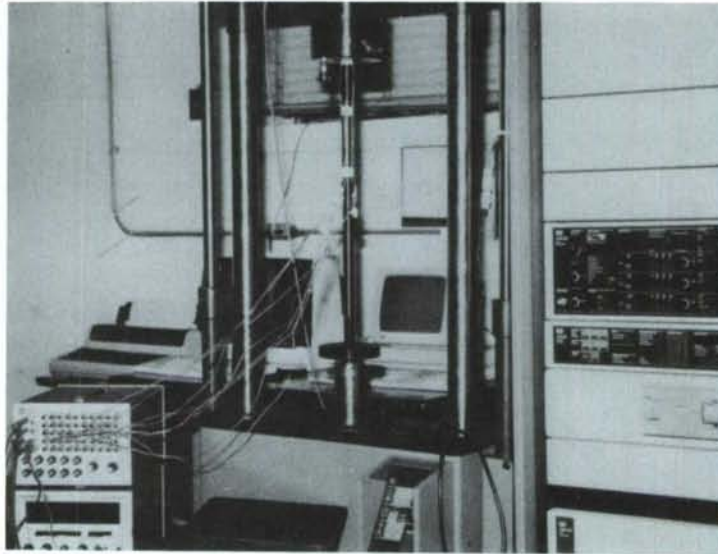


Fig. 1. MTS 880 Automated Materials Testing Machine with Computer Controls.

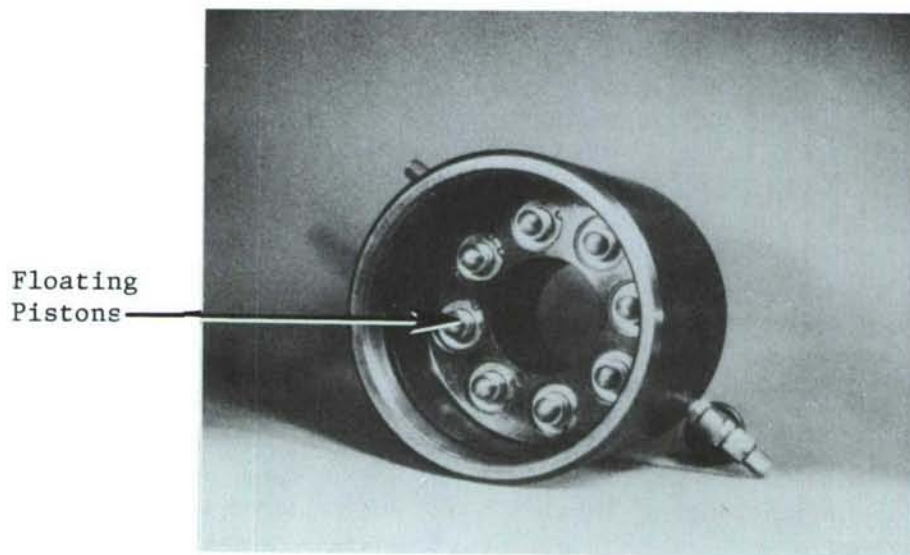


Fig. 2. Hydraulic self-aligning system with free floating pistons.

the equal reactive forces and the forces being equally spaced in a circle ideal concentricity can be achieved. For further detail, refer to Liu's report [1].

The set-up used to fill the hydraulic in the reservoir of the grip system is shown in Figure 3. First the hydraulic reservoir area was evacuated using a vacuum pump. Then using special one-way valves the hydraulic Texaco HD 46 was filled in the reservoir container using the created vacuum force and gravity. The pistons were pulled in and out sufficiently to release the air traps, if any, in the system.

Right now the mechanical testing equipment and the grip systems are being evaluated for their alignment characteristics. The Uni-Axiality of the self aligning hydraulic grip mechanism was tested with the help of a special "spider arm" load applicator instrumented with strain gages, as shown in Figures 4-6. Four sets of strain gages were bonded on the radial cantilever arms to monitor the distribution of the resulting tensile and compressive strains on the arms after application of load. Eight tests were performed. For each test, the load applicator was rotated by 45 deg. and the strains were measured on each arm using a switching and balancing unit and a digital strain indicator. A quarter bridge circuit was used for the strain measurement. The strains were monitored continuously while a tensile load was being applied. A load range of 4 kips was used and the strains were measured while the load was varied using the Set Point control, the maximum load being 3.2 kips (80% of the load range). To counter the transverse sensitivity of the foil strain gages, the strains were measured both during the loading and unloading cycles. Initial examination showed that there was good reproducibility of the data from cycle to cycle.

#### Status of Milestones

Tasks 1-4 are complete. High temperature grips are being fabricated now. Furnace specifications and extensometry are being modified to accommodate the new high temperature grip design (Task 5). Tensile samples which are behind schedule by six (6) months are expected to arrive from GTE during the fourth (4) week of December. Test plan for the program (Task 6) is ready and the testing will start as soon as the samples arrive.

#### References

1. K. C. Liu and C. R. Brinkman, "Cyclic Fatigue of Toughened Ceramics," pp. 168-174 in Ceramic Technology for Advanced Heat Engines Project Semiannual Progress Report for Period April 1985-September 1985, ORNL/TM-9947, Oak Ridge National Laboratory, Oak Ridge, Tenn., May 1986.

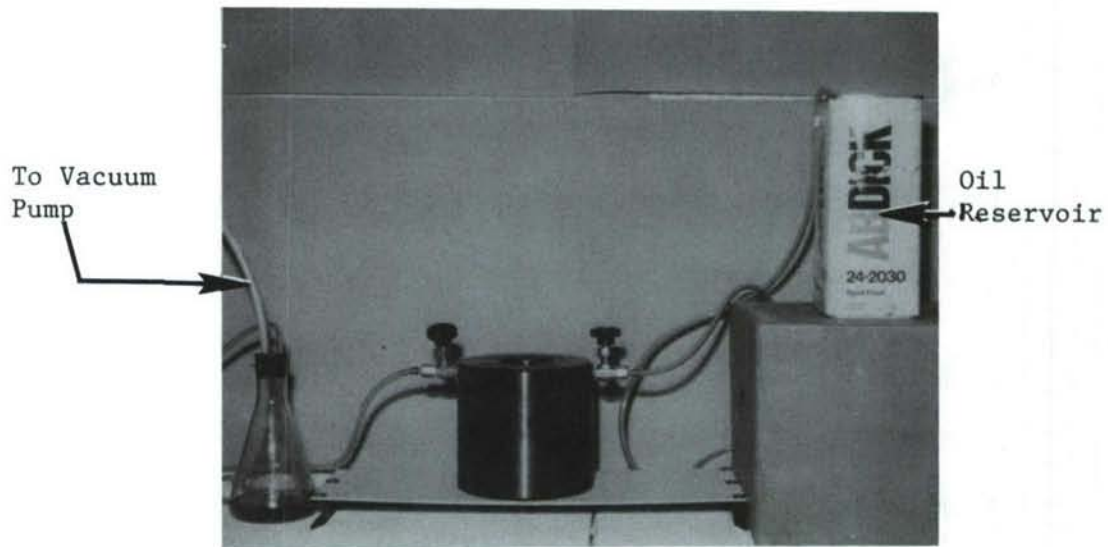


Fig. 3. Set-up for filling hydraulic oil in the self-aligning hydraulic grips.

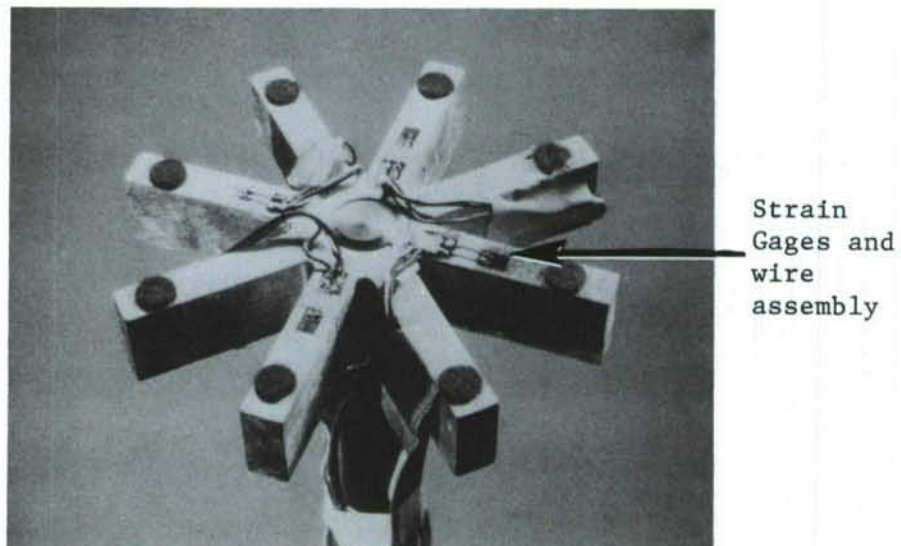
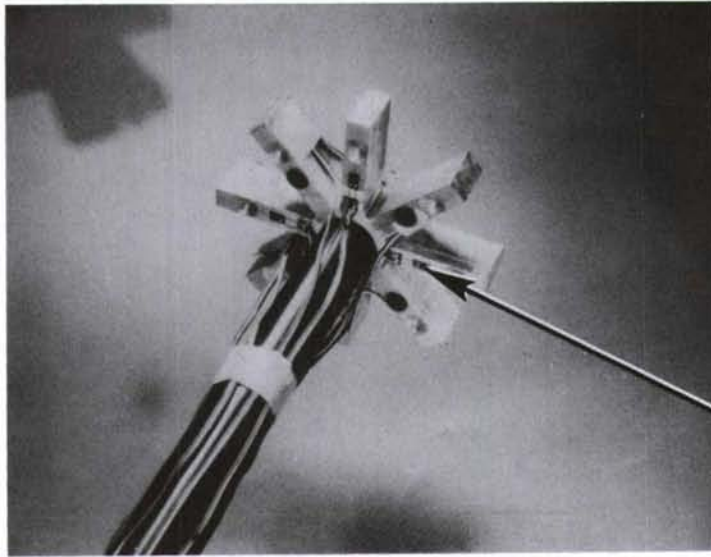


Fig. 4. Top view of the aluminum "Spider Arm" load applicator and calibration rod.





Strain Gages and  
wire assembly

Fig. 5. Bottom view of the Aluminium "Spider Arm" calibration rod.

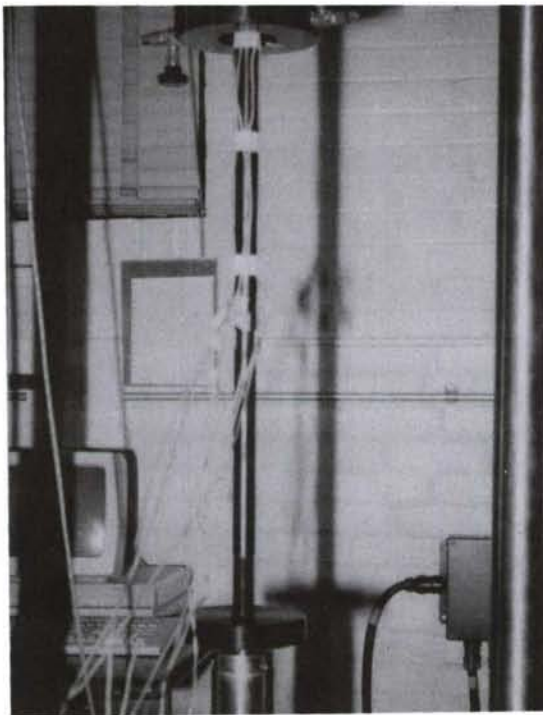


Fig. 6. Close-up view of the calibration set-up.

Standard Tensile Test Development

S. M. Wiederhorn, Leon Chuck, Tze-jer Chuang and D. E. Roberts  
(National Bureau of Standards)

K. Jakus

(University of Massachusetts)

Objective/Scope

This project is concerned with the development of test equipment and procedures for measuring the strength and creep resistance of ceramic materials at elevated temperatures. The goal of the project is to assist in the development of a reliable data base that can be used for structural design of heat engines for vehicular applications.

The mechanical strength of ceramic materials is usually measured in a flexural test configuration because of the ease of conducting such tests on these materials. Flexural tests are also relatively inexpensive to run, requiring a minimum of effort in the way of specimen preparation and test facility construction. Specimens consisting of small rectangular parallel pipeds are prepared by simple grinding and polishing operations, and testing is usually conducted with a simple compressive load train.

Despite the usefulness of flexural testing as a general means of characterizing strength, the technique is not capable of providing critical engineering data for structural design. At low temperatures the technique measures strength on a limited volume, which is usually not adequate for the extreme value statistics required for lifetime prediction on these materials. At elevated temperatures creep occurs in ceramics and as a consequence the stress distribution within the test specimen changes with time, precluding an accurate analysis of the creep and creep rupture process. Crucial for purposes of design, such analyses require testing in pure states of stress: both compressive and tensile testing are required. Whereas compressive testing is relatively simple, tensile testing is not, and there is a pressing need for a relatively inexpensive tensile test that can be used routinely to obtain strength and creep data.

In this program, techniques of measuring the creep and strength of ceramics at elevated temperatures are being developed and evaluated, and will be used to characterize the mechanical behavior of structural ceramics at elevated temperatures. Test methods will be inexpensive, using self aligning test fixtures, and simple grinding techniques for specimen preparation. Creep data obtained with these techniques will be compared with data obtained using flexure and compressive creep techniques.

Technical Highlights

Tensile creep tests on siliconized, silicon carbide specimens prepared by the NBS grinding shop are being carried out at 1300°C at applied stresses ranging from 75 to 130 MPa, for periods of at least 200 hours. The clothespin design tensile fixture, described in the last



report, is being used for these studies. The system is capable of determining displacements to an accuracy of  $\pm 2$  microns, which permits creep rates as low as  $10^{-10}$  sec $^{-1}$  to be measured. In the nine tensile tests conducted to date, the equipment has performed remarkably well. An earlier problem with broken fixtures was corrected by building a stouter fixture. Transition state creep occurs in siliconized, silicon carbide for 20 to 60 hours after load application, depending on the creep rate. Transition state creep lasts a longer time for lower creep rates. This observation suggests that the long time process for transient creep in bending for this material is an artifact of the test and represents a gradual shift in the stress distribution of the specimen as a consequence of the bending.

The transient nature of creep in bending is confirmed by an experimental investigation of the stress dependence of the creep rate, and by a theoretical study of the flexure test configuration. By varying the applied stress from 70 MPa to 130 MPa at 1300°C it was possible to show that the stress exponent for the creep rate increased from approximately 4 between applied stresses of 70 and 100 MPa to approximately 10 between 100 and 130 MPa, figure 1. This increase in the value of the stress exponent was attributed to cavitation creep at the higher loads. Indeed, microscopic examination of the gauge section of the test specimen indicates that considerable cavitation occurs above 100 MPa, whereas below 100 MPa cavitation is sparse. These data are consistent with those collected by Carroll and Tressler at Pennsylvania State University who obtained similar results at 1100°C on the same material.

A theoretical analysis of the flexure configuration has used the findings of this study to predict the shift of the neutral strain axis, and the size of the cavitation zone as a function of creep strain. The model assumes a bilinear creep behavior on the tensile side of the bend bar, and a linear creep behavior on the compressive side of the creep bar. Because of the complexity of the test configuration, a computer solution of the creep problem was necessary. The analysis suggests a gradual increase in the size of the creep cavitation zone and a shift of the neutral axis of the test specimen towards the compressive side of the specimen as the strain increases. Both predictions are consistent with experimental observations conducted on bend bars. Over the coming months, additional data will be obtained to put this type of calculation on a firmer basis. If data and theory are reasonably consistent, this type of calculation will be extended to other more complex configurations.

Since bending in tensile specimens leads to parasitic stresses, which are not a result of the applied tensile stress, a full evaluation of the accuracy and reproducibility of the tensile creep test being developed requires an evaluation of the bending that occurs during the test. The amount of bending is being determined using an apparatus, figure 2, that was designed and constructed for us by Prof. K. Jakus of the University of Massachusetts. The equipment is similar to that of a Talysurf Profilometer, but is capable of measuring surface displacement over much longer distances ( $\approx 5$  cm). The stylus used to contact the surface is a sapphire sphere which reduces wear during contact. The equipment is controlled by a computer so that the curvature of the specimen can be calculated directly from the displacement data.



To date, data has been obtained on three of the nine test specimens used in the present study. A sample of data collected on this apparatus is shown in figure 3, where the inverse radius of curvature of the surface is plotted as a function of position along the surface. The radius of curvature of the as received specimens, figure 3a, exhibits a minimum of  $\approx 10$  meters within the gauge section. The variation in curvature along the gauge section of the specimen is an indication of the surface roughness due to machining of the specimens. After subjecting the specimens to tensile loads under creep conditions, the radius of curvature of the test specimens has decreased from 10 meters to approximately 3 meters, indicating some bending in the test specimen, figure 3b. The strain due to bending is approximately 8 to 10 percent of the total strain in tension.

The apparatus has also been used to measure the radius of curvature of specimens subjected to creep deformation by Carroll and Tressler. Their specimens were much smoother and flatter than ours, having an initial curvature of approximately 30 meters. After testing, the curvature of their specimens was qualitatively the same as our own, being equivalent to a strain in bending of from 6 to 8 percent of the total strain in tension. Perhaps the most interesting observation in this study concerns the variation of curvature along the length of the gauge section. Such variation in curvature was observed on tensile test specimens from both the National Bureau of Standards and Pennsylvania State University, and may arise, in part at least, from non-homogeneous flow of the specimen during deformation. This possibility is currently being explored.

In addition to the creep studies conducted on the clothespin design apparatus, a pin and clevis fixture has been completed and has been used in two creep studies. In this fixture a dogbone specimen, figure 4, is held in the test apparatus by an  $\alpha$ -SiC pin through each end of the specimen. As with specimens for the clothespin design, each specimen is made by simple grinding operations, using a shaped grinding wheel. Specimen cost is approximately the same as that for the clothespin design fixture. Creep is measured from the gauge section of the specimen using flags of the same design as that used earlier in this study. Creep data obtained at 75 MPa and 1300°C indicate a similar behavior to that already obtained in this study: a short transient creep period followed by a lengthy steady state creep period. Within the scatter of the measurements, the creep rate measured in steady state is about the same for the pin and clevis design as that obtained on using the clothespin design.

#### Status of Milestones

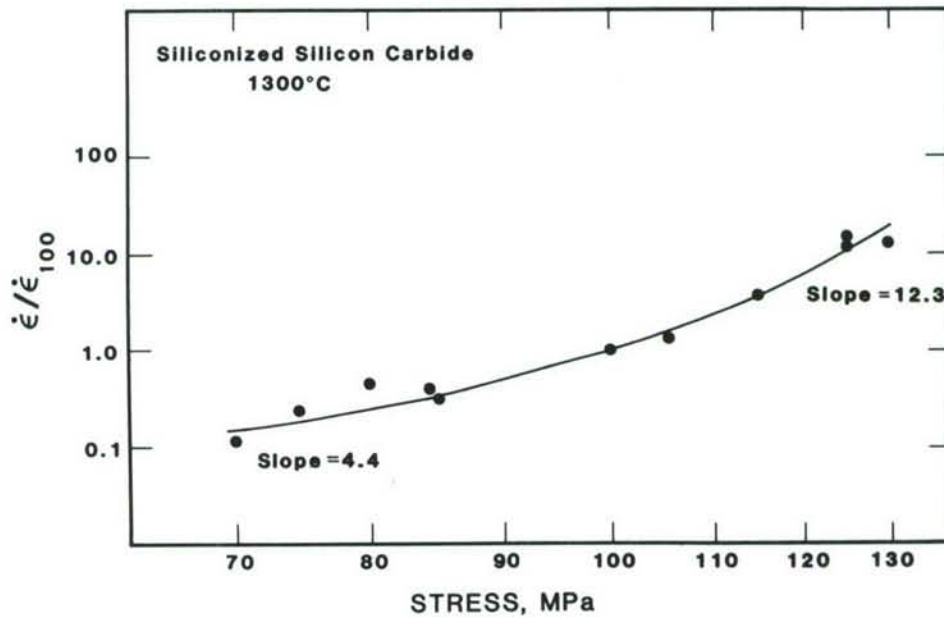
Test technique development: To date all milestones have been met on schedule. The clothespin design test fixture and the pin and clevis test fixture are both operational and are being characterized for degree of bending. If agreement is obtained between these two techniques and if the fixtures can be shown to apply a uniform stress in the gauge section, the construction of a third type of test fixture (powder grip design) will be canceled.

Comparison of creep data obtained in tensile testing with that obtained in compression and bending: This portion of the program is ahead of schedule. Creep data has already been obtained in bending; compressive creep equipment is being constructed. Although some data has already been collected in compression, the test fixture was not functioning well and had to be redesigned. Data collection on this portion of the program is expected to be completed as of 12/86. Two lectures on this subject were presented at the Annual Meeting of the American Ceramic Society in May. A paper on this subject has been written and will be submitted for publication by 12/86.

Inter-laboratory comparison of tensile test method: Although the milestones for this portion of the program lie in the future, a comparison is being made between our data and that collected at Pennsylvania State University on the same material. We view this comparison as a prelude to a inter-laboratory comparison on tensile test techniques for ceramic materials at elevated temperatures. In addition, the possibility of collaborative work with Mr. Leon Chuck of the Norton Company, (formerly with NBS) and with Mr. Ho Fang of Garret Aerospace is currently being explored.

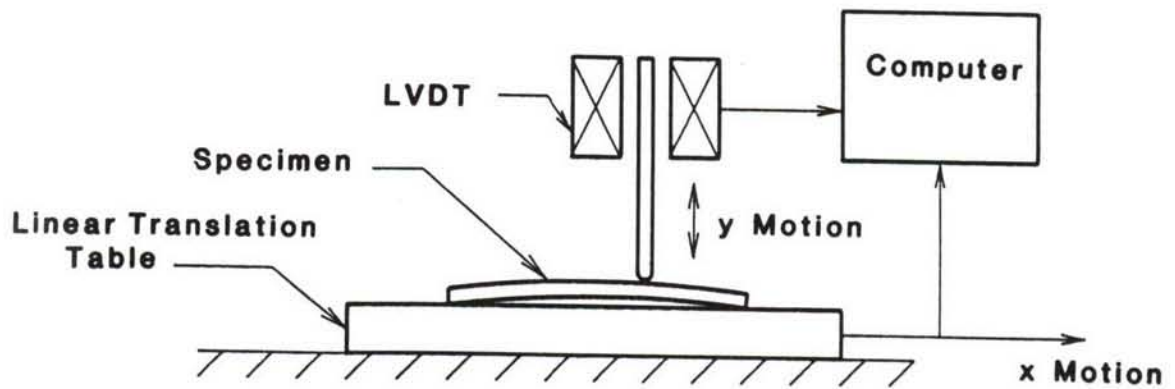
#### Publications

"Influence of Microstructure on Creep Rupture,"  
S.M. Wiederhorn, B.J. Hockey and R.F. Krause, Jr., Presented at Ceramic Microstructures '86: Role of Interfaces," University of California, Berkeley, California, July 28-31, 1986.

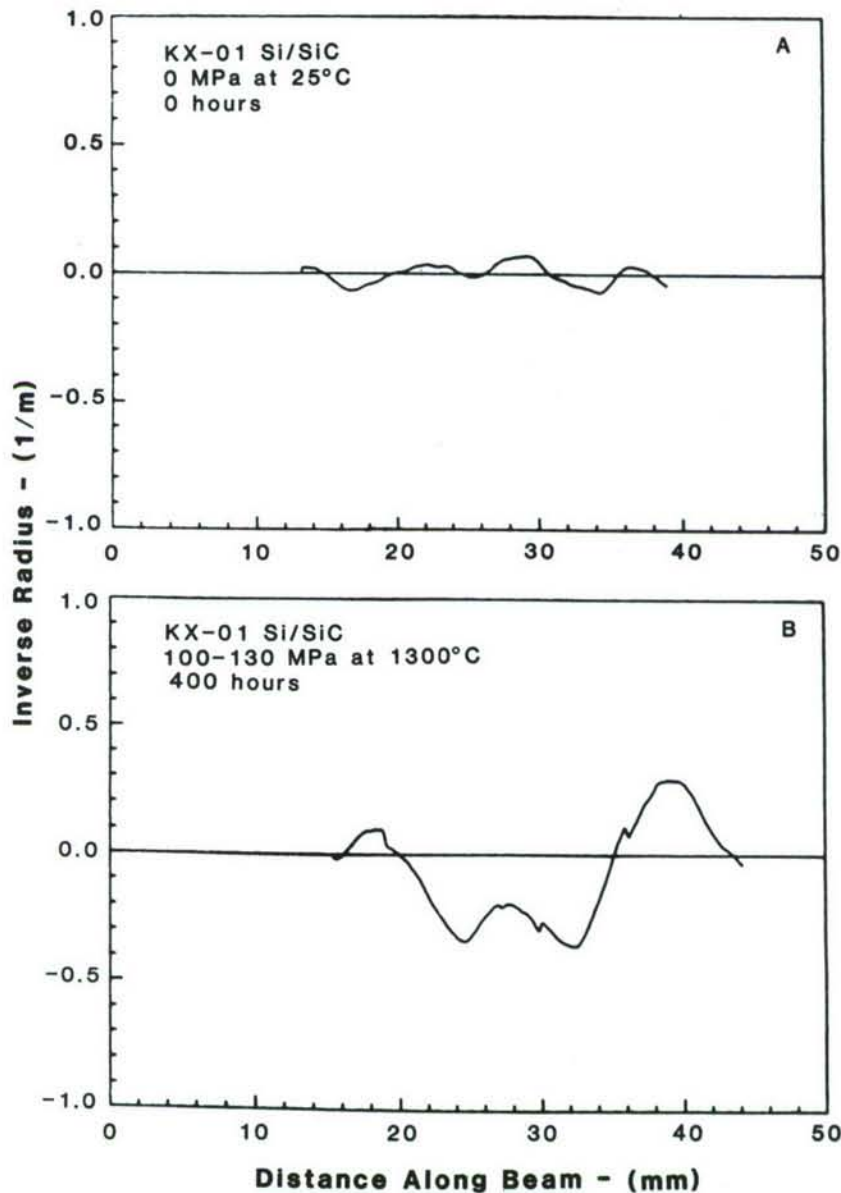


1. Dependence of creep rate on applied stress. As can be seen, the stress dependence of the creep rate is much less below 100 MPa than above this value. This enhancement of creep rate is the result of cavity formation, which is confirmed by a microstructural examination of the test specimens after testing.

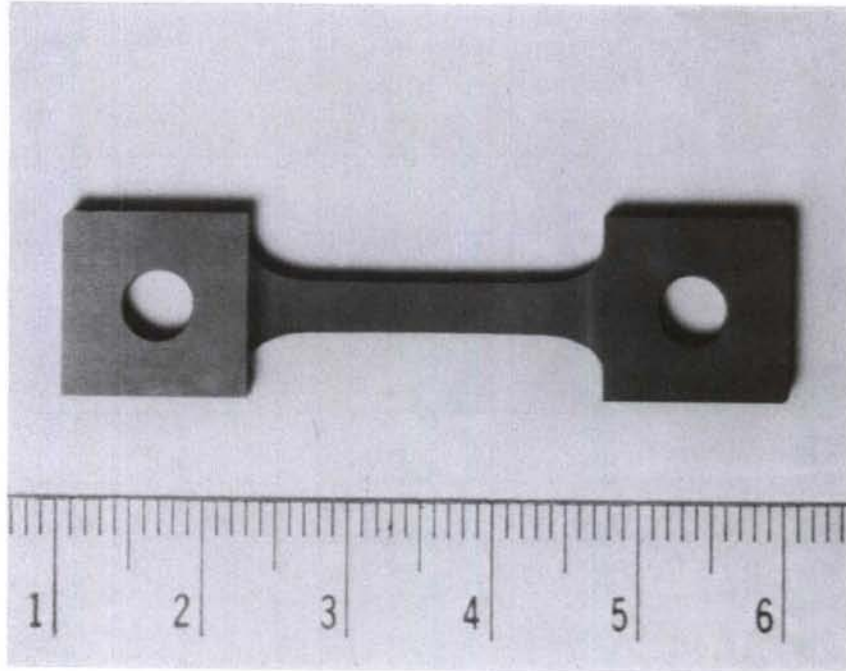




2. Schematic diagram of the equipment used to determine the amount of bending occurring during creep tests.



3. Curvature of specimens used in the present study: (a) As-machined specimen; (b) Deformed at 1300°C. The inverse radius of curvature is plotted as the ordinate because it is proportional to the amount of flexural strain in the specimen. In fact,  $\epsilon = b/R$ , where  $2b$  is the thickness of the test specimen (3 mm in the present case) and  $R$  is the Radius of curvature.



4. Specimen configuration used for the pin and clevis apparatus. The specimen is held by two  $\alpha$ -SiC pins that pass through the holes.



### 3.5 NONDESTRUCTIVE EVALUATION DEVELOPMENT

#### Nondestructive Characterization

R. W. McClung (Oak Ridge National Laboratory)

#### Objective/scope

The purpose of this program is to conduct nondestructive evaluation (NDE) development directed at identifying approaches for quantitative determination of conditions (including both properties and flaws) in ceramics that affect the structural performance. Materials that have been seriously considered for application in advanced heat engines are all brittle materials whose fracture is affected by structural features with dimensions on the order of the dimensions of their microstructures. This work seeks to characterize those features using high-frequency ultrasonics and radiography to detect, size, and locate critical flaws and to measure nondestructively the elastic properties of the host material.

#### Technical progress

We completed ultrasonic studies on three composite ceramic specimens consisting of 0.5- $\mu\text{m}$ -diam silicon carbide whiskers in an alumina matrix. The fiber length varies, but the most probable value is about 30  $\mu\text{m}$ . The specimens exhibited three degrees of fiber clumping as determined by SEM analysis: the first had fiber clumps about 200  $\mu\text{m}$  in diameter, the second had similar clumps 100  $\mu\text{m}$  in diameter, and the third appeared to be free of fiber clumps.

The specimens were examined with a 50-MHz center-frequency ultrasonic transducer. As expected, large numbers of indications were detected in the specimen containing 200- $\mu\text{m}$ -diam clumps (Fig. 1). The largest of these indications was elliptical, almost 1.6 mm long and 0.6 mm wide. The average indication was approximately circular with a diameter of about 250  $\mu\text{m}$ .

The second specimen, containing 100- $\mu\text{m}$  fiber clumps, also yielded large numbers of ultrasonic indications (Fig. 2). However, the intensity of scattering from the clumps was considerably less than that from voids of the same diameter in alumina. This result is not really surprising, but it is contrary to the results obtained on the first specimen, where the scattering appeared to be roughly comparable to that from equivalent size voids.

The third specimen yielded relatively few indications, whose intensities were considerably smaller than those from the 100- $\mu\text{m}$  bundles in the second specimen (Fig. 3). It is not known whether the source of the scattering is related to the fibers or is engendered by flaws in the alumina matrix, but the results are similar to those obtained on monolithics.

Following flaw testing, we obtained transfer curves on the three specimens. As expected, the transfer characteristic (frequency-dependent attenuation) of the clump-free specimen approximated that of monolithic alumina. This result is reasonable because the very small size of the whiskers limits scattering losses at frequencies below the 100-MHz limit of our ultrasonic system. For the other specimens, however, the transfer curve reflects the increased scattering losses caused by the fiber bundles.



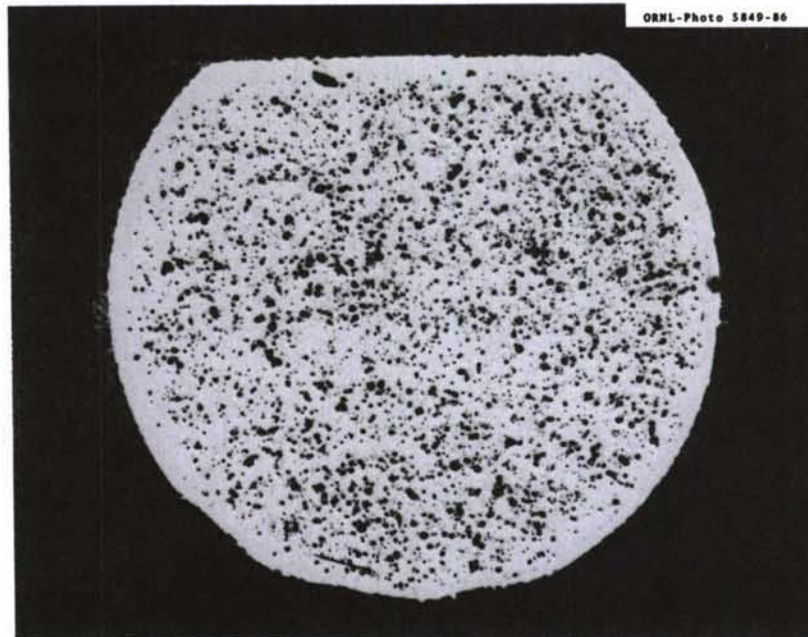


Fig. 1. Ultrasonic scattering data showing large (200- $\mu$ m-diam) fiber clumps in a composite ceramic.



Fig. 2. Ultrasonic scattering data showing detection of 100- $\mu$ m-diam fiber clumps in a composite ceramic.

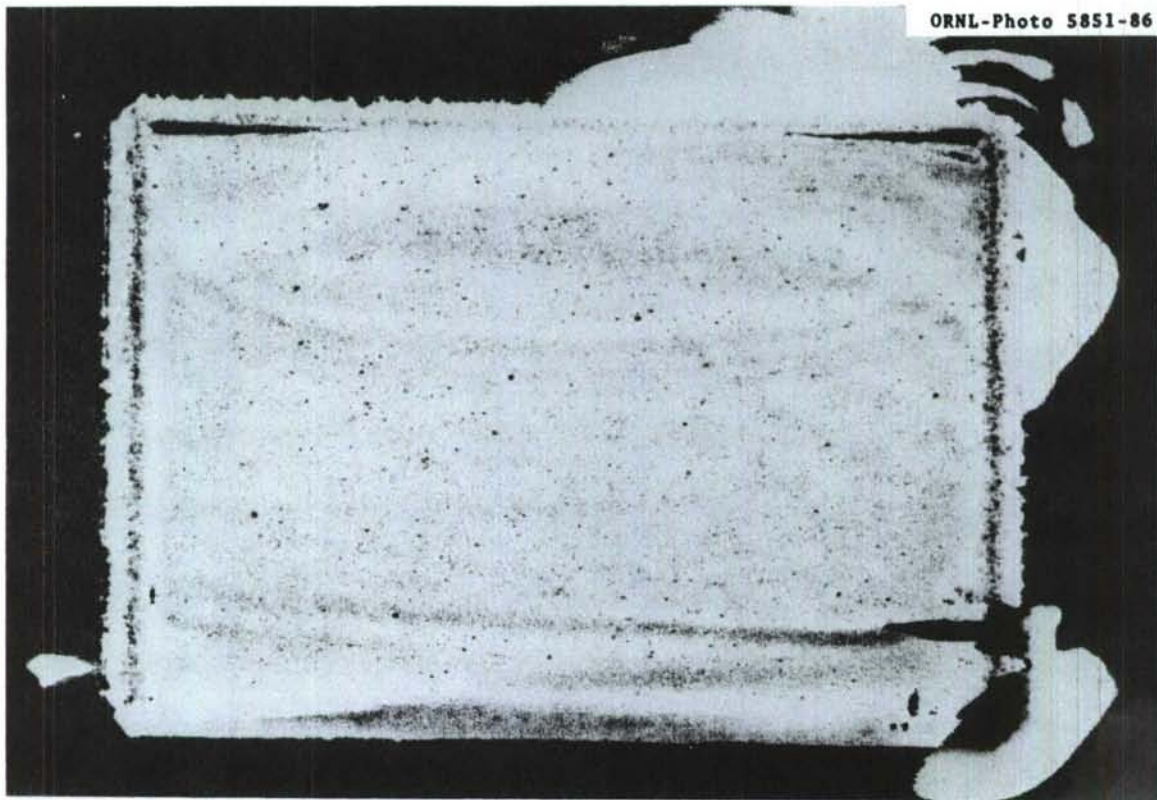


Fig. 3. Ultrasonic scattering data showing detection of natural flaws in a clump-free specimen of composite ceramic.

For such specimens, the presence of clumping can be inferred from the transfer curve without the necessity for detailed scanning of the part. This would not be the case if the density of clumps were very low or for the determination of individual clumps. Nevertheless, the results suggest that the transfer characteristic, which can be computed in a matter of seconds, could be used to reject composite ceramics that exhibit fiber clumping, thus saving the expense of further processing or testing.



Figure 4 shows the transfer curve obtained on a clump-free specimen and Fig. 5 that on a specimen containing 100- $\mu\text{m}$ -diam fiber clumps. Note the considerable increase in attenuation in the latter case.

High-frequency surface wave probing of composite ceramics indicated that the Rayleigh angle backscattering from samples with fiber clumping was more intense than that from samples with no clumping. This constitutes a second test for clumping that can be performed much more rapidly than scanning for discrete flaws.

For composite samples with proper fiber distribution, the techniques that we have developed previously in monolithics for sample characterization and flaw detection have been entirely adequate.

We have continued our investigation of leaky surface-wave probing of monolithic ceramics for detection of surface and near-surface flaws. Using maximization of the surface backscattering to locate the Rayleigh angle accurately, we have examined a highly polished silicon carbide piston wrist pin for surface flaws using 50-MHz energy. Although only a small portion of the total surface was examined because of the lack of suitable fixturing to rotate the cylindrical specimen, two natural defects were easily detected. The first was a roughly cylindrical pit 75  $\mu\text{m}$  in diameter and 25  $\mu\text{m}$  deep. The second was a cracklike feature about 200  $\mu\text{m}$  long, 50  $\mu\text{m}$  wide, and 25  $\mu\text{m}$  deep. All dimensions were determined by light microscopy.

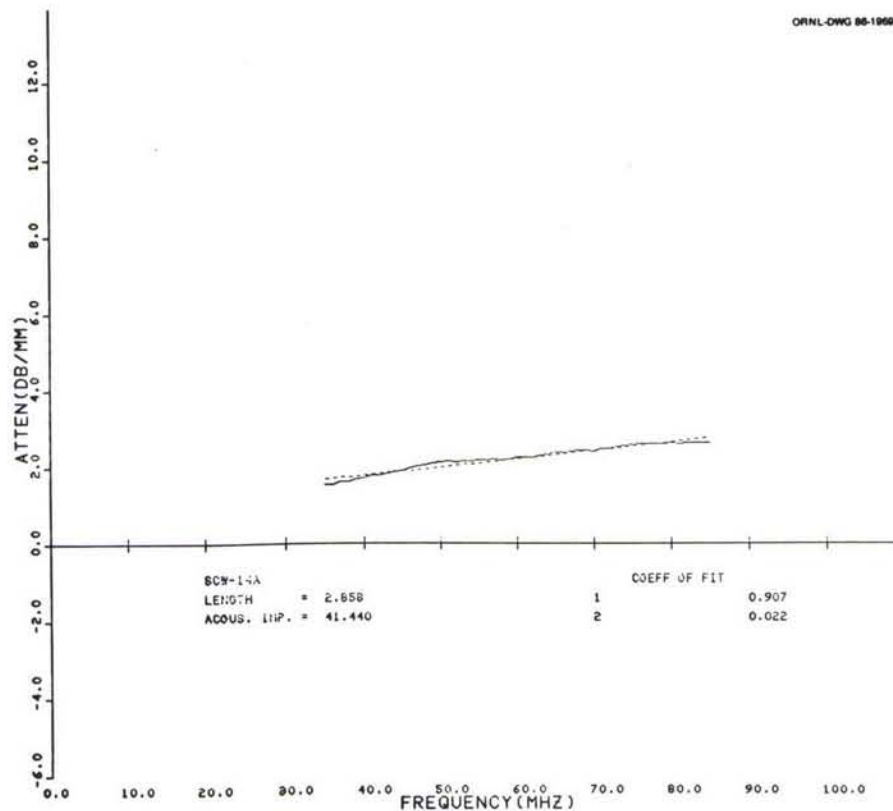


Fig. 4. Transfer curve for a clump-free sample of composite ceramic.

the SiC fabric was apparent in the radiographic images as well as the presence of voids. Each of the samples differed in overall density and variability. Approximate values of density variation were obtained within each sample (difference between highest and lowest value). Measurements were made only through fiber images, avoiding the voids. The radiographic images showed sample 2 to be the most uniform in density (only about 5% variation) as well as the highest in overall density. Sample 3 was next in overall density with subtle localized variations of about 15%. Sample 4 and then sample 1 were next in overall density with localized variations of some 20%.

The periphery of the 75- by 53-mm area of samples 1, 3, and 4 exhibited higher density than the central portion of that defined area. These samples were returned to CSSG, where they were sectioned to produce four small rectangular specimens that had been selected to be nearly uniform individually but varied from specimen to specimen. Each specimen was approximately  $25 \times 6 \times 2.5$  mm. Percentage differences in apparent density were related to the percentage changes of aluminum thickness for comparable values of X-ray attenuation (that result in values of X-ray film density). Film density measurements were made with different densitometer apertures and with both random measurement positions and selected positions on fiber-bundle images (as observed in the texture of the SiC fabric). Physical density measurements on the four specimens revealed an 8% difference between the highest and lowest value. Initial radiographic measurements indicated a 14% difference. We thought the difference in apparent value was due to a bias introduced by too high a film density and/or porosity when the specimens were radiographed through the 2.5-mm thickness. Further studies confirmed that the bias was caused by the porosity. The specimens were radiographed through the 6-mm thickness, and good agreement was obtained between radiographic and physical density measurements.

We obtained a short section (approximately 30 mm long) of 30-mm-diam by 2-mm-wall composite tube (20% SiC whiskers in alumina matrix). A segment that had been removed prevented mechanical positioning for exploratory studies with our microfocus rod-anode X-ray unit. However, initial single-wall radiographic images were made with our low-voltage, contact microradiographic system. Preliminary evaluation has shown the presence of texture that may be related to whisker distribution, small high-density inclusions, and a subtle step change in density at one position on the circumference. Further studies are planned.

A second specimen (approximately 133 mm long) of 30-mm-diam by 2.5-mm-wall composite tube (20% SiC whiskers in alumina matrix) was obtained. Preliminary evaluation using our low-voltage, contact microradiographic system has shown the presence of many small (25- to 675- $\mu$ m-diam) high-density inclusions. The larger inclusions appear to be randomly located, but many of the 25- to 75- $\mu$ m inclusions are oriented straight-line fashion in the axial direction in the specimen. In addition, two cracks were imaged. Further studies are planned with our micro focus rod-anode X-ray unit.

Radiographic studies were performed on a short length of thick-walled silicon nitride tube made for experimental studies as a piston wrist pin. Double-wall radiographic techniques disclosed the presence of apparent localized density variations near one end of the specimen and a few small discontinuities. The boreside rod-anode microfocus X-ray unit was



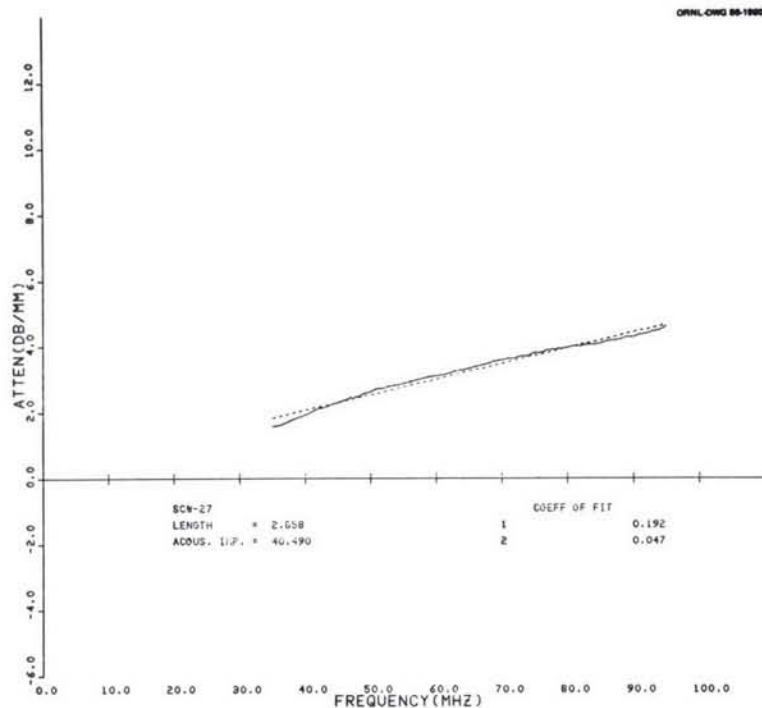


Fig. 5. Transfer curve for a composite ceramic specimen exhibiting fiber clumping.

The small size and cylindrical shape of the specimen makes it difficult to introduce much energy at the Rayleigh angle, but the above results indicate that, even for non-ideal geometries, flaws of the order of a wavelength can be detected easily.

We have successfully seeded an alumina test blank with styrene divinylbenzene spheres having diameters of 115, 60, and 30  $\mu\text{m}$ , arranged in linear arrays. Proper placement of objects this small was quite difficult, but the spheres were arranged regularly so as to distinguish them from natural flaws that might be present in the blank. The sample was prepared by pressing a blank of half the desired thickness at 60 MPa. The spheres were then placed on the surface of the blank and the die lightly reseated to press the spheres into the powder. This step was found necessary because very slight air currents dislodge the spheres if they are not embedded. The remaining powder was then added and the blank press to 120 MPa. The green-state blank will be annealed to vaporize the spheres, leaving spherical voids, and the sample will be sintered to produce the test standard.

We obtained four ceramic-matrix composite samples from the Ceramic Surface Systems Group (CSSG) for radiographic studies. These samples were identified as fiber-reinforced SiC composites fabricated by chemical vapor infiltration. The CSSG had identified the samples as 1, 2, 3, and 4 (top, top-mid, bottom-mid, and bottom). The dimension of each sample were approximately  $76 \times 53 \times 2.5$  mm. These thin sections were removed from a thicker specimen. Approximately 25-kVp X rays were used. The texture of



applied, revealing the localized density variations and much improved sensitivity, showing a large number of very small discontinuities (less than 100  $\mu\text{m}$ ), and showing several larger-diameter but quite thin (disklike) discontinuities.

Several modulus of rupture (MOR) bars have been prepared with small drilled holes to be used in radiographic sensitivity studies. The diameters of the holes are 75, 100, 125, and 250  $\mu\text{m}$ . Depths range from 10 to 70  $\mu\text{m}$ . These bars will be used for both contact microradiographic and projection microradiographic (with microfocus equipment) techniques. Specimens containing a few holes have been provided to two suppliers of microfocus X-ray equipment for preliminary studies prior to our visit with a more extensive group of specimens. Earlier visits to one supplier were unfruitful because of equipment malfunctions.

#### Status of milestones

Milestone 351102 was completed as scheduled.

#### Publications

None.

Computed Tomography - W. A. Ellingson, E. Segal, and M. W. Vannier  
(Argonne National Laboratory)

### Objective/scope

The purpose of this program is to develop X-ray computed tomographic (CT) imaging for application to structural ceramic materials. This technique has the potential for mapping density distributions, detecting and sizing high- and low-density inclusions, and detecting cracks in green-state and densified ceramics. CT imaging is capable of interrogating the full volume of a component, and is noncontacting. It is also relatively insensitive to part shape and thus can be used to inspect components with complex shapes such as turbocharger rotors, rotor shrouds, and large turbine blades.

### Technical progress

Efforts during the current reporting period included extensive analytical and experimental work on implementing a proposed linearization beam-hardening (BH) correction method for polychromatic-source CT scanners typical of those used in medical applications. Linearization of polychromatic CT scanners (i.e., ensuring that the log of the measured X-ray intensity is linearly related to the thickness of a uniform mass) for extended density ranges of materials is a very difficult task.<sup>1,2</sup> Nonlinearity is primarily (but not exclusively) caused by BH. BH correction methods that can provide highly accurate attenuation coefficient determinations for a range of materials and complex component geometries involve a significant computational burden, particularly when high spatial resolution is desired, such as in flaw detection or material characterization of ceramics.

### Approaches to beam hardening corrections

The "water bag" approach. Beam hardening is a function of the depth of penetration and/or the geometry of the object. In a noncylindrical object, different CT projections will undergo different BH effects because of different ray-path lengths. In the early days of medical tomographic scanning with polychromatic radiation, patients were surrounded by a water bag to avoid BH artifacts in the resulting images. A "water bag equivalent" for ceramics is a fitted symmetric structure of a "similar" material (Fig. 1). Putting the object of interest inside a cylinder of a similar material ensures that all rays from all directions will be subjected to similar BH effects.

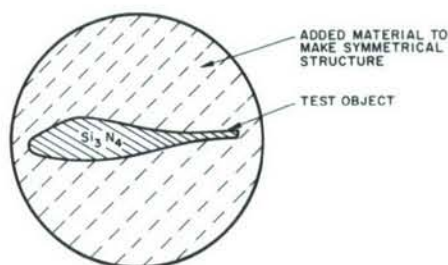


Fig. 1. "Water Bag" Method to Reduce BH Effect in Ceramics.

To estimate the effectiveness of this method, a cold-pressed MgO cylinder ( $\rho = 1.8 \text{ g/cm}^3$ ,  $z_{\text{eff}} = 10.7$ ) was scanned with and without a ceramic "water bag equivalent" -- in this case, a Teflon ring ( $\rho = 2.15 \text{ g/cm}^3$ ,  $z_{\text{eff}} = 8.2$ ). Figure 2 shows a CT image of the MgO ceramic scanned without a "bag"; the BH effect is about 8.7%. Figure 3 is a similar CT scan with the MgO surrounded by the Teflon ring. As the object and the ring are symmetrical, the BH is the same for all directions. The ring reduces the BH effect in the ceramic to <3%. In this case, however, since the ring reduces the number of photons reaching the object, it increases the statistical noise and reduces the contrast resolution of the reconstructed image. This approach, in principle, can only reduce the BH effect but not eliminate it.

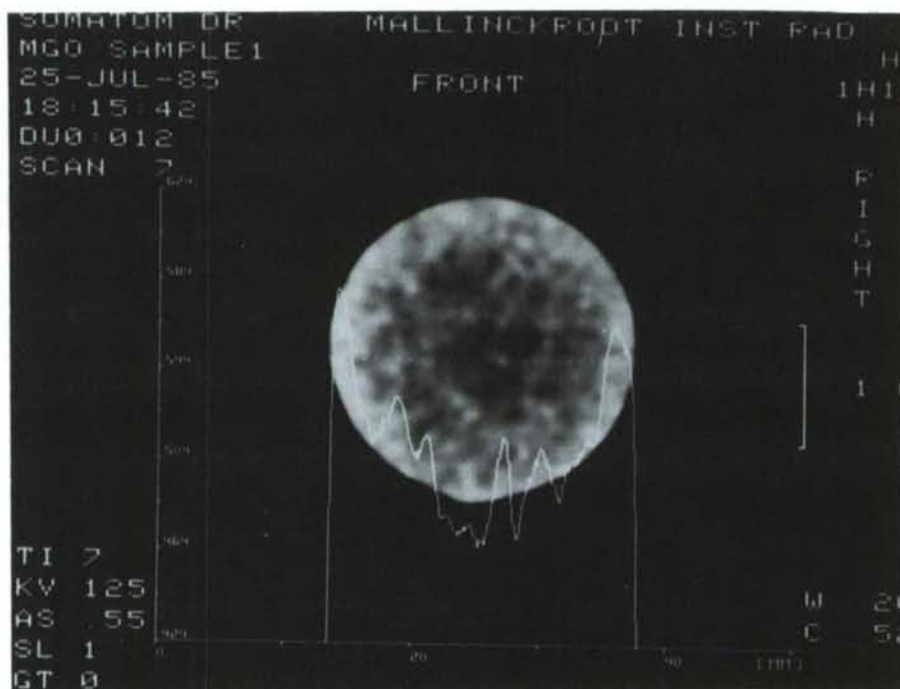


Fig. 2. CT Image and Density Trace of MgO Specimen Without "Water Bag Equivalent" (Teflon Ring).



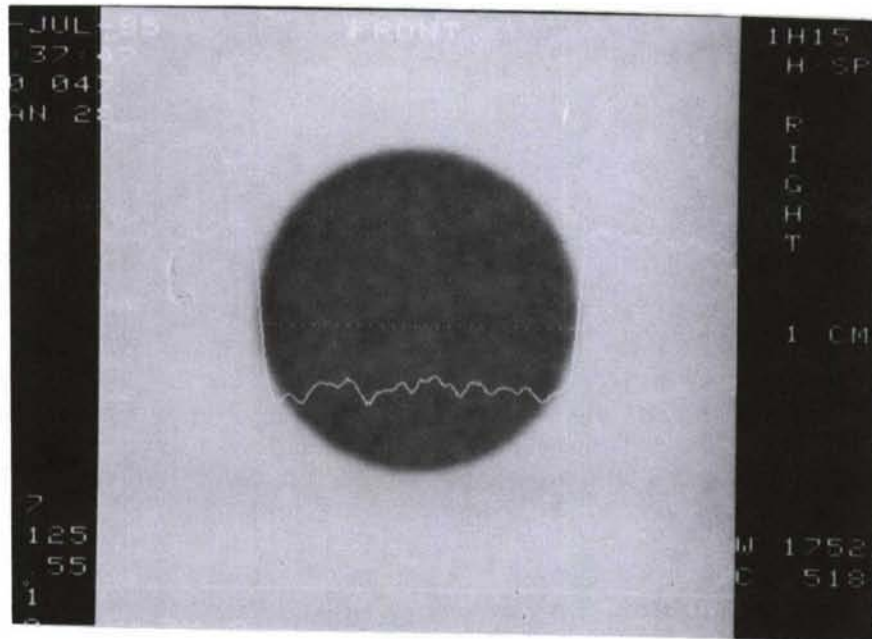


Fig. 3. CT Image and Density Trace of MgO Specimen Inside "Water Bag Equivalent" (Teflon Ring). The density trace no longer shows the very high-density outer region seen within the MgO in Fig. 2.

Pre-specimen beam filtering. A second approach to BH correction is to make the BH correction in the machine itself prior to irradiation of the object, by use of a special filter made of a "similar" material. The thickness and shape of the filter must be tailored to the material and geometry of the object to ensure that all parts of the object have the same effective BH. For example, a cylindrical object would require the special filter geometry shown in Fig. 4.

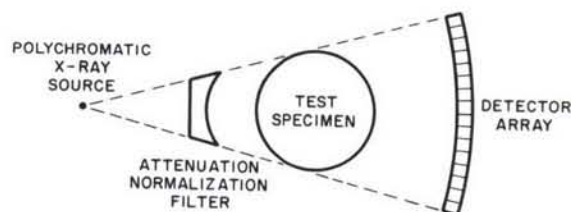


Fig. 4. Prefiltering of the X-Ray Beam to Reduce BH Effects.

The disadvantages of this BH correction approach, besides the difficulty and inconvenience of designing the filter, are similar to those of the water bag approach: (1) it will reduce the BH but will not eliminate it and (2) the hardening of the beam lowers the contrast resolution and increases the noise of the image, because the optimal energy for typical ceramic components is in the low-energy region of the X-ray spectrum.<sup>3,4</sup>

Proposed BH correction. The approach taken in this project is to correct the nonlinear preprocessed CT data for BH by establishing a new effective linear attenuation coefficient (LAC),  $\mu_l'$ , which makes the function  $\ln I/I_0 = -\mu_l' x$  linear as a function of penetration depth  $x$ . These values of  $\mu_l'$  are calculated for a specific ceramic material and a specific polychromatic photon spectrum. By linearizing the function  $\ln I/I_0$ , one obtains an effective monoenergetic beam. Images reconstructed with  $\mu_l'$  will be free of BH effects. (However, this may come at the expense of increased image reconstruction time.) Such a linearization correction requires access to the raw projection data sets in a CT scanner after normalization. (In medical CT scanners, special agreements may be required for such access.)

In order to establish the validity of this linearization approach, a test scan was made on a second-generation CT machine (Elscint Model 2002) in which a linearization correction had already been implemented. The specimen was a 5-cm-diam green  $\text{Si}_3\text{N}_4$  sample ( $\rho = 1.2 \text{ g/cm}^3$ ,  $z_{\text{eff}} = 12.1$ ). The CT image obtained with the linearization correction is shown in Fig. 5. No BH is apparent at the outer edge; however, an apparent "negative BH" (i.e., higher density in the center) is present. Of course, the linearization correction used here had been optimized for tissue and water-like materials, and is not suitable for ceramics. In practice, a correction for the particular ceramic material of interest, based on the measured attenuation coefficient of that material, is needed. Details of implementing such a linearization correction are discussed below.

#### Implementation of beam hardening correction

Implementation of the linearization correction discussed above requires knowledge of the type of detector being used, the spectrum of the X-ray head, and the composition of the material being studied, as well as access to the raw detector data. Several excellent references<sup>5</sup> are available on CT detectors and we will not discuss detection here. In order to evaluate the accuracy of the effective LAC method for a known X-ray spectrum and a homogeneous material, a theoretical calculation was completed and compared with an experimental measurement on a green-state  $\text{Si}_3\text{N}_4$  specimen ( $\rho = 1.995 \text{ g/cm}^3$ ) with dimensions of  $5.7 \times 4.3 \times 3.1 \text{ cm}$ . Figure 6 shows a comparison between the experimental data and theoretical calculations based on the X-ray head spectrum of a Siemens Somatom DR scanner operated at 125 kV. The excellent agreement between the experimental and theoretical results demonstrates that the BH effect can be calculated for ceramic materials. Figure 6 also shows how severe the BH effect can be.



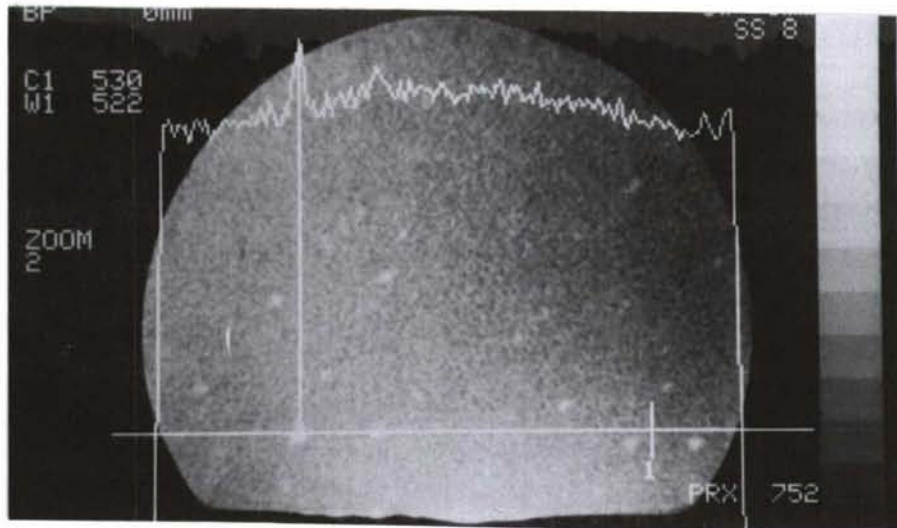


Fig. 5. CT Scan of Green  $\text{Si}_3\text{N}_4$  Specimen, Obtained with a Second-Generation Elscint Model 2002 Machine. No BH effect is apparent at the outer edge, but an apparent "negative BH" of about 0.5% is present.

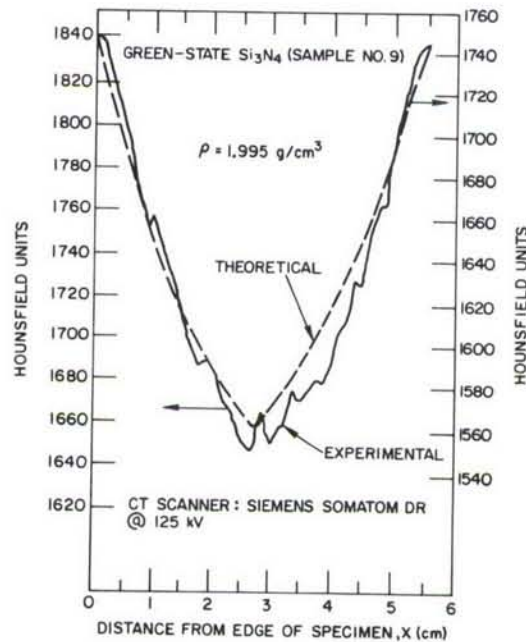


Fig. 6. Comparison between Theoretically Calculated BH Effect and Experimentally Measured BH Effect for a Green-State  $\text{Si}_3\text{N}_4$  Specimen.



The linearization BH correction method for ceramic materials was further experimentally verified with an Elscint Excel 2002 second-generation medical CT scanner. Access to the normalized detector data for this scanner was obtained. An approximate energy spectrum,  $S(E)$ , was used to represent the polychromatic source. Freon TF was chosen as the test material because this fluid has a mass density ( $\rho = 1.565 \text{ g/cm}^3$ ) and an electron density ( $z_{\text{eff}} = 14.4$ ) close to those of both green and dense  $\text{Si}_3\text{N}_4$ . The test specimen was a 53-mm-diam, thin-walled polyethylene bottle filled with Freon TF and placed in the CT machine so as to produce a circular cross-sectional image. Figure 7 shows a plot of the uncorrected nonlinear attenuation and the linearization correction obtained by using  $\mu_l(\text{eff})$  at an equivalent monoenergetic photon energy (60.6 keV). The third-order polynomial-curve coefficients were empirically established during tests on the machine.

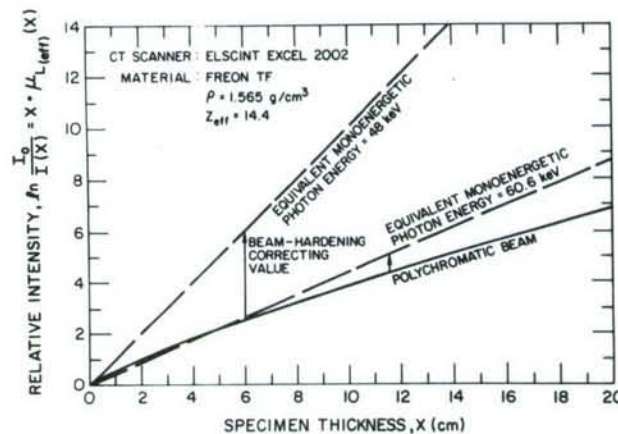


Fig. 7. Comparison of Theoretically Derived Uncorrected Linear Attenuation with Corrected Linear Attenuation for Estimated X-Ray Spectrum of Polychromatic Source from Elscint Excel 2002 CT Scanner.

Figure 8 shows the CT image of Freon TF obtained with a standard "water equivalent" BH correction. The BH effect is about 10%. Figure 9 shows the CT image obtained when the linearization BH correction was implemented. In this case the BH was reduced to <1%.

The results presented here show that a linearization BH correction procedure which takes into account the material composition of the specimen and the X-ray spectrum of the CT scanner can reduce the BH effect to less than 1%. Further reduction of the BH effect to the 0.1% level may not be possible, as scattering effects are present at the detector and may be difficult to convolve out of the image reconstruction process. Theoretically, a special BH calibration should be performed for the material of interest and for each density of this material. This presents a problem for ceramic components, as uniform ceramic calibration blocks may be difficult to produce. It would be very useful if the material mass-density/electron-density trade-off could be established so that calibrations could be done on known homogeneous substances such as the liquid Freon used in these experiments.

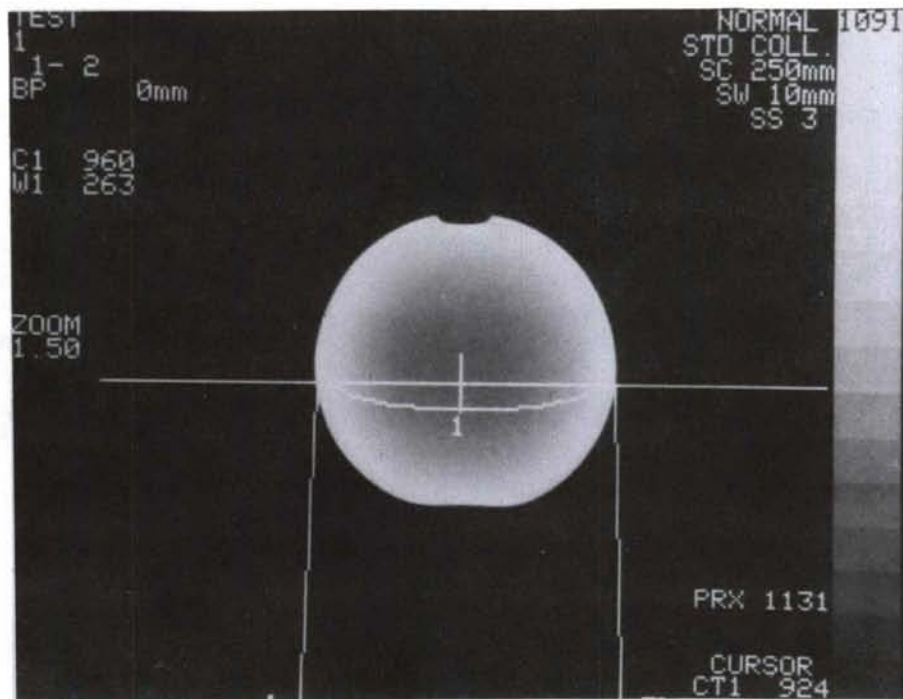


Fig. 8. CT Image (10-mm Slice) of 53-mm-Diameter Polyethylene Bottle Filled with Liquid Freon TF, with Water BH Correction. BH effect is  $\sim 10\%$ .

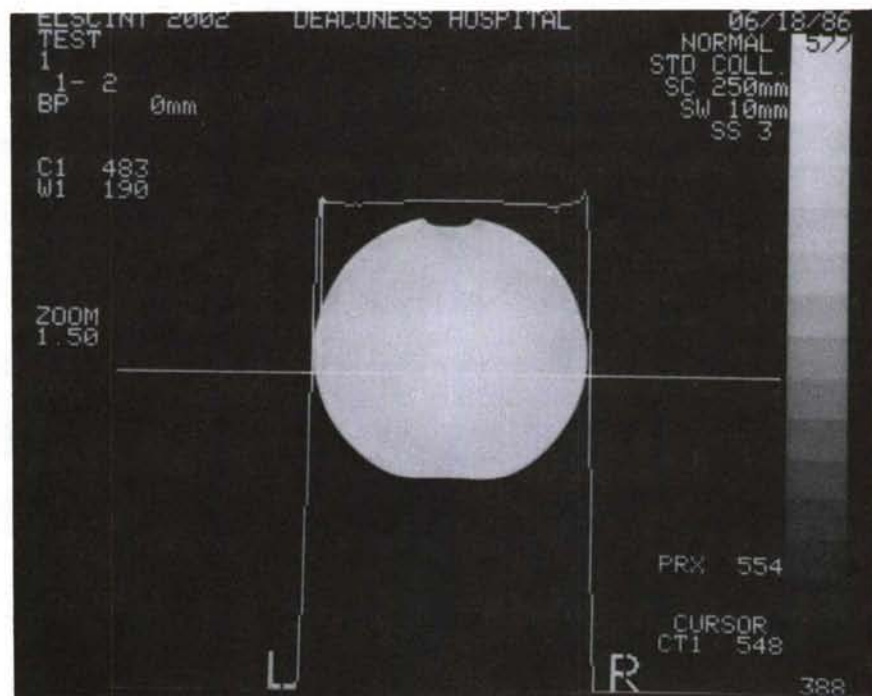


Fig. 9. CT Image (10-mm Slice) of Same Specimen Shown in Fig. 8, with a Third-Order Polynomial Linearization BH Correction. BH effect is  $< 1\%$ .



### Status of milestones

All milestones are on schedule.

### Publications

1. E. Segal and W. A. Ellingson, "Beam-Hardening Correction Methods for Polychromatic X-Ray CT Scanners Used to Characterize Structural Ceramics," to be published in the Proceedings of the 2nd Intl. Symposium on The Nondestructive Characterization of Materials, Montreal, Canada, July 21-23, 1986.
2. E. Segal, W. A. Ellingson, Y. Segal, and I. Zmora, "A Linearization Beam-Hardening Correction Method for X-Ray Computed Tomographic Imaging of Structural Ceramics," to be published in the Proceedings of the Review of Progress in Quantitative NDE, La Jolla, CA, August 3-8, 1986.
3. W. A. Ellingson and E. Segal, "Computed Tomography," in *Ceramic Technology for Advanced Heat Engines Project Semiannual Progress Report for Period October 1985-March 1986*, ORNL/TM-10079, Oak Ridge National Laboratory, Oak Ridge, Tenn., August 1986.

### References

1. G. T. Herman and R. G. Simmons, "Illustration of a Beam-Hardening Correction Method in Computerized Tomography," SPIE Vol. 173, Application of Optical Instrumentation in Medicine VII (1979), pp. 264-270.
2. I. J. Kalet, "Uncertainties Generated by Computed Tomography (CT) Beam-Hardening Corrections," SPIE Vol. 173, Application of Optical Instrumentation in Medicine VII (1979), pp. 258-263.
3. Y. Segal, A. Notea, and E. Segal, "A Systematic Evaluation of NDT Methods," in Research Techniques in NDT, Vol. III, Chapter 9, pp. 293-321, R. S. Sharpe, ed., Academic Press, New York (1977).
4. L. Grodzings, "Optimum Energies for X-Ray Transmission Tomography of Small Samples," Nucl. Instrum. Meth. 206, 541-545 (1983).
5. P. Haque and J. Stanley, "Basic Principles of Computed Tomography Detectors," in Radiology of the Skull and Brain, Vol. 5, Technical Aspects of Computed Tomography, T. H. Newton and D. G. Potts, eds., C. V. Mosby Co., St. Louis, Missouri (1981), pp. 4096-4103.



Methodology for Intelligent Processing of Reliable Engineering Ceramics  
 T. M. Resetar, J. V. Marzik, and J. W. McCauley (U.S. Army Materials  
 Technology Laboratory)

Objective/Scope

The Materials Characterization Division of the U.S. Army Materials Technology Laboratory (MTL) is currently undertaking the development of a data base for the purpose of intelligent processing of reliable engineering ceramics. This data base will allow for detailed quantifiable powder characterization which is focused on:

- A. Establishment of a set of quantifiable powder characteristics including those measurements like permeametry and flowability which may reflect several characteristics at once.
- B. Investigation of available data base management and artificial intelligence software for potential use in this program.
- C. Collection of data on  $\text{Si}_3\text{N}_4$ ,  $\text{SiC}$ , and  $\text{ZrO}_2$  powders and merging of data into selected data base management software.

Technical Progress

This study is directed toward developing a systematic knowledge representation for both quantifiable powder (Task 1) and ceramic characteristics (Task 2) and ultimately joining the powder and ceramic data bases with selected property data (Task 3). The quantifiable unique signature concept (Ref. 1) was used to establish the framework for constructing a computer accessible basic set of powder characteristics (Task 1).

The initial task for this project was the procurement of computer hardware and software for the storage and manipulation of powder data. The hardware obtained was a Rainbow personal computer (Digital, Inc.) along with a Digital LA-50 printer. The procured software was Symphony (1.01) with an MS DOS (Version 2.11) operating system. A feasibility study of this personal computer system (with additional memory to enable future communication capabilities) was done using data obtained from the characterization of zirconium powders.

Table 1 contains the basic set of quantifiable powder characteristics which will unambiguously define a particulate system. This basic set includes; a) physical and b) chemical properties, c) physical defects, and d) other characteristics distinctive for specific materials (i.e. burn time is traditionally used as a specification for zirconium powders.) The headings are broad enough to encompass a variety of classic powder characterization techniques and to include various property information specific to each different material.

To date, essentially all data organization and representation been based on previously characterized zirconium powder data. Table 2

Table 1. Basic Set of Quantifiable  
Powder Characteristics

---

CHARACTERIZATION

---

A. PHYSICAL CHARACTERISTICS:

- 1) Particle Size (dg, dv)
- 2) Particle Size Distribution ( $\sigma_g$ )
- 3) Surface Area ( $S_w$ )
- 4) Permeametry # (Fisher Sub-Sieve Size)
- 5) Material Density (Pycnometer, etc.)
- 6) Aspect Ratio (Long/Short)

B. CHEMICAL CHARACTERISTICS:

- 1) Major Elements
- 2) Minor Elements
- 3) Trace Elements
- 4) Volatile Analysis
- 5) Weight Loss in Air to 110°C
- 6) Phase Analysis (X-ray Diffraction)

C. PHYSICAL DEFECTS:

- 1) Agglomeration: Percent/Size

D. OTHER CHARACTERISTICS:

Table 2. Preliminary Data Base Format  
for Type II Zirconium Powder

Sample	Sedigraph		$\sigma_g(84)-$		FSSS APS- $\mu\text{m}$	% Free Zr	Sw(BET)/ Sw(dg)	ten <sup>3</sup> /sec Burn Time
	dg(50%)	$\sigma_g(84,16)$	$\sigma_g(16)$	Sw(BET)-m <sup>2</sup> /g				
J5042A-1	1.3	1.60	0.2	1.67	2.35	87.7	3.27	2.3
J5042A-2	1.75	1.56	0.22	1.69	2.35	87.1	3.22	2.6
J5042A-3	1.85	1.57	0.13	1.64	2.2	87.4	3.30	2.2
J5042A-4	1.75	1.67	0.29	1.68	2.2	87.7	3.20	2.1
J5043A-1	1.35	1.67	0.20	1.52	2.15	88.5	3.06	2.0
J5043A-2	1.38	1.61	0.22	1.61	2.20	87.1	3.29	2.2
J5043A-3	1.30	1.54	0.40	1.38	2.10	87.7	3.58	2.4
J5043A-4	1.75	1.65	0.17	1.72	2.12	87.1	3.27	2.3
J5051A-1	1.35	1.69	0.29	1.66	2.25	87.3	3.34	2.7
J5065A-1	1.30	1.65	0.32	1.70	2.25	87.4	3.33	2.4
J5068A-1	1.97	1.71	0.27	1.57	1.3*	86.1	3.40	2.7
J5068A-2	2.70	1.32	-0.31	1.64	1.3*	88.6	4.32	2.3
J5068A-3	1.88	1.64	0.15	1.74	2.4*	89.0	3.56	3.3
J5068A-4	1.92	1.69	0.17	1.76	2.5*	88.3	3.68	3.1
J5078A-1	3.15	1.75	0.23	1.23	4.3		4.22	6.1
J5116A-1	1.89	1.65	0.15	1.67	2.9*	88.9	3.44	3.2
J5116A-2	1.89	1.73	0.15	1.75	3.8*	88.7	3.60	2.4

\*Ventron Data



is the preliminary data format for Type II Zirconium Powder and contains a portion of the basic set of quantifiable powder characteristics and properties to measure. The first column contains the sample identification number. Columns 2-5 contain physical characterization parameters and column 6 lists the available chemical characterization information. The last two columns contain "other characteristics", which in the case of zirconium powder is a morphology descriptor ( $Sw[BET]/Sw[dg]$ ) and measurable property (burn time). This is a preliminary format and can be easily rearranged as more information is obtained (i.e. chemical composition).

Rarely does a particle have a perfectly spherical shape and a single size. In an attempt to quantify powder morphology and further characterize median particle size and distribution, an image analysis software package was used. This software package was installed on a Tracor Northern TN-5500 X-ray Analyzer for use of a JEOL JXA-840 scanning electron microscope. The image analysis system is capable of collecting information on individual particles for the average, maximum and minimum diameters, the area and perimeter. Once these values are stored, the program is capable of summarizing and tabulating data on all particles or converting to histogram form.

An initial assessment of this image analysis system was performed using zirconium powder J-5079 A-1 from the data base (Table 2). The zirconium powder was suspended in methanol in a glass sample vial. The vial was shaken vigorously and placed into a vibrating sample packer to prevent settling of the powder. While in the sample vibrator, a portion of the suspension was drawn into a glass pipette. The pipette was mounted onto a modified aerosol gas duster and the suspension was dispersed onto a sample holder for the SEM.

For the initial evaluation, the number of particles sized was limited to 100. Results are summarized in Table 3 and Figure 1. The average particle size was determined as 2.0  $\mu m$ . The median particle size for this same powder sample as determined by the Micromeritics X-ray SediGraph 5000D is 5.02  $\mu m$ , nearly two and a half times greater than that obtained from the image analysis system (Table 4). This large difference in average particle size values can be seen in the tendency for the powder to rapidly settle out of the methanol suspension. This would make it difficult to collect a suspension sample which is representative of the true particle distribution of the zirconium powder, since the larger particles settle first. This results in a collection of the fines fraction for the analysis, thereby giving a smaller average particle size than the Micromeritics SediGraph 5000D. It was also observed that suspension samples taken from vials which were not agitated resulted in even smaller particle sizes.

The sample preparation of the zirconium powder for image analysis on the JEOL JXA-840 is currently under evaluation since the results are dependent on the preparation procedure. Two possible options which are being evaluated to keep the particles in suspension include inserting an ultrasonic probe into the suspension as well as the use of a more viscous suspension media.

The high density for zirconium (6.49 g/cc) exacerbates the difficulty of making a representative suspension. For silicon nitride (3.44

Table 3. Particle Sizing of Zirconium Powder  
by Image Analysis

## SUMMARY OF RESULTS

LABEL: ZR POWDER J-5079 A-1

NUMBER OF FRAMES 6

NUMBER OF PARTICLES 100

MAGNIFICATION 2000

FIELD WIDTH= 43.48 um

OFF PARTICLE SPACING= 0.14 um

ON PARTICLE SPACING= 0.01 um

FIELD AREA= 1.89E+03 um<sup>2</sup>

TYPE	NAME	AVE.DIA. MICRONS	MAX MICRONS	MAX/MIN	AREA um <sup>2</sup>	PERIMETER MICRONS
0	ALL TYPES	1.87E+00 +- 1.50E+00	2.78E+00	2.21E+00	4.894E+00	7.855E+00
1	ZR - RICH	2.02E+00 +- 1.58E+00	3.00E+00	2.15E+00	5.362E+00	8.455E+00
62	NON-INT	4.00E-01 +- 1.90E-01	5.95E-01	2.77E+00	1.624E-01	1.781E+00

## PARTICLE COUNT SUMMARY

TYPE	NAME	NUMBER	#(%)	T.AREA(%)
0	ALL TYPES	100	100.00	4.31
1	ZR - RICH	91	91.00	4.30
62	NON-INT	9	9.00	0.01

AVERAGE DIAMETER HISTOGRAM FOR TYPE: 1 NAME: ZR - RICH

BIN MAX(um)	NO.	%	00---10---20---30---40---50---60---70---80---90---100
0.67	17	18.6	[*****]
1.33	23	25.2	[*****]
2.00	19	20.8	[*****]
2.67	10	10.9	[*****]
3.33	4	4.3	[***]
4.00	7	7.6	[****]
4.67	3	3.2	[**]
5.33	3	3.2	[**]
6.00	3	3.2	[**]
6.67	1	1.0	[*]
7.33	0	0.0	[
8.00	1	1.0	[*]
8.67	0	0.0	[

Figure 1. Histogram of Zr Powder Size Distribution  
by Quantitative Image Analysis

Table 4. Comparison of Different Particle Sizing Techniques

	Average Particle Size ( $\mu\text{m}$ )	Standard Deviation ( $\mu\text{m}$ )
Tracor PRC Image Analysis	2.02	1.58
Micromeritics, 5000 Sedigraph	5.80	2.19
Fischer Sub-Sieve Sizer	3.25	----



g/cc) and silicon carbide (3.21 g/cc) this difficulty should be minimized.

#### Status of Milestones

Milestone #351401 (Establish a set of quantifiable powder characteristics and properties to measure) is completed.

Milestone #351402 (Establish data base for recording, storing analyzing and retrieving data) is on schedule.

Milestone #351403 (Incorporate chemical and physical characteristics of the three powders into data base) is behind schedule due to delays in powder delivery from NBS.

#### Publications

None

#### References

1. J. W. McCauley, "The Role of Characterization in Emerging High Performance Ceramic Materials," Am. Ceram. Soc. Bull., 63 (2), 263-265 (1984).

## 4.0 TECHNOLOGY TRANSFER

### 4.1.1 Technology Transfer

#### Technology Transfer

D. R. Johnson (Oak Ridge National Laboratory)

Technology transfer in the Ceramic Technology Project is accomplished by a number of mechanisms including the following:

Trade shows. A portable display describing the program has been built and used at several trade shows and technical meetings, most recently at the Annual Meeting of the American Ceramic Society, May 5-7, 1985, in Cincinnati, Ohio.

Newsletter. A Ceramic Technology Newsletter is published bimonthly and sent to a large distribution.

Reports. Semiannual technical reports, which include contributions by all participants in the program, are published and sent to a large distribution. Informal bimonthly management and technical reports are distributed to the participants in the program. Open-literature reports are required of all research and development participants.

Direct Assistance. Direct assistance is provided to subcontractors in the program via access to unique characterization and testing facilities at the Oak Ridge National Laboratory.

Workshops. Topical workshops are held on subjects of vital concern to our community. During this period a workshop on material requirements for advanced heat engines was held during the Automotive Technology Development Contractors Coordination Meeting, October 21-24, 1985.

International Cooperation. Our program is actively involved in and supportive of the cooperative work being done by researchers in West Germany, Sweden, and the United States under an agreement with the International Energy Agency. That work, ultimately aimed at development of international standards, includes physical, morphological, and micro-structural characterization of ceramic powders and dense ceramic bodies, and mechanical characterization of dense ceramics. Detailed planning and procurement of ceramic powders and flexural test bars were accomplished during this reporting period.

IEA Annex II Specimens and Support

V. J. Tennery (Oak Ridge National Laboratory)

Objective/scope

The IEA Annex II agreement between the United States, the Federal Republic of Germany, and Sweden concerning structural ceramics for advanced heat engines and other conservation applications was recently signed by all three countries. This agreement includes four subtasks: (1) information exchange, (2) ceramic powder characterization, (3) ceramic chemistry and structural characterization, and (4) ceramic mechanical property characterization. Each country has agreed to provide selected ceramic powders and sintered structural ceramics for study in all three participating countries. Participating laboratories in all three countries have agreed to share all resulting data with the intent of using the knowledge gained for the purpose of evolving standard measurement methods for characterizing ceramic powders and sintered structural ceramics.

The lack of such standard measurement methods has severely hampered the evolution and development of structural ceramics, and this new Annex II agreement will greatly accelerate the development of standard methods for determining important properties of these materials.

In the United States, many companies and their research laboratories have agreed to contribute significant resources in performing the required measurements. For example, in Subtask 2, twelve laboratories are participating; in Subtask 3, seven laboratories are participating; and in Subtask 4, eight laboratories are participating.

For Subtask 2, five ceramic powders are being studied in the initial phase of this work. For Subtasks 3 and 4, three sintered ceramics are being studied, including one from each of the three countries. The ceramic from the United States is a silicon nitride, SNW-1000 from GTE-Wesgo, that from Germany is a hiped SiC from ESK Kempton, and that from Sweden is a silicon nitride from Asea Cerama.

Technical progress

As a result of several meetings of representatives of the three countries over the past two years, it has been agreed that the ceramic powders to be studied in Subtask 2 will be provided by the United States and these will be distributed by the National Bureau of Standards. The first of these powders is scheduled to be distributed to the participating laboratories in October 1986. The sintered ceramics required for Subtasks 3 and 4 are in the form of machined flexure bars. The ESK SiC bars to be studied in the United States are anticipated to be shipped to the Oak Ridge National Laboratory by the end of October 1986. The requisite number of bars will then be reshipped to the participating U.S. laboratories. An indication from Sweden as to the anticipated shipping date for the Asea Cerama silicon nitride bars is expected by October 1986. ORNL is responsible for purchasing the GTE-Wesgo SNW-1000 bars and distributing them to all participants in Subtasks 3 and 4. In addition, ORNL (with assistance from Professor M. K. Ferber of the University of Illinois) is distributing a template written for LOTUS 1-2-3 for data entry and statistical analysis of fracture strength data required in



Subtask 4. This template was prepared and distributed to all participants during August 1986. In addition, ORNL is responsible for providing metric four-point flexure fixtures on a loan basis to all U.S. participants who request them. These fixtures were fabricated and distributed following certification testing during the latter part of August. The specimens utilized for this certification are of alumina and were provided by NASA-Lewis Research Center, as this laboratory is also using this material to certify fixtures to be used at NASA-Lewis prior to fracturing specimens of nitride and carbide from the three countries.

The status of the SNW-1000 silicon nitride bars from GTE-Wesgo follows. The purchase order was placed on August 12, 1985, with a requirement that a total of 2875 bars be delivered to ORNL by January 1986. In January, ORNL was informed that a powder batch compositional error had occurred at Wesgo and that a delay in bar delivery was anticipated which may delay delivery until May 1986. In early June, ORNL was informed that the bars may be delayed until July. From the beginning of July until the present, Wesgo has been unsuccessful in sintering a "thick" billet of SNW-1000 which has the required Weibull modulus of 19-20 with a flexure strength of >100 ksi. A series of processing studies are now underway to identify the critical variables which have prevented achievement of the required properties, and it is anticipated that these problems will be resolved by the end of August. If this is done successfully, the silicon nitride bars will be distributed by ORNL in the first quarter of calendar year 1987, following ultrasonic and radiographic NDE characterization.

#### Status of milestones

On schedule.

#### Publications

None

Standard Reference Materials

A. L. Dragoo (National Bureau of Standards)

Objective/Scope

Ceramics have been successfully employed in engines on a demonstration basis. The successful manufacture and use of ceramics in advanced engines depends on the development of reliable materials that will withstand high, rapidly varying thermal stress loads. Improvement in the characterization of ceramic starting powders is a critical factor in achieving reliable ceramic materials for engine applications. The production and utilization of such powders require characterization methods and property standards for quality assurance.

The objectives of the NBS program are (1) to assist with the division and distribution of five ceramic starting powders for an international round-robin on powder characterization; (2) to provide reliable data on physical (dimensional), chemical and phase characteristics of two silicon nitride powders: a reference and a test powder; and (3) to conduct statistical assessment and modeling of round-robin data. This program is directed toward a critical assessment of powder characterization methodology and toward establishment of a basis for the evaluation of fine powder precursors for ceramic processing. This work will examine and compare by a variety of statistical means the various measurement methodologies employed in the round-robin and the correlations among the various parameters and characteristics evaluated. The results of the round-robin are expected to provide the basis for identifying measurements for which Standard Reference Materials are needed and to provide property and statistical data which will serve the development of internationally accepted standards.

Technical ProgressDivision and Distribution of Ceramic Starting Powders.

Bulk lots of zirconia (Toyo Soda TSK-ZR-3Y) and silicon nitride (H. C. Starck LC-10)<sup>a</sup> powders were divided into small samples in a process consisting of a manual splitting stage and three stages in which spinning rifflers were used. The spinning riffler used for the first and second riffling stages was described in the previous report. The final stage of riffling was carried out with a small riffle, shown in Figure 1. The riffler was operated in a glovebox that was flushed continuously with dry argon.

---

<sup>a</sup> Certain commercial equipment, instruments, or materials are identified in this paper in order to adequately specify the experimental procedure. Such identification does not imply recommendation or endorsement by the National Bureau of Standards, nor does it imply that the materials or equipment identified are necessarily the best available for the purpose.



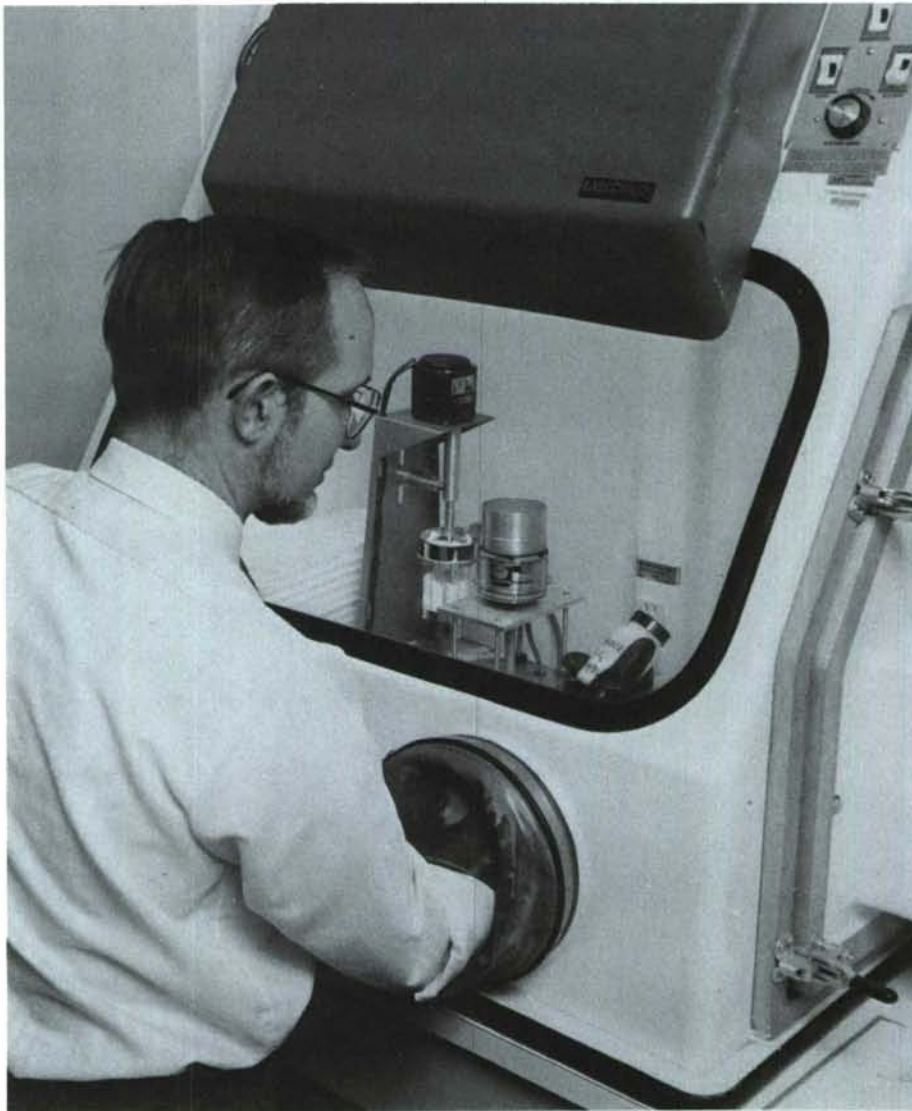


Figure 1. Processing of powder samples in the final riffing stage. The riffing operation is carried out in glovebox which is continuously flushed with dry argon so that samples are exposed to and sealed under an inert atmosphere.



A 25 Kg lot of zirconia was mixed in a cone blender and was split manually into 8 samples. The weight of each sample was determined. Samples from each stage were selected at random and were processed through the subsequent riffing stages. To determine the recovery of the powder through the first and second riffing stages and the sample-to-sample variability, the amount of powder transferred into the hopper of the small riffler was measured at the beginning of the final riffing stage. The results for the division of the zirconia powder are summarized in Table 1.

A comparison of the relative standard deviation (RSD) of the sample size following manual splitting with that for the quantity transferred to the hopper of the small riffler suggests that most of the variation in sample size was introduced when the powder was manually split. The recovery of powder after two riffing stages was 98.7 percent. Ninety-six of the 256 96-g samples obtained from Stage 2 were processed in the final riffing stage. The remaining 96-g samples will be used for test requiring "large" samples or will be riffled into a second batch of 12-g test samples.

Table 1. Summary of Riffing of Zirconia Powder (Toyo Soda TSK-TZ-3Y)

Stage	No. of Samples	Size of Sample
As Received		25 Kg
Blend and Split	8	3120 g (avg) 1.28 % s.e.
Stage 1 Riffle	64	390 g (approx.)
Stage 2 Riffle	256	97.5 g (approx.)
96 of the Stage 2 bottles transferred to Stage 3		
	Average quantity transferred	96.2 g 1.70% s.e.
Stage 3 Riffle	768	12.0 g
64 samples for certification analysis		
15 samples for preliminary tests		
2 samples lost		
687 samples for distribution		

The carousel of the small riffler was modified, see Figure 2, so that the sample vials could be accommodated on the riffler. This modification simplified the vial filling process and assured that all of the riffled powder was collected in the vials. The vials were capped with polyethylene caps as the vials were removed from the riffler; randomly selected vials were set aside for certification analyses; and the remaining vials of test samples (687) were arranged on polystyrene trays and sealed under dry argon in metallized polymer bags. Certification analyses are in progress. In early November, the test samples will be flame-sealed in glass envelopes in collaboration with Dr. Howard Kenare of the Construction Technology Laboratory of the Portland Cement Association. A schematic of a flame-sealed sample is shown in Figure 3.

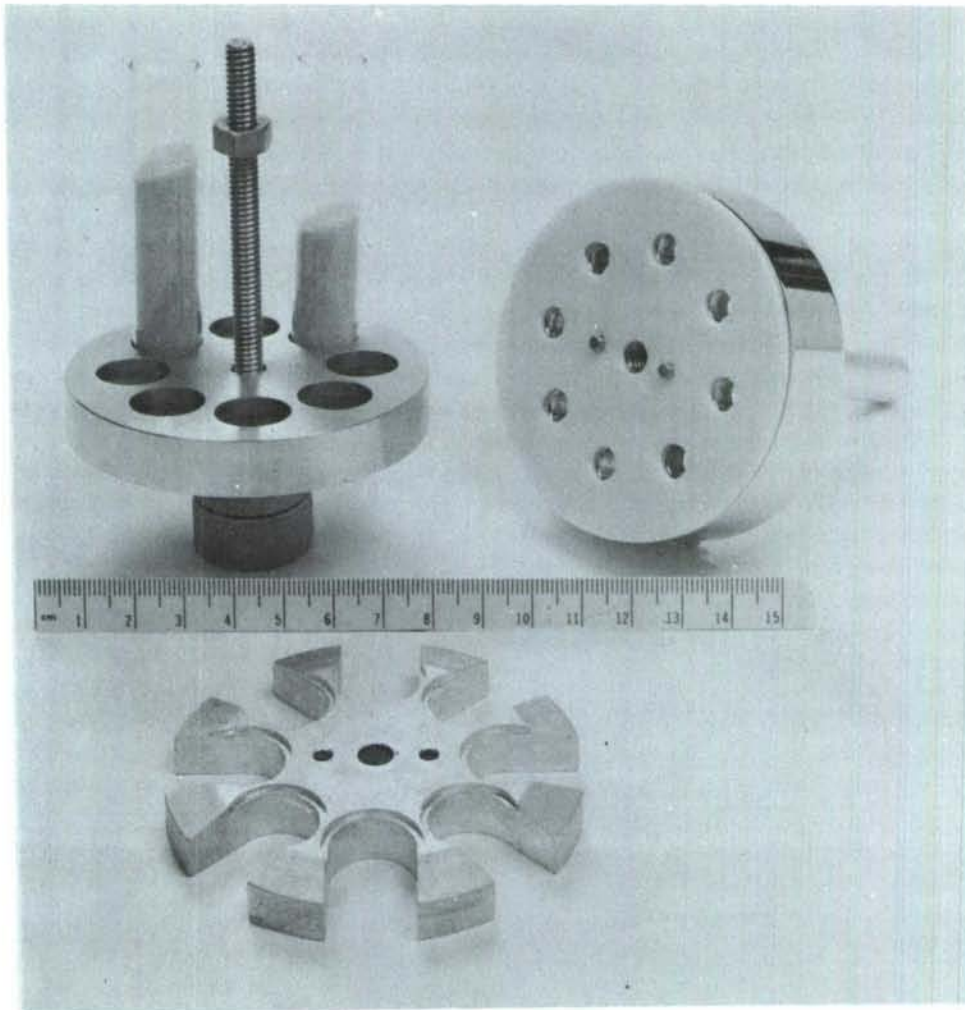


Figure 2. Modification of the carousel of a small riffler to permit direct loading of sample vials.

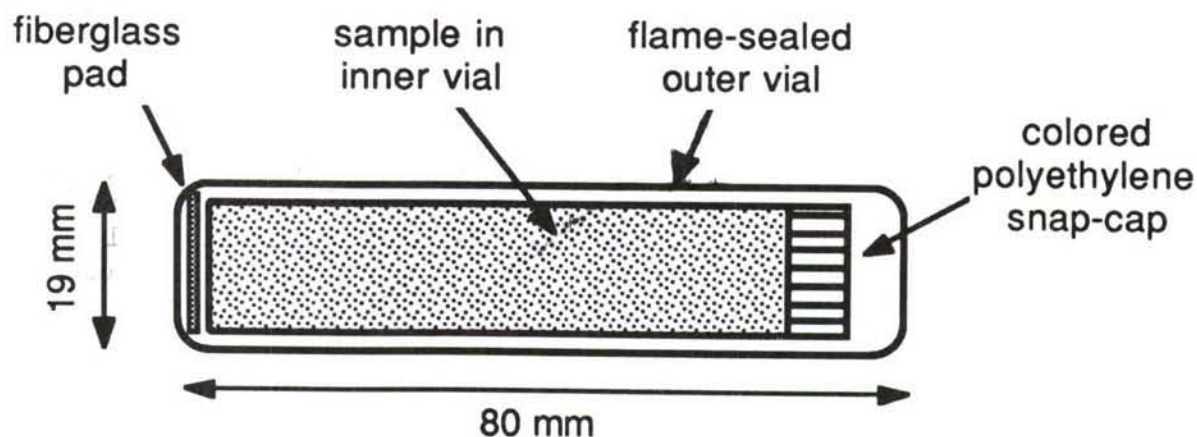


Figure 3. Schematic of flame-sealed sample showing the double vial arrangement of inner vial with powder sample and outer, flame-sealed vial.

A 100 Kg lot of silicon nitride powder was blended and manually split into 48 samples, weighing approximately 2-Kg each. The 2-Kg samples were processed through the first riffing stage and most of the resulting 260-g samples were process through the subsequent riffing stage. Due to the large number of samples produced in the manual splitting stage, samples were randomly paired before riffing in the next two stages. This pairing of samples is expected to reduced the sample-to-sample variation. An analysis of the processing times for the various stages showed that overall processing rates are controlled by the number of samples to be process, the ease with which the powder flows and sample size. Times required to riffle samples are shown in Table 2. To reduce the process times for the riffing stages an order was placed recently for a second large riffler.

Table 2. Processing Time for Riffing of Powders

Powder	Initial Amount (Kg)	Processing Time (Days)		
		Stage 1	Stage 2	Stage 3
Zirconia	25 Kg	5	20	7
Silicon Nitr.	100	45	70 <sup>a</sup>	--

<sup>a</sup> 75 percent of the bottles from Stage 1.



Experimental Design and Statistical Assessment of Round-Robin Data.

Data reporting forms were drafted for the following characteristics:

Physical Characteristics - Size and Size Distribution

Physical Characteristics - Morphology

Chemical Characteristics - Composition

Chemical Characteristics - Phases

Physical Defects and Other Properties.

Each form provides for a tabular summary of data plus summaries of methods, experimental procedures, and data analysis and statistical analysis. In addition, instructions for reporting experimental results were drafted. The data reporting forms and instructions will be distributed with the zirconia test samples.

A first version of a template for an electronic spreadsheet was designed for reporting particle size and size distribution data. Revision of the template is now in progress. The revision will include: (1) more convenient access to template menus and instructions, (2) conversion of size statistics to common basis (lognormality assumed), and (3) plotting of size distribution data. A version of this template will be distributed with zirconia test samples for evaluation by the participants in the round-robin.

Status of Milestones

Division of zirconia powder completed.

Publications

"Critical Assessment of Requirements for Ceramic Powder Characterization," A. L. Dragoo, S. M. Hsu and C. R. Robbins, Proceedings of the 1986 Conference on Ceramic Powder Science and Technology, Boston, August 4-6, 1986.

## INTERNAL DISTRIBUTION

- |                                    |                           |
|------------------------------------|---------------------------|
| 1-2. Central Research Library      | 34-38. D. R. Johnson      |
| 3. Document Reference Section      | 39. R. R. Judkins         |
| 4-5. Laboratory Records Department | 40. M. A. Karnitz         |
| 6. Laboratory Records, ORNL RC     | 41. M. P. Kertesz         |
| 7. ORNL Patent Section             | 42. T. B. Lindemer        |
| 8. S. Baik                         | 43. K. C. Liu             |
| 9. R. L. Beatty                    | 44. E. L. Long, Jr.       |
| 10. P. F. Becher                   | 45. W. D. Manly           |
| 11. J. Bentley                     | 46. R. W. McClung         |
| 12. T. M. Besmann                  | 47. D. L. McElroy         |
| 13. A. Bleier                      | 48. A. J. Moorhead        |
| 14. E. E. Bloom                    | 49. J. L. Rich            |
| 15. K. W. Boling                   | 50. C. R. Richmond        |
| 16. W. D. Bond                     | 51. J. M. Robbins         |
| 17. R. A. Bradley                  | 52. M. W. Rosenthal       |
| 18. C. R. Brinkman                 | 53. M. L. Santella        |
| 19. V. R. Bullington               | 54-77. A. C. Schaffhauser |
| 20. A. J. Caputo                   | 78. J. H. Schneibel       |
| 21. R. S. Carlsmith                | 79. J. L. Scott           |
| 22. P. T. Carlson                  | 80. G. M. Slaughter       |
| 23. J. A. Carpenter, Jr.           | 81. E. J. Soderstrom      |
| 24. J. V. Cathcart                 | 82. D. P. Stinton         |
| 25. R. H. Cooper                   | 83. R. W. Swindeman       |
| 26. S. A. David                    | 84. V. J. Tennery         |
| 27. J. H. DeVan                    | 85-87. P. T. Thornton     |
| 28. W. P. Eatherly                 | 88. T. N. Tieg            |
| 29. J. I. Federer                  | 89. J. R. Weir, Jr.       |
| 30. W. Fulkerson                   | 90. F. W. Wiffen          |
| 31. R. L. Graves                   | 91. R. K. Williams        |
| 32. D. L. Greene                   | 92. C. S. Yust            |
| 33. M. A. Janney                   | 93. A. Zucker             |

## EXTERNAL DISTRIBUTION

- |  |   |
|--|---|
| 94. Donald F. Adams<br>Composite Materials Research Group<br>Mechanical Engineering Department<br>University of Wyoming<br>Laramie, WY 82071 | 96. Donald J. Adrian<br>Chief Engineer<br>High Velocity Tool Corp.<br>2015 Indiana Street<br>Racine, WI 53405 |
| 95. Jane W. Adams<br>Corning Glass Works<br>SP-DV-21<br>Corning, NY 14831  |   |

97. Bruce J. Agle  
Metallurgical Engineer  
Sundstrand Corporation  
Turbomach Division  
Advanced Technology Group  
4400 Ruffin Road  
PO Box 85757  
San Diego, CA 92138-5757
98. Richard T. Alpaugh  
Department of Energy  
Office of Transportation  
Systems  
Forrestal Building CE-151  
1000 Independence Avenue  
Washington, DC 20585
99. H. Arbabi  
Brunel University  
Department of Materials  
Technology  
Uxbridge Middlesex UB8 3PH  
United Kingdom
100. James P. Arnold  
U.S. Army Belvoir  
R&D Center  
ATTN: FTRBE-EMP  
Fort Belvoir, VA 22060
101. V. S. Avva  
North Carolina Agricultural and  
Technical State University  
Department of Mechanical  
Engineering  
Greensboro, NC 27411
102. John M. Bailey  
Research Consultant  
Research Dept.  
Technical Center  
Caterpillar Tractor Company  
100 NE Adams  
Peoria, IL 61629
103. Murray Bailey  
NASA Lewis Research Center  
21000 Brookpark Road, MS 77-6  
Cleveland, OH 44135
104. R. R. Baker  
Ceradyne, Inc.  
3030-A S. Red Hill Avenue  
Santa Ana, CA 92705
105. J. Gary Baldoni  
GTE Laboratories, Inc.  
40 Sylvan Road  
Waltham, MA 02254
106. Ken Baumert  
Air Products and Chemicals,  
Inc.  
Box 538  
Allentown, PA 18105
107. A. L. Bement, Jr.  
Vice President  
Technical Resources  
TRW, Inc.  
23555 Euclid Avenue  
Cleveland, OH 44117
108. M. Bentele  
Xamag, Inc.  
259 Melville Avenue  
Fairfield, CT 06430
109. Clifton G. Bergeron  
Head, Department of  
Ceramic Engineering  
University of Illinois  
204 Ceramics Building  
Urbana, IL 61801
110. William D. Bjorndahl  
TRW, Inc.  
TRW Energy Development Group  
Materials Characterization  
and Chemical Analysis Dept  
One Space Park  
Building 01, Room 2060  
Redondo Beach, CA 90278
111. James A. Black  
Vice President  
American Matrix, Inc.  
118 Sherlake Drive  
Knoxville, TN 37922
112. John Blum  
Norton Company  
High Performance Ceramics  
Goddard Road  
Northboro, MA 01532-1545



113. Paul N. Blumberg  
President  
Integral Technologies Inc.  
415 E. Plaza Drive  
Westmont, IL 60559
114. Wolfgang D. G. Boecker  
Sohio Engineered Materials  
Company  
Niagara Falls R&D Center  
PO Box 832  
Niagara Falls, NY 14302
115. Tibor Bornemisza  
Sundstrand Corporation  
Project Engineer,  
Turbomach Division  
Advanced Technology Group  
4400 Ruffin Road, PO Box 85757  
San Diego, CA 92138-5757
116. Seymour A. Bortz  
Manager, Nonmetallic Materials  
and Composites  
Materials and Manufacturing  
Technology  
10 West 35th Street  
Chicago, IL 60616
117. H. K. Bowen  
Department of Materials Science  
and Engineering, Room 12-009  
Massachusetts Institute of  
Technology  
Cambridge, MA 02139
118. Richard C. Bradt  
Chairman, Materials Science and  
Engineering  
University of Washington  
Dept. of Materials Science and  
Engineering  
Roberts Hall, FB-10  
Seattle, WA 98195
119. Raymond J. Bratton  
Manager, Ceramic Science  
Westinghouse Electric Corporation  
R&D Center  
1310 Beulah Road  
Pittsburgh, PA 15235
120. Catherine E. Brown  
E. I. DuPont de Nemours &  
Company  
Experimental Station  
Information Center E302/301  
Wilmington, DE 19898
121. J. J. Brown  
Virginia Polytechnic  
Institute and State  
University  
Department of Materials  
Engineering  
Blacksburg, VA 24061
122. W. Bryzik  
U.S. Army Tank Automotive  
Command  
R&D Center, Propulsion  
Systems Division  
Warren, MI 48090
123. S. T. Buljan  
GTE Laboratories Inc.  
40 Sylvan Road  
Waltham, MA 02254
124. John M. Byrne, Jr.  
Manager, Business  
Development Co  
Development Department  
PPG Industries, Inc.  
One PPG Place  
Pittsburgh, PA 15272
125. Donald J. Campbell  
Air Force Wright  
Aeronautical Laboratory  
AFWAL/POX  
Wright-Patterson Air Force  
Base  
OH 45433
126. Harry W. Carpenter  
Rockwell International  
Rocketdyne Division  
J39-169-FB39  
6633 Canoga Avenue  
Canoga Park, CA 91304

127. David Carruthers  
Garrett Turbine Engine  
Company  
111 South 34 Street  
PO Box 5217  
Phoenix, AZ 85010
128. Se-Tak Chang  
GTE Laboratories  
40 Sylvan Road  
Dept. 312  
Waltham, MA 02254
129. R. J. Charles, Manager  
Ceramics Branch  
Physical Chemistry  
Laboratory  
General Electric Company  
PO Box 8  
Schenectady, NY 12301
130. En-sheng Chen  
B&C Engineering Research  
13906 Dentwood Drive  
Houston, TX 77014
131. Albert A. Chesnes  
Director, Heat Engine  
Propulsion Division  
Office of Transportation Systems  
Department of Energy  
Forrestal Building CE-151  
1000 Independence Avenue  
Washington, DC 20585
132. Frank Childs  
EG&G, Inc.  
Idaho National Engineering  
Laboratory  
PO Box 1625  
Idaho Falls, ID 83415
133. Gilbert Y. Chin  
Bell Telephone Laboratories  
Research & Development  
Murray Hill, NJ 07974
134. Melvin H. Chiogioji  
Director, Office of  
Transportation Systems  
Department of Energy  
Forrestal Building CE-15  
1000 Independence Avenue, SW  
Washington, DC 20585
135. William J. Chmura  
The Torrington Company  
Corporate Research  
59 Field Street  
Torrington, CT 06790
136. Eugene V. Clark  
Vice President  
Technology Engineering  
Turbine Metal Technology,  
Inc.  
7327 Elmo Street  
Tujunga, CA 91042-2204
137. William L. Cleary  
Associate Division Director  
ORI, Inc.  
1375 Piccard Drive  
Rockville, MD 20850
138. Jack L. Clem  
General Manager  
Carbon Black Division  
Huber Technology Group  
J. M. Huber Corporation  
PO Box 2831  
Borger, TX 79008-2831
139. Philip R. Compton  
Energy Systems Office  
National Aeronautics and  
Space Administration  
Code REC-1  
Washington, DC 20546
140. Harry E. Cook  
Director, Automotive  
Research and Technical  
Planning  
Chrysler Corporation  
PO Box 857, CIMS:  
44-01-22  
Detroit, MI 48288
141. Stephen Copley  
Professor and Chairman  
Materials Science  
Department  
University of Southern  
California  
Los Angeles, CA 90089-0241



142. John A. Coppola  
Manager, Advanced Programs  
Structural Ceramics  
Division  
Standard Oil Engineered  
Materials Company  
PO Box 1054  
Niagara Falls, NY 14302
143. William J. Croft  
U.S. Army Materials  
Technology Laboratory  
Arsenal Street  
Watertown, MA 02172
144. Gary M. Crosbie  
Ford Motor Company  
PO Box 2053, Room S-2079  
Ceramics Materials Department  
Dearborn, MI 48121
145. Floyd W. Crouse, Jr.  
Department of Energy  
Morgantown Energy Technology  
Center  
PO Box 880  
Morgantown, WV 26505
146. Raymond Cutler  
Ceramatec, Inc.  
163 W. 1700 South  
Salt Lake City, UT 84115
147. David A. Dalman  
Research Manager  
Central Research  
Organic Specialties Lab  
Dow Chemical Company  
M. E. Pruitt Building  
Midland, MI 48640
148. Stephen C. Danforth  
Rutgers University  
PO Box 909  
Piscataway, NJ 08854
149. Stanley J. Dapkunas  
Ceramic Division  
Institute for Materials Science  
and Engineering  
National Bureau of Standards  
Gaithersburg, MD 20899
150. Robert F. Davis  
North Carolina State  
University  
Materials Engineering  
Department  
232 Riddick Laboratory  
Raleigh, NC 27607
151. Evelyn M. DeLiso  
Assistant Research Professor  
Center for Ceramics Research  
Rutgers University  
College of Engineering  
PO Box 909  
Piscataway, NJ 08854
152. Alan L. Dragoo  
Materials Scientist  
Inorganic Materials  
Division  
National Bureau of Standards  
Center for Materials Science  
Gaithersburg, MD 20899
153. Keith F. Dufrane  
Battelle Columbus  
Laboratories  
505 King Avenue  
Columbus, OH 43201
154. Robert J. Eagan  
Manager, Chemistry and  
Ceramics Department 1840  
Sandia National Laboratories  
Albuquerque, NM 87185
155. Christopher A. Ebel  
Program Manager  
High Performance Ceramics  
Norton Company  
Goddard Road  
Northboro, MA 01532
156. J. J. Eberhardt  
Director, Energy Conversion  
and Utilization  
Technologies Program  
Department of Energy  
Forrestal Building CE-12  
1000 Independence Ave SW  
Washington, DC 20585



157. E. E. Ecklund  
Office of Transportation  
Systems  
Department of Energy  
Forrestal Building CE-151  
1000 Independence Avenue  
Washington, DC 20585
158. William A. Ellingson  
Argonne National Laboratory  
9700 South Cass Avenue  
Argonne, IL 60439
159. Director, Applied Technology  
Laboratory  
U.S. Army Research and Technology  
Laboratory (AVSCOM)  
ATTN: SAVDL-ATL-ATP  
(Mr. Graydon A. Elliott)  
Fort Eustis, VA 23604
160. A. Erdely  
Chemical Engineer  
26 Av. Gare des Eaux-vives  
1208 Geneva  
Switzerland
161. Charles D. Estes  
U.S. Senate  
Professional Staff Member  
Committee on Appropriations  
SD-152 Dirksen Senate Office  
Building  
Washington, DC 20510
162. Anthony G. Evans  
University of California  
College of Engineering  
Santa Barbara, CA 93106
163. Robert C. Evans  
Asst. Manager, Vehicular Gas  
Turbine and Diesel Project  
Office  
NASA Lewis Research Center  
21000 Brookpark Road  
Cleveland, OH 44135
164. Katherine T. Faber  
Assistant Professor of Ceramic  
Engineering  
Ohio State University  
2041 College Road  
Columbus, OH 43210
165. John Facey  
National Aeronautics and  
Space Administration  
Energy Systems Office  
Washington, DC 20546
166. John W. Fairbanks  
Office of Transportation  
Systems  
Department of Energy  
Forrestal Building CE-151  
Washington, DC 20585
167. Larry Farrell  
Babcock and Wilcox  
PO Box 1260  
Lynchburg, VA 24505
168. M. K. Ferber  
University of Illinois  
105 S. Goodwin Avenue  
203 Ceramic Building  
Urbana, IL 61801
169. H. W. Foglesong  
Dow Corning Corporation  
3901 S. Saginaw Road  
Midland, MI 48640
170. Thomas F. Foltz  
Manager, Product  
Applications  
Avco  
Special Materials Division  
Two Industrial Avenue  
Lowell, MA 01851
171. Robert G. Frank  
Manager, Non-Metallic  
Materials  
General Electric Company  
One Neumann Way  
Mail Drop M-87  
PO Box 156301  
Cincinnati, OH 45215-6301
172. Frank Gac  
Los Alamos National  
Laboratory  
PO Box 1663  
MSP6 MS G-770  
Los Alamos, NM 87545

173. George E. Gazza  
U.S. Army Materials  
Technology Laboratory  
Ceramics Research Division  
Arsenal Street  
Watertown, MA 02172
174. Charles M. Gilmore  
Department of Civil, Mechanical,  
and Environmental Engineering  
The George Washington University  
Washington, DC 20052
175. Paul Glance  
Director, R&D  
Concept Analysis Corporation  
9145 General Court  
Plymouth, MI 48170
176. Fred M. Glaser  
Department of Energy  
Office of Fossil Energy, FE-14  
Washington, DC 20545
177. Joseph W. Glatz  
Naval Air Propulsion Test Center  
Science and Technology Group  
Systems Technology Division  
Box 7176, PE 34  
Trenton, NJ 08628
178. Stephen T. Gonczy  
Allied Signal Research Center  
Materials Science Department  
50 UOP Plaza  
Des Plaines, IL 60016-6187
179. Robert J. Gottschall  
Office of Material Sciences  
Department of Energy  
ER-131 GTN  
Washington, DC 20545
180. Kenneth Green  
Senior Development Engineer  
Coors Porcelain Company  
Golden, CO 80401
181. Michael Greenfield  
National Aeronautics and  
Space Administration  
Energy Systems Office  
Washington, DC 20546
182. Lance E. Groseclose  
General Motors Corporation  
Allison Gas Turbine Division  
Indianapolis, IN 46206-0420
183. T. D. Gulden  
Manager, Ceramics and  
Chemistry  
GA Technologies, Inc.  
PO Box 81608  
San Diego, CA 92138
184. M. D. Gurney  
NIPER  
PO Box 2128  
Bartlesville, OK 74005
185. J. J. Habeeb  
Senior Chemist  
Research Division  
Esso Petroleum Canada  
PO Box 3022  
Sarina, Ontario  
Canada N7T 7M1
186. H. T. Hahn  
Pennsylvania State  
University  
ESM Department  
227 Hammond Building  
University Park, PA 16802
187. Nabil S. Hakim  
Staff Research Engineer,  
Engineering R&D  
General Motors Corporation  
Detroit Diesel Allison  
Division  
36880 Ecorse Road  
Romulus, MI 48174
188. John W. Halloran  
Ceramic Process Systems  
128 Spring Street  
Lexington, MA 02173
189. R. A. Harmon  
25 Schalren Drive  
Latham, NY 12110

190. Stephen D. Hartline  
Norton Company  
High Performance Ceramics  
Goddard Road  
Northboro, MA 01532
191. Willard E. Hauth  
Section Manager, Composite  
Development Ceramics Program  
Dow Corning Corporation  
Midland, MI 48640
192. Norman L. Hecht  
University of Dayton Research  
Institute  
300 College Park  
Dayton, OH 45469-0001
193. S. S. Hecker  
Deputy Division Leader  
Material Science and Technology  
Division, G-756  
Los Alamos National Laboratory  
PO Box 1663  
Los Alamos, NM 87545
194. Peter W. Heitman  
General Motors Corporation  
Allison Gas Turbine Operation  
PO Box 420, W-5  
Indianapolis, IN 46206-0420
195. Richard L. Helferich  
The Duriron Company, Inc.  
PO Box 1145  
Dayton, OH 45401
196. H. E. Helms  
General Motors Corporation  
Allison Gas Turbine Operations  
PO Box 420  
Indianapolis, IN 46206-0420
197. Thomas L. Henson  
Director of Research and  
Engineering  
Chemical & Metallurgical  
Division  
GTE Products Corporation  
Hawes Street  
Towanda, PA 18848-0504
198. Thomas P. Herbell  
NASA Lewis Research Center  
21000 Brookpark Road  
MS 105-1  
Cleveland, OH 44135
199. Ben Heshmatpour  
Thermo Electron Corporation  
101 First Avenue  
Waltham, MA 02154
200. Hendrik Heystek  
Bureau of Mines  
Tuscaloosa Research Center  
PO Box L  
University, AL 35486
201. Robert V. Hillery  
Manager, Coating Materials  
and Processes  
General Electric Company  
Cincinnati, OH 45215
202. Jonathan W. Hinton  
Vice President and  
General Manager  
Structural Ceramics  
Division  
Standard Oil Engineered  
Materials  
PO Box 1054  
Niagara Falls, NY 14302
203. Stephen M. Hsu  
Chief, Ceramics Division  
Institute for Materials  
Science & Engineering  
National Bureau of Standards  
Gaithersburg, MD 20899
204. Harold A. Huckins, President  
Princeton Advanced  
Technology, Inc.  
56 Finley Road  
Princeton, NJ 08540



205. Joseph E. Hunter, Jr.  
General Motors Corporation  
Research Labs, Metallurgy  
Department  
12 Mile and Mound Roads  
Warren, MI 48090-9055
206. Louis C. Ianniello  
Director, Office of Materials  
Sciences  
Department of Energy  
ER-13 GTN  
Washington, DC 20545
207. Robert H. Insley  
Champion Spark Plug Company  
Ceramic Division  
20000 Conner Avenue  
Detroit, MI 48234
208. Curt A. Johnson  
General Electric Company  
Ceramics Branch  
Physical Chemistry  
Laboratory  
PO Box 8  
Schenectady, NY 12301
209. Douglas C. Johnson  
Technology Development Manager  
Sundstrand Corporation  
Turbomach Division  
4400 Ruffin Road, PO Box 85757  
San Diego, CA 92138-5757
210. Larry Johnson, Director  
Center for Transportation Research  
Argonne National Laboratory  
9700 S. Cass Avenue, Building 362  
Argonne, IL 60439
211. R. A. Johnson  
General Motors Corporation  
Allison Gas Turbine Division  
PO Box 420  
Indianapolis, IN 46206-0420
212. L. A. Joo  
Associate Director of Research  
Great Lakes Research Corporation  
PO Box 1031  
Elizabethton, TN 37643
213. A. David Joseph  
Vice President, R&D Engineering  
Sealed Power Corporation  
100 Terrace Plaza  
Muskegon, MI 49443
214. Roy Kamo, President  
Adiabatics, Inc.  
630 S. Mapleton  
Columbus, IN 47201
215. Allan Katz  
Air Force Wright  
Aeronautical Laboratory  
Materials Laboratory,  
AFWAL/MLLM  
Metals and Ceramics Division  
Wright-Patterson Air Force Base  
OH 45433
216. R. N. Katz  
Chief, Ceramics Research  
Division  
U.S. Army Materials  
Technology Laboratory  
Arsenal Street  
Watertown, MA 02172
217. P. Victor Kelsey  
Ceramics Technical Leader  
Materials Science Division  
Aluminum Company of America  
Alcoa Technical Center B  
Alcoa Center, PA 15061
218. Frederick L. Kennard, III  
Supervisor, Ceramic Research  
General Motors Corporation  
AC Spark Plug Division,  
Dept. 32-24  
1300 N. Dort Highway  
Flint, MI 48556
219. J. R. Kidwell  
AGT101 Assistant Project  
Engineer  
Garrett Turbine Engine Company  
111 S. 34th Street  
PO Box 5217  
Phoenix, AZ 85010

220. Max Klein  
Senior Scientist, Thermodynamics  
Gas Research Institute  
8600 West Bryn Mawr Avenue  
Chicago, IL 60631
221. C. E. Knapp  
Norton Company  
8001 Daly Street  
Niagara Falls, Ontario  
Canada
222. A. S. Kobayashi  
University of Washington  
Dept. of Mechanical Engineering  
MS FU10  
Seattle, WA 98195
223. James F. Kolbe  
Group Vice President  
Product Development and  
Engineering Services Group  
Sealed Power Corporation  
100 Terrace Plaza  
Muskegon, MI 49443
224. David M. Kotchick  
AiResearch Manufacturing Company  
2525 W. 190th Street  
Torrance, CA 90509
225. Bruce Kramer  
George Washington University  
Aerodynamic Center, Room T715  
Washington, DC 20052
226. Saunders B. Kramer  
Manager, AGT Program  
Office of Transportation Systems  
Department of Energy  
Forrestal Building CE-151  
1000 Independence Avenue  
Washington, DC 20585
227. D. M. Kreiner  
AGT101 Project Manager  
Garrett Turbine Engine Company  
111 S. 34th Street, PO Box 5217  
Phoenix, AZ 85010
228. Pieter Krijgsman  
Ceramic Design Int.  
Hold., Ltd.  
PO Box 68  
8050 AB Hattem  
The Netherlands
229. W. J. Lackey  
Georgia Tech Research  
Institute  
Energy and Materials  
Sciences Laboratory  
Georgia Institute of  
Technology  
Atlanta, GA 30332
230. Everett A. Lake  
Air Force Wright  
Aeronautical Laboratory  
AFWAL/POOS  
Wright-Patterson AFB  
OH 45433
231. Fred F. Lange  
University of California  
College of Engineering  
Santa Barbara, CA 93109
232. James Lankford  
Department of Materials  
Sciences  
Southwest Research Institute  
6220 Culebra Road  
PO Drawer 28510  
San Antonio, TX 78284
233. John G. Lanning  
Corning Glass Works  
Advanced Engine Components  
HP-BB-2  
Corning, NY 14830
234. David C. Larsen  
Corning Glass Works  
Materials Research  
Department  
Sullivan Park, FR-51  
Corning, NY 14831



235. Patrick Lauzon  
Ontario Research Foundation  
Glass and Ceramics Centre  
Materials Division  
Sheridan Park Research  
Community  
Mississauga, Ontario  
Canada L5K 1R3
236. Harry A. Lawler  
Senior Product Specialist  
Structural Ceramics Division  
Standard Oil Engineered  
Materials Company  
PO Box 1054, Bldg. 91-2  
Niagara Falls, NY 14302
237. Alan Lawley  
Drexel University  
Materials Engineering  
Philadelphia, PA 19104
238. Daniel Lee  
2850 7th Street  
Berkeley, CA 94710
239. June-Gunn Lee  
Head, Refractory Materials  
Laboratory  
Korea Advanced Institute of  
Science and Technology  
PO Box 131, Dong Dae Mun  
Seoul  
Korea
240. E. M. Lenoe  
Office of Naval Research  
Air Force Office of  
Scientific Research  
Liaison Office, Far East  
APO San Francisco, CA 96503-0110
241. Stanley R. Levine  
NASA Lewis Research Center  
21000 Brookpark Road  
Cleveland, OH 44135
242. David Lewis  
Naval Research Laboratory  
Code 6360, Materials Science  
and Technology Division  
4555 Overlook Avenue, SW  
Washington, DC 20375
243. Winston W. Liang  
Director of Program  
Development  
Amercom, Inc.  
8948 Fullbright Avenue  
Chatsworth, GA 91311
244. Bill Long  
Babcock and Wilcox  
PO Box 1260  
Lynchburg, VA 24505
245. L. A. Lott  
EG&G, Inc.  
Idaho National Engineering  
Laboratory  
PO Box 1625  
Idaho Falls, ID 83415
246. Bryan K. Luftglass  
Staff Consultant  
Chem Systems, Inc.  
303 S. Broadway  
Tarrytown, NY 10591
247. Michael J. Lynch  
General Electric Company  
Medical Systems Group  
PO Box 414, 7B-36  
Milwaukee, WI 53201
248. Vincent L. Magnotta  
Senior Principal Development  
Engineer  
Technical Diversification  
R&D Dept.  
Air Products and Chemicals,  
Inc.  
PO Box 538  
Allentown, PA 18105
249. Tai-il Mah  
Technical Manager, Ceramics  
and Composites Research  
Universal Energy Systems  
4401 Dayton-Xenia Road  
Dayton, OH 45432



250. L. Manes  
Material Scientist  
Division of Prospective  
Studies and Knowledge  
Transfer  
Commission of the European  
Communities  
Joint Research Centre  
Ispra Establishment  
1-21020 Ispra (Varese)  
Italy
251. Gerald R. Martin  
Manager, Technology  
Fleetguard, Inc.  
Cookeville, TN 38501
252. John Mason  
Vice President, Engineering  
The Garrett Corporation  
9851 Sepulveda Boulevard  
PO Box 92248  
Los Angeles, CA 90009
253. J. McCauley  
U.S. Army Materials Technology  
Laboratory  
DRXMR-MC  
Arsenal Street  
Watertown, MA 02172
254. Robert R. McDonald  
President  
Boride Products  
2879 Aero Park Drive  
Traverse City, MI 49684
255. William J. McDonough  
Department of Energy  
Office of Transportation Systems  
Forrestal Building CE-151  
1000 Independence Avenue  
Washington, DC 20585
256. Thomas D. McGee  
Iowa State University  
Department of Materials Science  
and Engineering  
Ames, IA 50011
257. Malcolm G. McLaren  
Head, Department of Ceramics  
Rutgers University  
Busch Campus  
Bowser Road, Box 909  
Piscataway, NJ 08854
258. Arthur F. McLean  
Manager, Ceramics Materials  
Department  
Ford Motor Company  
20000 Rotunda Drive  
Dearborn, MI 48121
259. Brian L. Mehosky  
Development Engineer, R&D  
Standard Oil Engineered  
Materials  
4440 Warrensville Center Rd.  
Cleveland, OH 44128
260. P. K. Mehrotra  
Kennametal, Inc.  
PO Box 639  
Greensburg, PA 15601
261. Joseph J. Meindl  
Reynolds International, Inc.  
PO Box 27002  
6603 W. Broad St.  
Richmond, VA 23261
262. D. Messier  
U.S. Army Materials  
Technology Laboratory  
DRXMR-MC  
Arsenal Street  
Watertown, MA 02172
263. Arthur G. Metcalfe  
Director  
Research Department  
Solar Turbines, Inc.  
2200 Pacific Highway  
PO Box 80966  
San Diego, CA 92138
264. Thomas N. Meyer  
Senior Technical Specialist  
Alumina, Chemicals and  
Ceramics Division  
Aluminum Company of America  
Alcoa Technical Center  
Alcoa Center, PA 15069

265. W. Miloscia  
Standard Oil Engineered  
Materials  
Research and Development  
4440 Warrensville Center Rd.  
Cleveland, OH 44128
266. Bill Moehle  
Ethyl Corporation  
451 Florida Blvd.  
Ethyl Tower  
Baton Rouge, LA 70801
267. Helen Moeller  
Babcock and Wilcox  
PO Box 11165  
Lynchburg, VA 24506
268. Thomas Morel  
Vice President  
Integral Technologies Inc.  
415 E. Plaza Drive  
Westmont, IL 60559
269. Frederick E. Moreno, President  
Turbo Energy Systems, Inc.  
350 Second Street, Suite 5  
Los Altos, CA 94022
270. Peter E. D. Morgan  
Member Technical Staff  
Structural Ceramics  
Rockwell International  
Science Center  
1049 Camino Dos Rios  
PO Box 1085  
Thousand Oaks, CA 91360
271. Solomon Musikant  
General Electric Company  
Space Systems Division  
PO Box 8555, Mail Stop U-1219  
Philadelphia, PA 19101
272. Pero Nannelli  
Pennwalt Corporation  
900 First Avenue, PO Box C  
King of Prussia, PA 19406-0018
273. Robert M. Neilson, Jr.  
EG&G Idaho, Inc.  
Materials Research  
PO Box 1625  
Idaho Falls, ID 83415
274. Dale E. Niesz  
Manager, Materials  
Department  
Battelle Columbus  
Laboratories  
505 King Avenue  
Columbus, OH 43201
275. William D. Nix  
Stanford University  
Dept. of Materials Science  
and Engineering  
Stanford, CA 94305
276. Dick Nixdorf  
Vice President  
American Matrix, Inc.  
118 Sherlake Drive  
Knoxville, TN 37922
277. Norton Company  
HPC Library/D. M. Jacques  
Goddard Road  
Northboro, MA 01532-1545
278. W. Richard Ott  
New York State College of  
Ceramics  
Alfred University  
Alfred, NY 14802
279. Muktesh Paliwal  
GTE Products Corporation  
Hawes Street  
Towanda, PA 18848
280. Hayne Palmour III  
North Carolina State  
University  
Engineering Research  
Services Division  
2158 Burlington Engineering  
Laboratories  
PO Box 5995  
Raleigh, NC 27607

281. Joseph N. Panzarino  
Norton Company  
Director, R&D, High Performance  
Ceramics  
Goddard Road  
Northboro, MA 01532-1545
282. Pellegrino Papa  
Manager, Technical and Business  
Development  
Corning Technical Products  
Division  
Corning Glass Works  
Corning, NY 14831
283. James G. Paschal  
Chemical Sales, Regional Manager  
Reynolds Metals Company  
PO Box 76154  
Atlanta, GA 30358
284. Arvid E. Pasto  
Member of Technical Staff  
Precision Materials Technology  
GTE Laboratories, Inc.  
40 Sylvan Road  
Waltham, MA 02254
285. James W. Patten  
Director, Materials Engineering  
Cummins Engine Company, Inc.  
Box 3005, Mail Code 50183  
Columbus, IN 47201
286. Robert A. Penty  
Development Engineer  
Manufacturing Technology Dept.  
Apparatus Div.  
Eastman Kodak Company  
901 Elmgrove Road  
Rochester, NY 14650
287. Gary R. Peterson  
U.S. Department of Energy  
Idaho Operations Office  
785 DOE Place  
Idaho Falls, ID 83402
288. Dan Petrak  
Babcock and Wilcox  
PO Box 1260  
Lynchburg, VA 24505
289. R. Byron Pipes  
University of Delaware  
Center for Composite  
Materials  
2001 Spencer Laboratory  
Newark, DE 19716
290. Robert C. Pohanka  
Office of Naval Research  
800 N. Quincy Street  
Code 431  
Arlington, VA 22217
291. Stephen C. Pred  
Product Manager  
ICD Group, Inc.  
641 Lexington Avenue  
New York, NY 10022
292. Karl M. Prewo  
United Technologies Corp.  
Research Center  
Silver Lane, MS 24  
East Hartford, CT 06108
293. Hubert B. Probst  
Chief Scientist, Materials  
Div., MS 49-1  
NASA Lewis Research Center  
21000 Brookpark Road  
Cleveland, OH 44135
294. Carr Lane Quackenbush  
Norton Company  
High Performance Ceramics  
Goddard Road  
Northboro, MA 01532-1545
295. George Quinn  
U.S. Army Materials  
Technology Laboratory  
Arsenal Street  
Watertown, MA 02172
296. Dennis T. Quinto  
Kennametal, Inc.  
Phillip M. McKenna  
Laboratory  
PO Box 639  
Greensburg, PA 15601



297. S. Venkat Raman  
Manager, New Technology  
Marketing  
Contract Research Dept.  
Air Products and Chemicals, Inc.  
PO Box 538  
Allentown, PA 18105
298. Dennis Readey  
Department Chairman  
Ceramic Engineering  
Ohio State University  
2041 College Road  
Columbus, OH 43210
299. Robert R. Reeber  
U.S. Army Research Office  
PO Box 12211  
Research Triangle Park, NC 27709
300. K. L. Reifsnider  
Virginia Polytechnic Institute  
and State University  
Department of Engineering  
Science and Mechanics  
Blacksburg, VA 24061
301. Paul Rempes  
Champion Spark Plug Company  
Ceramic Division  
20000 Conner Avenue  
Detroit, MI 48234
302. T. M. Resetar  
U.S. Army Materials Technology  
Laboratory  
DRXMR-MC  
Arsenal Street  
Watertown, MA 02472
303. K. T. Rhee  
Rutgers University  
College of Engineering  
PO Box 909  
Piscataway, NJ 08854
304. Roy W. Rice  
W. R. Grace and Company  
7379 Route 32  
Columbus, MD 21044
305. David W. Richerson  
Ceramatec, Inc.  
163 West 1700 South  
Salt Lake City, UT 84115
306. Paul Rieth  
Ferro Corporation  
661 Willet Road  
Buffalo, NY 14218
307. Michael A. Rigdon  
Institute for Defense  
Analyses  
1801 Beauregard Street  
Alexandria, VA 22311
308. John E. Ritter, Jr.  
University of Massachusetts  
Mechanical Engineering  
Department  
Amherst, MA 01003
309. Giulio A. Rossi  
Norton Company  
High Performance Ceramics  
Goddard Road  
Northboro, MA 01532-1545
310. Barry R. Rossing  
Aluminum Company of America  
Alcoa Technical Center  
Alcoa Center, PA 15069
311. David J. Rowcliffe  
SRI International  
333 Ravenswood Avenue  
Menlo Park, CA 94025
312. Donald W. Roy  
Manager, Carbide and  
Optical Material  
Research and Development  
Coors Porcelain Company  
Golden, CO 80401
313. Bruce Rubinger  
Gobal  
50 Milk Street, 15th Floor  
Boston, MA 02109
314. Robert Ruh  
Air Force Wright  
Aeronautical Laboratory  
Materials Laboratory,  
AFWAL/MLLM  
Metals and Ceramics  
Division  
Wright-Patterson AFB,  
OH 45433

315. Robert J. Russell, Sr.  
Divisional Vice President  
Technology and Planning  
High Performance Ceramics  
Norton Company  
Goddard Street  
Northboro, MA 01532-1545
316. George P. Safoi  
Westinghouse Electric  
Corporation  
R&D Center  
Pittsburgh, PA 15235
317. J. Sankar  
North Carolina Agricultural and  
Technical State University  
Department of Mechanical  
Engineering  
Greensboro, NC 27411
318. Maxine Savitz  
Assistant to Vice President,  
Engineering  
The Garrett Corporation  
PO Box 92248  
Los Angeles, CA 90009
319. Richard Schapery  
Texas A&M University  
Civil Engineering Department  
College Station, TX 77843
320. J. L. Schienle  
Garrett Turbine Engine Company  
111 S. 34th Street  
Phoenix, AZ 85034
321. L. J. Schioler  
Aerojet Tech Systems Company  
PO Box 13222  
Dept. 9990, Bldg. 2001  
Sacramento, CA 95813
322. Arnie Schneck  
Deere and Company  
PO Box 128  
Wood-Ridge, NJ 07075
323. Matthew Schreiner  
Project Manager  
Ceramic Materials  
and Components  
Gas Research Institute  
8600 W. Bryn Mawr Avenue  
Chicago, IL 60631
324. John Schuldies  
Industrial Ceramic  
Technology, Inc.  
141 Enterprise Drive  
Ann Arbor, MI 48103
- 325-345. R. B. Schulz, Manager  
Advanced Materials  
Development  
Office of Transportation  
Systems  
Department of Energy  
Forrestal Building CE-151  
1000 Independence Avenue  
Washington, DC 20585
346. Wesley J. C. Schuster,  
President  
Thermo Electron Corporation  
Metals Division  
115 Eames Street  
PO Box 340  
Wilmington, MA 01887
347. Murray A. Schwartz  
Bureau of Mines  
2401 Eye Street, NW  
Washington, DC 20241
348. Douglas B. Schwarz  
Dow Chemical U.S.A.  
52 Building  
Midland, MI 48674
349. Thomas M. Sebestyen  
U.S. Army Tank-Automotive  
Command  
AMSTA-RGRT  
Warren, MI 48397-5000
350. Brian Seegmiller  
Senior Development Engineer  
Coors Porcelain Company  
17750 North 32 Street  
Golden, CO 80401



351. S. G. Seshadri  
Research Associate  
Standard Oil Engineered Materials  
Company  
Niagara Falls R&D Center  
PO Box 832  
Niagara Falls, NY 14302
352. Peter T. B. Shaffer  
Executive Vice President  
Advanced Refractory Technologies,  
Inc.  
699 Hertel Avenue  
Buffalo, NY 14207
353. Maurice E. Shank  
Director, Engineering Technology  
Assessment  
United Technologies Corporation  
Pratt and Whitney Engrg. Div.  
MS 162-31  
East Hartford, CT 06108
354. Laurel M. Sheppard  
Associate Editor  
Advanced Materials and Processes  
Route 87  
Metals Park, OH 44073
355. Dinesh K. Shetty  
The University of Utah  
Dept. of Materials Science and  
Engineering  
Salt Lake City, UT 84112
356. Jack D. Sibold  
Coors Porcelain Company  
17750 North 32 Street  
Golden, CO 80401
357. Neal Sigmon  
Appropriations Committee  
Subcommittee on Interior and  
Related Events  
U.S. House of Representatives  
Rayburn Building, Room B308  
Washington, DC 20515
358. Richard Silberglitt  
DHR, Inc.  
6849 Old Dominion Drive  
Suite 228  
McLean, VA 22101
359. Maurice J. Sinnott  
University of Michigan  
Chemical and Metallurgical  
Engineering  
438 W. Engineering Building  
Ann Arbor, MI 48109
360. S. R. Skaggs  
Los Alamos National  
Laboratory  
PO Box 1663  
MS F-682, Program Office  
Los Alamos, NM 87545
361. J. Thomas Smith  
Director, Precision  
Materials Tech.  
GTE Laboratories, Inc.  
40 Sylvan Road  
Waltham, MA 02254
362. Jay R. Smyth  
Senior Development Specialist  
Garrett Turbine Engine  
Company  
PO Box 5217  
MS 93-172/1302-2K  
Phoenix, AZ 85010
363. Rafal Sobotowski  
Standard Oil Engineered  
Materials  
Research and Development  
3092 Broadway Avenue  
Cleveland, OH 44115
364. Boyd W. Sorenson  
E. I. DuPont de Nemours  
& Company  
Textile Fibers Dept. -  
E304C123  
Wilmington, DE 19898
365. Richard M. Spriggs  
National Materials Advisory  
Board  
National Research Council  
2101 Constitution Avenue  
Washington, DC 20418



366. John D. Spuller  
Division Manager  
Government Products  
Deere and Company  
John Deere Road  
Moline, IL 61265
367. M. Srinivasan  
Standard Oil Engineered  
Materials  
Niagara Falls R&D Center  
PO Box 832  
Niagara Falls, NY 14302
368. Gordon L. Starr  
Manager, Metallic/Ceramic  
Materials Dept.  
Cummins Engine Company, Inc.  
Box 3005, Mail Code 50183  
Columbus, IN 47202-3005
369. Harold L. Stocker  
Manager, Low Heat Rejection  
Program  
General Motors Corporation  
Allison Gas Turbine Operations  
PO Box 420, T-23  
Indianapolis, IN 46206-0420
370. Roger Storm  
Director, Niagara Falls R&D  
Center  
Standard Oil Engineered Materials  
Company  
PO Box 832  
Niagara Falls, NY 14302
371. E. E. Strain  
Program Manager AGT-101  
Garrett Turbine Engine Company  
111 S. 34th Street  
PO Box 5217, Mail Stop 301-2N  
Phoenix, AZ 85010
372. Thomas N. Strom  
NASA Lewis Research Center  
21000 Brookpark Road, 77-6  
Cleveland, OH 44135
373. Richard Suddeth  
Boeing Motor Airplane Company  
PO Box 7730, MS K-76-67  
Wichita, KS 67277
374. Paul Sutor  
Midwest Research Institute  
425 Volker Blvd.  
Kansas City, MO 64116
375. J. J. Swab  
U.S. Army Materials  
Technology Laboratory  
Ceramics Research Division  
Arsenal Street  
Watertown, MA 02172
376. Lewis Swank  
Ford Motor Company  
PO Box 2053  
Building SRL, Room E3172  
Dearborn, MI 48121
377. Anthony C. Taylor  
Staff Director,  
Subcommittee on  
Transportation, Aviation,  
& Materials  
Committee on Science and  
Technology  
U.S. House of Representative  
Rayburn Building, Room 2321  
Washington, DC 20515
378. W. H. Thielbahr  
Chief, Energy Programs  
Branch  
Department of Energy  
Idaho Operations Office  
550 2nd Street  
Idaho Falls, ID 83401
379. John K. Tien  
Director of Center for  
Strategic Materials  
Columbia University  
1137 SW Mudd Building  
New York, NY 10027
380. T. Y. Tien  
University of Michigan  
Materials and Metallurgical  
Engineering  
Dow Building  
Ann Arbor, MI 48109-2136

381. Julian M. Tishkoff  
Air Force Office of Scientific  
Research  
Directorate of Aerospace Sciences  
Bolling AFB  
Washington, DC 20332
382. Louis E. Toth  
National Science Foundation  
Division of Materials Research  
1800 G Street, NW  
Washington, DC 20550
383. Richard E. Tressler  
Chairman, Ceramic Science and  
Engineering Department  
The Pennsylvania State University  
201 Steidle Building  
University Park, PA 16802
384. Donald R. Uhlmann  
Professor, Ceramics and Polymers  
Department of Materials Science  
and Engineering  
Massachusetts Institute of  
Technology  
Cambridge, MA 02139
385. Edward C. van Reuth  
President  
Technology Strategies, Inc.  
10722 Shingle Oak Court  
Burke, VA 22015
386. Thomas Vasilos  
Manager, Electro Chemical  
Facility  
Avco Corporation  
201 Towell Street  
Wilmington, MA 01887
387. V. Venkateswaran  
Standard Oil Engineered Materials  
Company  
PO Box 832  
Niagara Falls, NY 14302
388. John B. Wachtman, Jr.  
Director, Center for Ceramics  
Research  
Rutgers University  
PO Box 909  
Piscataway, NJ 08854
389. Richard B. Wallace  
Manager, Government  
Research and Development  
Programs  
General Motors Corporation  
Detroit Diesel Allison  
Division  
36880 Ecorse Road  
Romulus, MI 48174
390. Harlan L. Watson  
Subcommittee on Energy  
Research and Production  
U.S. House of Representatives  
Committee on Science and  
Technology  
Rayburn Building  
Suite 2321  
Washington, DC 20515
391. Steven G. Wax  
Department of Defense  
Advanced Research Projects  
Agency  
Materials Science Division  
1400 Wilson Boulevard  
Arlington, VA 22209
392. Albert R. C. Westwood  
Corporate Director, R&D  
Martin Marietta Laboratories  
1450 South Rolling Road  
Baltimore, MD 21227
393. Thomas J. Whalen  
Principal Research Scientist  
Ford Motor Company  
Scientific Lab, Room 2023  
Dearborn, MI 48121
394. Sheldon M. Wiederhorn  
U.S. Department of Commerce  
National Bureau of Standards  
Inorganic Materials Division  
Mechanical Properties Group  
Gaithersburg, MD 20899
395. James C. Williams  
Dean, Carnegie Institute of  
Technology  
Carnegie-Mellon University  
Schenley Park  
Pittsburgh, PA 15213



396. Roger R. Wills  
Manager, Advanced Ceramic  
Components  
TRW, Inc.  
Automotive Worldwide Sector,  
Valve Division  
Cleveland, OH 44110
397. J. M. Wimmer  
Supervisor, Nonmetallic Materials  
Group  
Garrett Turbine Engine Company  
111 S. 34th Street, PO Box 5217  
Phoenix, AZ 85010
398. David Wirth  
Vice President, Technical  
Operations & Engineering  
Coors Porcelain Company  
17750 North 32 Street  
Golden, CO 80401
399. Thomas J. Wissing  
Manager, Government Contract  
Administration  
Eaton Corporation  
Engineering & Research Center  
26201 Northwestern Highway  
PO Box 766  
Southfield, MI 48037
400. George W. Wolter  
Howmet Turbine Components  
Corporation  
Technical Center  
699 Benston Road  
Whitehall, MI 49461
401. James C. Wood  
NASA Lewis Research Center  
21000 Brookpark Road  
MS 500-210  
Cleveland, OH 44135
402. Hun C. Yeh  
Ceramic Supervisor  
AiResearch Casting Company  
19800 Van Ness Avenue  
Torrance, CA 90509
403. Thomas M. Yonushonis  
Cummins Engine Company, Inc  
Box 3005, Mail Code 50183  
Columbus, IN 47202-3005
404. Don Zabierek  
Air Force Wright  
Aeronautical Laboratory  
AFWAL/POTC  
Wright-Patterson AFB,  
OH 45433
405. Charles Zeh  
Department of Energy  
Morgantown Energy  
Technology Center  
PO Box 880  
Morgantown, WV 26505
406. Klaus M. Zwilsky  
Executive Director  
National Materials  
Advisory Board  
National Research Council  
2101 Constitution Avenue  
Washington, DC 20418
407. Department of Energy  
Oak Ridge Operations Office  
Assistant Manager for  
Energy Research and  
Development  
PO Box E  
Oak Ridge, TN 37831
- 408-437. Department of Energy  
Technical Information  
Center  
Office of Information  
Services  
PO Box 62  
Oak Ridge, TN 37831
- For distribution by  
microfiche as shown in  
DOE/TIC-4500,  
Distribution Category UC-95.